Ultraviolet Detectors for Solar Observations on the SOHO Spacecraft

Alice Antonia Breeveld

Mullard Space Science Laboratory

Department of Space and Climate Physics

University College London

A thesis submitted to the University of London

for the degree of Doctor of Philosophy

November, 1995

ABSTRACT

This thesis describes the complete development of four ultraviolet detectors for use at grazing incidence angles in a solar science instrument. The instrument is one of twelve on board the Solar Heliospheric Observatory (SOHO), a satellite to be launched in November 1995 with a minimum design lifetime of two years. The accurate measurement of abundances and small scale motions in the sun's atmosphere, requires that the detectors combine high speed and resolution with the low power and mass compatible with space flight.

These detectors represent a novel use of microchannel plates (MCPs), in the detection of extreme ultraviolet at grazing angles of incidence and at high count rates. Furthermore, this is the first time a SPAN anode will have been used on a flight instrument.

In order to get the maximum science out of the mission, it is crucial that the instrument be fully calibrated. For this reason emphasis is placed, in the thesis, on dividing the detector into its constituent parts and on understanding the various processes involved, from the arrival of the photon to the output spectrum. Computer modelling as well as experimentation is used in the investigation.

Starting with an introduction to SOHO in the context of Solar Physics, a description of the instrument reveals the requirements of the detectors. As one of the key parts of the detector, MCPs are described and results are presented from experiments investigating their behaviour. The thesis then describes how the SPAN readout is made and used, and how it is configured to suit the MCP set up.

Finally, the flight design, building and testing is described, followed by results from the flight calibration test and predictions of problems and successes in the detectors' mission.

In summary, the detectors meet the requirements of resolution (<50 μm FWHM), speed (>10^5 random), background count rate (<0.2 c s^{-1} cm^{-2}) and integral non-linearity (<0.03%). They fulfil the expected quantum efficiency (3–12%). However, limitations from using 8-bit digitisation with the SPAN anode, leads to a high level of differential non-linearity (27% r.m.s.). There are also problems with count rate dependence and long term gain depression in the MCPs. The sources of the problems are analysed and modelled where practicable, so that they can be minimised for flight operations.

‘ο βιος βραχυς, ‘η δε τεχνη μακρη,
‘ο δε καιροσ ’οξυσ,
‘η δε πειρα σφαλερη, ‘η δε κρισισ χαλεπη.

Hippocrates, 5th c. B.C.

Life is short, but the art is long,
the opportunity fleeting,
the experiment perilous, the judgement difficult

TABLE OF CONTENTS

LIST OF ABBREVIATIONS

ADC	Analogue to Digital Converter
AU	Astronomical Unit (mean distance from earth to sun)
AXAF	Advanced X-ray Astrophysics Facility
BEARS	Berkeley EUV Airglow Rocket Spectrometer
BESSY	Berlin Electron Storage ring
$c\ s^{-1}$	counts per second
CCD	Charge Coupled Device
CDGD	Count rate Dependant Gain Depression
CDHS	Command and Data Handling System
CDS	Coronal Diagnostic Spectrometer
CEM	Channel Electron Multiplier
CHASE	Coronal Helium Abundance Spacelab Experiment
CODACON	CODed Anode CONverter
DAC	Digital to Analogue Converter
DM	Development Model
DNL	Differential Non-Linearity
EGSE	Experiment Ground Support Equipment
EM	Engineering Model
EMC	ElectroMagnetic Compatibility
EPROM	Erasable, Programmable, Read Only Memory
EPS	Experiment Power Supply
ESA	European Space Agency
EUV	Extreme UltraViolet
EUVE	Extreme UltraViolet Explorer
EXOSAT	European X-ray Observatory SATellite
FET	Field Effect Transistor
FIFO	First In First Out buffer
FITS	Flexible Image Transfer System
FM	Flight Model
FS	Flight Spare
FUV	Far UltraViolet

FWHM	Full Width at Half Maximum
GIS	Grazing Incidence Spectrometer
GSPC	Gas Scintillation Proportional Counter
HRC	High Resolution Camera
HRI	High Resolution Imager
HV	High Voltage
IDL	Interactive Data Language (trade mark)
INL	Integral Non-Linearity
LLD	Lower Level Discriminator
LRGD	Long Range Gain Depression
LSB	Least Significant Bit
LTGD	Long Term Gain Depression
LUT	Look Up Table
MAMA	MultiAnode Microchannel plate Array
MCP	MicroChannel Plate
MHD	MagnetoHydroDynamic
MOS	Metal-Oxide-Silicon
MSB	Most Significant Bit
MSSL	Mullard Space Science Laboratory
MTF	Modulation Transfer Function
NIM	Nuclear Instrumentation Module
NIS	Normal Incidence Spectrometer
OM	Optics Model
OPS	Offset Pointing System
PAPA	Precision Analog Photon Address
PC	Personal Computer
PHD	Pulse Height Distribution
PMT	PhotoMultiplier Tube
PSF	Point Spread Function
PSPC	Position Sensitive Proportional Counter
PTB	Physikalisch-Technische Bundesanstalt
QE	Quantum Efficiency
QM	Qualification Model
RAL	Rutherford Appleton Laboratory
RAM	Random Access Memory
RANICON	Resisitive ANode Image CONverter

RC	Rowland Circle.
RM	Research Model
r.m.s.	route mean square
ROSAT	Röntgen SATellite
SDDA	Science Data Display Adapter
SM	Structural Model
SOHO	SOlar and Heliospheric Observatory
SPAN	SPiral ANode
SPD	Self-scanned Photodiode Array
STM	Structural Thermal Model
SUMER	Solar UV Measurement of Emitted Radiation
UCLAN	University of Central LANcashire
ULD	Upper Level Discriminator
UV	UltraViolet
VDS	Viewfinder Detector Subsystem
VUV	Vacuum UltraViolet
WFC	Wide Field Camera
WSA	Wedge and Strip Anode
XMM	X-ray Multi Mirror
ZOD	Zero Order Detector

LIST OF ILLUSTRATIONS

LIST OF TABLES

CHAPTER 1.

OBSERVING THE SUN IN ULTRAVIOLET LIGHT

1.1. INTRODUCTION

The Solar and Heliospheric Observatory (SOHO) is a European Space Agency (ESA) project scheduled for launch in 1995. Together with the multisatellite mission CLUSTER, SOHO forms the first cornerstone of ESA's Horizon 2000 programme. One of the twelve instruments on SOHO is the ultraviolet Coronal Diagnostic Spectrometer (CDS) which itself involves two spectrometers called the Grazing Incidence Spectrometer (GIS) and the Normal Incidence Spectrometer (NIS).

In this thesis my work on the design, construction, testing, integration and finally the calibration of the grazing incidence detectors for the GIS are described. The experiments, calculations and computer models presented in Chapters 2–8 are entirely my own except where explicitly referenced to other people. In Chapter 7, Table 15 details my particular work.

The thesis starts with a comprehensive review chapter, introducing SOHO in the context of solar physics. A broad description of CDS reveals how the detectors were selected and how their scientific requirements were defined. A review of broadly similar detectors is also included in this chapter.

The GIS and particularly the detectors are explained in more detail in Chapter 2, showing how I established the detector requirements. Chapters 3 to 6 break down the detector, conceptually, into its constituent parts, describing how I developed it and my experiments to establish its performance. They include background work which contributed to the design and expected performance.

Chapter 3 deals with the MCPs, including background information and theoretical models. My choice of MCP configuration for the GIS is explained, supported by results from my experiments. In Chapter 4, I present my results from further experiments investigating the behaviour of MCPs in a grazing incidence configuration with extreme ultraviolet (EUV) light, at a range of count rates. Chapter 5 explores the theory of the detector readout, including theoretical and computer modelling. Chapter 6 describes

how I made the readouts and used them with the MCPs. It also gives the results of my characterisation of the flight model detectors.

Chapter 7, in addition to the chronology, describes the detectors in the context of the space mission and flight operation. Finally, in Chapter 8, I present my analysis of results from the flight model calibration test.

1.2. SOHO AND THE SUN

SOHO is basically a 'quiet sun' mission, aimed at studying the physics of the typical sun. The main goals are to discover the nature of the solar corona, the internal structure of the sun and the forces which accelerate the solar wind. The twelve instruments can be grouped according to these three goals. Three instruments will use helioseismology to study the internal structure of the sun. Coronagraphs in white light and UV will image the corona, while EUV imaging and spectroscopy will study the structure and evolution of the low corona. Particle detectors will monitor the solar wind directly. Anisotropies in the solar wind will be measured through the imaging of the hydrogen Lyman-α line.

The CDS will use EUV spectroscopy to enable the determination of some of the physical parameters in the corona. Meanwhile SUMER (Solar UV Measurement of Emitted Radiation) will be used to study the fine structures in the chromosphere and transition region, recording flows and wave motions.

The launch of SOHO will be on an Atlas Centaur II AS rocket from the Kennedy Space Center in Florida. After a four month cruise phase it will reach the L1 Lagrangian point, 1.5×10^6 km away. At this point the gravitational pull of the sun and the earth balances the centripetal force required for the satellite to orbit the sun synchronously with the earth. It will be injected into a halo orbit around the L1 point, with an orbital period of 180 days. The advantage of this position is that it will have an uninterrupted view of the sun, pointing with an accuracy of 10 arcseconds. Being outside the magnetosphere, it will continuously sample the solar wind and particles.

The mission is planned to last for 2 years, extendable to 6. Communication with the spacecraft will take place via the Deep Space Network, for three short (1.6 hour) and one long (8 hour) contact per day.

1.2.1. Corona

In visible light the corona can be seen during eclipses or using coronagraphs. It appears as tenuous streamers and plumes extending out from the sun's disk. The white light corona is photospheric light scattered into the line of sight by electrons and dust grains. The electron scattering, known as the K-corona, dominates for the first 700,000 km or 2½ Solar radii, varying by up to 50% with the solar cycle. The electron density de-

creases slowly with distance from the sun. Scattering from a disk of dust particles—tiny solid grains a few microns in diameter—extends to many Solar radii. This is the F-corona, which is the source of Zodiacal light. Its emission has been detected by spacecraft out to 3 AU. Because of the scattering, the corona is polarized parallel to the solar limb.

Spectroscopy of the visible corona reveals the presence of the green line of Fe XIV at 530.3 nm, and the red line of Fe X at 637.5 nm. Fe XIV has only 13 of the 26 electrons and therefore produces an aluminium-like iso-electronic line sequence. It has two resonance lines, caused by transitions between the 4d and two closely spaced 3p states, in the X-ray region at 5.90 and 5.96 nm. The green line is a forbidden line from transitions between the two 3p states. The fact that the red and green lines are present means that the temperatures are very high (~10^6 K) and the presence of a forbidden line implies that the electron density is low (~10^{14} electrons m^{-3}). In active regions above sunspots, the yellow line of Ca XV at 569.4 nm is observed, implying a temperature of 4×10^6 K. Figure 1 shows how the mean temperature of the sun's atmosphere varies with height above the photosphere.

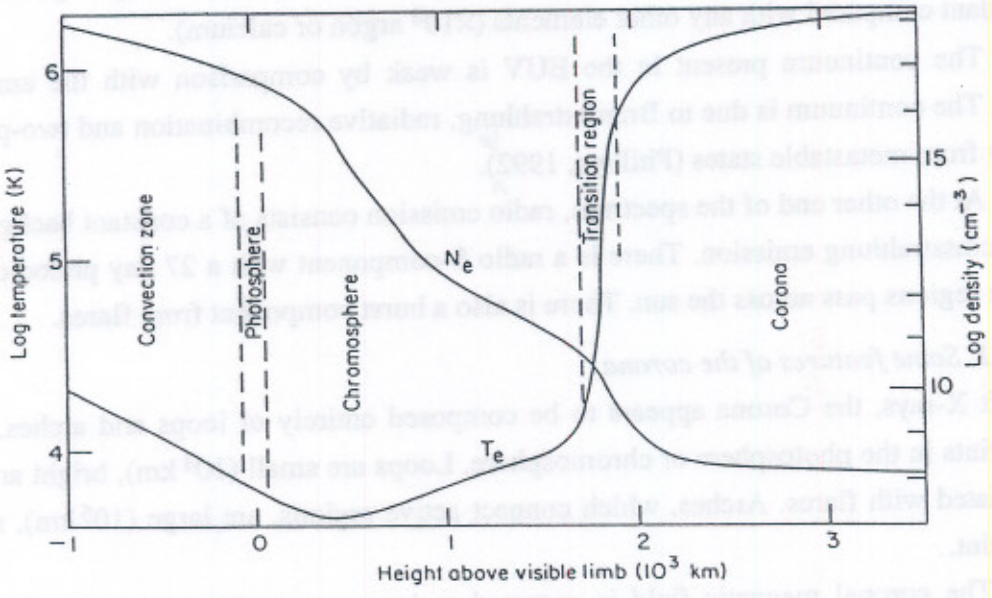

Figure 1. The variation of temperature and density in the outer layers of the sun. The mean values plotted vs. height from the limb of the sun (Gabriel and Mason, 1982).

The fact that the corona is at about 2×10^6 K, and that this figure is even higher in active regions, means that the gas, a large proportion of which is hydrogen, is a highly ionised plasma, emitting X rays, EUV and radio radiation. Whilst it is not possible to

see the visible corona against the background of the photosphere, X-rays, EUV and radio radiation are not strongly emitted by the photosphere. Observations of the corona in these wavelength bands can therefore be made on the disc as well as off limb.

The X-ray band consists of continuum and emission lines from highly stripped ions, *e.g.* the two Al-like Fe XIV resonance lines mentioned above, as well as the He-like C V, O VII, Ne IX and H-like C VI and O VIII. The continuum radiation is caused by recombination of electrons with the bare nuclei of carbon or oxygen. Bremsstrahlung radiation also contributes. The continuum peak is at 4 nm.

The EUV region is normally considered to be from 10–100 nm. In this wavelength band several Li-like ions can be detected *e.g.* Mg X at 61.0 and 62.5 nm and Si XII at 49.9 and 52.1 nm. In addition the 3p-3d transition is observed from the ions Fe X to Fe XIV. Lithium-like ions have 3 electrons with the outer in the $n=2$ orbit; the outer electron can be excited from the 2s to the 2p level and de-excited back to 2s giving a doublet separated by the spin energy.

There is a strong neutral hydrogen Ly-α line, caused by photo-ionisation from the $n=1$ to the $n=2$ level by photons from the chromosphere, at 121.6 nm. Although only 1 in 10^6 atoms are in the neutral state at any one time at 2×10^6 K, hydrogen is very abundant compared with any other elements ($\times10^6$ argon or calcium).

The continuum present in the EUV is weak by comparison with the emission lines. The continuum is due to Bremsstrahlung, radiative recombination and two-photon decay from metastable states (Phillips, 1992).

At the other end of the spectrum, radio emission consists of a constant background of Bremsstrahlung emission. There is a radio S-component with a 27 day periodicity as active regions pass across the sun. There is also a burst component from flares.

1.2.1.1. Some features of the corona

In soft X-rays, the Corona appears to be composed entirely of loops and arches, with footprints in the photosphere or chromosphere. Loops are small (10^4 km), bright and are associated with flares. Arches, which connect active regions, are large (10^5 km), stable and faint.

The coronal magnetic field is assumed to be an extension of the photospheric field. Because of the high electrical conductivity, the field is "frozen" into the plasma. Field lines therefore follow the shape of the arches (see Figure 2). When the electrons, spiralling round the field lines, reach the footprint of the arch where the densities are higher, they tend to collide and dissipate energy. By this means, heat is taken from the upper loop to the chromosphere.

Spicules originate in the chromosphere. They are very numerous, fine, jet-like structures, a few hundred kilometres in diameter. They ascend into the corona with velocities of 30 km s^{-1}, to altitudes of 9000 km. Each one lasts only 15 minutes or so. Spicules appear at the cell boundaries of a network, which is comprised of the tops of the convection cells in the body of the sun.

X-ray bright points in the corona can appear anywhere on the surface. These are regions of magnetic reconnection. Usually about 40 are visible per day, the smallest are less than 7000 km in diameter and have a temperature of 2.5×10^6 K.

Prominences (called filaments when seen against the disc) consist of very dense, cool tongues of material in the corona emitting a visible Hα spectrum typical of the chromosphere. The material is at a temperature of only 10,000 K, but is surrounded by the much hotter corona. They therefore look like thin dark filaments on the disk, extending to about 50,000 km above the photosphere. They can appear anywhere on the sun and last typically for a few months, after which time they may become unstable and 'erupt': ascending rapidly (up to a few km s^{-1}) and finally disappearing.

Flares, which are rapid brightenings in the corona and chromosphere, appear near sunspot regions. Sunspots appear as cool dark areas in the photosphere with extremely strong magnetic fields (~3 kG). Active regions are areas of moderate field strength (~300 G) in the chromosphere above sunspots. Sunspots often occur in pairs, with numbers varying with the eleven year solar cycle. Fibrils are dark elongated (~20,000 km long) features in the area of sunspots, often arranged in a radial pattern, following magnetic field lines, centred on the sunspot. They are low lying and do not therefore appear above the limb. Mottles are smaller features than fibrils and appear in quiet-sun areas.

Coronal holes are defined by the absence of X-ray emission. They are cool regions in the corona. Up to 20% of the hemisphere can be covered with coronal holes when they are most prevalent *i.e.* a few years before solar minimum. The holes start small then expand until they meet the coronal hole at the pole of the same polarity. They can be enormous, spreading to the pole from the other side of the equator. Coronal holes have magnetic field lines open to space and are the source of high-speed particle streams.

Ulysses, a joint ESA and NASA mission, launched in 1990, confirmed the presence of a coronal hole at the sun south pole in summer 1994 during its orbit over the polar regions, in an orbit inclined 80° to the sun's equator (Marsden, 1995). This was near the time of a minimum in the solar activity cycle. At latitudes above 40°, Ulysses became totally immersed in a fast solar wind from the polar coronal hole flowing continuously at an average speed of 750 km s^{-1}. It was found to originate in the chromosphere at a lower temperature than a slower wind, which emerges from the corona in a

streamer belt that encircles the sun at the magnetic equator. Both fast and slow winds are highly directional and distinctly separated, despite being created at different heights in the atmosphere.

Coronal mass ejections, gas bubbles of 10^{13} kg, are present in the fast wind. The bubbles are projected into space by magnetic forces. They travel at the same speed as the fast wind but expand rapidly, sending shock waves towards and away from the sun.

The magnetic field was measured by Ulysses as having no concentration at the pole, unlike the expected dipole structure, suggesting that the sun's magnetic field is not carried out by the solar wind.

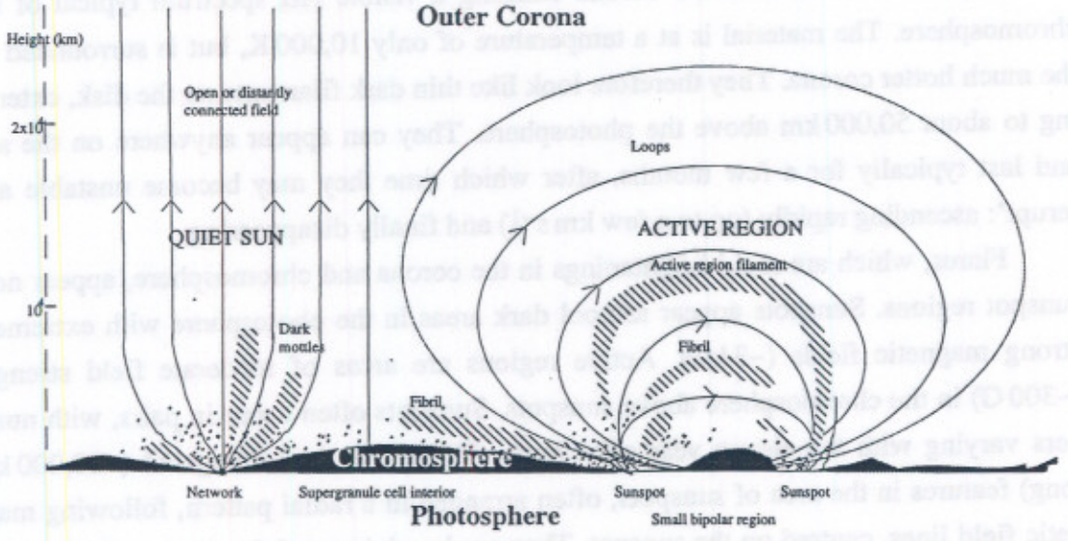

Figure 2. Diagram of the sun's atmosphere after Durrant (1988). On the left, the network feature has field lines returning to the surface at a distant point or extending out into the solar wind. On the right two sunspots form a small bipolar region with an active region above. The hatched areas represent areas where the high temperature chromospheric material is extending into the corona. The dots indicate the position of material at transition region temperatures.

1.2.1.2. Heating and cooling the corona

More is known about cooling the corona than heating it. Several cooling mechanisms are already understood. Some loss of energy from the corona can readily be seen in the form of X-ray radiation into space. Meanwhile, plasma in closed loops, in the quiet corona, transports energy back to the chromosphere via the free electrons and gas. If all the sun were covered in quiet corona, the total lost from the solar surface by this mechanism would be ~300 W m^{-2}. Coronal holes lead to loss of 1000–3000 W m^{-2} into space via the solar wind.

It is not yet known how the energy gets into the corona from the photosphere. Waves generated at the top of the turbulent convection cells may propagate into the corona before dumping their energy. Magnetic field line reconnection may give rise to the many small nano-flares, observed to last just a few seconds, and may provide enough energy to heat the corona. In slowly evolving active regions, twisting of the magnetic flux tubes could continuously dissipate energy (Patchett *et al.*, 1990).

Alfvén waves are set up when a magnetic field line is displaced sideways and then released. Tension restores them to the original shape, setting up an oscillation. If there is perfect electrical conductivity, the field lines are frozen into, and oscillate with, the ionised gas. Alfvén waves at 60 km s^{-1} from below the photosphere can be converted to fast and slow magnetohydrodynamic (MHD) waves in the corona leading to small and large loops. The conversion leads to energy dissipation. Alternatively Alfvén waves could provide energy for the solar wind.

Acoustic waves are a source of heating but are not thought to be sufficient. Jets at 400 km s^{-1} from the transition region could give rise to MHD shocks, heating the corona at 60 W m^{-2}.

H I Ly-α	121.5 nm	20,000 K
C IV	155 nm	110,000 K
O VI	103.2 and 103.8 nm	320,000 K
Ne VII	46.5 nm	500,000 K
Si XII	49.9 and 52.1 nm	2×10^6 K

Table 1. Some temperature dependent lines in the EUV.
Numbers taken from Phillips (1992).

1.2.2. Transition Region

The transition region lies between the chromosphere and the corona where the temperature rises from 2×10^4 K to 2×10^6 K. Table 1 gives some temperature dependent lines observable from the transition region which starts at about 2500 km above the photosphere. The corona is reached at about 5000 km. The EUV is particularly suitable for viewing the transition region. Below 140 nm the continuum fades out, leaving emission lines. As with the corona, the Li-like ions are present (*e.g.* C IV, O VI and Si XII in Table 1), as well as many Fe ions. The Lyman continuum edge, formed by recombination of free electrons with protons to form neutral hydrogen, is at 91.2 nm and extends to shorter wavelengths.

Thus by looking at radiation of 10–160 nm, the whole range of temperatures may be studied (see also Figure 3). For instance, imaging the cool transition region shows the

network of supergranules, on the scale of 20,000 km. At the boundaries the magnetic field lines are tightly bound together. The network is steadily less well defined as the temperature increases and is not traceable in the hot corona where the magnetic field lines spread out to form a canopy.

From the EUV line intensities, it is possible to work out the number densities of the elements if the probabilities of excitation and de-excitation are known for the relevant temperatures.

From the line profiles, it is possible to measure Doppler shifts from mass motions revealing information about energy transport in the transition region *i.e.* the random velocities due to the gas turbulence, as well as the jets (400 km s^{-1}) and 'turbulent events' (3000 km at 250 km s^{-1}). At a rate of about 20 per second all over the sun, jets could be responsible for heating the corona. Alternatively, even smaller structures (<100 km), which have not been properly resolved by earlier research, may be responsible.

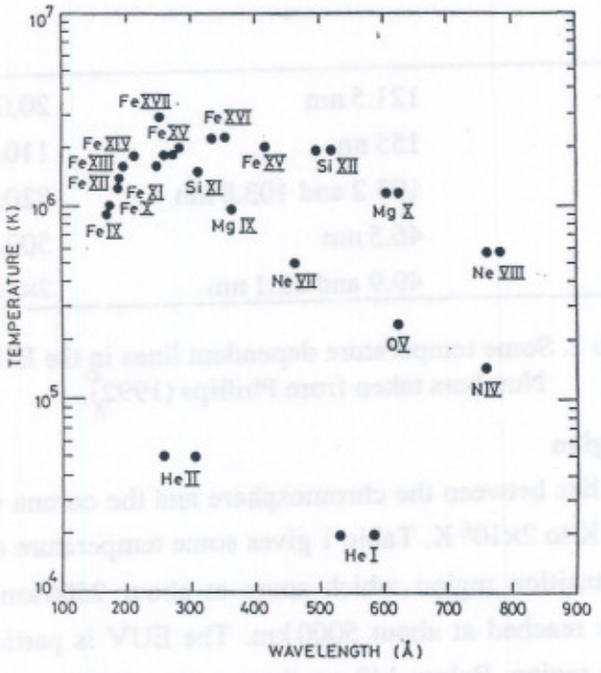

Figure 3. The temperature dependence of some strong EUV lines (Patchett *et al.*, 1989) in the range 10–90 nm.

1.3. THE CORONAL DIAGNOSTIC SPECTROMETER

The CDS is designed to concentrate on the questions of coronal heating and the mechanisms for the acceleration of the solar wind. These questions can only be

addressed by studying the solar EUV, which is only possible from above the earth's atmosphere. Few studies have been made in this region of the spectrum.

Observations began in 1946 with a photograph of a UV spectrum taken from a V2 rocket flight. By the 1960s, grazing incidence telescopes were developed for rocket flights, allowing the EUV sun to be imaged. Several of the OSO series of rockets between 1962 and 1972 carried EUV instruments. The NASA Skylab missions (SO55 and SO82A), flown in 1973/4, carried EUV spectrometers, as well as an imaging UV instrument, which showed the network structure in the chromosphere and transition region. The Space Shuttle was used for a week long Spacelab 2 mission in 1985, which included a spectrometer (CHASE), designed primarily to measure those spectral lines in the EUV needed to calculate the coronal helium abundance. Four EUV rockets, MSSTA, NIXT, LASP and SERTS, flew between 1988 and 1993. Of all these instruments, only OSO VII (1972), CHASE and SERTS (1989,91,93) extended to wavelength regions below 30 nm and provided unambiguous spectral and spatial information. CHASE and SERTS were only of short duration.

CDS views a wide wavelength range between 15 and 80 nm. Meanwhile another SOHO instrument, SUMER, will detect lines in two small wavelength bands between 50 and 160 nm, with a very high spectral resolution. Together the two instruments will provide an unprecedented view of the solar atmosphere from the chromosphere upwards, with excellent density, temperature and flow diagnostic capabilities (Patchett, 1991).

1.3.1. Science requirements

As described in §1.2.1., plasmas at temperatures of 10^4–2×10^6 K, such as in the transition region and corona, generate strong emission lines in the EUV. For a particular element the proportion ionised to a particular level depends on the balance between ionisation and recombination, which are a function of temperature. Measurement of absolute intensities and intensity ratios of the lines produced by the ions should reveal the temperatures and densities in the emitting regions. The wavelengths 15.0–80.0 nm have been chosen for CDS to cover the most important line ratios.

Lines to study may be selected by a number of criteria. Lists of prime lines have been constructed including a selection of density diagnostic pairs; lines from a good range of temperatures; and iso-electronic sequences, such as Li-like or Be-like ion lines, which will be used in differential emission measure studies. In addition, very high temperature lines have been included for the analysis of hot-spots or microflare activity. Tables 2, 3 and 4 are lists of the prime lines selected. They are taken from Harrison and Fludra (1995).

Ion	Lines (nm)	Ion	Lines (nm)	Ion	Lines (nm)
Mg VI	31.455/40.068	Mg VI	31.468/40.068	Mg VII	31.903/27.840
Mg VII	28.074/27.840	Mg VII	31.903/36.767	Mg VII	31.903/42.993
Mg VII	28.074/42.993	Mg VII	32.050/42.993	Mg VIII	43.047/43.662
Mg VIII	31.502/33.523	Mg VIII	31.502/43.047	Mg VIII	43.662/31.374
Si VIII	27.684/31.983	Si VIII	21.692/31.983	Si IX	34.987/34.195
Si IX	34.513/34.195	Si IX	29.276/34.195	Si IX	29.612/34.195
Si X	34.740/35.604	Si X	18.072/26.424	Si X	17.755/26.424
Si XI	21.593/28.142	Si XI	19.037/28.142	Si XI	21.764/28.142
Si XII	28.841/29.950	Fe X	17.527/17.453	Fe XI	18.041/18.114
Fe XI	18.441/18.114	Fe XI	17.976/18.114	Fe XI	18.470/18.114
Fe XII	18.687/19.351	Fe XII	19.664/19.351	Fe XII	33.827/36.447
Fe XIII	19.653/20.002	Fe XIII	20.204/20.002	Fe XIII	20.112/20.002
Fe XIII	20.204/20.379	Fe XIII	31.812/32.080	Fe XIII	32.080/34.818
Fe XIII	31.812/34.818	Fe XIII	35.964/48.18	Fe XIV	21.912/21.132
Fe XIV	26.480/27.420				

Table 2. Prime density diagnostic line ratios.

Ion	Lines (nm)	Ion	Lines (nm)	Ion	Lines (nm)
O III	70.298/59.959	O V	17.217/62.973	O VI	17.3/103.2
O VI	18.4/103.2	Ne V	35.9/57.220	Ne V	36.5/57.220
Ne V	41.620/56.920	Ne V	41.620/57.220	Mg IX	70.580/36.806
Mg IX	70.580/74.9	Si XI	60.400/58.090		

Table 3. Some temperature sensitive ratios.

Accurate atomic physics parameters will be important in analysing data. The intensity of an optically thin spectral line from a low density plasma is given by:

$$I = \frac{1}{4\pi} A \int G(T)\phi(T)dT \quad \text{photons m}^{-2}\,\text{s}^{-1}\,\text{st}^{-1} \qquad (1)$$

where A is the abundance of the element, $G(T)$ contains the atomic physics parameters relevant to the transition and $\phi(T)$ is the differential emission measure, which is a measure of the amount of hot plasma at temperature T.

Ion	Lines (nm)	Ion	Lines (nm)	Ion	Lines (nm)
O III	70.298	N IV	76.514	Ne VI	40.114
Ne VII	46.522	Ne VIII	77.04	Fe IX	17.107
Fe X	17.453	Fe XI	18.822	Fe XII	19.512
Fe XIII	20.379	Fe XIV	21.132	Fe XV	28.416
He I	58.43	O III	59.959	O IV	55.452
Ne VI	56.283	Mg VIII	31.373	Mg IX	36.81
Fe XII	36.447	Fe XIII	32.080	Fe XIV	33.417
Fe XV	32.702	Fe XVI	33.540		

Table 4. Prime lines for dynamic analyses.

The measurement of the abundance therefore depends not only on a measurement of the intensity but also on knowledge of the atomic physics involved and the nature of the emitting plasma. Often it is the differential emission measure which is required, because it is a primary characteristic predicted by models of the atmosphere. By using ratios of intensities from different lines of the same element, the A of equation (1) cancels out, allowing the rate of change of $\phi(T)$ with temperature to be calculated. Alternatively, the ratio of two lines can give a direct measure of the ratio of two atomic level populations which can be combined with models of temperature and density.

The transition region is thought to be a violent and magnetically active region, with small-scale disturbances. Small-scale mechanisms such as jets, may be important for heating the corona which is itself highly structured and dynamic. Wave activity may be detected by the presence of oscillations in intensities and velocities. Sporadic reconnection sites may be detected as patches of transient acceleration or localised bright spots. An understanding of the region therefore depends on high spatial and temporal resolution. The instrument must be able to resolve these structures spatially (a few arc seconds), with suitable temporal resolution (1 second). The spectral resolution needs to be able to reveal modest flow patterns ($<100\,\mathrm{km\,s^{-1}}$). From the Doppler effect, the required resolving power is given by

$$\frac{\lambda}{\Delta\lambda}=\frac{c}{\Delta v} \qquad (2)$$

where c is the velocity of light. With $\Delta v=\pm 100\,\mathrm{km\,s^{-1}}$ the ratio is 1500. Spectral resolving power therefore needs to be at least 1500.

Chapter 2 describes the impact of the science requirements and the instrument configuration on the GIS detector requirements (tabulated in Table 6 and Table 7).

1.3.2. CDS instrument

The CDS is made up of two components; a Normal Incidence Spectrometer (NIS) and a Grazing Incidence Spectrometer (GIS). Both use the same telescope and slit, but they use different optical paths and have separate gratings and detectors (see Figure 4).

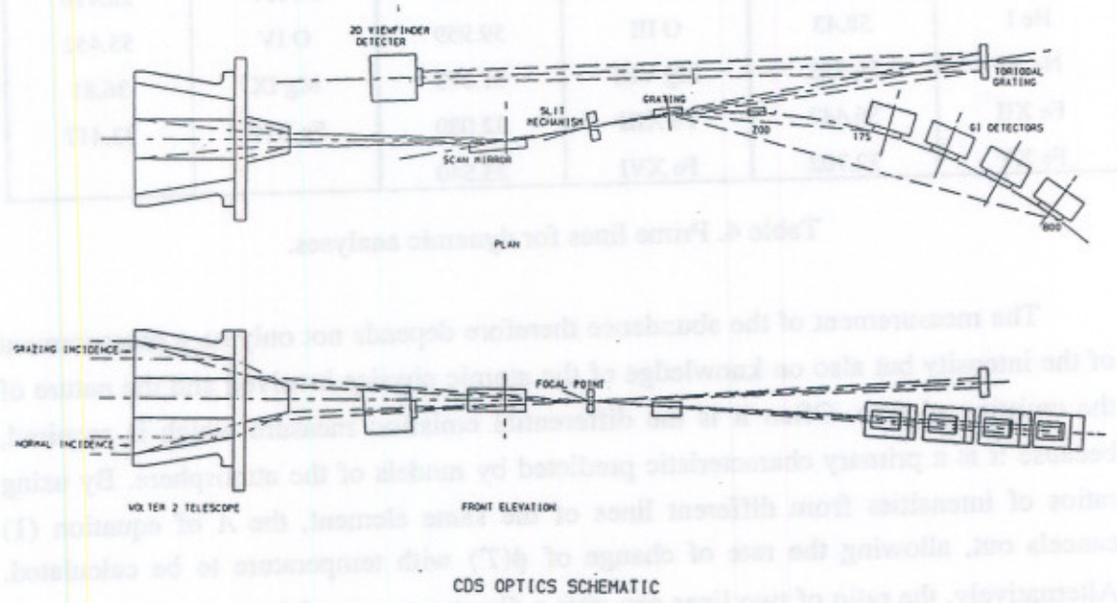

Figure 4. Diagram of the CDS Optical layout.

The wavelength range covered by CDS is 15–80 nm. Below 30 nm, the efficiency of reflection falls dramatically, unless the radiation is incident at a grazing angle, typically 1°–2°. Thus, paraboloid telescopes can only be used away from the vertex of the paraboloid. This restricts the field of view, but is only a small problem when observing the sun, which is an intense source.

Grazing incidence mirrors, especially two component mirrors, provide good spatial resolution at small field angles and have a relatively high reflectivity which is almost independent of wavelength (Negus, 1974). Grazing incidence optics are used for the CDS telescope and the GIS grating, whereas the NIS uses a novel multi-layer grating.

The telescope is a grazing incidence Wolter-Schwartschild Type II focused onto a variable slit mechanism. This type of telescope has a paraboloid primary mirror and hyperboloid secondary mirror. Table 5 summarises the instrument characteristics. Before arrival at the slit, the beam is intercepted by a flat scan mirror which scans the image of the sun across the entrance slit. A further function of the mirror is to straighten

out the optical design, which allows the instrument to be more conveniently packaged. The slit itself can be moved in an orthogonal axis to the scan mirror. Combining the movements of the slit and mirror allows two-dimensional mapping of regions of the sun. The slit mechanism also functions as a slit changer.

The image of the sun is rastered across the pinhole slit in the East-West direction by rotating the scan mirror (±2 arcmin, in 2.032 arcsec steps). This is motion in the 'yaw' direction, labelled instrument Y axis (see Figure 13). The slit is moved in the X axis or 'pitch', direction (North-South) (±2 arcmin, in 1.016 arcsec steps) to build up a spatially-defined raster of spectra of one 4×4 arcmin area of the sun.

With all grazing incidence telescopes, the field of view is restricted by severe off-axis aberrations. Therefore, to cover a wider range than the 4 arcminutes given by the slit and scan mirror movement, an offset pointing system (OPS) is required. Pitch and yaw movement is achieved by using a system of 6 legs with hemispherical bearings at each end to support the telescope structure. Two of the legs are linear actuators with stepper motors and screw jacks. Positional information is fed back by inbuilt linear positional transducers.

The OPS allows CDS to point to anywhere within a square of sides 1.15° centred on sun centre, which has a photospheric angular diameter of approximately 32' (½°). The pointing mechanism provides a step size of 1 arcsec, but the whole instrument moves much more slowly than scanning with the slit and mirror and there is a measurable hysteresis. Therefore, the OPS is used only to point at the start of a raster of spectra.

Two segments on opposite sides of the full telescope aperture are used by the spectrometers. Beyond the slit, one of the two separate and diverging beams feeds the NIS which is sensitive in the two bands 30.8–38.1 nm and 51.3–63.3 nm. The NIS uses a twin toroidal grating assembly which is stigmatic and focuses the slit onto a two-dimensional detector. The spectrum is dispersed in one direction, and the image of the slit in the other. A tall narrow slit, together with movement of the scan mirror, is sufficient to build up images of the sun. The use of two sets of grating rulings allows the two regions of the spectrum to be imaged.

The NIS detector, also known as the Viewfinder Detector Subsystem (VDS), is an intensified CCD camera (Thompson *et al.*, 1992) consisting of a single windowless MCP converting the EUV to electrons, coupled with a fibre optic lens system and phosphor screen to transform the electrons to visible photons. A CCD, cooled to −70°C, is used as the readout. The CCD has 1024×1024, 21 µm pixels and it takes 3.7 s to read out a full image.

General	Total Mass	100 kg
	Overall length	1.7 m
	Average Power	58 W
The Telescope	Outer f-number	9.38
	Effective Focal length	2.58 m
	Plate Scale	12.5 μm arcsec^{-1}
	Full Geometric Area	289.3 cm^2
	Half Energy Width	~ 3 arcsec
	PSF FWHM	~ 3 arcsec
	Field of View	4×4 arcmin
	Pointing	On disc and low corona
	Step sizes	E–W: 2.032 arcsec (mirror) N–S: 1.016 arcsec (slit)
The NIS	Telescope Area Available	34.3 cm^2 per grating
	Wavelength Range	30.8–38.1 nm, 51.3–63.3 nm
	Prime Slits (slit nos. 4,5,6)	2×240, 4×240, 90×240 arcsec
	Grating Ruling	2400 and 4000 lines mm^{-1}
	Slit-Grating distance	736.5 mm
	Grating-detector distance	744.6 mm
The GIS	Telescope Area Available	47 cm^2
	Wavelength Range	15.1–22.1, 25.6–33.8, 39.3–49.3, 65.6–78.5 nm
	Prime Slits (slit nos. 1,2,3)	2×2, 4×4, 8×50 arcsec
	Grating Ruling	1000 lines mm^{-1}
	Radius of Rowland Circle	750 mm

Table 5. CDS characteristics
taken from Harrison and Fludra (1995).

The NIS, being able to view a larger portion of the sun faster than the GIS, will be used as a viewfinder to locate features of interest. It will also be used to produce spectra in its own right. The resolving power is 4550–5550 for both wavelength ranges, allowing plasma velocities of 54–66 km s^{-1} to be detected.

The second beam is directed to the GIS which consists of a spherical grating with 1000 lines mm^{-1} and four detectors on a Rowland circle with a radius of 750 mm. There is also a visible light sensitive photodiode detector at the zero order position on the Rowland circle. This is called the zero order detector (ZOD) and is used for aligning the spectrometer with the instrument sun sensor.

Because the GIS is a one-dimensional spectrometer, it is necessary to use a pinhole slit with movement of the slit as well as of the mirror to look at the whole sun. The detectors consist of MCP stacks with SPAN readouts (also described in Breeveld *et al.*, 1992). They were developed as identical units in order to maintain interchangeability.

The MCPs and anodes are mounted on housing which contains the High Voltage distribution boards and pre-amplifier components for the position encoding electronics. The housing is also used to locate the detectors accurately on the Rowland Circle.

1.3.2.1. Scattered light

The scattered light is mainly due to the wings of the telescope point spread function (PSF), the shape of the telescope's image of a point source. The CDS must be able to point to small regions on and off the sun, minimising contamination of the radiation from the observing direction with radiation originating from all other points on the sun's disk. The sun's disk gives a 24 mm diameter image in the telescope focal plane. Only a small fraction of the beam getting through the aperture plate is wanted. All the rest is potential stray light. The number of surfaces illuminated by unattenuated sunlight is minimised and the orientation and surface finish are designed to reduce scatter in the critical direction.

During off-limb measurements, the count rates will be low. The background intensities due to stray light from the telescope and gratings will become important. The telescope has a half energy width of less than 3 arcsecs. The Gaussian point spread function falls to 10^{-3} of the maximum by 10 arcsecs to 10^{-5} at about 1 arcmin from the core of the PSF, 10^{-6} by 2' and 10^{-7} by 4'. (Harrison and Kent, 1994). This represents an almost flat distribution over the 4 arcmin field of view, adding a nearly constant background. If the disc is considered to have an intensity of 100, then at 0.1, 0.2 and 0.3 solar radii above the limb, the detected intensity from scatter will be 18.47, 6.15 and 0 respectively (Harrison, 1993). If the ratio of intensities on the disc to off limb is very high, *e.g.* for cool lines like He II, the scatter from the bright line on the disc may swamp the weak line off limb. Most prime lines, however, will have intensities greater than their scatter components.

The H Ly-α line at 121.5 nm will not be imaged on the detectors but, being an intense line, could scatter inside the optics bench. It is estimated that scatter from this line should contribute no more than 0.05 c s^{-1} to the GIS. The He II 30.4 and 58.4 nm bright lines will contribute as well.

Although the OPS will allow the CDS to view from the sun centre out to 3.3 solar radii, above 2 solar radii (0.5°) the sun's disc can illuminate the scan mirror through an abnormal beam path. One solar radius above the limb is therefore the practical limit.

The EUV continuum is expected to be as low as $0.6\,c\,s^{-1}$ on the GIS with the largest GIS slit (8×50"). This should be just detectable above the background and scatter.

Baffles are installed inside the optics bench to minimise contamination from scattered light and to prevent reflection from one detector to another.

1.4. REVIEW OF U.V. PHOTON DETECTORS

Common requirements for detectors for X-ray or UV astronomical telescopes are for spatial resolutions between 10 µm and 1000 µm, in formats up to 150 mm diameter. In many cases photon energy resolution is also required. Other important features include low particle background rates and high quantum efficiency (QE)—the ratio of photons detected to those incident on the detector. Culhane (1991) and Fraser (1989) present reviews of the current state-of-the-art X-ray detectors. Many of the detectors discussed can be used in the UV with modifications.

The following section reviews photon detection and multiplication and is followed by a review of position readout schemes.

1.4.1. Photon detection

Of primary importance in photon detectors is the ability to detect the absolute intensity of the radiation. Apart from this, the choice of detection method may depend on the speed of response, the sensitivity at the wavelengths of interest or the spatial resolution. The spatial resolution is normally expressed in terms of the full-width-at-half-maximum (FWHM) of the point spread function. In the EUV region the initial photon is normally detected by fluorescence, photoelectric emission or gas photo-ionisation, followed by electron multiplication to increase the sensitivity. MCPs, photomultipliers, proportional counters or channeltrons can be used as electron multipliers.

1.4.1.1. Channel electron multipliers

Two Channel Electron Multipliers (CEMs) are shown in Figure 5. They comprise a horn supported on a channel with a high length-to-diameter ratio. Both horn and channel are made of glass, covered with a semiconducting layer of high secondary electron emissivity. The output end is held at 1–3 kV positive with respect to the horn. Therefore electrons or photons with high enough energy incident on the horn or just inside the channel emit secondary electrons which are attracted down the channel, repeatedly impacting the wall and gaining energy. At the output, a cloud of up to 10^8 electrons is

detected as a pulse of charge. Each input photon or electron leads to no more than one charge pulse. If the event rate is higher than about $10^6\,s^{-1}$, however, the CEM can be used as a current amplifier with lower gains.

Efficiencies are very high (60–90%) but vary, by up to a factor of three, between photons arriving at the horn and the channel (Seah and Smith, 1991).

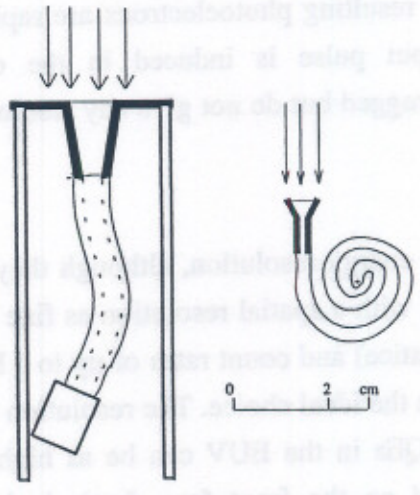

Figure 5. Schematic diagram of two CEMs.
Left, a Galileo (Bendix) 4729 CEM; right a Philips X919 CEM. Figure from Seah and Smith (1991).

CHASE (Coronal Helium Abundance Spacelab Experiment), an 8 day Spacelab 2 mission in 1985, (Patchett *et al.*, 1981) used an array of CEMs as the detection element in the spectrometer, with one CEM detecting each spectral line of interest. Rocking the grating allowed scanning of the line profiles. This method has excellent count rate characteristics and good signal to noise, but only a few well spaced (15 mm apart) lines can be observed. For GIS there are many lines of interest, some of them very close together, requiring a spatial resolution of 50 μm (FWHM) or better to resolve them.

1.4.1.2. Proportional counters

For both gas-filled position sensitive proportional counters (PSPC) and gas scintillation proportional counters (GSPC) (Peacock *et al.*, 1981) the spatial resolution and energy resolution is proportional to $E^{-½}$, for low photon energy, E. Quantum efficiencies of up to 80% can be obtained with X-rays if the appropriate window materials and gas are used. For UV, the QE is lower. Background rates can be as low as $10^{-4}\,c\,s^{-1}\,mm^{-2}$.

A thin lexan-windowed imaging proportional counter was baselined in the ESA EXUV mission study in the 0.6–25.0 nm band, but for wavelengths greater than

20.0 nm, a 0.15 µm pressure tight window and a gas supply system would achieve resolutions of only 300 µm (FWHM), (Fraser, 1991). The resolution is limited by the transverse motion of the photoelectron, but also because the initial photon energy is too low to achieve a good signal to noise ratio.

1.4.1.3. Photodiodes

In a photodiode the photons pass through an input window and mesh anode and strike an opaque photocathode. The resulting photoelectrons are rapidly accelerated towards the mesh anode and an output pulse is induced in the cathode connector. Optical photodiodes are small and rugged but do not give any resolution information beyond the size of the device.

1.4.1.4. MCPs

MCPs provide no effective energy resolution, although they can be used with filters or in spectrometers. However, with a spatial resolution as fine as the pore structure (down to 8 µm pores in a 12 µm lattice) and count rates of up to 1 Hz/pore or even higher with 'hot' plates, they can still be the ideal choice. The resolution in nearly all current devices is limited by the readout. QEs in the EUV can be as high as 50% depending on the photocathode material used on the front face. Intrinsic background count rates are typically 3×10^{-3} c s^{-1} mm^{-2}.

MCPs have been used in a number of space flight experiments. Ultraviolet experiments include CHASE; the Extreme Ultraviolet Explorer (EUVE) (Vallerga, Kaplan *et al.*, 1989); the Wide Field Camera (WFC) on ROSAT (Röntgen Satellite; Wells, 1985); FAUST Spacelab (Siegmund *et al.*, 1987a); BEARS (Cotton *et al.*, 1989); Mariner Jupiter/Saturn UV Spectrometer (Broadfoot and Sandel, 1977); the EUV spectrometers on Voyager and EXOSAT (Taylor *et al.*, 1981). Many X-ray experiments have also used MCPs, such as the Einstein HEAO-B X-ray Observatory (Henry *et al.*, 1977); ROSAT HRI (Gerdes, 1985), the AXAF High Resolution Camera (Winkler *et al.*, 1986) and EXOSAT (Mason *et al.*, 1984).

For X-ray or optical detectors, MCPs are often used as the multiplier, with a high QE photocathode for detecting the photons. For example, an alkali halide scintillator crystal coupled by fibre optic to an MCP with a bi-alkali photocathode has been developed for use in the X-ray region (Hailey *et al.*, 1990).

1.4.1.5. Photomultiplier tubes

The original photomultiplier tube used a set of discrete dynodes. Secondary electrons are accelerated from dynode to dynode, multiplying in number and energy.

One type of optical PMT is described by Johnson (1989). It uses an electrostatic lens between the cathode and the discrete 6 dynode electron multiplier. With 2500 V between the cathode and anode it has a rise time of 1.5 ns and can give a pulse of 5×10^4 electrons.

PMTs often use MCPs as the electron multiplier. Many include high photoelectron emission photocathodes and fibre optics. They use electrostatic, magnetic or proximity focusing between the various components (*e.g.* Ceckowski *et al.*, 1981). Proximity focusing means that the field between the photocathode and the MCP is sufficiently high that the photoelectrons do not move far in a transverse direction, thus impacting on the MCP at the same co-ordinates as they hit the photocathode. Proximity focusing has the advantage of immunity to magnetic fields, small size and volume. However, care has to be taken to avoid breakdown with the high electric fields involved. Sometimes the detector is gated by changing the electric field between the photocathode and MCP.

A curved channel MCP (C-plate) followed by a straight channel MCP, with 50 µm between them, is used in the intensifier tubes of Read *et al.* (1990). These are sealed tubes with an S20 photocathode for high QE at optical wavelengths. Because the tubes are sealed the MCPs have to be suitably scrubbed before assembly, extracting 2.6 C cm^{-2} from the C-plate, and 1.0 C cm^{-2} from the straight channel plate. A Thomson CCD is used as the readout in conjunction with transputers using programmable centroiding enabling data up to a division of 1/64th of a 23 µm square CCD pixel. Resolution of the device is, however, limited to 25 µm by the photocathode and fibre optic taper taking the output of the MCP to the CCD.

1.4.2. Position readout

Conceptually, the simplest type of position readout is the discrete-anode readout, where each pixel is defined by a separate anode complete with amplifier and counting circuit. Distortion-free imaging at high speeds is attractive, but the number of pixels is limited. For GIS, any system using such an array of discrete anodes behind an MCP, with each anode acting as one pixel, (of which 2000 per detector would be needed), and requiring its own set of electronics, would use too much power and would obviously be prohibitively cumbersome, expensive and heavy for space flight.

Readouts can be divided into two simple categories: digital or analogue. In the digital case, the co-ordinates of the centroid of the charge cloud pulse produced by the multiplier is determined by a digitally encoded discrete conductor pattern. These readouts use charge detection alone but require a large number of independent electrodes and electronics. An analogue device normally produces 2 to 6 signals, the relative size or timing of which depend on the position of the photon. To achieve high

accuracy, they require precise charge measurement, usually to a level higher than the position accuracy.

The main disadvantage in the case of the digital schemes is electronic complexity. The anodes are usually multilayer, difficult to construct and expensive. Analogue readouts, on the other hand, while being much simpler electronically, suffer from contamination of the signal by electronic noise. They rely on a high signal to noise ratio for each photon initiated event. The high accuracy required can be achieved only at the expense of speed.

1.4.2.1. Coincidence arrays

The MAMA (Multianode Microchannel plate Array, Timothy *et al.*, 1981) and CODACON (Coded Anode Converter, McClintock *et al.*, 1982) detectors use a system of coincidence arrays, grouping discrete anodes, so that fewer electronics are needed than in the straightforward discrete-anode system. The MAMA (see Figure 6), with its multi-channel system was designed to cope with high count rates given by laboratory spectroscopy or solar physics (Timothy and Bybee, 1975) and uses two orthogonal grids of anodes insulated from one another. The CODACON uses charge spreader pixels to couple capacitively to code tracks, which are paired in such a way as to produce a position in ~~grey~~ Gray code directly. Both types of anode can operate at high resolution (<25 µm depending on the size of the anodes); the resolution is only determined by the anode geometry, as the output data is recorded directly in digital format. They can operate at high speed (100 ns and 500 ns dead time respectively) and are forgiving of MCP gain depression problems (§3.4.) because they do not depend on a large spatial spread of the electron cloud. However, an event is only considered valid if the charge detected on adjacent anodes is co-incident. This requires a very fast time resolution if the detector is going to run at high speed. Coincidence arrays still require a large number of electronics channels. *e.g.* for MAMA to obtain N×M pixels, N+M channels are used, with each event spreading to two anodes. For CODACON $n+1$ channels are needed to encode 2^n pixels.

A crossed grid detector system is described by Chappell and Murray (1989) for the AXAF High Resolution Camera, which achieves a resolution of 25 µm over a 100 cm^2 area. The charge cloud from the MCP is accelerated towards two isolated orthogonal wire planes made of parallel wires 100 µm in diameter and 200 µm apart. The wires are resistively coupled by 10 KΩ thin film resistors. Every 8th wire is connected to a charge-sensitive amplifier. The amplifier collecting the most charge gives a coarse position. An algorithm is used to calculate the centroid using the two neighbouring amplifiers.

Particular problems are caused when the charge cloud is so large that some of the charge is not collected within the area covered by the three amplifiers.

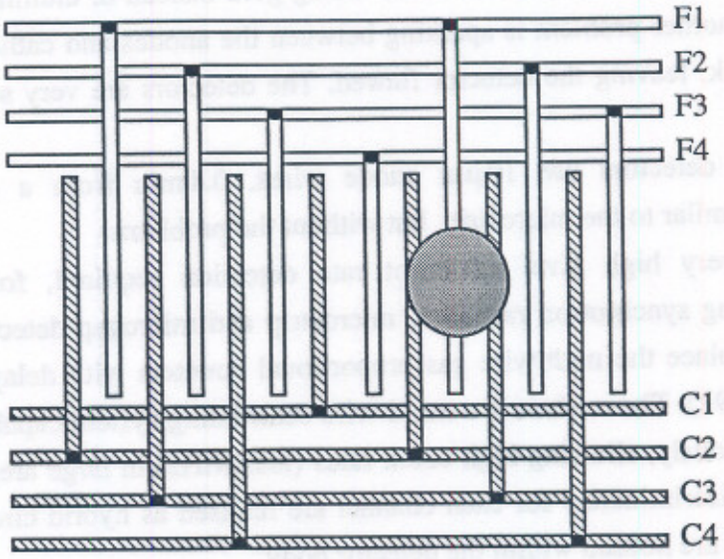

Figure 6.The MAMA detector
works by co-incidence detection. If there are signals on C2+F1+C3, as here, the event is accepted and the position interpolated. In the case of other combinations, *e.g.*F1+C3+F4, the event is rejected.

1.4.2.2. PAPA

For speckle imaging in astronomy a sequence of short (~ 10 ms) exposures is taken, the time depending on atmospheric conditions. For faint objects there are therefore only a few photons per exposure. The PAPA detector (Precision Analog Photon Address, described by Papaliolios *et al.*, 1985), with a narrow bandwidth, has been developed so that each photon may be time-correlated. The PAPA detector uses an MCP backed by a phosphor (Sams, 1991). A lens collimates the light from the phosphor which is then divided among a number of channels each consisting of another lens, a series of masks and a photo multiplier tube. The masks are arranged in Gray code to encode the position of the event. Gray code is used rather than binary because it has the property that only 1 bit changes in the digital address from one pixel to the next, reducing ambiguities. Any inherent non-linearities due to mask misalignments *etc.* can be eliminated by standard flat-fielding techniques. Resolutions of 100 μm across a 25 mm tube have been obtained.

1.4.2.3. Microstrips and microgaps

These readouts are designed for use in gas proportional counters. Microstrips are aluminium with coplanar anode and cathode strips. 8 μm wide anodes spaced at 1 mm

are separated from the cathode strips by 0.3 mm. A Problem has been found with irreversible radiation-poisoning of the microstrips under high rate testing, causing a drastic local fall in pulse height with time. Using gold instead of aluminium may solve the problem. Another problem is sparking between the anodes and cathodes which can evaporate a track, leaving the detector flawed. The detectors are very sensitive to gas-poisoning.

Microgap detectors use 10 µm anode wires, 0.4 mm from a cathode plane. Properties are similar to the microstrip, but without the problems.

For the very high level of count rate detection required, for example, in experiments using synchrotron radiation, microstrip and microgap detectors have been developed to replace the multiwire gas proportional counters with delay line readouts (Lewis *et al.*, 1992). The readout is a multi-wire centroiding system capable of handling events simultaneously, allowing high count rates (tens MHz) in large area formats. The amplifiers and discriminators for each channel are realised as hybrid circuits to reduce their volume and are housed within the detector body.

Another approach to position measurement is to divide the charge output from the MCP between electrodes such that the ratio is a function of the position. Readouts that use this technique include delay lines, resistive anodes and special geometry conducting anodes, such as the Quadrant anode (described in Lampton and Malina, 1976), Wedge and Strip anodes (WSA) and the Spiral Anode (SPAN).

A readout which combines a multi-wire approach with charge division is the graded-density cathode. This has been used with proportional counters (Mathieson *et al.*, 1980) and MCPs (Smith *et al.*, 1982). It comprises a plane of wires, with uniform pitch, connected electrically into two groups such that the density of each group changes approximately linearly across the cathode width. Provided the charge cloud spreads across a sufficient number of wires, the fraction of charge induced on each component varies progressively with position. Due to the constant pitch requirement, it is not possible to group the wires truly linearly. Increasing the height available for the charge cloud to spread and decreasing the pitch size improve linearity. Non-linearity of less than 0.25% has been obtained with a 9.5 cm cathode, giving a position resolution better than 150 µm (FWHM). Advantages of this method include a small number of electronic channels with low inter-electrode capacitance (44 pF for 1 mm pitch).

1.4.2.4. Delay lines

A pulse of charge arriving at a delay line divides into two pulses which propagate in opposite directions along the line. The difference in time taken by the signals to reach

the ends is used to determine the arrival position of the event. Delay lines have been used with proportional counters and MCPs. The difference in signal arrival times extends from −50 ns to +50 ns for photon initiated events that occur at the extreme ends of the delay line. With timing down to a few tens of picoseconds, several thousand resolution elements may be obtained. Resolutions down to 18 µm (FWHM) have been obtained in formats of 140 mm × 140 mm (Williams and Sobottka, 1989). This technique is slow; approximately 1 µs per event. Linearity to within ~50 µm has been obtained.

The delay line anode structure is composed of an orthogonal pair of flattened helical delay lines, wound one inside the other on a square frame. The windings are 200 µm diameter bare copper wire with 1 mm pitch. The anode is held 10 mm from the back of the MCP stack to allow sufficient spreading of the charge cloud to cover several turns of each delay line. Interpolation between positions is therefore possible.

Other schemes use individual parallel strips, zigzag patterns etched into copper on an insulating substrate, crossed delay lines (Siegmund *et al.*, 1989), or a combination of delay lines and special geometry charge division anodes (see §1.4.2.6.) (Lampton *et al.*, 1987).

1.4.2.5. Resistive anodes

An early example of a resistive anode is described in Lawrence and Stone (1975). In a resistive anode, the relative amounts of electrical charge arriving at its four corners or edges depend only on the x and y location of the centroid of the event. The co-ordinates of each event can therefore be determined in real time with a pair of ratio circuits fed by these signals. The spatial resolution is dependent on the gain of the MCP: for the best resolution more than 10^7 electrons per event are needed. Resistive disc readout anodes have achieved FWHM resolutions between 40 µm and 120 µm with formats between 25 mm and 50 mm. The difference in the rise times of the signals can also be used for the position calculation (Chauvet *et al.*, 1987).

Resistive anodes, like delay lines, have far simpler electronics than MAMA or CODACON, needing only 2 channels of electronics per dimension. They are relatively simple to manufacture and are mechanically robust. They can run at reasonably high count rates (300 ns processing electronics), the limit being set by the time taken for computation of the position. The Mepsicron position sensitive resistive anode gives very fast (<80 ps) time resolution, developed especially for time-resolved or time-gated spectroscopy (Courtney and Wilson, 1991).

Prompt signal collection requires low resistivity, whereas, in contrast, a low level of thermal noise necessitates a higher resistance: the resistivity chosen is therefore a compromise between the two. The optimum is to use a value for which the charge

collection time is much less than the preamplifier time constant. The anodes often have ~0.5 MΩ resistance. Formats up to the size of 100 mm active diameter are possible, but a major problem with large resistive anodes is the increased capacitance which increases the time constant of the readout. An advantage, however, is that they are free of the crosstalk problems of multi-anode systems. Crosstalk is an effect where signal is 'shared' between electrodes because of the capacitance between them.

Resistive anodes are insensitive to variations in MCP gain as long as the signal to noise ratio is maintained, although if the gain is poor ($< 10^6$), small changes in gain may result in measurable loss of resolution, especially in regions of gain depression (Clampin and Edwin, 1987). Firmani *et al.* (1982) and Paresce *et al.* (1987) used four or five MCPs with a gap of 1 mm in between the chevron stacks in order to get enough gain (10^7–10^8) together with sufficient control on charge cloud size.

Resistive anodes are susceptible to non-linearities in the ADCs which translate directly into non-linearity in the calculated position. This type of anode can suffer from variations with temperature and thermal noise. Geometric distortion may transform a rectangular test grid to an output with 'pincushion' or 'barrel' curvature. The amount and form of the distortion may be controlled by careful choice and shaping of the electrodes for a particular application and set of readout electronics (Fraser and Mathieson, 1981).

The WFC on ROSAT is sensitive in the range 6.0–30.0 nm. It uses grazing incidence telescopes and two-dimensional detectors—curving the MCPs and the resistive anodes to match the focus of the optics. The resistive anodes, with 45 mm active diameter, gave excellent local and global uniformity and minimal temperature sensitivity. Noise levels were below the detector resolution (Barstow *et al.*, 1985). The pixel size was 78 μm (10 bits in 45 mm) and the noise 1820 electrons r.m.s, which, at a modal gain of 3.1×10^7, gives a broadening due to noise of just 2.7 μm.

The Resistive Anode Image Converter (RANICON) is described by Lampton and Paresce (1974) and later by Clampin *et al.* (1988). The RANICON consists of an MCP intensifier tube with a uniform continuous resistive anode with appropriately shaped electrodes. Spatial precision of 45 μm FWHM across a 25 mm diameter active area has been obtained with 1 μs time resolution. The measurement of the position can be made either by comparing the ratios of the charges collected or by noting the difference in the signals' rise times. This system has been used for UV Rowland circle spectroscopy. A newer version for fast time resolved ground based optical astronomy at red wavelengths uses a GaAs photocathode, but has a resolution of only 76 μm (Clampin and Paresce, 1989a and b).

1.4.2.6. Special geometry charge division anodes

Special geometry, conducting anodes use a small number of electronic channels. For example, the one-dimensional Wedge and Wedge anode (also known as the backgammon anode) has only two electrodes. The electrodes are shaped as rows of interlinked isosceles triangles. A charge cloud landing at one end will be collected predominantly by the bases of one set of triangles. In the middle it will be spread evenly between the two sets. Thus, measuring the ratio gives the position: one ratiometric ADC is sufficient. Some of the above discussion on resistive anodes also applies to this particular type of anode; the maximum number of pixels is again equal to the number of bits in the ADC. Thus resolution and linearity is restricted to the ADC. Speed is dependent on the speed of the electronics. Thermal noise is not a problem however because of the use of a conductive, rather than resistive, surface. Crosstalk can be a problem with this type of anode.

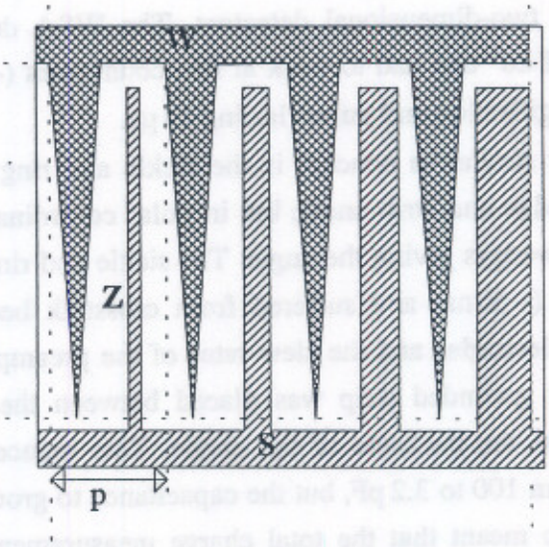

Figure 7. Diagram of a Wedge and Strip anode.
The anode is shown for clarity with only 4 repeat pitches. An individual pitch of p is indicated. The fractional range of both wedges and strips is from 0% to 50% of p along the horizontal and vertical axes respectively. The active area is outlined with dashed lines.

One of the two-dimensional versions is the very widely used Wedge and Strip anode (WSA) (*e.g.* the Tauvex detector described in Lapington, 1994a), as depicted in Figure 7. It consists of three electrodes in the form of two interlocking combs: the wedge and strip electrodes, with an interleaved Z electrode. Usually the charge pulse is measured with 11 or 12-bit accuracy, to achieve the required resolution. This limits the

speed to $1–2\times10^5$ events s^{-1}. Position resolutions of down to 35 µm (FWHM) on a 23 mm format or 80 µm in a 50 mm format have been achieved with Wedge and Strip anodes. There are many other similar designs such as the early design by Anger with two wedges for one axis and two strips for the other (Martin *et al.*, 1981). The disadvantage of this design was that two of the electrodes required interconnects. With the wirebonding technique that we use now at MSSL this would be no problem, but for Anger the only solution was to use circuit board and drill through to make solder connections. WSAs of all two-dimensional designs suffer from asymmetry, in that, while one axis is encoded continuously, the other relies on discrete strips, limiting the resolution in that axis.

Advantages of WSA type anodes over resistive anodes include the simplicity of manufacture, speed, and uniformity of resolution over a large area. The advantages are discussed in Lapington and Schwarz (1986).

The EUVE was sensitive to 10–100 nm. Like the ROSAT WFC it used grazing incidence telescopes and two-dimensional detectors. The WSA detectors were at a grazing incidence angle of 20° and had to work at low count rates (<40% dead time at 9000 c s^{-1}), with 15-bit digitisation and pulses lasting 15 µs.

Another anode very similar in concept is the sickle and ring (Knibbeler *et al.*, 1987), which is like a wedge and strip anode but in polar co-ordinates with the strips giving the radius and the wedges giving the angle. The sickle and ring anode was to be used at high count rates (~ 50 ns) and suffered from crosstalk because of the high capacitance between the electrodes and the slew rates of the preamplifiers. In order to reduce the capacitance, a grounded strip was placed between the electrodes and a grounded plate was put on the backside of the anode. This reduced the capacitance between the electrodes from 100 to 3.2 pF, but the capacitance to ground was increased. Having the grounded strip meant that the total charge measurement required for the algorithm had to be obtained from the sum of the charge deficit pulses on the front and backside of the bottom MCP. This is within 1% of the total charge signal.

The diamond cathode (Allison *et al.*, 1985) was designed for very large detectors, up to 300 m^2, for identifying muons against a background of hadrons in electron-positron colliders. It comprises two sets of two interlocking diamond-shaped electrodes. Both sets repeat in shape and are identical except that one set is offset 180° from the other. Yet another electrode is needed to measure the coarse position, the fine position being given by the ratio of the signals collected on the diamond electrodes. The reason for using two sets of diamonds is that at the vertices of one set the resolution is poor. At

this position the other set has good resolution, enabling a resolution of 1 mm in 5 m to be obtained.

The SPAN anode (which will be explained in detail in Chapters 5 and 6) can be thought of as an extension to the wedge and wedge anode. It is a charge division position sensitive readout which can be incorporated in one or two-dimensional detectors. It has been developed for use with MCPs in X-ray or UV detectors, to meet the space flight requirements of high speed and positional sensitivity together with electronics of low power and mass. Instead of using just two electrodes, as with the wedge and wedge, to encode one dimension, it uses three, combined in such a way as to maximise resolution and minimise non-linearities. This greatly reduces the required charge measurement precision for a given spatial resolution.

The electrode areas vary non-linearly along the position axis they encode so that the number of pixels does not map directly from the ADC channels. Thus ADC non-linearities are not carried directly to the image, as is the case with a WSA. Using 8-bit ADCs allows a higher count rate than WSAs. With the two-dimensional, six electrode version, a resolution of 24 µm (FWHM) on a 25 mm wide anode has been achieved (Lapington, Breeveld *et al.*, 1990).

The GIS detectors were chosen as the first ever to use this type of readout for flight, the reasons behind the choice depending mainly on the ability to encode a high number of pixels (11-bit; 2048) with only two 8-bit ADCs (the function of the third electrode being to normalise the signal from the other two). Very fast, flash ADCs, of low power and mass, could be readily bought for this precision, whereas no flash 11-bit ADCs were available commercially. In addition, reference to look-up-tables stored in memory on board, rather than real-time calculation, allows these detectors to operate at the required speed (10^5 c s^{-1} random with 10% loss).

1.4.2.7. Solid state

This group of detectors includes the CCD (charge coupled device), SPD (self-scanned photodiode array), Silicon Drift Chamber and Vidicon. For descriptions of solid state detectors see reviews by Talmi and Busch (1983) and Allinson (1982). In the case of the CCD, photons are absorbed by MOS capacitors and converted into electron-hole pairs. To increase the efficiency for detection of UV, MCPs are often used in front of CCDs. The charge produced is clocked out of the pixels serially. The position resolution of a CCD is usually limited by the size of the elements in the array; typically arrays are of 1000 by 1000, 25 µm pixels. Higher resolutions can be obtained by using centroiding algorithms. For example, the RAL Photon Counting Detector (van Breda *et al.*, 1992) involves eight transputers to calculate the positions of charge cloud centroids down to

1/128th of a pixel (0.5 μm). This detector cannot distinguish multiple events and works fairly slowly (200 ms from event to address), but can handle up to 10^5 c s^{-1} with 20% loss. Higher local speeds can be achieved by software windowing.

The NIS on CDS uses a CCD camera with MCPs and a phosphor screen. Unfortunately, CCDs need to be operated at less than 180 K and have a temperature dependent background which has to be subtracted. If the CCD is used in saturated mode, where each event from the MCP has enough charge to saturate a CCD pixel, then the CCD effectively has to be read out after every event, which is much too slow. If, on the other hand, an event provides just some fixed portion of the pixel saturation charge, so that an image can be accumulated before reading out, then the MCP must give the same charge for each event. Because an MCP gives a spread of energies, this will add considerably to the error, especially if the MCP itself is not operating in saturated mode.

Alternatively, the CCD can be back-illuminated, which does away with the need for the MCP. The efficiency can be 55% for the 5–200 nm band. Hier *et al.* (1989) describe a back-illuminated CCD and special techniques of side-stepping (clocking partial pixels) and centroiding to increase the resolution.

A DIGICON does not use MCPs either, but obtains all its gain from the silicon. Electrons from a photocathode are accelerated to 8–9 keV before colliding with the silicon and generating electron-hole pairs, the number being restricted by energy conservation to 1 pair per 3.6 eV. MCP count rate limitations and gain variations are therefore avoided.

Vallerga and Lampton (1987) compare CCDs and MCPs for windowless detectors for space astronomy. For them MCPs are preferable because of their automatic suppression of visible light while counting photons at all wavelengths shortward of the photoelectric cutoff. Furthermore, MCPs offer greater flexibility of format, less susceptibility to contamination and no need for cryogenic cooling. Allington-Smith and Schwarz (1984) present the advantages of MCP detectors for astronomical optical telescopes. MCPs allow the achievement of high signal to noise ratios at very low light levels. Additionally, they offer distortion free imaging over wide fields and act very fast. At high flux levels the CCD may be superior. CCDs are becoming ever more popular as the pixel size and noise is reduced and formats increase in size (Jorden, 1990). Efficiencies as high as 80% can be obtained at visible wavelengths.

CHAPTER 2.
THE GRAZING INCIDENCE SPECTROMETER

I designed the detectors for GIS to meet the scientific goals which have already been described. In this chapter, I expand these goals to give the detector specifications. I also give an introduction to the MCPs and anode chosen.

2.1. GIS DETECTORS

The four GIS detectors, one of which is pictured in Figure 8, are identical and therefore interchangeable. They are described briefly in Breeveld and Thomas (1992). Due consideration was given to making each of the detectors specific to a particular wavelength range. This would have given scope for detector active areas of different sizes to ensure that important lines were included. Apertures could have been adjusted to minimise line spread in some detectors or maximise intensity in others. A method for baffling the very high count rate He 30.4 nm line was investigated. However, building four identical units has the advantages of allowing bulk purchases of parts (*e.g.* sets of MCPs) which cuts down costs. It facilitates manufacture in the workshop and on the laser cutting machine where many identical parts may be produced easily after the initial design. This expedites the process of manufacture and assembly. Test equipment can be used identically for each detector without any need for the building or purchase of new mounting equipment. The breadboard, engineering model (EM) and qualification model (QM) stages were able to be completed with only one detector and set of associated electronics per model. Tests performed on one unit could be extrapolated to the others. In addition, it meant that only two spare detectors were sufficient. It was therefore decided to compromise on the detector design to keep the flexibility of interchangeability.

On the spectrometer the detectors are known as FM or GI 1, 2, 3 and 4. During the flight build and testing, the flight detectors and spares were instead given the letters I, J, K, L, M and N to allow them to be mounted in the spectrometer in any order without confusing their identity. They were nicknamed Isaiah, Jeremiah, Kings, Leviticus, Malachi and Nehemiah.

Each detector is made up of three main sections: the detector head, the HV box and the preamplifier box (see Figure 9). Three, rectangular (25×50 mm), double-

thickness MCPs, arranged in a 'z-stack', with conductive nickel shims of 25 and 12.5 μm between the MCPs, are used for photon detection and electron multiplication. The term 'z-stack' can be understood by looking at the schematic diagram of the MCPs in Figure 10, where the angles of the channels in the three MCPs form a 'z' shape. This configuration has been selected in order to achieve maximum gain and to maintain a narrow pulse height distribution (PHD). The following section explains these terms in detail.

Figure 8. Photograph of one of the flight detectors.
The detector, on the right side of the picture, is about 15 cm high. The MCP front face can be seen as the black rectangle towards the top of the detector. On the left of the photograph is the HV card. In the middle is the stack of three preamplifier cards and one trigger amplifier card, which fits into the detector black box. The wires connect to the HV card with enough spare length to allow the stack to be withdrawn from the body for testing.

The EUV spectrum is dispersed along the longer (50 mm) MCP axis, with an exposed height of 16 mm. Behind the MCPs is a position sensitive Spiral Anode (SPAN), which determines the arrival position, in one dimension, of each EUV photon.

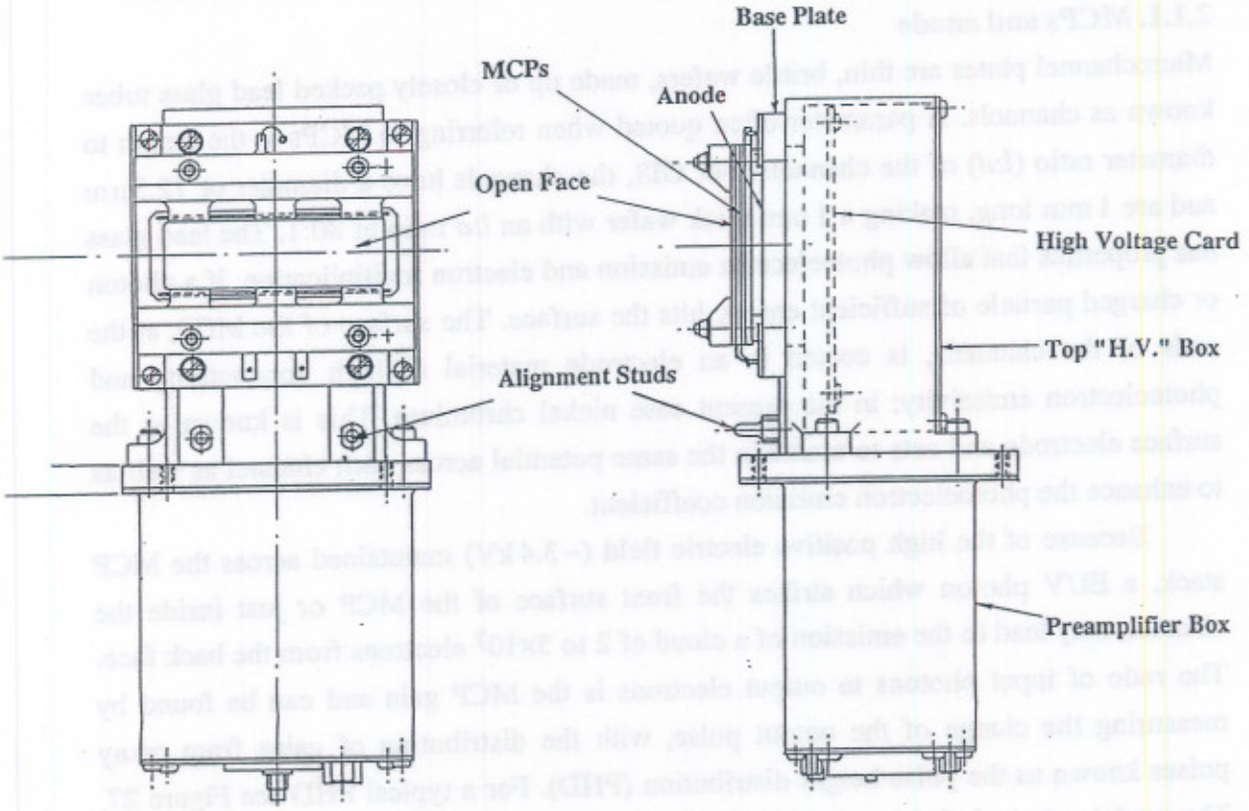

Figure 9. GIS detector.
A mechanical drawing of a detector, showing the complete assembly.

As Figure 9 shows, the detector head with MCPs and anode is mounted on the 'HV box', which houses the High Voltage distribution board. A resistive bias chain on this board, in parallel with the MCPs, maintains the plate potentials, keeping them stable in respect of temperature variation and ageing of the plates. On this housing two studs are fitted for accurate location of the detectors on the Rowland Circle (RC). Below the optics bench hangs the 'preamplifier box', which contains the three preamplifier cards and a trigger amplifier card, allowing as short a cable length as possible between the detector head and the preamplifiers. On the panel on the bottom of the box, there are connectors for the signal processing harness and the high voltage supply. Each detector has its own separately controlled HV power supply.

Two tungsten filaments are mounted in front of the four detectors in the optics bench cavity. An electric current, programmable on command, is used to heat one of

them. Electrons, emitted by thermionic emission from the filament, illuminate the detector front faces, which may be biased at either –12 V or +12 V relative to the chassis ground. The –12 V setting is for normal use with UV illumination, to repel background electrons. The +12 V setting may be used to increase the electron flux to the detectors.

2.1.1. MCPs and anode

Microchannel plates are thin, brittle wafers, made up of closely packed lead glass tubes known as channels. A parameter often quoted when referring to MCPs is the length to diameter ratio (*l:d*) of the channels. For GIS, the channels have a diameter of 12.5 µm and are 1 mm long, making a 1 mm thick wafer with an *l:d* ratio of 80:1. The lead glass has properties that allow photoelectron emission and electron multiplication, if a photon or charged particle of sufficient energy hits the surface. The surface of the MCP, at the ends of the channels, is coated in an electrode material of high conductivity and photoelectron emissivity; in the present case nickel chromium. This is known as the surface electrode and acts to maintain the same potential across each channel as well as to enhance the photoelectron emission coefficient.

Because of the high positive electric field (~ 3.4 kV) maintained across the MCP stack, a EUV photon which strikes the front surface of the MCP or just inside the channel, may lead to the emission of a cloud of 2 to 5×10^7 electrons from the back face. The ratio of input photons to output electrons is the MCP gain and can be found by measuring the charge of the output pulse, with the distribution of gains from many pulses known as the pulse height distribution (PHD). For a typical PHD see Figure 27. The modal gain is defined as the gain corresponding to the peak of the distribution. The full width at half maximum (FWHM) is the width of the peak measured as a percentage of the modal gain. Typically the FWHM is less than 100%.

Figure 10 illustrates the principle of operation of a detector. The anode is held at a higher potential than the back of the MCPs so that the electron cloud is attracted across the 3 mm MCP-anode gap. The gap allows the cloud to expand to a radius large enough to spread over the three SPAN electrodes.

The SPAN anodes (Lapington, Breeveld *et al.*, 1990 and Lapington, Breeveld *et al.*, 1991) are manufactured at MSSL (see §6.2.), starting with a quartz substrate and coating it with a thin layer of aluminium. The electrode pattern (see Figure 108) is scribed into the coating with a laser. Selected conductive elements are wire-bonded together to form three continuous electrodes.

A charge division technique is used to encode the position of the centroid of the charge cloud, which represents the position of the original photon interaction. The insulating lines which divide the electrodes take the form of damped sine waves. The

surface areas of the electrodes thus vary in a sinusoidal way along the dispersing plane (the axis of the spectrum), with the decreasing relative amplitudes ensuring that the relative areas are unique at any position along the anode .

The charge cloud emitted by the MCPs is thus divided between the electrodes according to their relative areas in that region and the charge is then collected by three charge-sensitive preamplifiers. Two of these electrode signals are digitised by ratiometric ADCs; driving the reference input dynamically with the sum of all three signals. This gives two normalised 8-bit values to be used directly as the address in a look up table (LUT) which gives the location of the original photon, to 11-bits accuracy, in one dimension.

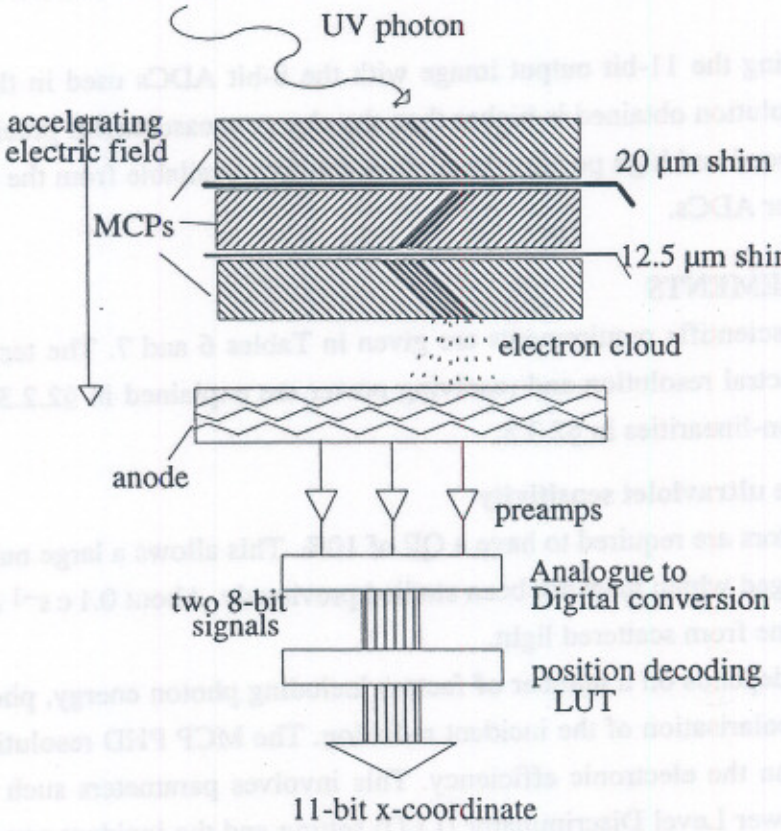

Figure 10. Schematic diagram of a GIS detector showing the path through a detector from a single photon to a single co-ordinate in the output image.

There are therefore 2048 (2^{11}) pixels along the 50 mm length, each being 24.4 µm wide. A spectrum is built up during a chosen exposure time, by counting the number of photon initiated events in each pixel. For the LUT to map the events to the pixels correctly, it has to be calculated such that it accurately matches the response of each

detector. A separate LUT is required for each detector, because, although they are identical in design, there is always a variation in component values and MCP response which may affect their performance.

The LUTs are 128 kBytes per detector (256×256×16bits) and therefore would take too long (~35 minutes) to telemeter to the spacecraft. For this reason, the LUTs are calculated on board with just 11 8-bit parameters to be up-loaded per LUT. Data taken with uniform illumination, known as flat fields, for all detectors is transmitted regularly to the ground for fitting of LUT parameters. If any change is required they may be up-linked to the spacecraft for re-calculation of the LUTs by the on-board processor. The disadvantage in having programmable LUTs is that, if for any reason the on-board processor is switched off, it may loose the LUTs. It takes 20 minutes to rebuild the whole set.

Comparing the 11-bit output image with the 8-bit ADCs used in the processing, the spatial resolution obtained is higher than the charge measurement precision. In other words, high speed and high position resolution are both available from the SPAN anode, with low power ADCs.

2.2. REQUIREMENTS

The principal scientific requirements are given in Tables 6 and 7. The terms positional resolution, spectral resolution and resolving power are explained in §2.2.3.; differential and integral non-linearities in §2.3.3.

2.2.1. Extreme ultraviolet sensitivity

The GIS detectors are required to have a QE of 10%. This allows a large number of faint lines to be imaged which have not been studied previously. About 0.1 c s^{-1} is required to distinguish a line from scattered light.

The QE depends on a number of factors including photon energy, photon incident angle and the polarisation of the incident radiation. The MCP PHD resolution will have a large effect on the electronic efficiency. This involves parameters such as the MCP voltage, the Lower Level Discriminator (LLD) setting and the incident count rate. If the PHD is too wide, many of the photons will be lost by producing pulses that fall below the LLD or above the Upper Level Discriminator (ULD). The open area ratio, which is the ratio of pore area to total area of the MCPs front face, will also affect the QE, as will the photocathode or electrode material and the shape of the electric field at the end of the channels (end spoiling). It is therefore possible to optimise, to some extent, the MCPs for the wavelength range to be detected.

Detector number:	1	2	3	4
Wavelength range—first order (nm and (eV))	15.5–22.4 (80.3–55.6)	26.1–34.6 (47.7–36.0)	39.5–49.6 (31.5–25.1)	66.2–78.7 (18.8–15.8)
Wavelength range—second order (nm)	7.8–11.2	13.1–17.3	19.8–24.8	33.1–39.4
Mean angle of incidence	77.6°	74.9°	72.0°	67.4°
Mean dispersion (nm mm^{-1})	0.138	0.17	0.202	0.250
Positional resolution (μm) (FWHM)	82[a]	68[a]	58[a]	47
Resolving power[b]	1292–1867	2175–2883	3292–4133	5517–6558

Table 6. Scientific requirements for the individual detectors.

[a] In fact using 47 μm as the requirement for all detectors for interchangeability

[b] See Table 8 for predicted values.

Sensitive area (aperture)	50×16 mm
Number of pixels in 50 mm	2048
Pixel width	24.4 μm
Pixel height	16 mm
Spectral resolution[c]	0.012 nm
Differential non-linearity (DNL)	<0.1%
Integral non-linearity (INL)	<0.1% = <50 μm
Quantum efficiency	>10%
Maximum throughput per detector (10% loss)	10^5 c s^{-1} random
Maximum output from all detectors, in TOTAL[d]	8.9×10^4 c s^{-1}

Table 7. Requirements and specifications applying to all four detectors.

[c] See Table 8 for predicted values.

[d] Limited by hardware link between the detector electronics and the command and data handling system (CDHS).

MCPs are sensitive to light of wavelengths shorter than about 180 nm. This implies that photons (or charged particles *etc.*) of energy greater than about 7 eV may be energetic enough to release an electron from the front face electrode or channel wall, although the probability is low.

From Wiza (1979):

$$\delta = A\sqrt{V_C} \tag{3}$$

where δ is the number of secondary electrons produced, A is a constant, approximately 0.2, and V_C is the voltage across the channel. Photons at the GIS wavelengths, 15–80 nm, have energies of 83–15 eV. From experiments performed at the Bendix Research Laboratories (Schmidt and Hendee, 1966), $\delta = 1$ if the primary electrons have energy, $V_C = 25$ eV (49 nm). Eberhardt (1981) estimates the value as 20 eV (62 nm). At higher energies, at least one electron should therefore expect to be released on impact, although there will be a disadvantage from the severe angles of incidence (see Table 6), such that the photon is less likely to be absorbed.

At the GIS longer wavelength (low energy) end of the range, δ will be less than 1 so that the efficiency will be poor. At very low incident photon energy the gain will also tend to be low because the initial electron, emitted with little energy, will be accelerated down the channel faster and further before crossing the channel diameter. Therefore, it may travel a long way through the top channel plate before it can cause secondary electron emissions and thus there will be a smaller number of electrons in the discharge.

For these reasons it is expected that detector 1 will be more efficient than detector 4 (15.8–18.8 eV at ~68°), whose wavelength range is entirely greater than 49.8 nm, but none of them very efficient compared with, say, the MCP detectors used for X-ray detection or in low incident angle configurations. In fact during the flight calibration test at RAL, the efficiency of detector 4 was observed to be 1.5–3.5 times less than that of the other detectors (see Table 20).

The EUV QE was shown by Tomc *et al.* (1984) to be a strong function of the linear polarisation of the test beam, even out to angles of incidence of 60°. At this angle the MCPs are about 1.35 times more sensitive to 58.4 nm light linearly polarised parallel to the surface than perpendicularly. There are many reflections taking place in the CDS. Therefore, it is important that these are reproduced faithfully in the calibration setup if the intensity measurements are to be consistent.

It was originally proposed to coat the front face of the top MCP with MgF_2 to enhance the QE in this wavelength range. For reasons given in §3.3.3. this was not done.

2.2.2. Grazing incidence

The four detectors are not curved to fit the RC, but are tangential and therefore set at an angle appropriate to the mean wavelength. These angles are given in Table 6.

Pre-flight measurements for CHASE suggested a drastic fall off in QE for incident angles above 80°. More recent measurements by Siegmund (private communication, 1991) follow the same general trend. The angle of the channels relative to the incident

beam and the depth of the end spoiling can be expected to have an effect. The end spoiling (see Figure 11) is where the Nichrome electrode has been deposited onto the surface and down the channels of the MCP to a depth which is dependent on the angle of deposition. Normally the depth is equal to the pore diameter because deposition takes place at 45°. Because of the low resistance of the surface electrode, the accelerating potential field is not felt at the ends of the channels. Photons hitting the surface electrode may release electrons, but many will be lost because they are not attracted by the electric field down the channel. For GIS a depth of half a pore diameter was specified to reduce this loss.

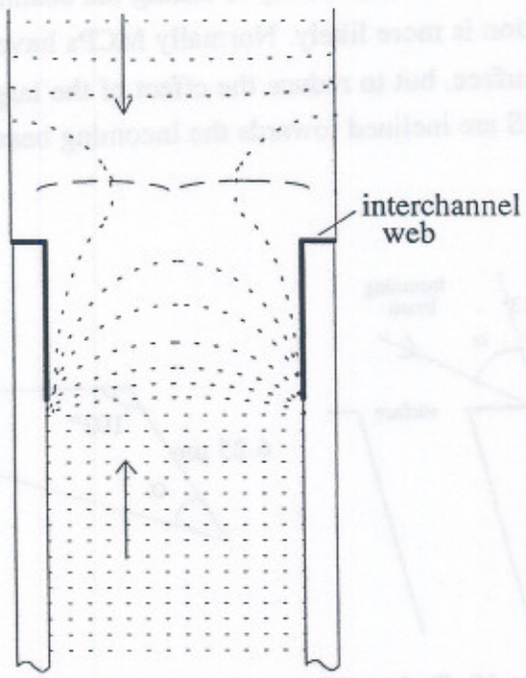

Figure 11. Shape of potential at the input of a MCP channel (as shown by Fraser *et al.*, 1984). The heavy black lines represent the end-spoiling electrode. Electric fields inside the channel and above the MCP front surface are antiparallel (arrows). Note the presence of a weak field region at the channel entrance, resulting from electrode penetration down into the channel. The broken line represents the contour of zero electric field.

One technique commonly used in MCP detectors is to put a negatively charged repeller grid above the first MCP, reversing the field above the channel. When photons hit the inter-channel web, the photoelectrons are forced back towards the MCP surface by the electric field formed between the grid and the front face. They can then enter a pore and be detected. However, unfortunately for the CDS experiment, any repeller grid

would necessarily obscure the incoming light to an unacceptable level for the following detector because of the grazing incidence configuration.

To prevent shadowing of the grazing incidence radiation, no physical clamping of the MCPs is allowed along the short edges. The MCPs are therefore used in an 'open face' (*i.e.* not in a sealed tube) configuration with just 4.2 mm along each long edge used for clamping the MCPs.

The MCP pores are each 12.5 µm in diameter, arranged hexagonally 15 µm apart, giving an open area ratio of 0.58. The efficiency of the inter-channel web is negligible. The efficiency of the channels is at a maximum (for EUV illumination) at MCP incident angles of between 10° and 20° so that the ray is hitting the channel wall at near grazing incidence, where absorption is more likely. Normally MCPs have a channel angle of 8° from the normal to the surface, but to reduce the effect of the large angles of incidence, the MCP channels for GIS are inclined towards the incoming beam at an angle of 13° to the normal to the surface.

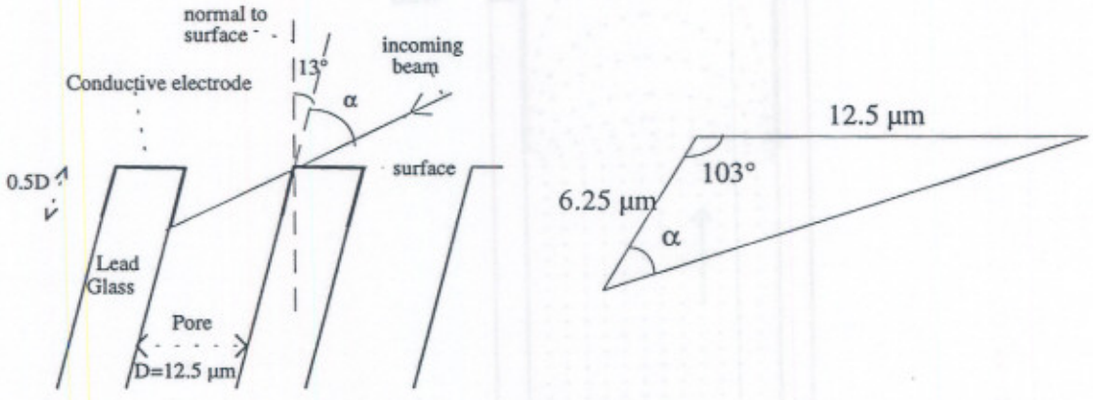

Figure 12. End spoiling and grazing incidence.
The picture on the left is a diagram of the end of one channel of an MCP. On the right, the triangle is constructed between the end of the channel and an incoming ray hitting the lead glass beyond the end spoiling. The angle α is found to be 66°. The angle of incidence of the photon therefore is 66°+13°=79°, which is marginally higher than on any of the GIS detectors.

Figure 12 shows the geometry of the end of the channels. The triangle on the right is used to calculate the maximum angle of incidence at which a beam of light may still directly hit the lead glass on the inside of the channel. At any angle steeper than this, the photons are bound to meet the surface electrode first. Although this may mean that more electrons are emitted, they may be lost if the component of their initial velocities away from the front face are high enough to escape from the electric field in the channel. It

might be expected therefore that we would see a reduction in QE above this angle of incidence. From the triangle illustrated, the angle is 79°, which corresponds to the fall-off above 80° mentioned above. However, the measurements described in Chapter 4 show a gradual decline in efficiency as the angle is increased, with no particular increase in fall-off above 79°. The most extreme angle of incidence is on detector 1 at 78.6°.

There is a probability that a photon hitting the inter-channel web will be spectrally reflected. The probability of reflection decreases with energy because of the increase in the critical angle of reflection (Barstow *et al.*, 1985). If reflection does take place, light intended for one detector may be reflected onto the following detector. For this reason, baffles (known as inter-detector shields) have been fitted to the first and second detectors to trap any reflected rays.

Further details about the MCP choice and characteristics are given in Chapters 3 and 4.

2.2.3. Resolution and resolving power

Because the detectors are one-dimensional, any spatial information is defined by the small fraction of the sun imaged by the telescope onto the entrance slit of the spectrometer (see Figure 13). For fine spatial resolution, a pinhole entrance slit has to be used. The effective spatial and spectral resolutions of the instrument will also be dependent on the PSF of the telescope, which takes the form of a sharp peak with scatter, giving wings extending right across the field of view. The FWHM of the peak defines the resolution whereas the peak to wing intensity ratio determines the ability to resolve weak features, without their being dominated by the scatter (see §1.3.2.1).

The CDS telescope was originally intended to have a PSF of 2"×2" (FWHM) (CDS Proposal, 1987), which is therefore the smallest area of the sun that could be resolved. In order to use the resolution to the full, the smallest pinhole had to subtend 2"×2". This resolution goal was subsequently reduced to 3"×3" (Harrison and Sawyer, 1993), although the small slit remained.

A point source at the pinhole slit is imaged as a line on the focal plane, at the RC, of height somewhere between 6.5 mm (at the short wavelength end) and 11 mm (long wavelengths). The height and width of the image will increase with the size of the slit. During the rastering, the positions of the images on the detectors move up and down so that, for example, an image which is 12.5 mm high takes up 17.3 mm (Lidiard, 1991a), hence the requirement for an aperture at least 16 mm high to prevent loss of efficiency.

The smallest pinhole is 25×25 µm which, with a plate scale of 12.7 µm arcsec^{-1}, is designed to image a 2"×2" area of the sun, giving the highest possible spatial resolution. Other slits are available sized 4"×4" and 8"×50" (to the nearest arcsec). There are also 3

slits intended mainly for use with the NIS, sized 2"×240", 4"×240" and 90"×240", which could be used with GIS.

When spatial resolution of the detector is referred to, however, it normally means the FWHM width of the image of a hypothetical infinitely narrow spectral line falling on the front face. It can be converted into spectral resolution if the dispersion and resolution of the spectrometer are known. Spatial resolution (dx) is a meaningful concept for a detector and associated electronics standing alone, but spectral resolution ($d\lambda$) and resolving power ($\lambda/d\lambda$) are only useful terms when discussing the whole instrument.

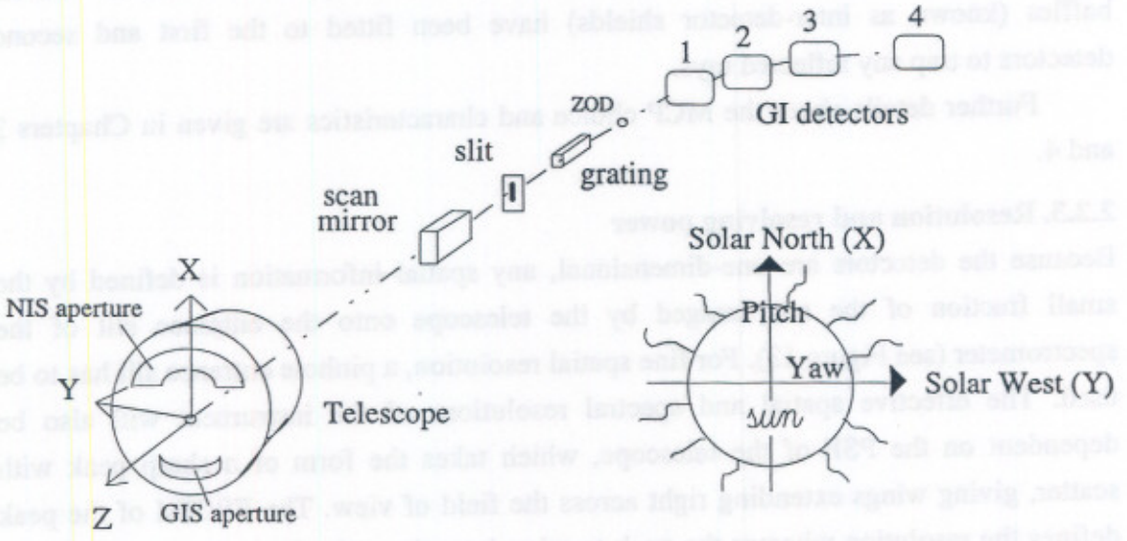

Figure 13. Orientation of CDS with respect to the sun.

The GIS needs to be able to isolate the lines whose intensities are needed for diagnostic information and to detect movement in the lines. This is hardest in the 15.5–22.4 nm range (detector 1) where there is a high line density but the lowest resolving power of any of the ranges, due to the fact that the geometrical properties of this position lead to a broader slit image on the detector. Analysing the spacing between the prime lines, Harrison (1993) has calculated that, even with a spectral resolution of 0.01 nm, 11% of the prime lines would be lost, *i.e.* the lines would be closer to each other than the resolution. At 0.02 nm, 30% would be lost and at 0.03 nm, 59%. The absolute requirement limit is set therefore at 0.03 nm, with 0.02 nm as a realistic goal.

The effective resolving power is a function of the size of the slit-image on the detector plane as well as the resolution of the detector itself. The highest required resolution is for detector 4, at 47 µm, which gives a resolving power of 2997–3716

(Table 8). If this resolution is also achieved on detector 1, the resolving power will nevertheless be worse than 1016 because of the image size of the slit at this position and the spreading due to the optics. The calculation of effective resolving power therefore has to include the dispersion; the size of the slit; the broadening and curvature of the slit image by the grazing incidence geometry; the broadening of the slit by the fact that the detectors are flat on a curved RC; the detector positional resolution and finally, the telescope PSF.

Ray tracing through the CDS (Lidiard, 1991b) has taken into account all of these factors except the size of the slit, the angle of the detector to the image and the detector resolution itself. In the following subsections, the factors affecting image width will be explained and a table presented of expected line widths after combining all the effects.

2.2.3.1. Calculations of required detector resolution

As has been mentioned in §2.1.1., there are 2048 resolution elements along the 50 mm active length, giving a pixel size of 24.4 µm×16 mm. Chapter 5 and the paper by Lapington, Breeveld *et al.* (1990) explain how the detector achieves this with only 8-bit charge measurement accuracy. However, this does not constitute the only measure of the detector spatial resolution which is a function of the pixel size and the electronic processing.

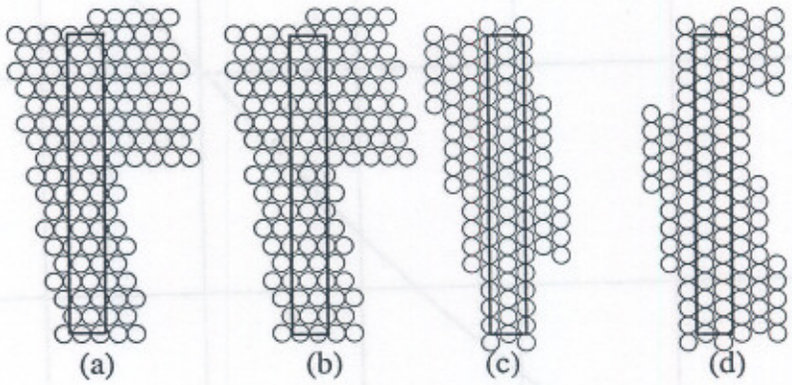

Figure 14. Convolving the pore structure with a slit image 25 µm wide. (a) gives a FWHM of ~44 µm, (b) of ~35 µm, (c) of 30 µm and (d) of ~27 µm. Other orientations will give something in between the extremes.

The absolute limit on the resolution would be the quantisation imposed by the discrete pore structure of the MCP itself, which is a hexagonal packing of pores 15 µm apart. The SPAN readout in the two-dimensional format (Lapington, Breeveld *et al.*, 1992), has achieved position resolutions down to this limiting level, which makes this type of detector ideally suited to high resolution applications. The width of a line image

will depend on the convolution of the line with the hexagonal matrix of the pore. It will also depend on the angle of the line relative to the pore structure. For instance, a line of 25 µm width, when convolved with the pore structure, gives an image of between 27 and 44 µm wide, depending on how well the line is aligned with the pores (see Figure 14).

We can assume that the image of a spectral line on the detector will have a top hat intensity profile. The aim of the optics was to produce lines on detector 1 with a PSF of no more than 50 µm FWHM. A 25 µm pinhole projected onto the midpoint of detector 1, assuming that the midpoint is on the RC, gives an image 117 µm wide (from equation 9 and using the angle from Table 6). Adding this to the ideal PSF vectorially, gives an r.m.s. width at the midpoint on detector 1 of 127 µm (Lidiard, 1991b). At the longest wavelength on this detector, the width would be 120 µm and, at the shortest wavelength, 136 µm. Multiplying 136 by the dispersion factor given in Harrison (1993) of 0.146 nm mm^{-1}, gives a spectral resolution of 0.02 nm, which is the goal given in the previous section.

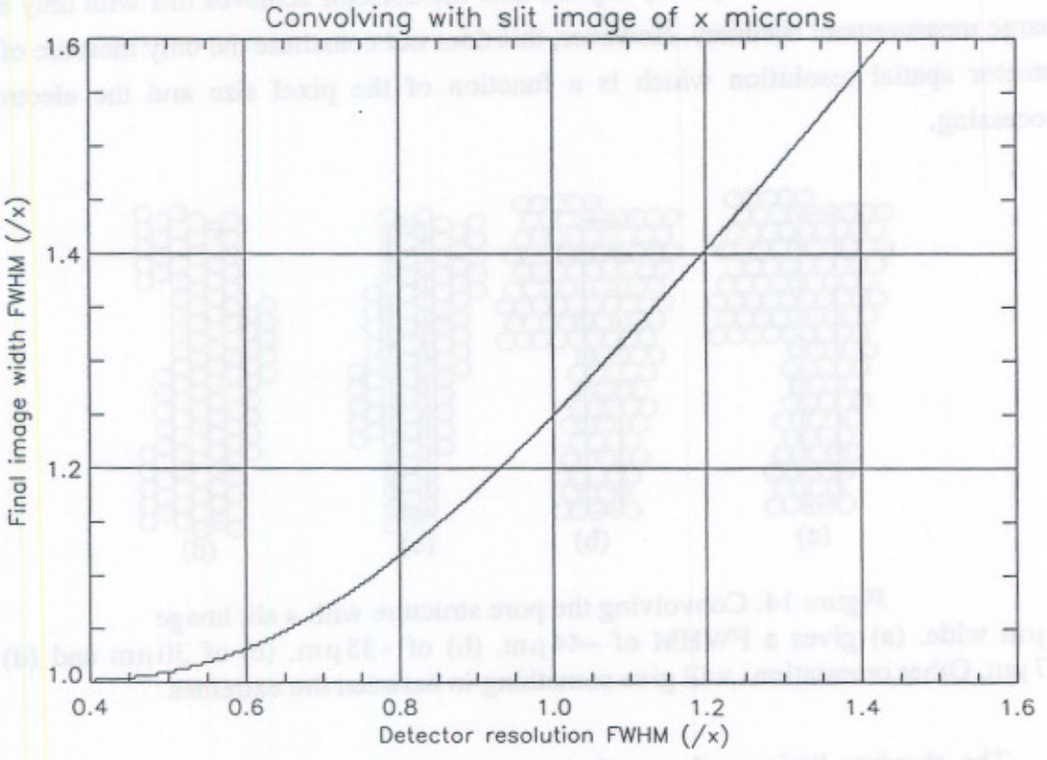

Figure 15. FWHM of the convolution of a Gaussian with a top hat function.
The convolution in this graph was done using an IDL routine. A similar graph was used to calculate the requirement for the detector resolution. This graph shows axes normalised to the image size so that it can be used for any sized image, if the detector resolution is similar to the image width.

If the detector response is assumed to be Gaussian, the final width of the line obtained is a convolution of the Gaussian with the top hat distribution. Figure 15 shows a plot of the widths of the results of Gaussian distributions convolved with top hat functions using an IDL routine. Using this convolution, together with the requirement that the detector should not increase the minimum projected slit line width (120 μm) by more than 10%, the resolution requirement for detector 1 is found to be less than 90 μm.

At the other end of the spectrum, however, a line of 78.7 nm wavelength has a projected image 62.56 μm wide. The 10% allowance on this gives a much tighter constraint on the detector resolution: 47 μm. Since the detectors are identical, this tougher requirement has been adopted for all the detectors.

In fact the expected minimum line width on the centre of detector 1 is 151 μm (see Table 8), because a point source at the centre of the slit is predicted by ray-tracing (including the geometrical factors, §2.2.3.4., and image curvature off axis) to produce a line width of 111±12 μm at 19.0 nm, not 50 μm as hoped (Lidiard, 1991b). This means that at this point the predicted resolution is 0.023 nm and resolving power is 864. For comparison, the absolute limit (given in §2.2.3.) of 0.03 nm (Harrison, Feb. 1991) is equivalent to 210 μm.

2.2.3.2. Reflection grating spectrometer

The grating is spherical, curved to a radius of 1500 mm. It is made of a glass ceramic called 'Zerodur' and coated with gold. 1000 lines mm^{-1} are ruled in an area 10×66 mm, with the blaze angle optimised for 35.0 nm light in the first order (Browning and Lidiard, 1991). 50 mm of the length will be illuminated by the telescope.

The location of a particular wavelength (λ) on the detector on the RC can be found by using the angle at which it leaves the grating (see Figure 16). The equation is:

$$\ell' = 2R\cos\alpha \tag{4}$$

where ℓ' is the chord length of the ray between the grating and the RC of radius R (750 mm) and α is the angle of reflection off the grating, which can be obtained from:

$$n\lambda = g(\sin\theta + \sin\alpha) \tag{5}$$

where n is the order of the line, g is the grating ruling spacing (1000 lines mm^{-1}), θ is the angle of incidence on the grating (84.75°). Using the angle α the size of the image of the slit on the detector face can be calculated as follows. First differentiate equation (5) with respect to θ keeping λ constant. Because n and g are constant:

$$d\theta\cos\theta + d\alpha\cos\alpha = 0 \tag{6}$$

Defining angles $d\theta$, $d\alpha$, distances ℓ and ℓ', slit size s and images s' and s'' as in the diagram (Figure 16), it follows that

$$d\theta = \frac{s}{\ell} \text{ and } d\alpha = \frac{s'}{\ell'} \Rightarrow s' = \frac{s\ell' \cos\theta}{\ell \cos\alpha} \quad (7)$$

$$\text{and } s'' = \frac{s'}{\cos\alpha'} \quad (8)$$

Substituting equation 7 into equation 8 and using the fact that $\cos\theta = \ell/2R$ and $\cos\alpha = \ell'/2R$ so that $\ell\cos\alpha = \ell'\cos\theta$:

$$s'' = \frac{s\ell' \cos\theta}{\ell \cos\alpha . \cos\alpha'} = \frac{s}{\cos\alpha'} \quad (9)$$

This gives the size of the slit image at the centre point of the detector, assuming the detector were tangential to the RC at the midpoint, in which case $\alpha' = \alpha$. This does not include the fact that the grating is of a finite size. This will be added to the image width in the next sub-section.

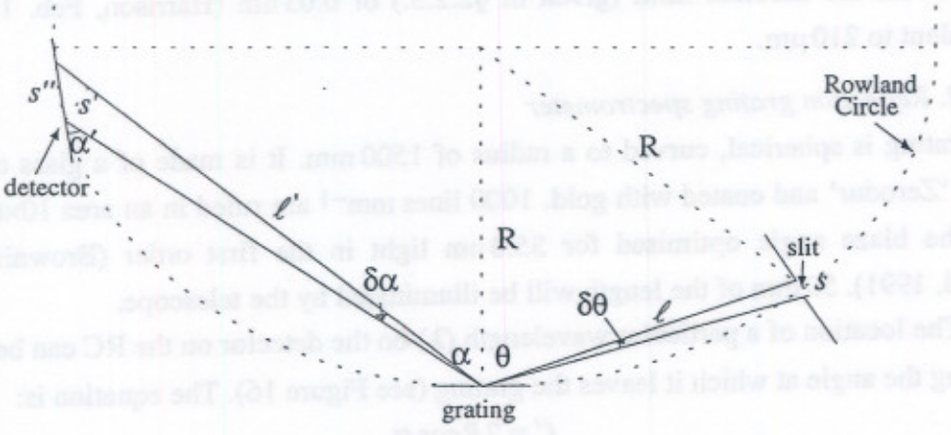

Figure 16. Diagram of the slit, grating, detector geometry.

In addition, the detector is not tangential at the midpoint, but cuts the RC in two places so as to minimise the distance of the detector from the RC along its whole length (§2.2.3.4.), which gives rise to some defocusing. Following on from the equations (7) to (9), let ℓ'_n be the distance from the grating to the detector, where the detector is no longer tangential to the RC, i' be the width of the image parallel to the beam at the position where the detector intersects it and i'' the width of the image on the detector face, so that,

$$\ell'_n = \ell' - \frac{d}{\cos\alpha} \quad \text{and,} \quad i'' = d\alpha . \ell'_n \quad (10)$$

where d is the distance of the front face from the RC. As in equation (7),

$$i' = \frac{s\ell'_n \cos\theta}{\ell \cos\alpha} \quad \text{so that,} \quad i'' = \frac{i'}{\cos\alpha'} = \frac{s\ell'_n \cos\theta}{\ell \cos\alpha . \cos\alpha'} \tag{11}$$

Substituting equation (10) and equation (9) into equation (11):

$$\frac{i''_n}{s''} = 1 - \left[\frac{d\cos\theta}{\ell \cos^2\alpha}\right] \tag{12}$$

which, with the real values for d ($d \sim 200\,\mu m$ at the centre of the detector is calculated in §2.2.3.4.), ℓ, θ and the range of real values for α substituted, gives a range of negligible correction factors between 0.997 and 0.9996.

Now to calculate dispersion, differentiating equation (5) with respect to λ gives the angular dispersion with wavelength:

$$\frac{d\alpha}{d\lambda} = \frac{n}{g\cos\alpha} \tag{13}$$

The arc length l around the RC from the grating to the intersection of the reflected ray is given by:

$$\frac{l}{2\pi R} = \frac{\pi - 2\alpha}{2\pi} \quad \text{or} \quad l = R(\pi - 2\alpha) \tag{14}$$

Differentiating this and using equation 13 gives the wavelength dispersion along the RC:

$$\frac{d\lambda}{dl} = \frac{d\lambda}{d\alpha}\frac{d\alpha}{dl} = \frac{g\cos\alpha}{2Rn} \tag{15}$$

Or it can be re-written as the resolving power:

$$\frac{\lambda}{d\lambda} = \frac{2nR\lambda}{g.\cos\alpha.dl} \tag{16}$$

where dl becomes the resolution element scale. So, for example, with the 127 µm slit image described above, the resolution $d\lambda$ would be 0.0181 nm and the resolving power 1046.

2.2.3.3. Expected image widths

In the previous sub-section the defocusing due to the finite slit width was discussed and the correction factor with the detector displacement from the RC was found to be negligible. However, the defocusing caused by the fact that the grating has a finite illuminated length of 50 mm, is more severe.Tracing a ray from each end of the grating to focus on the RC, as in Figure 17, allows the spreading due to displacement of the detector from the RC to be calculated.

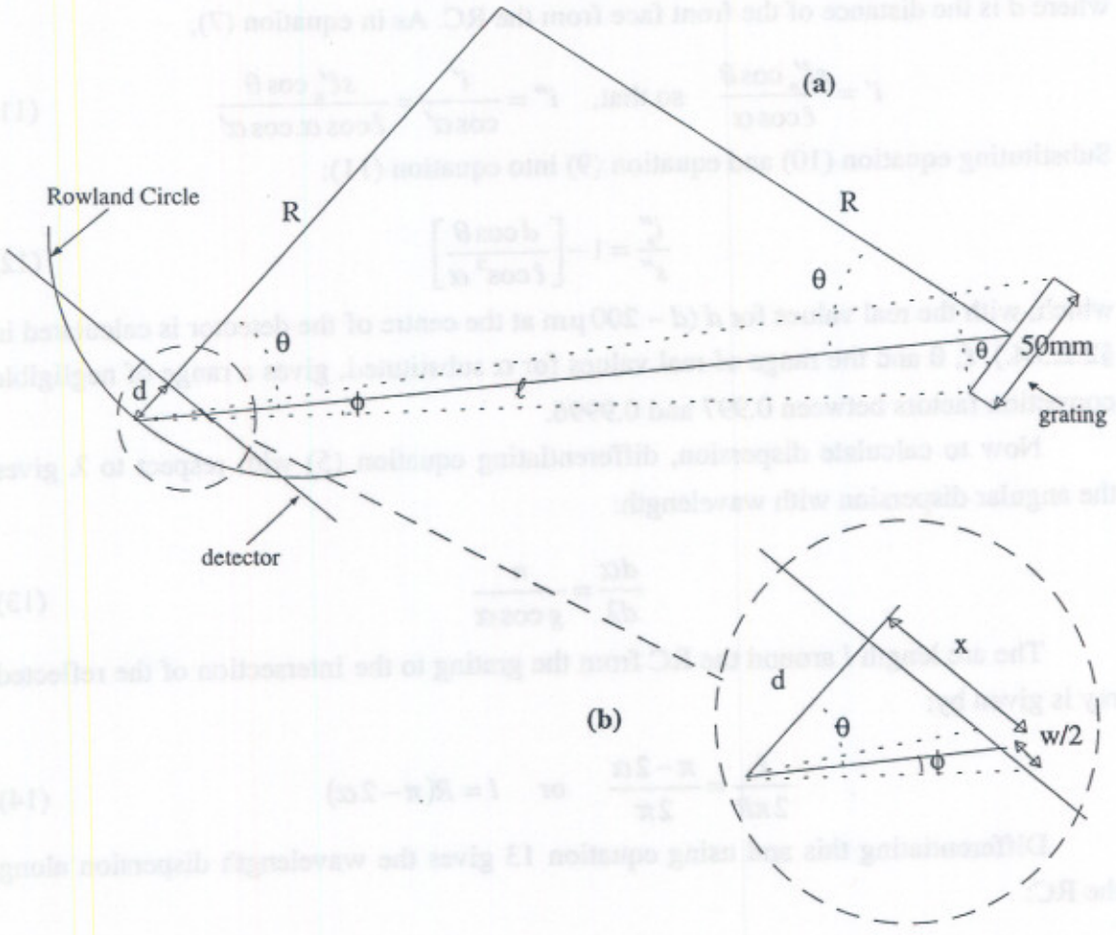

Figure 17. Illustration of defocusing due to the width of the grating (not to scale). w, the width of the image on the detector is the quantity to be calculated. (b) is an enlargement of part of (a).

From Figure 17(a): $$\tan\varphi = \frac{25\cos\theta}{\ell} \qquad (17)$$

From Figure 17(b): $$\tan\theta = \frac{x}{d} \quad \text{and} \quad \tan(\theta+\varphi) = \frac{x+w/2}{d} \qquad (18)$$

Combining these two equations gives:

$$w = 2d\left(\tan(\theta+\varphi) - \tan\theta\right) \quad \text{where} \quad \varphi = \tan^{-1}\left(\frac{25\cos\theta}{\ell}\right) \qquad (19)$$

Section 2.2.3.4. gives d as 208 µm. Inserting values of $\theta = 67.43°$ and $\ell = 575.7$ mm for the midpoint of detector 4, gives $w = 49.0$ µm. For detector 2 with

$\theta = 74.89°$ and $\ell = 390.9$, $w = 108.8\,\mu m$. Detector 1 has a midpoint angle of 77.65° and $\ell = 320.9$, so that $w = 164.0\,\mu m$.

Figure 18 shows the variation in expected r.m.s. line widths falling on the detector front face, depending on their position relative to the detector or the position of the slit.

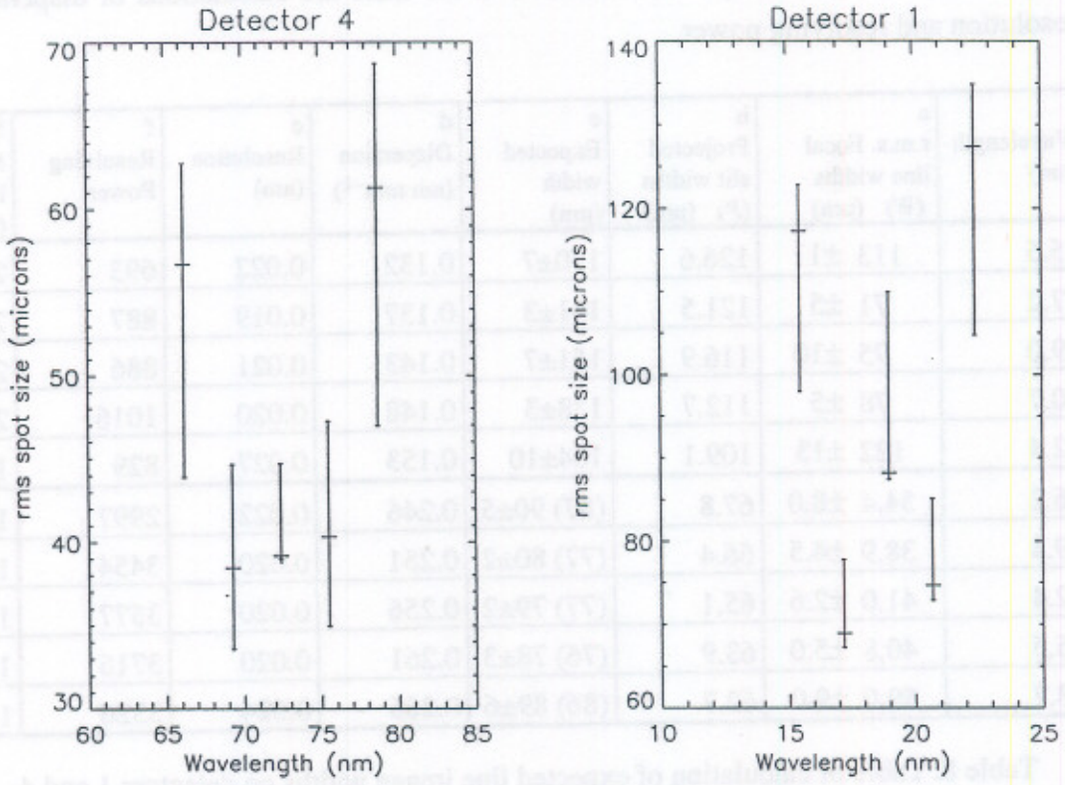

Figure 18. Plot of r.m.s. focal line widths calculated by ray tracing on detectors 1 and 4, taking into account the optical and geometric factors described above. These widths, which are given in Table 8 (column a), do not include slit width or grazing incidence angle. The error bars indicate the predicted spread of widths (to 1σ) in scanning the pinhole between the extremes of its range. Numbers are taken from Tables 2 and 5 of Lidiard (1991b). In these tables, the measurements from the actual grating are used to calculate the widths, not the theoretical grating.

Table 8 sets out the line widths of detectors 1 and 4, starting with the r.m.s. focal line widths found by ray tracing (see Figure 18). The ray tracing (Lidiard, 1991b) combined the effect of the telescope, the geometrical effects of the RC geometry and the detector mounting. For each line the projected slit width was calculated (by means of a computer program) to generate a number for 'expected line width', given the smallest slit. The expected width in column (c) includes the convolution with the detector resolution. For detector 4, the expected width pre-convolution is also included in

brackets to show the effect of the detector resolution. The detector resolution has a negligible effect on the detector 1 widths. Note (in column c) how little effect the detector response has on the effective width of even the narrowest lines.

The expected width can be compared with the upper limit allowed by the CDS specifications (in column g). Also included in the table are calculations of dispersion, resolution and resolving power.

Wavelength (nm)	a r.m.s. Focal line widths (W) (μm)	b Projected slit widths (P) (μm)	c Expected width (μm)	d Dispersion (nm mm^{-1})	e Resolution (nm)	f Resolving Power	g Maximum line width (μm)
15.5	113 ±11	126.6	170±7	0.132	0.022	693	227
17.2	71 ±5	121.5	141±3	0.137	0.019	887	219
19.0	95 ±10	116.9	151±7	0.143	0.021	886	210
20.7	78 ±5	112.7	138±3	0.148	0.020	1016	203
22.4	122 ±13	109.1	164±10	0.153	0.027	829	196
66.2	54.4 ±8.0	67.8	(87) 90±5	0.246	0.022	2997	122
69.3	38.9 ±4.5	66.4	(77) 80±2	0.251	0.020	3454	120
72.4	41.0 ±2.6	65.1	(77) 79±2	0.256	0.020	3577	117
75.5	40.8 ±5.0	63.9	(76) 78±3	0.261	0.020	3716	115
78.7	59.0 ±9.0	62.7	(86) 89±6	0.266	0.024	3326	113

Table 8. Table of calculation of expected line image widths on detectors 1 and 4.

[a] taken from Lidiard (1991b) Tables 2 and 5
[b] using equation (9) and a slit of 25×25 μm
[c] using $\sqrt{W^2 + P^2}$, to give number in brackets, and then convolving with detector resolution of 47 μm.
[d] using equation (15)
[e] using column c × column d
[f] using equation (16)
[g] required upper limit to line width given resolution of 0.03 nm by Harrison (1991)

2.2.3.4. Alignment and construction

Because of the one-dimensional nature of the detectors and the 16 mm high aperture, it is necessary to have very accurate alignment of the anode with the RC spectrum. Using simple geometry, a skew of θ between the anode pattern and the image broadens the image by 16 mm × tan θ, *e.g.* 1 arcmin rotation leads to an additional 4.7 μm width. In addition, any displacement from the circumference of the RC will lead to defocusing.

Note that the effects of the defocusing caused by the tangential rather than curved nature of the detectors has already been taken account of in the ray tracing. Therefore, it is only additional defocusing due to error in mounting the detectors relative to the RC which has to be dealt with in this section.

On detector 4, if it is perfectly positioned in the focal plane (on the RC), the mean r.m.s. focal line width of the point spread function would be 45±5.7 µm FWHM. If the detector were defocused by moving 300 µm along the radius of the RC, the mean r.m.s.. focal line width would become 56±13.3 µm. Parts of the detector would be better focused whereas the focus of other parts would deteriorate, because of the fact that the detector front face cuts the RC in two places; *e.g.* the midpoint becomes 118 µm if the 300 µm is in addition to the 208 µm. For detector 1 a movement of 100 µm increases a 96±15.1 µm mean line width to 107±31.7 µm (Lidiard, 1991b). Both of these are well over the 10% requirement (given in §2.2.3.1). The 10% point for detector 1 is 94 µm radial movement, for detector 4 is191 µm.

Bearing these two alignment constraints in mind, one starts the detector construction by mounting a blank coated anode into the base plate and then cutting the anode pattern with the laser, using the bottom edge of the base plate as an alignment reference. The base plate is pushed up against two alignment surfaces on the HV box and the MCP stack is built up from this. Finally, the flat front face of the MCPs must intercept the curved focal plane of the RC such that the defocusing is kept to a minimum. This is achieved by positioning two round headed studs on the HV box at the calculated intercept points and using a CCD microscope and surface table to match their height to within 20 µm of the MCP surface. These studs can then be pushed up against the RC jig in the instrument or in the test spectrometer (see Figure 19).

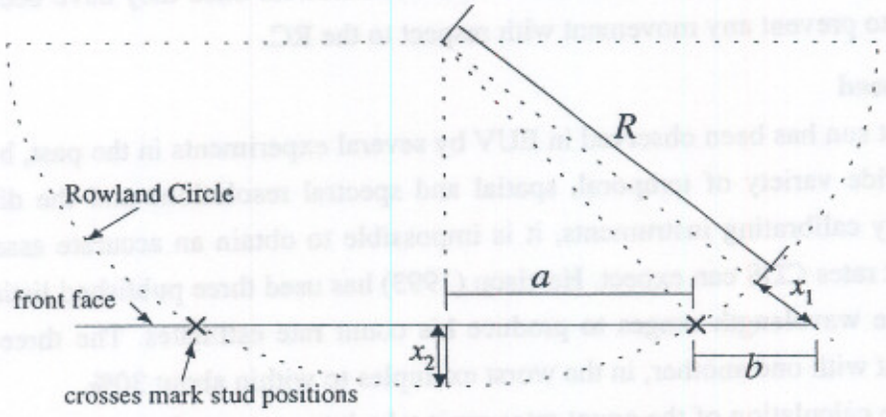

Figure 19. Geometrical alignment of detector front face with RC.
The position of the studs is calculated to minimise the displacement and hence the defocusing of the front face from the RC. *i.e.* the distances x_1 and x_2 are minimised.

To calculate the position of the studs, let:

$$a+b=l \tag{20}$$

Using the smaller right angled triangle:

$$x_2 = R-\left(R^2-a^2\right)^{\frac{1}{2}}$$

$$\Rightarrow a^2 = x_2\left(2R-x_2\right) \tag{21}$$

and the larger right angled triangle:

$$\left(R+x_1\right)^2 = \left(R-x_2\right)^2 + l^2$$

Letting $x_1 = x_2$,

$$\Rightarrow x = \frac{l^2}{4R} \tag{22}$$

Substituting this into equation (21) gives:

$$a^2 = \frac{l^2}{4R}\left(2R-\frac{l^2}{4R}\right) \tag{23}$$

Knowing that $R=750$ mm and $2l=50$ mm, gives:

$$2a=35.4\text{ mm} \quad \text{and} \quad x=0.208\text{ mm}$$

In fact the lengths of the optical paths (which are at approximately 78° to the normal) from the RC to the detector front face should be equalised. If the equations are worked through with this factor in mind, a ratio is obtained of $x_1 = 0.925 \times x_2$. This leads to $x_2 = 216\,\mu$m and $x_1 = 200\,\mu$m, with $a = 18$ mm.

Because the detector has to be electrically isolated from the optics bench, the studs are set back by 0.5 mm with a micrometer after alignment with the MCP surface. A 0.5 mm spacer is then used between the studs and the RC during detector mounting. The detectors are kept in place by means of insulated dowels once they have been mounted in order to prevent any movement with respect to the RC.

2.2.4. Speed

The quiet sun has been observed in EUV by several experiments in the past, but because of the wide variety of temporal, spatial and spectral resolutions and the difficulty of accurately calibrating instruments, it is impossible to obtain an accurate assessment of the count rates CDS can expect. Harrison (1993) has used three published listings spread over wide wavelength ranges to produce his count rate estimates. The three are fairly consistent with one another, in the worst examples to within about 30%.

The calculation of the count rates must take into account the telescope, mirror and grating reflection efficiencies (*qt, qm, qg,* which are approximately 50% for each of the

two reflections, 80% and 3% respectively), the detector QE (*qd*, assumed to be 5%), as well as the area of the sun being viewed by the telescope.

The data published are in the form of intensity, I (ergs $cm^{-2}\,s^{-1}\,st^{-1}$). To convert from ergs to photons, I must be divided by photon energy (hc/λ).

The area of the sun which is being viewed is:

$$A = \frac{abR^2}{f^2} \tag{24}$$

where $a \times b$ are the dimensions of the slit, R is the distance from CDS to the sun and f is the focal length of the telescope. The solid angle is therefore:

$$\Phi = \frac{A}{R^2} \tag{25}$$

The number of photons per second is:

$$Photons.s^{-1} = \frac{I.\lambda.ab.A}{hc.f^2} \tag{26}$$

Now, multiplying by the efficiencies, the count rate becomes:

$$c.s^{-1} = \frac{I.\lambda.ab.A}{hc.f^2} \times q_m q_g q_d q_t \tag{27}$$

Using this method on past quiet sun data, Harrison has estimated that, using a 2"× 2" slit, 63 emission lines will have count rates of between 1 and 5 $c\,s^{-1}$; 14 will have 5 to 10 $c\,s^{-1}$; and 22 will have intensities high enough to give more than 10 $c\,s^{-1}$ (see Figure 77). These numbers will be increased for larger slits and for the active sun. For the wavelengths of detector 1 (shortest wavelengths) and part of detector 2, active region count rate data are not available.

	2"x2"slit Quiet	2"x2"slit Active	4"x4"slit Quiet	4"x4"slit Active	8"x50"slit Quiet	8"x50"slit Active
Detector 1	100	1100	400	4400	10,000	110,000
Detector 2	260	1600	1040	6400	26,000	160,000
Detector 3	30	240	120	960	3000	24,000
Detector 4	20	300	80	1200	2000	30,000
Totals	**410**	**3240**	**1640**	**12960**	**41,000**	**324,000**

Table 9. Estimated total count rates per GIS detector.
Table taken from Harrison (RAL, private communication, 1995). For the first detector, active count rates are simply quiet count rates multiplied by 11 because of a lack of data for this wavelength range.

From the estimated count rates in Table 9 it can be seen that the requirement on an individual detector to cope with 1×10^5 c s^{-1} will probably only be needed for the large slit (8"×50") in an active region. Harrison states that even these count rates could be too high because an active region is unlikely to cover such a wide area of the sun.

The temporal resolution required to look at the formation and changes in *e.g.* spicules is a few seconds. The temporal resolution of the GIS depends on obtaining sufficient counts, in a given time, to form a line profile. This will be limited by the line intensity, lines being dominated by telescope scatter or by bright lines swamping the weaker ones, rather than on the count rate limit of the detectors. The detectors are each able to sustain a non-random count rate of 1.42×10^5 c s^{-1} (see §2.3.4).

All four detectors supply information (events) to the same GIS processor, which deals with each event in accordance with the priority of arrival. The count rate is limited by the rate at which information can be sent to the CDHS (Command and Data Handling System) from the GIS Processor box, which is 8.9×10^4 c s^{-1}. This is only just fast enough to cope with the largest slit with even a quiet sun. A FIFO buffer, 512 events deep, is used to store bursts of events which arrive closer together, allowing short bursts of events at a higher count rate. For higher continuous count rates, data will simply be lost over this limit. Using the smaller slits should meet with no problems with respect to count rate limitations.

The temporal resolution may, however, ultimately be limited by the rate at which the data can be telemetered to the ground from the CDS (see Chapter 7).

For very high point source count rates, the MCPs limit the maximum local count rate and counting linearity of the detectors (§3.4.1). High local count rates (~1 c s pore^{-1}) can paralyse the illuminated areas and can even produce a gain suppression effect for a large surrounding region (Edgar *et al.*, 1989). There is a particularly bright HeII line at 30.4 nm which will fall on detector 2. It is estimated that there could be a count rate from this line of more than 2500 c s^{-1} in active sun conditions with the 2"×2" slit. For the 8"×50" slit it could rise to 250,000 c s^{-1}. The MCP pores are 15 µm apart, hexagonally packed. The area occupied by each pore is therefore 15×15×sin60°. If the line width is 95 µm for the 2"×2" slit (this is the minimum line width, assuming no broadening due to optics), then the number of pores in the top MCP stimulated by the light across the 16 mm height is:

$$\frac{95\mu m\times 16mm}{15\mu m\times 15\mu m\times \sin 60^\circ} = 7800\, pores \qquad (28)$$

Therefore, at minimum, there will be 2500/7800 = 0.32 c s^{-1} pore^{-1}. Wider slits will admit more photons, but would also illuminate more pores. With the 4"×4" slit,

there will be approximately twice as many pores illuminated (depending on the height of the image), but four times the count rate, giving 0.64 c s^{-1} $pore^{-1}$. The 8"×50" slit, however, will have a count rate 100 times that of the 2"×2" slit and will illuminate only four times as many pores. Therefore, the count rate will be 250,000/31,200 = 8 c s^{-1} $pore^{-1}$. So by this analysis gain depression is expected to be a big problem when using large slits.

The next brightest lines are Fe XVI lines; a doublet on detector 4 and a single line on detector 3. These are expected to give up to 400 c s^{-1} with the smallest slit and an active sun. This will be a mere 0.07 c s^{-1} $pore^{-1}$ and should be no problem, with this slit.

Various schemes were considered to reduce the intensity from the bright HeII line, because of the way it will tend to dominate the GIS processing, *i.e.* fewer counts will be observed in the weaker lines because of the dead time surrounding the many photons falling at 30.4 nm. A permanent baffle would be too inflexible, not allowing the count rate from this line to be determined properly even though it is a prime line. As stated above, the greatest restriction on count rate is the rate at which information can be sent from the GIS Processor box to the CDHS. A software baffle would allow a higher proportion of counts from the weaker lines to be sent, but only after the analogue processing, with its associated dead times, has taken place. This would make calculation of real intensities from the observed count rates complicated. It is nevertheless the intention to include software baffles and windowing facilities in the GIS operation code.

Again from Table 9, it can be seen that the minimum count rate any detector is expected to record is 20 c s^{-1}. This was used to decide the requirements on detector dark counts and also on scattered light. The detector background count rate requirement has been given as 'constant but with a variance at less than 0.1c s^{-1} $pixel^{-1}$'. To obtain a variance as low as this, with Poisson statistics, the mean number of background counts per second per pixel has to be greater than 100! A more realistic assessment of the required background is that it has to be low enough for the detection of the weakest line to be observed. The lowest listed count rate expectation is 0.08c s^{-1}. The detector background count rates measured in the laboratory of less than 1 c s^{-1} per detector amply meet the requirement.

2.2.5. High voltage anode

In a space environment, it is highly undesirable to have a sensitive element at a much higher or lower potential than the rest of the spacecraft structure. The front face of the MCP stack is kept near ground potential (−12 V) to avoid a high background due to field emission, ambient or thermal electrons. Low energy photoelectrons from light scattered inside the telescope are repelled by the −12 V bias. Therefore, the anode has to be held

at high positive voltage in order to maintain the accelerating voltage across the plates. The voltage between the front of the MCPs and the anode is variable up to 5 kV with up to 4.3 kV across the MCPs. It allows the potential to be increased to maintain the gain of the plates, which tends to fall with time as charge is abstracted from them.

A switchable front face potential is achieved by connecting HV return, at the end of the resistive bias chain, to ±12 V at the power supply. All detectors are switched together.

Filtering has to be added to stop noise from the HV converter from being carried straight to the anode. A carbon composition 10 kΩ resistor, in series with the HV return, reduces the possibility of HV breakdown pulses damaging the preamplifiers by discharging through signal ground. It is worth noting that the screen of the HV supply cable was originally connected to signal ground, but was removed to prevent breakdown energy from the supply reaching the signal ground. It also had the effect of reducing the noise by preventing ripple from the HV unit coupling capacitively to signal ground. The HV screen is connected to secondary ground in the HV supply unit.

Holding the anode at high potential requires special precautions (see Figure 20). The base plate into which the anode is sunk is made of polycarbonate. The bolts which form the MCP stack pass through holes in the base plate. They are all held at the front face potential, being used to supply this potential, and therefore have to be kept at least 5 mm from the anode, as well as clear of the MCPs. Polycarbonate spacers are used not only to space the MCP back face from the anode but also to form the MCP locators. The base plate has two Oxley pins (silver plated pins with a polycarbonate bush) set in it to carry the voltage to the MCP mid-contact shims. The MCP base contact plate is supplied by a HV wire, which is pushed through a hole in the base contact plate.

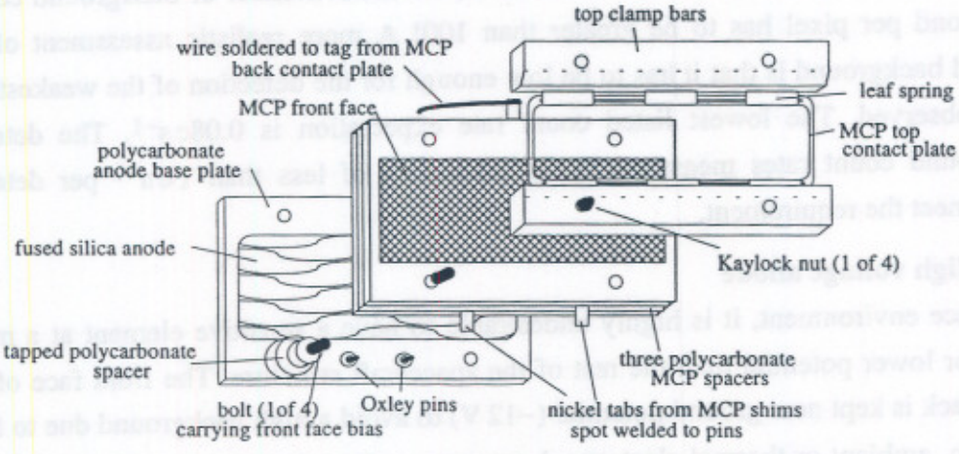

Figure 20. HV breakdown protection of anode and MCPs.

One of the early problems found with using a high voltage anode was that any differential voltage between the electrodes could lead to breakdown from one to another or from the electrodes to the 'anode surround'—the aluminium coating the anode outside the active electrode area. Differential voltages could be encountered during switch-on, if the rise times of the voltages of the electrodes were not equal. To overcome this, pairs of low capacitance diodes with fast switching time and high surge current were employed between each pair of electrodes including the anode surround, to clamp the potentials together.

Two copper strips are set into the base plate behind the anode to act as capacitive (each ~2 pF) stimulators (stims) of the anode and hence the electronics. They mimic an electron cloud arriving at the anode. They are used as an end to end test of the electronics and to provide a repeatable measurement. Their particular advantage is that they can be applied without any high voltage, which allows testing at atmospheric pressure. This was used extensively during System Functional Tests on the instrument and after integration with the spacecraft. The stims are kept at ground potential, but the anode cannot break down to them because of the 3 mm-thick fused silica of the anode between them. A problem did occur, however, in one of the flight detectors where gas was trapped in the pocket housing the stims behind the anode plate. Under vacuum, the gas pressure in this volume dropped to a pressure at which a high voltage discharge can be maintained. The high voltage tracked across the surface of the polycarbonate, through the gas, from the edge of the anode to the stims. This problem was solved by providing additional holes in the base plate for outgassing.

Inside the HV and preamplifier boxes, clearances and insulation are very important. The sides of the boxes near to any high voltage component are protected with two layers of 0.005" kapton sheet, which is fastened down with kapton tape. This provides insulation up to 5 kV (2.5 kV per layer). Screened HV wire (CSSH 7/0.2mm) is used to carry signal from anode to preamplifiers. Other non-screened HV wire is used whenever it has to lie near a pillar of much higher or lower potential than itself. Local epoxy encapsulation is used on exposed areas of high voltage. In addition, the detector electronics are conformally coated to protect against particulate contamination, although this step was not taken without due consideration of the potential outgassing of the conformal coating into the optics bench where a very high degree of cleanliness is required. It was concluded that the benefits outweighed the risks for very small amounts of epoxy.

Additional protection will be provided in flight by the GIS processor, which reads the current drawn by the MCPs every two seconds. If the current exceeds a

programmable limit, the HV to that detector is tripped out. This will occur if there is a breakdown or a sudden burst of out-gassing. It will also provide protection against very high count rates caused, for instance, by an energetic solar event, provided the current limit is set close enough to the normal operational value.

2.3. ELECTRONICS

2.3.1. Detector encoding electronics

At any position along a SPAN anode (explained in detail in Chapter 5), the ratio of the charge collected on one electrode to that collected on another electrode is unique, provided they are both normalised. Measurement of the charge on two electrodes is therefore sufficient if the third is used for normalisation.

As described briefly in §2.1.1., after the charge from the MCPs is collected by the electrodes, it is converted into a voltage step by charge-sensitive preamplifiers and measured and normalised by ratiometric ADCs. Finally, the two numbers are passed to the LUT, which gives the one-dimensional location of the event. The sum is digitised separately to be used directly for building up a PHD.

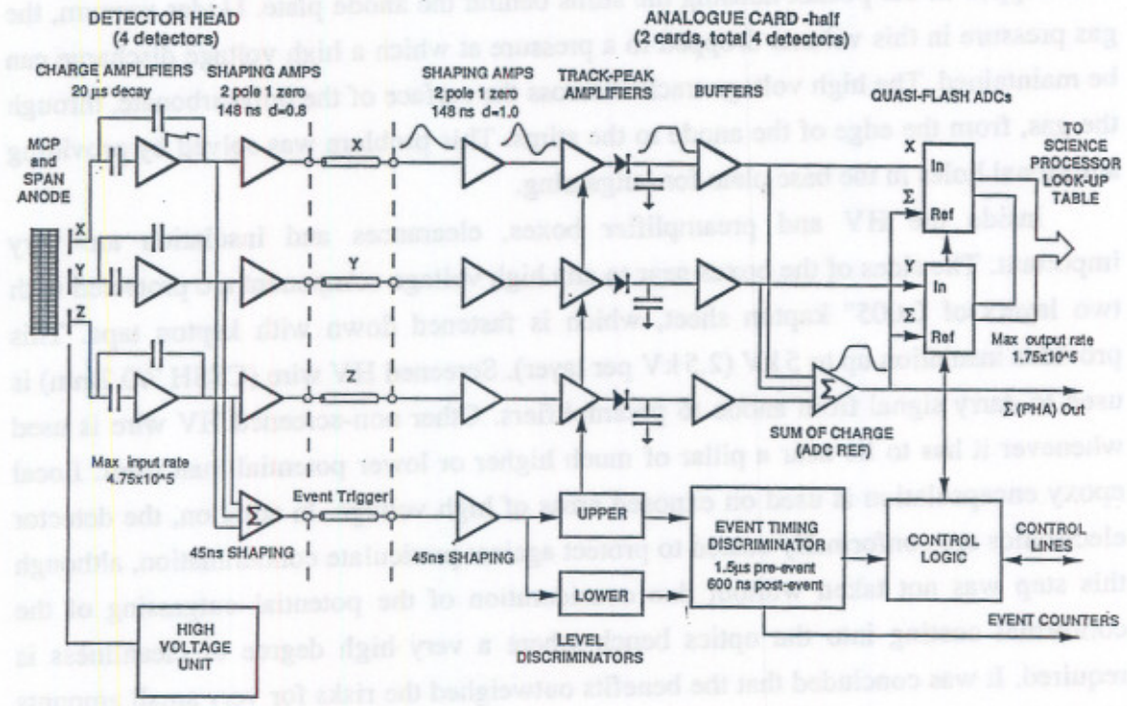

Figure 21. Diagram of the GIS processing electronics (from Thomas, MSSL). This figure shows the how the signal from the detectors is converted to values to be used in the LUT.

Figure 21 is a diagram of the analogue electronics, designed by Thomas, MSSL. Each detector has its own set of digital electronics, including a unique LUT. Each analogue card services two detectors and is therefore divided into sides A and B. After amplification and shaping, the charge pulses are peak-detected and summed. The *sum* signal drives the reference input of two low power (approx. 50 mW) 8-bit quasi-flash ADCs (MP7683). Quasi-flash means that the measurement is made in two steps, first the 3 most significant bits, then the 5 least significant bits. This requires the signal to be held steady for the minimum conversion time (1 µs). A peak and hold circuit is therefore used.

The preamplifier rise time is 19–25 ns with a 25% overshoot. Settling to 1% takes 150 ns and the decay time constant is 20 µm. The second stage of shaping has a time constant of 145 ns. The shaping scheme is bipolar, to give auto-baseline restoration, removal of drifts and offsets in the electronics and rejection of charge amplifier decay characteristics. An event-trigger channel provides the timing for the circuitry. For this, the outputs of the charge amplifiers are summed in a fast shaping amplifier. This event-trigger channel has a two pole, two zero characteristic and a shaping time of 45 ns, producing a fast bipolar pulse. Events less than 50 ns apart (measured) are rejected by the ULD.

The PHD is windowed by use of low and high level discriminators to remove invalid events: that is to say, those generated by noise or background from the low energy end or double events which appear at the high energy end. Use of the discriminators and a narrow PHD ensures that all events have good signal to noise ratios and that the denominator stays approximately uniform for the signal-processing electronics.

The use of ratiometric ADCs means that the digitisation level is not dependent on the pulse height, but on the position of the event on the anode. The true *sum* signal is reduced by 5/9 to shift the spiral image towards the upper part of the ADCs, giving an apparent ADC range of 0 to 460. Figure 22 shows the range of the ADC values used by the anode. Nearly all events are digitised to a level better than 7-bits, which is half way along each axis at (230, 230).

The LLDs are charge thresholds, programmable to 8 levels between 1.4×10^7 and 3.5×10^7 electrons. The actual values vary slightly between analogue cards. Each event reaching the LLD is counted as a 'raw event'. The ULD is fixed at 8×10^7 electrons. Events which are large enough to achieve this level are rejected and counted. After the analogue processing, normalised data passes to the science data processor including the LUT (designed by McCalden, MSSL). The science data processor also independently

counts the number of accurately digitised events, the 'processed events', which is approximately the number of raw events, minus the ULD events.

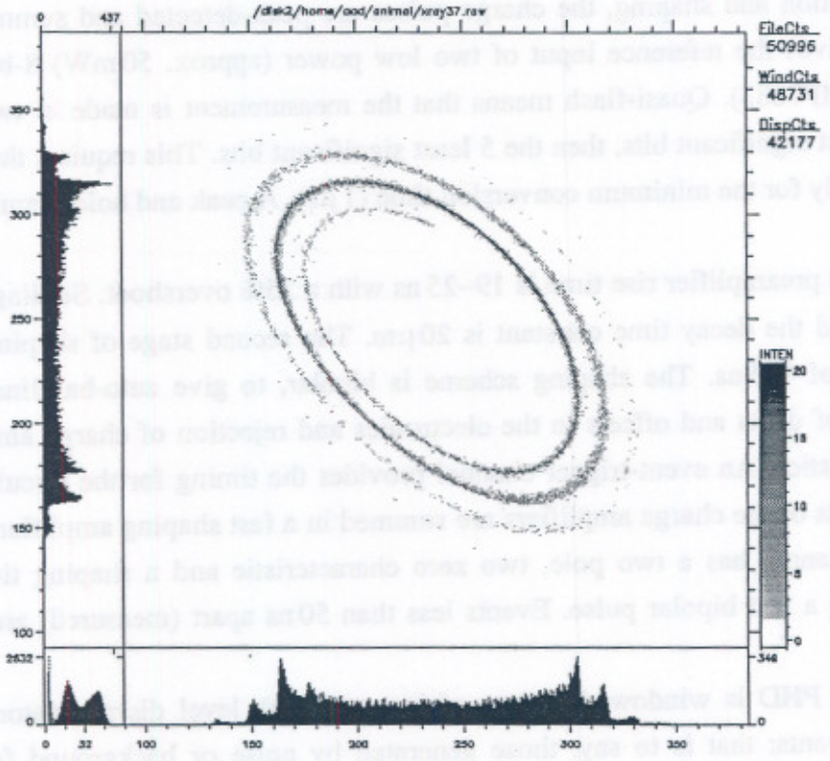

Figure 22. Spiral image plotted in normalised co-ordinates.
The *x*-axis gives the value from the *A/Sum* ADC, the *y*-axis being the *B/Sum* ADC

The two copper stims which are set into the base plate behind the anode can be stimulated with pulses of 1 to 5 V, programmable in 256 steps, at a constant rate of $\sim 1.3 \times 10^4$ c s^{-1}. The capacitive coupling with the anode, through the fused silica of approximately 2 pF, provides signals from two known positions. The stims provide an extremely accurate assessment of the LUT, as the positions of the two lines per detector can be predicted in advance to within a couple of pixels for a given LUT. The stim signals can even be split by varying the LUT to give 'ghosts' in known positions.

2.3.2. Linearity

A mean MCP charge gain of 3 to 4×10^7 with a PHD FWHM of less than 100% makes optimum use of the ADC dynamic range, minimising contributions from ADC integral and differential non-linearities. The dynamic range at the DC reference input is 0 to 2.5 V, with a pulse of 3×10^7 electrons giving 1.5 V. The requirement on the ADCs was to allow no more non-linearity than ±0.5 of the least significant bit (LSB).

The ADC is basically a circuitry system which takes an analogue pulse from an amplifier and classifies it, based on its pulse height, (corresponding to the number of electrons), as belonging to a given channel. The ADC channels have a definite width, expressed in volts, which corresponds to the amplitude range within which all pulses get classified to the same channel.

The ADC transfer characteristics may be represented as a staircase plot as shown in Figure 23. Integral linearity represents the overall linearity of this staircase—that is the proximity of the centre points of all the steps to the straight line. Differential linearity reflects the equality of all the step sizes with respect to each other. It may be seen from the diagram that good integral linearity may be obtained even with poor differential linearity because short and long steps may compensate each other, resulting in an overall straight line.

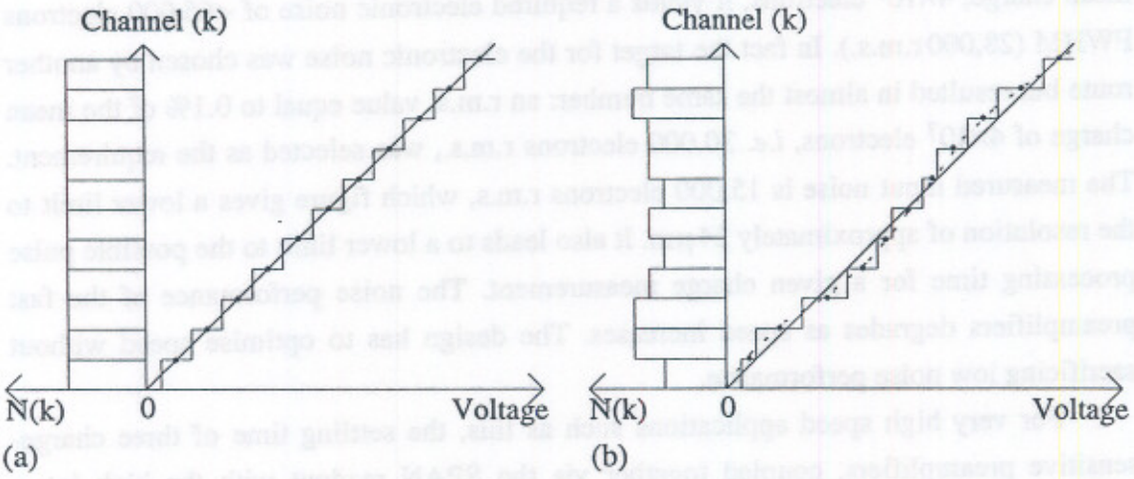

Figure 23. Diagram of ADC characteristics.
Each step represents horizontally the voltage intervals and vertically the channel number (k). Plot (a) has perfect linearity, whilst plot (b) has non-linearity. The histograms on the 'channel' axes give the number of events in channel k, N(k), showing how the DNL would affect a flat field. The dotted line through the steps on plot (b) represents the INL.

If the width of a given channel (step) is greater than that of the mean channel, then there will be more pulses classified in that channel than intended and, in the same way, fewer pulses will be appointed to narrow channels. The effect, illustrated in Figure 23(b), is to distort the spectrum. It may lead to ghost peaks or distort the shape of real peaks. This matter is particularly important when one is measuring low-intensity lines in the presence of a strong background or when looking at line widths or shifts.

For GIS, the ADC DNL has been measured statically as ±0.45 LSB (max.) and INL as no more than ±0.2 LSB. This folds into a projected detector DNL of ±0.02% and an INL of no more than 10 µm.

2.3.3. Noise and crosstalk

Amplifier noise is dominated by inter-electrode capacitance. If the anode pattern is enlarged, or the repeat pitch reduced, the capacitance increases and the amplifier noise dominates. Some other detectors overcome this by linking small patterns as a mosaic with a consequent increase in the number of electronics channels required (Rasmussen and Martin, 1989).

The maximum signal from any one SPAN electrode is 5/9 of the total signal from the three combined electrodes. This occurs at just one position along the spectral axis. When this figure is combined with a signal to noise ratio of greater than 1 in 256 and the mean charge, 4×10^7 electrons, it yields a required electronic noise of <65,000 electrons FWHM (28,000 r.m.s.). In fact the target for the electronic noise was chosen by another route but resulted in almost the same number: an r.m.s. value equal to 0.1% of the mean charge of 4×10^7 electrons, *i.e.* 30,000 electrons r.m.s., was selected as the requirement. The measured input noise is 15,000 electrons r.m.s, which figure gives a lower limit to the resolution of approximately 24 µm. It also leads to a lower limit to the possible pulse processing time for a given charge measurement. The noise performance of the fast preamplifiers degrades as speed increases. The design has to optimise speed without sacrificing low noise performance.

For very high speed applications such as this, the settling time of three charge-sensitive preamplifiers, coupled together via the SPAN readout with the high inter-electrode capacitance, can be significant. The capacitance for SPAN is about 200pF between one electrode and both its neighbours connected. Capacitance to ground is 128–135 pF. The inter-electrode capacitance (between one electrode and all the others, including the electrode contact wires) is about 320 pF. The use of a low dielectric constant material for the anode substrate, *i.e.* quartz, as well as keeping the conductive coating as thin as possible, minimises the capacitance..

Signal crosstalk, which is proportional to inter-electrode capacitance and the effective input impedance of the preamplifiers, reduces the dynamic range and hence the resolution. This problem occurs particularly at high speeds, as crosstalk is affected by charge amplifier rise time, dynamic capacitance and shaping time. A rise time of less than 25 ns with 25% overshoot and a dynamic capacitance of at least 50 times the inter-electrode capacitance (>15 nF) yields a crosstalk of between 1.5 and 3%, which is within the 4% set in the Performance Specifications (Thomas and Breeveld, 1993) and has

virtually no effect on position encoding. These values have been confirmed by measurement.

In the early designs, the detector housing was grounded to the optics bench (chassis ground) and was isolated from signal ground. However, the signal ground picked up noise from the chassis ground. To minimise this pick-up of common mode noise at the detector front end, the detector housing was instead connected to signal ground potential. The housing therefore had to be isolated from the rest of the instrument by a 1 mm thick epoxy glass-fibre cushion between the detector and the optics bench, which gives approximately 100 pF (measured) isolation capacitance. The studs, which were intended originally to be pushed up against the optics bench RC jig, are set back 0.5 mm from it, so that a spacer has to be used in setting up.

To minimise common mode noise currents, the harness must have a low impedance compared with the capacitance between the detector and ground. At a frequency of 1 MHz, from the 145 ns shaping time constant, the total reactance of the isolation and harness capacitances is at least 10^3 times the harness series impedance.

2.3.4. Throughput

The SPAN anode with 8-bit ADCs, together with the on-board LUT, is designed to achieve individual detector count rates of $1\times10^5\,c\,s^{-1}$. A real-time calculation of the event locations directly from the three electrode outputs, by means of the SPAN algorithm, would be prohibitively time consuming. All the calculations are done in advance and loaded into the LUT so that obtaining the position is merely a question of looking up the answer using the ADC outputs as an address.

Following an event, the pulse amplifiers require a certain time to recover. If a second event occurs during this period and no pile-up rejecter is employed, the calculated co-ordinates will be perturbed by the remnant of the previous event. If a pile-up rejecter is employed, the image quality does not suffer, but the count-rate dependent dead time correction will be larger.

The analysis by Becker *et al.* (1981) of throughput and its relationship to dead time in signal processing can be applied in this case. The analogue processing has two inherent dead times. The first is the pre-event dead time T_w which allows for settling of the shaping amplifiers (and prevents pulse pile-up). The second is the post-event dead time T_p which prevents pile-up in the peak-detectors while analogue to digital (A to D) conversion is in progress. If any event occurs within T_w or T_p after the current event, both the current event and the new one are invalidated and the dead time will be extended a further time period T_w or T_p. It is therefore referred to as an 'extending dead

time'. As the A to D conversion itself takes place after the event (during T_p), it does not contribute further to the dead time.

In the GIS detector system, the settling time constant T_w is 1.7 µs, with a filter centre frequency of 1 MHz (145 ns). T_p is 900 ns, resulting in an additive extending dead time of 2.6 µs. For extending dead times, the theoretical output rate follows the law:

$$R_o = R_i . e^{(-R_i . T_d)} \tag{29}$$

where R_i is the input rate, R_o is the output rate and T_d is the dead time ($=T_w+T_p$). The graph of equation (29) is plotted in Figure 133.

Differentiating R_o with respect to R_i and setting it equal to zero to find the maximum output count rate:

$$\frac{dR_o}{dR_i} = (1 - R_i T_d) e^{(-R_i . T_d)} = 0 \quad \Rightarrow \quad R_i = \frac{1}{T_d} \tag{30}$$

With T_d at 2.6 µs, $R_i = 3.85\times10^5$ c s^{-1}, allowing a maximum random output count rate of 1.42×10^5 c s^{-1} per detector: a factor ($1/e$) of the input rate. There will be a gradual reduction for input count rates above this and eventually pulse pile up will occur. At the required maximum input count rate of 1×10^5 c s^{-1} there is a loss of 23% resulting in an output count rate of 7.7×10^4 c s^{-1}.

The science data processor is composed entirely of logic circuitry and is therefore extremely fast. A parallel-to-serial conversion is performed on the data prior to transmission to the CDHS at a maximum rate of 8.9×10^4 events per second, which is then the total for all four detectors. As this is the slowest part of the procedure, the LUT feeds a first-in-first-out (FIFO) buffer, 512 events deep and 11 bits wide, which provides a de-randomising buffer between the random detector events and the serial science data interface to the CDHS. For a purely random input, the FIFO will be empty most of the time at input count rates of less than the output rate. At an input rate of 8.9×10^4 the FIFO will have a maximum of 12 events in it at any one time. Over this rate, the FIFO rapidly becomes full.

The first of the four detectors to have a valid event, sends a signal to a 'one of four buffer' which selects the detector, allowing it to transmit its event data to the FIFO. This takes 600 ns. In the meantime, approximately 200 ps after the event was indicated by a data valid high from the detector, an acknowledge signal is sent to all four detectors to reset them ready to receive another event. Thus the data is selected according to the order of arrival. The processed event is counted when the data valid line from the detector is set high. Therefore if more than one event arrives within 200 ps, both can be counted, although neither of them will be processed. This can lead to discrepancies

between the count rates transmitted and the sum of the valid counts in the science stream (see discussion in Chapter 6).

2.4. SIMULATORS

One very important aspect of building instruments for space flight is the construction of sufficient simulators, for instrument testing and development. Every piece of equipment needs to be simulated as simply as possible in hardware or software, either by use of commercially available equipment (*e.g.* laboratory power supplies) or specially built. The reason for this is to allow testing of sub-units independently without necessarily needing all the flight equipment to be ready at the same time and in the same place. It allows parallel work on different aspects of the instrument. It can high-light problems long before integration takes place, giving time for remedial action. Sometimes, several simulators are required for different aspects of the same item, for the testing or setting up of a particular mechanism.

Simulator	Use	Developed at MSSL by:
GIS_SIM	Software model of whole detector system	Breeveld, Edgar, Smith
Charge Cloud Model	Software model of interaction between MCP output with anode	Breeveld
Stim Capacitive Probe	Stimulation of anode with capacitive probe	Breeveld
Pseudo-random detector simulator	Four simultaneous pseudo-random signal channels	Thomas
DET_SIM	Software and hardware detector simulator	Chun, Thomas
ALLSINGN	Data acquisition and analysis program	Edgar, Breeveld
IDL LUT programs	Data display and LUT parameter programs	Breeveld
CDHS and EGSE simulator	Transputer based simulator	McCalden
SDDA	Science data display adapter for displaying data from GIS box	Chun

Table 10. Summary of simulators directly involved with detector development.

2.4.1. Software detector simulators

Early on in the project much was learnt by writing a software model of the whole detector system. This is a PC-based simulator known as the GIS detector simulator (*GIS_SIM*). It was used to show how every part of the system is related and how the whole GIS system would work from photon to output spectrum. Secondly, it showed

how, for example, electronic noise in the preamplifiers or non-linearity in the ADCs would affect performance. It allowed specific predictions of performance for expected or measured error configurations and thus aided in assigning requirements to the design of various sub-units. The simulator is based on a Monte Carlo approach and, as far as possible, incorporates actual measurements. For instance, the pulse height distributions are taken from one of the development detectors.

The Charge Cloud Model was written to help with the design of the anode itself. It simulates the interaction between the charge cloud from the MCP with the anode. Using the dimensions of a charge cloud thought to be typical, the anode parameters could be varied until the happy medium between 'modulation' and 'spiral size reduction' had been found.

These two computer models and results from them are described in Chapters 5 and 6.

2.4.2. Hardware detector simulators

One of the first hardware simulators was an anode stimulated with a small capacitive probe connected to a pulse generator, the pulses simulating real events. The probe could be moved along the anode and data read out through the analogue card with an analogue test box connected to the PC for data capture and display. This allowed an early test of the anode design and analogue electronics. The same simulator was also used for the first test of the LUT and the GIS processor box.

An alternative was a pulse generator connected via a three-way splitter and attenuaters and capacitors (to simulate variable electrode signals) and thence to a set of preamplifiers, analogue card *etc.* This way pseudo-events could be precisely controlled and pulse heights known. This was useful for setting up preamplifier gains to match each other and in calibrating the analogue electronics. It was also useful in timing experiments.

The Pseudo-Random Detector Simulator supplied a repeated pattern of events simultaneously to all four channels. This was used in the testing of the GIS processor box and again in timing experiments.

In *DET_SIM,* event values, based on a user defined spectrum or pattern, are selected randomly in software on a PC. The user can choose the gain of the PHD, the rate of events and whether to have a flat field or events at a single position. The event information is then converted into real event signals via a digital to analogue converter and shaping amplifier circuit. So far two channels have been completed and it has already been useful for testing the Flight Spare (FS) and Engineering Model (EM) instrument. It will be the only way of simulating any problems seen during flight, as

there will be only one detector on the GIS EM, which is going to be kept operational throughout flight.

2.4.3. GIS processor box simulators

The *GIS_SIM* software model described above includes the simulation of the LUT on-board generation and subsequent use. The Occam code used in the GIS processor box is based on the code in this model.

The development and Research Model (RM) detectors are run using laboratory electronics (Ortec preamplifiers, NIM shaping amplifiers and three ADCs), the output of which is bussed to a PC. The PC reads in the three ADC values and plots the events in a choice of formats. The data acquisition and analysis program is known as '*ALLSINGN*' and is described in detail in Chapter 4. This configuration was also used for operating the detector in the Optical Calibration tests at RAL, avoiding the need for the flight-style processor electronics to be available. Another version of *ALLSINGN* can be used with the flight analogue electronics and test box, without the flight processor.

More recently, a suite of software has been written in IDL to perform the duties of plotting the raw data in a number of ways and simulating the LUT itself. It does not perform data acquisition. It was particularly useful in sorting out problems with the on-board LUT writing code. This software will be available with the EGSE (Experiment Ground Support Equipment) during flight.

2.4.4. CDHS and EGSE simulators

An important simulation to test the on-board software for detector commanding and science collection, in the absence of the real CDHS and EGSE, used a transputer development system. The display of the spectra from the on-board LUT which would normally be done by the EGSE was provided by the Science Data Display Adapter (*SDDA*). This program displays the output from all four detectors on one screen or one detector at a time. Every channel (numbering 2048 per detector) is displayed. Count rates for each channel are calculated, taking into account the dead time caused by the PC and can be read out using the cursors. Spectra can also be printed out.

Using the CDHS and EGSE simulators, together with the *SDDA*, it was possible to simulate the whole procedure for obtaining spectra when in flight (see flow diagram Figure 146).

2.5. DETECTOR CHARACTERISATION PLAN

Any measurement of the spectral line intensity has to be corrected for electronic dead time, losses from the LUT, gain depression, detector dark count and scattered background. The wavelength calibration, linearity and the line profile are affected by

fixed patterning, non-uniformity, electronic non-linearity, the LUT and any pulse height dependent position effect. For the science data to be useful therefore, all these effects have to be well understood. The purpose of the detector testing was to assess some of these characteristics, such as the effects of high count rates on the electronics and MCPs and to quantify the effects of photon energy and angle of incidence.

1.	Rowland Circle → MCP surface	
	Mechanical Alignment	2.2.3, 4.1.3
	Slit size	4.1.3
2.	MCP surface → Anode Surface	
	Gain and PHD variation with voltage	3.2.3
	Background events	4.2
	Uniformity	4.3
	Count rate linearity	4.4. 3.4
	Efficiency variation with wavelength	4.5
	Efficiency variation with angle	4.6
	Electron cloud distribution	6.1.4, 6.1.5
	Life Test	4.7
3.	Anode → Analogue Electronics Output	
	Capacitance of anode	2.3.3
	Linearity	4.3
	Electronic noise	2.3.3, 4.8
4.	Analogue Electronics → ADC output	
	ADC Integral non-linearity	2.3.2
	ADC Differential non-linearity	2.3.2
5.	ADC output → Final Spectrum	
	Fixed patterning	5.1.4
	LUT	5.1.2
6.	Final Output	
	Resolution	6.4.2
	Differential and Integral non-linearities	6.4.3, 6.5
	Throughput (global maximum)	6.4.4

Table 11. Outline of characterisation tests.
The right hand column gives the thesis section where the results of tests I performed are given or discussed.

The concept for the characterisation plan (Breeveld, 1992) was to examine transformations at each interface in the detector, (*i.e.* from photons to electrons, to voltage signals, to LUT addresses), as well as end to end calibration, from U.V. spectral lines to the output spectrum.

Two detectors, two sets of electronics and two vacuum chambers were involved in the characterisation. The QM detector was mounted with flight-style electronics, either in the clean room, on the RC with the UV discharge lamp as illumination, or in the laboratory, with the mercury Penray lamp providing a flat field. The RM detector was kept in the clean room on an X-Y-rotary table on the RC. It could be used with either flight-style or laboratory electronics, and could be moved across the light beam to simulate a flat field. Masks were designed and used on either detector for the various tests. Table 11 lists the tests incorporated in the characterisation plan.

CHAPTER 3.

USING MICROCHANNEL PLATES TO DETECT UV

Microchannel Plates are chosen for Extreme UV, Far UV and soft X-ray astronomy because of their ability to detect single photons (*i.e.* potentially weak sources) efficiently with low photon energy (long wavelengths, up to 180 nm). They can provide high resolution, both spatial and temporal, low background and low non-uniformity. MCP detectors can be made with a relatively large sensitive area, up to 100 mm diameter.

MCPs were first made in the 1960s as a development of the Channeltron[1] (channel electron multiplier or CEM) technology and as an extension to the discrete dynode photomultiplier tubes (Leskovar, 1977). Development was made possible by research into secondary electron emission and also the technique of baking lead glass in a reducing atmosphere at high temperatures, producing in the glass a semiconducting resistive surface just a few microns thick. Fibre drawing techniques, developed for the manufacture of fibre optic devices, allowed the glass tubes to be made very thin (as small as 8 μm diameter) (Wiza, 1979).

This chapter starts with an overview of MCPs introducing the main concepts. The following section describes my choice of MCPs and their configuration for GIS including some results from my experiments and other authors' models of MCP gain. The conclusion takes the form of a discussion of two MCP properties of particular interest: quantum efficiency and count rate linearity (gain depression). My own experiments on these two topics are given in Chapters 4 and 6.

3.1. MCPS—OVERVIEW

The MCPs selected for GIS have already been described in Chapter 2. More detail is now given about MCPs in general, starting with a description of their predecessors, CEMs.

CEMs (see Figure 5) are glass tubes with a resistive coating on the inside, typically 1 mm in diameter, by 5 mm long, (Adams and Manley, 1965). The resistive tube acts like a continuous dynode (see Figure 24). When a high potential is established

[1] "Channeltron™" is a registered trademark of Galileo Electro-Optics Corporation, USA

between the ends of the tube, any secondary electrons generated at the low potential end by incident radiation are accelerated down the tube until they strike the wall again, generating more secondaries. Thus, a cascading process is started, which results in the emergence of a large cloud of electrons (up to 10^8), from a single photon event.

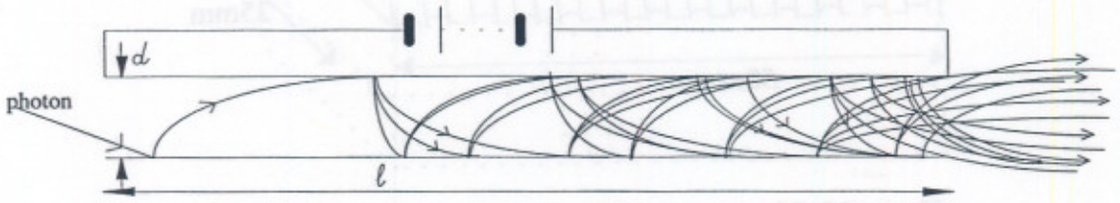

Figure 24. Operation of single-channel electron multiplier taken from Mullard (1976).

The number of electrons produced per event is a function only of the length to diameter (*l:d*) ratio and voltage down the tube, but not of the size of the tube. The dimensions can thus be scaled down to make a smaller device with better spatial resolution, limited only by manufacturing technology. A Microchannel plate consists of an array of millions of short, straight channeltrons or continuous dynodes, all bonded closely, parallel to each other and arranged in a hexagonal lattice pattern (see Figure 25). Each channel is like a CEM: the high resistance semiconductive layer has a secondary emission coefficient of 1.1–3.5, (Leskovar, 1977). The channels or 'pores' typically have diameters between 10 µm and 100 µm and length to diameter (*l:d*) ratios between 40 and 100. A plate with an *l:d* ratio of 40 is known as a 'single thickness plate'. MCP channel axes are often biased at a small angle, typically 8°, to the normal to the surface.

Conducting coatings on the front and rear surfaces allow a bias voltage (around 1000 V) to be applied to the channels in parallel, providing a potential gradient along the length of the channels. A photon arriving at the MCP surface and interacting with the inside wall of a channel releases a photoelectron which, as with a CEM, is attracted and accelerated down the tube by the electric field. If the electron gathers sufficient energy (20–50 V) between each collision with the wall, secondary electrons are emitted from the wall surface, until there are enough electrons to detect as a pulse of charge. From a single-thickness plate with 1000 V bias, one would expect 10^3 to 10^4 electrons. Simultaneous events can be amplified by the plate, although in the case of an MCP stack, they may not be distinguishable if they are closer than about 1 mm, because of the spread of the electron cloud in the bottom plate. The readout usually limits the rate of simultaneous event detection. A second event arriving in the same location before the channel has fully recharged may not be detectable.

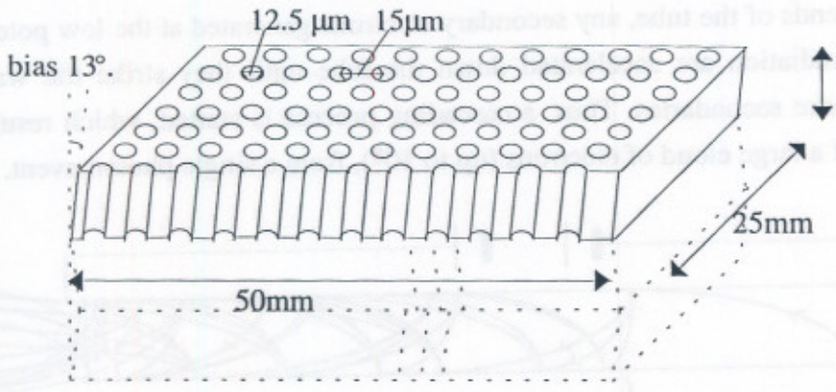

Figure 25. Diagram of a GIS microchannel plate (not to scale).
Three channel plates like this one are used in each detector, arranged in a '*z*-stack' with the bias angle in alternate directions. The dotted lines indicate the positions of the lower two plates. The top one here has been sectioned in order to show the channel structure.

3.1.1. Manufacture

The manufacturer starts with a number of thin-walled lead glass cylinders containing soluble cores of soft glass (see Figure 26). The core is required to stop the cylinder from distorting and collapsing. Glass (50% PbO, 40% SiO_2 and several alkali oxides) is used because techniques involving it are well known, the process is very repeatable and the channels are regular in size and internal diameter. The cylinders are drawn to a small diameter (from *e.g.* 35 mm to 0.8 mm) and then cut, stacked and fused into a bundle, called a hexagonal multi-fibre, which is itself re-drawn to 0.8 mm. Many of these bundles are then stacked together and fused into a larger bundle called a boule, which is sliced into thin wafers and polished. The cores are etched away leaving the microchannel plate structure. Enhanced resolutions can be obtained by reducing the pore size. Small format MCPs with 4 and 6 µm channels have been made (Laprade and Reinhart, 1989).

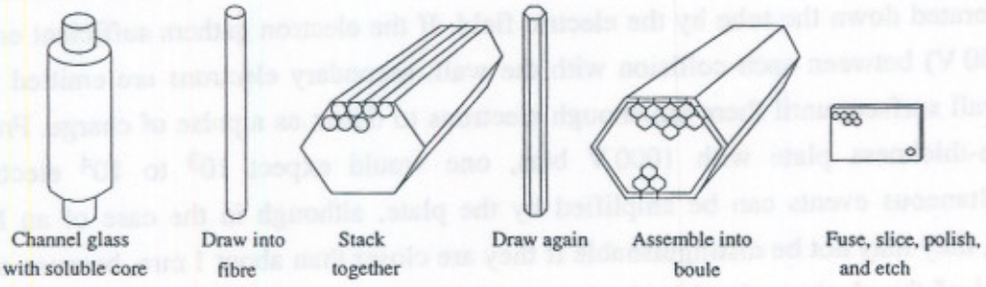

Figure 26. Steps in the manufacture of microchannel plates.
Picture adapted from Mullard (1976).

The plate is made partially conductive by removing the oxygen from the lead by heating for a few hours at 250–450°C in a hydrogen atmosphere. Finally, the channels are electrically connected in parallel by vacuum-depositing Nichrome (a nickel chromium alloy) or equivalent electrodes onto both sides. The film fills the space between the channels, but leaves the mouths or pores of each multiplier open. Most of the reduced lead evaporates from the surface. The rest coalesces into metallic clusters which gives the characteristic black colour. The resistance of one channel can be in the range 10^8 to $10^{14}\,\Omega$ (Guest, 1971b). MCPs with specially low resistances are manufactured for high count rate measurements (see §3.1.5).

3.1.2. Pulse height

The gain of an MCP is the ratio of the output current to the input current. If only one initial electron is assumed, the gain is the number of electrons in the output charge cloud. The incoming photon can be thought of as equivalent to one electron so that the meaning of the term 'gain' is consistent.

The number of electrons in the output pulse varies from event to event, because of the statistical uncertainty inherent in secondary electron emission and the depth of the initial photon interaction. Of secondary importance is the statistics governing the number of photoelectrons produced by the incident photon collision, which may depend on the photon energy or incident angle. The amplitude distribution of the output pulses is known as the Pulse Height Distribution (PHD).

A simple theory from Wiza (1979) describes how the gain depends on the voltage applied across the plate. The secondary emission yield increases with voltage, because each collision occurs at higher energy. At the same time, the number of collisions in the channel must decrease, because the electrons travel further before interacting with the wall. Eventually saturation occurs. The gain also depends on the *l:d* ratio of the plate (see §3.2.1.1).

3.1.3. Saturation

When the MCP bias voltage is too low for saturation, the amplitude distribution of output pulses is quasi-exponential. As the voltage is increased, the PHD can be seen to change as saturation is reached, from the quasi-exponential to a peaked distribution, with a low energy exponential tail (see Figure 27). Normally the gain and FWHM of the PHD are quoted. The gain is the modal gain ('g' in Figure 27) and the FWHM is the half width of the distribution given in terms of a percentage of the modal gain. The peak can have a FWHM as low as 50%.

Saturation allows pulse height discriminators to be set at either side of the peak for noise discrimination in event counting. A narrow PHD peak also reduces the dynamic range requirements of the following electronic processing. All threshold circuits are subject to a pulse height dependence factor (sometimes called 'walk') due to the rise time of an event. This is minimised if the PHD is peaked. In saturated mode, the output count rate should not vary with small changes in voltage.

In general, the smaller the pore diameter, the lower will be the gain at which saturation starts to occur. The reason for saturation is that the output current is limited by the secondary electron coefficient, which varies with the impacting electron energy, which is in turn controlled by the electric field inside the channel.

Schmidt and Hendee (1966) show that, for large diameter CEMs, the major cause of saturation is the limiting of space charge density, due to the cloud of multiplied electrons in the channel, particularly at the output end where most electrons are being stripped from the surface. Therefore at high enough gains, the space charge density at the rear of the channel reduces the kinetic energy of the electrons as they interact with the channel walls until the coefficient of emission is reduced to unity. A decrease in density allows the kinetic energy at each collision to increase, so that the density itself is increased and vice versa. Thus a dynamic equilibrium is reached and the gain fluctuations from event to event are reduced. In this way, the channel gain is limited by the space charge, which is itself governed by the voltage and the channel geometry.

Evans (1965), from his experiments on smaller diameter channeltrons, believed that the electron multiplication process was limited by the charging of the channel walls, because the wall charge cannot be replenished on the time scale of the passage of the pulse of electrons. Positive wall charging is also the explanation of saturation for MCPs (Fraser *et al.*, 1983). At the output end of the channel, the potential gradient is flattened and the cascading electrons can no longer acquire the energy needed to multiply. Furthermore, this portion of the tube tends to become an electron sink. Evans observed this from the capacitive coupling of a wire tightly wrapped around the outside of the tube. Positive pulses could be detected everywhere except, in the saturated mode, at the output end, where the pulse became negative. The decay time of these pulses was greater than 50 µs, indicating that the effect was in the resistive layer, rather than an effect associated with the passage of the space charge electron cascade.

Note that saturation does not prevent the modal gain from increasing further with increased bias voltage; as the voltage is increased, a larger part of the last channel becomes saturated.

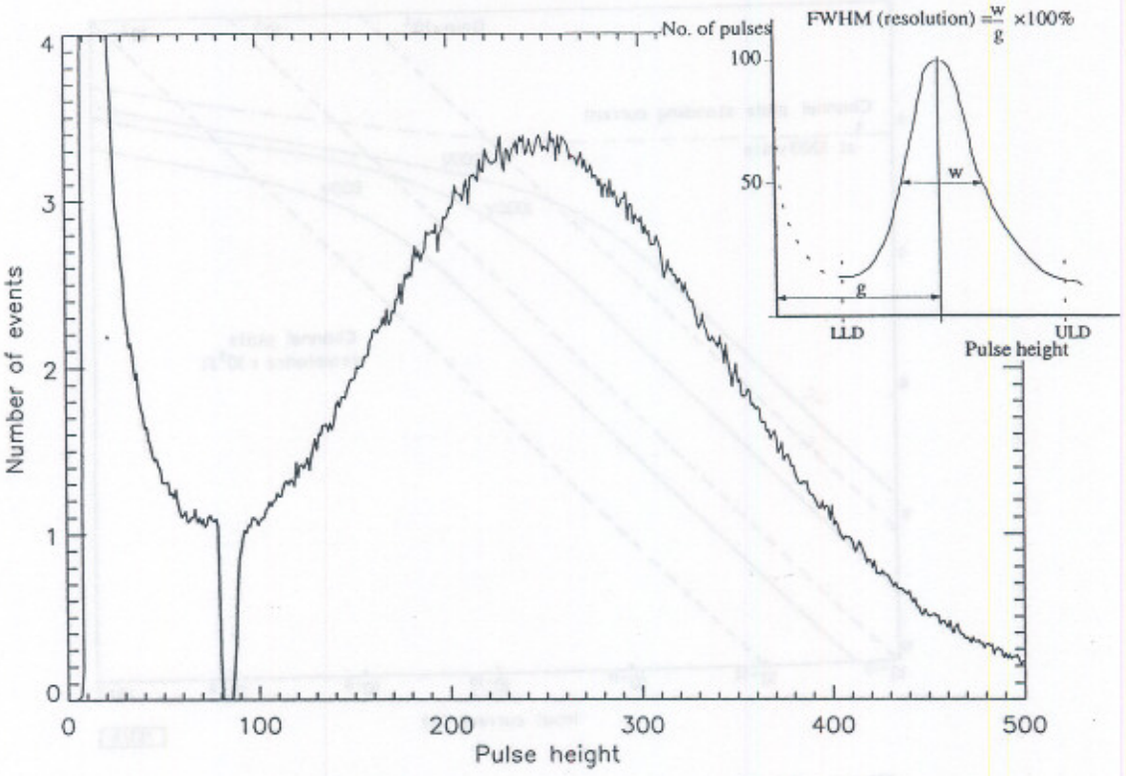

Figure 27. Typical pulse height distribution from one of the flight spare detectors. It has a modal gain at channel 250 ~ 4×10^7 and a FWHM of 75%. The inset shows how the FWHM is calculated and also typical positions for the discriminator settings, marked LLD and ULD for lower and upper level discriminators.

In saturation, most of the output electrons come from the distributed capacitance of the channel wall through the current in the channel walls, often termed the strip current. The current is too small to recharge any significant fraction of the electrons depleted from the channel wall during the passage of the pulse. For continuous, uniform illumination, the output current is usually 10–30% of the strip current. Figure 28 gives an example of the relationship between the input current and output current for continuous illumination. It shows the strip (or standing) current, below which the output current is limited. If the resistance of the plate remained constant, the output would have to saturate at a value below the nominal strip current. However, the effective resistance decreases with the cascade of electrons through the channels, because they form a parallel resistive path, so that the strip current increases. With pulsed illumination or illumination of a small area, currents higher than the nominal strip current can be observed (Guest, 1971a).

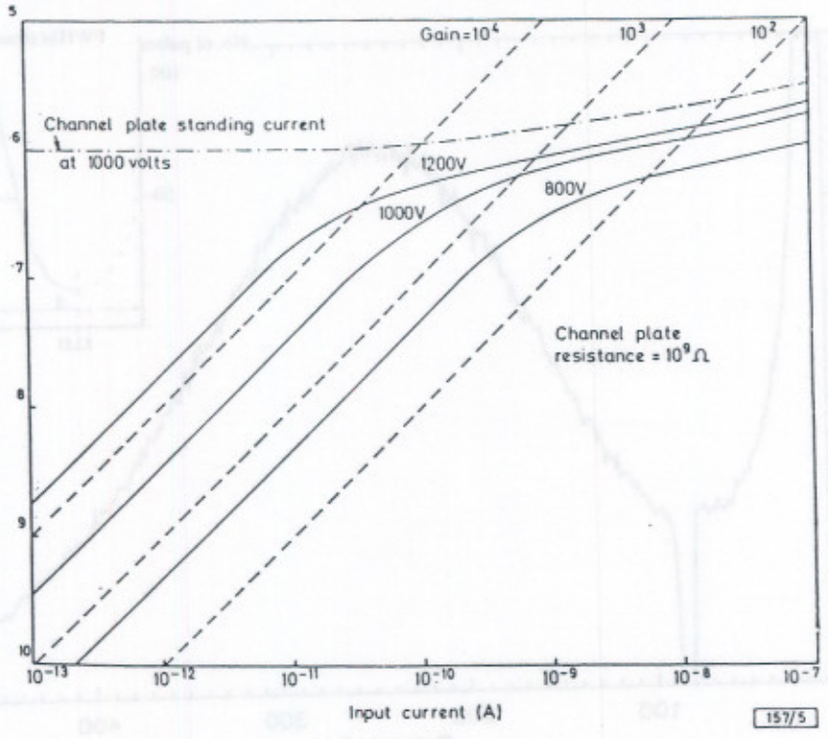

Figure 28. Current transfer characteristics of a channel plate taken from Guest (1971b).

The PHD width is reduced with increasing saturation, but there are a number of other refinements which can minimise the width. With a distance of only 150 µm between the MCPs, 100 to 300 channels in the second MCP will be excited by one channel in the first MCP (Kersten, 1982). According to Anacker and Erskine (1991) the diameter of the electron cloud emerging from a single channel, if there is no voltage bias across the gap, is given by:

$$D_2 = D + \frac{2d}{\tan(90° - \Delta\theta)} \tag{31}$$

where D is the diameter of the pore, $\Delta\theta$ is the characteristic emission angle (10–20°) and d is the distance between plates. For MCPs mounted with no gap, d must come from a measure of MCP surface flatness, *i.e.* d is the mean peak to trough difference.

Applying an accelerating voltage across the inter-plate gap can reduce the number of channels illuminated in the second MCP by a factor of three (Wiza, 1979). This reduces the gain, but also the PHD width, because a larger proportion of the channels will saturate. According to Kersten (1982), the narrowest PHD can be obtained with an electric field in the gap of 5×10^6 V m^{-1}, which works out at 300 V across a 50 µm gap.

Increasing the count rate, as well as reducing gain by gain depression (see §3.1.5.), broadens the PHD. In view of the fact that the MCP channel acts capacitively, the height of a pulse becomes a function of the time interval since the one preceding.

3.1.4. Ion feedback

If the voltage along the channel is high enough, the cloud of electrons arriving near the output end of the channel may be sufficiently dense to ionise, by electron bombardment, any residual gas atoms inside the channel or atoms absorbed on the channel wall. Positive ions will be accelerated up the channel towards the front face. If they travel far enough up the channel, they may interact with the wall with sufficient energy to initiate a new avalanche of electrons. Despite the fact that the output end of the last channel may have a high local positive potential preventing secondary electrons from becoming free, due to the removal of electrons by the real event cascade, there is still sufficient charge left in the front portion of the channel and in other plates in the stack to give a small secondary event. The secondary event effectively contributes to the background. In the worst situation it is possible to obtain an extra peak at the upper energy end of the PHD, because the ion feedback events are almost coincident with real events and thus are not discounted by any time discrimination in the processing electronics.

Ion feedback is normally unwanted because it limits the ultimate gain that can be achieved. It is also essentially unreliable, giving variable results depending on pressure, the nature of the residual gas, the surface properties of the channel wall and the voltage applied across the plate. The pressure dependence, which gives a gain increase with increasing pressure, presents a problem for any experiment where the pressure may vary. It is usually necessary to put discriminators either side of the PHD. Ion feedback has the effect of broadening the range of pulse heights.

Those ions which reach the MCP front face may damage any photocathode which is being used to enhance the electron emission coefficient. If ion barriers (*e.g.* Al_2O_3 and SiO_2 5–10 nm membranes, which are transparent to visible light and to photoelectrons from 800 eV, Clampin and Edwin, 1987) are used, the QE is reduced.

For a straight channel single CEM, the ion feedback can lead to saturation at a lower voltage than would otherwise be possible. Evans (1965) demonstrated that, having set the bias voltage to obtain a saturated PHD, a decrease in pressure causes the PHD to lose saturation unless the bias voltage is increased. If a new saturating voltage is found at the lower pressure and then the pressure is increased, the PHD becomes distorted with spurious counts—often, continuous, uncontrollable pulsing. Using the ion feedback as a mechanism to saturate the channel, leads to a much slower rise time of the output pulse

(typically 0.5 μs rather than the tens of nanoseconds without ion feedback), because it is made up of multiple pulses.

Evans (1965) further showed that curving the channeltrons completely removes the problem of ion feedback, allowing them to be operated over a range of pressures (below 10^{-3} mm Hg) and a range of voltages (provided the voltage was high enough for saturation) and a range of incident particle energies, without any significant change in count rate. The channeltrons could be operated at up to 10^5 c s^{-1} without any gain reduction.

If the channel walls are curved, ions are very likely to interact with the wall before they have gained enough energy to initiate an event or, in any case, secondary electrons produced by the ions cannot multiply sufficiently in the available length. The secondary emission for electrons is not affected by the curvature since they need to gain only about 50 eV between collisions, whereas an ion needs considerably more to liberate a secondary electron (Adams and Manley, 1965). Just putting a shallow curve or angle into the channel is sufficient to inhibit ion feedback at normal operating gains. Curved channel MCPs ('C-plates', made by Galileo Electro-Optics Corp.), are sometimes used, but more commonly, two or three straight channel MCPs with the channels biased at a small angle, are built in a stack with the angles opposing. This leads to a higher gain and a more spatially extended output pulse than for a C-plate and, provided that the anode is a centroiding device, this does not degrade the spatial resolution. An increase in gain is a benefit in increasing the signal to noise ratio.

Disadvantages of the C-plates include the fact that each charge cloud comes from just one channel and therefore channel to channel irregularities in length, width, curvature and material are directly transmitted to the image. With a multi-stack in contrast, many channels in the bottom plate are stimulated for each event, averaging out any irregularities. Irregularities are in any case more likely with the C-plate, due to the difficulty of making the curved channels. The gain is also lower at about 10^6, ion feedback being observed at gains higher than this (Henkel *et al.*, 1978).

Timothy (1981) quotes a curved channel plate's gain as stabilising after 10^{11} counts mm^{-2} and not reaching the end of its useful lifetime. He claims narrower PHD widths for C-plates (being between 40 and 60% FWHM), although there are many published results of PHDs as narrow as this from pairs of straight channels arranged as chevron stacks, which furthermore demonstrate more reproducible results from plate to plate. C-plates may suffer from less count rate dependent gain depression (Timothy *et al.*, 1979). The main advantage seems to be the longer useful life and stability of the C-plate.

Another method of bending the channel is found in Sandwich channel plates, made by Phillips, where three 40:1 MCPs are bonded together in permanent contact. This makes them stronger and simpler than conventional stacks of separate MCPs, with gain and PHD characteristics similar to that of a single C-plate (Pearson *et al.*, 1988). The fact that the electrons cannot spread between channels means, as in the case of the C-plate, that irregularities are not ironed out in the final image, and that there are problems with aliasing, where a pore in one plate may line up with one, two or three pores in the next plate in the stack (Kawakami, MSSL, private communication, 1994).

3.1.5. Time of response and dead time

Many experiments, which are undertaken during the course of atomic and molecular fluorescence-decay measurements and nuclear research, require that the MCPs have a very fast (sub nanosecond) time response (Leskovar, 1977). As with the pulse heights, there is some variation in the time response of the MCP, due to the variation in times of flight of the photoelectrons and secondary electrons, as well as to different trajectories and a variety of initial velocities. Again, saturation has the effect of standardising the time response of the MCP from event to event. The time spread of one event typically has a peak with a FWHM of less than 1 nanosecond and a rise time of 100 picoseconds. In general, the time from the initial excitation to reaching a given current level at the output is a linear function of channel length. The application of an accelerating voltage between the plates in the stack can speed up the transit.

After an event has stripped electrons from the wall, the channel takes a finite time to recharge. The typical RC time constant is tens of milliseconds, depending on the open area ratio of the MCP, the glass dielectric constant and the channel diameter. In §3.4.1., the dead time for the GIS MCPs is calculated. If an event arrives during the recharge period, the gain of the event is reduced. Thus at high local count rates, the phenomenon of count rate dependent gain depression (CDGD) is observed. A reduction in output count rate is seen in the region of gain depression, resulting in a non-linear count rate response across the detector. It can even lead to distortions and ghosting in the image with some readout techniques.

Reduced resistance plates have been manufactured (termed 'Hot MCPs' by Galileo Electro-Optics Corporation) for the sake of operating at high count rates. A reduced lead surface has a negative temperature coefficient of resistance, so that if the resistivity is too low, a thermal runaway condition may occur at high voltage and high count rates, resulting in a catastrophic breakdown of the MCP. The resistance can change with bias voltage applied due to resistive heating of the channel plate (Pearson *et al.*, 1987). Actively cooled MCPs with resistances of only 500 kΩ have been developed,

which can operate up to 10^4 c s^{-1} $pore^{-1}$ (Fraser, 1991). Non-uniform resistivity may also decrease gain depression and increase MCP life (Matsuura *et al.*, 1984).

Another type of gain depression occurs gradually during use of the MCP as charge is extracted from it. This is discussed in detail in §3.4. For example, with the GIS development model detector the gain dropped 30% after 5×10^{-4} C was extracted. There are Long life (L^2) MCPs which have good gain and PHD characteristics up to 6×10^4 c s^{-1} cm^{-2}. These MCPs (manufactured by Galileo) drop to only half their initial gain values after 0.1 C cm^{-2} has been extracted (Fraser *et al.*, 1988b).

The modal gain drops with increasing temperature at a rate of about –0.12% per °C (Slater and Timothy, 1993). This is probably due to an axial temperature gradient within each channel (hotter in the centre) causing a variation in the resistivity and hence the electric field. Alternatively it could be due to a negative temperature dependence of the secondary yield of the MCP glass.

3.1.6. Background

The 'dark count' is the number of events observed per second without any illumination on the front of the detector. The PHD for background events may be different from that produced by photons or other radiation. Typically it has a negative exponential shape, even when the gain for photon events is highly saturated. This is because a photon event is initiated at the top of the MCP stack, whereas background events may be initiated at any depth. The greater the depth, the lower the gain. Thus, assuming a uniform distribution of depths, a negative exponential is expected.

The causes of the background may include MCP 'hot spots', thermal electron emission, field emission, cosmic rays and radioactive decay in the MCP glass. The background rate is normally very reproducible, at ~0.4 events cm^{-2} sec^{-1}, for plates which have been baked, scrubbed to stabilise the gain by extracting large quantities of charge, and kept under vacuum (Siegmund *et al.*, 1988). The scrubbing method used by Siegmund *et al.* extracts ~0.1 C cm^{-2} with UV flux. Exposure to atmosphere can increase the background count rate by up to 10 times because the subsequent outgassing of the channel walls causes the release of ions and neutral atoms which initiate background events.

Any particulate matter on the MCPs may give rise to 'hot spots', which are regions of very high background count rates. The debris on the surface produces field emission when charged up. Hot spots are most likely if the particles are conductive and are lodged inside a channel, where the field strength is high and emitted electrons are trapped by the MCP. This can occur easily if the MCPs are physically damaged in some

way. In order to keep the background rate low, it is consequently necessary to maintain a very high level of cleanliness and careful handling (see §4.1.1).

The surface area of a MCP (including the channels) is large, (~3100 cm^2 for a GIS plate), and therefore thermal electrons from the detector surface and surrounding instrument could contribute to the dark count. The work function of the glass (~10 eV) is high enough to exclude most thermionic electrons of ~5 eV, because they do not have enough energy, (Evans, 1965). According to Siegmund *et al.* (1988) there is no variation in background count rate with temperature. Visible light does not contribute, again because visible photons have too little energy.

Field emission from structures or defects on the channel walls could contribute to the background count rate. In this case, the number of events would be expected to rise as the MCP bias voltage is increased. The gain of the background events certainly increases with voltage and the gain rises faster than the modal gain of the photon PHD. This relative change is attributed to the fact that the background events do not saturate like the events initiated in the front of the MCP and therefore can increase more in gain as the voltage is raised. However, over a factor of 30 in MCP gain, there is no significant change in the overall dark count (Siegmund *et al.*, 1988).

External events such as cosmic rays or environmental gamma rays are a contributory factor. By measuring coincident events in a scintillator and MCP stack, Siegmund *et al.* (1988) showed that only 4% of MCP background events are caused by cosmic rays if the MCPs are horizontal and about 2.2% if they are vertical. They showed that each event may initiate up to about 10 electrons. The number of cosmic rays detected compared with the cosmic event flux of ~ 0.024 events cm^{-2} sec^{-1} implied a 64% MCP efficiency at detecting these events. The efficiency and the number of secondary electrons produced however depends on the MCP thickness and angle of penetration.

Radioactive decay occurring in the channel plate glass itself contributes to the dark count. The internal radioactive emission is mainly from ^{40}K or ^{87}Rb (Fraser, 1992). Potassium contains ^{40}K at a level of 0.0118%, which emits β particles (1.32 MeV, with a half life of 1.43×10^9 years) and γ rays (1.46 MeV, half life 1.2×10^{10} years). Most of the dark count comes from the β decay—up to 0.52 decays cm^{-2} sec^{-1}—which is close to the total background count rate. The magnitude of the dark count is closely related to the manufacturing process of the MCPs and may vary from one MCP to another. As a result of collaboration between Fraser and the manufacturers, it is now possible to obtain "low noise" MCPs, which are made of radioisotope-

free lead glass. With low noise MCPs, the background can be reduced to cosmic events only ($\sim 0.01\ c\ s^{-1}\ cm^{-2}$) (Fraser, 1992).

The number of background events was observed to increase by up to a factor of two for the EXOSAT CMA detectors in a highly elliptical deep space orbit, and similarly for the Einstein HRI instrument in low earth orbit, *e.g.* Fraser *et al.* (1986). Analysis of the expected radiation environment for SOHO has been performed by ESA. Although the satellite will be outside the magnetosphere, highly energetic particles, mainly bursts of protons, will be received from the sun.

3.1.7. Photon detection efficiency

The quantum detection efficiency (QE) is the percentage of incident photons producing detectable pulses at the output of the plate. The QE depends on the probability of a photon's entering a channel rather than hitting the inter-channel web, the secondary electron coefficient and the voltage across the plate.

The first of these probabilities depends on the open area ratio of the plate and the geometry of the detector. It can be enhanced by putting a repeller grid in front of the front face, in order to force any electrons emitted from the inter-channel web to enter a neighbouring pore. This method has been seen to enhance the QE by as much as 70% (*i.e.* 1.7 times the QE of a bare plate) as described by Barstow *et al.* (1985) for the Wide Field Camera (WFC) on ROSAT. The disadvantage is that the 'neighbour' may be some distance from the original arrival point. Thus there is a trade-off between QE and spatial resolution. The repeller grid also has a finite transmission and effectively shades the MCP front face so that some photons will hit the repeller grid itself and be lost.

It is easy to establish how many events are saved by using the grid, by measuring the count rate first with the grid at the same voltage as the MCP front face and then at a relative positive voltage. At zero voltage difference, the count rate will not include any photons that hit the inter-channel web.

Photons which successfully enter a channel may still fail to produce a secondary electron or the cascade may die out after a few stages. The secondary electron coefficient, δ, is affected by the energy of the radiation being detected and the condition of the plate. At high energies a photon can penetrate far into the MCP, exciting more than one channel. It may excite a channel even if it hits the inter-channel web. At lower energies (*e.g.* UV radiation), any photons hitting the inter-channel web are lost (provided there is no repeller grid) so that the QE is limited to a maximum of the open area ratio of the plate. In this case, the photons do not have enough energy to penetrate more than one channel, which is an advantage in the case of very high positional resolution detectors. With an incident energy of 300 eV, δ reaches a maximum of about

3.5 (Fraser, 1983) and the QE can be as high as 90% (Richter and Ho, referring to CEMs, 1986).

The angle of incidence also has a direct effect on the QE. If the photon trajectory is parallel to the channel axis, it is more likely to penetrate deep into the channel before interacting with the wall. A low gain pulse will be produced. The angle of maximum efficiency is generally reported to be about 6° from the channel axis.

The QE may be enhanced by coating the front MCP with a photocathode material. (*e.g.* MgF_2 or CsI). This topic is dealt with in detail in §3.3.3.

A new method of enhancing QE is to use square pore MCPs with neither any coating nor repeller grid. They can deliver very high (up to 80%) QEs (Fraser, 1991) not only because of a higher open area ratio, but also because of the angles of incidence of the electron with the channel wall. In round channel MCPs, with illumination at an angle of incidence θ, a photon will meet the wall at any angle from $(90°–\theta)$ down to zero depending on its arrival position relative to the pore, (see Figure 48). For square pores, there are only two angles of incidence which interchange at each reflection. Therefore, the likelihood of the occurrence of more than one reflection down the channel is much smaller for the square than the round MCP channels.

In general the QE cannot easily be predicted for a given configuration. The measurement has to be made.

3.1.8. Applications

MCPs have many uses, such as very precise measurement of the arrival position of photons. The narrowness and closeness of the channels provide high position resolution, limited only by the channel size.

MCPs can be operated in the unsaturated 'DC mode', where the MCP is subjected to a low level slowly varying input electron image, which is amplified by the electron cascade process within the MCP channels and emitted as an intensified output electron image. In this mode, the current transfer characteristic (ratio of output current to input current) is linear, up to 10% of strip current (Figure 28). This mode is employed in generation 2 image intensifier tubes with phosphor readout.

In 'pulse counting' mode the MCP is subjected to a higher bias voltage. A high proportion of the incident photons or particles will lead to the emission of a saturated pulse from the MCP. This mode allows an individual photon to be counted, with a confidence limit set by the probability that it will give a detectable event. It is possible to discriminate photons from the noise (see Figure 27).

MCPs may be used to detect electromagnetic radiation from soft X-ray to extreme UV wavelengths and they may be combined with a photocathode in a sealed tube for use

at UV, visible and near infrared wavelengths. The capability of MCPs includes the detection of protons, positive ions, energetic atomic hydrogen, electrons if accelerated to a high enough energy and metastable thermal molecules. If MCPs with a high lithium content were manufactured they could be used to detect thermal neutrons with efficiencies up to 28%. The plausibility of this has been demonstrated by the comparison between 'low noise' MCPs containing ^{6}Li and normal MCPs (Fraser and Pearson, 1990).

MCPs are not as susceptible as channeltrons to magnetic fields. The gain of a curved-channel MCP is not affected by 0.09–0.2 T axial magnetic flux density. Oba (1976) reports that when the channel axis is perpendicular to the magnetic field, the gain decreases as the field strengthens. The electrons' trajectories are forced into the wall in a short distance, before gathering sufficient energy to emit the usual number of secondary electrons. If the magnetic field is parallel to the channels, there is a range of field strengths (0.02–0.1 T depending on the MCP voltage) which actually increases the gain by extending the range of the electrons, by causing them to rotate around the field direction. At higher field strengths the gain is once again reduced because the rotation radius becomes too large. In their study of the affect of magnetic field perpendicular to the plate surface, Schecker *et al.* (1992) observed an initial increase in gain and thereafter a linear drop in gain to about 30% by 2.5 T.

MCPs can be used in image intensifiers with a proximity focused photocathode and a phosphor screen, as well as in quantum position-sensitive detectors. X-ray imaging, neutron radiography, electron microscopy, ultra fast cathode ray tubes and streak cameras (Leskovar, 1977), have all made use of MCPs.

The popularity of MCP detectors is explained by their small size, light weight and so-called 'ruggedness'. They give a high gain for little power consumption and are fast. Although they have been developed mainly as electron image amplifiers for use in high gain compact image intensifier tubes, they are flexible enough to serve in many different ways with a variety of readouts. Their disadvantages include ease of damage or contamination, necessity of storage under vacuum or in a dry atmosphere and loss of gain with use. They are also non-linear at high count rates.

3.2. MCP CONFIGURATION EXPERIMENTS

One of the first decisions to be taken in connection with the detector design for GIS was the number and type of MCPs. Much work has been done on comparing plates and their configurations. For instance, Malina and Coburn (1984) tested a large number and variety of plate configurations from seven manufacturers covering pore diameters between 12.5 and 25 µm and *l:d* ratios between 40:1 and 80:1, with a number of surface

electrode materials. They assessed background count rate, EUV quantum efficiency (30.0–120.0 nm), gain and PHD. They could find no particular significance in the type of glass or electrode material, although they established differences in operating characteristics between even apparently identical MCPs from the same source. Most of these differences were induced as a result of post-delivery handling, mounting and processing techniques, although some appeared to be intrinsic. They chose for EUVE, MCP chevron or *z*-stacks of *l:d* of 80:1, to get gains of 3×10^7 and saturations of less than 40%.

Many imaging systems, *e.g.* MAMA and CODACON (§1.4.2.1.), require a gain of 10^6, with a tight PHD and a small charge cloud size. For these C-plate MCPs are ideal. For charge division or resistive anodes, a high gain ($>10^7$) is required and a wider charge cloud size is needed. A narrow PHD is still preferred for the sake of optimising the electronics and count rate stability. In this case a chevron pair with high *l:d* or a *z*-stack are the possible configurations.

For GIS, to give a signal to noise ratio of better than 2000, the MCP configuration needs to supply charge clouds of 4×10^7 electrons on average. This is at bias voltages of less than 4 kV, in order to allow some head room for voltage increase up to the 5 kV supply. Since it is necessary to set lower and upper level discriminators on the PHD in order to select events for subsequent processing, it is required that the PHD FWHM be less than 100% to include most of the events. This is essential if the detector is used to measure intensities. Less than 100% is also found to be necessary to prevent ambiguities in the position as measured by the SPAN anode (see Chapter 6).

The spread of the charge cloud from the MCP has to be controllable and matched to the SPAN anode pattern dimensions. Other constraints on the configuration are engineering simplicity and minimising the opportunities for breakdown between the MCPs, shims or from the MCP to the anode.

The three available choices were a chevron pair of double-thickness (1 mm, *l:d* = 80:1), or triple-thickness (1½ mm, *l:d* = 120:1) plates, or a *z*-stack of double-thickness plates. Furthermore, there was the possibility of putting a conducting or non-conducting shim of a variety of thicknesses between any two MCPs in the stack. Another variable was the size of the gap between the MCP and anode.

3.2.1. Gain and pulse height predictions

In the case of a chevron or *z*-stack, the gain and PHD depend not only on the diameter of the pores, the *l:d* ratio of the MCPs and the voltage across them, but also on the gaps between the MCPs where electrons can spread. With small gaps, saturation tends to

occur at a lower voltage and the distribution is tighter. Larger gaps give more gain, because more channels are stimulated by electrons in the second and third MCPs.

A voltage can be applied across the inter-MCP gaps. The effects have been tested using two plates in a chevron stack. A change in the whole plate bias voltage has more effect on the gain than the interplate gap voltage, but a positive voltage across the gap decreases the width of the PHD. This is because the electrons are divided between fewer channels in the second MCP so that most channels have enough 'primary' electrons to make them saturate. For this reason, a higher voltage across the top plate has more effect on reducing the width of the PHD than if it were across the bottom plate. The latter is demonstrated in the interplate gap experiment by Smith and Allington-Smith (1986).

Following the same argument, Malina and Coburn (1984) explain their finding that, all other things being equal, the maximum achievable gain can be obtained with smaller diameter pores. They say that, assuming that the electrons spread the same amount in the interplate gap regardless of pore diameter, a greater number of channels will be stimulated per event for small pores, thus giving larger pulses. Siegmund *et al.* (1987a) compare the saturation with increasing voltage in a stack of three 80:1 plates and a stack of six 40:1 plates. The stack of three saturates first, because the charge does not have so much opportunity to spread into many channels. The six stack also shows a poorer PHD width.

Experiments have also been done with combinations of chevrons and *z*-stacks of MCPs. Floryan and Johnson (1989) described the importance of positive or negative fields between the stacks in determining the gain and width of the distribution.

Audier *et al.* (1978) found that the saturated gain from a chevron geometry (G_C) can be expressed as:

$$G_C = n_e . N_C . G'_R = G_F^{1-\alpha} . G_R . N_C^{\alpha} \qquad (32)$$

where G_F and G_R are the gain of the front plate and the rear plate respectively, N_C is the number of channels in the rear MCP excited by one channel of the front MCP, n_e is the number of electrons entering each pore of the rear MCP ($\approx G_F/N_C$) and giving a gain of G'_R. α is an empirical parameter such that $G'_R = G_R . (\overline{n}_e/n_e)^{\alpha}$; $\alpha \approx 0.6$ for 12.5 µm diameter channels and $\overline{n}_e \approx 1$, is the number of electrons required to enter a pore for it to saturate. If there is no inter-plate gap, Fraser *et al.* (1983a) say that N_C is typically seven. N_C can be manipulated by the inter-plate gap voltage.

This has been extended to an equation for gain of a *z*-stack by Siegmund *et al.* (1985):

$$G_Z = G_R G_M^{(1-\alpha)} G_F^{(1-\alpha)^2} N_R^{\alpha} N_M^{\alpha(1-\alpha)} \qquad (33)$$

where M refers to the middle plate, R to the rear and F to the front, so that N_M is the number of channels excited in the middle plate *etc.* Typical values are $\alpha = 0.85$, $N_M = 7$ and $N_R = 40$.

3.2.1.1. Models of gain with voltage

Gatti *et al.* (1983) show, by solving Laplace's equation, that under steady conditions the electric field in an MCP is parallel to the channel axis.

Adams and Manley (1966) give a simple ballistic model to find an equation for channel electron multipliers for the dependence of gain on applied voltage. This is valid for MCPs being used in the linear mode where the PHD is quasi-exponential (not saturated). In this case each channel can be modelled individually as a series of discrete dynodes.

Assuming that the secondary electron is emitted normally to the channel wall and thus leaves with no axial kinetic energy, the distance travelled down the tube between collisions of the electron with the channel wall S, is:

$$S = \tfrac{1}{2} E \frac{e}{m} t^2 \tag{34}$$

where E is the electric field down the channel and t is the time between collisions, such that:

$$t = d\sqrt{\frac{m}{2eV}} \tag{35}$$

where d is the channel diameter and eV the initial energy, perpendicular to the channel axis, of a secondary electron leaving the channel wall.

The collision energy, V_C, depends on the distance travelled in the electric field.

$$V_C = ES \quad \text{and} \quad E = \frac{V_o}{l} \quad \Rightarrow \quad V_C = \frac{V_o^2}{4V\alpha^2} \tag{36}$$

where V_o is the applied voltage and l is the length of the channel, α is the $l{:}d$ ratio. S has been substituted from equation (34). If it is assumed that the secondary electron emission coefficient is:

$$\delta = KV_C \tag{37}$$

where K is a constant (in fact δ is greater than one only for a specific range of primary electron energies and reaches a maximum before dropping slowly back below one; Amnicoli, 1985), then the gain, G is

$$G = \delta^n \quad \text{where} \quad n = \frac{l}{S} = \frac{\alpha d}{S} \tag{38}$$

Substituting equations (34), to (37) into this gives:

$$G = \left(\frac{KV_o^2}{4V\alpha^2} \right)^{\frac{4V\alpha^2}{V_o}} \tag{39}$$

The model shows that for a given bias voltage, the gain depends only on α, the length to diameter ratio. However, it also predicts that the gain will rise to a maximum value and then decrease as the voltage is increased. In practice, the gain is not seen to decrease if the voltage is raised beyond the maximum value.

Guest (1971a) takes the ballistic model further, using a Monte Carlo computer model, although, like the Adams and Manley model, it is not appropriate to saturation. Inputs to the model include the energy of the electron and the angle at which it strikes the wall, with a secondary electron emission function dependent on these parameters. A Poisson distribution based on the function is used for the random selection of the number of secondary electrons. A cosine distribution assigns the angle of each secondary electron, the energy being selected from a Rayleigh distribution with a variable modal energy. Each secondary electron trajectory is calculated in three dimensions using ballistic equations so that after many iterations the number of electrons emitted and the pulse transit time can be obtained from this model. A PHD can be built up. However, Guest does not include space charge effects and therefore, the model is of limited use to saturation of MCPs.

From this model, though, Guest predicts that "for each particular applied voltage, there is an optimum value of the *l:d* ratio which gives the maximum gain and near this value the gain is least sensitive to the small variations in channel diameter which occur in practice".

One version of the model predicts that the output energy distribution from the plate is like a negative exponential function. Comparing this with an experiment using a retarding grid gives very close agreement. For a *l:d* ratio of 60 and 1 kV bias, 25% of electrons leaving the MCP have energies greater than 77 eV.

Eberhardt (1979) and (1981), still relying on the idea of a MCP acting as a discrete stage electron multiplier with a fixed number of dynodes, developed a model whereby the log of the gain is proportional to the log of the voltage. This would seem to be borne out by the experiments illustrated in his papers. However, it is still not relevant to saturation of the MCP. What is of particular interest in Eberhardt's papers, however, is the prediction that the secondary electrons should actually tend to focus or converge toward particular regions inside the channel (illustrated in Figure 29). His argument assumes a direct proportionality between the bombarding primary electron/photon

energy and the average radial emission energy of the secondary electron. The regions lie at a fixed distance apart (z), depending on the voltage, so that the MCP tends to act as if it were a discrete stage electron multiplier. The importance of this is that during use or scrubbing at a given voltage, the MCP will be scrubbed more in these regions than elsewhere. The voltage should be varied during scrubbing to cover as large an area as possible. This theory suggests that after scrubbing at a particular voltage, a small change of voltage up or down may increase the gain by a larger amount than otherwise expected. In practice, a range of voltages is normally used in scrubbing to compensate for the fall in gain with charge extraction.

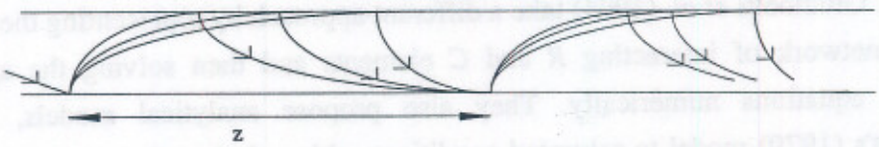

Figure 29. Focused electron trajectories in a cylindrical channel from a diagram by Eberhardt (1979).

In saturation, Loty (1971) found that the gain (Q) is a function of voltage and both the pore diameter (d) and the length to diameter ratio (α) according to:

$$Q = e.G = \frac{\pi\varepsilon_0}{4} V_0 . d . \alpha^{-1} \qquad (40)$$

where V_0 is the voltage applied along the channels. Leonov *et al.* (1980) confirm that Q is proportional to d and α^{-1}.

Fraser *et al.* (1983a) describe a model of MCP peak gain, including saturation. Starting with equations of motion according to the radial and axial electric fields in the channel, they solve them numerically iterating over a series of dynodes. This model leads to the prediction that the collision energy V_C is reduced during the passage of the electrons down the channel until it reaches the value such that the secondary electron coefficient δ_e is unity and that the spacing between the dynodes decreases.

This model agrees with the others in that, in unsaturated mode, the gain is dependent only on α, but when saturation starts, it depends on diameter too. Saturation starts at a lower voltage for small values of d. The voltage required to produce saturated pulses (V_S) increases with increasing α and

$$V_S \cong V_T + 450 \ \ V \qquad (41)$$

where V_T is the voltage at which the MCP gives unity gain between collisions.

This voltage can be found from equation (36), with V_C set to 20 eV for $\delta = 1$ (§2.2.1.) and $V = 1$ volt (Adams and Manley, 1966) so that:

$$V_T = \alpha\sqrt{4.V.V_C} = 8.94 \times \alpha \qquad (42)$$

For the GIS MCPs with $\alpha = 80$, this gives $V_S = 3.5$ kV across the z-stack, which is close to the experimental value of about 3.3 kV. However, as is the case for the MCP QE (§3.1.7.), it is very difficult to make predictions about gain when there can be so many configurations, including the type of stimulation, the angle of incidence, the end-spoiling, the temperature *etc.*

All the above models compute the trajectories of electrons inside the MCP channels. Giudicotti *et al.* (1994) take a different approach by representing the MCP as a discrete network of interacting R and C elements and then solving the appropriate Kirchoff equations numerically. They also propose analytical models, extending Eberhardt's (1979) model to saturated conditions, although they do not claim that these represent MCP behaviour as closely as numerical models. Starting with a general equation giving the gain as a function of input current, they solve it for particular situations, *e.g.* for operation of the MCP in current mode or in pulse mode. The result includes predictions of the behaviour of MCPs with regard to CDGD and the narrowing of the PHD.

3.2.2. Experimental setup

Each of the three main configurations was tried out on the development model detector which consisted of a bracket onto which anode and MCPs were mounted. The development model detector had a larger anode than for flight, measuring 25×60 mm with four holes in it for the MCP stack pillars. The MCPs were also a slightly different dimension—20×50 mm for the development model detector, 25×50 mm for flight. The dimensions were altered before flight for two reasons. The first was that the requirement for the active area of the detector changed from 50×12 mm to 50×16 mm. The other was that holes in the quartz anode substrate compromised the strength. On one occasion, during the tightening of the MCP stack pillar nuts, the quartz cracked. The design was therefore changed to move the pillars further apart and to use a smaller anode set into a polycarbonate base plate, through which the pillars pass.

The development model detector was operated in a glass cylinder vacuum chamber with an oil diffusion pump backed by a rotary pump. Pressures of 4×10^{-6} mbar were obtainable. Dry nitrogen was used to back-fill the chamber whenever it was necessary for it to be opened. All connections to the anode and the high voltages were made through the aluminium end flange of the vacuum chamber using HV BNC feedthroughs. Connections onto the MCP stack itself were made using spot-welding. For

the anode, spot-welds joined aluminium wire to copper strips stuck to the aluminium anode surface using conductive epoxy. Extra connections could be made between the anode and the copper strips by ultrasonic wire-bonding. Initially, the anode was at ground potential, the front of the MCP stack being held at high negative potential. During development the orientation was changed to that of the flight detectors with the anode at high voltage.

Figure 30 shows how the apparatus was set up. Outside the chamber was a die cast box containing a variety of resistive chains for connecting in parallel with the MCP-anode stack. High voltage was supplied by a 5 kV variable power supply. The signals from the detector were processed by three parallel channels of electronics, each consisting of an Ortec 109 charge-sensitive preamplifier followed by an Ortec 572 shaping amplifier, which could give unipolar or bipolar shaped pulses with a wide range of amplifications and shaping times and finally a peak-detecting Canberra 8075 ADC, with up to 11-bits digitisation. The shaping amplifiers and ADCs were all mounted in a NIM rack. The digital data, 'data-ready' and 'reset' from the ADCs were multiplexed onto a Parallel Interface chip card, PC8255, controlled by a Research Machines Nimbus IBM compatible PC. For the earliest experiments a parallel piconet box was used as the interface to a 80186 equivalent computer.

The computer continuously examines the status of the data-ready line from each ADC. When an ADC has digitised a pulse, its data-ready line goes high and the computer begins a timing loop. If data-ready is indicated by the other two ADCs within their conversion time, then the event is accepted and the data is read from each ADC in turn. Otherwise the event is considered invalid and all the ADCs are reset ready for another event. The LLD levels of the ADCs could be controlled and the ULD was normally set to equal the highest level of the ADC.

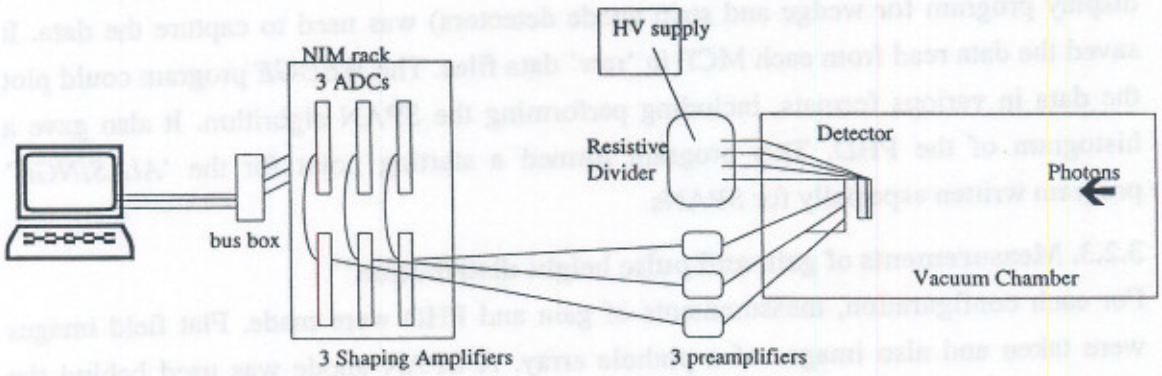

Figure 30. Diagram of laboratory apparatus.

The ADCs could digitise to 8-bits or up to 11-bits. For much of the early developmental work 11-bits were used. For flight, the ADCs digitise to 8-bits. This limits the resolution and gives certain digitisation effects which are discussed in Chapter 5. Using 11-bits for testing, detector effects and resolution could be separated from digitisation effects.

To set up the gains and DC offsets of the three electronics channels so that they were identical, a computer program (*TURBOCAL*) was developed by Trow and Edgar, MSSL, to send a range of digital signals to a high precision DAC. This analogue signal is used as a reference for a pulse generator which feeds the test capacitances of the preamplifiers. The signal height covers the full ADC range in about 20 steps (user defined). The resulting data, consisting of many pulses (usually 20–100) per step, is averaged by the computer and compared with the set signal height using a least squares fit or single value decomposition routine. The gradients and intercepts of the lines are displayed on the screen as the gains and offsets, so that they may be adjusted by iteration. The goodness of fit is also given as a χ^2.

The absolute gains can be calculated by feeding a known step voltage (V), through a known capacitance (C), to the input of each preamplifier in turn, in order to by-pass the small differences in values of the internal test capacitances. The resulting sum of ADC values is associated with the gain as the ratio of output to input electrons thus:

$$Gain = \frac{CV}{q_e} \tag{43}$$

where q_e is the charge of one electron. The total gain is the sum of the three channels. This method can also be used to measure the width of the electronic noise distribution of each preamplifier.

A computer program, written by Walton of MSSL, called '*WEDGE*' (written as a display program for wedge and strip anode detectors) was used to capture the data. It saved the data read from each MCP in 'raw' data files. The *WEDGE* program could plot the data in various formats, including performing the SPAN algorithm. It also gave a histogram of the PHD. This program formed a starting point for the '*ALLSINGN*' program written especially for SPANs.

3.2.3. Measurements of gain and pulse height distribution

For each configuration, measurements of gain and PHD were made. Flat field images were taken and also images of a pinhole array. A SPAN anode was used behind the MCPs.

Two different photon sources were used. At first the UV discharge lamp which had been involved in the development of detectors for CHASE was used. This had a number of different filters for selecting different UV wavebands. Secondly, the detector was stimulated by means of a collimated X-ray source. The K-shell X-rays are emitted from an aluminium target when it is struck by electrons produced by thermionic emission from a tungsten filament at high voltage (2 to 3 kV).

3.2.3.1. Chevron of double-thickness plates

Before the GIS development model detector was built, much work was done on the prototype two-dimensional SPAN detector, which was being developed for the Optical Monitor, an optical/UV telescope on XMM (X-ray Multi-mirror Mission—ESA's second cornerstone mission in its Horizon 2000 programme). The two-dimensional version can use a continuous SPAN pattern for one axis and discrete strips in SPAN ratios for the other, in a similar manner to the strips in a wedge and strip anode. The triplet of discrete strip electrodes is slotted between the pitches of the continuous axis. The widths of the strips are chosen to vary along the discrete axis in such a way as to mimic the continuous axis. The disadvantage is, as with the WSA, that the axes are not symmetrical and do not necessarily require the same charge cloud characteristics. It is difficult to get both axes to work well with the same MCP voltages. An alternative is to draw both axes as continuous SPAN patterns, but set at 45° to the measurement axes. This was the later design for the Optical Monitor, where the whole anode is symmetrical about the $x = y$ axis, which leads to some simplifications in the manufacture.

The original continuous-discrete detector was used to investigate the possible range of MCP voltages, interplate voltages and MCP-anode gap voltages with a view to their affect on the image produced. This work was therefore of direct relevance to the GIS detectors. A chevron set of double-thickness MCPs with 12.5 µm holes was used. A mask with a diagonal row of pinholes was put in front of the detector. Two different MCP-anode gaps were tried: 1 and 2.5 mm. The mid-MCP gap was varied between −40 and +60 V, anode gaps between 100 and 600 V and MCP voltage between 2700 and 3200 V, giving gains of $1–5\times10^7$.

The size of the spiral image is an indication of charge cloud spread (see Chapter 5 for explanation). If the spread is too small, modulation will occur. This results from the fact that the charge cloud does not average across all the electrodes and causes image distortion. If too large, the charge cloud smothers the pattern so that the full range of amplitude during one wavelength is not used, reducing the position resolution. Between the extremes, a larger spiral implies a smaller charge cloud and vice versa. It

was found that as the MCP voltage was increased, the gain would go up and that the spiral would reduce in size. This is the expected behaviour.

It was also found (see Figure 31) that as the mid-MCP gap voltage was reduced, the gain went up. This is understood from the above discussion as being due to the fact that more channels in the second MCP were being stimulated. With a negative mid-MCP gap voltage however, the gain was very low, presumably due to the deceleration of electrons in the gap. The MCP-anode gap voltage did not have much effect on the gain. The spiral reduced in size for a lower voltage, in line with a less well-defined charge cloud in a weaker electric field.

The resolution of the image improved with increasing gap voltage. It was discovered that even a very small mid-MCP gap voltage could have a significant effect on the image. While the continuous SPAN axis gave the best image at 0 V, 2 V was preferred for the discrete axis.

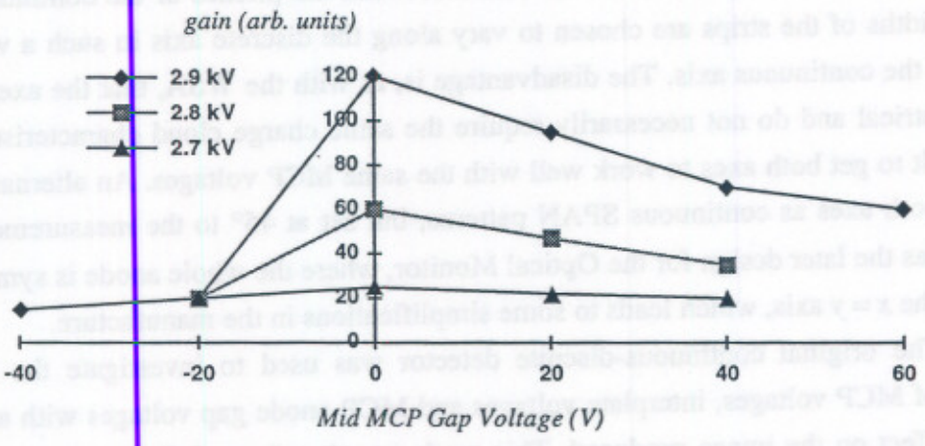

Figure 31. Variation of gain with mid MCP gap voltage
measured at 3 different MCP bias voltages (given in the key). The *y*-axis is measured in channels and is a relative measure of gain.

The first configuration used in the GIS development model detector was also a chevron double-thickness stack. The MCPs had been used in the development of detectors for the CHASE experiment and were in poor condition. They had very low resistances—1.5 MΩ and 3.5 MΩ and looked 'mouldy'. This turned out to be due to a crystalline deposit of degraded MgF_2 on the surface of the MCPs. The clean-up process involved rinsing and ultrasonic bathing in de-ionised water, in IPA, and finally a rinse in Arklone vapour. After evacuating the cleaned plates, the resistances had increased to 60 and 100 MΩ. At first, there were many problems with high count rate hot spots, but with

scrubbing and use, these were reduced to an acceptable level. The resistance of the MCPs gradually (over a few weeks) rose to ~400 MΩ across the stack.

The maximum gain obtained with these plates was about 1×10^7, with a PHD FWHM of 50–100%. The gain would probably have been higher when the plates were new.

This configuration was used mainly to develop and prove the concept of the one-dimensional SPAN anode detector.

3.2.3.2. Chevron of triple-thickness plates

A new set of Mullard triple-thickness plates was baked to 240°C for 48 hours before being mounted in the development model detector. They were initially butted together with no shim between them. The resistance was 900 MΩ across the stack.

At first it seemed to be very difficult to get a comprehensible PHD. There were many events (~600 per second) showing very low energy. There appeared to be breakdown problems at about 2.5 kV. However, the MCPs were persuaded to work eventually with the anode at high voltage and the front of the MCPs at ground.

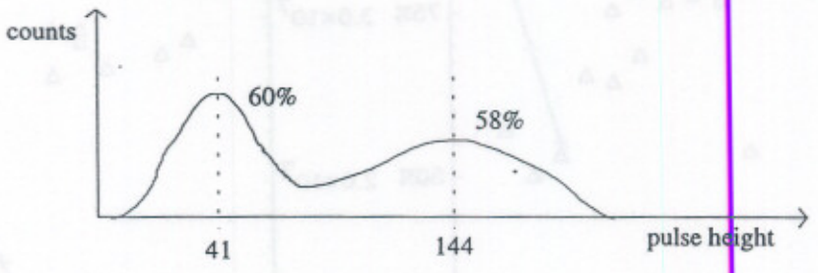

Figure 32. Twin peak pulse height distribution.
A sketch of an example PHD from the triple-thickness plates. The percentages refer to the FWHM of the peaks.

The plates exhibited a rare phenomenon of two distinct peaks in the PHD at certain voltages (see Figure 32). At low voltage, one peak would be evident, with the second 'high gain' peak growing as the voltage was increased. The gain of the low gain peak scarcely changed. At high voltages, the high gain peak would predominate.

Figure 33 shows the voltage and PHD width curve for these plates without any shims. For the measurements in Figure 33(a), the Penning gauge was used as a source of ions with the MCP front face at ground potential. As can be seen, the voltage has to be greater than 3.8 kV to obtain a gain of 10^7. For 4×10^7, more than 4.0 kV is needed. It is not necessarily easy to establish which is the 'real' photon peak. The measurements were repeated but with a source of X-rays instead of ions. The X-ray graph (b) is similar

except that the gain of the high gain peak is lower, with a maximum of 3×10^7 at 4.0 kV. This is presumably due to the higher number of initial photoelectrons produced by the ions as compared with the X-rays.

After taking these measurements, a 14 μm shim was inserted between the plates. Use of a conductive shim did not allow voltage to be put across the mid-plate gap, but different voltages could now be put across the top and bottom plates as well as across the MCP-anode gap. The shim allowed a larger number of pores in the back plate to be illuminated by electrons from the front. In this configuration the twin peaks were still evident. The overall gain increased by nearly an order of magnitude (*e.g.* at 3.5 kV with a shim gives 1.2×10^7, without gives 2.2×10^6 gain) while keeping the PHD width narrow (50–60%).

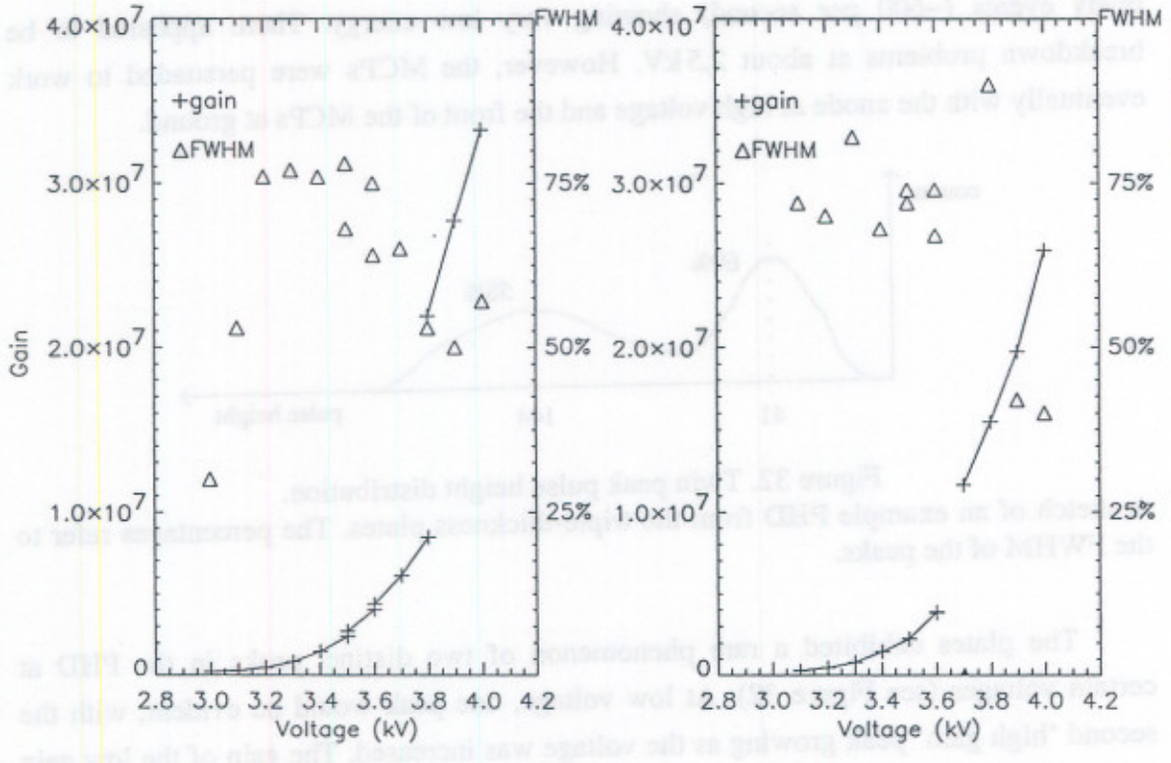

Figure 33. PHD for triple-thickness plates.
The MCPs exhibit a double pulse height peak. The discontinuity arises from the fact that measurements were taken first of the low gain peak and then of the high gain peak. The measurements in (a) were made using the Penning gauge to provide a wide spatial distribution of events. The pulse width is plotted on the same graph with 100% as full-scale. In (b) for comparison, is shown the gain with X-rays.

The preamplifiers had to be adjusted to allow them to operate at higher gains. The graph in Figure 34 was produced starting with an MCP-anode resistance of 10 MΩ. The gap resistance was reduced to 4.7 MΩ to allow the MCP voltage to go up to 4.3 kV.

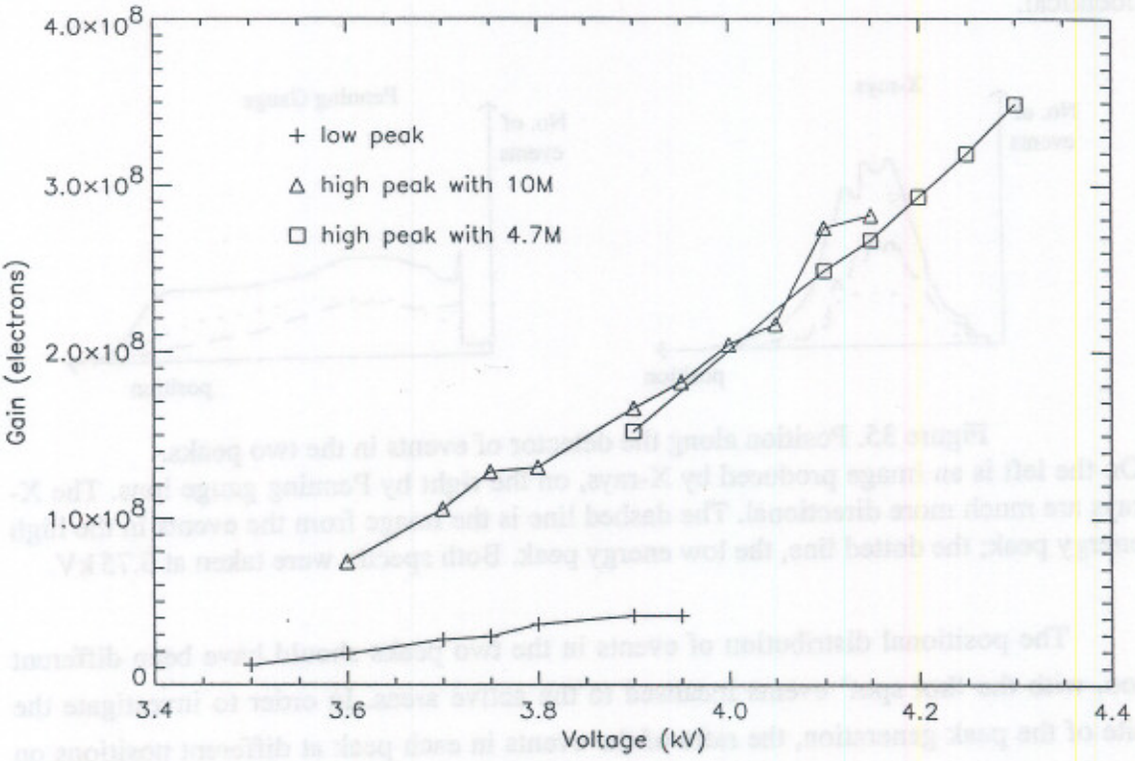

Figure 34. Gain of triple-thickness plates with shim with a MCP-anode gap resistance of 10 MΩ or 4.7 MΩ.

3.2.3.3. Investigating the twin peaks

It is well known that ion feedback can cause a second peak, but putting a bend into the path by using a chevron or *z*-stack is designed to eliminate ion feedback. The comparatively low gains and pressures involved did not suggest ion feedback.

Hot spot hypothesis

The first of many possibilities investigated, was that the low gain peak could be due to hot spot activity and not related in any way to photon events. In this case the hot spot peak may reduce with use and time. However, the background event rate was measured and found to be very low (less than 10 c s^{-1}) without a source on. Background events do contribute to the lower gain peak, but mainly occupy the low energy exponential tail.

If hot spots were the cause, then the ratio of counts in the peaks should vary with X-ray count rate. At higher event rate, the hot spot events would become less significant. The X-ray beam current was varied between 1 and 4 mA, giving a range of count rates of 700–2500 c s^{-1}. The positions and ratios of the peaks remained nearly identical.

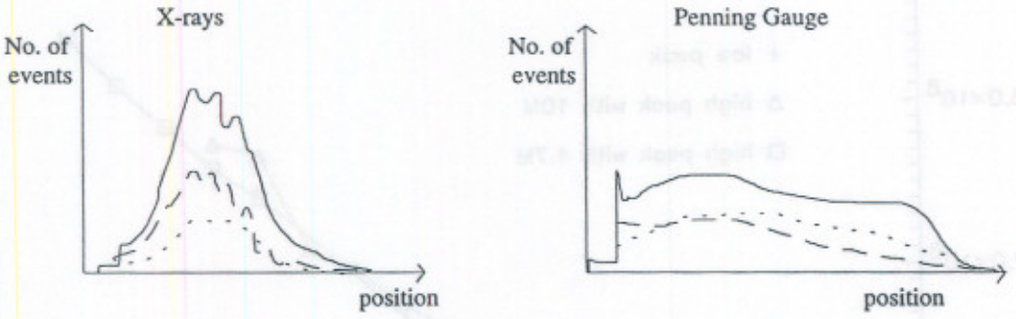

Figure 35. Position along the detector of events in the two peaks.
On the left is an image produced by X-rays, on the right by Penning gauge ions. The X-rays are much more directional. The dashed line is the image from the events in the high energy peak; the dotted line, the low energy peak. Both spectra were taken at 3.75 kV.

The positional distribution of events in the two peaks should have been different too, with the 'hot spot' events localised to the active areas. In order to investigate the site of the peak generation, the ratio of the events in each peak at different positions on the detector was measured. This could easily be done because for every event captured on the computer, its pulse height as well as position were recorded. A simple way of seeing the spatial distribution of the event energies was to consider the data as a one-dimensional image, windowing to select events of given energy ranges (see Figure 35). Although there is no particular positional dependence of either of the peaks, there are more high energy events with the X-ray source than with the ion source (note the swapping of the dashed with the dotted line).

The 'wiggles' appearing in the X-ray plot of Figure 35 could be due to modulation, where the charge cloud is too small to sample the anode pattern sufficiently (see Chapter 5). Alternatively, it could be due to the maximum charge level of the preamplifiers (1.3×10^8 electrons) clipping events in certain high ratio positions. It is noticeable that the wiggles are provided by the high energy part of the PHD which may account for the events meeting the preamplifier maximum level. It was confirmed, however, that the charge cloud for these events was spatially smaller than for the low gain events, because the spiral was larger for the high energy peak. This was not evident when the highest MCP-anode electric field was used (10 MΩ resistor giving 660 V), but

was apparent at all the lower voltages (5.6, 4.7 and 3.5 MΩ resistors giving 330, 300 and 230 V respectively). This suggests that the higher gain events have a smaller spatial distribution, leading to modulation.

Peaks dependent on photon or ion energy

It could be that ions produce one peak (the higher energy one) while X-rays give the lower one. However, then one would expect to see only one peak with the Penning gauge used as the source. Alternatively, since the detector front face is at ground, the higher peak could be the real X-ray or ion peak, while the lower one is given by stray low energy electrons.

The fact that the ratio of peaks does not vary with count rate suggests that both peaks are produced by the source. If the lower peak were produced by stray electrons then both the X-ray source and the Penning source must have a mechanism to produce electrons. It is possible that they are photoelectrons produced from the surrounding detector body. As the front face is at ground there would be very little acceleration onto the front face, so that the gain produced would be small. Ions may be expected to release more photoelectrons from the surrounding area than X-rays, both because they are more massive and also because they are less directional and would hit more of the detector body. This ties in with the fact that there are more low energy peak events in the Penning plot (comparing the plots of Figure 35).

To test this idea the X-ray source was run at lower voltages to reduce the energy of the incident photons. The k-edge of aluminium is at 1.562 kV. Since aluminium is used in the detector body and mounting stage, the source voltage was reduced from 2.0 kV to 1.4 kV in 0.2 kV steps, to span the k-edge. While the total count rate was much reduced (from 700 to 40 c s^{-1}), the ratio of counts in the low gain to high gain peak changed significantly as the edge was crossed. The data was corrected by subtracting the few hot spot events so that they did not distort the number of events in the low gain peak. The result was that the ratio increased as the X-ray energy decreased—the opposite to what was expected, if stray electrons caused by the interaction of X-rays with the detector body had been the cause.

Another test for the stray photoelectron hypothesis was to apply a bias to the front face of the MCP in order to repel electrons. A variable voltage of −100 to +100 V was applied to the detector front face from outside the chamber. No significant change in the ratio of peaks was found between these two extremes; it was therefore concluded that neither peak was caused by stray electrons, assuming that the stray electrons had energies of less than 100 eV.

Ion feedback

If ion feedback in the top plate were the explanation for the high gain peak, then it should get more pronounced at higher pressures. This was tested by looking at the ratio of the peaks with ions at a range of pressures of $2–5\times10^{-6}$ mbar. The ratio changed from 2.5 ± 0.3 at 5×10^{-6} mbar to 3.5 ± 0.4 at 2×10^{-6} mbar, so there was a significant increase in the high gain peak with pressure. The total count rate nearly doubled over this range too, due to the fact that the Penning gauge produces more ions at higher pressures. It was difficult to isolate the effects of count rate and pressure.

Reduction of ion feedback may be achieved by simply keeping the MCPs under vacuum and it may be accelerated by scrubbing the plates to remove their impurities. A scrub at 15000 c s^{-1} was carried out for 13½ hours, removing 1.1×10^{-8} C s^{-1} to a total of 5×10^{-4} C. Over this time, the gain of the plates fell by 30% and the ratio of low gain peak to high gain peak changed from 0.9 to 1.38 *i.e.* there was less and less in the high gain peak. This supports the ion feedback theory.

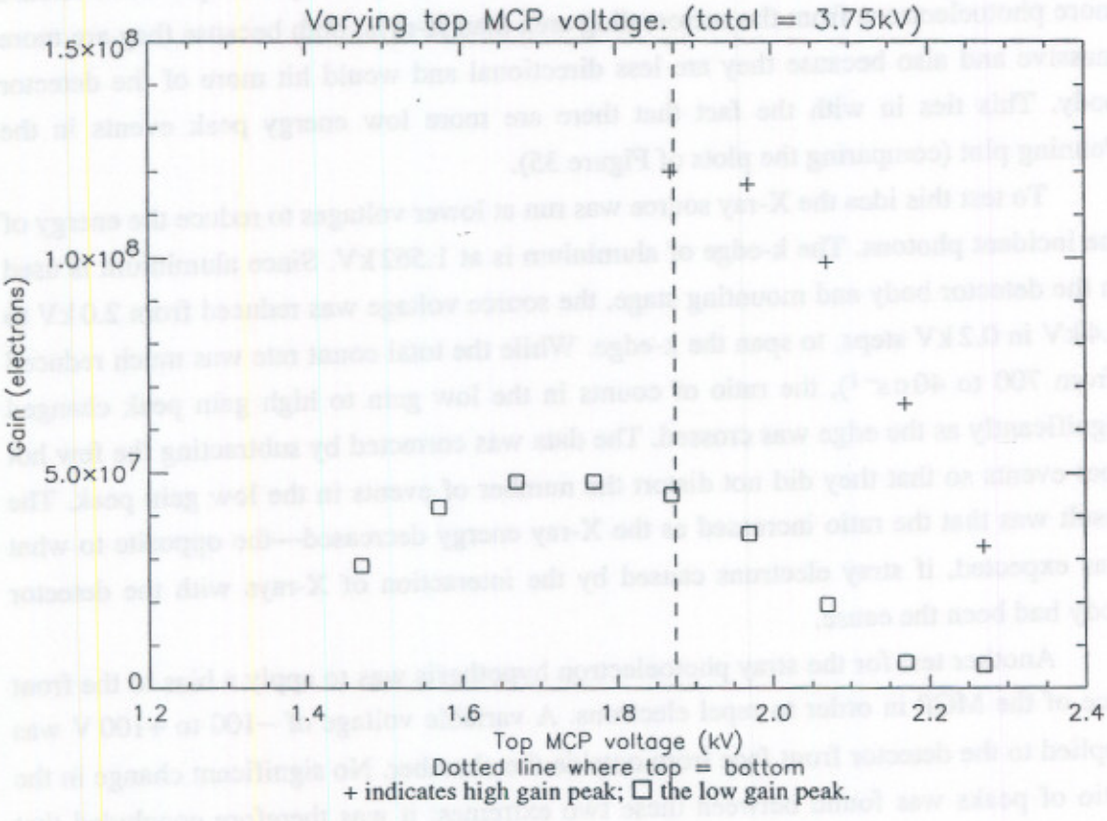

Figure 36. Gain of triple-thickness stack with shim.
Varying the top plate voltage while keeping total equal to 3750V.

It was instructive to put different voltages across the top and bottom MCPs, while keeping the total voltage constant. At two different voltages, 3.75 kV and 3.9 kV, the voltage across the top plate was varied between 1.45 and 2.3 kV (see Figure 36). At both voltages, the high gain peak did not appear unless the top plate voltage was equal to or greater than 1.8 kV. The gain of both peaks was at a maximum at the equality, dropping off either side, although the total count rate was maintained at a maximum between 1.8 and 2.2 kV across the top plate. The widths of the peaks were at a minimum (~ 50%) near equality but did not vary much across the range.

Four other experiments were carried out, keeping one plate constant first at a low voltage (1.65 kV) then at a high voltage (2.25 kV), while varying the other (see Figure 37). From this it appeared that the gain of both peaks was dominated by the lower plate voltage, even though, as stated above, the high gain peak did not appear until the top plate was above about 1.8 kV setting, except when the bottom plate was itself at its maximum voltage (see graph (b) in Figure 37). The discontinuity in graph (b) is associated with a reduction in the voltage across the anode gap in order to get sufficient total MCP voltage from the power supply. Keeping the bottom plate constant while increasing the top plate voltage leaves the low gain peak at approximately the same gain, while the high gain peak increases rapidly. Keeping the top plate constant while increasing the bottom plate voltage causes the gain to increase gradually linearly.

The results of these experiments suggest that the twin peaks are caused by an effect in the top plate. This supports the ion feedback hypothesis.

Number of pores stimulated in bottom plate

If the electrons from the top plate illuminated just a small number of pores in the second plate, then the difference between illuminating one pore or several pores may give two distinct peaks. According to data on charge cloud sizes and distributions (see Chapter 5), beyond a certain voltage the distribution starts to form wings. The spread of gains from the top plate may include some with and some without wings. This would account for the fact that the high gain peak switches on at a certain top plate voltage and the percentage of events in this peak gradually increases.

However, from the measured spiral image, the charge cloud extent appeared to become smaller as the top plate voltage increased, with the rate of change at a maximum near the equality. This fact contradicts the possibility that the greater spreading in the gap might give the high gain peak, because the greater spreading would be expected to lead to a larger cloud.

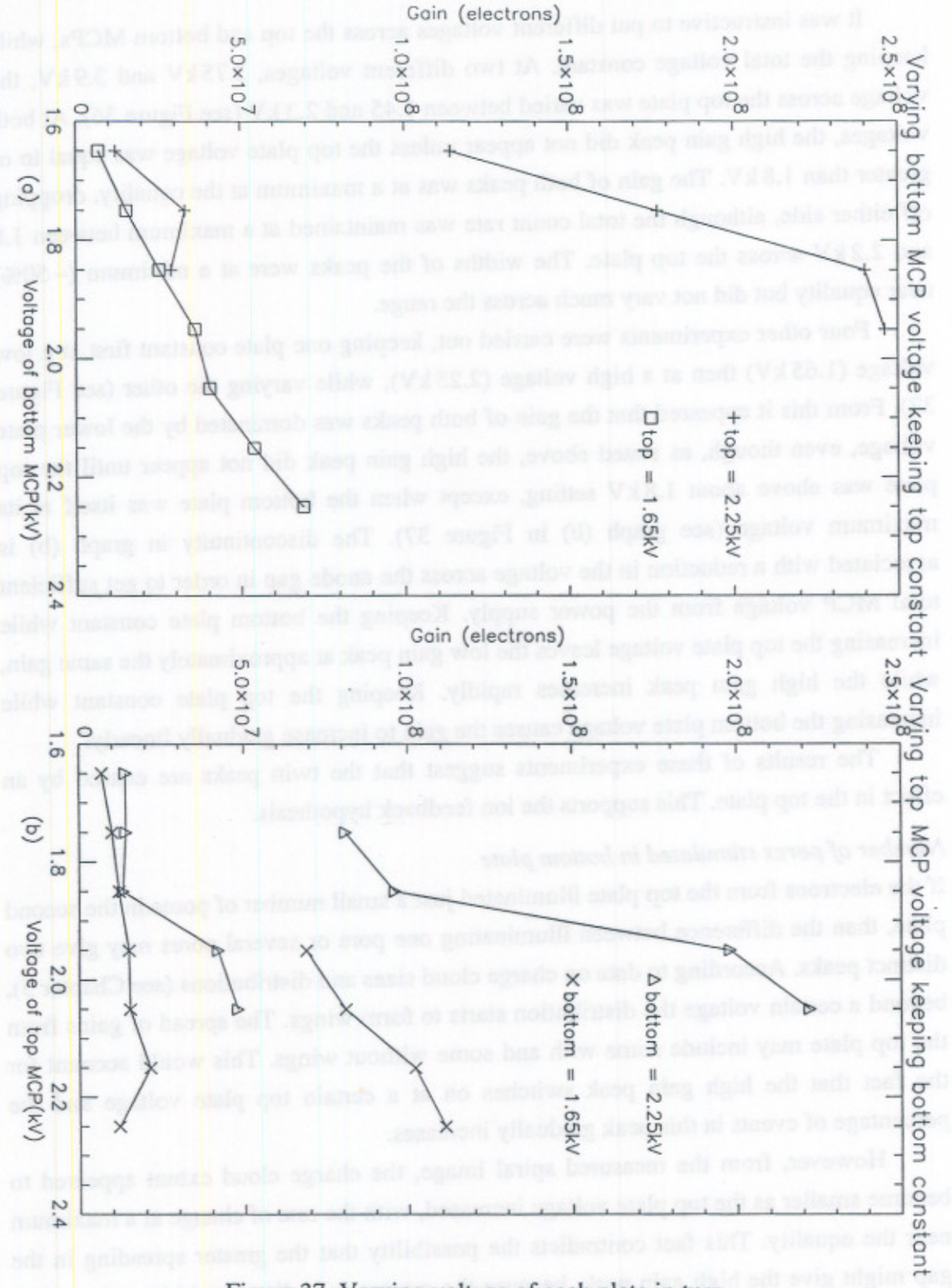

Figure 37. Varying voltage of each plate in turn keeping the other plate at either 1.65 kV or 2.25 kV throughout. Graph (a) is varying the bottom plate voltage and (b) the top plate voltage. Both low and high gain peaks are plotted.

In an attempt to find out whether different numbers of pores illuminated could give the two peaks, equation (32) (in §3.2.1.) was fitted to the data in the graph in Figure 34. From equation (40) the gain of each plate should be proportional to voltage. Note that α in equation (40) is the *l:d* ratio, whereas in equation (32) α is the number of pores stimulated in the lower plate per event.

As a trial at one voltage, inserting the values for π, ε_0, e, d and α into equation (40), with a voltage of 1850 V (3.7 kV across both plates), gives a theoretical gain of 8400. In practice this voltage across both plates in the chevron stack gives a measured total gain of 9×10^7 (high gain peak). It is necessary for α to be greater than zero physically. A value of less than zero would imply that the more pores illuminated in the rear plate by the front plate, the smaller the gain. Using these values for total, front and rear plate gain in equation (32) the only method of arriving at a positive value for α is to have N_C bigger than 8400, which is unreasonable. Adjusting the value of single plate gain to 1×10^5 allows values of $\alpha=0.6$ and $N_C=3.7$, which are physically reasonable. If a value for N_C of 1 is used, a gain of 1×10^7 is obtained, which is close to the low gain peak value at this voltage. However, this is only at one voltage.

In order to find out whether it is possible to use this model at more than one voltage, it was necessary to fit to the available data. For this the assumption that gain is proportional to voltage found in equation (40) was used for both MCPs. Assuming the voltage across both MCPs is the same:

$$G_C = (AV)^{1-\alpha}.BV.N_C{}^{\alpha} \qquad (44)$$

where V is the voltage across either detector. A and B are constants of proportionality to be found. Plotting the logarithm of G_C versus that of V, using the data of Figure 34, a straight line is obtained, the gradient of which is given by $m=2-\alpha$ and the offset of which is $c=(1-\alpha)\ln A+\ln B+\alpha\ln N_C$. A straight line was fitted to the high gain peak by the least squares method. The gradient gave a negative value of α. The low gain peak was tried but with similar results. As explained above, it is unphysical to have a negative α. The reason this model fails is most likely because the front MCP is not saturated and therefore does not give a gain proportional to voltage.

Using an exponential model for the individual MCP gains does allow reasonable values of N_C and α to be found using a least squares fit. The high gain peak fits to $N_C=7$ with $\alpha=0.66$ and for the low gain $N_C=2$ fits. However, this model does not fit to the data with different voltages across each plate. It is therefore inconclusive as to whether the difference in gain of the two peaks could be due to a simple difference in the number of pores stimulated in the rear plate.

The only hypothesis that fits the data is that the high gain peak is caused by ion feedback in the top MCP.

3.2.3.4. Z-stack of double-thickness plates

The z-stack, like the chevron, was a new set of Mullard plates. They were baked at the same time as the triple-thickness ones, to 240°C for 48 hours. The z-stack consisted of three double-thickness (80:1) plates; one straight channel MCP and two with a 13° bias in the plane of the short side. They were first mounted with the straight channel MCP on the top of the stack, with 50 µm shims between each one:

There was a very high resistance, 1.6 GΩ, across the whole stack. The resistive divider chain outside the vacuum chamber had 20 MΩ across each MCP.

Ion feedback was not a problem with this configuration. Although the total channel length is the same as with the triple-thickness chevron, the extra bend was enough to prevent ion feedback. The chevron had a bias of only 8°, whereas the z-stack had a 13° bias. This more severe bias is another contributory factor to preventing ion feedback.

A number of conductive nickel shims, in different configurations, were inserted between the plates, (see Figure 38). As the two 50 µm shims gave plenty of gain but a poor PHD width (not getting below 60% by 6×10^8 electrons), the lower shim was replaced with a 14 µm shim. This allowed plenty of gain by spreading in the top gap, but a reduction in the bottom gap spreading to tighten up the PHD. However, although the gain was reduced marginally, the PHD was scarcely affected. Both shims were removed and the 14 µm one inserted in the top gap. This gave a significant reduction in gain at a given voltage, but also a desirable reduction in the PHD width. The MCP-anode gap resistor of 10 MΩ was reduced to 3.6 MΩ to allow the voltage to be raised. This gave a smaller anode-MCP voltage and is plotted as a different symbol in Figure 38.

Interestingly, in plotting the PHD FWHM against the voltage across the MCPs, results from all configurations lie on approximately the same curve (Figure 39). Although the PHD is narrower for thinner shims, the gain is lower too. A possible explanation for this phenomenon is as follows: it can be assumed that every channel in the bottom plate which is stimulated by electrons will be saturated. The depth of saturation depends only on the voltage. If the FWHM is determined solely by the depth

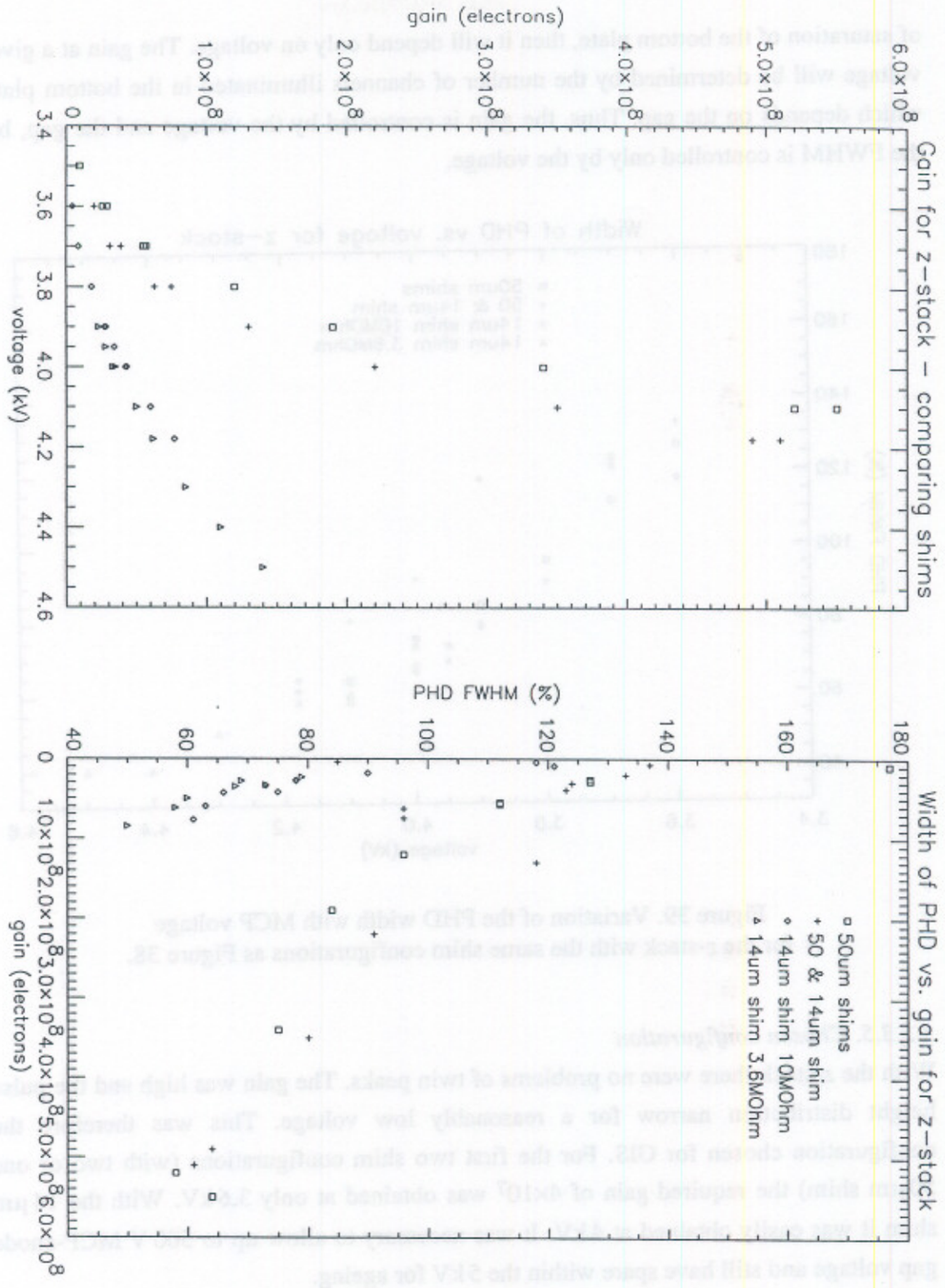

Figure 38. Characteristics of the *z*-stack varying with shim thickness. The four configurations are described in the text. For the first two, the anode-MCP voltage was set by a 10 MΩ resistor.

of saturation of the bottom plate, then it will depend only on voltage. The gain at a given voltage will be determined by the number of channels illuminated in the bottom plate, which depends on the gap. Thus, the gain is controlled by the voltage and the gap, but the FWHM is controlled only by the voltage.

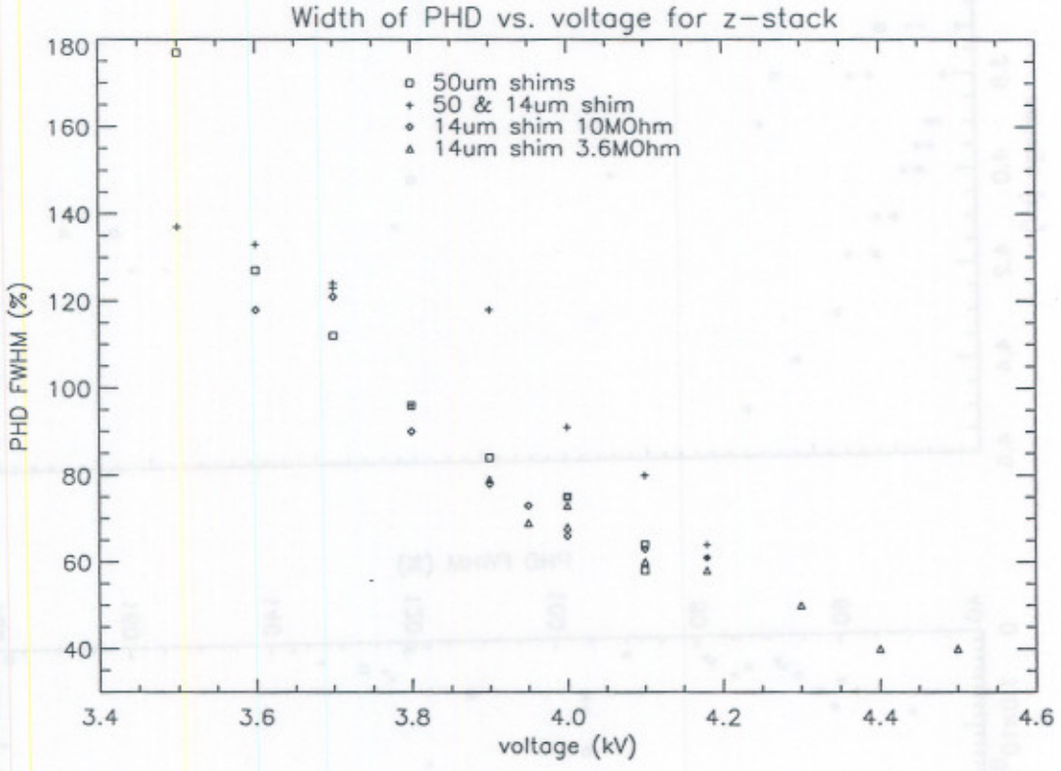

Figure 39. Variation of the PHD width with MCP voltage for the *z*-stack with the same shim configurations as Figure 38.

3.2.3.5. Chosen configuration

With the *z*-stack there were no problems of twin peaks. The gain was high and the pulse height distribution narrow for a reasonably low voltage. This was therefore the configuration chosen for GIS. For the first two shim configurations (with two or one 50 µm shim) the required gain of 4×10^7 was obtained at only 3.6 kV. With the 14 µm shim it was easily obtained at 4 kV. It was necessary to allow up to 500 V MCP-anode gap voltage and still have spare within the 5 kV for ageing.

For the 50 µm shim configurations the gain at 4×10^7 produced a width of ~110–120%, which was too wide. The thinner shims gave a width of less than 70% at this gain. A compromise between gain and PHD width was chosen in two shims: a 25 µm

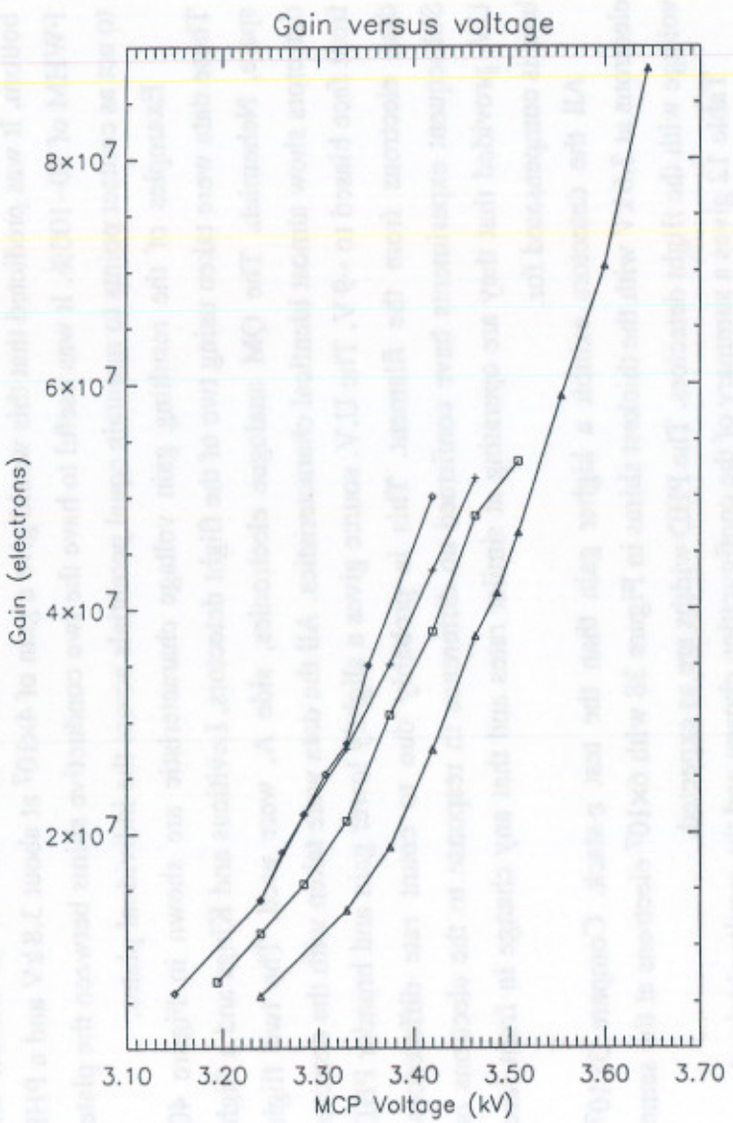

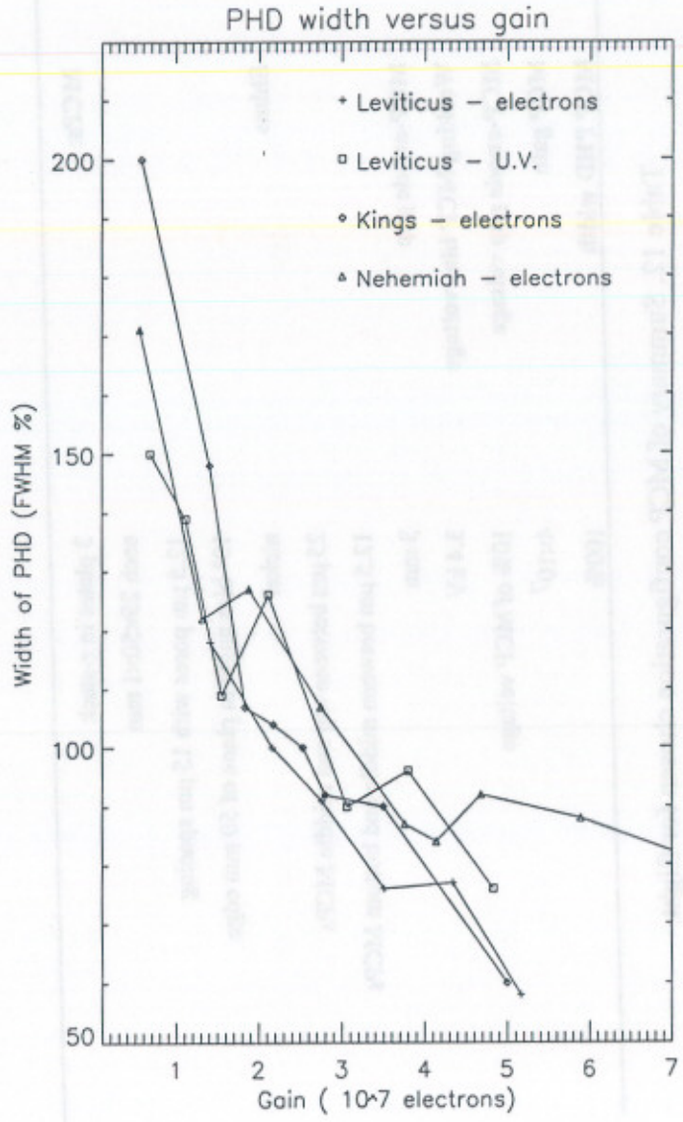

Figure 40. Gain plotted against applied voltage.

shim between the top and middle plate and a 12.5 µm shim between the middle and bottom. It was predicted that this would give a gain of 4×10^7 at about 3.8 kV and a PHD FWHM of 90–100%. It was useful to have the two conductive shims between the plates to act as contact points to maintain equal potentials across the individual plates.

Examples of the resulting gain voltage characteristic are shown in Figure 40. These data were taken using two of the flight detectors, Leviticus and Kings and a flight spare, Nehemiah. The QM analogue electronics, side A, were used. The two flight detectors show almost identical characteristics. All the data were taken with the detector front face biased to –9 V. The U.V. source gives a slightly lower gain and broader PHD than electrons from the filament. This is probably due to count rate differences. Subsequent experiments have confirmed no difference in response to the electrons or UV, provided that they are operating at similar rates and that any change in front face bias is compensated for.

All the detectors exhibit a higher gain than the test *z*-stack. Compare 3×10^7 electrons at 3.6 kV with the thickest shims in Figure 38 with 6×10^7 electrons at the same voltage with the flight detectors. The PHD widths are as expected.

Table 12 gives a summary of the configuration chosen and the results obtained.

MCPs:	3 plates in *z*-stack
	each 25×50×1 mm
	12.5 µm pores with 15 µm spacing
	13° bias angle in plane of 50 mm edge
Shims	nickel
	25 µm between top and middle MCPs
	12.5 µm between middle and bottom MCPs
MCP-anode gap	3 mm
Working MCP bias voltage	3.4 kV
MCP-anode gap voltage	10% of MCP voltage
MCP gain	4×10^7
MCP PHD width	100%

Table 12. Summary of MCP configuration chosen for flight.

The selection of MCP configuration, working gain, expected PHD and energy window were made on the basis of the experiments that have been described here. With hind-sight, given the gain depression problems (see §3.4.), it may have been better to

have chosen a much narrower PHD (<50%) even if it had meant a loss of gain for a given voltage, especially since the gain turned out higher than expected. No shims, or just one between the top and middle plates, as with the 14 μm shim setup, would have allowed a gain of 4×10^7 and a narrow PHD. The energy acceptance window (between the lower and upper level discriminators) could have been set wider too. These changes would have allowed more scope for variations in gain in a given input spectral line without changing the intensity measurement. However, the changes would have led to the following disadvantages: a narrower PHD obtained at the expense of gain would imply a shorter MCP lifetime before reaching the limit of 5 kV HV supply. Widening the energy acceptance window at the lower end admits events with poorer signal to noise, reducing the resolution. Thus there is a trade-off between lifetime, resolution and linear intensity measurements.

3.3. QUANTUM EFFICIENCY OF MCPS

The absolute QE of the GIS MCPs has to be calculated from the results of the flight calibration test with a calibrated discharge lamp (see Chapter 8). Relative responses to the wavelengths and angles can be measured more easily in the laboratory and results are presented in Chapter 4. This section discusses the expected QE for GIS.

3.3.1. Efficiency with wavelength

Most recent research into EUV QE has been associated with alkali halide coatings for MCPs or for MCPs used at near normal incidence. However, there are some results and models for bare MCPs in the wavelength range of relevance.

Figure 41 gives QE measurements, by various authors, made at near normal incidence, covering the GIS 15.5–78.7 nm range. The angles quoted below are relative to the MCP bias angle *e.g.* an angle of 8° is obtained by normally illuminating an 8° bias plate. Taylor *et al.* (1983), using an 80% transmitting repeller grid at zero voltage and a 30° angle of incidence, obtained 10% at 17.0 nm, 6.5% at 30.4 nm and 58.4 nm and 1% at 121.6 nm. At an angle of 8°, Martin and Bowyer (1982) found 4% at 20 nm and 6% for 30–80 nm. Kowalski *et al.* (1986), also with an 8° angle of incidence obtained 10% at 15 nm, falling to 5% by 40 nm. Bowyer *et al.* (1981) gave a graph of efficiency with increasing angle for 30.4, 58.4, 92.0 and 121.6 nm, starting at 20°. The 20° measurements are included in the figure.

More recently, Siegmund made a series of measurements covering wavelengths between 30 and 120 nm. These measurements, taken at 15°, are plotted on Figure 41. As can be seen here, they are much higher than the measurements taken by the other authors.

From these results and from a model of response with wavelength by Fraser *et al.* (1982), it is not expected that there will be much change across the range, although there may be a reduction above about 60 nm.

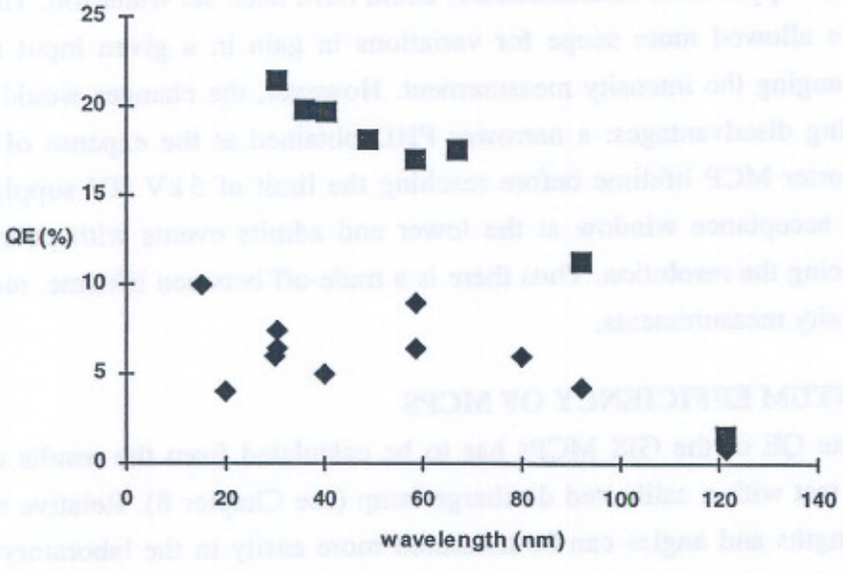

Figure 41. Quantum efficiencies measured at EUV wavelengths at near normal incidence. ◆ are measurements taken from Taylor *et al.* (1983), Martin and Bowyer (1982), Bowyer *et al.* (1981) and Kowalski *et al.* (1986); ■ are from Siegmund (1991). The Siegmund data also appears in Figure 45.

3.3.2. Grazing incidence—expected response

The incident angles (relative to the detector front face, not the channel bias angle) on the GIS detectors range between 67.4° at the longest wavelength to 77.6° at the shortest wavelength.

The best response from MCPs is obtained at incident angles of between 5° and 10° relative to the angle of the channel. At angles lower than this, photons tend to penetrate deep into the channel, resulting in lower gain. In addition, the angle of incidence to the channel wall is high, thus increasing the likelihood of reflection of the photon even further down the channel. At angles above 10° there is a decreasing photoelectric yield but also decreasing reflectivity. For longer wavelengths (*e.g.* 121.6 nm), these seem to cancel each other out, giving a flat response with angle. At shorter wavelengths, the decrease in photoelectric yield dominates. The effect of the reduced electric field due to end spoiling is also more important at high angles of incidence. Figure 42 shows the

relative response of a MCP to X-ray illumination from different angles of incidence and different energies.

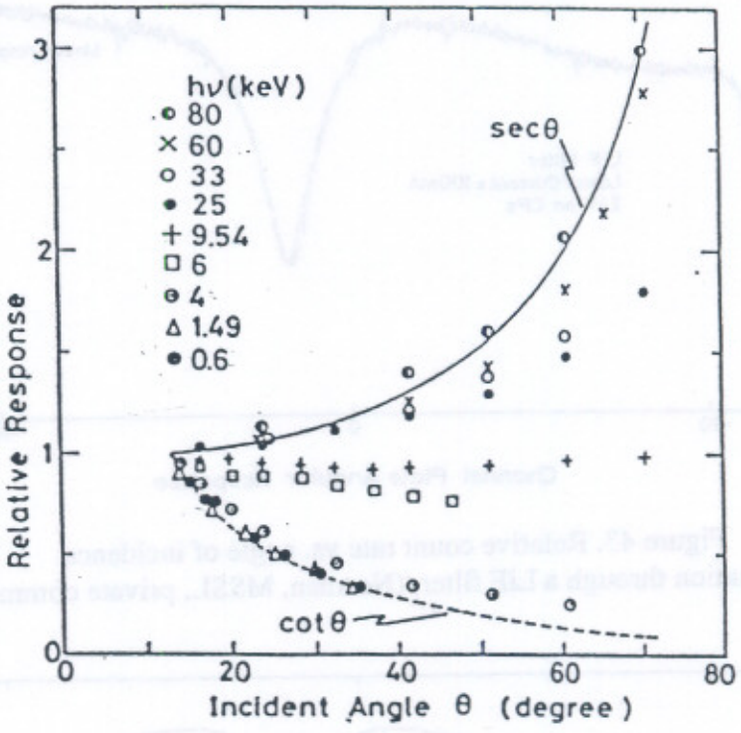

Figure 42. Response of MCP to X-rays of various energies and incident angles taken from Yamaguchi *et al.* (1989).

As can be seen in the diagram, for the lower energy X-rays (<4 keV) the response follows approximately a cot(θ) curve. At higher energies (>60 keV) it has a sec(θ) dependence. In between there is a region at about 10 keV where there is no angular dependence. At low energies, any interaction will take place near the surface of the channel wall. Therefore, the efficiency will depend on the amount of wall exposed to incoming radiation, which is proportional to cot(θ). At high energies, the incoming X-ray will pass through the MCP, exciting any channels on the way. Thus the response is proportional to the thickness of the MCP traversed by the beam, which is sec(θ). In respect of the detectors in this study a cot(θ) dependence may therefore be expected.

The angle at which the efficiency is at a peak rises as the photon energy decreases because the critical angle of reflection increases, (Barstow *et al.*, 1985). For a bare MCP, the XUV QE at an incident angle of 25° is less than 15%.

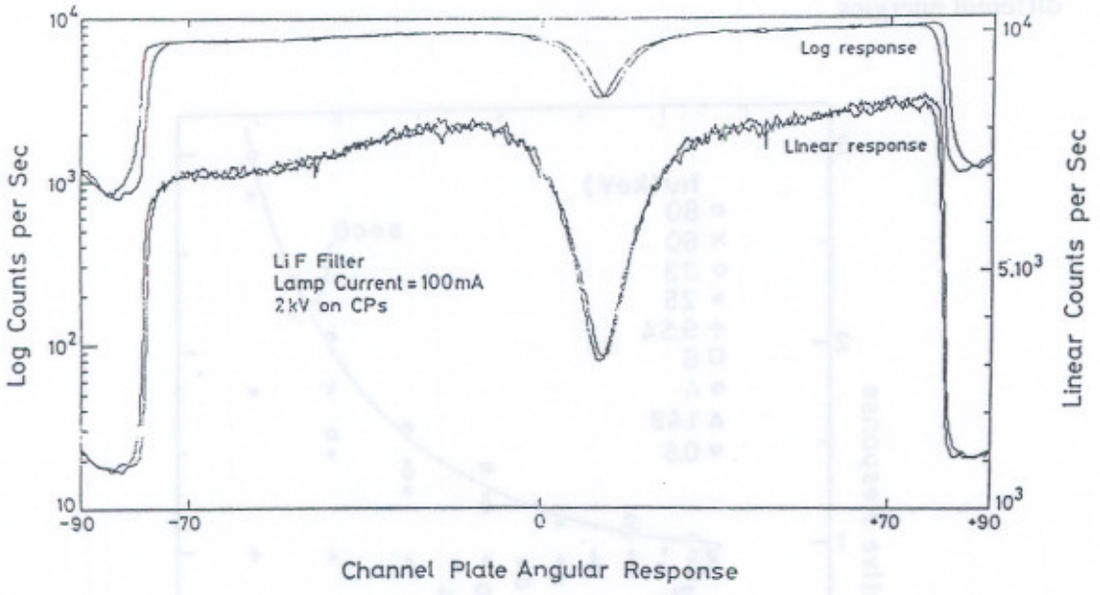

Figure 43. Relative count rate vs. angle of incidence
for UV illumination through a LiF filter, (Norman, MSSL, private communication).

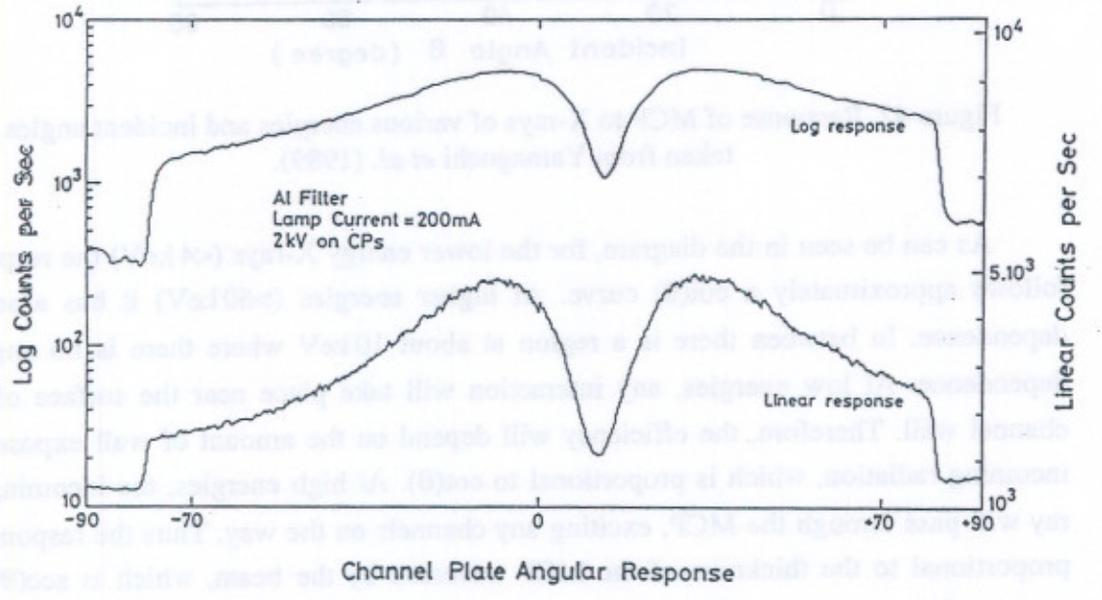

Figure 44. Relative count rate vs. angle of incidence for Al filter
(Norman, MSSL, private communication).

Fraser (1983) describes a model for the quantum detection efficiency of an MCP detecting electrons, in terms of electron energy and angle of incidence. He uses an MCP with a zero bias angle and no coating in addition to the nichrome. According to him, for

electron energies of less than 100 eV, the secondary electron yield of lead glass has a negligible dependence on the grazing angle α'.

Norman made a number of relative angle of incidence measurements for CHASE. He used two different filters to select UV light. A lithium fluoride filter selected wavelengths longer than 105 nm, which is at too low an energy to release an electron from the lead glass, so that only the nichrome electrode response was being measured. An aluminium filter selected wavelengths between 17 and 75 nm. With LiF, there was no change in response up to 80°, after which the count rate dropped off rapidly. With Al, there was a reduction to half the maximum by 80°.

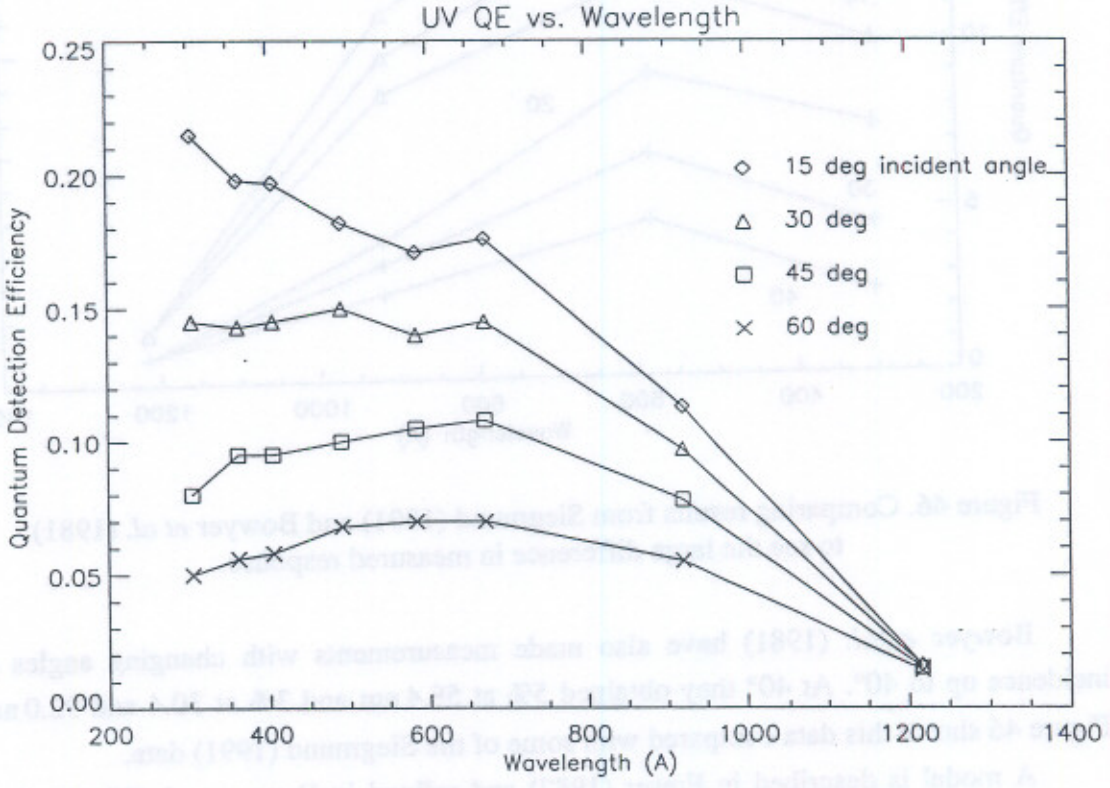

Figure 45. Summary of results from Siegmund (1991) showing the response of MCPs to light of wavelengths between 30 and 120 nm, falling on the MCPs with an incident angle between 15 and 60°.

Siegmund (private communication, 1991) also considered the EUV response of the MCPs with angles of incidence. He produced a series of curves showing absolute QE at a range of wavelengths, between −35° and +60°. They all follow similar trends to the curves in Figures 43 and 44 and show the same reduction in sensitivity to angle with

increasing wavelength. In Figure 45 the results from four angles have been selected and plotted versus wavelength.

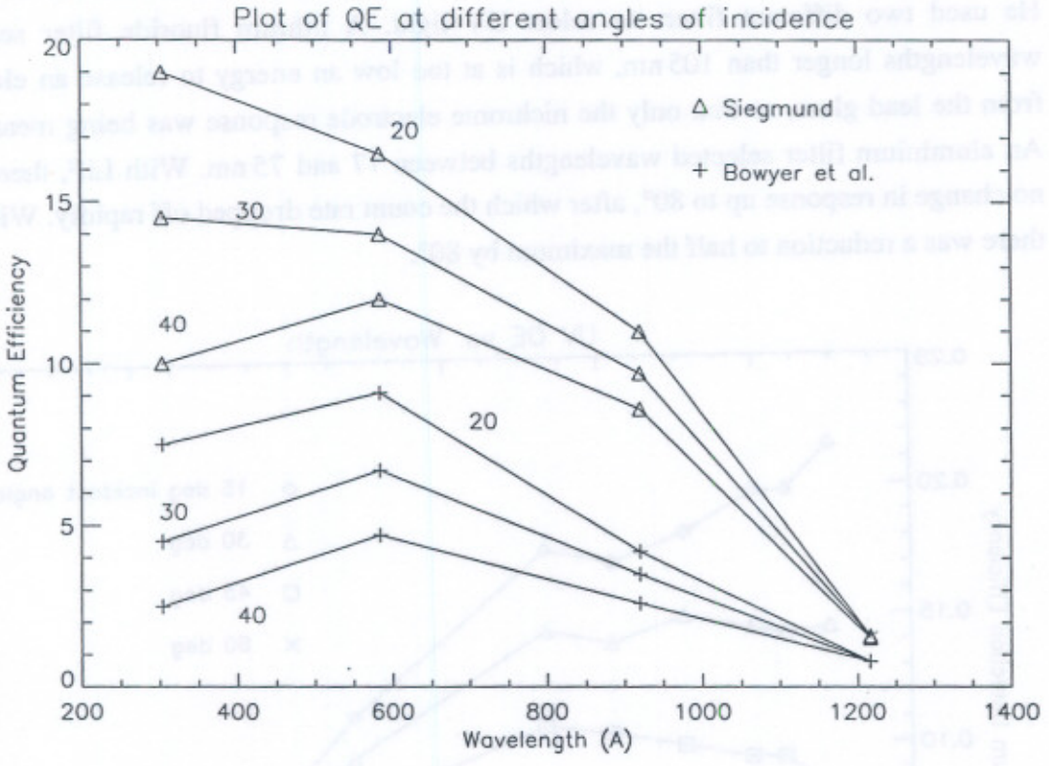

Figure 46. Comparing results from Siegmund (1991) and Bowyer *et al.* (1981) to see the large difference in measured response.

Bowyer *et al.* (1981) have also made measurements with changing angles of incidence up to 40°. At 40° they obtained 5% at 58.4 nm and 3% at 30.4 and 92.0 nm. Figure 46 shows this data compared with some of the Siegmund (1991) data.

A model is described in Fraser (1982) and refined in Fraser *et al.* (1984) which predicts the EUV response of MCPs between 5 and 60 nm, for incident angles of 10°, 20° and 30°. This anticipates a fairly flat response across the wavelength range, but a cosec(θ) dependence with angle of incidence. Fraser (1990) uses this proportionality on the data compiled by Bowyer *et al.* (1981), taken at angles of incidence of less than 40°, in order to make predictions about the response at high angles of incidence. Given the relatively poor fit of the real data to the cosec(θ) curve, the accuracy of the predictions is limited. As was shown in the scatter plot of Figure 41 and in Figure 46, where part of Siegmund's data from Figure 45 and the data from Bowyer *et al.* are plotted together,

there is a variety of numbers one could use as a starting point. Ignoring the results taken at an 8° angle and the very high Siegmund values, Figure 47 shows a possible range.

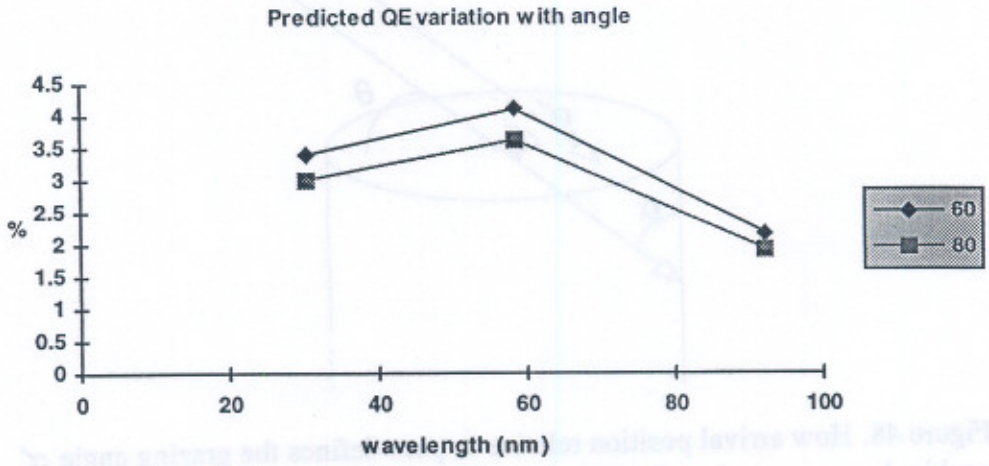

Figure 47. Predicted variations in sensitivity with angle over the angles of incidence 60 to 80°.

The depth to which the nichrome extends has a significant effect. If it is deposited at the usual 45° to the normal, then the QE at 40° angle of incidence is ~25%. If the nichrome is deposited at near normal incidence so that it penetrates further down the channel, the QE at 40° is reduced to just 5%. For GIS the depth of nichrome was specified as half a pore diameter in depth. In §2.2.2. a simple model was illustrated, describing how the response to end spoiling depends on the angle of incidence of the photon. In that model, a value of 79° was found for the maximum angle of incidence at which the photon should not meet the end electrode.

In fact, at an incident angle of 79° only a very small fraction of the incoming photons hit the channel wall below the end spoiling. If they arrive at a position such that they do not cross the whole diameter of the channel, they meet the wall higher up. The position also determines the angle at which they intersect the wall. If ψ is defined as in Figure 48, to give the angle of arrival around the pore perimeter, then the angle of incidence between the channel and the wall, α, is modulated by a cosine of ψ thus (Fraser, 1983):

$$\sin\alpha' = \sin\theta.\cos\psi \qquad (45)$$

The results given above of near normal incidence, 30°, 40°, 80° and the range of angles used by Siegmund, justify a prediction of between 2–5% for GIS, bearing in mind

the enhancements in QE from increased channel angle and a reduced electrode end-spoiling depth.

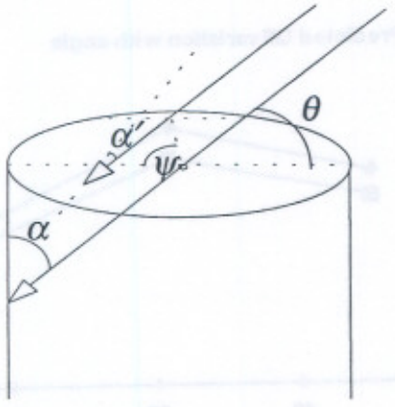

Figure 48. How arrival position relative to pore defines the grazing angle α'. Relationship between angle of incidence (θ) between photon and MCP, position of photon relative to pore (ψ) and angle of incidence between photon and wall of MCP (α').

3.3.3. Effect of coating MCPs

Useful photo-emission can be obtained from many metals in this region of the spectrum and can be enhanced by evaporating thin layers of insulating material onto the metal surface. The particular high emission qualities of certain substances such as CsI have been well known and in circulation since at least 1962 (Dunkelman *et al.*, 1962).

Some coatings commonly used to enhance the QE of MCPs include CsI, KBr, KCl and MgF_2. The MCP detectors in CHASE were coated with MgF_2 for EUV enhancement. Sometimes efficiencies as high as 40% may be achieved in the EUV by using photocathode coatings. CsI can be particularly effective for soft X-rays (<7 nm) (Fraser *et al.*, 1982).

The photocathode may be deposited to a variety of thicknesses, typically of the order of 1.5 μm, while the MCP is heated to 100°C. If the deposition angle is 10°, there is 100 nm deposited inside the walls. If the insulating material is too thick, saturation effects can be caused by the fact that the insulating surface continually charges up when exposed to radiation. The current given by MgF_2 evaporated onto a stainless steel substrate and illuminated by light at 58.4 nm was measured by Samson (1984). The maximum current is evident with a very thin coating. The current carries on rising with time, due to the fact that the increasingly charged up photocathode repels electrons more readily from the surface, resulting in their detection. This is the opposite of what would

be required from an MCP coating, where the electrons need to be directed towards the open pores rather than away from the surface.

Barstow *et al.* (1985) describe how a coating of CsI increases the QE in the soft X-ray (0.21–6.77 nm) and EUV (25.6–200 nm) bands. For ROSAT, CsI was coated at 11° to a thickness of 1.4 μm, giving 82 nm on the walls. These researchers found it practicable to use a high transmission (92%) tungsten mesh as a repeller grid.

The QE depends, as always, on the energy and incident angle of the photons. The QE enhancement for a particular photocathode depends on the absorption coefficient of the material, the mean diffusion length of an electron, the electron escape probability at the photocathode surface, the photoelectron energy distribution and the probability that an emitted electron will be detected by the MCP.

Siegmund *et al.* (1987b) show structures in the wavelength dependence of the QE, due to the valance to conduction band energy gap and the onset of atomic-like resonant transitions. Barstow *et al.* (1985) also note that in using CsI there is a strong peak at 10.0 nm because of a *4d-4f* absorption feature.

Figure 49 presents a collation of results of QE measurements. According to this graph, all the photocathodes give convincing enhancement of the QE, although it must be remembered that the results are not all taken with the same configuration and MCPs.

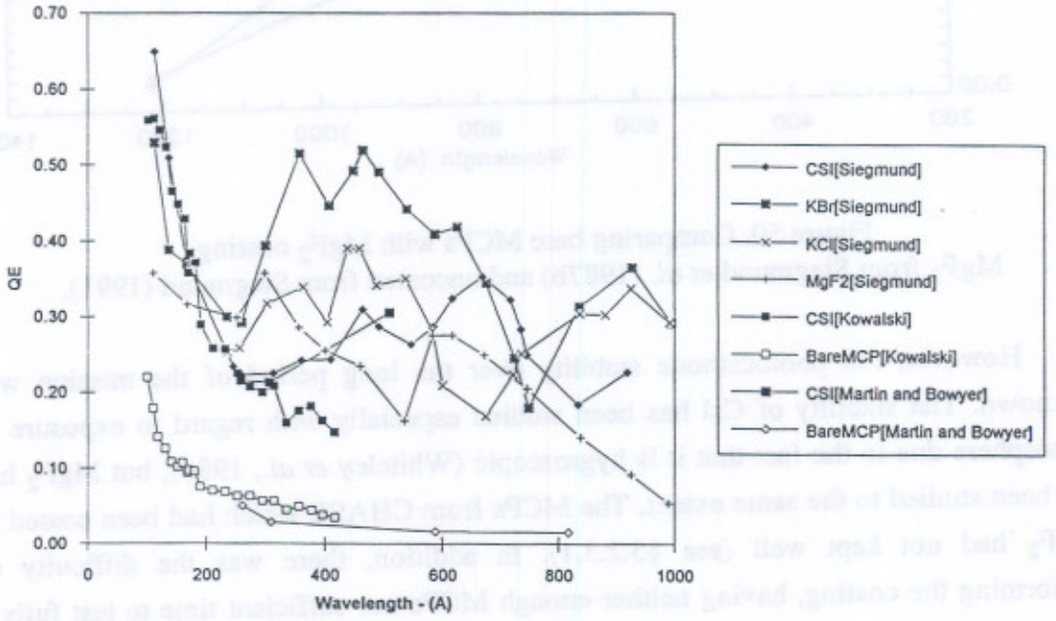

Figure 49. Quantum efficiency of MCPs with a variety of photocathodes.

For GIS, the original intention was to coat the front MCP with MgF_2. This was believed to enhance the QE by up to a factor of two and was chosen rather than CsI

because of its stability with water vapour (Fraser, 1983 and Samson, 1984). It was therefore the only material suitable for an open channel plate. MgF_2 was used as a photocathode material for detectors on Einstein, EXOSAT and P78-1 (Eng and Landecker, 1981) to enhance X-ray efficiencies in the 0.3–2.5 nm range and on some of the EUVE detectors, which detected photons between 10 and 100 nm.

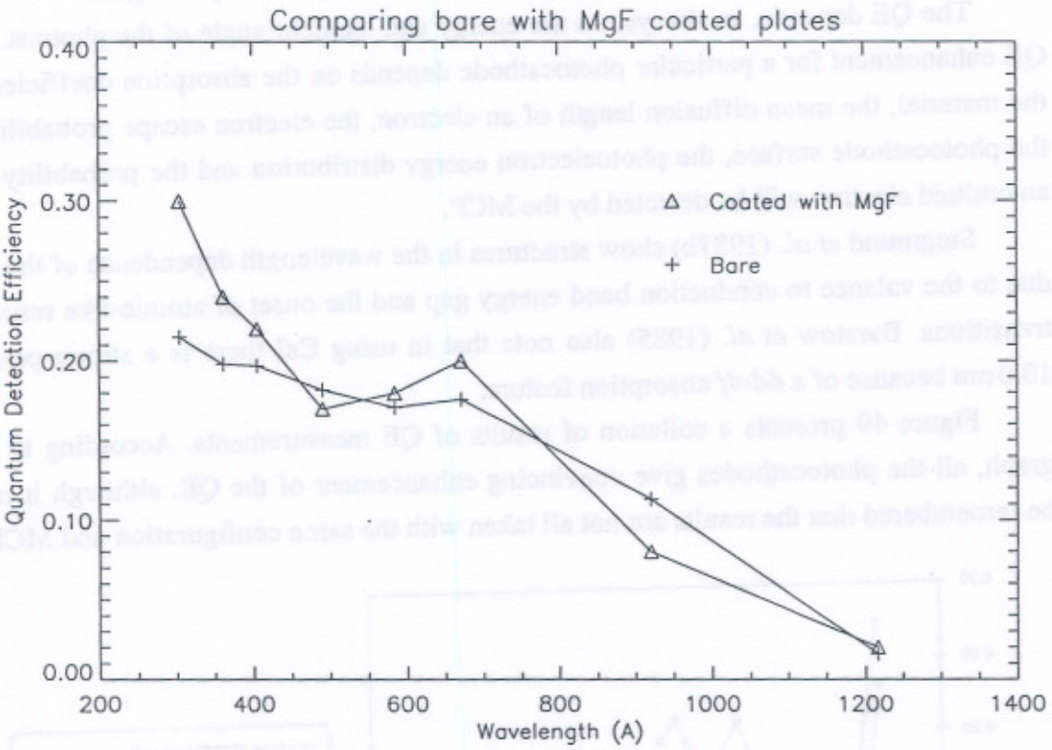

Figure 50. Comparing bare MCPs with MgF_2 coating.
MgF_2 from Siegmund *et al.* (1987b) and uncoated from Siegmund (1991).

However, the photocathode stability over the long period of the mission was unknown. The stability of CsI has been studied especially with regard to exposure to atmosphere due to the fact that it is hygroscopic (Whiteley *et al.*, 1984), but MgF_2 has not been studied to the same extent. The MCPs from CHASE which had been coated in MgF_2 had not kept well (see §3.2.3.1). In addition, there was the difficulty of performing the coating, having neither enough MCPs nor sufficient time to test fully a variety of coating techniques, thicknesses and configurations. The process and repeatability was not well understood and would have risked the integrity of very expensive MCPs. It was not known how well the deposition could be controlled, nor how well it would stand vibration, radiation exposure or vacuum. Nor was it clear how

durable the coating would be in orbit. Pieces breaking off and lodging in MCP pores could be fatal. Moreover, it was thought to be unnecessary, as a QE of 10% may have been obtainable from the detectors. All these factors, plus the fact that the predicted improvement would be only moderate, led to a decision to drop the proposal to coat the MCPs.

Siegmund *et al.* (1987b) measured the QE of a MgF_2 photocathode coating, 1.5 µm thick, as a function of wavelength for an incident angle of 15° to the microchannel axis, with 150 V mm^{-1} retarding field. His measurements are incorporated in Figure 49. Without including the web contribution because the GIS detectors have no retarding grid, the QE is ~22% at 60 nm, then drops to a minimum of ~12% at 54.0 nm. It increases for wavelengths below this and then peaks again at a maximum of ~30% at 30 nm and 10 nm. Note that this was at 15°. At grazing incidence angles the QE would be substantially lower than this. Figure 50 is a plot of the response from the graph in Figure 45 together with measurements of the uncoated plate response also made by Siegmund, but in 1991. Both were made at an incident angle of 15°.

3.3.4. Non-uniformities

It is normal to see small-scale non-uniformities from the hexagonal packing of the MCP fibre bundles, often termed the chickenwire effect. The non-linearities are due to the multifibre boundaries in the back MCP. Given that the charge cloud profile varies with gain, if the gain varies from bundle to bundle it can give rise to mismatch of the image between consecutive hexagons. Other explanations for this effect include displacement of the output electrons (see Figure 51), reduced open area ratio at the hexagon boundaries or reduced gain at the boundaries (Barstow *et al.*, 1990). For GIS, which involves imaging in one dimension, the chickenwire distortions are integrated along the 16 mm axis and therefore not noticeable. There are approximately 20 hexagons in 16 mm.

In the detectors used on the EUVE, described by Vallerga, Gibson *et al.* (1989), the flat field response varies by only 10% over large scales of the plates. Large scales are useful here because every line is scanned over the whole plate so that small-scale non-uniformities will not be seen. The writers are able to quote one QE for the whole plate, except at the edges where there is significant non-linearity. For the GIS detectors, the positions of the spectral lines will remain fixed. The calibration can give a different QE for each wavelength.

In the same paper, Vallerga, Kaplan *et al.* describe an experiment to test the variation in QE with wavelength. Between 11.4 and 58.4 nm the features that they could see in the flat field image did not vary. The uniformity of illumination was not as good

at the longer wavelengths because of the structure of the emitting region in the hollow cathode discharge lamp. But, nevertheless, the flat fields at short and long wavelengths were identical to within Poisson statistics.

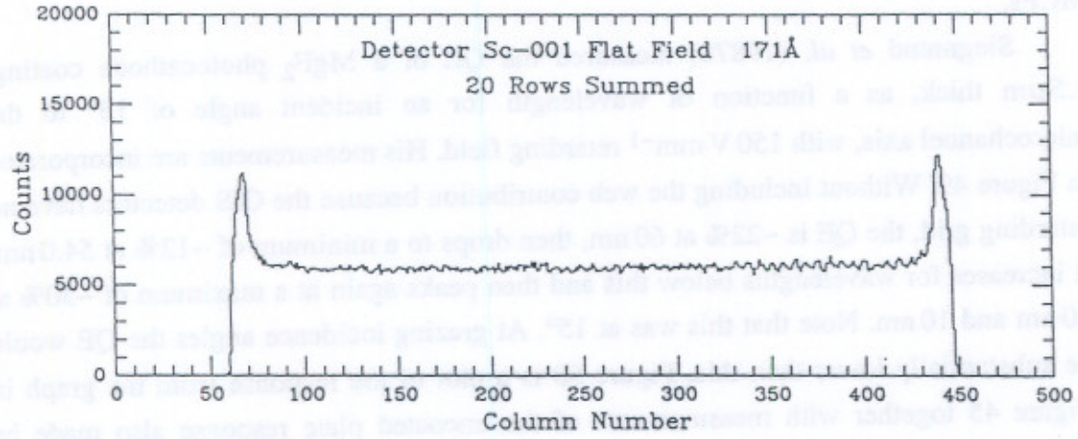

Figure 51. Hexagonal boundaries giving non-linearities from Vallerga, Kaplan *et al.* (1989). A horizontal cut through the centre of a two-dimensional image. At the hexagonal boundaries there is an enhancement followed by a deficit in the response. This implies that the photon events are not lost but mislocated. This image also shows brightening at the edges of the field of view.

3.4. CHANGES WITH TIME—GAIN DEPRESSION AND SCRUBBING

One of the decisions which had to be made before delivering the flight detectors was whether or not to scrub the MCPs. Scrubbing is a method of extracting a large amount of charge from a plate by illuminating it at a high count rate for a long period of time. The purpose is to aid outgassing and thereby reduce background count noise and to reduce the gain of the plate to a stable level. An additional purpose is to produce a narrow PHD. Mainly H_2, H_2O and HO are released during this process, in the approximate ratio 9:3:1. The presence of these molecules on the surface of the channel glass can give a high secondary electron coefficient, so scrubbing tends to reduce the gain. If plates are scrubbed excessively it is possible to start removing other materials from the plates, *e.g.* sodium, and this can lead to a rapid and unrecoverable fall in gain (Smith, MSSL, private communication, 1994). A scrubbed region can be permanently affected, possibly due to the fact that changes in the material of the channel walls cause distortion of the equipotential field near the channel exit, or changes in the secondary electron coefficient.

In fact, time under vacuum also reduces background noise, gain and to some extent the width of the PHD. Exposure to oxygen or atmosphere can restore the gain after evacuating or scrubbing. This is believed to be due to partial re-reduction of the lead-glass when it is exposed to the atmosphere, giving rise to an increase in the secondary emission coefficient, (Smith and Allington-Smith, 1986). Even without exposure to atmosphere complete recovery of gain has been observed a few days after a GIS high count rate experiment.

3.4.1. Gain reduction with high count rate

In addition to the long term gain depression (LTGD) associated with charge extraction, MCPs are vulnerable to count rate dependent gain depression (CDGD) (*e.g.* Zombeck and Fraser, 1991).

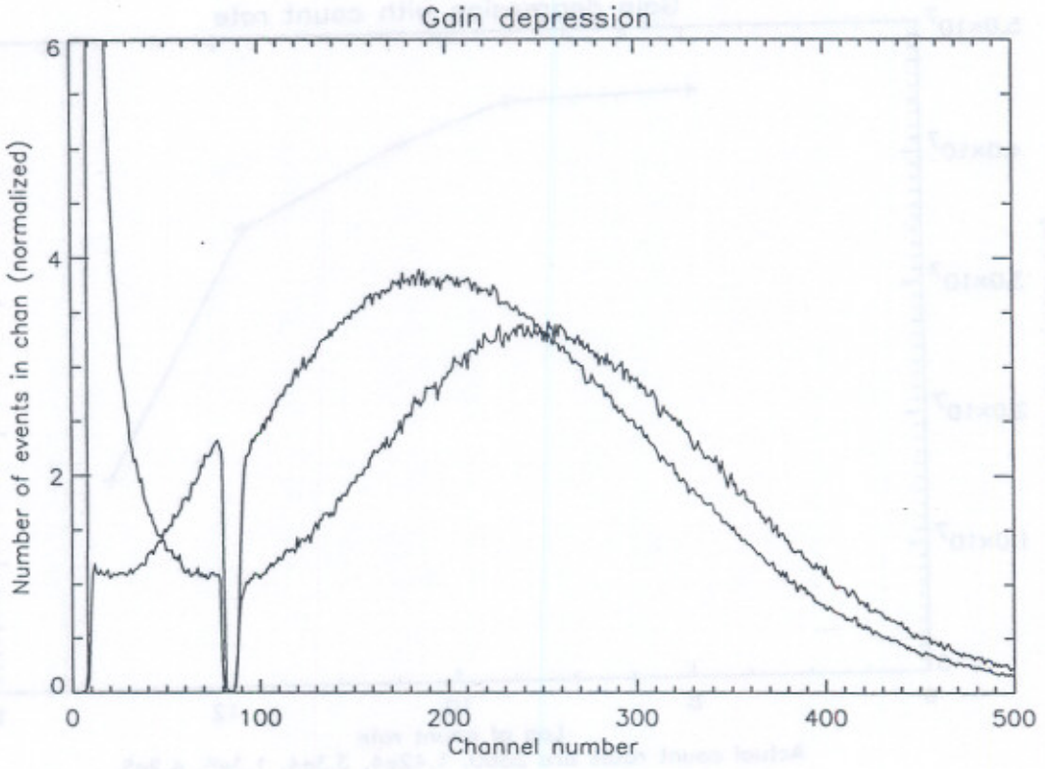

Figure 52. Measured pulse height distributions with increasing count rate. Measured using Nehemiah with the filament as an electron source with the front face biased positive. The two count rates are 2800 and 1.3×10^5 c s^{-1}. The higher count rate PHD looks taller because the exponential noise tail becomes less significant with increased rate of real events. The gain at channel 250 is 4×10^7.

Chapter 2 discussed the dead time of the electronics processing. After the arrival and detection of a photon there follows a finite time before a new event can be detected, within which any new events will be discarded by the electronics pile-up discrimination. This limits the rate at which events may be detected and results in a non-linear relationship between the input and output count rates. The reduction of the global count rate of the detector can be calculated or measured and therefore compensated for. Provided there is no rapid change in the input image, this dead time does not alter the distribution of detected events in the output image. Every 'pixel' is available to detect a new photon within the same time period—the length of the period is reduced by dead time by the same amount for each pixel. *i.e.* the detection of a photon depends only on its arrival time, not on its position.

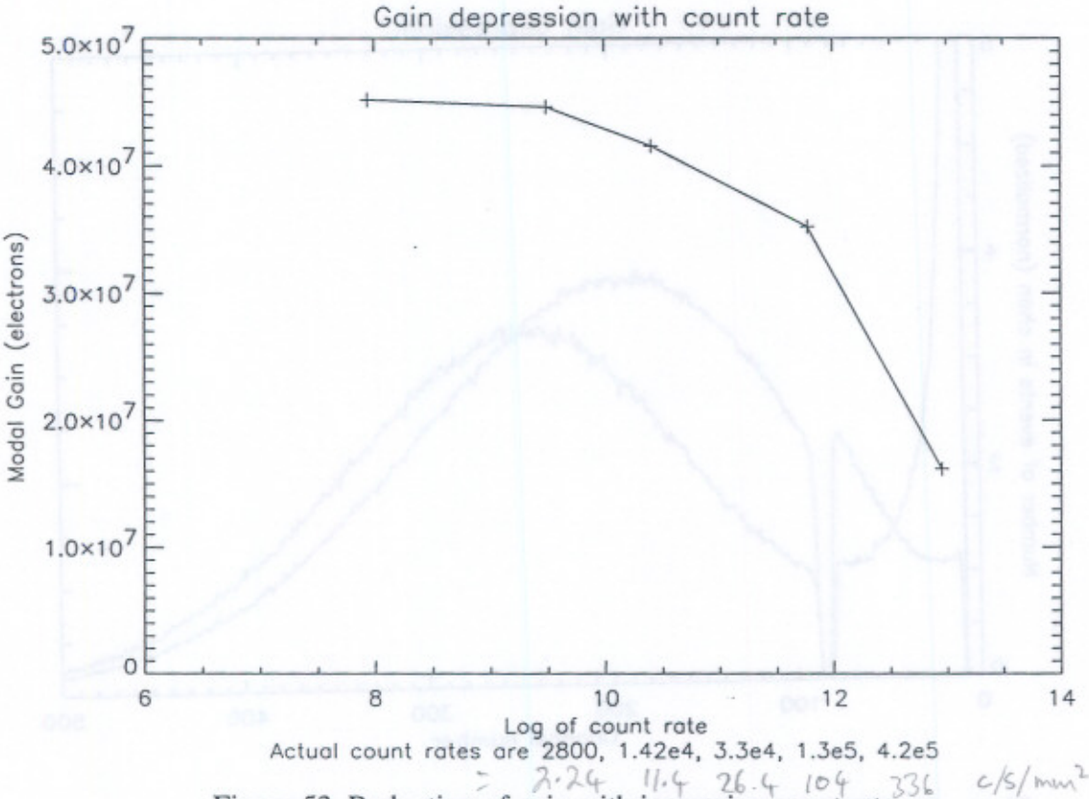

Figure 53. Reduction of gain with increasing count rate. (The *x*-axis is in natural logarithms) This data was taken using the setup described in Chapter 4. Nehemiah, with a positively biased front face was stimulated by electrons from the filament.

The dead time of the MCPs, however, certainly can have an effect on the distribution of output events. There is a finite time (between 3 and 100 ms) required to recharge the channels after a pulse of electrons has been released and therefore the gain

sustainable by the channel plate is inevitably reduced as the photon count rate increases (Figure 52). If too many events fall within a short time and in a small area then the count rate in that area will be reduced relative to the rest of the detector. Figure 53 shows the result from an experiment measuring the reduction of gain with count rate on one of the flight spare detectors. The illumination was not flat but peaked, covering approximately half the active area. Assuming this, the incident count rates per input pore corresponding to the data points are: 0.0014, 0.007, 0.016, 0.065 and 0.205 c s^{-1} $pore^{-1}$. The gain falls to half at an input count rate of 0.14 c s^{-1} $pore^{-1}$.

Many authors have reported this effect: for instance Siegmund *et al.* (1985) show the gain starting to fall off at just 0.2 c s^{-1} per input channel, for their *z*-stack at gains of 1.5×10^7. Sams (1991) explains how gain depression can lead to errors in the position calculated by the PAPA detector. Sharma and Walker (1989) derive expressions for the reduced mean count rates in MCPs using a probabilistic non-paralysable local dead time model. The effect can also be paralleled with count rate dependent gas gain depression in proportional counters (Trow, 1991).

Reducing the temperature of the MCPs increases their resistance and hence the recharge time constant. Schecker *et al.* (1992) observed the maximum output count rate fall with temperature. They operated MCPs down to a temperature of 14K. The strip current had fallen exponentially from 5 µA at room temperature to 1 nA at 18K, with the plate resistance increasing from 180 MΩ to 900 GΩ.

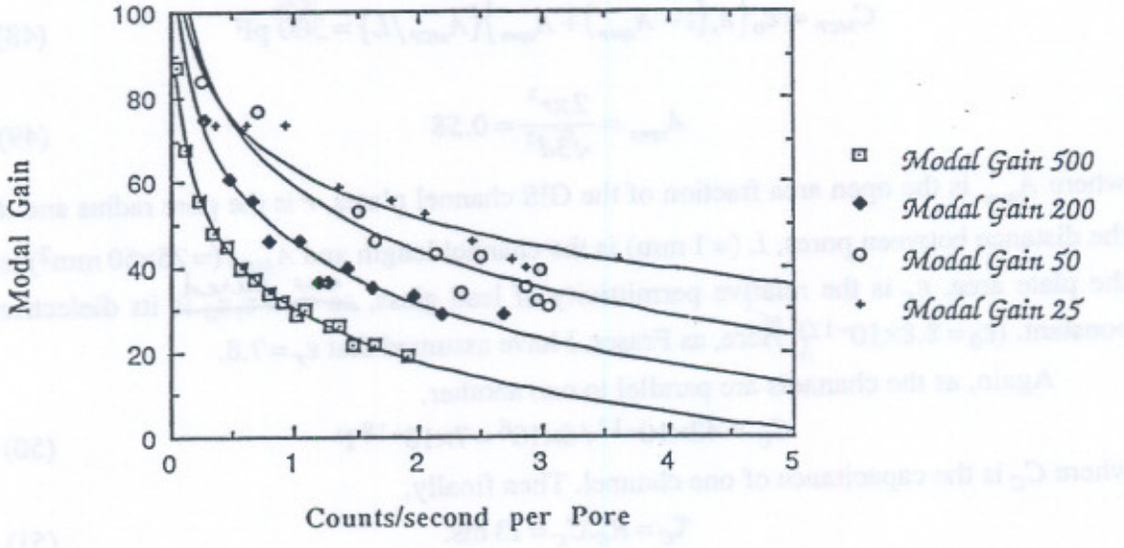

Figure 54. Variation of gain depression with area illuminated
from Nartallo Garcia (1990). The numbers 500, 200, 50 and 25 refer to the diameter in µm of the pinhole illuminated.

The count rate per pore is the important parameter—a high count rate across the whole plate where an individual channel is not 're-fired' within its recharge time constant will not produce gain depression, whereas the same number of counts concentrated in a smaller area may have an effect. However, there is an added complication, namely an effect known as 'adjacency' (Sharma and Walker, 1989; Cho and Morris, 1988) where the behaviour of the electron multiplication process in one channel depends on the transverse electric fields from neighbouring channels. The strip current and recharge time constant are not necessarily constant. The gain depression depends (inversely) on the area illuminated (see Figure 54).

3.4.1.1. Predicting gain depression

An estimate of the steady state recharge time constant τ_c can be obtained by knowing the resistance and capacitance of one channel. For GIS, the plate resistances are 250–300 MΩ. There are 5132 pores mm^{-2} (§2.2.4.) and therefore,

$$5132 \times 50 \times 25 = 6415000$$

pores in the plate. As the M channels are parallel to one another,

$$R_C = MR_{MCP} \tag{46}$$

$$\therefore \quad R_C = 6\times10^6 \times 3\times10^8 = 1.8\times10^{15}\,\Omega \tag{47}$$

where R_C is the resistance of one channel for a 300 MΩ plate.

Using equation A1 for the capacitance of a MCP from Fraser *et al.* (1991) which is basically the equation for a parallel plate capacitor:

$$C_{MCP} = \varepsilon_0\left\{\varepsilon_r\left(1-A_{open}\right)+A_{open}\right\}\left\{A_{MCP}/L\right\} = 300\ \text{pF} \tag{48}$$

$$A_{open} = \frac{2\pi r^2}{\sqrt{3}d^2} = 0.58 \tag{49}$$

where A_{open} is the open area fraction of the GIS channel plates, r is the pore radius and d the distance between pores, L (= 1 mm) is the channel length and A_{MCP} (= 25×50 mm^2) is the plate area. ε_r is the relative permittivity of lead glass, so that $\varepsilon_r\varepsilon_0$ is its dielectric constant. ($\varepsilon_0 = 8.8\times10^{-12}$). Here, as Fraser, I have assumed that $\varepsilon_r = 7.8$.

Again, as the channels are parallel to one another,

$$C_C = 42\times10^{-12}/6\times10^6 = 7\times10^{-18}\,\text{F} \tag{50}$$

where C_C is the capacitance of one channel. Then finally,

$$\tau_C = R_C.C_C = 13\ \text{ms}. \tag{51}$$

It has been found experimentally (Natallo Garcia, 1990) that the local dead time of the plate depends on this time constant and also on the area illuminated, with a dependence:

$$\tau = k\tau_C = kR_C C_C = kR_{MCP} C_{MCP} \quad (52)$$

where k is an increasing function of illuminated area. (N.B. for a single-stage channel plate, k is area independent and ~5, suggesting that there is no adjacency in this case). As the area tends to zero, k becomes approximately the value for a single stage plate.

It used to be assumed that the strip current (I_S) in the MCP (calculated from the bias voltage and MCP single channel resistance, equation 54) gave a maximum to the output pulse current (I_P) obtainable (§3.1.3). (This is in fact true for a single stage plate, which has a maximum output of $0.5 \times I_S$). However, Fraser (1991) shows that the strip current need not remain constant during plate operation. If the ratio I_P/I_S is calculated using the quiescent value of I_S, it may exceed unity. Within a large scatter, the limiting current ratio is approximately inversely proportional to the number of channels illuminated, M (see Figure 55). An expression can also be found for this ratio using k and M. It is given in equation (59).

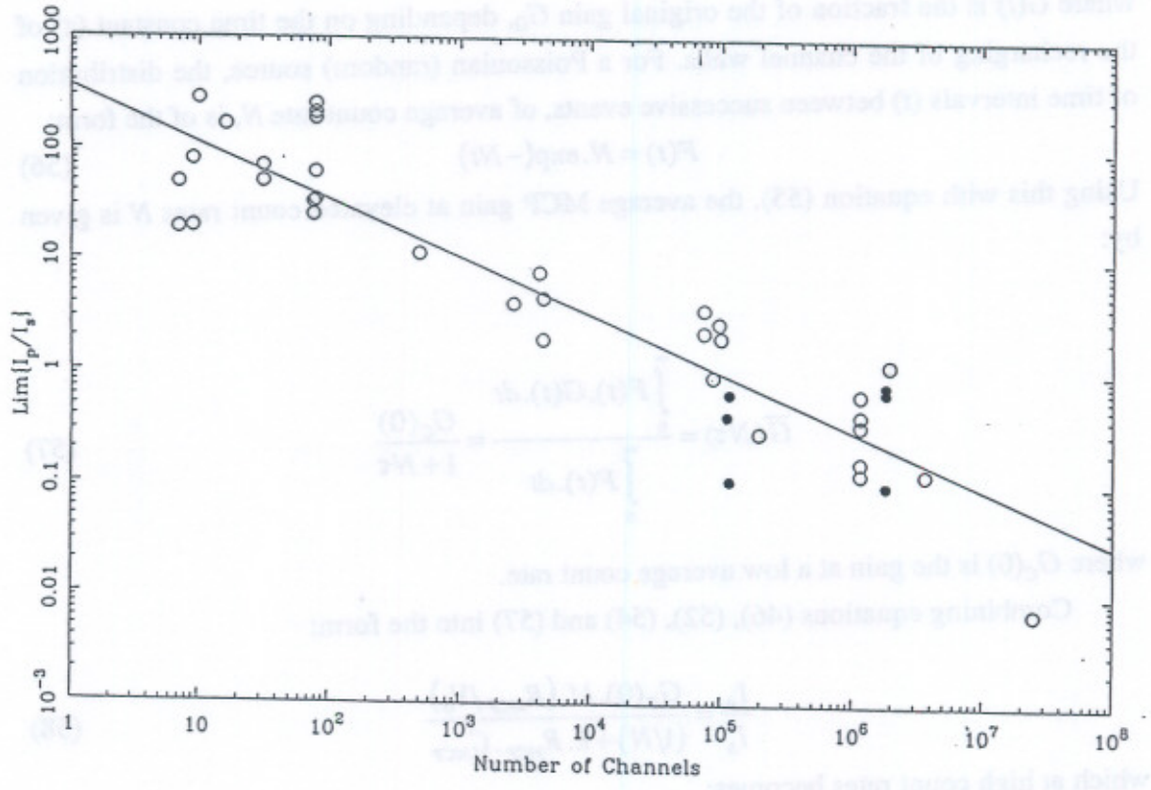

Figure 55. Variation of limiting ratio (I_P/I_S) with number of channels illuminated as the channel count rate tends to infinity (Fraser *et al.*, 1993 fig 1).

From Fraser *et al.* (1993) a fit to the curve in Figure 55 gives:

$$\log\left(\lim_{N\to\infty}\langle I_P/I_S\rangle\right) = -0.513.\log(M) + 2.57 \tag{53}$$

$$I_S = \frac{V_0}{R_C} \quad \text{and} \quad I_P = \overline{G}.N \tag{54}$$

where I_S and I_P are the strip and pulse current, respectively; V_0 is the bias across the channel, R_C is the channel resistance, $\overline{G}$ is the mean gain and N is the mean count rate.

On the time scales of the recovery time (tens of milliseconds), the removal of a pulse of charge (Siegmund *et al.*, 1986, measure 1-2 ns for a *z*-stack) can be considered instantaneous. Assuming that the gain available immediately after the MCP has fired is zero, the gain $G(t)$ of a second event occurring at a time t after the first one, will have an expected value of (Fraser, 1991):

$$G(t) = G_0\left\{1 - \exp(-t/\tau)\right\} \tag{55}$$

where $G(t)$ is the fraction of the original gain G_0, depending on the time constant (τ) of the recharging of the channel walls. For a Poissonian (random) source, the distribution of time intervals (t) between successive events, of average count rate N, is of the form:

$$F(t) = N.\exp(-Nt) \tag{56}$$

Using this with equation (55), the average MCP gain at elevated count rates N is given by:

$$\overline{G}(N\tau) = \frac{\int_0^\infty F(t).G(t).dt}{\int_0^\infty F(t).dt} = \frac{G_C(0)}{1+N\tau} \tag{57}$$

where $G_C(0)$ is the gain at a low average count rate.

Combining equations (46), (52), (54) and (57) into the form:

$$\frac{I_P}{I_S} = \frac{G_C(0).M.\left(R_{MCP}/V_0\right)}{(1/N) + k.R_{MCP}.C_{MCP}} \tag{58}$$

which at high count rates becomes:

$$\lim_{N\to\infty}\langle I_P/I_S\rangle = \frac{G_C(0).M}{k.V_0.C_{MCP}} \tag{59}$$

k can therefore be obtained if the ratio of strip to pulse current is measured at a very high count rate. An alternative way to measure k is given by equation (65).

A more realistic model (Amnicoli, 1985 and Fraser *et al.*, 1993), is one where the maximum charge which can be emitted depends on the amount of charge remaining in a 'reservoir' after previous pulses have depleted it and recharging has taken place in the time between pulses (see Figure 56).

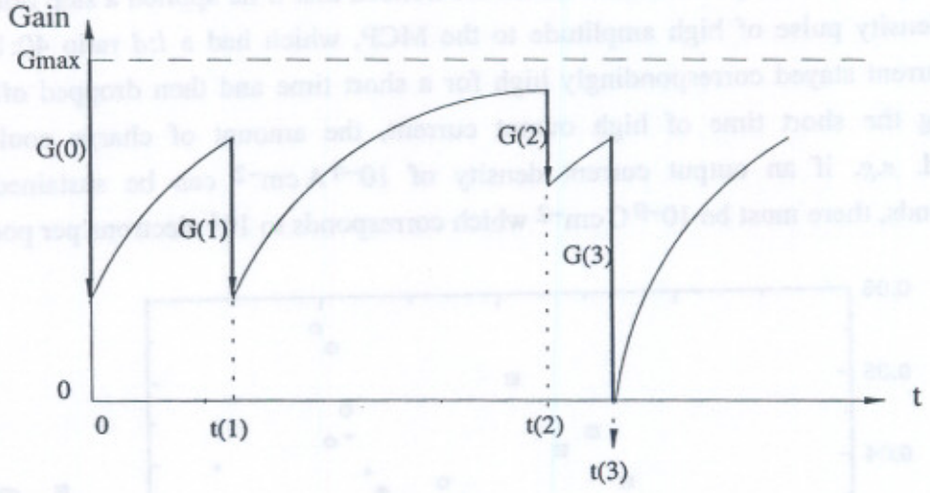

Figure 56. Model of charge in a reservoir of depth G_{max} taken from Fraser *et al.* (1993). Pulses of magnitude G(0)..G(3) occur after times t(0)..t(3). The gain of each pulse is restricted to no more than the charge remaining in reservoir.

In this case, after the first event at time $t=0$:

$$G(t) = G_{\max} - G(0)\exp(-t/\tau) \tag{60}$$

where $G(t)$ is the charge available for an event t seconds later than an event of size $G(0)$. After the second pulse of $G(1)$ is taken at time $t(1)$, the charge available for multiplication for the next electron is (using the short hand $t_1 = t(1)$ *etc.*):

$$G(t > t_1) = G_{\max} - \left[G_1 + G_0 \exp(-t_1/\tau)\right]\exp\left(-(t-t_1)/\tau\right) \tag{61}$$

If the MCP is saturated, then the pulse removed should be approximately the same size each time (say, G), provided there is enough charge in the reservoir. Assuming also that the pulses arrive within a characteristic time Δt, then equation (61) becomes:

$$G(t) = G_{\max} - G\left[1 + \exp(-\Delta t/\tau)\right]\exp\left((t_1 - t)/\tau\right) \tag{62}$$

After n–1 pulses of magnitude G separated by time Δt, long enough that there is always enough charge, this becomes:

$$G(t_n) = G_{\max} - \sum_{j=1}^{n-1} G_j \exp(-j\Delta t/\tau) \tag{63}$$

However the reservoir model would imply a constant value of G_{max}. In fact, G_{max} deduced from PHDs is seen to reduce with high count rates.

From Eberhardt (1981), the amount of charge stored in each channel and available for short pulse outputs can be determined experimentally by using an MCP in a photomultiplier tube in pulse current mode. He noticed that if he applied a step function current density pulse of high amplitude to the MCP, which had a *l:d* ratio 40:1, the output current stayed correspondingly high for a short time and then dropped off. By measuring the short time of high output current, the amount of charge could be calculated. *e.g.* if an output current density of 10^{-4} A cm^{-2} can be sustained for 10^{-5} seconds, there must be 10^{-9} C cm^{-2} which corresponds to 10^4 electrons per pore.

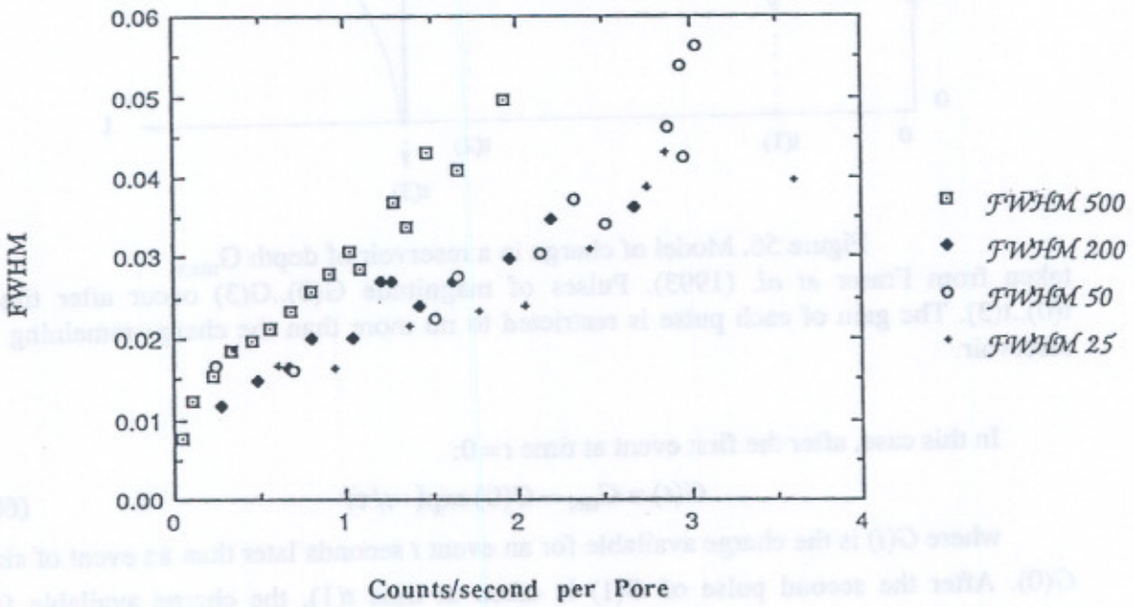

Figure 57. Change in width of PHDs with increasing count rate from Natallo Garcia (1990). The numbers 500, 200, 50 and 25 refer to the diameter in μm of the pinhole illuminated. It can be seen from this graph that the PHD FWHM (measured in arbitrary units) increases with count rate. For larger illuminated areas the effect is more pronounced.

By means of this experiment another estimate of the capacitance and hence the recharge time constant can be made, knowing the maximum linear DC output current. Eberhardt calculates that there should be at least 10 ms between high amplitude pulses if linearity is to be maintained. He goes on from this to calculate the capacitance per channel, using the channel resistance and obtains 2.5×10^{-16} F channel^{-1}, which is in fairly close agreement with the calculation of equation (50) for an MCP with an *l:d* ratio of 80:1.

Using equation (57) in a Monte Carlo model, Fraser has shown that the width of the PHD should increase with high count rate, while the gain falls. Figure 57 illustrates the increase in PHD FWHM.

Following on from equation (57) the high rate N_h at which the mean gain falls to a fraction a of its low rate value is then:

$$N_h = \frac{(1/a)-1}{\tau} \tag{64}$$

If, *e.g.* $a=0.5$, then:

$$N_h(0.5) = \frac{1}{\tau} = \frac{1}{(k.R_{MCP}.C_{MCP})} \tag{65}$$

using equation (52). k can be calculated from this equation or from equation (59).

From Figure 53, $N_h(0.5)=2.7\times10^5$ electrons. Using the MCP resistance and capacitance from equation (47) and those before, we obtain a value of $k=4\times10^{-5}$. Equation (65) predicts that $\tau=4\mu s$, which is much smaller than the value for an individual channel calculated directly from the resistances and capacitances of the channels in equation (51). Therefore the dead time of an area of the plate differs from the dead time of a single channel, depending on the area illuminated.

3.4.2. Long range gain depression

Edgar *et al.* (1992a) have shown that gain depression operates not only in the exact region of highest count rate, but also in the surrounding area out to a radius of about 1.5 mm or 100 pore diameters. The reduction in gain is linear, inversely proportional to radius and directly proportional to count rate. The time taken to recharge the illuminated channels therefore seems to depend on the ratio of active to quiescent pores. This is again the effect of adjacency.

Edgar *et al.* used a simple experiment to demonstrate the long range gain depression (LRGD). He illuminated a 100 µm diameter pinhole simultaneously with a diffuse, low count rate ^{55}Fe source of 5.9 keV MnK X-rays and a high flux of UV radiation from a mercury vapour lamp. The mask was made of aluminium so that the X-rays were able to pass through it to illuminate the whole MCP evenly, whereas the UV radiation was confined to the pinhole area. The diffuse count rate was ~5×10^{-4} c s^{-1} pore^{-1} and the UV high flux count rate was ~0.53–1.2 c s^{-1} pore^{-1}.

As the pulse magnitudes associated with every event were recorded on the computer taking the data, it was possible to build up PHDs for events arriving within annuli of a given radius from the centre of the pinhole. The PHDs associated with those events falling in annuli within 1.5 mm of the high flux region showed distinct gain

depression (see Figure 58), even though the rate of events falling in those annuli was very low (see Figure 59). This shows that adjacency has indeed a real physical effect. It is essentially a radial phenomenon.

Fraser (1991) repeated the experiment using UV to generate both the diffuse and the intense flux components by use of a photographic film mask containing a 0.5 mm pinhole. He obtained a result of 2 mm as the radius of influence of the bright spot. The higher the count rate in the pinhole region, the greater the effect on the gain in the surrounding region.

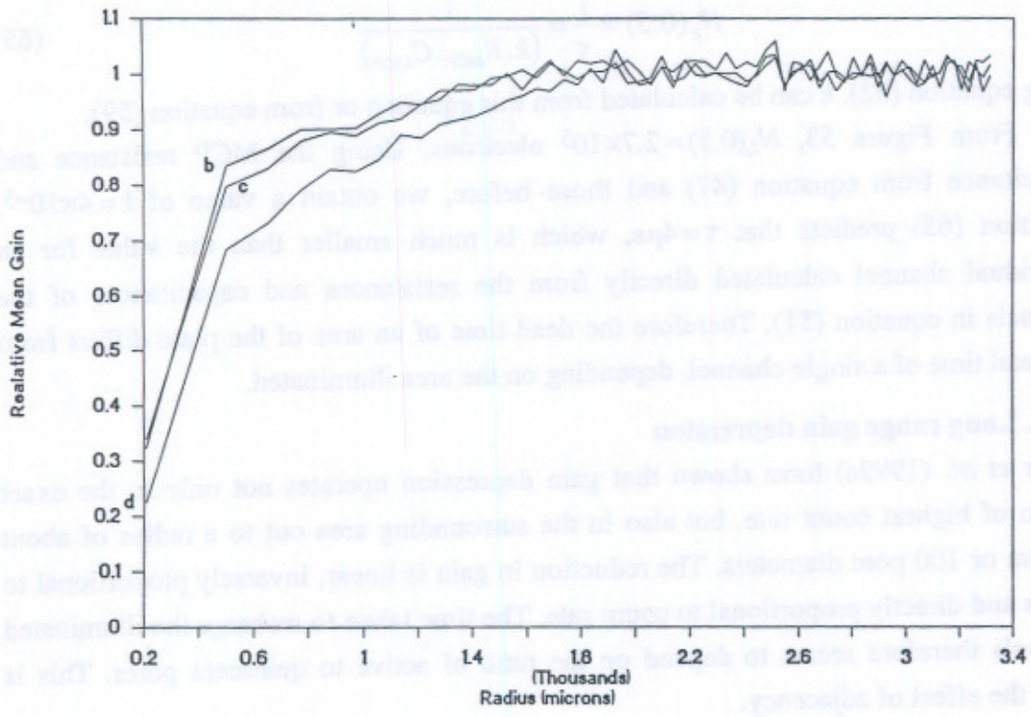

Figure 58. Relative mean gain vs. radius from centre of bright spot from Edgar *et al.* (1992a). Curves **b**, **c** and **d** represent UV fluxes of 2700, 2900 and 5900 c mm^{-2} s^{-1} respectively. They have been normalised with respect to the curve obtained with only X-ray illumination.

Fraser's data approximately fits to the function:

$$\overline{G}(r) = \begin{cases} \overline{G_0} & r < r_0 \\ \overline{G_0} + \left(G_P - \overline{G_0}\right)\left(1 - \dfrac{r_0}{r}\right) & r > r_0 \end{cases} \qquad (66)$$

where G_P is the gain in the 'plateau' region far from the pinhole, G_0 the gain in the central region and r_0 is the radius of the bright spot.

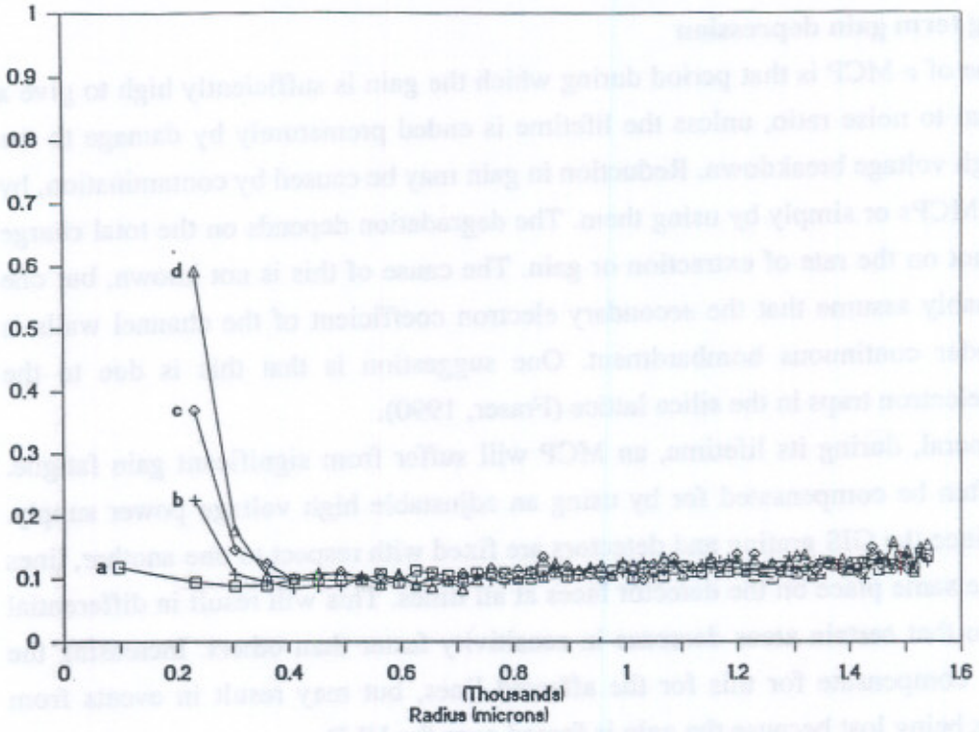

Figure 59. Count rates per annulus for the curves in Figure 58 from Edgar *et al.* (1992a). The high count rate region is only up to 0.5 mm radius. Curve a was obtained with only X-ray illumination.

The most likely explanation for adjacency is provided by Anacker and Erskine (1991). They suggest that the wall charge at the output end of the channels, due to the extracted electrons, produces a radial electric field, dependent on the dielectric constant of the lead glass, extending up to 20 channels away. The field is proportional to the wall charge and therefore to the gain and is inversely proportional to the radius. According to Gatti *et al.* (1983) the electric field is normally aligned with the channel axis (see §3.2.1.1). The gain is very sensitive to the angle of the electric field, so that if the angle is perturbed the gain can fall off sharply. If the field in an active channel linearly affects the gain reservoir of the surrounding channels adversely, then the extended gain depression would be seen to be following a function as in equation (66). With a number of channels in the second channel plate fired for each event, the effect could extend out to 1.5 or 2 mm.

Fraser (1992) writes "Obviously MCP adjacency will be a major concern in the calibration of many future experiments, especially those EUV and FUV spectrometers which are required to view intense isolated line fluxes."

3.4.3. Long term gain depression

The lifetime of a MCP is that period during which the gain is sufficiently high to give a useful signal to noise ratio, unless the lifetime is ended prematurely by damage to the MCP or high voltage breakdown. Reduction in gain may be caused by contamination, by baking the MCPs or simply by using them. The degradation depends on the total charge extracted, not on the rate of extraction or gain. The cause of this is not known, but one may reasonably assume that the secondary electron coefficient of the channel walls is reduced under continuous bombardment. One suggestion is that this is due to the creation of electron traps in the silica lattice (Fraser, 1990).

In general, during its lifetime, an MCP will suffer from significant gain fatigue. This can often be compensated for by using an adjustable high voltage power supply. However, since the GIS grating and detectors are fixed with respect to one another, lines appear at the same place on the detector faces at all times. This will result in differential scrubbing so that certain areas decrease in sensitivity faster than others. Increasing the voltage can compensate for this for the affected lines, but may result in events from weaker lines being lost because the gain is forced over the ULD.

Gain reduction by a factor of 10 has been reported, after the extraction of only 0.05 C from 1 cm^2. For a channel plate with 12 μm diameter pores and a mean pulse height of 4×10^7 electrons (6.4×10^{-12} C), this works out as 1.6×10^4 events $pore^{-1}$. At high local count rates of 1 c s^{-1} $pore^{-1}$ this extraction can be reached after just 4½ hours. Table 9 lists expected count rates during flight. Calculations in §2.2.4. show that the brightest line (He II 30.4 nm) will illuminate at the rate of 0.32 c s^{-1} $pore^{-1}$ with the smallest 2"×2" slit, rising to 8 c s^{-1} $pore^{-1}$ for the 8"×50" slit. Thus the gain of this line is expected to fall rapidly. Luckily, few observations have been proposed using this line.

3.4.4. Problems of gain depression and scrubbing

A great deal of discussion has been published concerning the desirability of scrubbing and the correct procedure.

In Fraser (1992) a chevron pair with *l:d* ratio = 80:1 and 10 μm diameter pores were scrubbed to remove 0.05 C cm^{-2}, which reduced the pulse height from 4 pC per event to 0.63 pC. This fall was easily restored by increasing the voltage from 1250 V per plate to 1375 V.

Malina and Coburn (1984) suggested a 10^{-3} Coulomb scrub for the plates for EUVE, which they claimed was required to reach a stable regime of gain. They also noticed that breaking the vacuum can alter the MCP characteristics, although most changes are reversed after 24 hours of evacuation. Vallerga, Gibson *et al.* (1989) say

that, in fact, a bake-out at 250°C for 8 hours was selected followed by a scrub to extract 0.1 C cm^{-2}.

Fraser (1990) discusses the usefulness of scrubbing for CDS in particular. He suggests that to burn in all the flight detectors and spares for CDS would produce, after great effort, only a reduction in the rate of decrease of modal gain and not achieve absolute gain stability. Furthermore, this benefit would be immediately compromised on any subsequent exposure of the detector to atmosphere. He advocates monitoring the gain of the plates closely throughout their lives and adjusting the voltage accordingly. In addition, a parallel 'life test' should be carried out in the laboratory to simulate the charge abstraction in flight (see also §8.3.1).

One of the main problems with this approach, caused by a short-coming in the electronic design, is that the gain in individual parts of the detector cannot be monitored—the PHD is transmitted without any positional information apart from detector number. Therefore, if the gain is depressed in any particular line by count rate dependent, long term or long range gain depression, it cannot easily be compensated for. During the calibration test, with fairly high count rate spectral lines, both count rate dependent and long term gain depression were seen.

With spectral lines continuously illuminating the same places on the detectors, there will therefore be different gains across the detector. Scrubbing prior to flight, with no pre-launch recovery period, would diminish the expected differences, but would not prevent position dependent gain depression. Several methods for monitoring gain depression are described in §8.4.1.

Monitoring changes in response does nothing for CDGD. This can only be compensated for using graphs of count rate out versus count rate in, obtained through calibration, or by adjusting the HV to find the maximum output count rate.

Weighing up all the above considerations, the decision was made not to scrub before launch, but to put in place procedures for monitoring the MCP health. The option remains of scrubbing in flight with the filaments, should it prove necessary.

CHAPTER 4.

PERFORMANCE—MCPS IN THE UV FACILITY

4.1. PRACTICAL SETUP FOR TESTING

This Chapter describes my work on the performance of the MCPs at grazing incidence angles and with high intensity EUV light. It also includes a description of the experimental configuration and methods I used.

4.1.1. Handling the MCPs for GIS

The MCPs for GIS came from Philips as sets of three with matched resistances because they were cut from the same boule. This meant that they did not need to have intermediate contacts to an external voltage network to maintain the same voltage across each plate, although, in fact, contacts were chosen to act as spacers as well as to protect against any change in resistance.

MCPs are delivered in little foil sachets surrounded by foam padding in plastic boxes. In the air flow bench (better than class 10) in the clean room, using powder-free, pure, natural, latex, clean-room gloves, the packaging is removed and the MCPs are examined for any travel damage and placed into watch glasses, supported on o-rings, in a locked desiccator cabinet. Thus, the MCPs are only supported by the extreme corners and are kept dry and protected. The o-rings and cabinet are kept scrupulously clean, using IPA and, for the watch glasses, an ultrasonic bath in Arklone. A record is kept of the serial numbers of each MCP, so that the sets do not get confused with each other.

Before use, a set of MCPs is mounted into a specially made stainless steel 'toast rack' and baked in the bake-out chamber at low pressure (less than 10^{-6} mbar) at 250°C for 48 hours. The bake-out chamber is protected by valves which isolate the chamber if the power fails, maintaining a vacuum until the temperature has dropped to normal.

The MCP stack (Figures 20 and 25) is built up from the back contact plate which defines the aperture with a chamfered edge. Polycarbonate spacers position the MCPs and a contact plate is held onto the top MCP face by copper leaf spring clamps. The front plate is in contact with the MCPs only along the long edges in order to prevent masking of grazing incidence radiation by structure along the short edges. Nickel shims, 25 µm and 12.5 µm thick, are placed between the MCPs (Figure 10). The inner aperture

of the back face contact plate is smaller than the apertures of the inter-MCP contact shims, which are themselves smaller than the front face contact plate, so that the edge of the aperture is well defined. This thereby avoids any edge noise which may occur due to the stack spring clamp on the top MCP or from the naked short edges of the MCPs. Once the stack is built, the order of the MCPs and their orientation is never changed, so that calibration may be maintained.

Cleanliness is vital for the proper functioning of the MCPs. They must have a secondary electron emission coefficient, δ, of at least 1.3 (Eberhardt, 1981) to obtain a desirable gain. Heavy hydrocarbons such as vacuum silicon pump oils, solder resins or epoxy deposited on the MCPs can break down under electron bombardment leaving mainly carbon, which reduces δ. Smaller hydrocarbon molecules, such as alcohol, trichlor and other similar solvents will not leave a carbon residue. Carbon has a very high work function and the process of deposition is irreversible and therefore has to be avoided. The degradation is proportional to the quantity of heavy hydrocarbons and also to the current through the MCP. Thus, the bottom plate is the most degraded. Particulate contamination must be kept to a minimum because of the risk of generating hot spots.

Evacuating an MCP to a low pressure allows it to desorb water vapour and other light molecules. When in use, electron multiplication and impact, together with the heating due to the current, continues the desorption process. At first application of high voltage, the gain may be unusually high because of the ionisation of the residual gas. Baking the MCP before use reduces the likelihood of this.

McComas *et al.* (1987) report a series of experiments on CEMs, exposing them to controlled quantities of contaminants at partial pressure including Teflon, eutectic 63/37 solder, Epotech H77 non-conductive epoxy and Epotech H21-D conductive epoxy. After taking $1–2\times10^{11}$ events, there was no degradation of the CEM gains. Repeating these experiments with Viton and Apiezon-L vacuum grease shows some degradation, but falling by only ~10% after 1×10^{11} counts. With the ability to increase the voltage to compensate for gain loss, they predict that a 10 year lifetime at 6.3 kHz counting rate is possible with gains greater than 1×10^{7}. Although these experiments were performed on CEMs and not MCPs, the results strongly suggest that use of these substances should not be prohibited for testing or in flight, although the use of hydrocarbons should always be kept to a minimum.

The detectors are operated, at MSSL, in a ultra clean UHV stainless steel chamber in a clean room, continually pumped to a pressure of no higher than 2×10^{-6} mbar, provided by an oil free turbo-molecular pump, backed by a rotary pump. If it is necessary to open the chamber, dry nitrogen is used to backfill the chamber to atmospheric

pressure. The first few monolayers of gas adsorbed by the MCPs are therefore dry nitrogen rather than water vapour.

A Penning gauge is used to measure the UHV pressure. It is baffled from the chamber by being mounted on an elbow on the side of the chamber. It can be used as an ion source for stimulating the detector at very high count rates. Fraser (1990) warns that after-imaging has been observed after using an ion gauge, even when it is only used with the detector HV switched off! During the experiments described here, this problem was never observed.

The detector body can be isolated from the chamber to simulate the actual isolation from the optics bench in the instrument.

A voltage of up to 5 kV is applied across the MCP stack and anode gap. Turning the HV on to the MCPs must be a gradual process, particularly for the first time, in case of bursts of out gassing leading to HV break down. The rise time of the power supply is limited to longer than 2.5 s and the on-board software ramps the voltage up over 5 s at each commanded voltage step. For the first switch-on after exposure to atmosphere the voltage is raised in 500 V steps until the MCPs start to emit electrons. Then the voltage is raised in steps of 100 V (the flight power supplies have 20 V steps) with plenty of time (up to an hour) at each stage for outgassing. In the flight HV power supplies, monitors report the current and voltage measured. If the current monitor exceeds a pre-determined value (selectable) the on-board software turns the power supply off to that detector. The voltage may then be re-applied more slowly with smaller steps in the hope that whatever caused the current trip can be removed by electron bombardment. Alternatively, the detector may just need more time to outgas. It is possible to have pressures of 10^{-4} mbar inside the channels (see below) when the gauge on the vacuum chamber is reading less than 10^{-6} mbar.

If a laboratory power supply is being used a current monitor is needed in series with it. Whenever the MCPs are active, the chamber pressure (the ion gauge is turned off before voltage is applied), voltage, current and count rate are noted. Where possible, gain and PHD FWHM are measured.

From Holland, Steckelmacher and Yarwood (1974), the pressure inside a channel can be calculated approximately as follows:

$$\text{Virtual leak}(Q) = \text{pressure}(P) \times \text{pumping speed}(U) \tag{67}$$

$$U = 116 \times \text{aperture} \times W \tag{68}$$

where $W = 1/\alpha \times \ln(\alpha)$, α being the length to diameter ratio of the channel. The channel aperture $= \pi r^2 = 1.3 \times 10^{-10}\ \text{m}^2$. $\therefore\ U = 6 \times 10^{-10}\ \text{m}^3\ \text{s}^{-1}$.

$$Q = \text{outgassing rate of glass} \times \text{surface area of channel} \quad (69)$$
$$= 1\times10^{-4} \times 6\times10^{-8}\ \text{Pa m}^3\ \text{s}^{-1}.$$
$$\therefore\ P = 1\times10^{-4} \times 6\times10^{-8} / 6\times10^{-10} = 0.01\ \text{Pa} = 1\times10^{-4}\ \text{mbar}. \quad (70)$$

Thus, the pressure in the channels depends on the outgassing rate of the glass, which depends on the glass material and conditioning (baking and scrubbing), not on the chamber pressure.

4.1.2. U.V. facility

A UV spectrometer was built in the clean room at MSSL (see Figure 60), simulating the instrument layout as closely as possible. A stainless steel vacuum tank with aluminium lid, large enough to hold a 750 mm RC and just high enough to mount the detectors on the RC with the front face on the spectral axis, was purchased from RAL, cleaned with sand blasting and refurbished. A stainless steel RC mounting plate was made and a diffraction grating purchased. Various slits and baffles can be mounted on the RC in the beam. A zero order box and a knife edge jig for setting up the optics were specially made. An oil free magnetic levitation turbo pump can evacuate the chamber to 8×10^{-7} mbar, although unfortunately, due to the large internal surface area of the tank (due to the sandblasting), it takes at least 24 hours to get down to the maximum operating pressure of 4×10^{-6} mbar.

To provide EUV light, a source is needed which can operate under vacuum, since no material exists which is transmissive in the EUV. A discharge lamp operating at low pressure with a pump to regulate the gas pressure can provide an emission source at these wavelengths. An ultraviolet discharge lamp is therefore mounted on the side of the main chamber, with a separate turbo pump. The lamp is separated from the chamber by a 1 mm diameter pinhole through which the UV illuminates the entrance slit. There is a manual valve for shutting the light off and pressure sealing the chambers from one another. The lamp is on a stand which can be moved bodily relative to the main chamber with a concertina tube connecting the two. The lamp itself is on a manipulator table so that fine adjustments can be made to its angle and position relative to the RC.

A diagram of the lamp is given in Figure 61. It is rotationally symmetric and has two anodes and one cathode, all made of stainless steel, with glass spacers between them. Water cooling is needed both for the pump and the lamp. The conical shape of the anodes, shown in the figure, reduces arcing and short circuiting through metal depositions.

Argon, neon or helium can be supplied to the lamp; the pressure being adjusted using a needle valve. A lamp power supply gives up to 3 kV at currents up to 500 mA.

Figure 60. Photograph of the UV chamber with the lid removed.
The lamp can be seen in the top left hand corner with gas supply and water cooling tubes showing. Inside the chamber, from left to right, are: the adjustable entrance slit with a baffle on the back side, grating, line selecting slit, zero order slit, zero order light collecting box, knife edge jig and detector. In front of the detector the filament can be seen. The viewing port is the nearest to the detector. The X-Y-rotary table driver is shown underneath the chamber beside the pump controls.

After a considerable amount of setting up the lamp has proved to be extremely easy to operate, quick to get started and reliable. It is possible to leave it on for hours with little change in current or voltage, provided the gas supply is steady. Unfortunately, the lamp rusts if the water cooling is left on for long enough for condensation to form. The water droplets can also provide a breakdown path if they are not dried up before operating the lamp. Apart from this, the only difficulty is in aligning the lamp with the RC in the main chamber.

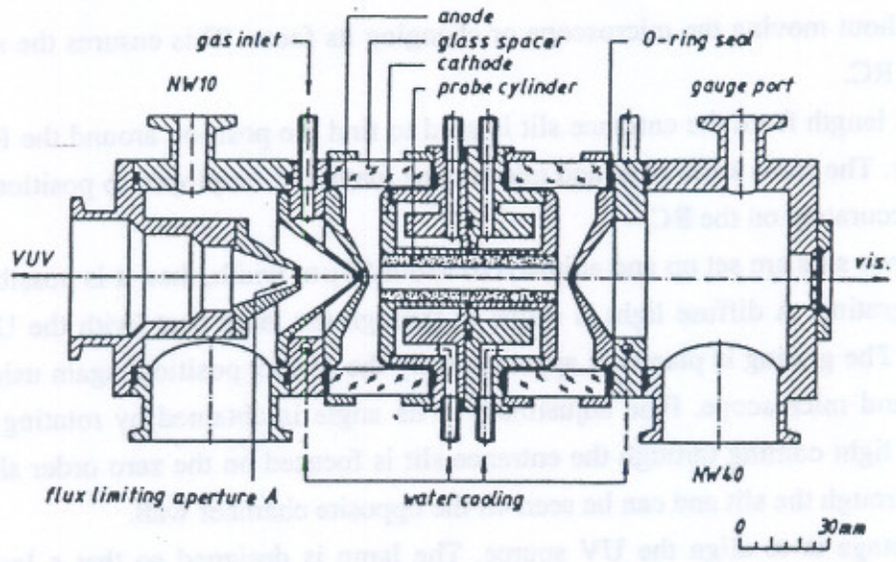

Figure 61. Diagram of the UV discharge lamp
from Danzmann *et al.* (1988).

4.1.3. Aligning the spectrometer

The basic alignment has to be done by measurement, because visible light cannot be used to align an RC designed for EUV. The angle of the beam entering the chamber and the RC is 84.5°, whereas in the flight GIS the angle is 84.75°, because of a late design change. This means that the calculations performed in Chapter 2 (see Figure 16) to find the angles and positions of the spectral lines had to be repeated for this different entrance angle.

It is very difficult for just one person to set up the alignment. The two most important pieces of equipment for the alignment comprise a knife edge jig which accurately brings the RC edge up to the height of the optical beam and a microscope which is small enough to put into the optical beam, but can be looked into from above, so that it is not necessary to put the eye in line with the beam—in an ultra clean chamber with little room for manoeuvre. The microscope was built by the author by combining a collimator and microscope, since it was impossible to buy a suitable device.

The knife edge jig was also specially made with two studs which can be pushed up against the RC jig to accurately locate the vertical knife edge on the RC. It is placed at the required position of the entrance slit (see Figure 16) by measurement from the edge of the chamber. The microscope is focused onto the knife edge at the height of the optical beam (indicated by a mark on the edge) and the cross hairs aligned with the edge. The knife edge jig is then removed and replaced with the adjustable slit. The slit position is adjusted until it is in focus and aligned with the cross hairs of the

microscope, without moving the microscope or changing its focus. This ensures the slit is placed on the RC.

The chord length from the entrance slit is used to find the position around the RC of the zero order. The same knife edge and microscope method is employed to position a zero order slit accurately on the RC.

Once the two slits are set up and adjusted to about 50 μm width, then it is possible to position the grating. A diffuse light is shone in through the lamp port (with the UV lamp removed). The grating is placed in approximately the correct position, again using the knife edge and microscope. Fine adjustment to its angle is obtained by rotating it until the diffuse light coming through the entrance slit is focused on the zero order slit. The light falls through the slit and can be seen on the opposite chamber wall.

The next stage is to align the UV source. The lamp is designed so that a laser beam can be shone right through it. Before re-assembling the lamp with the main chamber, a laser is set up to shine through the lamp port, through the entrance slit and to reflect off the grating through the zero order slit. Again the laser light can be seen on the opposite chamber wall.

At this point the lamp is re-joined to the main chamber and moved about bodily until the laser light can be seen to have travelled right through it and arrived in the main chamber. The lamp is now aligned.

But, when the lamp is evacuated, it moves. For this reason, the laser is left in position until the lamp has been evacuated, so that the lamp can then be moved again to re-align it. The problem here is that in order to allow the lamp light into the main chamber, the baffle between the chambers needs to be open. Therefore, the main chamber has to be evacuated with the lamp. With the lid closed on the main chamber it is very difficult to see whether the laser is shining through the zero order slit when moving the lamp around to align it. The zero order box, which is designed to absorb the zero order light and stop it from reflecting round the chamber giving scatter, is instead used to reflect the laser light from behind the zero order slit, out through the viewing port. In this way, the alignment can be checked provided that the laser has not been moved.

Unfortunately, if the entrance slit is narrowed down to 50 μm or less, there is not enough laser light to be seen from outside the chamber. The chamber therefore has to be opened up again for the entrance slit to be narrowed after the alignment has been set up. To set up the entrance slit, feeler gauges may be used to calibrate the vernier adjuster. Due to the difficulty of fitting feeler gauges in such a confined space, an alternative

method is to set up the zero order slit to the required width using the feeler gauges and then reduce the entrance slit width until all the light goes through the zero order slit.

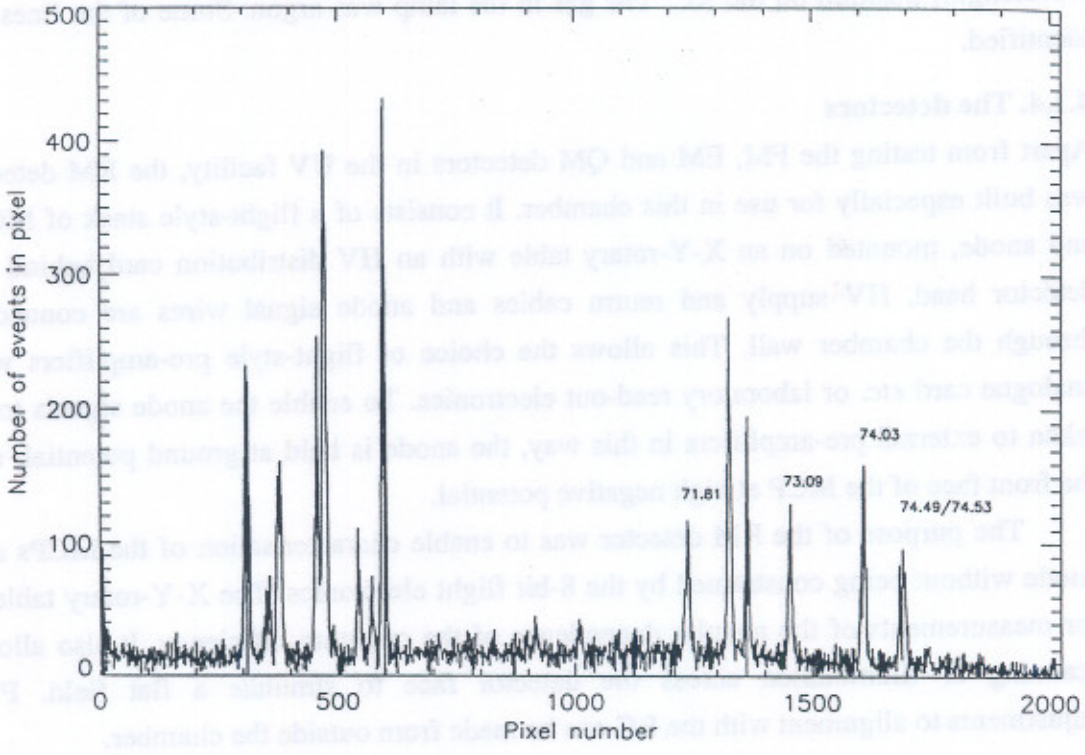

Figure 62. Spectrum obtained using the UV spectrometer with the detector Jeremiah in position 4 on the RC and argon used in the lamp. A few of the identified lines are labelled according to wavelength in nm.

The detector is mounted on the RC using a specially made mount, again with location studs for the lower RC and an accurately machined upper RC location for the detector studs to be pushed against. The lower RC jig plate had to be machined away where the detectors were to be mounted to allow room for the detector connectors. The detector can be isolated from the mount by using the fibre glass spacer manufactured for the flight GIS. The detector alignment studs then have to be set back by the 0.5 mm and pushed against the mount jig using a 0.5 mm spacer, just as in the flight GIS.

Baffles are required to cut down scattered light. A slit baffle is used on the chamber port to reduce the width of the beam arriving at the entrance slit. Another is mounted on the back side of the entrance slit to cut down the angle and height of the beam leaving the slit, reducing extra orders of diffraction. The grating is baffled with a glass slide on its edge, to stop UV light from hitting the edge or passing straight over the

top. Baffles are also used to stop any light from the grating except that which falls in the required region of the spectrum.

Figure 62 shows a spectrum obtained by placing the detector in the fourth (longest wavelength) position on the RC. The gas in the lamp was argon. Some of the lines are identified.

4.1.4. The detectors

Apart from testing the FM, EM and QM detectors in the UV facility, the RM detector was built especially for use in this chamber. It consists of a flight-style stack of MCPs and anode, mounted on an X-Y-rotary table with an HV distribution card behind the detector head. HV supply and return cables and anode signal wires are connected through the chamber wall. This allows the choice of flight-style pre-amplifiers with analogue card *etc.* or laboratory read-out electronics. To enable the anode signals to be taken to external pre-amplifiers in this way, the anode is held at ground potential, and the front face of the MCP at high negative potential.

The purpose of the RM detector was to enable characterisation of the MCPs and anode without being constrained by the 8-bit flight electronics. The X-Y-rotary table is for measurements of the angular dependence of the quantum efficiency. It also allows scanning of illumination across the detector face to simulate a flat field. Fine adjustments to alignment with the RC can be made from outside the chamber.

4.1.5. Data acquisition–*ALLSINGN* program

Data can be acquired in a number of different configurations. The full GIS electronics box may be used with the CDHS and EGSE simulators and *SDDA*. Alternatively, a single analogue card may be used with the analogue test box and a PC. A PHD can be built up in the PC using the *sum* signal feeding an MCA (multi-channel analyser) program, or images can be taken using *ALLSINGN*. The setup for laboratory electronics is shown in Figure 30.

'*ALLSINGN*' was developed by Edgar, MSSL, alongside the two-dimensional SPAN anode to display the output from the detectors on a Research Machines Nimbus microcomputer. It was adapted by the author to take in the data from just two normalising ADCs (rather than the original 6) and to plot it in four different ways, one of which was as a spectrum. It allows windowing with the mouse to enlarge an area of interest or to measure the mean event position in a certain region. There are options for histogramming, for reading the intensity in a pixel using the mouse and for using colour to display intensity or energy, with logarithmic or linear scales. The colour pallet can be chosen by the user. Prints can be made of the screen or the analysed data can be dumped

in ASCII or binary files. This powerful data acquisition and display program has been used extensively throughout the development of the detectors for GIS.

4.2. BACKGROUND NOISE TESTS

Having described the practical setup, the sections below detail the measurements made on the detectors, starting with the detector background noise.

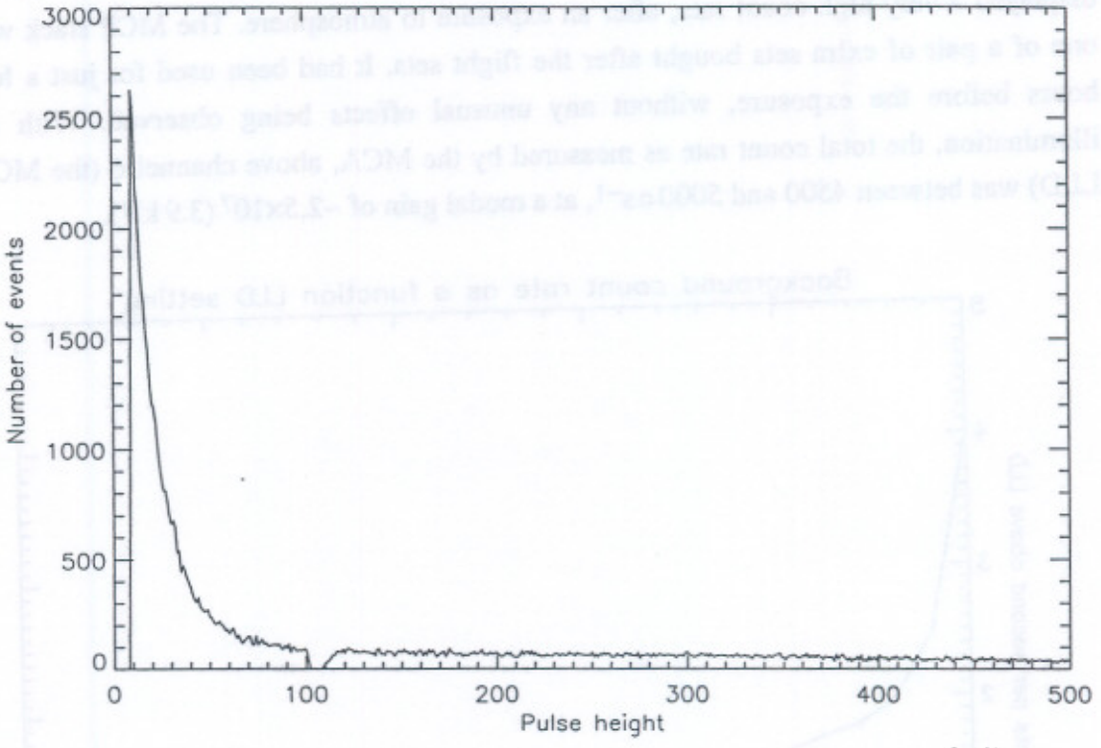

Figure 63. PHD of background events taken with the QM detector.

The required background event rate is less than $1\,c\,s^{-1}\,cm^{-2}$. The energy distribution of the events forms a quasi-exponential (see Figure 63), which may be described by the following equation (Parkes *et al.*, 1970):

$$n = n_0 \exp(-q/\overline{q}) \tag{71}$$

where n is the number of pulses of charge q and $\overline{q}$ is the mean charge or gain, of the distribution. n_0 is found by extrapolation. Therefore,

$$\overline{q} = \frac{q_2 - q_1}{\ln(n_1/n_2)} \tag{72}$$

where q_1 and q_2 can be conveniently set to two of the LLD levels and n_1 and n_2 are the numbers of events over those levels. The shape of the background PHD is not a perfect

exponential, but has a high energy tail. The mean gain in Figure 63, using equation (72) is 8×10^6.

The QM detector, with LLD set to 20% of the modal gain, had a count rate of $0.16\,c\,s^{-1}\,cm^{-2}$ (see Figure 64), which may be compared with Siegmund's value of 0.3 to $0.35\,c\,s^{-1}\,cm^{-2}$ with the same percentage LLD (Siegmund *et al.*, 1988).

With all the detectors the background count rate was very low (less than $2\,c\,s^{-1}$ over the LLD set at 35%), except for the flight spare detector Nehemiah, which displayed a very high count rate, after an exposure to atmosphere. The MCP stack was one of a pair of extra sets bought after the flight sets. It had been used for just a few hours before the exposure, without any unusual effects being observed. With no illumination, the total count rate as measured by the MCA, above channel 6 (the MCA LLD) was between 4500 and $5000\,c\,s^{-1}$, at a modal gain of $\sim2.5\times10^7$ (3.9 kV).

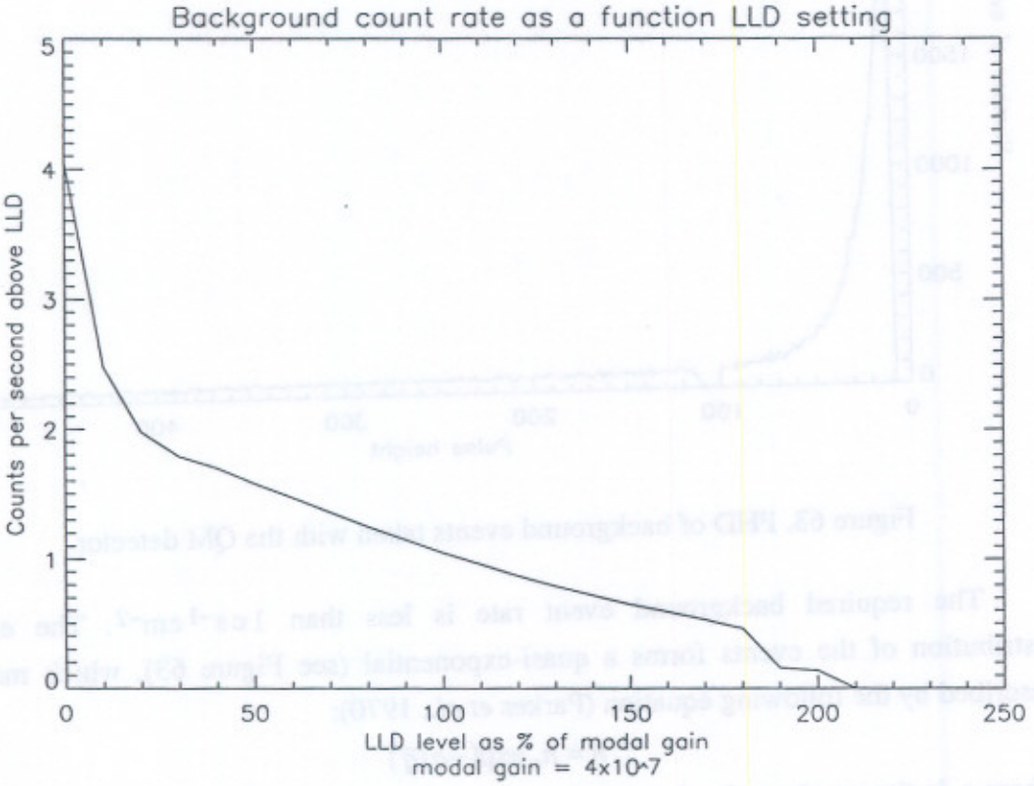

Figure 64. Background events in the QM detector.
The MCA was used to sum the number of events above each percentage level of the mean gain of 4×10^7.

The form of the PHD was of a negative exponential, which indicates that the events were not being initiated solely at the front face or else the gain would have been

similar to that for real events. When an image was taken of the background, with no source illumination, it was apparent that most events were occurring at either end of the detector. It has been observed (Parkes *et al.*, 1970) that continuous pulses can be observed from poor contacts, up to $10^4\,c\,s^{-1}$, either because of damage to the plate leaving debris or because of sparking between the contact and the MCP. Malina and Coburn (1984) also comment on the need for smooth, polished contact plates. However, in the case of the GIS detectors, the ends where the hot spots are observed is free from contacts because they are clamped only along the long edges to avoid shadowing at grazing incidence. It is possible that there is damage along the short edges. In baking, the short edges are held in the bake-out jig, but exactly the same technique was adopted for all MCP stacks suggesting that the damage may have occurred before delivery.

Malina and Coburn (1984) observed similar sudden appearances of hot spots in their MCP test (described in §3.1.6). Their phenomena lasted for anything between a few seconds and a few weeks. Often they could be removed by increasing the detector voltage from 1 to 2 kV above the normal operating voltage for five minutes or simply by pumping or scrubbing. Clampin and Edwin (1987) also observed hot spots around the peripheral of the plates.

The concern in finding hot spots is not the number of events produced at those positions, because those parts of the image can be ignored if necessary. Of more relevance are those events which fail to pass the LLD. They will not be rejected by the pulse pile up rejecter and will therefore add on to any other event being processed at the same time. The probability of co-incidence between one of the $5000\,c\,s^{-1}$ background events each of which takes 1.6 μs to process and a real event which takes 2.6 μs is 1.3%.

4.3. FLAT FIELDING AND UNIFORMITY

This section examines the non-uniformities due to the MCPs and the electric field between the back face and the anode. These include edge effects due to strong electric fields, any non-uniformity due to the hexagonal packing of boules in the MCPs and variations in gain across the active area. For these measurements 10-bit ADCs are used. Interactions of the charge cloud with the anode pattern are dealt with in §6.1., after the anode has been fully described. Non-uniformities of the whole detector including flight electronics effects are given in §6.4.3.

The effect of the non-uniform factors is to raise the pixel to pixel deviations above the photon statistical level. Poisson statistics lead to an expectation of an r.m.s. variation of $\sqrt{N}$, where N is the number of events per pixel. If the additional factors are systematic and vary only slowly with time, they may be removed by calibration.

Non-linearities may be due specifically to the fact that the centroid of the charge cloud is physically shifted. Assuming that the anode itself is working correctly, it will then record the event at the centroid position, which will not represent the true photon arrival position. These shifts can be due to distortions in the MCP-anode gap electric field, such as at the edges of the MCP below the contact plates; or they may be due to the velocity of the electron cloud as it leaves an angled pore.

Shifts can also occur if some MCP channels do not supply as many electrons as others. In this case, the centroid position will be weighted towards the higher gain channels. This has been observed (Vallerga, Kaplan *et al.*, 1989 and Vallerga, Siegmund *et al.*, 1989) near to dead spots, where the dead channels do not supply any electrons. It may also explain the chickenwire effect at the boundaries between hexagonal multifibres in the rear MCP.

There are several ways of assessing non-uniformities, both differential non-linearity (DNL) and integral non-linearity (INL). DNL can best be looked at by examining a flat field and measuring the variation in count rate across the MCP.

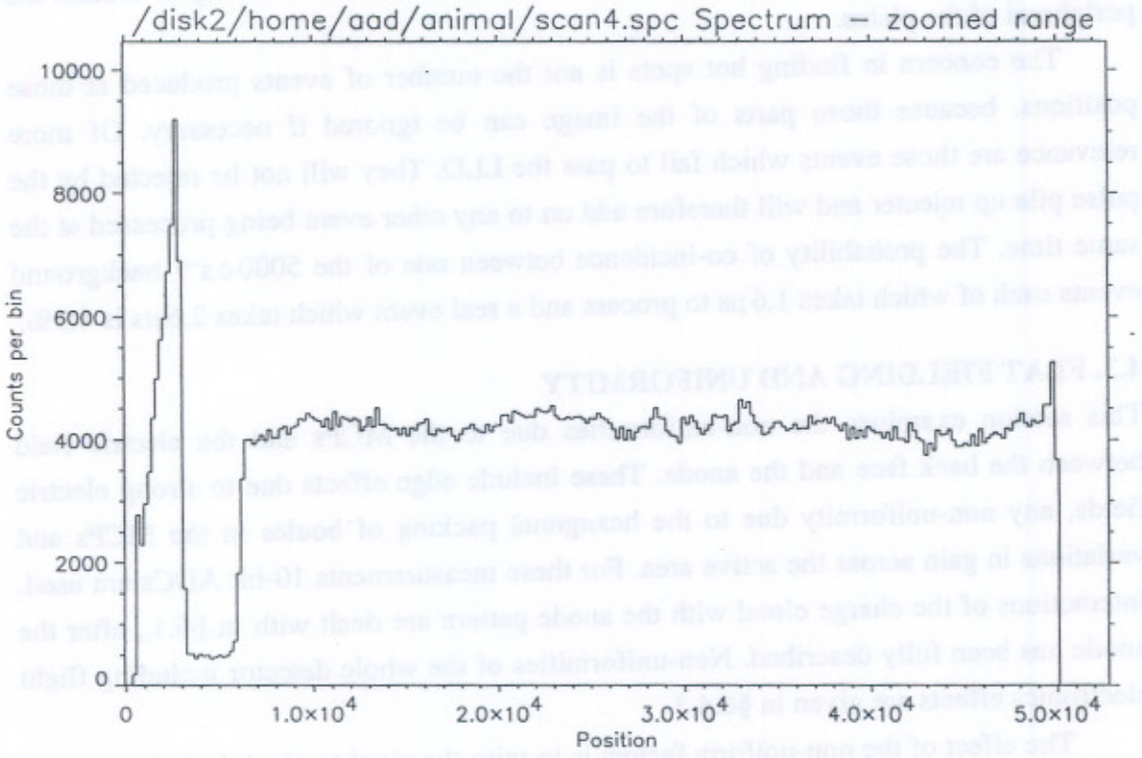

Figure 65. Time integrated flat field on RM detector obtained by scanning a beam across the surface. The x-axis is in μm units. Events with gains below 1.5×10^7 have been excluded to eliminate the small hot spot. Large scale deviations from the mean are due to variations in the lamp output.

4.3.1. Flat fielding

A flat field on the detector front face can test uniformity of gain and image quality. According to Poisson statistics, if there are more than 400 events per pixel, then there should be only a 5% random error in counts per pixel. To obtain this level requires 1 million events for a flat field, which at a rate of 10^3 c s^{-1} takes just 1000 s or 17 minutes.

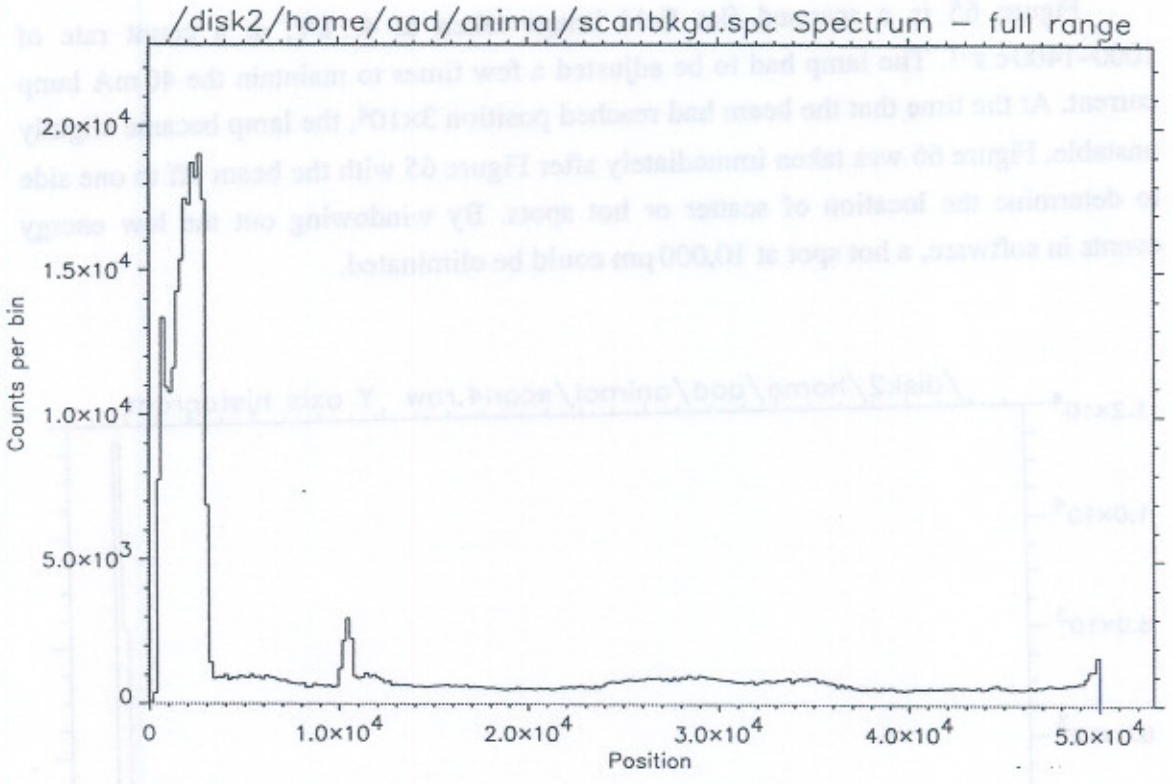

Figure 66. Background and scattered light events in the RM detector gathered for 8 hours. The x-axis is in μm units. The count rate was approximately 20–40 c s^{-1}. This included all events with gains greater than 1.6×10^6. Two high count rate areas are apparent. The one at position 10,000 consists almost entirely of very low energy events.

A reasonable flat field may be obtained by simply having a pinhole light source 1.5 to 2 m away from the detector. The spreading of the light beam is enough to cover the detector. This scheme was employed for the detector life testing.

Without a direct flat field, a spot of illumination can be moved across the front face to create a time-integrated flat field. The RM detector in the UV facility was suited to this method. The detector was scanned across a tall, narrow beam of light, which was

formed by a single Ne I (73 nm) spectral line, selected by a slit aperture. The detector was moved at a speed of 10 μm s^{-1} or less, starting with the beam beyond one edge of the detector. The maximum traverse of the X-Y table was 50 mm, which, given that the line did not fall in the middle of the detector when the table was at the origin, only allowed 44 mm of the detector to be scanned. However, the last 3 or 4 mm of the detector received a high count rate from scattered light and, therefore, it would not necessarily be useful to scan this region.

Figure 65 is a scanned flat field image taken at 4.1 kV, at a count rate of 1000–1400 c s^{-1}. The lamp had to be adjusted a few times to maintain the 40 mA lamp current. At the time that the beam had reached position 3×10^4, the lamp became slightly unstable. Figure 66 was taken immediately after Figure 65 with the beam off to one side to determine the location of scatter or hot spots. By windowing out the low energy events in software, a hot spot at 10,000 μm could be eliminated.

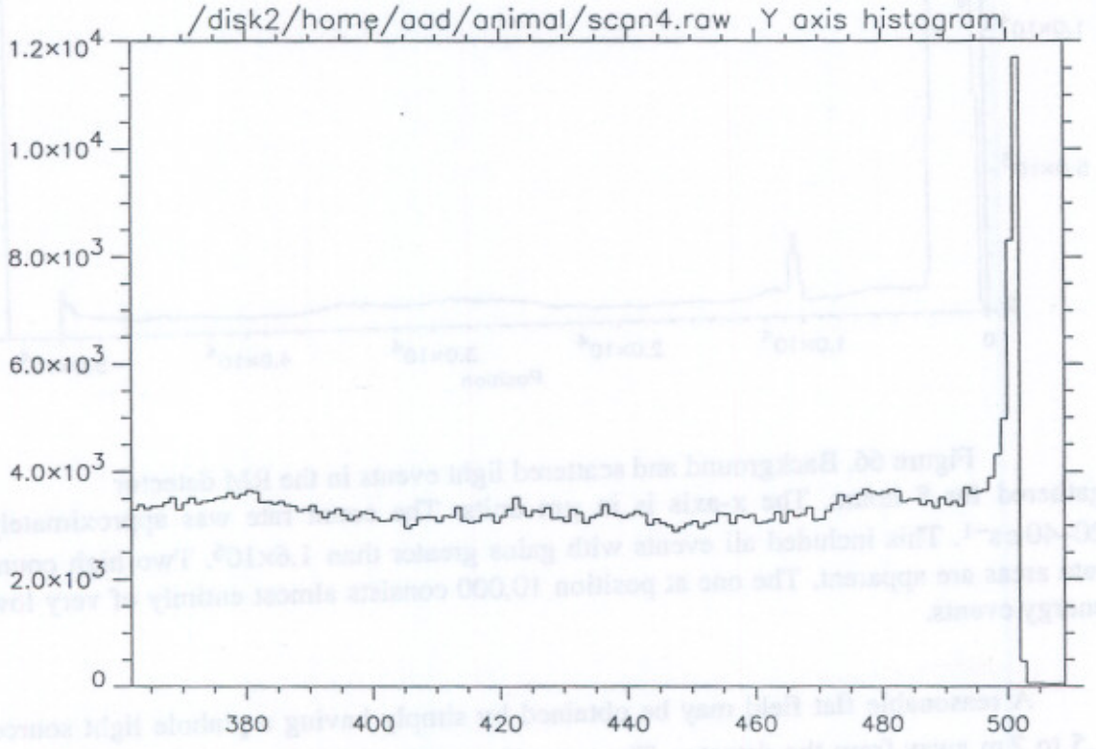

Figure 67. Expanded view of one end of the flat field image showing brightening for ~500 μm at edge of the field of view. The x-axis is in units of 100 μm.

Figure 67 shows an expanded view of the right hand end of the image in Figure 65, although the x-axis in Figure 67 is given in units of 100 µm. Brightening at the ends of the flat field image could be due to a radial electric field component in the MCP-anode gap due to the finite thickness of the MCP back contact plate. This field accelerates the charge clouds at the edge of the detector inward, but the field falls off very quickly towards the centre of the detector. Therefore, a pixel at the edge of the detector image represents a larger illuminated area on the front surface and will be brighter for an even illumination.

To look at small scale uniformity, such as the chickenwire effect (§3.3.4.), without integrating across the height of the detector, a mask with a slit oriented along the x-axis was fitted to the front face. The mask had a slot 250 µm high and 40 mm long. It was mounted onto the front of the RM detector and scanned by the Ne spectral line.

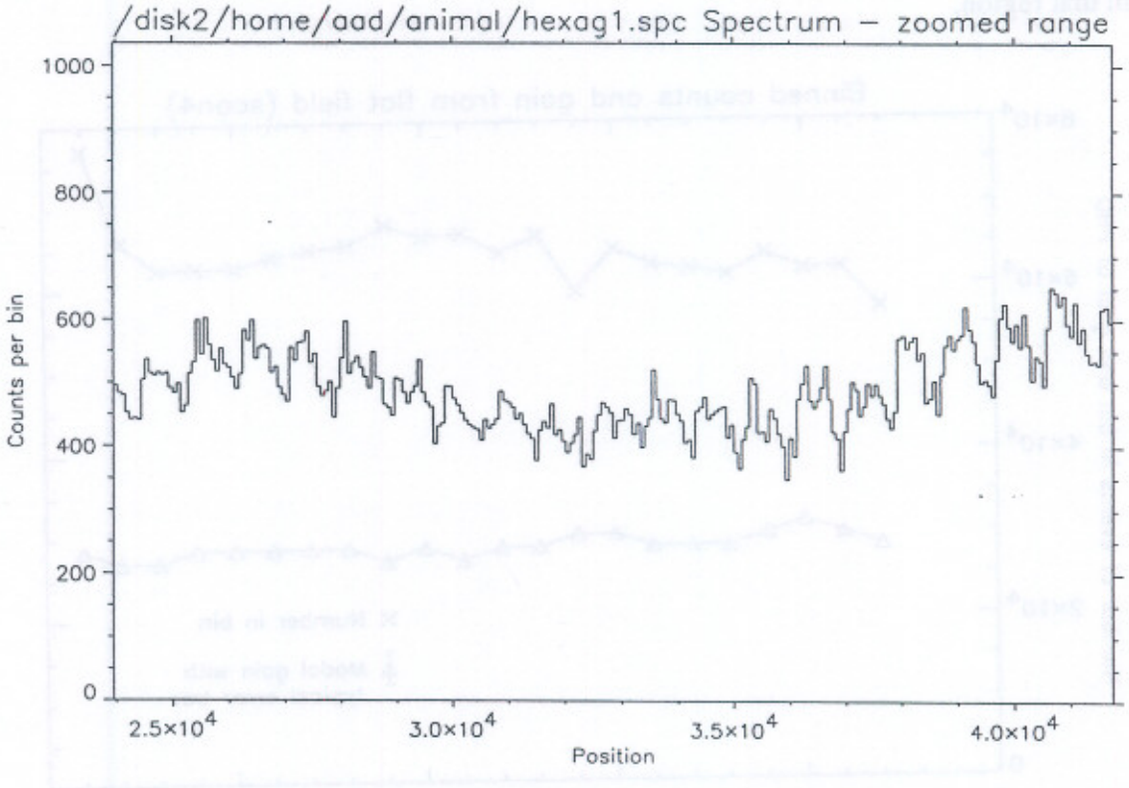

Figure 68. One dimensional chickenwire effect
obtained by illuminating a long slot mask. The irregularities have a scale of 900 µm.

Figure 68 is part of the image obtained. Castellation-shaped irregularities on the scale of 900 µm, due to the boule structure, are clearly shown. Many of the castellations have a dip in the middle. This suggests that the electron clouds are being displaced from

the boundaries towards the centre of each hexagonal bundle. These features are not seen when the whole 16 mm height is illuminated.

4.3.1.1. Gain uniformity

If the MCPs themselves are not uniformly made or have deteriorated in a non-uniform way, this may show up as a variation in gain across the active area. Any variation in inter-plate gap, due to warping of the plates or non-flat shims, will also show up as a large-scale variation in gain across the MCPs, because the number of pores stimulated in the middle and rear MCP will vary.

Uniformity in gain can be measured easily with a detector for which the position dependent PHD can be measured. It is far harder for a detector which only supplies an integrated PHD across the whole active area. If the flat field is perfectly uniform, then the count rate gives the same information—the lower the count rate, the lower the gain in that region.

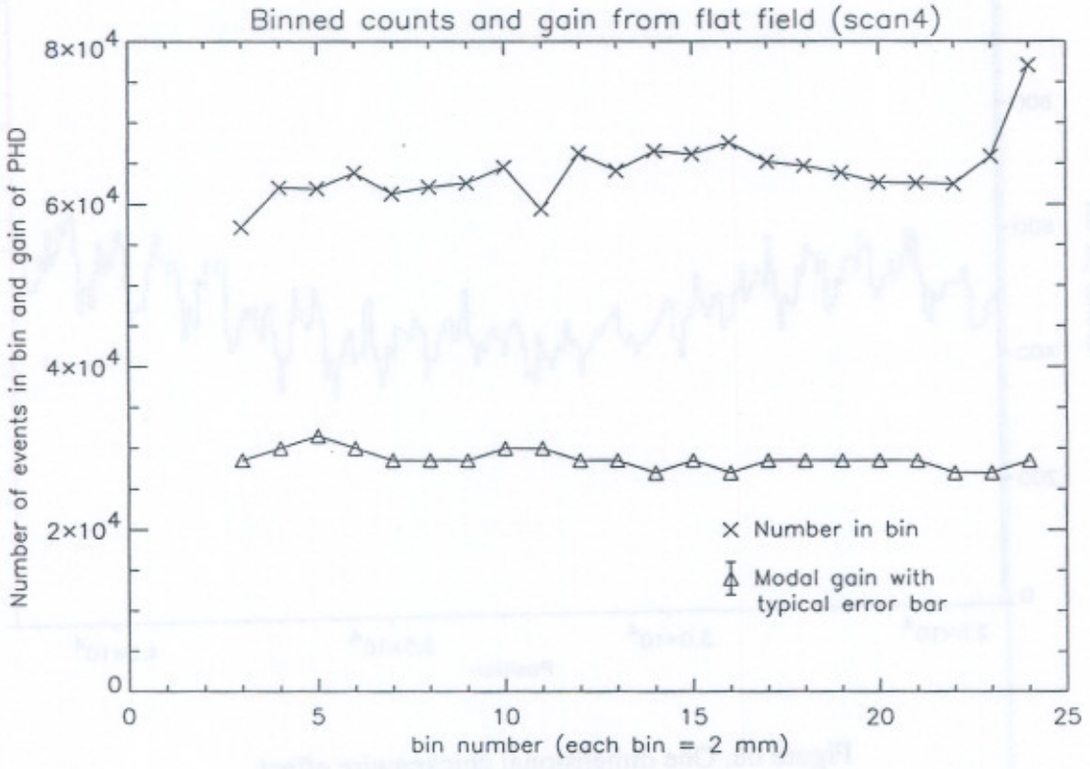

Figure 69. Variation in gain across RM detector as measured from a flat field scan image binned into 2 mm sections.

The image shown in Figure 65 was binned into 2 mm sections. For each section the total number of events and the PHD of the events was found. The modal gains

obtained from the PHDs are plotted in Figure 69. The ratio of the maximum to the minimum gain in the region scanned is 1.17. The difference in shape between the number-in-bin curve and the gain curve implies that the large scale irregularities in the flat field are not caused by gain variation. The variation in modal gain across the length of the detector used in the scan is, in fact, smaller than the error in measuring the gain. Thus, it may be concluded that the detector gain is uniform at least to within 17%.

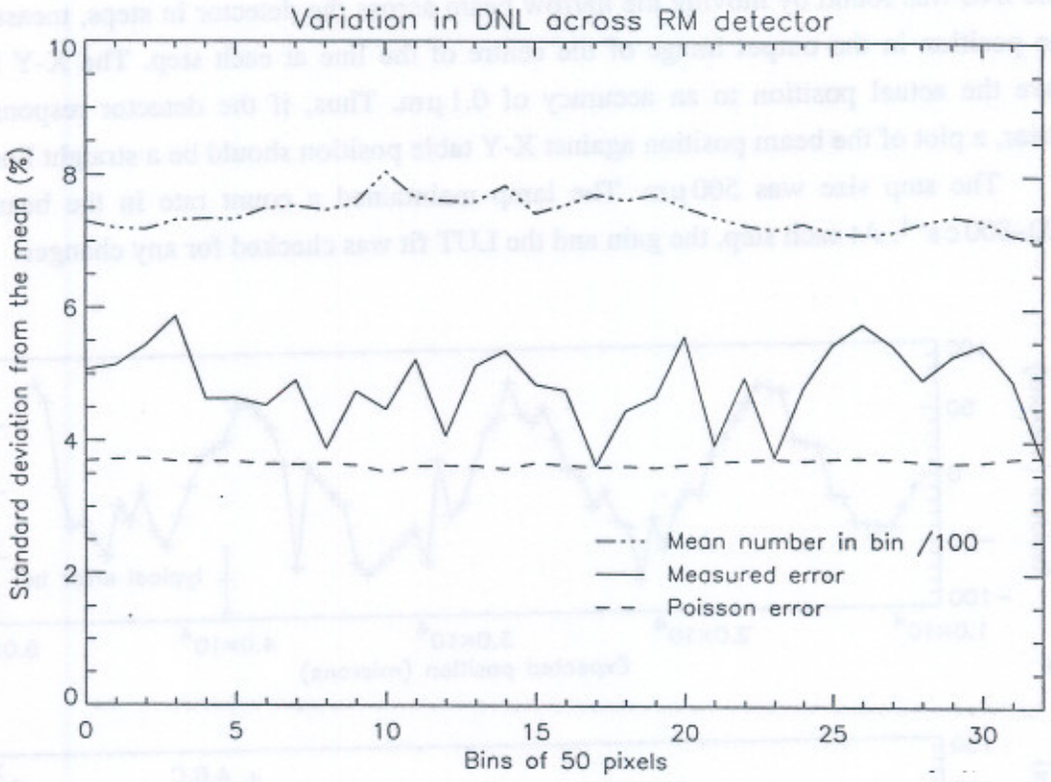

Figure 70. DNL measurement with the RM detector.
The data, taken using laboratory 10-bit readout electronics, is divided into 50 pixel sections. The Poisson error indicates the expected level of error. The mean number in each bin has been scaled so that it can be plotted on the same graph.

4.3.1.2. Differential non-linearity

The data shown in Figure 65 was further sub-divided into 25 µm pixels, in accordance with flight-style data. In order to measure the DNL, the mean counts per pixel and the standard deviation were calculated for each 50 pixel (1250 µm) section. The mean number of counts per pixel was 742, with an r.m.s deviation from the mean within each section of 36±4. The mean and deviation (as a percentage of the mean) are illustrated in Figure 70. The expected error, as calculated using Poisson statistics, is marked on the

graph for comparison. The measured error is approximately 1.3 times that expected. Subtracting the Poisson error from the measured error in quadrature, the resulting DNL is 3.1%. The DNL may be due in part to small changes in gain (up to 17%) as illustrated above, and in part to low level fixed patterning (§5.1.4.) from the 10-bit readout electronics.

4.3.2. Integral non-linearity

The INL was found by moving the narrow beam across the detector in steps, measuring the position in the output image of the centre of the line at each step. The X-Y table gave the actual position to an accuracy of 0.1 μm. Thus, if the detector response is linear, a plot of the beam position against X-Y table position should be a straight line.

The step size was 500 μm. The lamp maintained a count rate in the beam of 600–800 c s^{-1}. At each step, the gain and the LUT fit was checked for any changes.

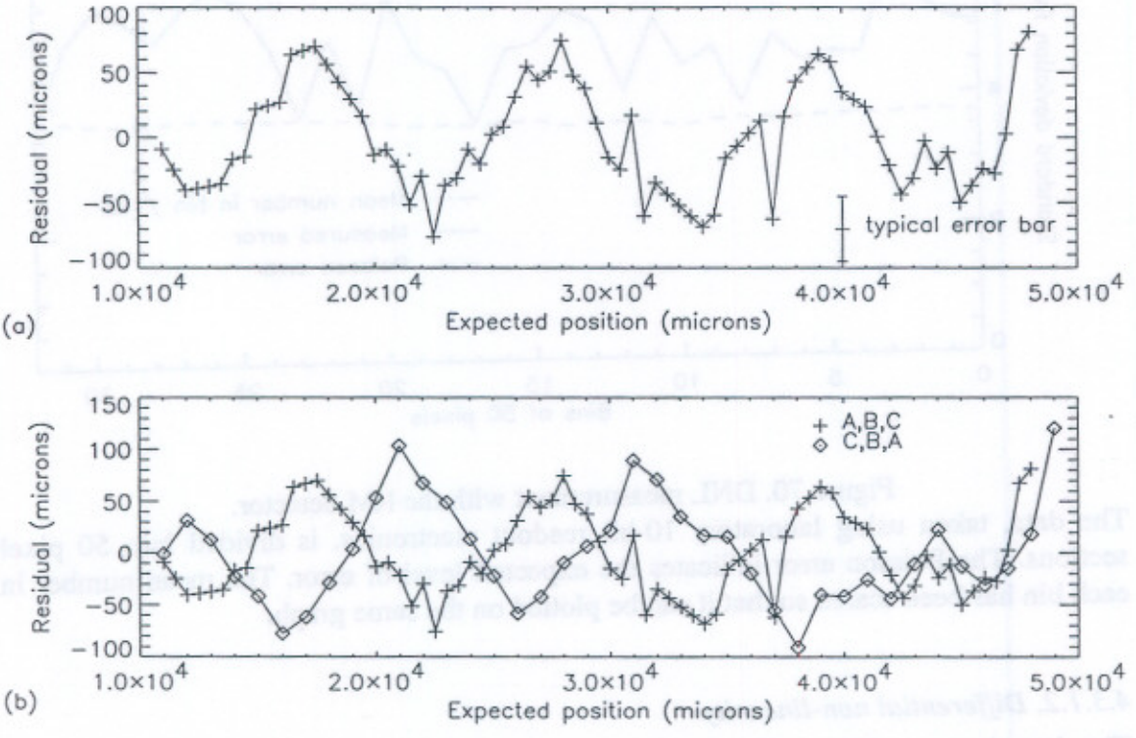

Figure 71. INL of RM detector with laboratory electronics.
(a) shows residuals from a straight line fit. (b) overlays the change in INL by swapping the electronics channels.

Figure 71 (a) shows the residuals of the spectral line position from a least squares fit to a straight line. As can be seen, there is a smoothly varying, cyclic error of ±50 μm

or ±2 pixels. The error follows the phase angles of the anode spiral arms, with minima and maxima corresponding to the axis of the *C* electrode. In fact, the *C* electronics channel had itself exhibited considerable INL when being set up by means of the *TURBOCAL* program (see §3.2.2.) of ±4 ADC channels. This channel was also the noisiest of the three. To test the hypothesis that the electronics response may be the cause of the non-linearity in the SPAN output, the *C* and *A* electronics were swapped. Figure 71 (b) shows that the hypothesis was correct. The error moved with the electronics.

A useful measure of INL is to calculate the r.m.s. deviations of images from their expected position. A distortion parameter (Barstow *et al.*, 1985) is defined thus:

$$\delta = \frac{1}{L}\sqrt{\frac{\sum_{N}(x_i - x_t)^2}{N}} \times 100\% \qquad (73)$$

where x_i is the position of the image and x_t is the true position. L is the length of the anode. Calculating this parameter for the data of Figure 71(a) gives 0.08%, and for (b) 0.096%.

This particular result is interesting in that it gives a direct measure of the relationship between ADC non-linearities and readout non-linearities. From the INL requirement on the flight ADCs of 0.5 LSB (§2.3.2.), the readout INL should be ~0.025%, within the requirement for the detector INL of 0.1%. The measured flight ADC INL was less than the requirement at 0.2 LSB, predicting a readout INL of just 0.01%. The flight detector INL will be presented in §6.4.3.

4.4. LINEARITY OF PHOTON COUNT RATE

A gain of 4×10^7 was chosen for the flight detectors as being easily obtainable within the high voltage available (§3.2.3.5). Initially, LLD levels were selectable between 2 and 5×10^7 with a ULD at 7×10^7. This setup appeared to be adequate while looking at the flat field spiral or the images of spectral lines. However, it did result in the discarding of a large number of real valid events, due to the ~100% FWHM.

In the calibration test (see Chapter 8), where spectral lines of known strength were used to illuminate the detectors, it was realised that the intensity measurements were not entirely linear. The relation between the PHD and the 'energy window' between the LLD and ULD was re-examined. The LLD levels were higher and the ULD lower than had been believed. This was due to the prototype preamplifiers having lower LLD discriminator levels (by a factor of 1.43) than the flight preamplifiers and the amplifier saturation point being mistaken for the ULD signature on the MCA. This had led to the

assumption that only a small part of the PHD was being thrown away by the discriminators.

The discriminator levels and MCA were re-calibrated using a known voltage across standard capacitors. A pulse generator supplied square waves of known voltage (V) with a fast rise time (6 ns) and slow fall time (20 µs), which simulated the rise and fall times of real events. A three way splitter divided the pulse amplitude between three matched 10 pF capacitors. This is equivalent to:

$$N = \frac{3 \times V \times \left(10 \times 10^{-12}\right)}{1.6 \times 10^{-19}} electrons \qquad (74)$$

The prototype preamplifiers were used together with the proto-flight analogue card and the analogue test box. The *sum* signal was digitised by the PC MCA card. As the voltage was changed, the 'event' pulse indicated whether or not the event was being discriminated. The ULD signal went low when the ULD was reached. In this way all the discriminators and the MCA channels were calibrated with respect to electron gain.

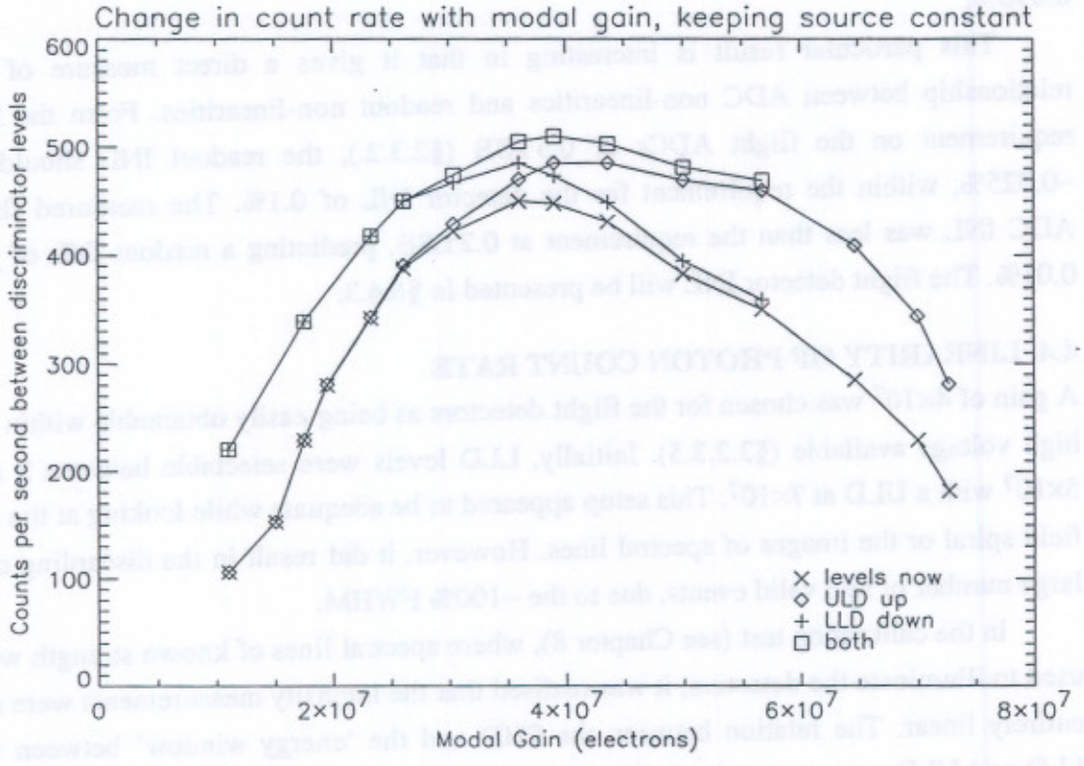

Figure 72. Stability of count rate with changing modal gain.
The crosses mark readings taken with LLD = 2×10^7 and ULD = 7×10^7. ULD was increased to 8.75×10^7 and LLD was reduced to 1.5×10^7 for the other readings.

Figure 72 was made using the RM detector, the UV lamp and the MCA card. The count rate between the discriminator levels could be found by integrating the relevant channels on the MCA. The MCP voltage was changed in 20 V steps to move the modal gain across the window. As can be seen in the figure, with the LLD and ULD set at the original levels, the count rate rises as more and more events reach the LLD. It peaks with the modal gain at 4×10^7, but then drops rapidly again as the events fall over the ULD. Increasing the ULD to 8.75×10^7 allows a plateau region between about 3 and 6×10^7 where changes in voltage or gain depression should not affect the count rate. The problem is that to have a PHD in the centre of the plateau would require a gain of 5×10^7, rather than the intended 4. Therefore the LLD was reduced to 1.4×10^7 to allow the gain to remain at 4×10^7 rather than having to run the plates harder, which would wear them out sooner and might lead to higher gain depression. The final value for the ULD was chosen to be 8×10^7 electrons to avoid being too close to the maximum obtainable output from the amplifiers.

4.4.1. Count rate dependent gain depression effects

The effect of CDGD is to force the PHD towards the LLD at high count rates. To a limited extent, the gain can be restored by an increase in HV, but at very high count rates the normal gain cannot be obtained. Figure 73 shows an example. The RM detector, with flight-style electronics, was mounted on the RC with two strong neon lines dispersed by the grating to illuminate very small areas of the MCP. The current in the UV discharge lamp was gradually increased to increase the count rate. The input count rate, which was not accurately known, was assessed by combining count rates below the LLD, above the ULD and processed events. The output count rate is the processed events only. As the current was increased (from 10 mA to 300 mA) the number below the LLD increased as the gain reduced. The experiment was repeated at a number of voltages.

The top graph in Figure 73 shows the CDGD curves for all voltages tried. The decline in output count rate can be seen. The middle graph is an expanded view of the lower count rate region of the top graph. In this one the loss of efficiency at low count rates with the very high HV setting can be seen. This is shown even more clearly in the bottom graph where the percentage of output to input count rates processed is plotted. The higher values of HV are better at high count rates but not low ones. However, with high HV the efficiency does not reach the 90% level achieved at lower HV.

Another experiment assessed the ability to reproduce accurately the ratio of intensities between two lines. The two bright neon lines falling at the position of

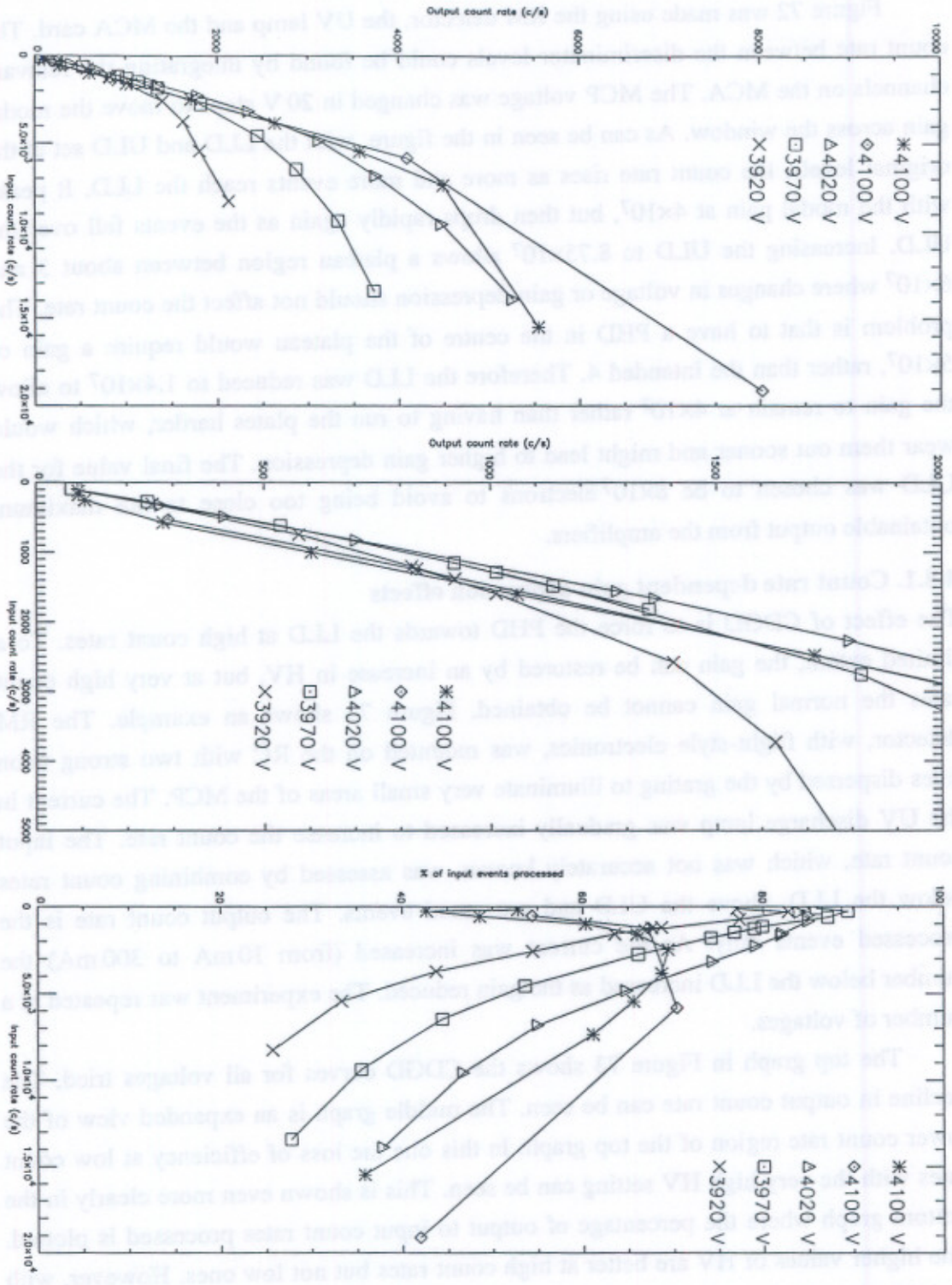

Figure 73. Count rate dependent gain depression with voltage.
Illuminating a small area of the MCP front face.

detector 4 were measured at a variety of input voltages. With a low current in the UV lamp, giving a count rate in the brightest line of about 150 c s^{-1}, a consistent ratio of ~0.2 between the 73.59 and 74.37 nm lines was obtained throughout the HV region 3.85–4.02 kV. At a higher count rate of 700 c s^{-1} in the brightest line, the same ratio was not obtained until 4.06 kV.

To choose a HV setting, and to create correction factors for CDGD, a matrix of output count rates at a wide variety of voltages and input count rates needs to be established. In the experiment described above, the voltage was kept steady while varying the input count rate, which was assessed from the PHD. In the following experiment, the input count rate was kept steady, and the voltage varied. This allowed comparison of response to the same stimulus, without having to make a judgement on the input count rate. The other main difference between this and the former experiment is that in this case one neon line only was allowed to illuminate the detector, selected using the slit. This meant that the measurement was more realistic in assessing the detector response to a single spectral line.

Accordingly, at six different lamp current settings, the count rate was measured at a range of voltages. The total processed count rate was read from a meter counting the number of data valid pulses and an image was recorded. The percentage of the total number of events which were falling in the line was obtained from the image. Multiplying this by the total count rate gave the output count rate in the line only.

Figure 74 shows the curves obtained for each run. At low voltages, the PHD is mainly below the LLD so the efficiency is low. At high voltages, it is above the ULD, again reducing the count rate. It can be seen clearly that the peak moves towards higher HV as the count rate increases. This is because with CDGD the HV needs to be raised to move the PHD back into the window between the discriminators. The value of HV at which the count rate is maximised—the optimal HV setting for that count rate—is plotted against maximum count rate in Figure 75(a). This type of graph will be used to select the best HV to view a particular line, during the mission.

In Figure 74(b) it can be seen that if the HV is too high, efficiency at low count rates is lost, as expected. This is seen even more clearly in Figure 75(b), in which the data matrix has been turned around to plot the response curves for a few of the voltage settings (not all the HV curves have been plotted for the sake of clarity), in a similar format to Figure 73. Ideally, the CDGD curves should be plotted against input count rate. In this case, this is assumed to be proportional to the maximum count rate, as seen at the optimal HV setting. The low HV settings give a good response at low count rate,

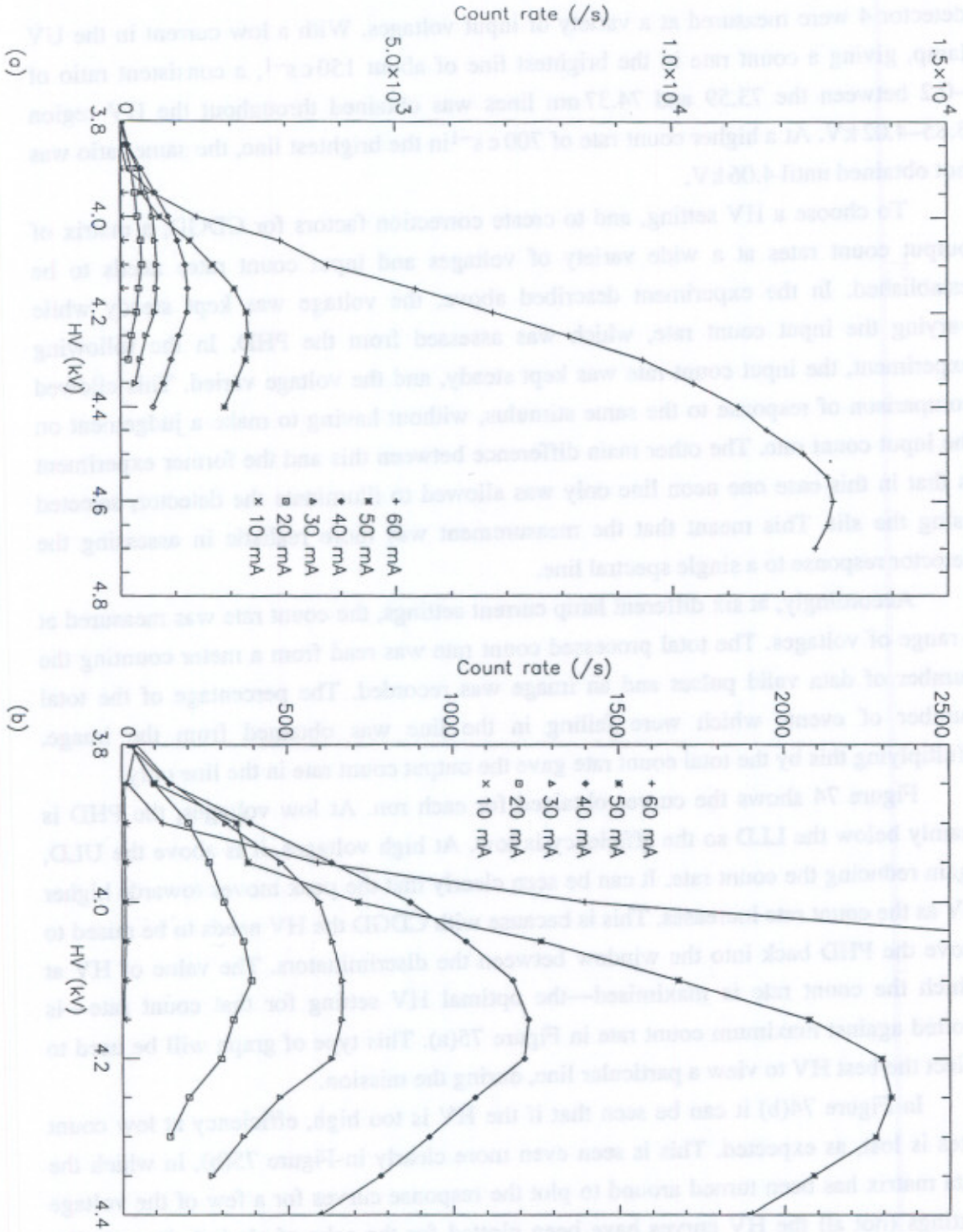

Figure 74. Change in processed count rate with HV.
In (a) the count rate in the neon line is plotted against HV for 6 lamp settings. (b) is an enlarged view of the low voltage part of graph (a).

but a poor response at high count rate. The high HV settings work vice versa. This shows the difficulty in choosing a HV setting for a range of count rates on one detector. In this particular case, to view lines with count rates between 0 and 2000 c s^{-1}, a HV setting of 4.1 kV would give good efficiency and, most importantly, a monotonic variation with count rate.

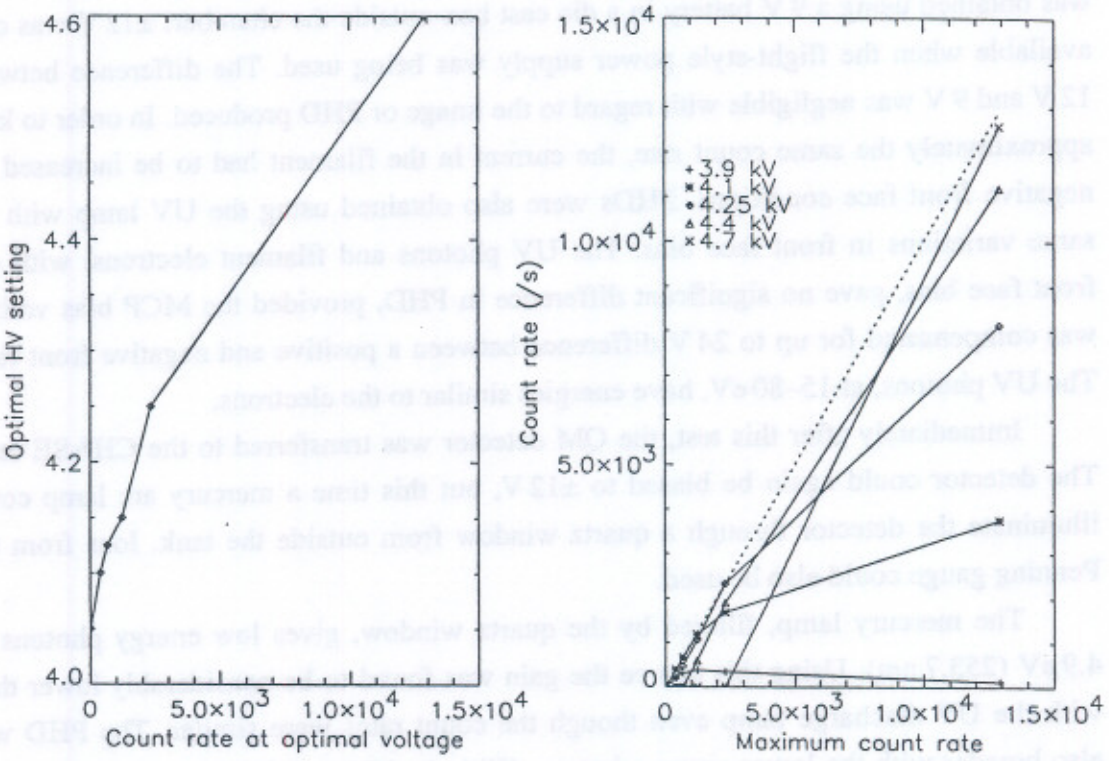

Figure 75. Optimal HV settings and CDGD curves.
In (a) the change in optimal voltage with input count rate is shown. (b) shows response curves to count rate for a variety of voltages. The ideal response curve, such that the optimum output count rate is given for any input count rate is shown as a dotted line.

4.5. EFFICIENCY VS. PHOTON ENERGY

Only one photoelectron can be released by one photon for EUV between 15 and 80 eV. Any incident ions or electrons with more energy than this can produce more than one photoelectron and therefore it may be expected that the PHD would peak at a lower gain for EUV than for ions or high energy electrons or even X-rays. Using an open face configuration for the MCP detectors allows the detector response to extend to low energy photons because there is no absorption in an entrance window. It was seen in

§3.2.3.2. that there was a difference in gain produced by the MCPs for X-rays and for ions, the gain from the ions being higher than from X-rays.

In this section, the detector response to electrons, ions and two wavelengths of EUV were measured with positive or negative front face bias.

In the UV chamber with the QM detector, the filament was used as an electron source with the front face of the detector at ±12 V, ±9 V or at chamber ground. The ±9 V was obtained using a 9 V battery in a die cast box outside the chamber. ±12 V was only available when the flight-style power supply was being used. The difference between 12 V and 9 V was negligible with regard to the image or PHD produced. In order to keep approximately the same count rate, the current in the filament had to be increased for negative front face conditions. PHDs were also obtained using the UV lamp with the same variations in front face bias. The UV photons and filament electrons, with any front face bias, gave no significant difference in PHD, provided the MCP bias voltage was compensated for up to 24 V difference between a positive and negative front face. The UV photons, at 15–80 eV, have energies similar to the electrons.

Immediately after this test, the QM detector was transferred to the CHASE tank. The detector could again be biased to ±12 V, but this time a mercury arc lamp could illuminate the detector through a quartz window from outside the tank. Ions from the Penning gauge could also be used.

The mercury lamp, filtered by the quartz window, gives low energy photons of 4.9 eV (253.7 nm). Using this source the gain was found to be considerably lower than with the UV discharge lamp even though the count rates were similar. The PHD was also broader with the lower energy photons. With the HV at 3.68 kV, the peak with the low energy UV was at channel 196, with a FWHM of 190%, whereas with the discharge lamp the peak was at channel 311 (~4×10^7) at this voltage, with a FWHM of 77%.

The ions are expected to give a higher gain than the UV discharge lamp, but the count rates from the Penning gauge are not controllable. As in the UV facility, the voltage always had to be increased for a positive front face, but the count rate of the ions changed little with the change in front face bias. With a much higher count rate the gain is expected to be depressed. This was indeed observed, with a PHD of peak 251. This shows that although ions should give a higher gain because they are more massive, the count rate effect dominates. Thus there is a dependency on photon energy, but the dependency is small compared with count rate effects.

4.6. EFFICIENCY VS. ANGLE

To measure the change in QE with angle of incidence, the RM detector was mounted on

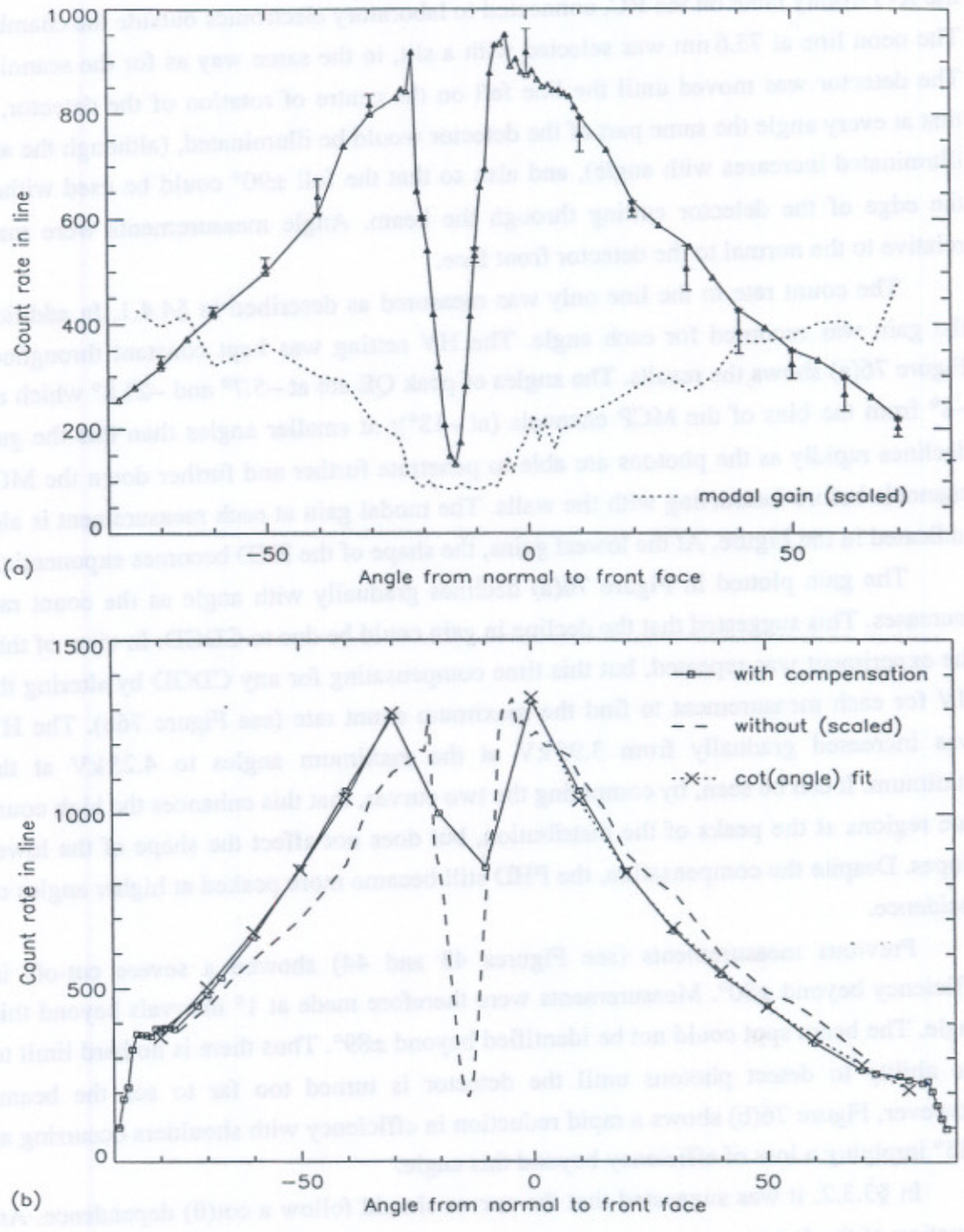

Figure 76. Dependence of QE on angle of incidence.
In (a) the HV was kept constant throughout. The modal gain is plotted over the top showing a decline in gain towards the centre. In (b) the HV was adjusted to find the maximum count rates. A cot(angle) fit is plotted over the top. For comparison the curve in (a) is reproduced here. The angles are measured relative to the normal to the front face, increasing with rotation away from the RC (with the detector parallel to the RC the angle is ~ –70°).

the X-Y-rotary table on the RC, connected to laboratory electronics outside the chamber. The neon line at 73.6 nm was selected with a slit, in the same way as for the scanning. The detector was moved until the line fell on the centre of rotation of the detector, so that at every angle the same part of the detector would be illuminated, (although the area illuminated increases with angle), and also so that the full ±90° could be used without the edge of the detector cutting through the beam. Angle measurements were made relative to the normal to the detector front face.

The count rate in the line only was measured as described in §4.4.1. In addition, the gain was recorded for each angle. The HV setting was kept constant throughout. Figure 76(a) shows the results. The angles of peak QE are at –5.7° and –21.8° which are ~8° from the bias of the MCP channels (at –13°); at smaller angles than this the gain declines rapidly as the photons are able to penetrate further and further down the MCP channels before interacting with the walls. The modal gain at each measurement is also indicated in the Figure. At the lowest gains, the shape of the PHD becomes exponential.

The gain plotted in Figure 76(a) declines gradually with angle as the count rate increases. This suggested that the decline in gain could be due to CDGD. In view of this, the experiment was repeated, but this time compensating for any CDGD by altering the HV for each measurement to find the maximum count rate (see Figure 76b). The HV was increased gradually from 3.95 kV at the maximum angles to 4.25 kV at the minimum. It can be seen, by comparing the two curves, that this enhances the high count rate regions at the peaks of the distribution, but does not affect the shape of the lower slopes. Despite the compensation, the PHD still became more peaked at higher angles of incidence.

Previous measurements (see Figures 43 and 44) showed a severe cut-off in efficiency beyond ±80°. Measurements were therefore made at 1° intervals beyond this angle. The beam spot could not be identified beyond ±89°. Thus there is no hard limit to the ability to detect photons until the detector is turned too far to see the beam. However, Figure 76(b) shows a rapid reduction in efficiency with shoulders occurring at ±85° implying a loss of efficiency beyond this angle.

In §3.3.2. it was suggested that the curves should follow a cot(θ) dependence. An equation of the form:

$$f = \frac{a}{\tan(b\theta + c)} \tag{75}$$

was successfully fitted to both slopes in Figure 76(b) with the following parameters:

$a = 600$; $b = 0.6$ radians; $c = 0.4$ radians; for +ve θ,

$a = 1200$; $b = -0.6$ radians; $c = 0.4$ radians; for –ve θ.

The fit is identical apart from the multiplier, a, which is higher for the angles towards which the channels are biased.

4.7. EFFECT OF TIME

Lifetime tests to examine the effect of the extraction of a large amount of charge from a detector were carried out on the QM, with new MCPs installed in it. The MCPs were first given the same treatment as those designated for flight, namely a vacuum bake-out to 250° for 48 hours, before being built straightaway into the detector and kept under vacuum. According to several authors, baking the MCPs has the same effect on the initial desorption process as the first part of a burn-in scrub, starting to move down the gain curve towards a stable regime, as well as reducing the background event rate.

A lifetime of 2 years for the detectors could mean an accumulation of 8×10^{10} events for the most-used detector. It was necessary for this to be simulated in the laboratory, but not just as a flat field case since in flight most of the events will be taken from small areas of the detectors where the lines fall. For this reason, it was decided to thoroughly test the QM with flat fielding and in addition to cover one half of the MCP front face with a slit mask. This allowed the effects of small area illumination to be investigated as well as giving a control area where no photons would reach the detector, except for the occasional gain measurement.

The experiment was performed in the CHASE vacuum tank, with the mercury Penray lamp just under 1 m from the detector, providing a reasonably flat field. A diaphragm in front of the lamp was used to control the flux rate. One major difference between this system and flight is the count rate, which has to be higher to enable the life test to be performed within a sensible time frame. Also, the wavelength is longer than in CDS, at 253.7 nm.

An HV protection network was added (by Thomas) to the QM power supply to disable the supply if the power was cut. It would also trip the HV if the current exceeded a pre-set value. These mechanisms prevented damage to the MCPs during the frequent failures of the vacuum system, allowing the test to be operated continuously.

4.7.1. Expected accumulation

To calculate the number of events which would need to be extracted, assumptions had to be made as to the form of the flight operation of the detectors.

From Harrison (RAL, private communication, 1995) there will be 1–3 GIS studies each day, each lasting several hours. It can be assumed that the HV is switched on for ~10 hours a day and that for ~10% of the time the studies will involve the active sun.

Within those studies, ~70% of the time will be spent with slit 1, ~20% with slit 2 and ~10% with slit 3. Slit 3 will never be used to view active sun regions.

From Table 9, detector 2 will receive the most photons, most of these being from HeII at 30.4 nm. Inserting those count rates into the above schedule gives an accumulation of 1.15×10^8 photons per day. Given the intended gain of 4×10^7 electrons photon^{-1} this amounts to an extraction of 736 μC per day. Over the two year period, 536 mC should be extracted from the whole detector. If, in the test, only half the detector is being illuminated, the equivalent per unit area, *i.e.* 0.67 mC mm^{-2}, is achieved after extracting 268 mC. This was the target for the flat fielding of one half of the detector. At a rate of 40,000 c s^{-1} this could be accumulated in 290 hours, although, as the gain falls below the maximum, the Coulomb accumulation rate reduces, which would also be the case during flight. The total charge extracted in a particular period was calculated from the PHD and mean count rate.

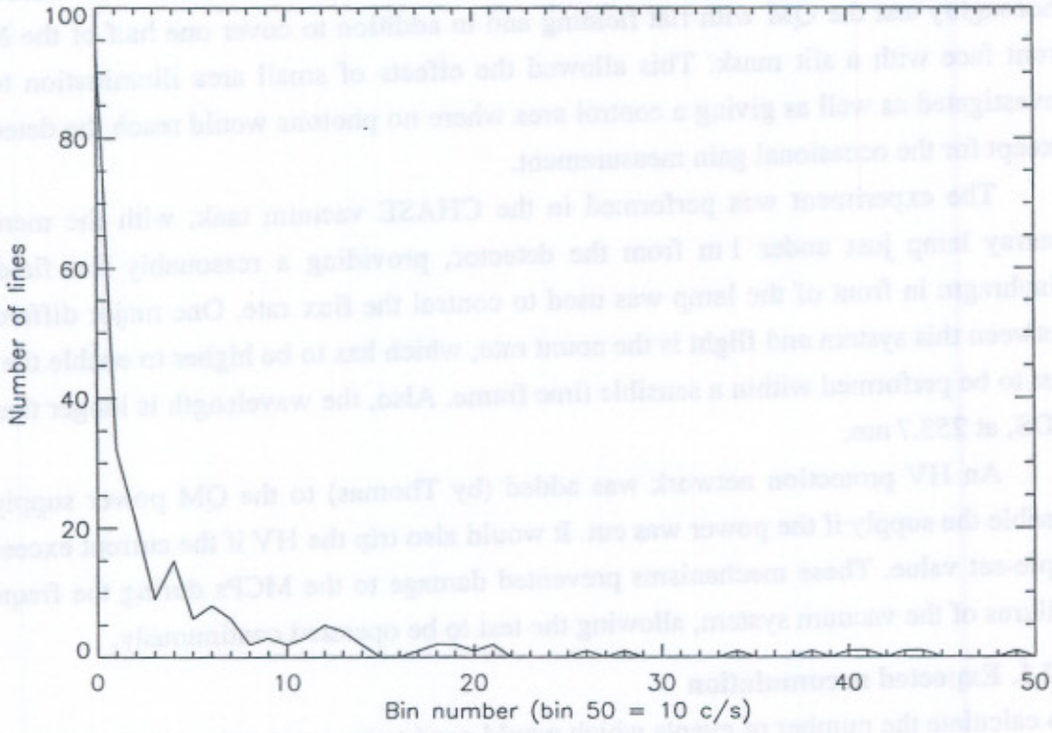

Figure 77. Expected distribution of spectral line count rates over all four detectors. A histogram of expected count rates listed by Harrison and Fludra (1995).

Disregarding the He II line at 30.4 nm, the next brightest line is the Fe XV line at 28.4 nm with a quiet sun, slit 1 count rate of 44 c s^{-1}. Assuming the same ratios of slit and quiet/active sun operation as above, the mean count rate over the 10 hours of operation per day is 572 c s^{-1}. Over two years this line would extract 96 mC of charge.

The slit in the mask had an area of 100 µm × 16 mm; typical dimensions for a spectral line. The mean count rate of the Fe XV line, 572 c s^{-1}, is already a very high count rate for this small area, at 0.07 c $pore^{-1}$. Significant gain depression occurs at count rates higher than this. For this reason, it was decided to perform the slit mask part of the life test at a rate no higher than this. Although the test could potentially be run for 24 hours a day, rather than the typical 10 hours/day in flight, to simulate 2 years would still take 300 days. However, this is a bright line. Figure 77 shows the distribution of expected count rates. Ninety-five percent of the lines will have count rates of less than 0.66 c s^{-1} with the smallest slit. Extracting just 1.4 mC (0.87 mC mm^{-2}) is therefore sufficient to illustrate the Coulomb loss from most of the lines. The aim was to extract as much charge as possible at 500 c s^{-1}.

4.7.2. Results of slit lifetest

The MCPs used in these tests were from the same batch as those mounted in Nehemiah. They likewise showed a high (800–1400 c s^{-1}) background count rate at operating voltages, with events coming from the short edges of the MCPs. This, together with the count rate of 500 c s^{-1}, and the low gain from the long wavelength mercury lamp UV, meant that the PHD was very wide (~200% FWHM).

The background count rate dropped gradually while the HV was switched on. It could be reduced by increasing the HV by a few hundred volts above the operating voltage for a few hours. For instance, turning up the HV from 4.06 kV to 4.2 kV increased the background rate from 1000 c s^{-1} to 8700 c s^{-1}. After it was left on overnight with no UV source, the rate fell to 2400 c s^{-1}, dropping to 200 c s^{-1} when the voltage was returned to 4.06 kV. However, whenever the voltage was turned off for a few hours (for instance during a power cut), the background count rate recovered completely, even though the gain of the plates did not recover. The most likely explanation for the cause of the background is field emission from the glass damaged by cutting at the edges of the plates. Once the voltage is switched on, the damaged areas charge up in such a way as to inhibit field emission, discharging again slowly when the voltage is switched off.

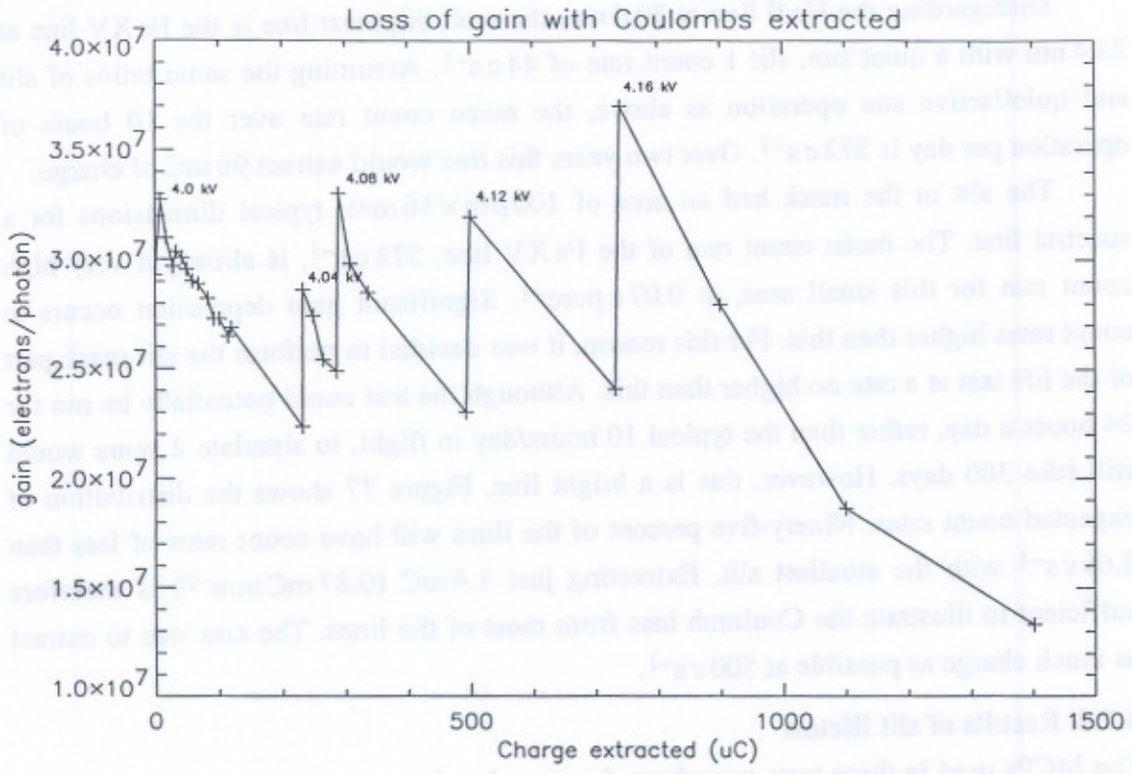

Figure 78. Single slit MCP lifetest.

As the charge was extracted it became increasingly difficult to identify the photon peak in the PHD from the background. After the extraction of 1.4 mC the vacuum pump repeatedly tripped out because of the high temperature of the cooling water in the hot weather. The test was therefore abandoned at this point. The amount of charge extracted covers the expected extraction of most of the spectral lines (see above).

Figure 78 gives the results. Whenever the gain became too low to recognise the peak from the background events, the HV was raised. The values of HV are marked on the graph. There is a gradual decrease in the rate of gain loss: at the end the gradient is 69% of the initial gradient. This suggests that eventually the fall in gain would become small.

4.7.3. Results of flat field lifetest

Problems with high background count rate were not so severe when illuminating half the detector because the event count rate could be maintained at a high enough rate (~40,000 c s^{-1}) to swamp the background. To obtain the desired flux level and a flat field it was necessary to put neutral density filters in the beam, as well adjust the entrance diaphragm aperture. The mercury lamp was mounted on an x-y-z manipulator

to achieve precise alignment through the filters and entrance aperture, giving a good flat field on the detector.

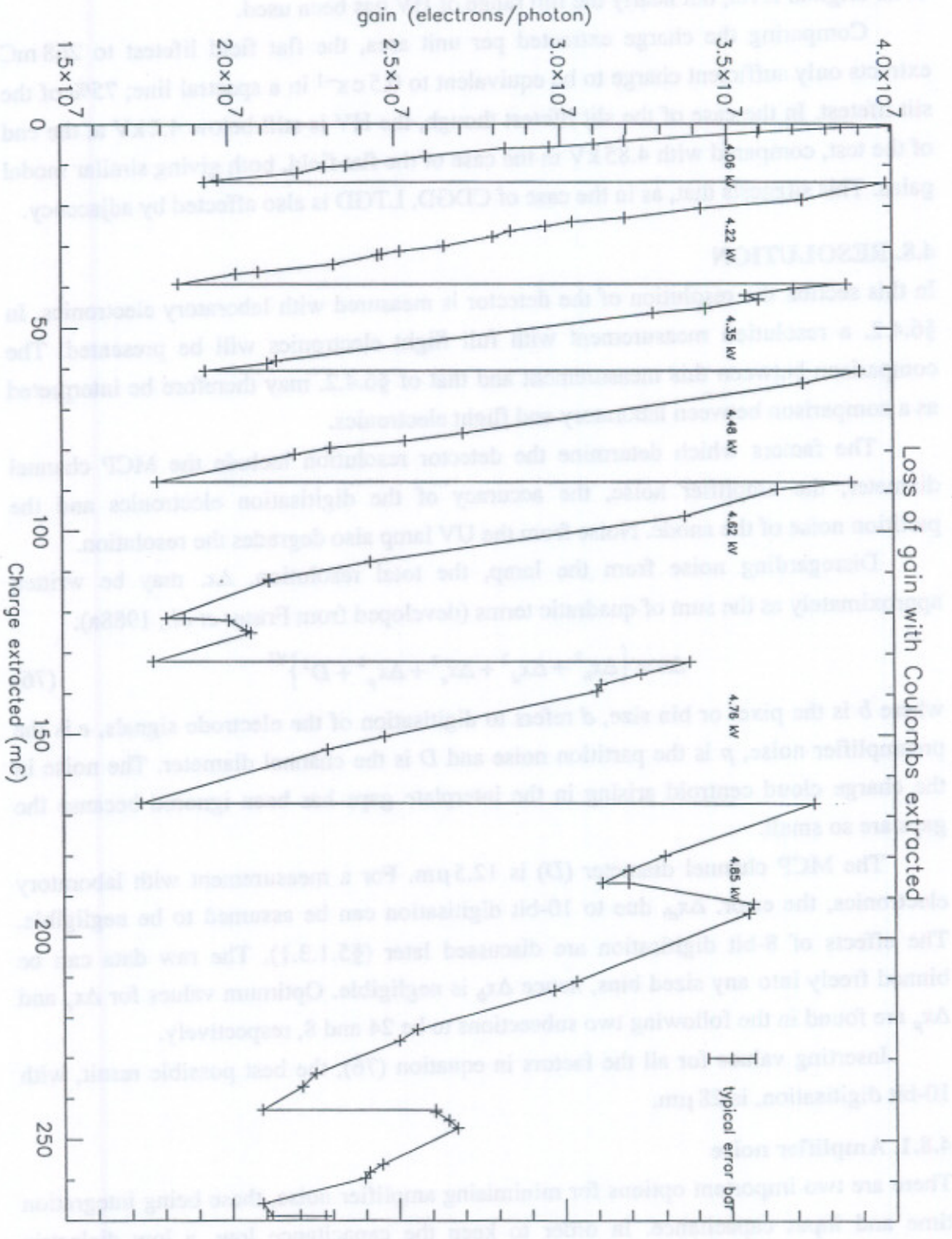

Figure 79. Flat field MCP lifetest.

This test is on-going. The results so far are given in Figure 79. The goal of 268 mC has been reached, equivalent to the 2 year life. The rate of decline has reduced to a sixth of its original level, but nearly the full range of HV has been used.

Comparing the charge extracted per unit area, the flat field lifetest to 268 mC extracts only sufficient charge to be equivalent to 0.5 c s^{-1} in a spectral line; 75% of the slit lifetest. In the case of the slit lifetest though, the HV is still below 4.2 kV at the end of the test, compared with 4.85 kV in the case of the flat field, both giving similar modal gains. This suggests that, as in the case of CDGD, LTGD is also affected by adjacency.

4.8. RESOLUTION

In this section the resolution of the detector is measured with laboratory electronics. In §6.4.2. a resolution measurement with full flight electronics will be presented. The comparison between this measurement and that of §6.4.2. may therefore be interpreted as a comparison between laboratory and flight electronics.

The factors which determine the detector resolution include the MCP channel diameter, the amplifier noise, the accuracy of the digitisation electronics and the partition noise of the anode. Noise from the UV lamp also degrades the resolution.

Disregarding noise from the lamp, the total resolution, Δx, may be written approximately as the sum of quadratic terms (developed from Fraser *et al.*, 1988a):

$$\Delta x = \left\{ \Delta x_b^{\,2} + \Delta x_d^{\,2} + \Delta x_e^{\,2} + \Delta x_p^{\,2} + D^2 \right\}^{1/2} \qquad (76)$$

where b is the pixel or bin size, d refers to digitisation of the electrode signals, e is the preamplifier noise, p is the partition noise and D is the channel diameter. The noise in the charge cloud centroid arising in the interplate gaps has been ignored because the gaps are so small.

The MCP channel diameter (D) is 12.5 µm. For a measurement with laboratory electronics, the error, Δx_d, due to 10-bit digitisation can be assumed to be negligible. The effects of 8-bit digitisation are discussed later (§5.1.3.1). The raw data can be binned freely into any sized bins, hence Δx_b is negligible. Optimum values for Δx_e and Δx_p are found in the following two subsections to be 24 and 8, respectively.

Inserting values for all the factors in equation (76), the best possible result, with 10-bit digitisation, is 28 µm.

4.8.1. Amplifier noise

There are two important options for minimising amplifier noise, these being integration time and input capacitance. In order to keep the capacitance low, a low dielectric material is used as the anode substrate. The metallic layer is kept thin to minimise the

inter-electrode capacitance. Typically, noise is reduced as the integration time is increased, which is achieved by increasing the shaping time constant, though this has the disadvantage of limiting the count rate. The Ortec shaping amplifiers used in these tests have a range of shaping times: 2 μs was selected for these experiments. The Ortec preamplifiers do not include any shaping. In the flight electronics, the shaping time is 1.7 μs.

Simple equations can be constructed to calculate the effect of an error in the ratio of the electrode signals. These can be used to give a rough idea of the effect of electronic noise. The angle given by the SPAN anode decoding algorithm represents the position along the anode. For the flight system the noise was measured as ±15,000 electrons on a 4×10^7 electron signal. Assuming this noise level on one of the three input signals, the resulting error on the SPAN angle is plotted in Figure 80 as two solid lines. It can be seen that the error is at a maximum where the signal is itself at a maximum or minimum (at 90° or 270°). The error due to the same noise on the other two signals is plotted as broken lines, assuming that the noise on all channels is the same.

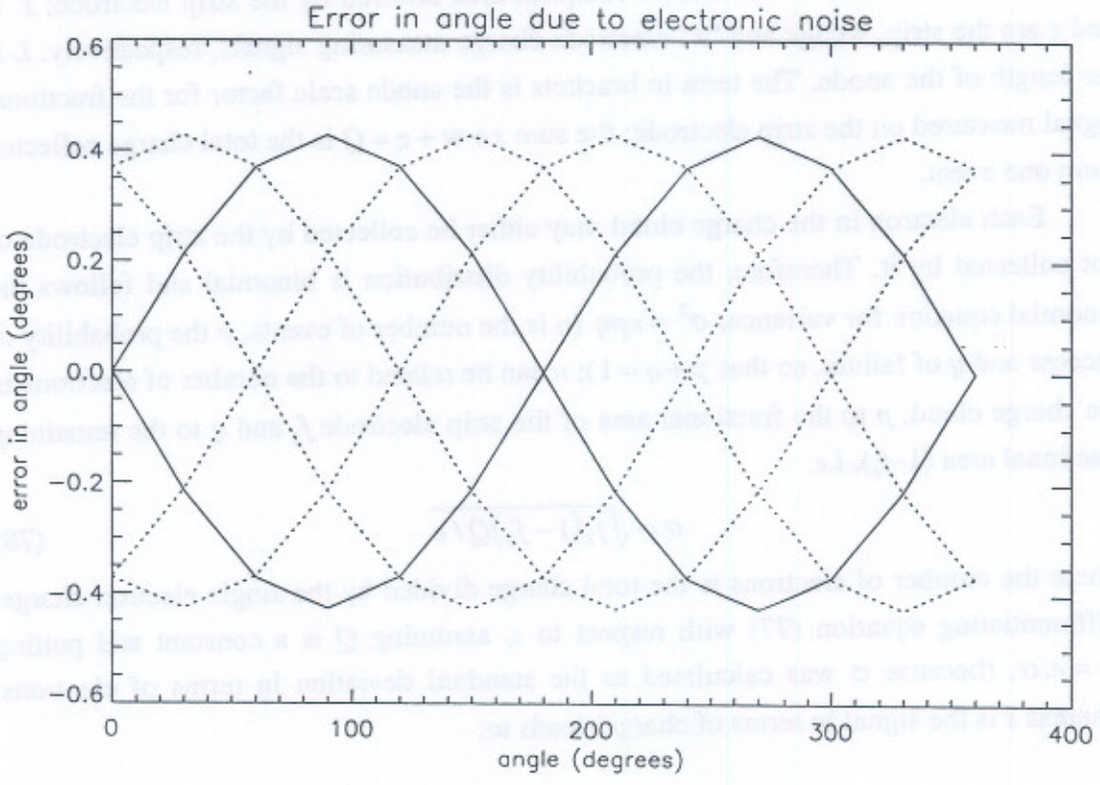

Figure 80. Error on resulting SPAN angle due to noise.
For explanation see text.

The maximum error on θ from this is ±0.45°. Assuming that this single revolution represents a fifth of the anode length which is 10,000 µm, then the error represents ±12 µm. This then is the order of r.m.s. error that could be expected due to the flight system electronic noise. With the laboratory electronics the noise was persistently higher, normally ~20,000–40,000: 70,000 electrons r.m.s. was the maximum noise measured. For 70,000 electrons an error of ±55 µm can be expected from this model.

4.8.2. Partition noise

Partition noise is that which is due to the statistical variation in the positions of the electrons in the charge cloud and the way they divide between the electrodes. For the WSA it is simple to calculate (Thornton, 1988 and Siegmund *et al.*, 1983).

Consider the strip electrode, which defines the position along the X axis via the equation:

$$X = \left(\frac{L}{f_{\max} - f_{\min}} \right) \frac{s}{s+w+z} \tag{77}$$

where f is the fraction of the cloud's footprint area covered by the strip electrode; s, w and z are the strip, wedge and "z" electrode charge measuring signals, respectively. L is the length of the anode. The term in brackets is the anode scale factor for the fractional signal measured on the strip electrode; the sum $s + w + z = Q$ is the total charge collected from one event.

Each electron in the charge cloud may either be collected by the strip electrode or not collected by it. Therefore, the probability distribution is binomial and follows the binomial equation for variance, $\sigma^2 = npq$ (n is the number of events, p the probability of success and q of failure, so that $p + q = 1$); n can be related to the number of electrons in the charge cloud, p to the fractional area of the strip electrode f_s and q to the remaining fractional area ($1–f_s$), *i.e.*

$$\sigma = \sqrt{f_s(1-f_s)Q/e} \tag{78}$$

where the number of electrons is the total charge divided by the single electron charge. Differentiating equation (77) with respect to s, assuming Q is a constant and putting $ds = e.\sigma$, (because σ was calculated as the standard deviation in terms of electrons, whereas s is the signal in terms of charge) leads to:

$$\text{partition noise, } dx(FWHM) = \frac{2.355L\left[f_s(1-f_s)e/Q\right]^{1/2}}{(f_{\max} - f_{\min})} \tag{79}$$

Assuming that each cycle of the SPAN pattern can be approximated by a wedge and strip pattern, if L is 10,000 µm (the average pattern repeat length), f_{max} is 0.556 and f_{min} is 0.097, Q is 4×10^7 electrons, then at $f = f_{max}$, the partition noise is about 6 µm and at f_{min} is 2 µm. Figure 81 is a graph of the partition noise with increasing gain.

Electronic noise for a wedge and strip detector affects the resolution as (Martin *et al.*, 1981):

$$\text{electronic noise, } dx(FWHM) = \frac{2.35L\left[N_w{}^2(1-f)^2 + f^2\left(N_s{}^2 + N_z{}^2\right)\right]^{\frac{1}{2}}}{Q\left(f_{max} - f_{min}\right)} \qquad (80)$$

where N_W is the noise on the wedge signal amplifier *etc.* Hence, both electronic noise and partition noise can be minimised by increasing $f_{max}-f_{min}$, and Q. However, partition noise is proportional to the inverse of the square root of the gain, unlike electronic noise which varies as the inverse of the gain. Therefore, partition noise will only be important at high gain when there are low electronic noise levels. Nevertheless, partition noise is still small at high gains.

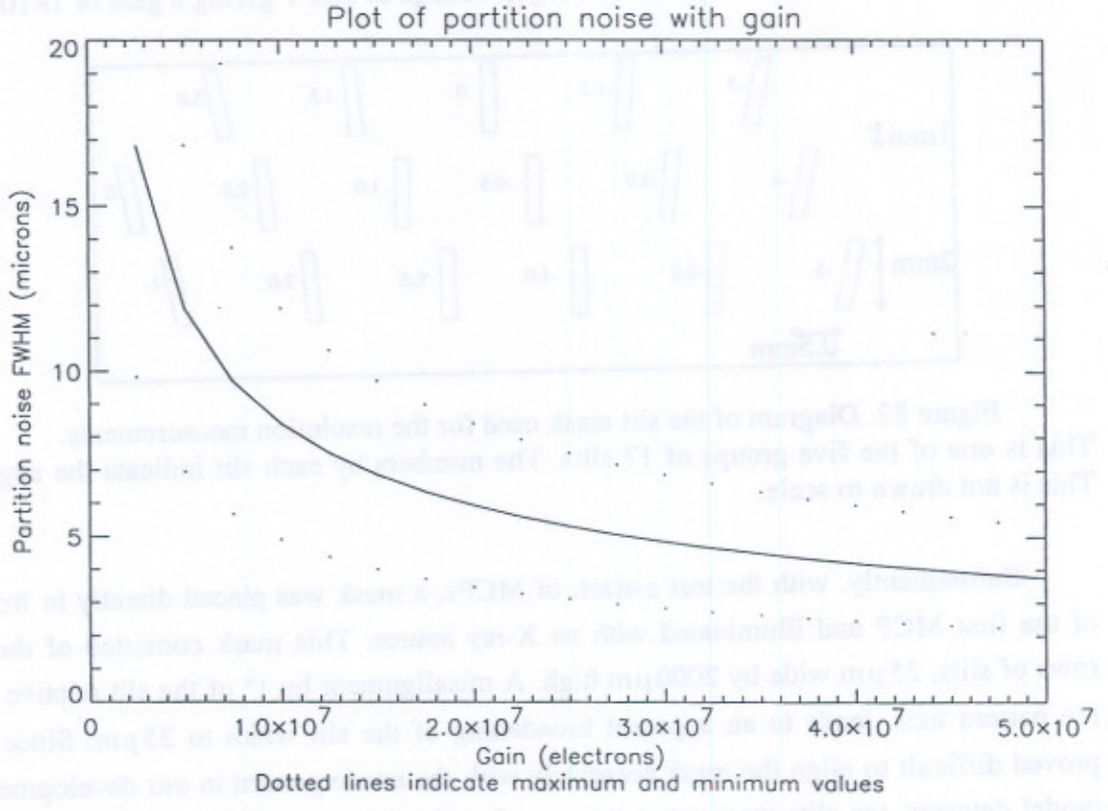

Figure 81. Calculated partition noise for the GIS SPAN anode vs. electronic gain showing that at the nominal gain, partition noise is negligible compared with the required resolution. Dots mark the range of values corresponding to $f_{min} < f < f_{max}$

4.8.3. Measurement with laboratory electronics

It is of crucial importance in this measurement to minimise the electronic noise. Low noise preamplifiers are needed, as well as a grounding scheme that eradicates ground loops and mains pickup.

The first one-dimensional SPAN anode was made with 7 spiral revolutions. The MCPs, as described in Chapter 3 were a chevron stack of 12.5 µm pore, 20×50 mm rectangular plates. They were old CHASE plates and had to be cleaned up before use. Repeated problems were encountered in connection with hot spots and a high background count rate. The detector was mounted in the CHASE tank, illuminated by a UV discharge lamp. Various filters could select particular wavelengths and control the count rate. Ions from the lamp tended to swamp the detector. This problem had to be overcome by running at a high lamp pressure, in order to reduce the mean free path of the ions.

At the first attempt at a resolution measurement in these less than ideal conditions, with a mask of 50 µm pinholes, a resolution of better than 100 µm was obtained. This was with a MCP voltage of 2.95 kV and a gap voltage of 500 V giving a gain of 1×10^7.

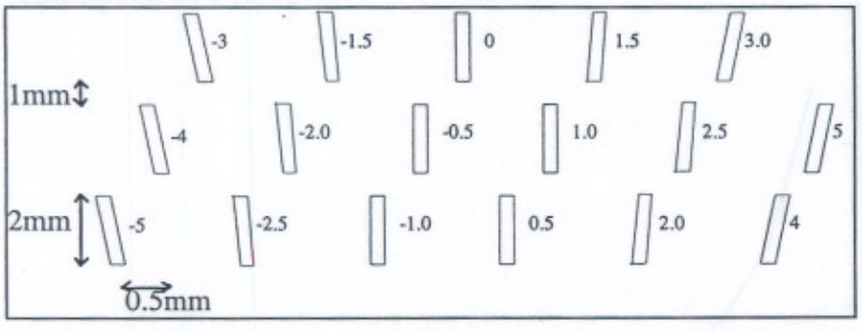

Figure 82. Diagram of the slit mask used for the resolution measurements. This is one of the five groups of 17 slits. The numbers by each slit indicate the angle. This is not drawn to scale.

Subsequently, with the test *z*-stack of MCPs, a mask was placed directly in front of the first MCP and illuminated with an X-ray source. This mask consisted of three rows of slits, 25 µm wide by 2000 µm high. A misalignment by 1° of the slit relative to the pattern axis, leads to an apparent broadening of the slit width to 35 µm. Since it proved difficult to align the mask accurately with the anode pattern in our development model detector, the slits were set at a range of angles between −1.3° and +1.3° from a nominal value. The separation between the slits was 300 µm. The data confirmed that the resolution depended upon the angular offset of the slit and indicated that the whole

mask was offset by a further few degrees from true alignment. The best measured resolution was 70 µm. For a perfect alignment with this configuration, and high electronic noise figure (50,000 electrons FWHM), a resolution of 60 µm was expected from the detector simulator program (§5.2.4.1).

A new mask was made with the angles even more extreme, between ±5°. This time there were 5 repeated groups of 17 lines 500 µm apart (see Figure 82), still in the three rows. Figure 83 is an example of the image produced. On this attempt, after deconvolution of the output image with a 25–36 µm top hat (slit) image, a measurement of 35–47 µm was made for the best aligned slit, successfully meeting the requirement.

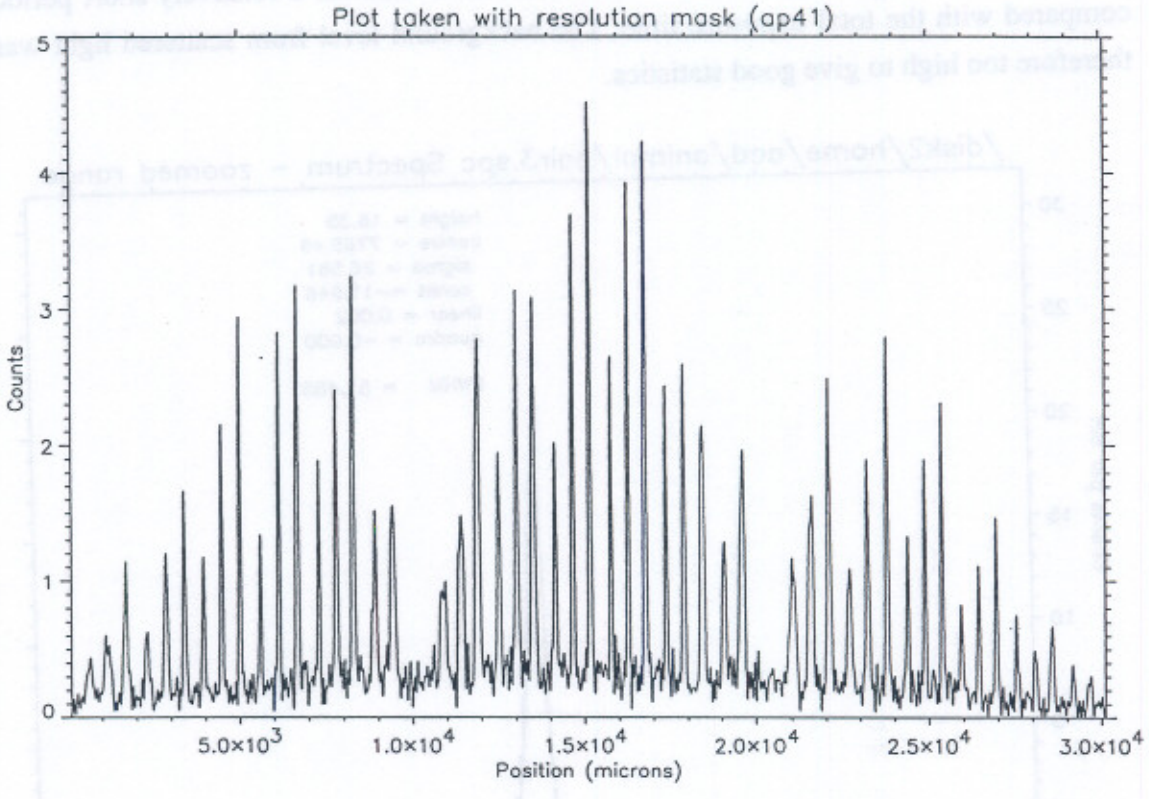

Figure 83. One-dimensional histogram of the position output using a mask illuminated with X-rays. The varying heights of the peaks in groups of three are caused by non-uniform vertical illumination of the mask. Each third peak corresponds to the same row of slits. Only three of the five groups of slits were sufficiently illuminated.

The resolution was also measured with the RM detector on the RC with the UV lamp. A mask with a series of square holes, of decreasing size and 1 mm apart, was clamped against the front face and illuminated by the brightest neon line from the UV lamp. Using a square hole rather than a slit reduced any problems with alignment

(calculated as an increase of 1.7% per degree rather than the 40% per degree in the case of the slit) but meant that the accumulation needed to last several hours for sufficient photons. Because of the low count rate through a small hole, it was difficult to identify when the beam was aligned with it. The detector was therefore scanned across the beam illuminating each hole in turn to calibrate the X-Y table co-ordinate relative to the beam. It was then moved so that the beam illuminated the 25 µm hole and left for several hours. The total count rate was $10\,c\,s^{-1}$, which was only just above the scattered light background count rate.

An attempt was made at a MTF measurement (see §6.4.2.1.), but using the spectral line and scanning technique illuminated each hole for a relatively short period compared with the total exposure time. The background level from scattered light was therefore too high to give good statistics.

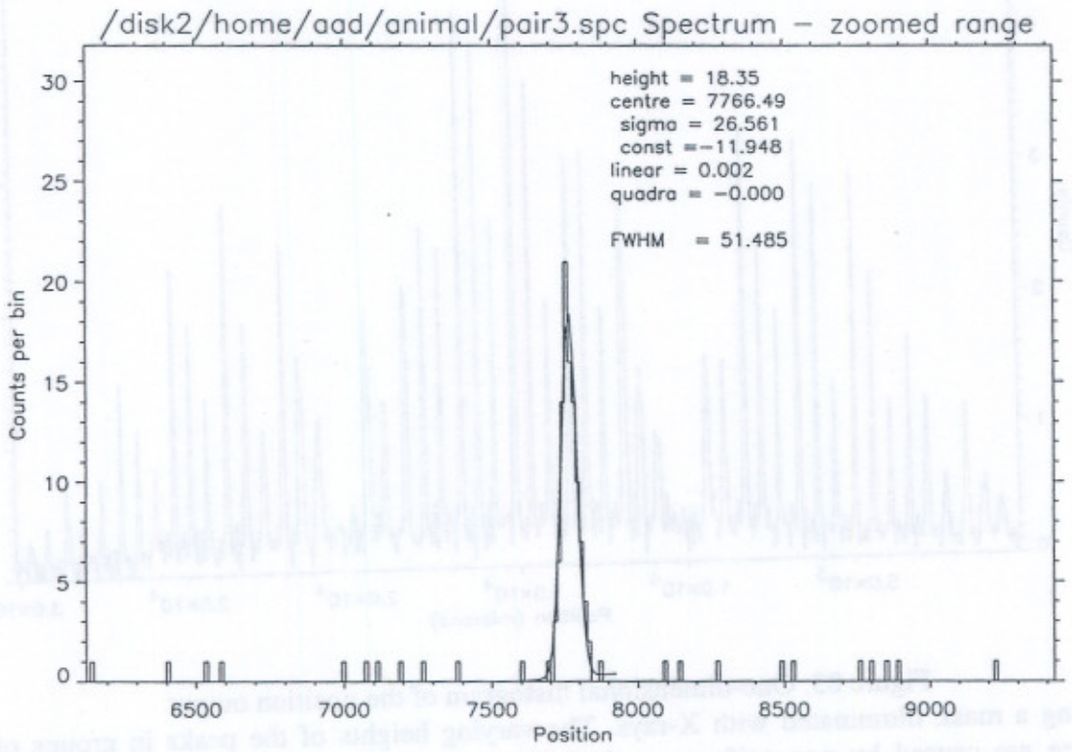

Figure 84. Image of 25 µm pinhole with RM detector and UV light.
The x-axis is measured in micrometers.

Figure 84 is the image obtained through the 25 µm pinhole. A Gaussian has been fitted with a width of 51 µm, which corresponds to a detector response of 47 µm after deconvolution. This resolution measurement corresponds closely to the previous result

obtained with the development model and X-rays. It is also close to the result of 50 µm obtained with the flight system and described in §6.4.2.

There are three explanations for the fact that it is higher than the optimum prediction of 28 µm. The main reason is due to the noise from the UV lamp, which was not included in the equation (76). Another is that the value of electronic noise effect calculated above assumes that every event contains 4×10^7 electrons. In fact, due to the width of the PHD, a substantial number of events are up to four times smaller than this, achieving a poorer signal to noise ratio. The third reason is that the value of D used in equation (76) is 12.5 µm, whereas the value should depend on the alignment of the hole with the pores, as described in §2.2.3.1.

CHAPTER 5.

SPIRAL ANODE THEORY AND GIS SIMULATOR

5.1. SPIRAL ANODE THEORY

The SPAN concept was developed by Lapington in the late 1980s (Lapington, Breeveld *et al.*, 1990) to meet the ever increasing demands of imaging detectors for space, at a time when space-approved, fast ADCs had a maximum resolution of 8-bits.

This Chapter describes my development of the theory of SPAN and my computer models of the detector system. It also discusses some of the features of the readout.

5.1.1. Description of SPAN

The anode consists of three co-planar, electrically isolated electrodes, *A*, *B* and *C*, spaced a few millimetres (3 mm for GIS) behind the MCPs. The pattern of electrodes has a repetitive structure covering the entire active area. The pattern is finely divided such that a single charge cloud is sufficiently large to spread to all the electrodes and to integrate out the fine structure. The electrons directly collected by the anode are divided between the electrodes according to the areas subtended by them at that point. Provided that the relative areas of *A*, *B* and *C* vary along the anode, the co-ordinates of the charge cloud, and therefore the initial photon, may be determined by measuring the relative magnitude of the charge collected on each electrode.

The whole anode is shown in Figure 108, which illustrates the variation in the electrode areas along the length of the anode. Because the detector is one-dimensional, the electrode areas need to vary in only one direction. In the figure, the horizontal or *x*-axis is the spectral axis. In the vertical direction, the triplet electrode structure is repeated identically.

The electrodes are continuous along the spectral axis, so that in analogue form the output position measurement is continuous. The measured position always corresponds to the centre of the charge cloud. The anode is therefore known as 'centroiding'.

In the flight GIS detectors, the 50 mm *x*-axis is divided up, conceptually and in software, into 2048 pixels, each of which is 24.4 µm wide and 22 mm high. The values for the relative areas can be calculated in advance for each pixel *x*-position, so that a look up table can be constructed, to decode *A*, *B* and *C* into positions.

5.1.2. Theory of readout

A diagram of one revolution of the pattern is shown in Figure 85. The area of an electrode within an infinitesimally small section of the x-axis (dx) is equal to the vertical height (h) of the electrode at that value of x multiplied by dx. Thus, since h varies slowly, looking at $h(x)$ reveals how the areas change.

For each electrode, the charge collecting area ($h(x)dx$), varies sinusoidally with the horizontal axis (x). The x-co-ordinate can therefore be determined in terms of degrees in the sine wave pattern. There are five complete sinusoidal revolutions in the GIS anode patterns. The form of each of the three electrodes is the same but with the sine wave offset from the other two by ±120°.

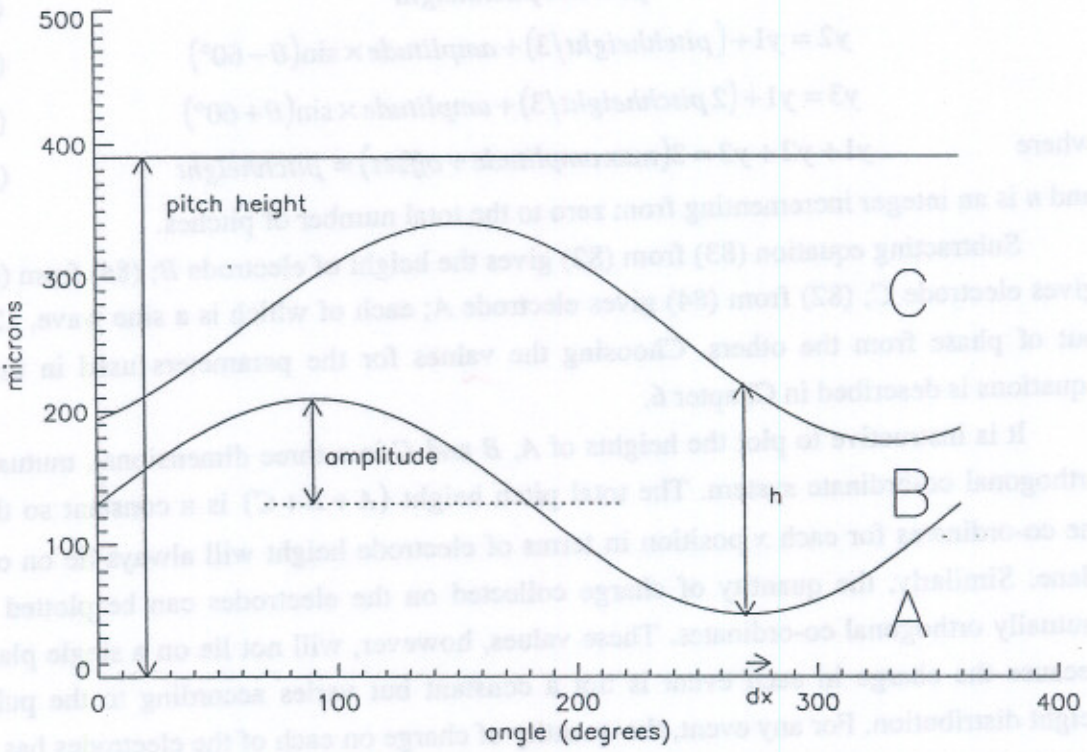

Figure 85. Diagram of the three electrodes making up SPAN.

If the electrodes varied simply with a sine wave of constant amplitude the pattern would be repeated with every revolution (360°). There would be no way of distinguishing between the revolutions. Each revolution is therefore made unique by changing the amplitude and wavelength of the sine wave continuously with position.

An alternative method of distinguishing between revolutions would be to make use of an additional electrode which itself varies in area along the length of the anode.

For example, for the vernier anode, (Lapington, Breeveld *et al.*, 1991) three additional electrodes are provided, similar in form to the first set but with wavelengths slightly different, so that for each revolution, the difference in phase measured by each set provides a measure of 'coarse' position. The mean phase is used to measure 'fine' position.

The equations governing the height (h) of each electrode for SPAN follow the form:

$$h = amplitude \times \sin(\theta + \phi) \tag{81}$$

where $\phi = 0°$, 120° or 240° for electrodes *A*, *B* and *C* respectively, with *amplitude* itself dependent on θ. In order to achieve this, the equations of the insulating lines defining the electrodes are:

$$y1 = n \times pitchheight \tag{82}$$

$$y2 = y1 + (pitchheight/3) + amplitude \times \sin(\theta - 60°) \tag{83}$$

$$y3 = y1 + (2\,pitchheight/3) + amplitude \times \sin(\theta + 60°) \tag{84}$$

where
$$y1 + y2 + y3 = 3(\max amplitude + offset) = pitchheight \tag{85}$$

and n is an integer incrementing from zero to the total number of pitches.

Subtracting equation (83) from (82) gives the height of electrode *B*; (84) from (83) gives electrode *C*; (82) from (84) gives electrode *A*; each of which is a sine wave, 120° out of phase from the others. Choosing the values for the parameters used in these equations is described in Chapter 6.

It is instructive to plot the heights of *A*, *B* and *C* in a three dimensional, mutually orthogonal co-ordinate system. The total pitch height $(A + B + C)$ is a constant so that the co-ordinates for each x position in terms of electrode height will always lie on one plane. Similarly, the quantity of charge collected on the electrodes can be plotted in mutually orthogonal co-ordinates. These values, however, will not lie on a single plane because the charge in each event is not a constant but varies according to the pulse height distribution. For any event, the quantity of charge on each of the electrodes has to be positive and the maximum ratio between one electrode and the other two is limited by the maximum ratio of the heights. In three dimensions, therefore, the events are constrained to lie within a cone with the origin at zero and the sides defined by the maximum ratio. Normalising the values by dividing by the *sum*, they are then constrained to lie on one plane such that:

$$A' + B' + C' = 1 \tag{86}$$

where
$$A' = \frac{A}{\Sigma} \quad B' = \frac{B}{\Sigma} \text{ and } C' = \frac{C}{\Sigma} \text{ given } \Sigma = A + B + C \tag{87}$$

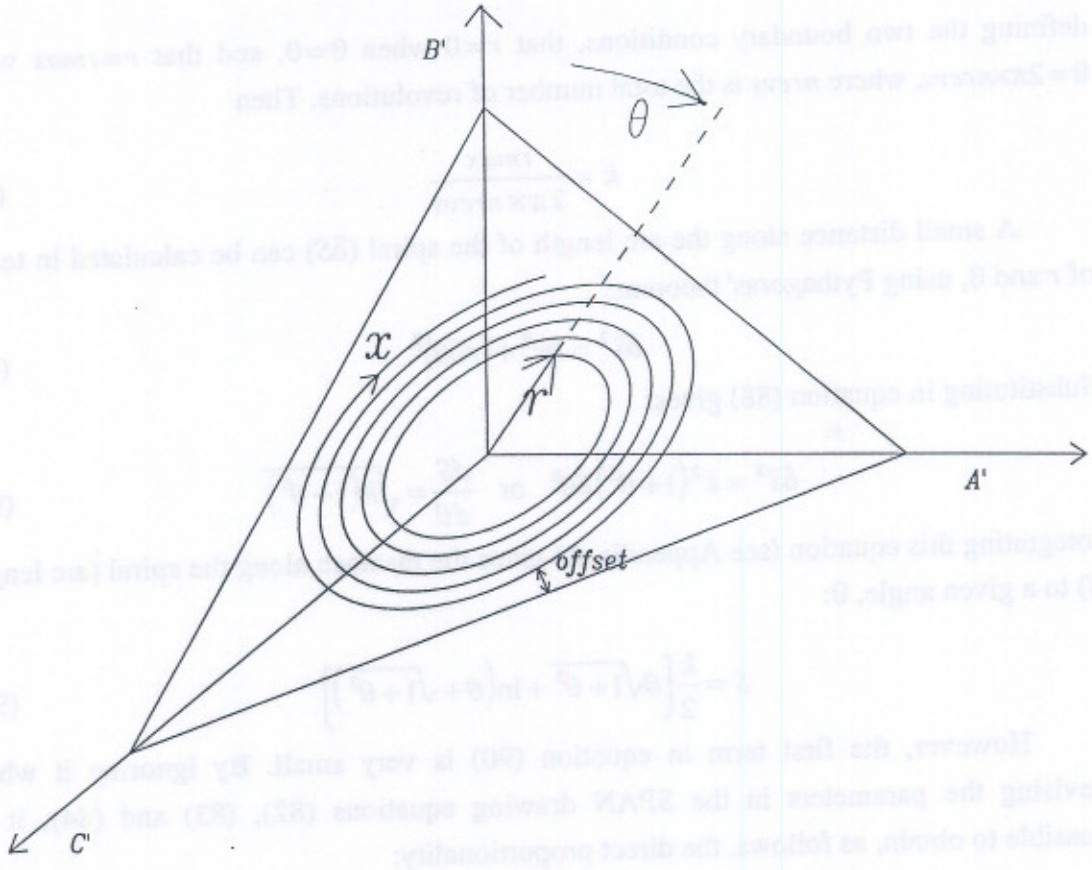

Figure 86. Event position, *x*, plotted in three dimensions.

Figure 86 shows the event positions in this plane. Moving from one end of the anode to the other, the event locus follows a spiral on the normalised plane with the radius (r) at any point defined by the *amplitude* of the electrodes at that point and the angle (θ) as used in equation (81). The distance between the maximum radius (*rmax)* and the triangle defining the limits of positive *A, B* and *C,* is set by the parameter *offset*. It can be seen from this plot, that for every x value, there will be a unique set of normalised values of A', B' and C'. The value of x is directly proportional to the distance (S) along the spiral from the start point.

In order to keep the distance between the spiral arms constant, an Archimedian spiral is used, with the radius proportional to the angle:

$$r = k\theta \tag{88}$$

where θ is defined as the total angle including whole numbers of revolutions, so that it can be thought of as $\theta + 2n\pi$, where n is the number of whole revolutions starting at $r = 0$. The constant k is known as the spiral expansion parameter. k can be calculated by

defining the two boundary conditions, that $r=0$ when $\theta=0$, and that $r=rmax$ when $\theta=2\pi\times nrevs$, where *nrevs* is the total number of revolutions. Then

$$k=\frac{rmax}{2\pi\times nrevs} \tag{89}$$

A small distance along the arc length of the spiral (δS) can be calculated in terms of r and θ, using Pythagoras' theorem:

$$\delta S^2=\delta r^2+(r\delta\theta)^2 \tag{90}$$

Substituting in equation (88) gives:

$$\delta S^2=k^2(1+\theta^2)\delta\theta^2 \quad \text{or} \quad \frac{dS}{d\theta}=\sqrt{k(1+\theta^2)} \tag{91}$$

Integrating this equation (see Appendix A) gives the distance along the spiral (arc length S) to a given angle, θ:

$$S=\frac{k}{2}\left[\theta\sqrt{1+\theta^2}+\ln\left(\theta+\sqrt{1+\theta^2}\right)\right] \tag{92}$$

However, the first term in equation (90) is very small. By ignoring it when devising the parameters in the SPAN drawing equations (82), (83) and (84), it is possible to obtain, as follows, the direct proportionality:

$$S\propto x\propto\theta^2 \tag{93}$$

In order to keep the resolution constant along the spectral axis, x, the condition has to be imposed that δx (a small element along the axis) is proportional to δS (an element of the arc length along the spiral). Assuming that δr is small so that the first term of equation (90) can be ignored:

$$\frac{dS}{dx}\approx\frac{rd\theta}{dx}=v \tag{94}$$

where v is a constant. Substituting in equation (88) and integrating with respect to x, leads to the equality:

$$\theta=\sqrt{\frac{2vx}{k}} \quad \text{or} \quad x=\frac{k\theta^2}{2v} \tag{95}$$

The constant v can be found by re-organising this equation. Using the boundary condition that $r=rmax$ at $x=xmax$ (the active length of the anode) and substituting in for k from equation (89) gives

$$v=\frac{rmax.2\pi.nrevs}{tmax} \tag{96}$$

Substituting this equation and equation (89) into equation (95) gives a simple relationship between x and θ:

$$\theta = 2\pi.nrevs\sqrt{\frac{x}{xmax}} \tag{97}$$

which, together with equation (88), defines the relationship between all the constants needed to plot y1, y2 and y3 against x (equations 82–84).

In order to save power and increase speed for flight it was decided to use ratiometric ADCs to digitise the signals from the electrodes using the *sum* signal (Σ) as the reference. Instead of obtaining A, B and C separately (as when using the laboratory electronics with the development model detector or RM detector), and then performing the normalisation by summing and dividing, we obtain straightaway the ratios A' and B' in equation (87). Each ratio is a number up to 256 (because the ADCs are 8–bit). This provides enough information to calculate the position x since it follows that

$$C' = 256 - (A' + B') \tag{98}$$

A' and B' are used to address the LUT which gives the appropriate value of x.

To plot the spiral in two dimensions as in Figure 93, mathematical functions have to be performed on A', B' and C' (see Appendix B). They are :

$$X = \frac{C' - B'}{\sqrt{2}} \quad \text{and} \quad Y = \frac{2A' - B' - C'}{\sqrt{6}} \tag{99}$$

The ratio A' can never exceed the ratio of the maximum height of A to the total height of the anode. This comes to 5/9 using the parameters chosen for GIS and by symmetry is the same for the other electrodes. Using 8–bit ratiometric ADCs, this would allow a maximum digitisation level of 142. In order to use the maximum range of the ADCs, the *sum* signal is multiplied by 5/9 in analogue, before the normalisation. This changes the constant given as 256 in equation (98) to 460 (see Figure 22).

Another helpful way of looking at the spiral image is by transforming X and Y in equation (99) into polar co-ordinates (equation 100) and then plotting radius against angle. In this form the spiral becomes a series of straight lines known as spiral arms, one for each revolution, with a gradient of k. Figure 87 is one such.

$$r = \sqrt{X^2 + Y^2}$$
$$\theta = \tan^{-1}\left(\frac{Y}{X}\right) = \tan^{-1}\left\{\frac{2 - 3(A' + B')}{\sqrt{3}(A' - B')}\right\} \tag{100}$$

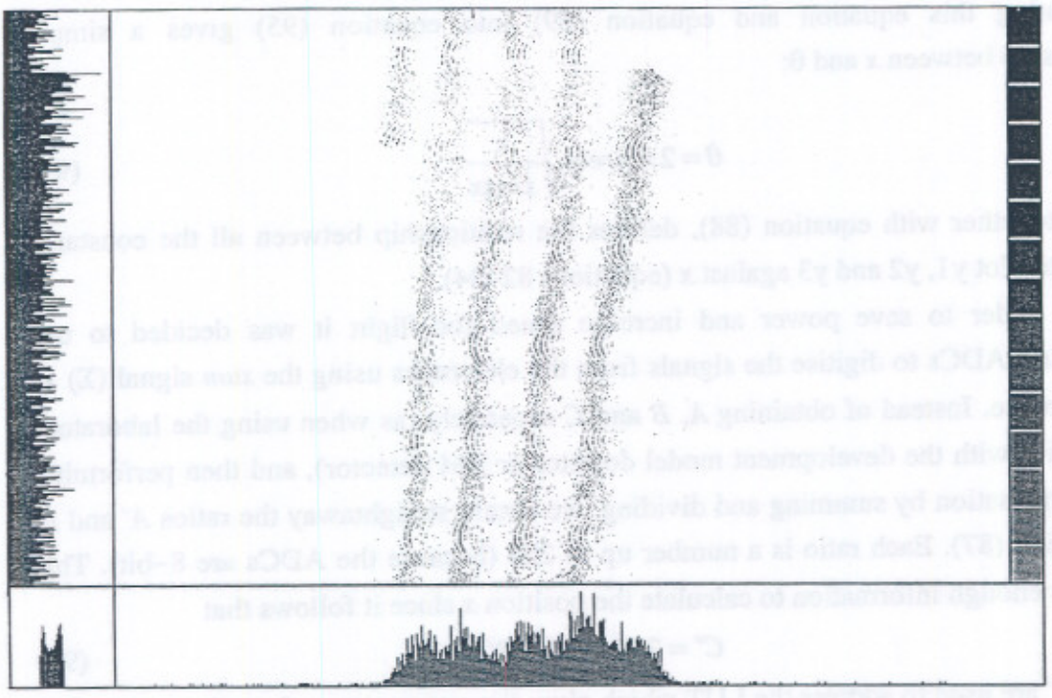

Figure 87. Plot in polar co-ordinates showing the spiral arms and their width. Data from the QM detector taken with the filament as a source and the detector front face negatively biased. The x-axis is the radius; the y-axis is the angle (0–2π).

5.1.2.1. Writing the look up table

Before starting to write the LUT, the spiral has to be well defined. For the GIS anodes, the spiral is clockwise, *i.e.* r increases as one goes from large A to large B to large C. The equations (99) which perform the transform on the normalised values of A' and B' must be consistent with this fact. An interchange of any two of A, B or C, or a change of sign in the first equation, leads to an anticlockwise spiral.

For every x position, there is a calculable ratio between A', B' and C'. However, given noise on the values, and certain charge cloud effects discussed later, there will be more than one ratio in terms of ADC values for each x. In other words, the resultant event spiral has width (see Figure 87).

The LUT is built by selecting each possible combination of ADC values in turn and using the chosen LUT parameters to calculate the value of x, if there is one, that could produce that combination. The allowed width of the arms has to be selected. Any ADC combinations lying in the space between the arms is rejected. Assignment to an incorrect arm leads to an error in position producing spurious images or 'ghosts'.

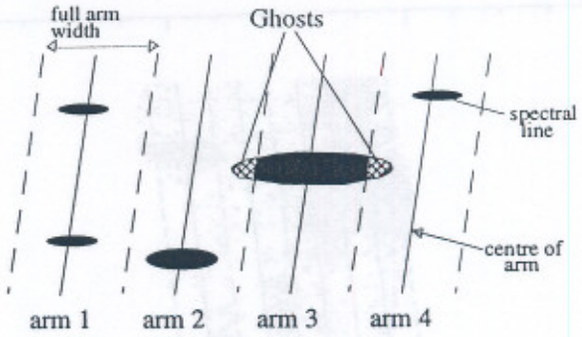

Figure 88. Demonstrating the cause of ghosting from one spiral arm to another. The co-ordinate system is the same as that in Figure 87. The centres of the arms are drawn as solid lines. Here, a spectral line which should be on arm 3 is spreading to give ghosts on arms 2 and 4.

As will be described in Chapter 6, the radius of the spiral arms reduces as the charge cloud spreads out. The charge cloud always has a finite size and therefore the radius is always less than *rmax*. For example, as the voltage across the MCPs is decreased from 4.0 to 3.6 kV, with a corresponding decrease in gain from 6.4×10^7 to 8×10^6, the radius of the tenth arm increases by a factor of 1.05 and of the fifth arm by 1.08. This shifts the tenth arm half way towards the eleventh arm of the LUT and the fifth arm is shifted even further. This order of radial change is significant, especially since the arms have a width of typically more than 50% of the distance between them.

To make sure, therefore, that any charge cloud or electronics effects are taken into account the LUT is not built using theoretical spiral parameters. It is necessary to fit a spiral to the real events to find out a value for *e.g.* the constant k which is used in equation (88). For the LUT to map the events to the pixels correctly, it has to be calculated such that it closely fits the output of each detector. Thus four separate LUTs are required.

For each detector, real events covering the whole range of the anode are captured and the data from the ADCs plotted. This data is referred to as 'raw' because it has not passed through any LUT. Data which does come through the LUT is referred to as 'science' data. The house-keeping processor can be commanded to transmit raw data from a particular detector so that A' and B' and PHD data is received. The transform equations (99) are performed on the ground to allow the data to be plotted in terms of a spiral, in polar co-ordinates. A spiral is then fitted to this data in the form of parallel straight lines (see Figure 89).

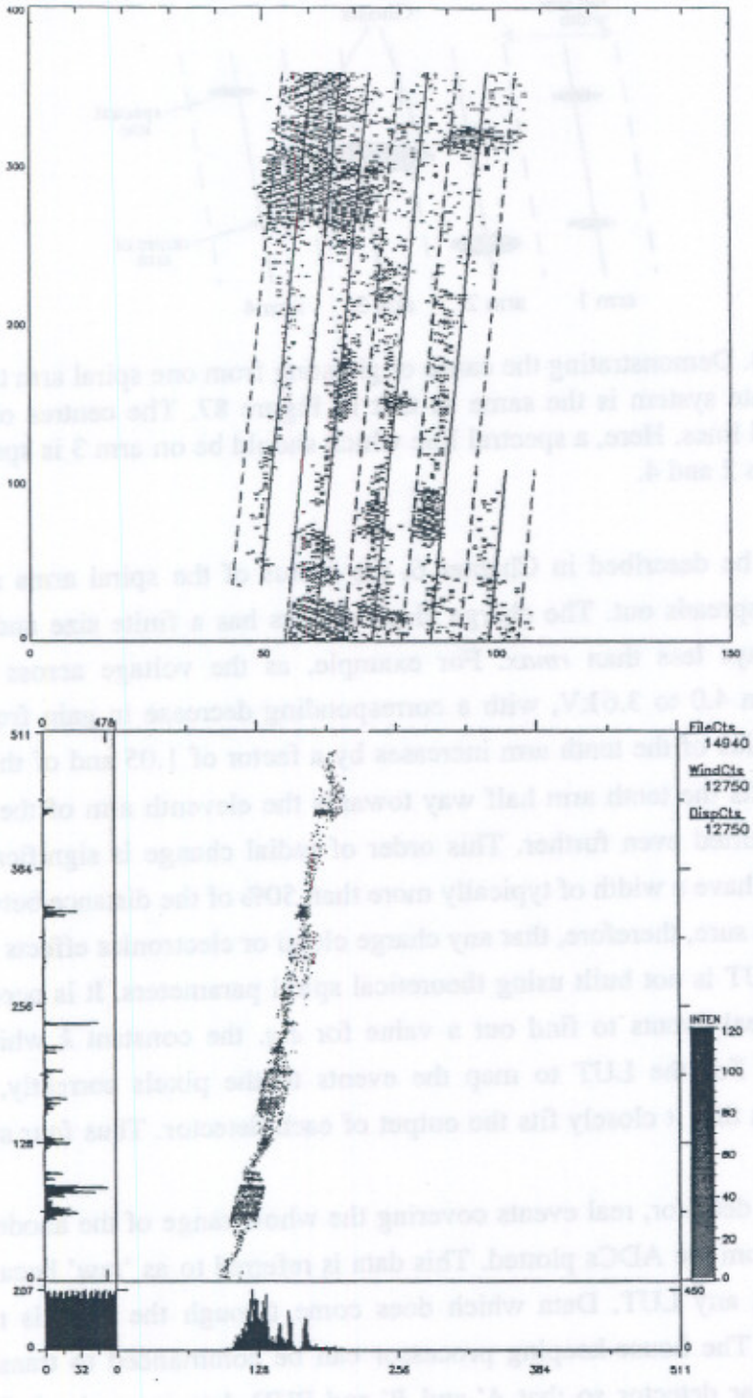

(a)

(b)

Figure 89. Showing a raw data file fitted to LUT parameters.
(a) In the polar plot, the dashed lines indicate the allowed width of the spiral arms; the solid lines follow the centres of the arms. (b) All the arms joined together according to the LUT parameters selected using (a). The histogram up the left hand side is the spectrum.

Equation (88) is modified to allow for the shrinkage of the spiral to the form:

$$r = k(\theta + \phi) \tag{101}$$

where ϕ allows for the spiral to begin at another angle than 0°. This is equivalent to allowing an offset from zero where the fitted spiral crosses the y-axis in the spiral polar plot. Fitting to equation (101) allows k and ϕ to be chosen. Note that the fitted k is not necessarily the same as the theoretical k used to draw the anode.

Figure 89 shows the fitting of a LUT to a normal raw file. In the case of bright lines, the events will tend to spread across to the neighbouring arm (usually towards smaller radius). Ghosts of the line will then appear in the wrong part of the spectrum. Because of the type of distortion, the ghosts will always appear in well defined positions (see Figure 88). The ghost intensity can be added to the true line intensity.

Other parameters which have to be selected before the LUT can be written include the angle defining the start and end of the anode (known as *start* and *stop*) and the width of spiral arm allowed for valid events (given as a *percentage* of the distance between the arms).

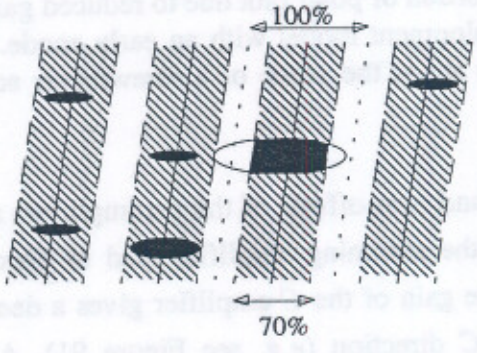

Figure 90. Use of 'percent' to minimise ghosts.

If the *percent* parameter in the LUT is set to 100%, then the maximum number of events will be captured in the science data. There will undoubtedly be some ghosts, because of small distortions in the data. By adding the intensities from all the ghosts back onto the true lines the true intensity can be obtained. However, problems may occur when the ghost of one line appears at the true location of another line. In this case, it may be better to reduce the *percent* parameter to cut out the possibility of ghosting (see Figure 90). The disadvantage of reducing percent is that the intensity in the spectral lines are no longer given by the number of events in the received spectrum, and that the percentage lost will vary along the spectrum.

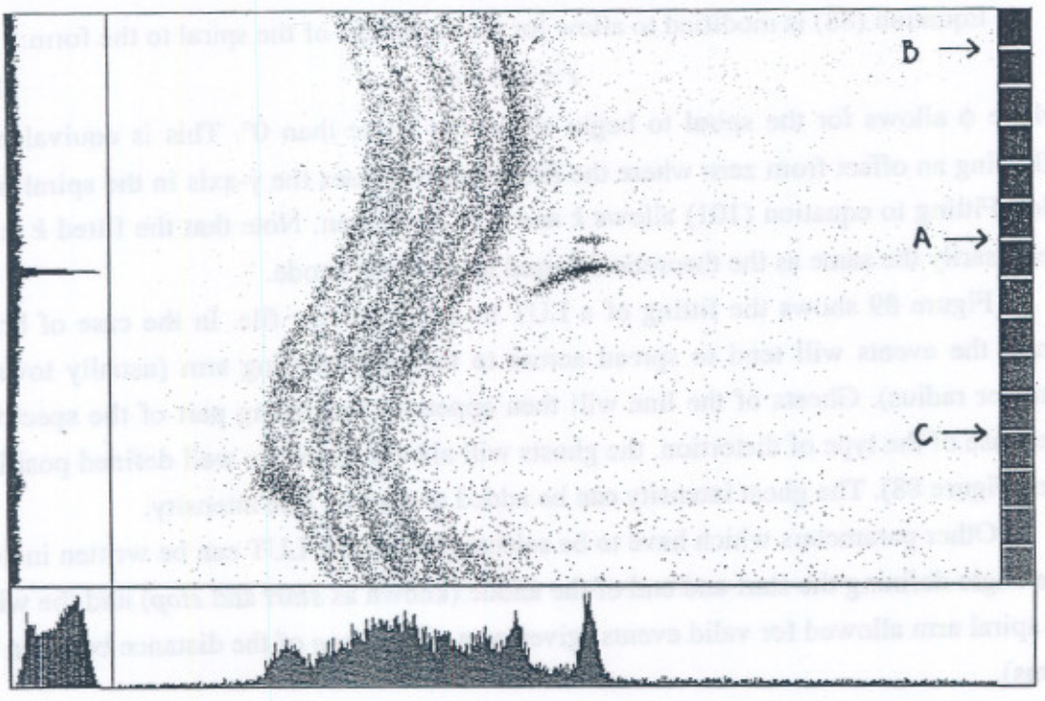

Figure 91. Distortion of polar plot due to reduced gain on channel *C*.
Data taken with the development model with an early anode. The two bright points in the middle of the picture are at the scene of a screwdriver accident on the MCP front face.

Drifts in the gains and zero offsets of the preamplifiers and shaping amplifiers of the electrode signals or the summing amplifier lead to distortions in the spiral. For example, a decrease in the gain of the *C* amplifier gives a decrease in the radius of the spiral in the maximum *C* direction (*e.g.* see Figure 91). An error in the summing amplifier, also affects *C* because *C* is derived directly from the *sum*, but it can also be thought of as determining the normalising plane which is being used. Multiplying factors can be put into the equations (99) to correct for the distortions and produce straight lines in the polar plot. These equations are used when calculating the LUT and therefore the multiplying factors can be taken into account in the calculation, to create a LUT which compensates for the distortions. In the event of a gradual change in the MCP output PHD, or drifts in electronics gains due to temperature changes or ageing, the LUT becomes progressively less optimum, leading to a degradation in accuracy of intensity measurements and an increase in ghosting. The LUT fitting therefore has to be checked on a regular basis. Distortions in the image which cannot be removed by adjusting the gain and offset parameters will lead to further ghosts.

To sum up, the parameters which have to be selected for writing the LUT are given in Table 13.

1	%	Width of arms in terms of percentage of the distance between arms.
2	stop	As for start (no. 3), but giving the angle of pixel 2048.
3	start	The start of the actual events imaged in terms of spiral arms, giving the angle of pixel one.
4	k	Defined in equation (101).
5	zpln	Constant in equation (98) which can correct for an offset error in *Sum* (default value 460).
6	phi	Defined in equation (101).
7	nobits	Constant specifying the range in powers of 2 for A' and B' in equation (99) for the LUT generation. It is set to 8 for GIS, but a lower number can be used for testing.
8	detno	There is a different LUT for each detector.
9	xgain	The factor to correct for the gain in the A' channel.
10	ygain	As for xgain but for B'.
11	zgain	The factor to correct for the gain of C' after calculating it using equation (98).

Table 13. The LUT parameter list.

An option in the *ALLSINGN* program allows the user to chose k and φ and see a spiral plotted over the top of the raw data plot. Edgar (1993) devised two methods of automatic fitting. One uses edge detection routines and robust line fits. Edgar evaluated several edge detection algorithms for this purpose. The other, implemented from an image analysis technique by Hough, is as follows.

Any straight line in Cartesian co-ordinates can be fully described by the normal distance, ρ, of the line from the origin and the angle of the normal, θ, with the equation $\rho = x\cos\theta + y\sin\theta$. If the line is plotted in (ρ, θ) co-ordinates, known as Hough space, it therefore becomes a point. However, for a single point (x,y) in Cartesian space, there are an infinite number of values of ρ and θ which would fit the equation. If these values are plotted in Hough space they form a sinusoidal curve. Any point in the curve represents a straight line passing through the (x,y) point. If there are two points in the Cartesian space, they may each be represented by a different curve. However, they will have one possible straight line in common—the line joining the two points. The Hough space

curves will therefore cross at the point at which ρ and θ define that line. Three co-linear points in Cartesian space will all have curves crossing at one place in Hough space.

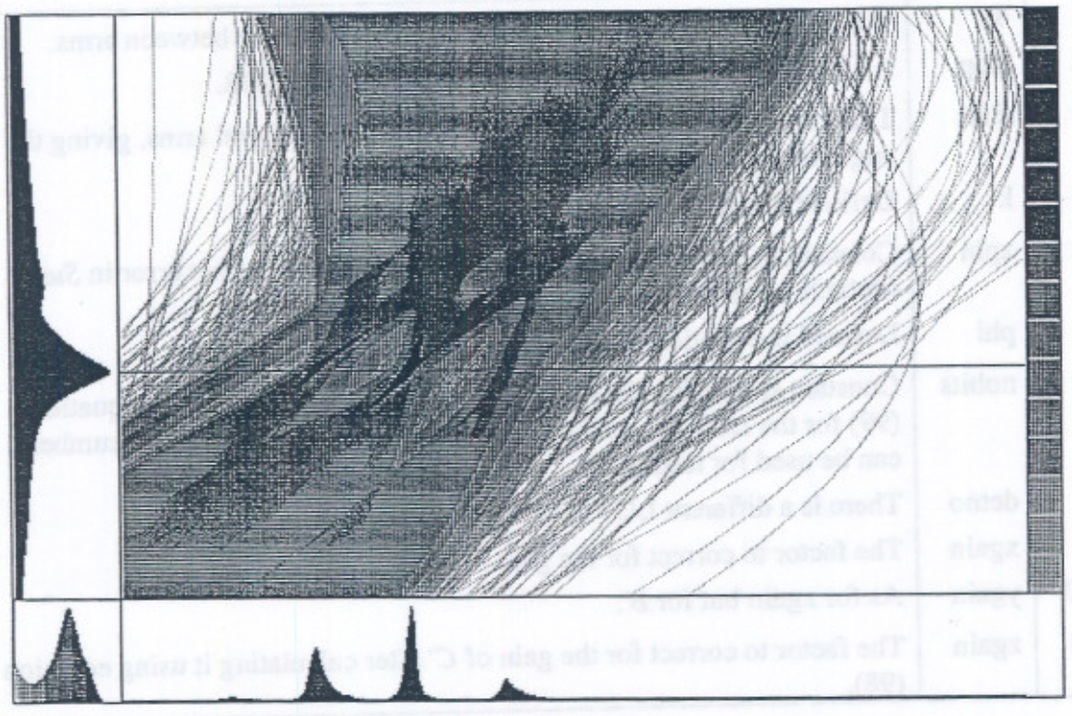

Figure 92. Hough transform of spiral arms.
The side histogram shows the variation of maximum intensity with θ. The histogram along the bottom window is the histogram of ρ along the line indicated.

The importance of this for the spiral fitting is that, ideally, all the events in one arm lie in a straight line in polar co-ordinates (Figure 87). Plotting each of the events in *n* spiral arms as a curve in Hough space leads to a mass of curves with *n* convergent points representing the straight lines along each of the spiral arms (see Figure 92). The arms of the spiral all follow the same gradient (determined by *k*) and therefore the convergent points all have the same value of θ. The convergent point on the θ-axis is found by determining the maximum intensity distribution for every value of theta. The value of θ that returns the largest maximum intensity is the value that represents the best fit. By histogramming the ρ-axis along this value of θ, the straight line fits are fully determined by the maxima and the widths of the peaks represent the widths of the arms. Figure 92 shows some data being analysed in this way. The three convergent points can be seen clearly in the histograms.

Many problems occur with the automatic fitting schemes. The first one (edge detection) cannot cope easily with any discontinuities in the lines of real data. It detects

edges within a spiral arm and fragments the arms. With the Hough scheme, there are problems in matching scale factors and getting the correct answer from it. In the end, it appears that nothing matches the human eye for ability to fit the best spiral with consistency. The user can decide how many of the data are noise or which points are the most important to fit if there are conflicts with distortions.

Similarly, choosing the gain and *sum* correction factors is performed by eye to achieve the straightest lines in the spiral polar plot. The Hough fit can be useful in assessing the straightness.

A suite of programs (see Table 14) has been written to help perform the LUT-fitting task in machine-independent IDL so that it can be done on the EGSE workstations, on a PC or on the MSSL VAX computer.

Program	Purpose	Author
ALLSINGN	PC program for capturing and displaying raw data.	Edgar, (Breeveld)
READ_RAW_GIS	Takes EGSE files and divides raw and PHD data	Alam
PLOTPHA	Plots PHD data.	Breeveld
VRAWNALL	Plots Raw data and fits LUT parameters	Breeveld
MYLUT	Calculates a LUT	Breeveld
USELUT	Makes spectrum from raw data via LUT written by *MYLUT*	Breeveld
GHOST	Calculates pixel numbers of possible ghost lines given the spectral line position	Breeveld
ARM_LINE	Calculates the position of a spectral line from position in terms of spiral arms	Breeveld
CURS_INT	Integrates area in spectral line selected by cursor	Breeveld
SPANIMAL	Raw data display and analysis program	Walton, (Breeveld)

Table 14. Raw data analysis programs.
All the programs are in IDL and can be run on a PC or work station, apart from *ALLSINGN*, which is in 'C'.

5.1.2.2. Spiral fitting programs

Raw data can be obtained from laboratory or flight style systems. It can be obtained directly in the laboratory by using the PC and *ALLSINGN*, which accumulates raw data files as the default. With the simulated flight system, the EGSE simulator can be requested to dump raw or pulse height analysis (PHA) data to separate files on diskette. With the full CDS instrument, the GIS, CDHS and EGSE can be put into raw data mode

to collect raw and PHD data. An IDL program by Alam, called *READ_RAW_GIS* takes the EGSE files and divides the data into raw and PHA data files.

VRAWNALL allows the user to view the raw data from any of these sources in all possible configurations: plotting the ADC values directly as B' against A'; plotting them as a spiral after using equation (99); plotting this same data in polar co-ordinates—angle against radius; plotting in polar co-ordinates but using a y-axis of 4π rather than 2π. Plots can be made with every event plotted or using contours or colour keys for intensity. From the polar plot, choices for the LUT parameters can be made and the effects illustrated. The percentage of events rejected or accepted in a given LUT scheme can help to choose a best fit. This facility can be used for finding the percentage rejected by the LUT for individual lines too, allowing a correction factor to be applied to the final spectrum if necessary. Finally, a list of the parameters is given in formats suitable for use with either the flight instrument (in decimal) or the test models (in hex).

These parameters can be loaded into a program called *MYLUT* which calculates a LUT in exactly the same manner as the on-board code in the GIS processor box. *USELUT* picks up the raw data file and plots the raw data as a spectrum using the LUT just generated. In this way the parameters used in the LUT building on board can be checked out thoroughly.

A number of ancillary programs were written for analysing the spectra. A program called *CURS_INT* is used to integrate the area in a line between two cursor positions. By this means, intensities can be obtained either from raw data via *USELUT* or science data. *GHOST* calculates the possible positions of ghost lines given a spectral line pixel position. *ARM_LINE* predicts the position of a spectral line in the spectrum given the position in terms of spiral arm numbers or vice versa. This is useful for identifying spectral lines in the spiral plot so that the percentage of a given line included in the arm width may be calculated with *VRAWNALL*. *PLOTPHA* simply plots the PHA data, first as they come and then as a histogram.

SPANIMAL (SPAN IMage AnLyser) is an IDL program (adapted from *ANIMAL* by Walton, MSSL), which performs a similar function to *ALLSINGN*, but in a faster and more sophisticated way, in displaying raw data with zoom, histogram and a variety of plotting functions. *SPANIMAL* can produce a floating point spectrum from the raw data using the LUT parameters obtained from *VRAWNALL*, avoiding the need to bin into 2048 pixels. It will form an important part of the raw data analysis for GIS.

5.1.3. Resolution of SPAN

As mentioned in §4.8., there are several factors affecting the detector resolution beyond the anode design with its associated partition noise. The accuracy of the digitisation

electronics, the binning and the MCP channel size turn out to be the limiting factors. The digitisation factor in (d in equation 76) is calculated below for 8-bits, giving $\Delta x_d = 10\,\mu m$. The software binning of the data into 2048 bins gives Δx_b equal to $25\,\mu m$. Other values are the same as those in §4.8., *i.e.*, Δx_p was found to be less than $8\,\mu m$ and Δx_e $24\,\mu m$. Inserting all these into equation (76) gives a result of just under $39\,\mu m$. This then is the estimated ultimate resolution achievable with the GIS SPAN anode.

5.1.3.1. Digitisation

The plot in Figure 86 illustrates how x is related to the angle of the event in the spiral plot. The values returned by the ADCs, A, B and C, represent the vertices of a cubic lattice in this plot. After normalisation, this lattice is sectioned by the plane so that the grid elements on the two-dimensional plane become rhomboidal in shape, with the vertices hexagonally packed, as shown in Figure 93. The rhomboids represent each discrete combination of ADC values allowable. (The rhomboid shape arises from the fact that only two ADCs are being used; with three, triangles result). The length of the sides of the triangle representing the limits of the usable plane is equal to $\sqrt{2\times460^2} = 651$, in terms of ADC values. In other words, this picture illustrates the pattern of the ADC digitisation elements, or bins, available to be used by the anode. If the spiral is superimposed on top of this pattern, the number of ADC bins cut through by the arms can be counted.

A program was written by Lapington to work out the maximum number of grid elements covered by a given spiral. The number of grid elements crossed by the theoretical GIS spiral (derived from the anode drawing parameters rather than a set of real events) is about 5000. This spiral is mapped to 50 mm, giving a digitisation limit of $10\,\mu m$. Thus, SPAN may obtain a higher resolution than the charge measurement accuracy: although there are only 256 bins in each of the two ADCs, the number of resolution elements can be much higher, depending on the spiral parameters. In general, the aim is to obtain as long a spiral as possible, *i.e.* with many arms and a large radius. However, it can easily be seen from the figure that the resolution will vary along the anode because the spiral sometimes crosses right through the long axis of a rhomboid and at another place touches just one corner.

There are physical restrictions on the length of the spiral. The centroiding nature of the anode allows a certain flexibility in charge cloud size—but if the charge cloud is large, small-scale structure in the anode pattern is integrated out, leading to a reduction in the spiral radius, so that fewer ADC values are crossed. Ideally there should be a negligible change in electrode height in the distance dx (see the discussion at the start of §5.1.2.) where dx is determined by the charge cloud spread. The wavelength of the

electrode sinusoid therefore needs to be long compared with the charge cloud. Thus, the innermost arms of the theoretical spiral are not useful.

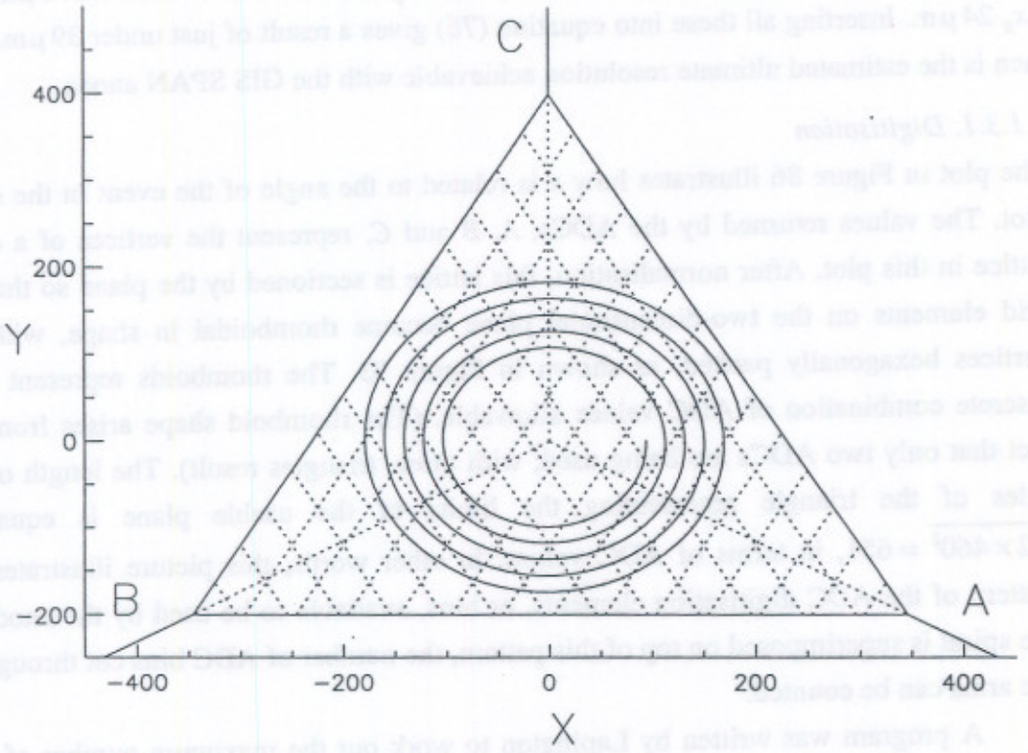

Figure 93. Illustrating the ADC grid in the spiral plane.

No other shape than a spiral could sample the ADC resolution elements as efficiently (Lapington, Breeveld *et al.*, 1992). A circle crosses only a fraction of the available bins. Any other shape must have a higher degree of curvature, corners or discrete elements (such as the strips in the WSA).

5.1.4. Fixed patterning

Fixed patterning has been observed in a number of systems and can be described as the problem of repeated digitisation. In moving from an analogue signal to one digitised to 8-bits by the ADCs, there is inevitably loss of information. However, the more serious problem arises when the two digitised values are put through the LUT. It has already been shown that the digital resolution varies with distance along the spiral in a pseudo-random manner (see Figure 93).

The position of an event is determined by the distance along the spiral, which is related to the angle subtended from the centre. The result is in practice given by the angle of the digital grid element within which the analogue event lies. If the spiral arm

of width (Δr) is divided into 2048 segments (pixels) of equal arc length (ΔS), it can be seen that in some segments there will be only one grid element whilst in others there will be several. This variation manifests itself as variation in the effective sensitivity from one pixel to another and will give non-linearity in the output (see Figure 94).

The magnitude of the fixed patterning has a clearly defined periodicity, becoming most prominent when a line perpendicular to the spiral arms lies along one of the axes of the lattice *i.e.* at 30°, 150° and the opposites, 210° and 330°. At these angles there is a high risk of hitting no digital elements at all, or with just a small shift of angle, a high number of elements. There is also a prominence at 90° and 270° where the perpendicular line cuts through the shorter width of the rhomboid. This is illustrated in Figure 102.

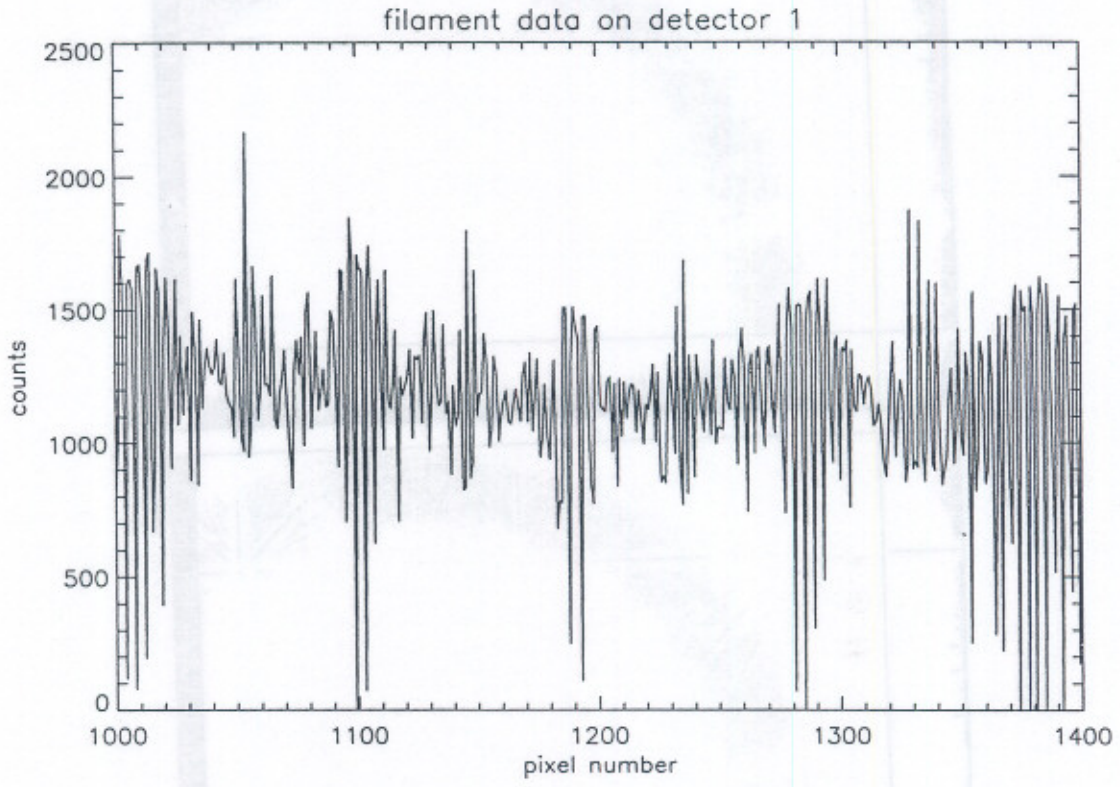

Figure 94. Short length of image clearly showing fixed patterning.
This is part of a flat field image taken with detector 1 in the instrument calibration.

Smoothing the image, by means, for instance, of a simple box car average, reduces the magnitude of the deviations from the mean. Summing together the pixels to make just 1024 or fewer also reduces the fixed patterning by increasing the length of the segment covered by each pixel. This reduces the likelihood of obtaining zero digital

values or particularly high numbers. Extending this argument, the spiral itself ought to be as long as possible. This is in agreement with the discussion of §5.1.3.1. on resolution. The number of arms and their radii need to be as large as possible without having the arms so close together that ghosting occurs.

There are several controllable parameters that will affect the amount of fixed patterning observed. The more ADC values covered by the data, the less the fixed patterning effect. Parameters such as the number of spiral arms, the starting angle and the maximum and minimum radii can be optimised and are fixed when the anode is designed.

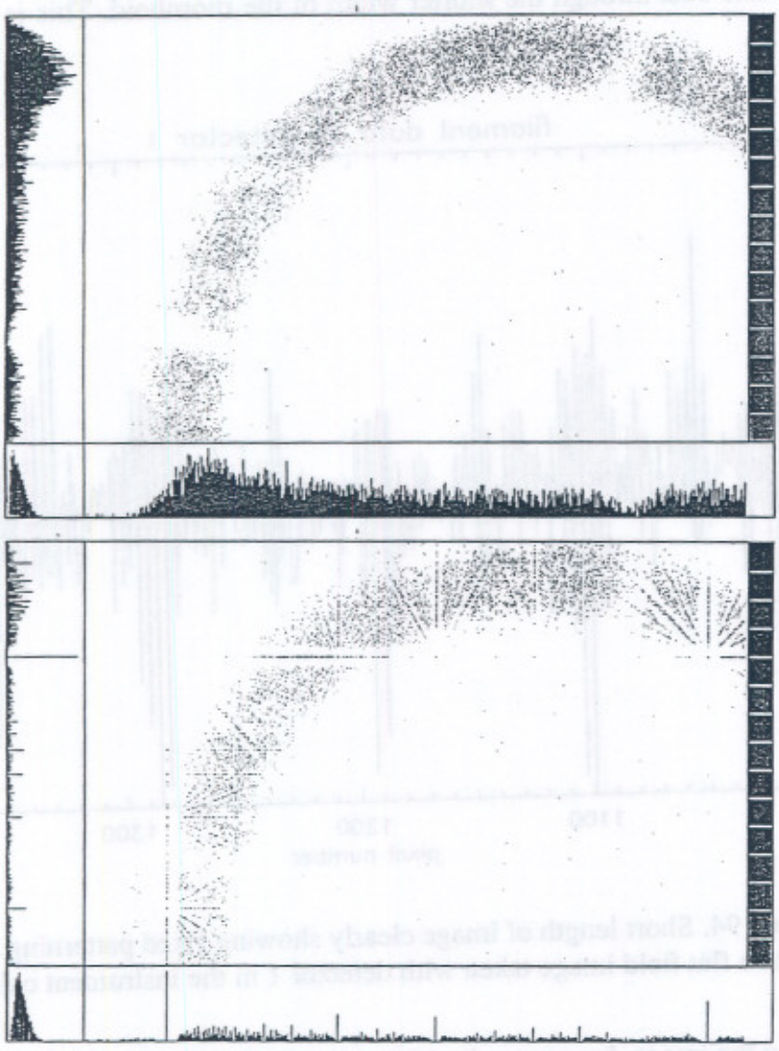

Figure 95. More bits leading to less fixed patterning.
Above 14-bits; below 8-bits. These are two-dimensional SPAN images taken by Edgar (1993).

The width of the spiral arms has a large effect on the fixed patterning as it affects the number of grid elements contained in a single segment. The spiral always has width, due to electronic noise and charge cloud effects and, from the point of view of fixed patterning, this is a distinct advantage. Because the radius of the spiral is approximately inversely proportional to charge cloud spread (see equation 107) and hence pulse height, the cross section of a spiral arm tends to follow more or less the shape of the PHD. Thus, it is important to have a wide PHD, without tight windowing by the discriminators and without tight restriction on the spiral arm width by the LUT. Unfortunately, these requirements are in opposition to those best suited to intensity measurements, where a tight PHD is needed. Of course, fixed patterning itself is disadvantageous in intensity measurements where the true position and extent of a spectral line may be masked.

It is important to digitise to a high level. The angle subtended by each grid element is then at a minimum. Figure 95 shows part of an image taken with a 2 dimensional SPAN detector. This does not use ratiometric ADCs but digitises each electrode independently. The ring mask has a 1 mm radius and the pixel size is 4 μm due to the computer screen. The top image is taken with 14-bit digitisation; the lower with 8-bits. Due to the low gain, as shown in the PHD in the bottom left hand corner of each picture, effective digitisation is nearer 12-bits and 6-bits. Re-binning the 8-bit data into larger bins improves the situation, but it would be necessary to have only 8 bins (*i.e.* 3-bits) to reduce the fixed patterning error to less than 1% (Edgar, 1993).

For this two-dimensional case, the size of the grid elements is the same in all planes because it is defined by the size of the ADC digitisation bins. However, the size of the triangle limiting the allowable extent of the plane varies with pulse height. Thus, making the plane as far as possible from the origin, by increasing the pulse height, raises the number of lattice points per unit angle, thereby reducing fixed patterning and increasing resolution. In using ratiometric ADCs, all the data is projected onto one pulse height plane, ensuring that the number of lattice points is constant and independent of pulse height. This advantage means that 10-bits rather than 12 as in Figure 95 is enough to reduce fixed patterning to an acceptable level (see Figure 96).

If the fixed patterning were perfectly constant, the spectra could be divided by a flat field pattern to remove the effects. If the data evenly fills wide arms it smoothes out the fixed patterning and, since it is repeatable, it is removable. However, the PHD obtained while a filament flat field is created for the denominator is not necessarily exactly equal to the PHD produced by UV light, particularly where there are regions of

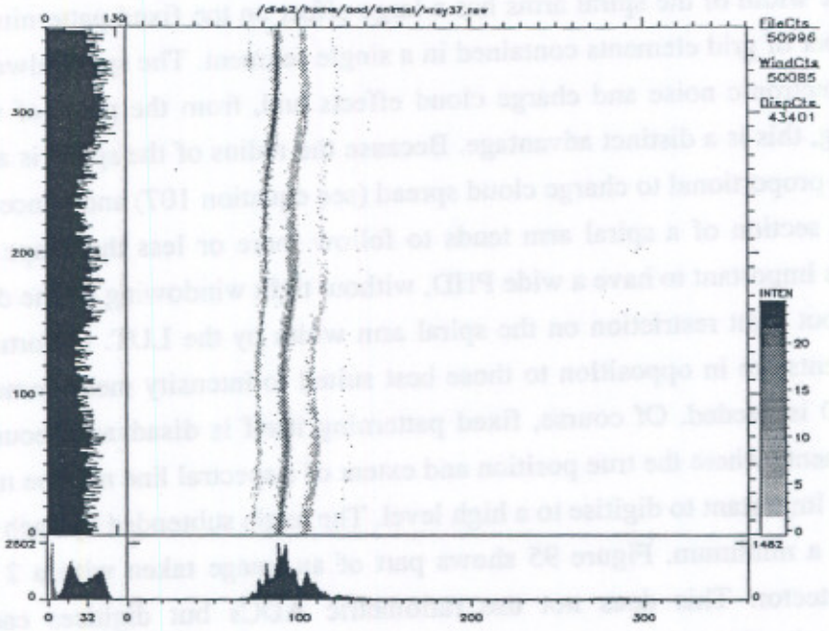

(a)

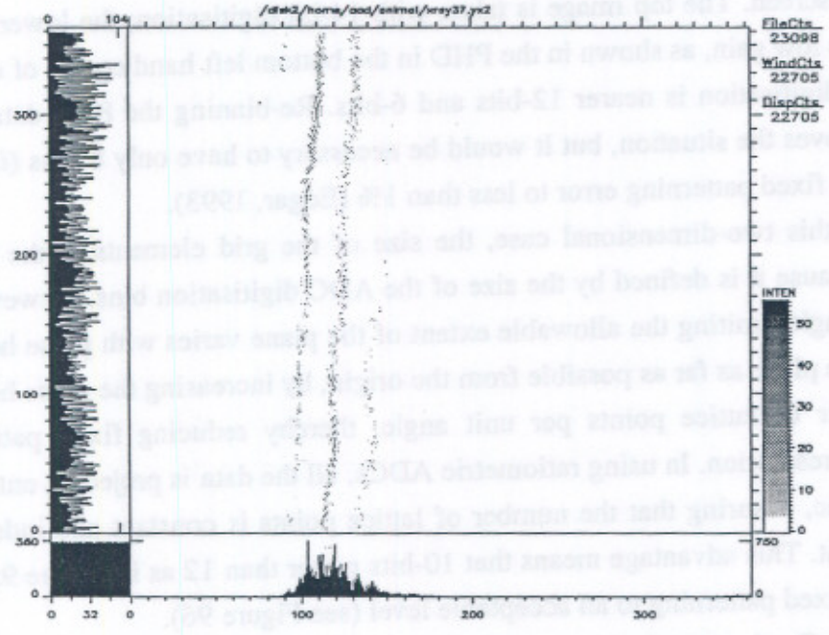

(b)

Figure 96. The same data in 10-bits and 8-bits taken with the development model detector with an X-ray source. (a) is the original 10-bit data. (b) has been converted to flight-style 8-bit data. The fixed patterning is noticeable in (b) as 'finger prints' in the data, and a more jagged histogram on the left hand side.

high count rate and hence gain depression. Therefore, the ADC values covered by a flat field created with a filament stimulus may not be the same as those covered by spectral data.

A number of other methods for reducing the effect of fixed patterning has been investigated, as described in the following paragraphs.

Although the fundamental ADC binning cannot be altered, the binning by the LUT into 2048 pixels can be changed. If a large raw data file is collected, it may be converted into a spectrum with infinitely small bins, *i.e.* a floating point spectrum. This returns the maximum position information from the data. Alternatively, a LUT can be created such that all 2048 pixels cover only a small part of the spectrum, in which case the pixels over-sample the ADC bins and contribute less to the fixed patterning.

Another way of reducing the effect is to use slightly different LUTs (for instance changing the *percent* or *start* and *stop* parameters) for the same data—dividing the ADC digitisation elements into pixels with different boundaries. Spectra produced with different LUTs may be summed together.

Other methods involve changing the distribution of events relative to the ADC bins. For instance, repeating an observation with more than one slit should show up the anomalous peaks and dips. Altering the HV changes the PHD and hence the distribution of events in the spiral plane.

5.2. MODELLING THE DETECTOR SYSTEM

It is of crucial importance to understand the detector performance over a wide range of operating conditions. Two computer models have therefore been written to predict the effects of PHDs, electronic noise and digitisation *etc.* The model described in this section looks at the detector and electronics as a whole system. Another model, described in §6.1.3., deals with the interaction between the charge cloud emanating from the MCP and the anode surface.

To predict performance characteristics, as well as to determine various requirement specifications for supporting sub-units, a PC-based GIS detector simulator (known as *GIS_SIM*) was developed. The simulator, written in the C computing language, is based on a Monte Carlo approach and, as far as possible, incorporates actual measurements. Both the anode parameters used in the detector and a measured PHD are loaded into the program. Values for electronic noise, partition noise, crosstalk and ADC non-linearities can be introduced to see how much they affect the image. ADC differential non-linearity figures are chosen covering the range expected and observed in the actual ADCs to be used in flight. By setting all the values to those typically measured, the simulator results can be directly compared with those of the detector.

Some of the subroutines were written by Smith. Edgar adapted many of the *ALLSINGN* subroutines, particularly the graphics, for *GIS_SIM*.

5.2.1. Required detector performance

The detector requirements have already been described in detail in §2.2. Two of the most important of these were first, to be able to process up to 10^5 c s^{-1} (random) with a linear response to the intensity of individual spectral lines up to the highest expected count rate. Disregarding the He II 30.4 nm line, the Fe XVI lines are the most intense lines expected, with 400 c s^{-1} for an active sun and the smallest slit.

Secondly, the detector resolution has to be better than 47 μm FWHM in order to broaden the minimum expected line width by no more than 10%.

Other requirements were non-linearities of no more than 0.1% and a quantum efficiency of greater than 10%.

5.2.2. Simulation

The simulation of the GIS performance involves a number of stages. In the first stage, a flat field is simulated by choosing a large number of closely and evenly spaced positions across the detector and initiating 'events' at these positions. Each event is assigned a pulse height according to a probability distribution taken from a PHD. The SPAN algorithm is then used to calculate the distribution of charge on the three electrodes. Random electronic noise and electronic crosstalk are added by subroutines using a normal distribution with the standard deviation chosen by the user. The quantity of charge collected is normalised and then digitised, or binned, by simulated ADCs, which add their own non-linearities. The number of bits can be selected. These values are then put into a file as simulated raw data.

The second stage (in a separate program, either *SPANFIT* or *HOUGH*) involves fitting the raw data from the first stage to an ideal spiral to obtain a best fit parameter set—simulating the real system described in §5.1.2.1. These parameters are then used to build a LUT with *LOOKUP*.

In the third stage, a spectrum defining the positions of photon events is selected as input to the model. The input spectrum is divided into 1 μm lengths, and may define one or more spectral line of a chosen width. A large number of events with these positions is generated. The charge values are modified by random noise, crosstalk and non-linearities as for the flat field case, but with an option to use different values from the first stage. The LUT calculated from *LOOKUP* is used to map the observed signals into a one-dimensional position spectrum. Finally, the output spectrum is compared with the input in order to calculate performance characteristics such as signal rejection, spatial resolution and non-linearities.

5.2.3. Use of the model

The simulator assisted with testing out the resolution and linearity requirements (§5.2.1). It showed that while the resolution is easily achievable, the linearity is limited by the fixed patterning.

Using just the first stage of *GIS_SIM* produced some enlightening results. A flat field can be created with unmatched preamplifier gains, ADC non-linearities, electronic noise and crosstalk, any PHD *etc.* It can also be plotted with co-ordinates defined by the ADCs or r-θ co-ordinates, polar or Cartesian, just as in *ALLSINGN*. Thus the gross effect of any source of error can be assessed very quickly.

If the LUT is built to compensate for unmatched gains and crosstalk, the effects of these errors cannot be seen in the final result. The second and third parts of the simulator process are therefore used mainly to assess the effects of a change in these particular errors between creating the LUT and using it. Noise, which appears as a broadening of the spiral arms in the flat field simulation, and non-linearities cannot be compensated for in the LUT.

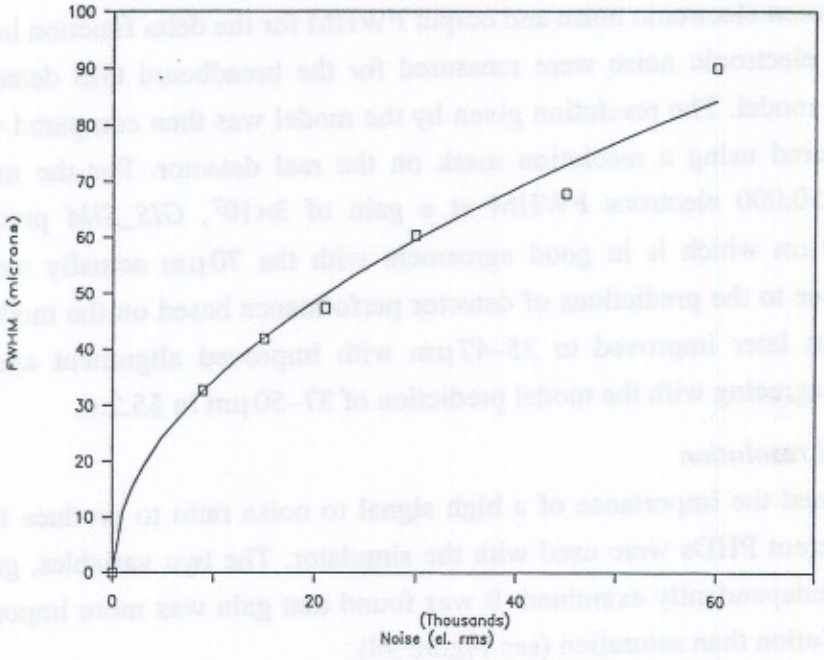

Figure 97. Spectral line FWHM with noise.
The points are FWHM measured by the model with different values of electronic noise. These have been fitted by a curve.

GIS_SIM was the first time the concept of the LUT was initiated and tested. The software for writing the LUT was complex and needed many iterations. Methods for

correcting for gains and offsets in the LUT were tested. Routines to fit a spiral automatically to the flat field were developed.

Once *GIS_SIM* was working reliably, a large part of the LUT code was incorporated in the on-board software in the GIS processor, but translated by McCalden, MSSL, into the Occam computing language.

5.2.4. Electronic effects

5.2.4.1. Noise and resolution

As expected, the effect of electronic noise is found to be a broadening of the output spectral lines. By using an input image of a series of delta functions (a 1 μm wide line is as near as the model can get), the broadening effects of electronic and partition noise can be isolated and the values obtained compared with those used in equation (76) for Δx_e and Δx_p. Because of the discrete nature of the output spectra from the simulator, the lines cover only a few bins. Therefore, in order to find the mean FWHM, the output lines were all summed together, matching up the peak bin. This had the effect of artificially broadening the lines, especially at low noise values. Figure 97 shows the relationship between electronic noise and output FWHM for the delta function input.

Values of electronic noise were measured for the breadboard GIS detector and inserted into the model. The resolution given by the model was then compared with the resolution measured using a resolution mask on the real detector. For the measured noise value of 50,000 electrons FWHM at a gain of 3×10^7, *GIS_SIM* predicted a resolution of 60 μm which is in good agreement with the 70 μm actually measured, lending confidence to the predictions of detector performance based on the model. This measurement was later improved to 35–47 μm with improved alignment and lower electronic noise, agreeing with the model prediction of 37–50 μm in §5.2.6.

5.2.4.2. Gain and resolution

GIS_SIM confirmed the importance of a high signal to noise ratio to produce the best resolutions. Different PHDs were used with the simulator. The two variables, gain and saturation were independently examined. It was found that gain was more important in determining resolution than saturation (see Figure 98).

If a single valued gain, ph_j, is considered *i.e.* a PHD consisting of a delta function, a Gaussian line width of resolution r_j will result when electronic noise is applied. Each real PHD is a function, $f(j)$, defining the distribution of the single-valued delta functions. Therefore the width of the resultant line is a sum of all the Gaussians, weighted according to the number of events at each pulse height:

$$Res^{n^2} \propto \sum r_1^{\,2} + r_2^{\,2} + \ldots . r_N^{\,2} / N = \sum_{0}^{j=N} r_j^{\,2} f(j) \Big/ \sum_{0}^{j=N} f(j) \qquad (102)$$

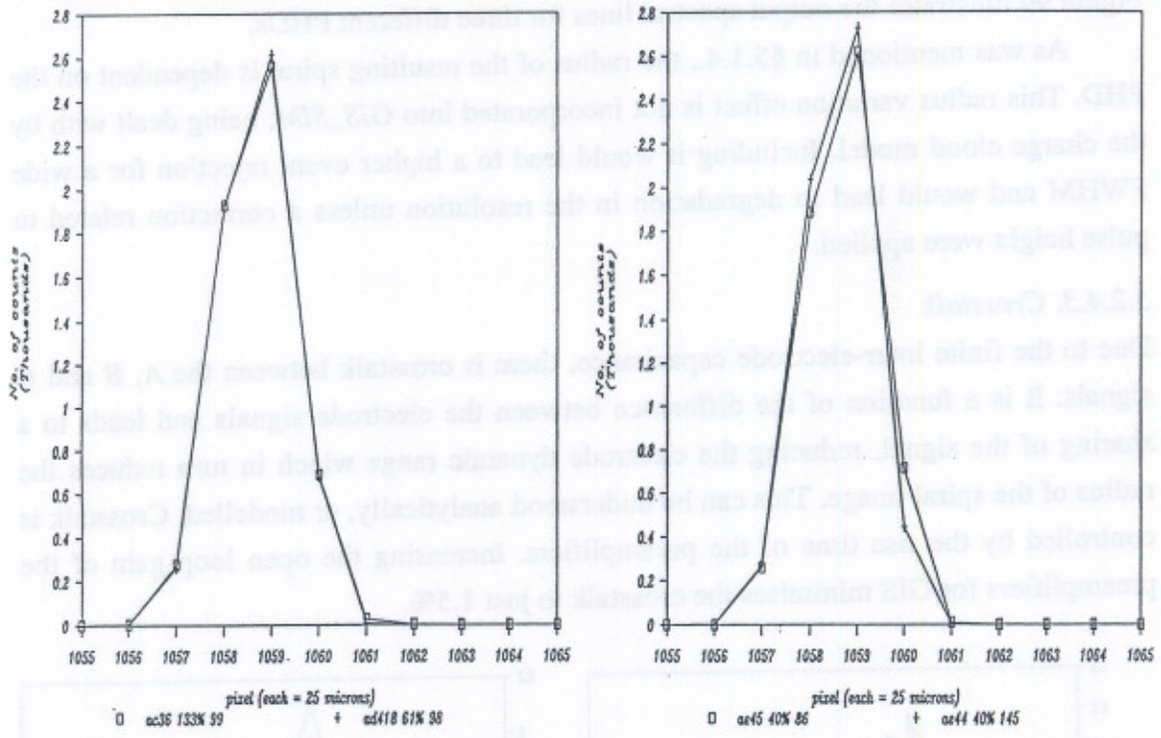

(a) (b)

Figure 98. Comparing the effect on resolution of gain and PHD width.
Plot (a) shows the modelled spectral line resulting from a top hat input 60 µm wide, with two PHDs of the same gain but different widths. For Figure (b), the PHD gains were different but the width was kept the same. The PHD with the higher gain produces the slightly narrower spectral line.

If the resolution r_j is inversely proportional to the gain, ph_j, then we can define RMSIG (r.m.s. inverse gain):

$$RMSIG = \sqrt{\frac{\sum f(j)/ph(j)^2}{\sum f(j)}} \qquad (103)$$

where $f(j)$ is the number of events falling into pulse height bin $ph(j)$. The value of RMSIG was calculated for the PHDs being used in the model, using a FORTRAN program, *RMSIG*. Consideration of the effects of noise indicates that the positional resolution will depend directly upon RMSIG. This was confirmed from *GIS_SIM* results, where PHDs with widely differing FWHM but similar RMSIGs, gave almost identical position resolutions. Given two PHDs of the same RMSIG, one with FWHM

of 133% and the other with 61%, the output spectra were almost identical, the difference being that for the 133% FWHM PHD, only 99.89% of the events were found to lie within the boundaries of the LUT compared with 100% for the narrower PHD. Figure 99 illustrates the output spectral lines for three different PHDs.

As was mentioned in §5.1.4., the radius of the resulting spiral is dependent on the PHD. This radius variation effect is not incorporated into *GIS_SIM*, being dealt with by the charge cloud model. Including it would lead to a higher event rejection for a wide FWHM and would lead to degradation in the resolution unless a correction related to pulse height were applied.

5.2.4.3. Crosstalk

Due to the finite inter-electrode capacitance, there is crosstalk between the *A*, *B* and *C* signals. It is a function of the difference between the electrode signals and leads to a sharing of the signal, reducing the electrode dynamic range which in turn reduces the radius of the spiral image. This can be understood analytically, or modelled. Crosstalk is controlled by the rise time of the preamplifiers. Increasing the open loop gain of the preamplifiers for GIS minimises the crosstalk to just 1.5%.

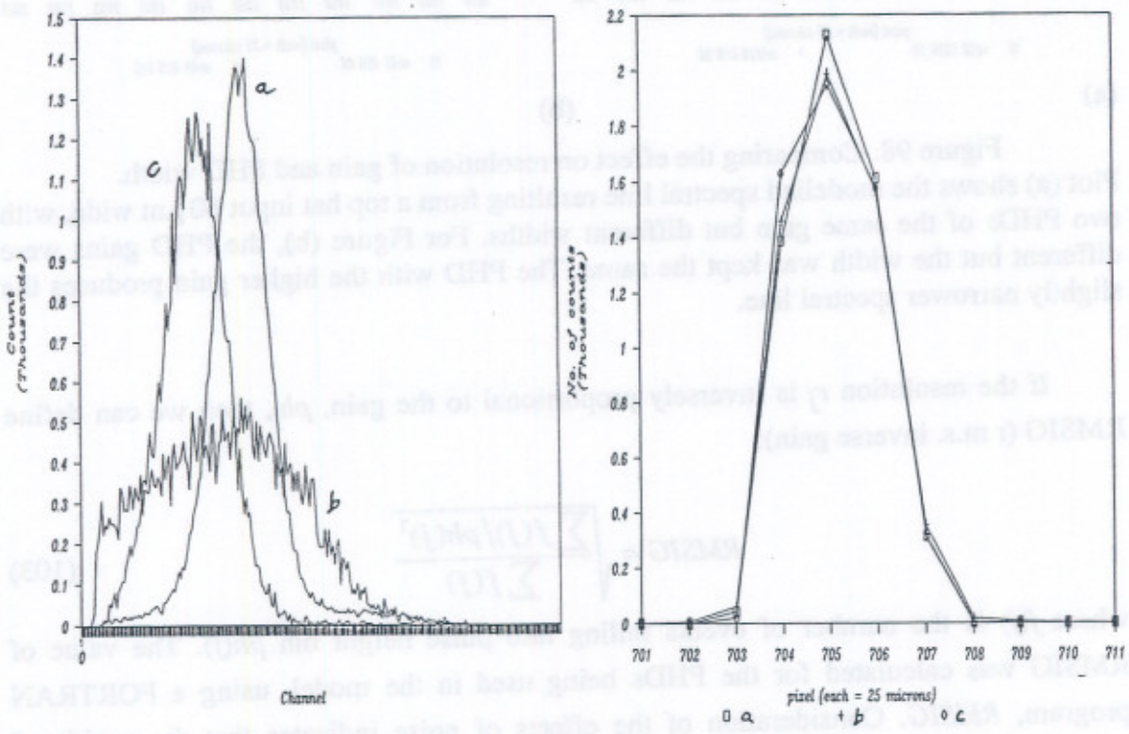

Figure 99. Effect of three different PHDs on a modelled output spectral line.

Crosstalk is not expected to vary greatly during the detector's lifetime. One of the first tests using the simulator was to see how crosstalk affects the image and how large the change in crosstalk can be before the image is significantly degraded or a new LUT needs to be generated.

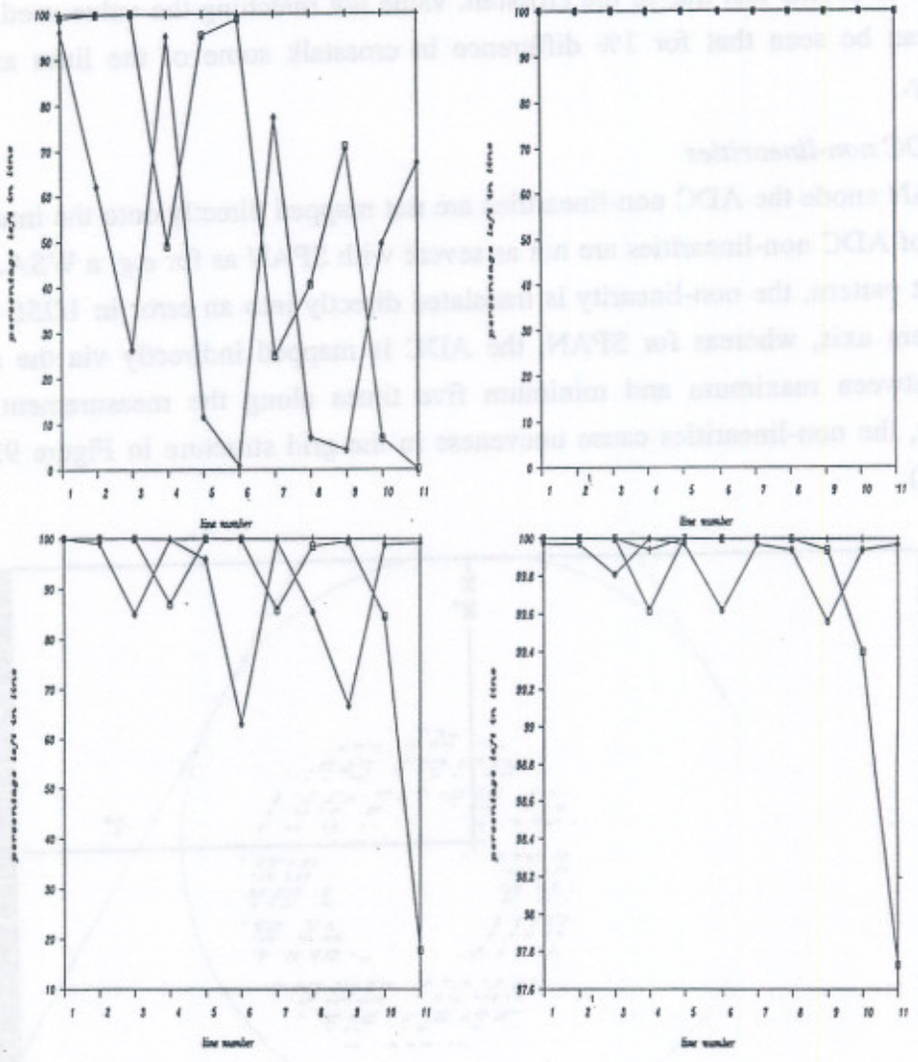

Figure 100. Percentage loss of events with crosstalk mismatch from the value used in the LUT. From left to right, top: ±1% ±0.1%, bottom: ±0.7%, ±0.4%,. Eleven spectral lines are simulated and the number of events in the output lines compared with the input.

The reduction of the radius of the resultant spiral due to crosstalk leads to a loss of resolution because of the reduction in ADC dynamic range. A LUT can be written to take the reduced spiral parameters into account, but if the crosstalk varies from the value used to generate the LUT, the resulting spiral will change and events will lie outside it.

In the creation of the LUT, an interval of finite width (controlled by the *percent* parameter) is left unmapped between the spiral arms, in which all events are discarded. Using a *percent* parameter of 50%, it is found that when the crosstalk is changed by 0.9%, the spiral no longer lies within the LUT envelope. Figure 100 shows the percentage of events lost due to the crosstalk value not matching the value used in the LUT. It can be seen that for 1% difference in crosstalk some of the lines are lost completely.

5.2.4.4. ADC non-linearities

In the SPAN anode the ADC non-linearities are not mapped directly onto the image, so the effect of ADC non-linearities are not as severe with SPAN as for *e.g.* a WSA. For a linear 8-bit pattern, the non-linearity is translated directly into an error in 1/256 of the measurement axis, whereas for SPAN, the ADC is mapped indirectly via the spiral, varying between maximum and minimum five times along the measurement axis. Effectively, the non-linearities cause uneveness in the grid structure in Figure 93 (see also §4.3.2).

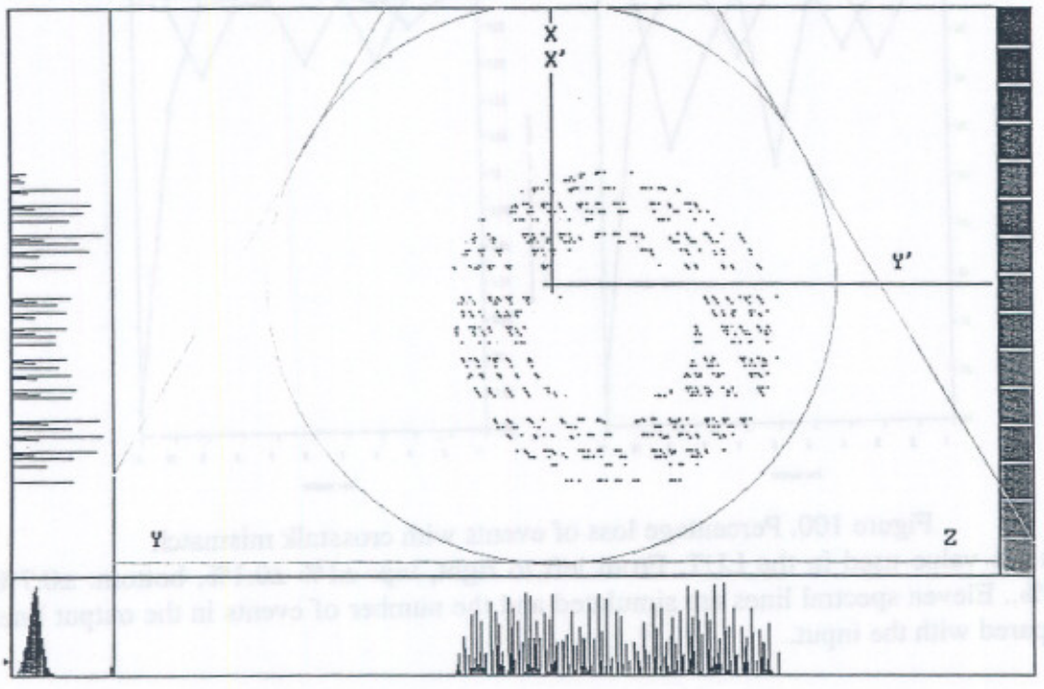

Figure 101. Geometrical effects on the simulated spiral caused by an offset on the ADC bits to simulate integral non-linearity.

Non-linearities can be applied in the ADC subroutine in several ways. The ADC is conceived as a number (256 for 8-bits) of evenly spaced discrete levels between 0 and

1.0. Differential non-linearity can be applied by adding a random offset to each ADC level. The random offset is selected using a normal distribution with the standard deviation, in terms of percentage of ADC level, chosen by the user. The differential non-linearity produces spiral arm broadening which is similar to electronic noise on the flat field spiral. However, this is an introduced systematic error rather than purely random and so cannot be avoided through long integration. A form of integral non-linearity is simulated by applying a non-random offset to each bit as it is set, such that a given level contains a binary sum of such offsets. This results in a spiral shifted from the origin, with geometrical effects as in Figure 101.

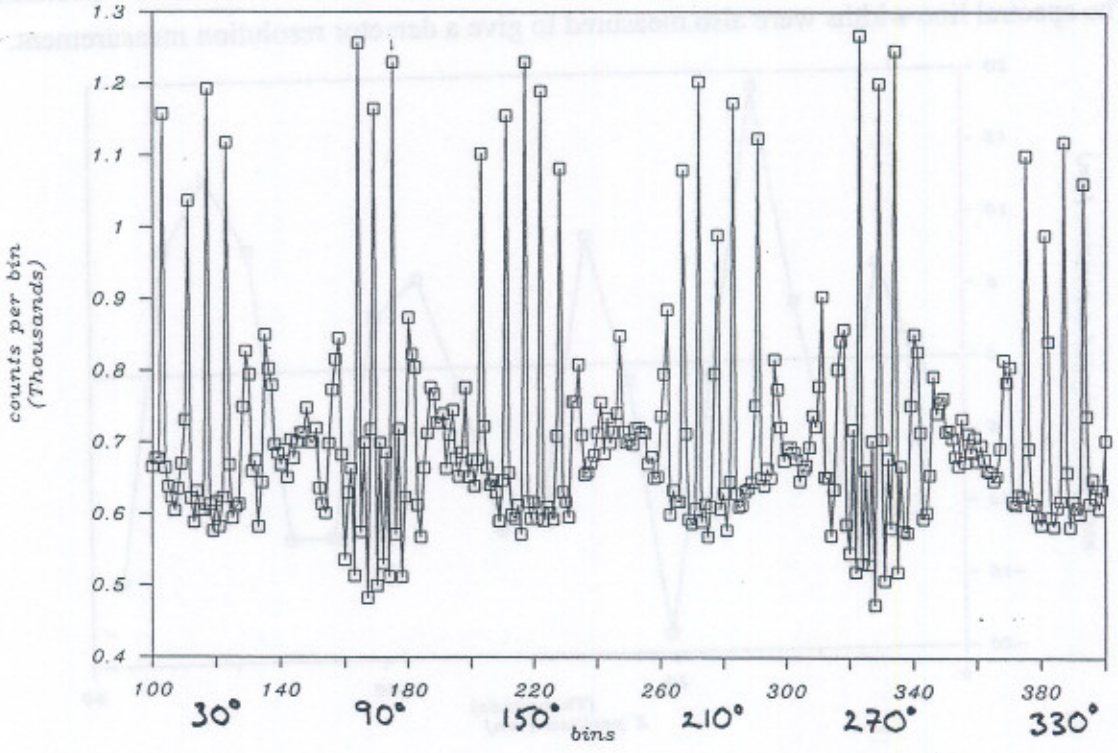

Figure 102. Example of simulated fixed patterning along a short length of an image . This is a simulated flat field. Note the particular problems at the angles 30°, 90°, 150°, 210°, 270° and 330°, as expected from §5.1.4. The noise was set to 6000 electrons r.m.s. and crosstalk to 4%.

5.2.5. Modelling fixed patterning

Clampin and Edwin (1987) attribute the presence of a fixed pattern noise to preferred codes in the analogue-to-digital ratiometric conversion leading to a non-linear conversion. In the case of SPAN this is what was discussed the previous section as ADC non-linearities. However, the fixed patterning most significant in SPAN is due to the

conversion of the spiral form to a linear image, as described in §5.1.4. The model shows very clearly how fixed patterning can distort a flat field (see Figure 102).

A large number of lines at regular intervals were put in to the simulator and the distances between output peaks were measured. It can be seen from Figure 104 that the positions of the peaks have been locally affected by the fixed patterning, although over the whole anode the effect cannot be seen.

In another test an input image consisting of 20 evenly spaced lines, each 60 µm wide was applied to the model, with a 60% width PHD. The values for noise, of 6000 electrons r.m.s., and the ADC non-linearities were as measured on GIS. For each output line, the expected position was calculated and compared with the measured position. The spectral line widths were also measured to give a detector resolution measurement.

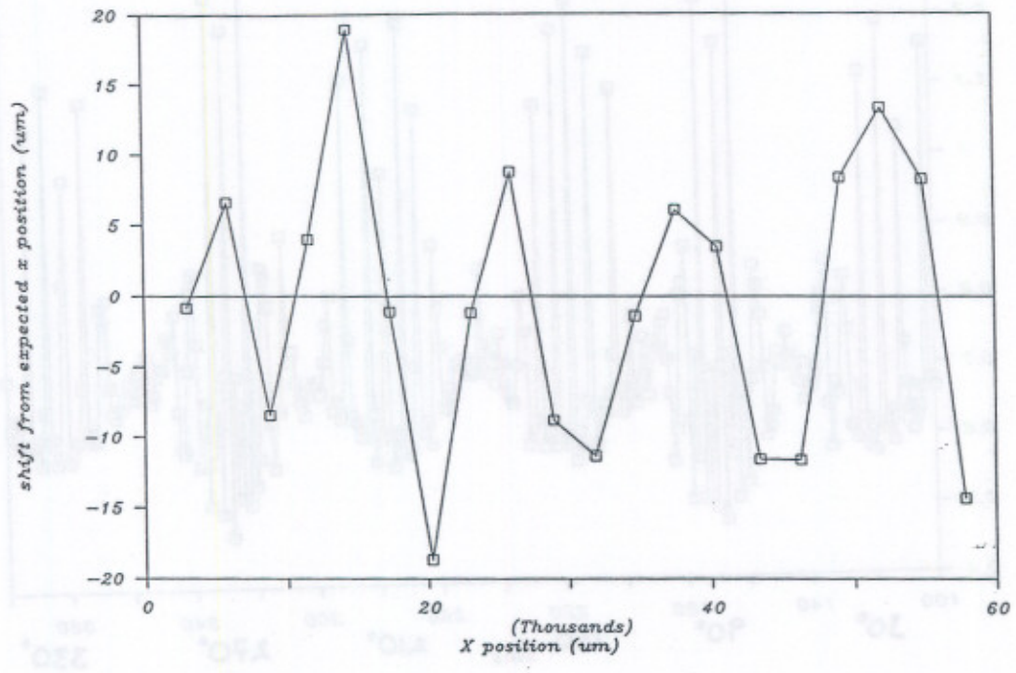

Figure 103. Output positions from the 20 60 µm lines input to the simulator (see text). The integral non-linearity of ±25 µm (±1 pixel) is due to fixed patterning.

The shift from the expected position for each line is plotted in Figure 103. An error of up to ±19 µm (almost ±1 pixel, or 0.04%) is observed. This is within the specification.

The stability of the fixed pattern noise introduced by the LUT is ultimately the limiting factor in the calibration of the instrument. If it is truly fixed, a measured, or even a calculated, flat field can be divided into any spectrum to correct for the effect. If there is any variability, however, the divided result may be more misleading than if left

uncorrected. Phillips (1992) describes how large errors can be introduced by using this type of data manipulation when the pattern is not static. The model was used to assess the stability of the fixed patterning.

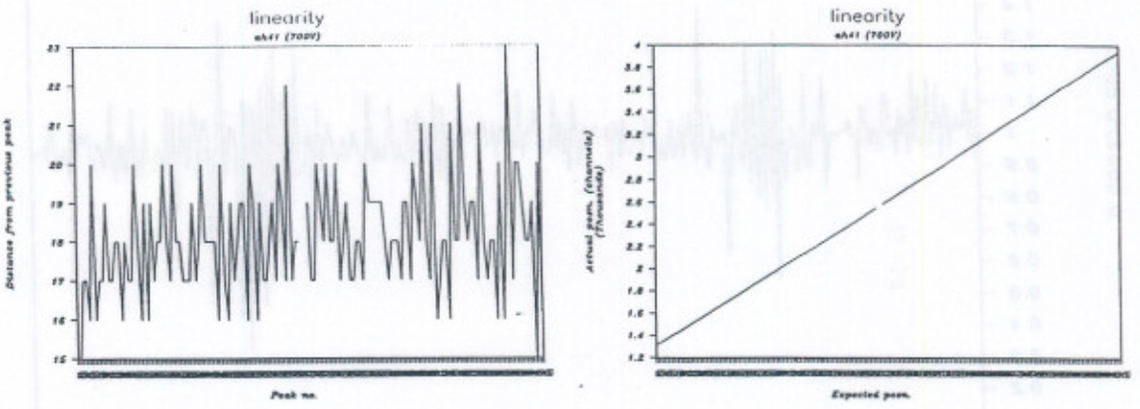

(a) (b)

Figure 104. Effects of fixed patterning on linearity from model.
(a) is a plot of the distance between each peak in the image and shows the differential non-linearity. (b) is the integral plot where the measured position is plotted against expected position.

In trying to find a way to reduce the effect of fixed patterning, it is important to know its sensitivity to various parameters. To investigate this, a flat field consisting of 25 events per point 1 µm apart in the input image was simulated. A measure used to assess the quantity of fixed patterning is the r.m.s. deviation of the number of events per pixel from the mean, calculated for a flat field. Figure 102 shows a section of the output flat field, equivalent to a single spiral arm. The flat field in this section was repeated for a number of values of electronic noise. Doubling noise decreases the amount of fixed patterning from 25% r.m.s. deviation to 20%. Figure 105 shows one of these flat fields divided by the other. It can be seen that the shape of the patterning matches well except at certain positions, which correspond to the angles of 90° and 270°.

Flat fields for two PHDs were also produced. The PHDs are shown in Figure 99. One (a) has a gain of 1.6×10^7 and a FWHM of 60%. The other (b) has a gain of 5×10^7 and a FWHM of 40%. These gave r.m.s. deviations of 23% and 20% respectively, showing that the higher gain produced less fixed patterning. Dividing the flat field for one by the other gives a r.m.s. error of 8%. Figure 106 shows how the deviation in the divided plot increases linearly as one PHD is gradually transformed into the other.

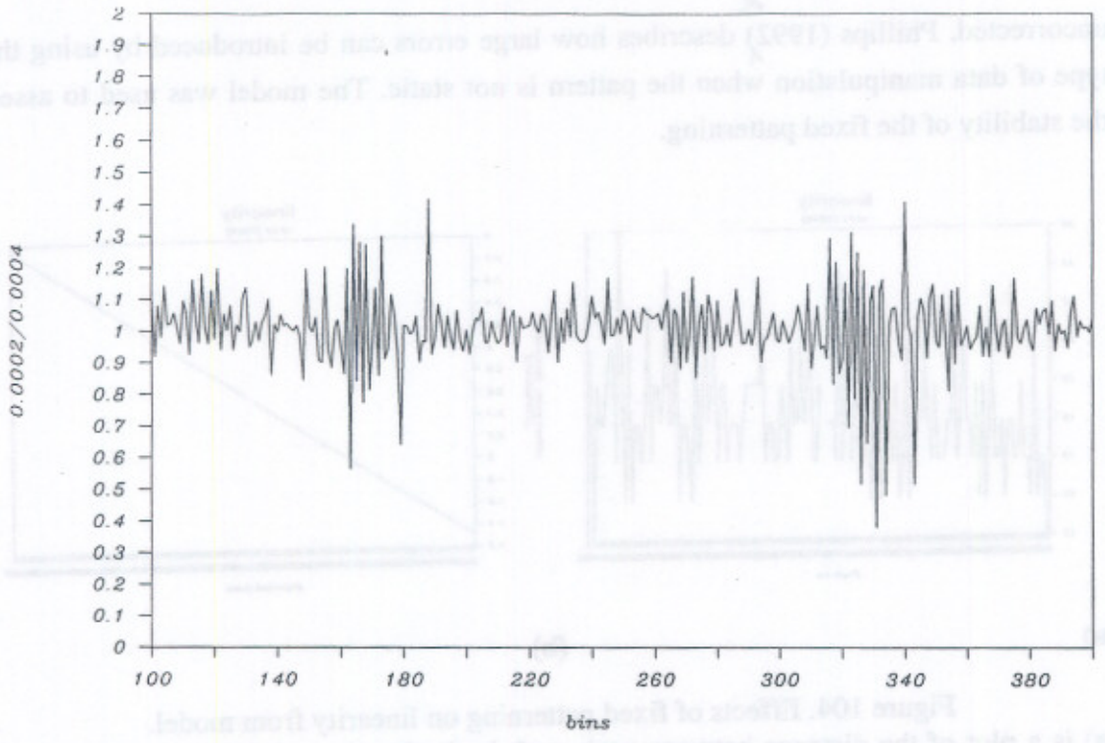

Figure 105. Dividing two flat fields, simulated with different electronic noise. 6,000 and 12,000 electrons r.m.s. noise on a gain of 3×10^7. The result has a 7% error from the desired value of 1.0. The x-axis covers one revolution of the spiral, with bin 100 at 0° and 400 at 360°.

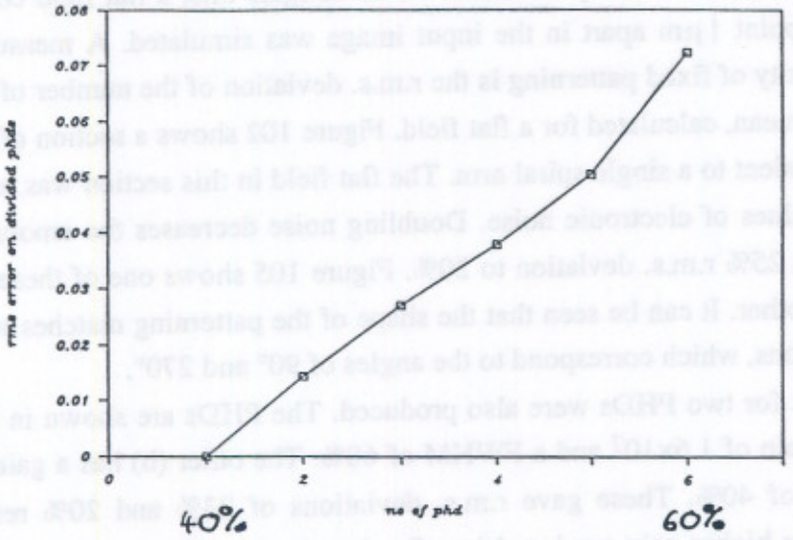

Figure 106. Variation in flat field with PHD.
The PHDs range from 40% to 60% FWHM and from 5×10^7 to 1.6×10^7 modal gain.

However, this is not a strictly fair trial—the 60% FWHM should help reduce fixed patterning if the radius pulse height dependence had been included in the model.

If a division method is to be used, a new flat field will have to be taken if the PHD or noise changes significantly.

5.2.6. Expected resolution

For the flight system, the electronic noise levels are approximately 15,000 r.m.s. at a gain of 4×10^7. Putting into *GIS_SIM* all the expected values for the error parameters including electronic noise, crosstalk and partition noise, we obtain a predicted resolution of 37–50 µm FWHM, which is within the specification and includes the 39 µm predicted in §5.1.3., and the 35–47 µm measured in §4.8.3. Modelling partition noise made a negligible difference to the line widths, as also predicted in §5.1.3.

5.2.7. Different approaches to the anode design

It was suggested, that since only two ADCs were being used, it would make sense to create the pattern with two electrodes 90° from each other instead of 120°, the third being reserved for normalising only. In that case, plotting the signals from the two ADCs against each other would be a simple Cartesian plot with a grid of square elements. No transformation such as equations (99) is required to form a spiral in the X,Y plane. The centre of the spiral lies at $\frac{1}{3}(Sum, Sum)$ so that the position of the centre, pre-normalisation, is pulse height dependent and lies along the line $X=Y$. The 90° anode lends itself to use in the normalised mode, when the event co-ordinate may be determined with very little calculation. Using the LUT method, however, it would not make any difference to the speed or ease of operation because the two ADC values do not have the transform performed on them in real time, but are simply used as addresses for the LUT.

It was also argued that the square grid elements would give less fixed patterning. As the worst fixed patterning lines up with the pixel boundaries, it was thought that the shorter edges of the square pixels would be an advantage over the longer edges of the rhomboids. Where θ is zero, the spiral path goes straight across each square grid element in turn and has a length of unity. At 45° the maximum length of the path crossing each element is $\sqrt{2}$. This compares with the $\sqrt{3}$ or $\sqrt{2}$ maximum distances across the rhomboidal element. The angles along which the greatest fixed patterning arises are moved to the diagonals.

Using the *GIS_SIM* model adapted to a 90° anode, a flat field was input with 25 events at each µm position as for the 120° case. The result is pictured in Figure 107. It can be seen that the patterning is indeed at its worst at positions where the spiral is at

45°, 135°, 225° and 315°. This can be compared with Figure 102. In fact the 90° anode gives slightly worse fixed patterning. Calculating the r.m.s. deviation from the mean number of events in each pixel gives 20% for the 120° anode and 25% for the 90° anode. The reason is that fewer grid elements are cut through by the spiral in the 90° pattern.

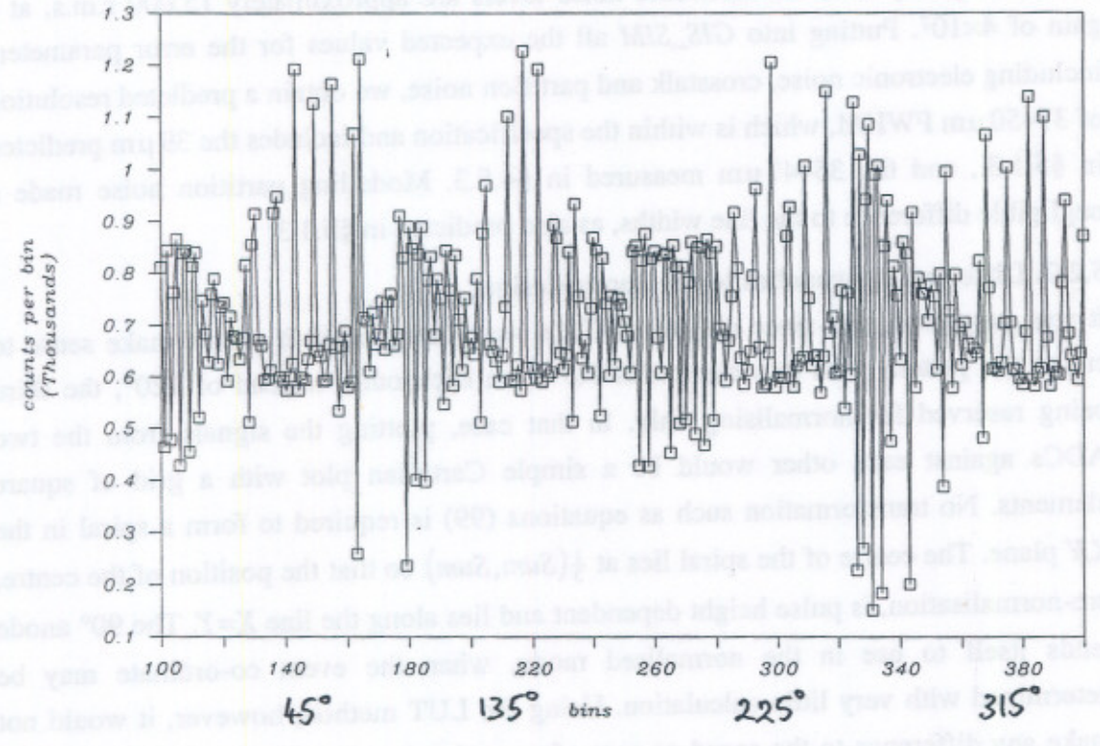

Figure 107. Modelled flat field output for the 90° anode.
It covers one spiral arm starting at $\theta = 0°$.

A histogram representing the number of pixels containing counts in ranges of 50 has been drawn up for this flat field, covering the whole length of the anode, not just the section shown in Figure 107. This histogram can be compared with a similar one for the 120° anode. The mean number of counts per pixel is the same for each. However, for the 120° anode the range was 708^{+722}_{-328}, whereas for the 90° anode the range was much more symmetrical, being 708^{+556}_{-557}. Presumably this is because the square grid elements have four degrees of rotational symmetry, whereas the rhomboid has only two degrees. For both flat fields the same PHD, noise and crosstalk values were used.

Better resolution was not demonstrated with the 90° anode. The advantages of changing for a simpler LUT calculation scheme were not sufficient to outweigh the

benefits of symmetry in the 120° design, in having identical electrode structures. An anode of this 90° type was manufactured, but was never put into operation.

Although the heights of the electrodes follow an identical form in the 120° case, it can be seen from the anode design that the actual shapes of the electrodes themselves are not of the same form. Electrodes *A* and *C* are both bounded by one straight edge, whereas electrode *B* has two wavy edges. Backlash in one axis of the laser cutting may therefore affect the electrodes in different ways causing irregularities in the spiral image. Furthermore, the convolution of the charge cloud with a curving edge would be different from convolution with a straight edge.

An anode was therefore designed that would use wavy lines between each electrode. The equations for the electrodes were simple although the top and bottom edges of the anode were not as tidy as for the straight version. However, again due to time constraints, this anode design was never implemented. Interestingly, a gain adjustment factor has to be applied to the *B* electrode in nearly all the flight detectors of +5%. This could well be because of the particular decrease in radius at this electrode because of convolution, or backlash.

CHAPTER 6.

ANODE DESIGN, MANUFACTURE AND TESTING

The anode active pattern area is 58×22 mm. Figure 108 shows the design of the anode, with the electrodes divided from one other by black lines which represent the laser-machined insulating tracks. The pattern is made up of groups or pitches of 3 electrode elements, (see Figure 85), which are identically repeated along the *y*-axis, to increase the charge collection area. There is no positional information along the *y*-axis.

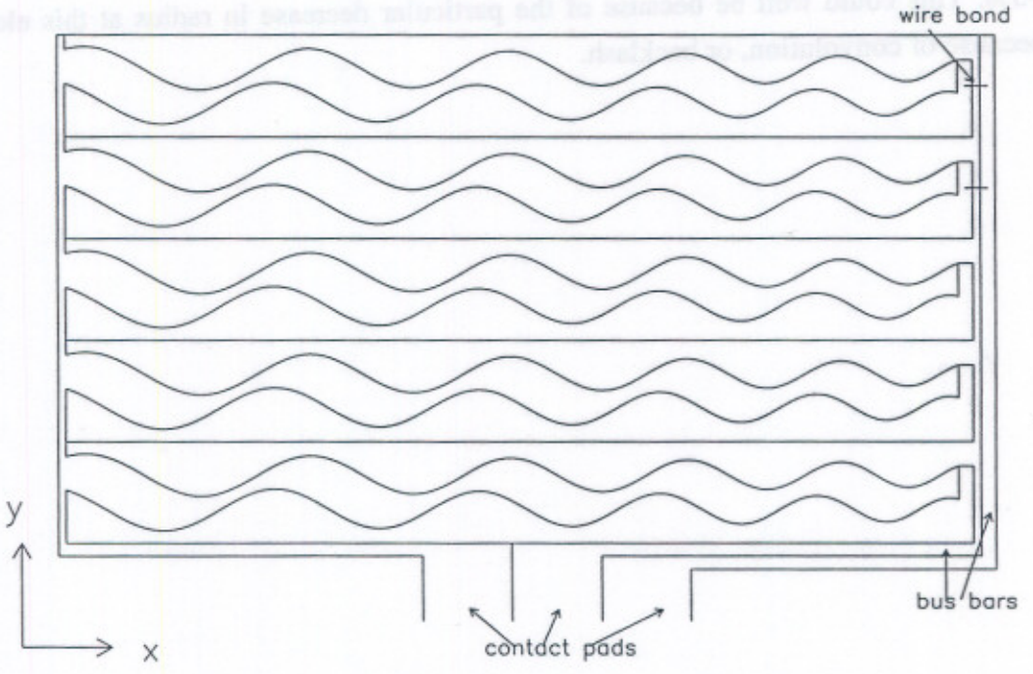

Figure 108. Diagram of anode electrode pattern.
The *x* and *y*-axes are indicated, the *x*-axis being the spectral dispersion axis. The positions of two of the wire bonds are indicated.

The horizontal elements of the three electrodes, *A*, *B* and *C* are interleaved in the pattern *A, B, C, A, B, etc.* The actual pattern used has a repeat pitch height of 390 μm.

There are a total of 56 pitches in the *y* direction, adding up to the active height of 21.8 mm. The figure shows only 5 pitches for the sake of clarity, but the edge geometry is an accurate representation of the anode showing how two of the electrodes are continuous, with all the elements joining bus bars leading to the contact pad. The last electrode has to be connected to its bus bar by wire-bonding. The whole anode is held at high positive voltage in order to provide an accelerating field behind the MCP stack. The outside area of the anode is also held at high voltage so as to prevent breakdown across the narrow laser tracks.

The position of two of the wire bonds linking together the elements of one of the electrodes is indicated by short 'stitches' down the right hand side of the figure. There are normally two stitches per element for redundancy. The electrodes are often referred to as the *A, B* and *C* or the *X, Y* and *Z* electrodes, but these names must not be confused with the *x* and *y* axes of the anode (in Figure 108) or of the instrument, illustrated in Figure 13.

6.1. CHARGE CLOUD INTERACTION—MCPS WITH ANODE

Once the charge cloud is emitted from the back of the rear MCP, its shape and direction of travel are governed by the initial velocity of the electrons, the forces between them and the electric field in the gap. Assuming conditions were ideal, the charge would be divided exactly as the anode area ratio. This is the basic ratio that is used in the *GIS_SIM* model.

The output energy from an MCP has been measured by putting a grid and collector with a range of retarding potentials behind the MCP (Koshida and Yoshida, 1979 and Koshida and Hosobuchi, 1985). Most electrons are emitted from an MCP with energies less than 10 eV, but a considerable number are emitted with higher energies, up to 60 eV or more, depending on the operating configuration of the MCPs and the end spoiling. The distribution consists of a sharp peak with the FWHM of a few eV and a long tail extending over a wide energy range as shown in Figure 109.

The output energy distribution of the electrons forms a peak at lower energy for increasing saturation. A decrease in potential gain between electron collisions with the wall near the output reduces the width and the peak of the energy distribution. This is particularly noticeable with changes in end spoiling depth (Koshida, 1986). As the depth is increased, the peak and width are both reduced (Koshida *et al.*, 1980). The gain is also reduced.

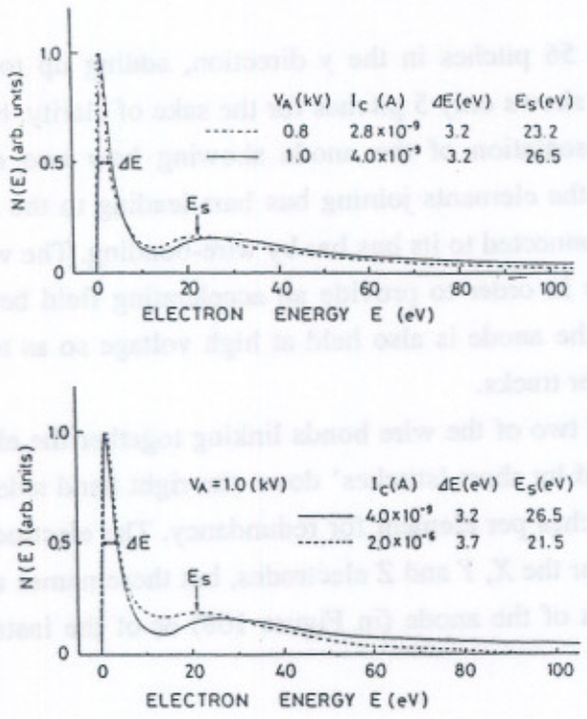

Figure 109. Example of the output electron energy distribution of an MCP. a) the output energy curves for two different applied voltages; b) for one applied voltage—in saturated and unsaturated mode. The voltages and currents are written on the diagram as well as the peak energy and width. Taken from Koshida *et al.* (1985).

6.1.1. Modulation and convolution

There are various output charge cloud effects coupled with the anode which can lead to small- and large-scale non-uniformities or non-linearities. If the charge cloud is spread over too small an area, of the order of one pitch dimension or less, it will fall preferentially onto one electrode or another, under sampling the electrode ratios. This will produce image modulation, which is a form of DNL. A spatially small charge cloud can occur either because of lack of electronic gain or because of an anode gap electric field which is too high to allow the charge cloud to spread out sufficiently. Conversely, it may be caused by an anode pitch which is too large for the MCP configuration. Martin *et al.* (1981) calculate that, for a wedge and strip anode, modulation should give less than 1% position error if the charge cloud r.m.s. radius is equal to the repeat pitch of the pattern.

Modulation effects in wedge and strip anodes are further described and modelled by Smith *et al.* (1989). An example of the effect of changing the anode-MCP gap voltage is shown in Figure 110. It is worth commenting that, in modelling an MCP output consisting of a uniform disk of charge, they showed that a sharp edge to the

charge cloud can cause modulation even when the disk has a radius as large as 20 pitch widths. A soft edge, such as the true exponential distribution is less likely to cause modulation. According to Guest (1978), deeper electrode penetration at the channel output end increases the collimation of the charge cloud and decreases the output energy, thereby increasing modulation.

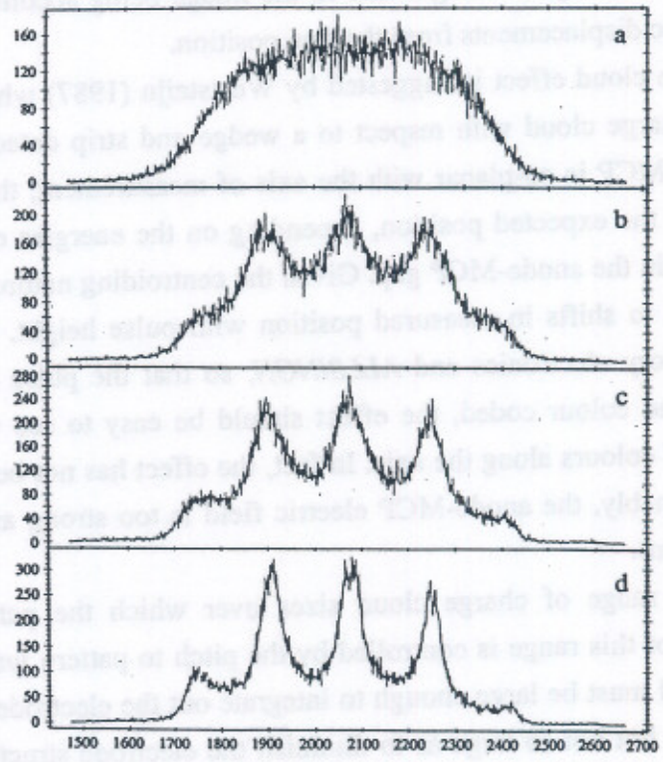

Figure 110. Increase in modulation with MCP-anode voltage from Smith *et al.* (1989). This is a collection of one dimensional positional histograms using a wedge and strip anode. MCP-anode voltages are: a) 100 V; b) 250 V; c) 400 V; d) 550 V.

Another effect occurs when the charge cloud is very large or has large spread-out wings. If they fall on the contacts or on the bus bars, the image will be distorted at the edges. This is equivalent to the 'S' distortion in wedge and strip anodes. For this reason the active area of the GIS anode, 58×22 mm, leaves a reasonable border around the 50×16 mm aperture area.

It is necessary for the charge cloud to integrate out fine structure in the *y*-axis direction to avoid modulation. It is also desirable to have as much charge as possible to improve the signal to noise ratio. However, an extended charge cloud will also tend to integrate out the fine structure in *x*-axis, leading to loss of resolution. The convolution of

the charge cloud distribution with the electrode structure effectively reduces the sinusoidal amplitude and hence resolution (Lapington, 1994a) *i.e.* the spiral shrinks towards the centre of the plane. As the charge cloud grows, the distinction between one spiral arm radius and another becomes blurred and eventually can lead to loss of uniqueness if it becomes impossible to distinguish between the spiral arms. Ghosting occurs in this case, resulting in a bright line in the image being accompanied by faint ghost lines at periodic displacements from the true position.

Another charge cloud effect is suggested by Weststeijn (1987) who examines the asymmetry of the charge cloud with respect to a wedge and strip detector. If the bias angle of the bottom MCP is co-planar with the axis of measurement, the charge cloud may be shifted from the expected position, depending on the energies of the electrons and the electric field in the anode-MCP gap. Given the centroiding nature of this type of anode, this will lead to shifts in measured position with pulse height. Using the RM detector with laboratory electronics and *ALLSINGN,* so that the pulse height of each event is measured and colour coded, the effect should be easy to see with a pinhole mask as a rainbow of colours along the axis. In fact, the effect has not been seen in this configuration. Presumably, the anode-MCP electric field is too strong and the gap too small (>360 V in 3 mm).

There exists a range of charge cloud sizes over which the pattern functions correctly. The width of this range is controlled by the pitch to pattern wavelength ratio since the charge cloud must be large enough to integrate out the electrode fine structure related to the pitches, but not so large as to diminish the electrode structure associated with the wavelength representing one revolution of the spiral. Thus the pitch to wavelength ratio as well as the electric field strength and MCP gain are crucial to image quality.

6.1.2. Split strip anode–charge cloud size

To achieve optimum performance from the detector, it is important, as set out above, to take into account the spatial distribution of the charge cloud in the anode design. The split strip anode was a method invented by Lapington *et al.* (1988) to measure the charge cloud spatial parameters directly. Figure 111 is a diagram of the split strip anode. It measures simultaneously both the position of an event and the fraction of charge falling on each side of the division. The detector is illuminated through a horizontal slot, allowing events at a variety of x-positions to be measured, whilst eliminating edge effects.

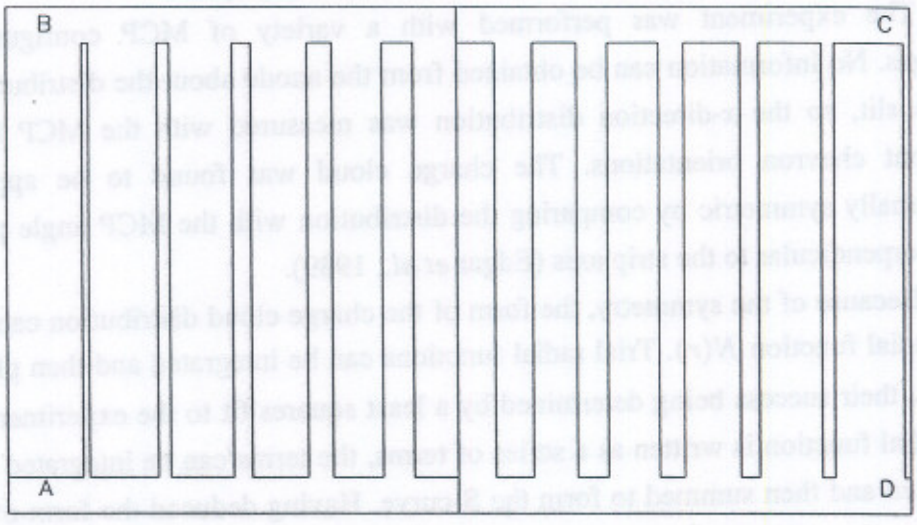

Figure 111. Split strip anode.
The strips have been expanded in the picture to show the detail.

The electrodes are paired in different ways to produce the two measurements. If the electrodes are summed together as A+B and C+D then the fraction of charge landing on the right hand side of the strip can be easily found from

$$fc = \frac{Q_C + Q_D}{Q_A + Q_B + Q_C + Q_D} \tag{104}$$

where Q_C is the charge collected by electrode C *etc.*

If the electrodes are paired with A+D and B+C summed, then the anode becomes position sensitive, with the fraction falling on A+D increasing linearly with x. The centroid position is found from

$$cp = \frac{Q_A + Q_D}{Q_A + Q_B + Q_C + Q_D} \tag{105}$$

Both *fc* and *cp* are calculated for each event. Plotting *fc* against *cp* produces a characteristic 'S-curve' (see Figure 112), which gives the average distribution for all the events. Events occurring towards one end of the slit will produce charge all of which is collected on the two electrodes on one side of the split, giving a value of *fc* of zero or

unity. For events near to the split, *fc* is a strong function of centroid position. Differentiating the curve gives a one-dimensional distribution corresponding to the mean charge cloud integrated over the axis parallel to the split.

The experiment was performed with a variety of MCP configurations and voltages. No information can be obtained from the anode about the distribution parallel to the slit, so the *x*-direction distribution was measured with the MCP having two different chevron orientations. The charge cloud was found to be approximately azimuthally symmetric by comparing the distribution with the MCP angle parallel and then perpendicular to the strip axis (Edgar *et al.*, 1989).

Because of the symmetry, the form of the charge cloud distribution can be written as a radial function $N(r)$. Trial radial functions can be integrated and then plotted as S-curves, their success being determined by a least squares fit to the experimental data. If the radial function is written as a series of terms, the terms can be integrated separately, weighted and then summed to form the S-curve. Having deduced the form of the radial function, the reduced χ^2 of the fit is used to determine the most successful weights and radial scale length parameters, using a computer-automated iterative procedure.

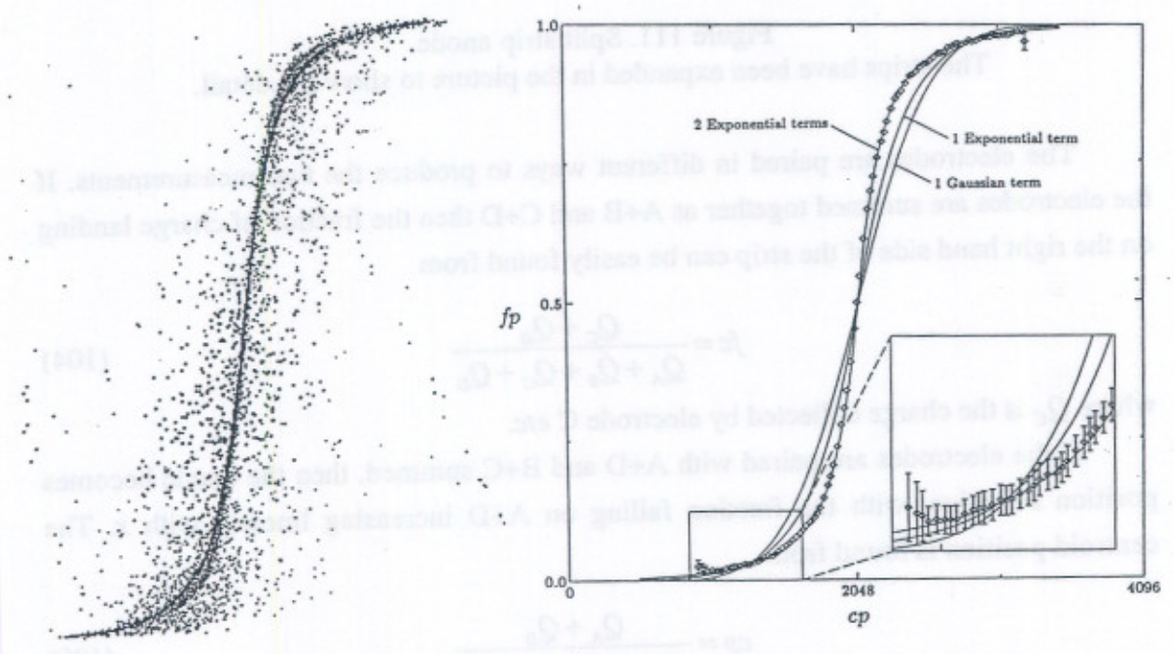

Figure 112. S-curve and comparison with a double exponential fit from Edgar (1993). In (a) each dot represents one of the 45000 individual events. The few events not lying on the S-curve are due to background events or measurement errors due to electronic pulse pile-up. In (b) the binned data is represented by diamonds with 3σ error bars relating to the width of the *fc* distribution per bin.

In general, the best fit was found to be the sum of two exponentials, one describing the centre portion of the cloud and the other the wings, as in equation (106). The scale and relative weights vary with the detector operating conditions. This radial function produces a minimum χ^2 approximately two to four times smaller than a fit where either one or two of the terms are replaced by a Gaussian.

$$N(r) = \frac{a_c}{2\pi r_c^2} e^{-r/r_c} + \frac{a_w}{2\pi r_w^2} e^{-r/r_w} \qquad (106)$$

where a_c is the weight in the centre component and a_w in the wing component, so that $a_c + a_w = 1$. r_c and r_w are the corresponding scale lengths.

6.1.2.1. Measured distribution

The narrow and well defined S-curve shown in Figure 112 shows that the distribution is relatively stable between individual events and from pore to pore. Variability would widen the curve. The central component scale length tends to be three to six times smaller than the wing component although most of the charge is usually in the central component. Using the automated routine on a number of data sets showed that the error associated with the central component parameters was less than 2% and that for the wing component less than 5%.

The experiments described in Lapington and Edgar (1989) were performed with two 36 mm diameter, 80:1 *l:d* ratio MCPs in a chevron configuration. The bias angle was 13°, the pore diameter 12.5 µm and the end-spoiling half a pore diameter. The MCP-anode gap could be 6.2 mm or 3 mm. Other variables were the overall MCP operating voltage (2.65–3 kV giving gains of ~ 1–5×10^7 electrons); the interplate voltage (+30 V to −30 V); the anode gap voltage (50–800 V). Illumination was with Al-K X-rays.

The main factors influencing the shape of the charge cloud are found to be, as expected, the MCP gain and the MCP-anode accelerating field and geometry. Interplate gaps and accelerations also have an effect. At higher gains the higher charge density results in a stronger mutual repulsion between the electrons and hence a broader charge cloud. The gain likewise affects the energy distribution of the output electrons, as described earlier (§6.1). Higher MCP-anode fields act as a focusing mechanism, preventing the charge from spreading.

The MCP-anode gap voltage is the dominant factor in determining the spatial distribution of the charge cloud (see Figure 113). When the anode gap voltage is

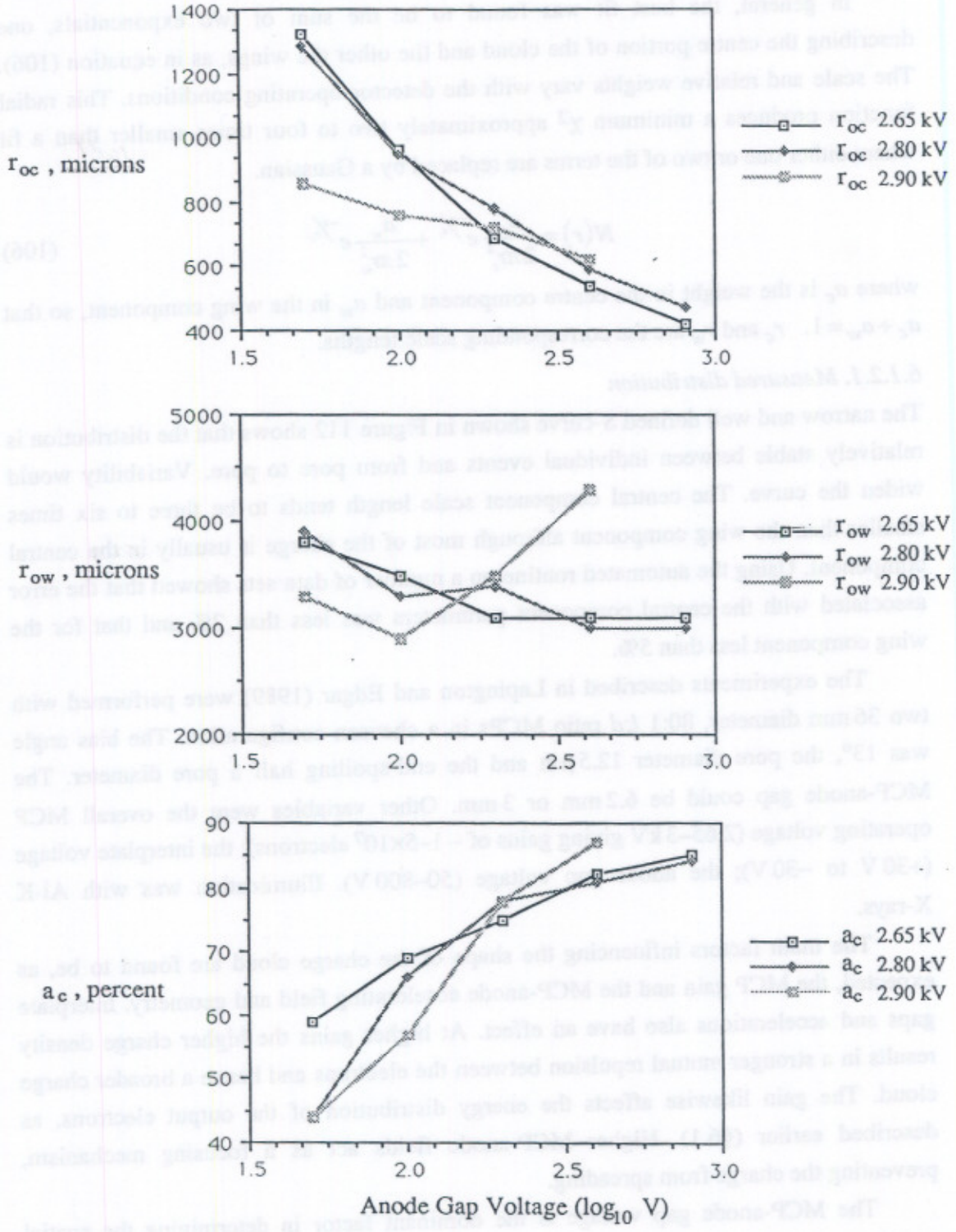

Figure 113. Plot showing charge cloud scale parameters with changing MCP (2.65–2.9 kV) and anode gap voltage (50 V to 800 V) for a gap of 6.2 mm, from Lapington and Edgar (1989). The interplate voltage was 0V. The parameters r_{ow} r_{oc} and a_c are described in the text as r_w r_c and a_c.

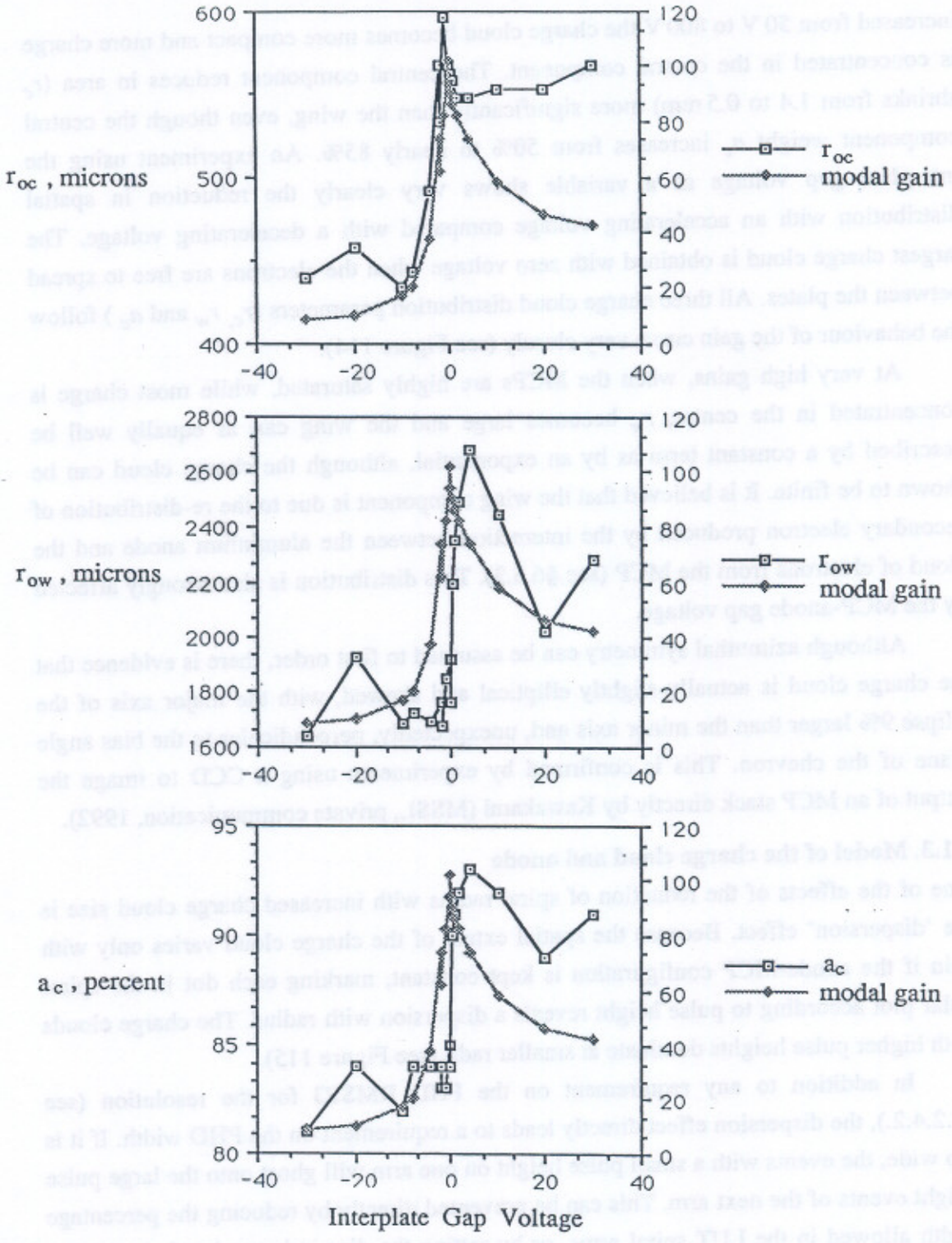

Figure 114. Parameters in Figure 113 plotted against interplate voltage from Lapington and Edgar (1989). Interplate voltage was varied between –30 and +30 V, with the MCP voltage kept at 3.0 kV and the anode gap voltage at 400 V.

increased from 50 V to 800 V the charge cloud becomes more compact and more charge is concentrated in the central component. The central component reduces in area (r_c shrinks from 1.4 to 0.5 mm) more significantly than the wing, even though the central component weight a_c increases from 50% to nearly 85%. An experiment using the interplate gap voltage as a variable shows very clearly the reduction in spatial distribution with an accelerating voltage compared with a decelerating voltage. The largest charge cloud is obtained with zero voltage when the electrons are free to spread between the plates. All three charge cloud distribution parameters (r_c, r_w and a_c) follow the behaviour of the gain curve very closely (see Figure 114).

At very high gains, when the MCPs are highly saturated, while most charge is concentrated in the centre, r_w becomes large and the wing can as equally well be described by a constant term as by an exponential, although the charge cloud can be shown to be finite. It is believed that the wing component is due to the re-distribution of secondary electron produced by the interaction between the aluminium anode and the cloud of electrons from the MCP (see §6.5.3). This distribution is also strongly affected by the MCP-anode gap voltage.

Although azimuthal symmetry can be assumed to first order, there is evidence that the charge cloud is actually slightly elliptical and skewed, with the major axis of the ellipse 9% larger than the minor axis and, unexpectedly, perpendicular to the bias angle plane of the chevron. This is confirmed by experiments using a CCD to image the output of an MCP stack directly by Kawakami (MSSL, private communication, 1992).

6.1.3. Model of the charge cloud and anode

One of the effects of the reduction of spiral radius with increased charge cloud size is the 'dispersion' effect. Because the spatial extent of the charge cloud varies only with gain if the anode-MCP configuration is kept constant, marking each dot in the spiral polar plot according to pulse height reveals a dispersion with radius. The charge clouds with higher pulse heights dominate at smaller radii (see Figure 115).

In addition to any requirement on the PHD RMSIG for the resolution (see §5.2.4.2.), the dispersion effect directly leads to a requirement on the PHD width. If it is too wide, the events with a small pulse height on one arm will ghost onto the large pulse height events of the next arm. This can be prevented directly by reducing the percentage width allowed in the LUT spiral arms, or by setting the discriminator levels to restrict the width of the pulse height window. This will determine the width of the spiral arms. However, if the discriminator levels are set close, and the PHD is not fully contained within those limits, there will be an error in the intensity measurement proportional to the number of events being rejected. Thus there is a trade-off between ambiguity in the

result due to ghosting, and accurate intensity readings. The ideal is to find the plateau region where a change in charge cloud extent does not greatly affect the radius of the spiral.

Another trade-off in this context is the number of spiral arms in the pattern and the difference in amplitude between them. It is desirable to have a large number of spiral arms, because the longer the spiral arc, the greater the possible position resolution. However, the distance between the arms has to be large enough to accommodate the range of charge cloud sizes without leading to ghosting. The extreme outside and inside arms must themselves be compatible with the same range of charge cloud sizes.

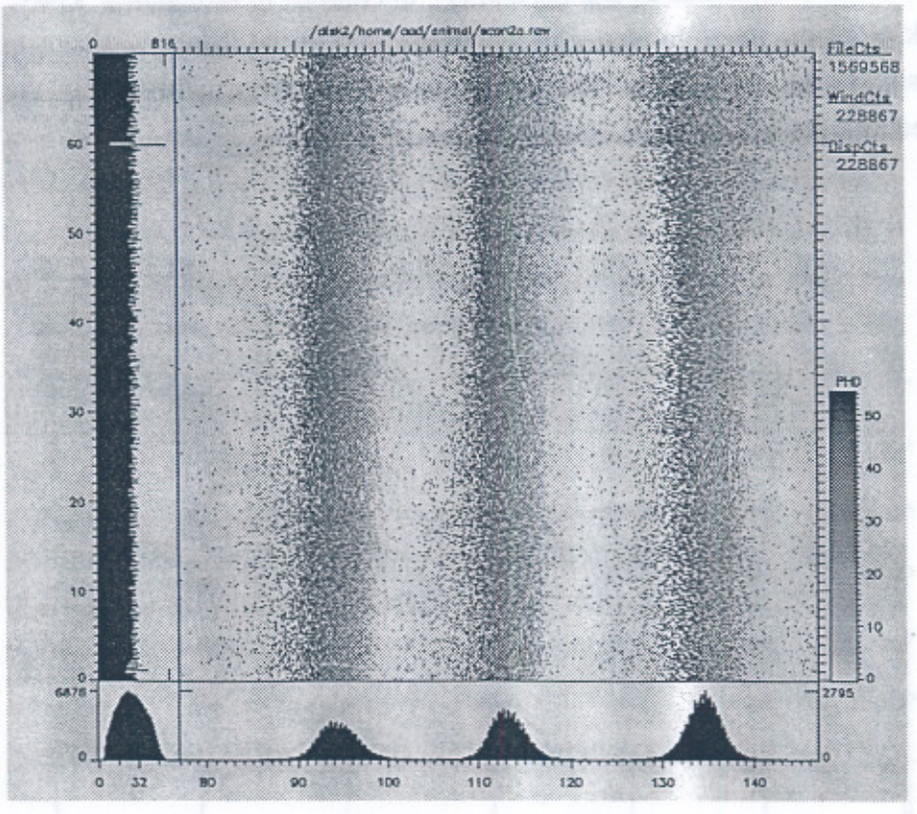

Figure 115. Dispersion effect in a spiral polar plot.
This image was taken with the RM with the UV spectral line scanned across the front face.

Although closely related, the effects of quantity of charge (*i.e.* gain) and of spatial extent (*i.e.* spread) have to be dealt with separately. A FORTRAN model (Breeveld *et al.*, 1992) was written to try to understand and quantify these effects. In the program (*SINEMOD*), a charge cloud of a given size and shape, described by the parameters r_c, r_w and a_c from equation (106), is 'deposited' onto a sinusoidal pattern with the charge

cloud centre at different positions. Given an azimuthally symmetric charge cloud as described in §6.1.2., with its centre at (X,Y), the quantity of charge gathered by each electrode is numerically integrated with a scale of 1 µm. From this a *measured* position (X',Y') is determined using the centroiding algorithm (given in equation 99). Modulation (§6.1.1.) is measured as the displacement of (X',Y') from the true centre position (X,Y). The program allows the scale parameters of the charge cloud distribution, $N(r)$, to be varied to examine the effects on modulation or spiral radius reduction. The calculation can be done for charge cloud centres at any position relative to the anode.

The model assumes three independent ADCs digitising the value of charge collected on each electrode as Q_a, Q_b and Q_c. In contrast to ratiometric ADCs, this uses the stack of all the possible planes in which the sum of the values is a constant, before normalising to the unity plane. The performance with different PHDs can therefore be compared in order to assess the effects of quantity of charge.

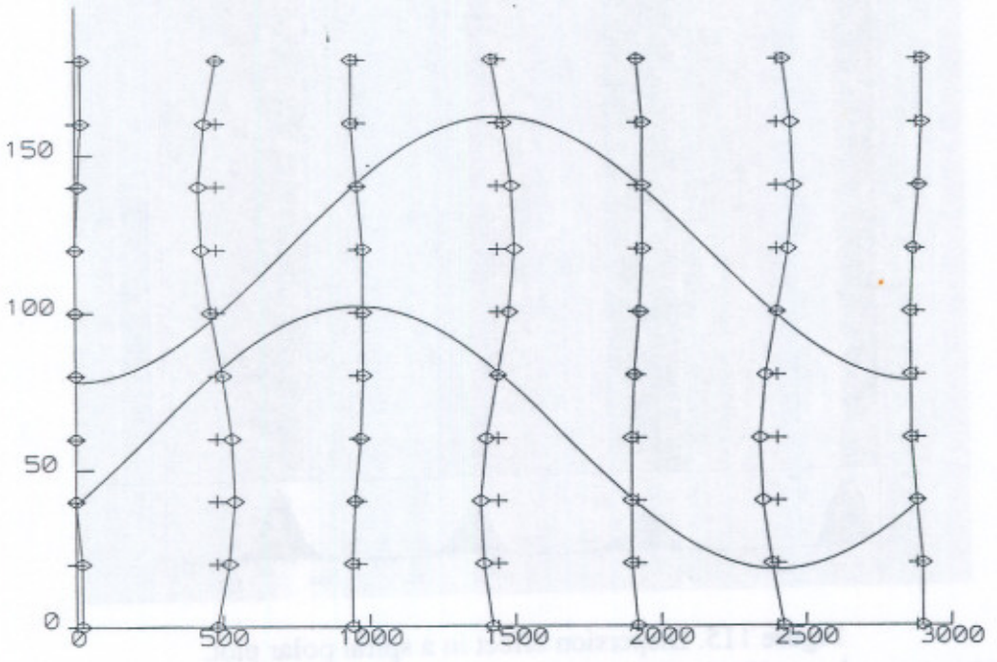

Figure 116. Modelling modulation.
The x-axis is the direction of measurement. The total length of the x-axis is 9 mm, (there is a scale factor of 3). The y-axis is 500 µm. The modulation error has been exaggerated by 20 times.

One simplification in the model was to encode an anode which does not have a decreasing sinusoid amplitude with each turn, but which has just one cycle repeated indefinitely in the x and y directions. This results in a single circle (ring) in the

$Q_a + Q_b + Q_c = 1$ plane which allows easy measurements of the resulting radius to be made. Additionally, it allowed an array describing just the one anode cycle to be used. The code was optimised to run as quickly as possible, but the large number of floating point calculations which were needed meant that a small charge cloud (1 mm radius) positioned at 70 different points, took about 5 hours of CPU time.

For the first tests the charge clouds were normalised to examine the effect of spatial extent only. The centre and wing parts of the calculation could be done either together, or separately and then summed with different weights to investigate the effect of varying a_c. Charge clouds of different spatial parameters were compared.

Figure 116 shows a typical output from the program. The underlying anode shape is shown with input and calculated centroid positions superimposed. The program also gives histograms of the errors. The radius of the resulting ring on the $Q_a + Q_b + Q_c = 1$ plane is also calculated.

The spiral pattern parameters used in the program were from the GIS development model: repeat pitch 500 µm; sine wave maximum amplitude 117 µm and wavelength 8 mm. The charge cloud distributions were taken from Edgar *et al.* (1989) and therefore correspond to a chevron of double-thickness MCPs, rather than the GIS *z*-stack, although the other MCP parameters were the same.

Because the charge cloud wings decay exponentially, an upper limit has to be placed on the radius to be included. The radius containing 99% of the charge was found to give accurate results: using a larger radius changed the results insignificantly, by less than 1%. It can be seen from the figure that there is position uncertainty produced by modulation where the error on X varies with Y, ($\Delta X(Y)$). There is also a non-linearity because the mean error, averaged over y, varies with X, ($\Delta X(X)$). The best results in both position uncertainty and non-linearity are obtained by a fairly large central component ($r_c \equiv 0.7$ mm) with the majority of charge therein (>90%), corresponding to an anode gap voltage between 200 and 400 V. For example, for $r_c = 0.62$ mm, $r_w = 4.3$ mm and $a_c = 0.87$ gives an error of ±10 µm.

The number of bits of digitisation can be selected in the program. With a saturated PHD of about 50% FWHM, the ADC scale is arranged such that half the events fall below a value of 0.85×full-scale. To examine the effect of moving away from this optimum setting, the ADC scale can be adjusted.

The ring radius bears a direct relationship to the resolution; a larger ring intersecting more ADC values. The ring radius is affected by spatial extent as well as quantity of charge and therefore both have to be included in this study.

The larger the charge cloud the less the error on X, but the smaller the radius of the ring (R_r). Comparing the ring radius and position error, it is found that with sufficient spread for the lowest position error, *i.e.* least modulation, the ring is already reduced to about half its maximum size. With $r_w = 0$, it is possible to find a plateau where the large ring radius is retained with minimum position error, but this is unrealistic. Assuming that wings are unavoidable, the actual value of r_w has very little effect on the ring radius. The radius within which a certain percentage of charge lies is, in fact, more significant than the distribution of that charge.

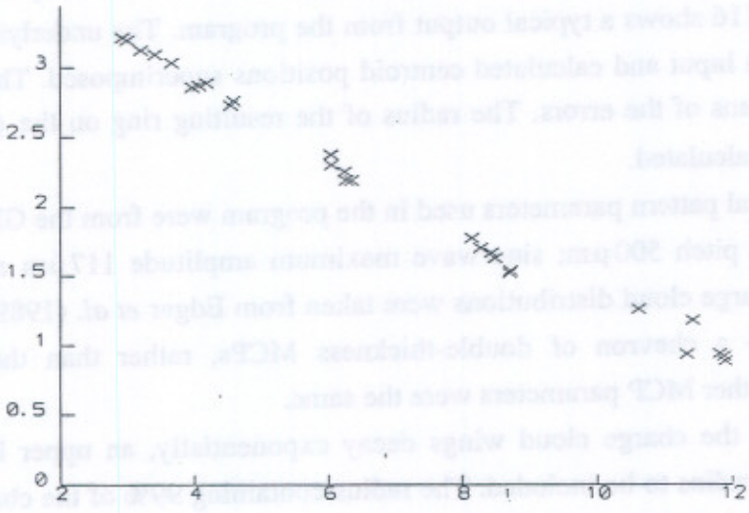

Figure 117. Radius of ring with radius of charge cloud (in mm).
The radius of the charge cloud is defined as that containing 99% of the charge.

Figure 117 shows a plot of ring radius as a function of charge cloud spatial size. A variety of real examples of charge cloud parameters, taken from Edgar *et al.* (1989), were modelled up to the radii containing 68%, 95% and 99% of their total charge, to see whether there was a critical radius. Each of these gives a straight line. At the 99% level as in Figure 117 the line can be fitted to:

$$R_r \propto \frac{-1}{4} \times R_{cc} + 3.9 \text{ mm} \qquad (107)$$

where R_r is the ring radius and R_{cc} is the charge cloud radius to 99%. The error on the radius of the resultant ring (ΔR_r) is found to be proportional to the modulation error (ΔX) and this is found in turn to be proportional to the radius (R_r) cubed.

The width of a resolvable line is proportional to the error on the position measurement, and inversely to the spiral length *i.e.* resolution is proportional to $\Delta X/R_r$. Figure 118 shows how small changes in the core parameters r_c or r_c/a_c can significantly

change the resolution, as measured by $\Delta X/R_r$, while there is a large scatter from the wing parameter r_w.

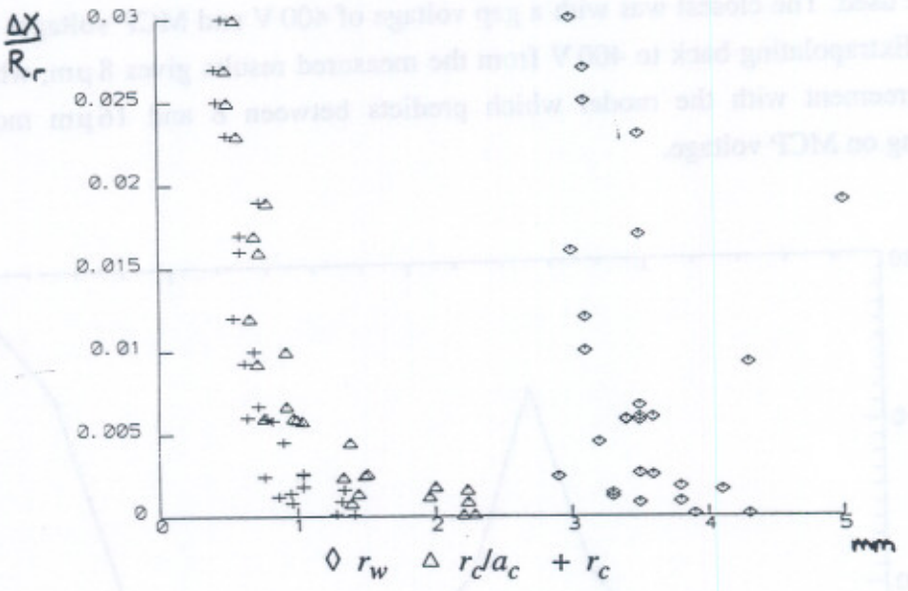

Figure 118. Resolution, or modulation error, vs. charge cloud parameters.

A relatively tight FWHM (<80%) is required to prevent an overlap of the spiral arms and so to ensure the uniqueness of the final derived position. A more robust method than relying on a well behaved PHD is to correct for the radius pulse-height dependence during position decoding by using the substitution:

$$R' = R + \alpha . ph \qquad (108)$$

where R' is the corrected radius, R is the original radius obtained from the transformation and polar equations, ph is the pulse height and α is the correction variable. This correction is straightforward to undertake if all the electrode signals are digitised or if a separate value of pulse height is associated with each event. In the case of using a LUT, it would be necessary to apply some real time correction to the values being used to address the LUT, or else to use a stack of LUTs: one for each value of *ph*. However, because of the limited resources available within the GIS instrument it has not been possible to associate particular events with their pulse heights. The PHD information is a random sample from the events collected. No pulse height correction can therefore be made.

6.1.4. Measured interaction—modulation

Modulation was measured using the development model by moving the detector up and down relative to a pinhole fixed in position (see Figure 119). The MCP voltage throughout was 3.05 kV. Gap voltages were varied between 500 V and 1100 V and

modulation increased smoothly through that range from 13 µm to 63 µm (peak to peak error). In the model, only voltage configurations which had been measured by Edgar could be used. The closest was with a gap voltage of 400 V and MCP voltages of 2.8 or 2.9 kV. Extrapolating back to 400 V from the measured results gives 8 µm, which is in good agreement with the model which predicts between 8 and 16 µm modulation depending on MCP voltage.

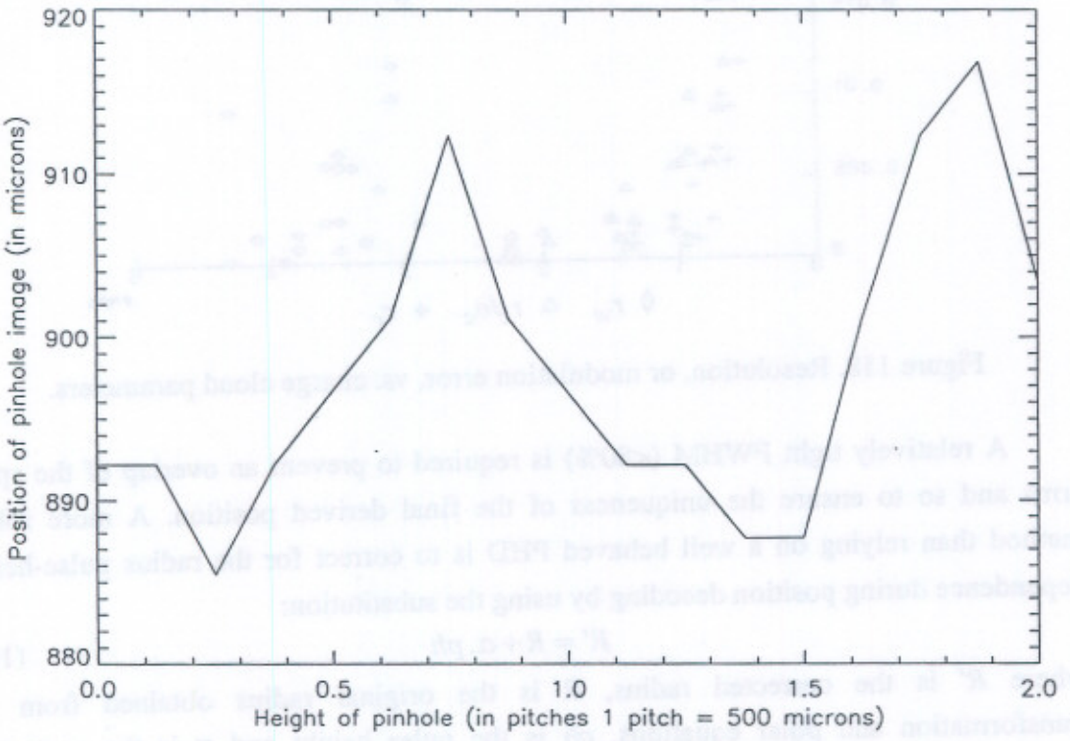

Figure 119. Modulation observed with development model detector using an MCP voltage of 2840 V and gap voltage of 1020 V. This 27 µm modulation was observed as the pinhole was moved across two pitches. A slight misalignment with the anode and the pinhole movement axis can be seen in the rising of the pattern from left to right.

Modulation is also thought to be the cause of the triplet effect with the development model detector when using the slit mask described in §4.8.3. The slits were in three rows, (see Figure 82). In the polar plot the radius of the slit images varies in triplets (see Figure 120). The PHD in each slit image is the same, so that the effect is not caused by charge cloud size or count rate. The only explanation is that each row corresponds to a slightly different level with respect to the anode pattern pitch and therefore it is modulation that is being observed. The slits were 2 mm high and the rows

1 mm apart. With a pitch height of 390 µm, the centres of the slits in each row correspond to a third of a pitch height apart.

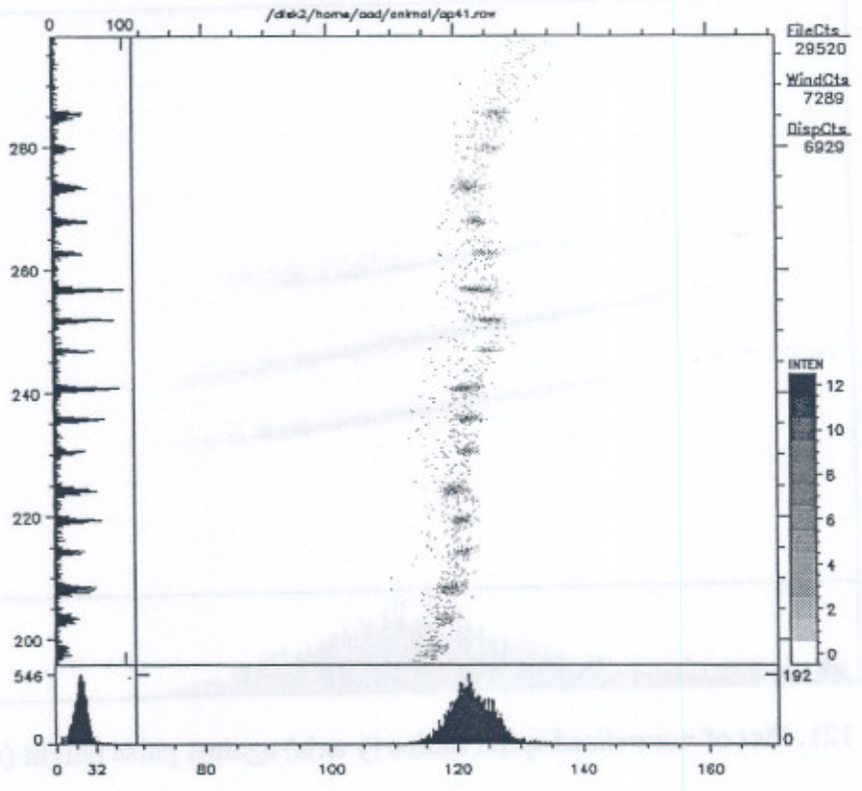

Figure 120. Slit mask polar plot from development model detector showing modulation. The plot is of angle vs. radius (arbitrary units).

6.1.5. Measured interaction—convolution

With the development model detector, an early experiment showed how the spread of the charge cloud could affect the radius of the output spiral. Keeping the MCP voltage constant, the MCP-anode gap voltage was varied between 100 and 850 V. Between 100 V and 700 V there was an 18% decrease in the radius of the spiral. Increasing the gap voltage further did not alter the radius much more. There was a tendency for the outer arms to become bunched closer together. There was no apparent change in the resolution of the detector throughout this range, as measured by the width of a slit image.

Using the development model detector, with every event assigned to a pulse height, it is possible to plot the normalised spiral radius, r, against pulse height. The result is a graph as in Figure 121. The straight lines are predicted by the model. The

parameter α is the gradient of the lines (see equation 108) and can be used as a measure of the 2nd order radius variation.

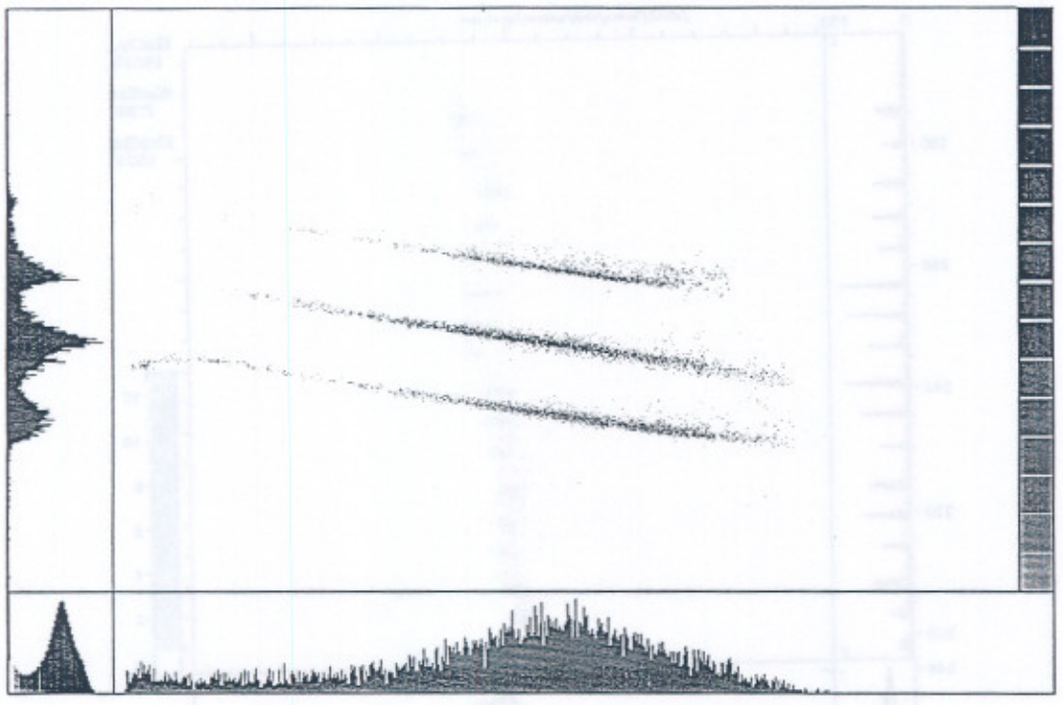

Figure 121. Plot of normalised spiral radius (y axis) against pulse height (x axis).

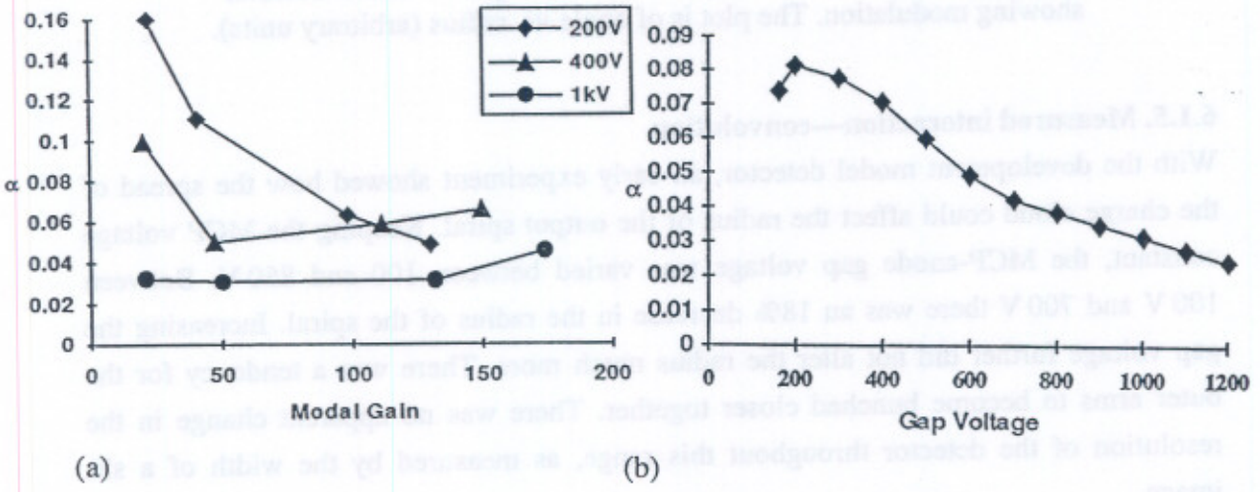

Figure 122. Plot of alpha against modal gain and gap voltage.
(a) Three different gap voltages are used. On *x*-axis 100=1×10^8 electrons. (b) The modal gain is 8×10^7 (equivalent to 80 in plot a).

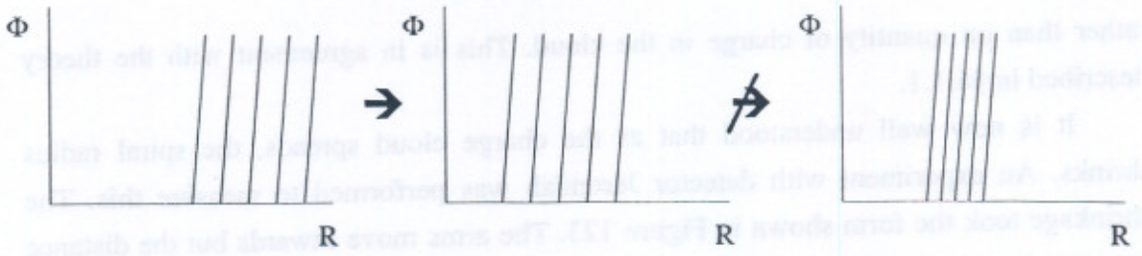

Figure 123. Shrinkage of spiral radius with charge cloud spread showing the arms moving towards the spiral centre but not getting close together.

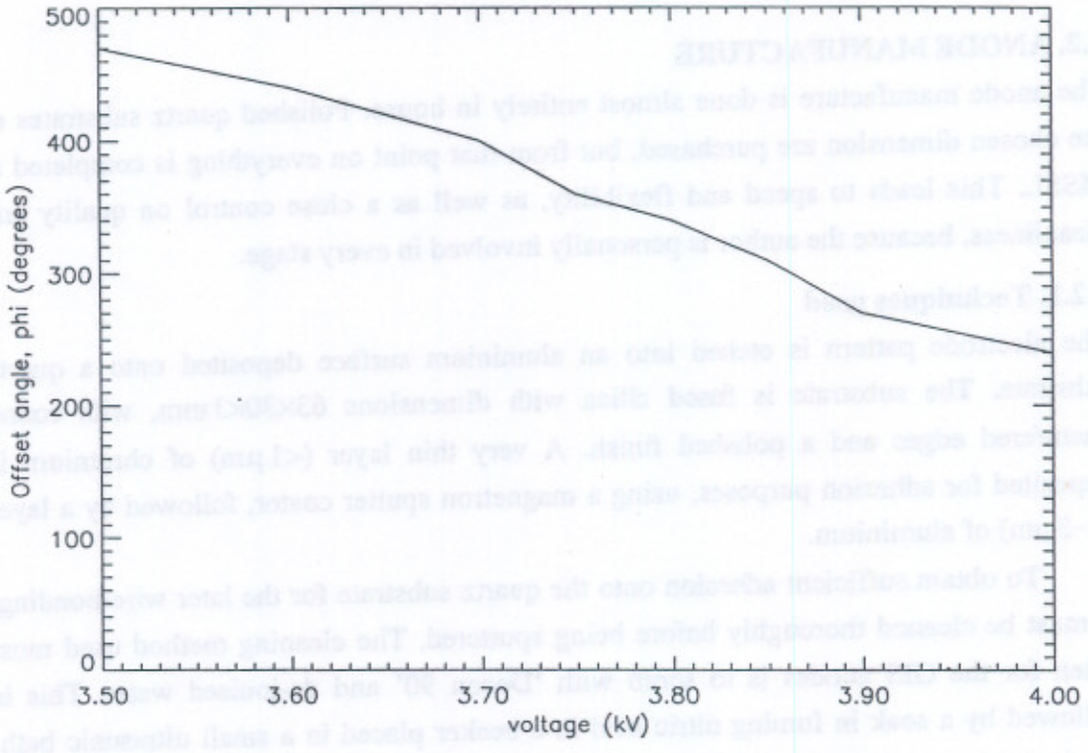

Figure 124. Change in the offset angle with gain.
Measurements taken with Jeremiah using the UV spectrometer.

The parameter α was calculated for a number of spirals obtained at different gains. It was calculated automatically for a large number of data sets using a Hough transform program. Plots of α against gain and also against anode gap voltage are shown in Figure 122. It transpires that α is very sensitive to gap voltage and fairly insensitive to gain at higher gap voltages. However, gain is independent of gap voltage. This suggests that α does not depend on the quantity of charge, but only on its distribution, as controlled by the gap voltage. Therefore, spiral radius does indeed depend on the charge cloud spread

rather than on quantity of charge in the cloud. This is in agreement with the theory described in §6.1.1.

It is now well understood that as the charge cloud spreads, the spiral radius shrinks. An experiment with detector Jeremiah was performed to measure this. The shrinkage took the form shown in Figure 123. The arms move inwards but the distance between them is maintained. The fit parameter k therefore can stay constant, if the offset φ and the starting arm number are changed. The change in offset is plotted in Figure 124. This covers a change in modal gain between 4×10^6 at 3.5 kV and 5.2×10^7 at 3.95 kV.

6.2. ANODE MANUFACTURE

The anode manufacture is done almost entirely in house. Polished quartz substrates of the chosen dimension are purchased, but from that point on everything is completed at MSSL. This leads to speed and flexibility, as well as a close control on quality and cleanliness, because the author is personally involved in every stage.

6.2.1. Techniques used

The electrode pattern is etched into an aluminium surface deposited onto a quartz substrate. The substrate is fused silica with dimensions 63×30×3 mm, with round chamfered edges and a polished finish. A very thin layer (<1 μm) of chromium is deposited for adhesion purposes, using a magnetron sputter coater, followed by a layer (2–3 μm) of aluminium.

To obtain sufficient adhesion onto the quartz substrate for the later wire-bonding, it must be cleaned thoroughly before being sputtered. The cleaning method used most often for the GIS anodes is to scrub with 'Decon 90' and de-ionised water. This is followed by a soak in fuming nitric acid in a beaker placed in a small ultrasonic bath. De-ionised water is used to rinse. An air gun dries the substrate so that water stains do not appear. After cleaning, the anodes are immediately coated and then kept continually in the clean room (class 100) in boxes to protect them from damage or contamination. All the detector assembly takes place in an air flow cabinet (typically better than class 10) in the clean room to protect the MCPs and anode from contamination by particulate matter.

6.2.1.1. Coating

Two substrates can be mounted in the sputter coater at once, in a specially made jig which masks the edges where aluminium is not required. The jig is bolted to the inside of the lid on a rotating table so that each substrate can be held directly over the target metal while coating.

Once in the sputter coater the substrates are further cleaned by using a glow discharge before starting the deposition. After the vacuum has reached about 2×10^{-6} mbar, using liquid Nitrogen to cool the diffusion pump, the pump valve is partly closed and argon gas bled through a needle valve into the chamber until a pressure of 4×10^{-3} mbar is reached. The lower the pressure used, the lower the final coating resistance. However, if it is too low, the laser-machining becomes more difficult. The chromium layer is deposited first using 100 W power and exposing the substrates for about 20 s each. For aluminium, 300 W for 4 minutes is used.

The metal is very soft so the surface of the anode must not be touched at all after coating, except by the wire-bonding tool.

6.2.1.2. Laser-machining

After coating, the anode pattern is cut into the metal layer using a laser, which removes insulating strips approximately 30 µm wide. A high degree of precision is required to manufacture the pattern to satisfactory tolerances. The laser is a 15 W, single-mode, ruby infrared, NdYAG (neodymium, yttrium, aluminium, garsonide) laser. The anode is mounted into the polycarbonate detector base plate into which the Oxley pin feed-throughs have already been fixed and the electrode contact wires soldered to them so that no soldering need be done near the anode—any solder or flux splash on the delicate pattern could ruin it. It is appropriate to mount the anode before laser-machining so that the pattern is aligned with the base plate rather than with the edge of the substrate. It is this base plate which is aligned to the Rowland circle via the detector housing.

The base plate plus anode is mounted flat in a jig on a precision co-ordinate table, 150×150 mm, controlled by a PC with a positional accuracy of 1 µm. The laser is stationary above the table and is focused onto the substrate. The SPAN pattern is drawn at 45° to the table axes, and all lines are drawn sequentially and uni-directionally, so that at all times the effects of hysteresis in the motors are negligible and any thermal expansion that takes place during the 7 hours will not cause an offset between the lines.

The table speed and laser Q-switch frequency (both specified in units of 500 ns) are selectable, allowing the laser to be switched off by turning off the Q-switch while the co-ordinate table moves the substrate to a new position to start laser-machining. The pattern drawing software is written in FORTRAN and linked to C subroutines which draw straight lines, circles *etc.* in terms of 1 µm steps. The C subroutines were written by Walton, MSSL. Before starting, the focus of the laser is checked and the table speed, Q-switch and laser current are selected by running tiny test spiral patterns on one corner of the anode which will be part of the 'anode surround'. Poor focusing may give lines in the x direction which are narrower than in the y direction. Poor selection of power,

Q-switch and table speed parameters can give jagged or incomplete lines. Typical values are table speed: 1 mm s^{-1}; Q-switch frequency: 3.2 kHz and current: 27.5 A. The alignment is then set up by repeatedly running the camera along the edges of the base plate, before the laser is switched on. The pattern software calculates the starting position from the corners of the substrate.

The 12.5 and 25 µm shims fitted between the MCPs are cut out by the same laser. The advantage, apart from accuracy and ability to cut without crinkling up the shim material, is that the laser does not leave burrs on the edges.

6.2.1.3. Wire-bonding

After laser-machining, ultrasonic wire-bonding is used to interconnect the elements of the non-continuous electrode. The technique of wire-bonding was taken from the integrated circuit manufacturers, where it is used to bond the chip electrically to its carrier. At each end of the wire bond, the 'footprint' is controlled by pre-set power and time parameters. These can be adjusted to optimise the bond strength without vaporising the aluminium wire. Wire bonds are small and lie close to the anode surface which makes them ideal for use in a gap which has a high field strength.

Two bonds are made per electrode element. The wire is 25 µm thick, pure aluminium. As long as the anode is sufficiently clean, the wire-bonding is very reliable with no failures having occurred in the interconnects during anode use or vibration tests. If the adhesion is not good, the bonds tend to lift the aluminium from the anode as the footprint is made. In this case the anode is discarded. The back of the substrate (the front will be permanently scarred by the laser) can be re-used once the coating has been removed. To prevent wasting time and substrates, a few wire bonds are tried out between coating and laser-machining to check adhesion.

Wire-bonding is also used to connect between the anode pads and the pin feedthrough heads. These bonds have to be more than 3 mm long and are formed in a loop for strain relief. To add security, two footprints are made at each end, so that if the bond is put under stress pulling one footprint from the surface the other may still hold. Eight bonds per contact are made, this being the maximum number which can easily be fitted into the space. On one of the flight detectors more than 50% of these wire bonds did fail during the building of the rest of the detector. On close inspection, the problem was traced to using too much power and almost burning through the heel of the bond. The footprints were still attached to the anode surface.

Wire bonds that come loose could short out the anode or, in zero gravity, float freely with other dangerous consequences.

Once all the bonding is complete, the anode is checked for shorts between electrodes using resistance, and for continuity using capacitance. Shorts are usually due to a small piece of metal bridging one of the laser-machined gaps. These are difficult to find because of the long total length of insulating gap. They can often be removed by blowing with an air gun, but can appear at any stage during the detector build which is why clean conditions are essential. Sometimes a bridge is left after laser-machining where a piece of dust does not allow coupling of the laser beam with the aluminium. These can only be found through a microscope and removed by running the laser to and fro across the short. At first, shorts frequently occurred where one line met another, because it is hard to cut through the 'wall' of melted aluminium which forms either side of the laser line. Pauses were added to the software at these points to dwell long enough to break through the wall. Attempting to make the insulating lines narrower than about 20 µm can also lead to shorts because the laser power simply is not high enough to cut through any debris or dust.

6.2.2. Polyimide

One major concern with the anode manufacture was the use of quartz as the substrate. Quartz is a brittle material so that there is no inherent mechanism to stop propagation of cracks. It is impossible to test the strength of the quartz to be used in flight, because any stress from the testing will lead to micro-cracks which will not show until the quartz breaks suddenly after further stress. Another problem with quartz is the difficulty in making permanent contacts with it for stim pads or external connections. Quartz is also difficult to manufacture to the required tolerances and difficult to mount in a way that avoids stress.

Although the problems with stim pads, mounting and external contacts have been solved satisfactorily for GIS, a non brittle material would have had significant advantages with its ease of machining, the ability to have bolts put through it *etc.* A programme was therefore initiated to investigate possible alternatives. The most probable materials were polycarbonate and sintimid, a type of polyimide.

It was necessary to be able to coat the materials, obtaining a good adhesion, to form insulting gaps in the coat by laser-machining and to wire bond to the coated surface. Only when all these properties were established could a material be used to manufacture a test anode.

Coating either polycarbonate or polyimide was successful. In cutting polycarbonate with the laser, the cut lines were always partly conductive, as the polycarbonate burned in the laser beam and a carbon deposit was left. However, it was possible to laser-machine polyimide. Wirebonding would also work using a softer

aluminium wire than normal, if the coating was thick. The coating never looked as pure as with quartz, but this was understood to be due to the fact that the substrate surface was rougher. The polyimide material was therefore put forward to be tested as an anode.

A piece of polyimide was shaped and polished to a shape and form which could replace both the anode and polycarbonate base plate in the development model detector. The polished surface was coated with chromium and 8 minutes of aluminium. It was machined with the standard pattern, using 25 A at 4 mm s^{-1} and 125 Hz Q-switch; then wire-bonded and mounted in the detector.

The resistance between the electrodes was infinite, but the capacitance was 280 pF between any pair, which was high. Contacts with the anode were made by bolting solder tags to the anode surround and wire-bonding to the bolt head. It was this which inspired the use of wire-bonding to the Oxley pins in the flight design.

Eventually the anode was ready to use. At first the anode was held at high voltage with the MCP front face at ground. Later the anode was grounded.

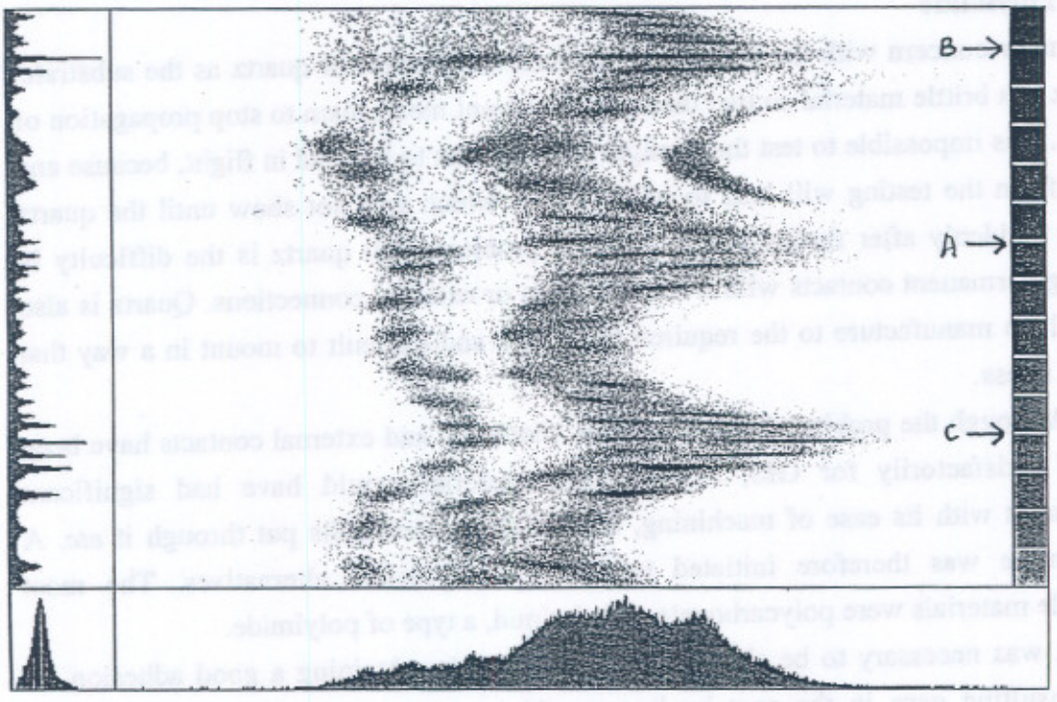

Figure 125. Output from development detector with a polyimide anode.
The output from this detector is completely useless. A slit mask was used with this detector which explains the blobby look of the output.

A number of MCP voltages and MCP-anode gap voltages were tried. The slit mask which had been used on the development detector for resolution measurements

was inserted. Flat fielding was also tried. However, it was impossible to get a sensible image out of the detector (see Figure 125). Perhaps the capacitance was too high, even though the material was chosen specifically for its low dielectric constant, leading to very high dynamic crosstalk (see §6.5.4). Maybe the surface properties made the material unsuitable because of secondary electron emission (see §6.5.3). Further work is needed to establish the reason for failure. Thus quartz is still used for the GIS.

6.3. ANODE PATTERN PARAMETERS

For a given electronic charge resolution and detector gain, the position resolution is dependent on the arc length of the spiral. This length can be maximised by choice of the best pattern and detector geometry. Trade-offs due to charge cloud effects have to be taken into account.

The laser may be used to machine gaps from 10 to 80 µm wide. For the anode, an insulating gap of 20–25 µm was found to be the narrowest which could be reliably cut. Either side of the insulating gap lies a line of damaged aluminium a few microns wide. In view of this, the minimum electrode width was chosen to be 45 µm. The original patterns had minimum widths of 35 µm, but the 10 µm conductor left after cutting the insulating gaps was too narrow. It led to a high resistance along the electrode (undesirable for high speed operation), and was too easy to break, leaving part of the electrode electrically floating.

The selected coating times give a resistance of about 40 Ω from the end of one electrode element to the other. The resistance is highest at the narrow 45 µm parts of the element: ~0.6 Ω mm^{-1} as compared with 0.06 Ω mm^{-1} in the wide 215 µm part. Given a laser line width of 25 µm, and a value for the bulk resistivity of aluminium of 2.65×10^{-8} Ωm, these measurements suggest the aluminium coating thickness is about 2 µm. This has been confirmed recently by direct measurement (Worth, MSSL, private communication, 1995).

To eliminate modulation, the charge cloud needs to sample about 8 pattern pitches. Assuming a charge cloud of about 3 mm diameter (§6.1.2.1.), a pitch height of 390 µm was chosen; a number divisible by three being desirable for the three electrodes given the discrete nature of the laser co-ordinate table. The pitch height controls the inter electrode capacitance, affecting crosstalk and noise. At 390 µm the capacitance is already 290 pF between one electrode and the other two; a higher value would increase the electronic noise and hence reduce the resolution obtainable. Therefore the pitch height could not be any lower than this.

Once the pitch height and minimum electrode width have been chosen, the maximum electrode *amplitude* has to be $(390/3)-45=85\,\mu m$. The maximum electrode width then becomes $(390/3)+85=215\approx(5/9)\times 390$. This is the origin of the 5/9 factor described in §5.1.2.

Once the *amplitude* has been chosen, the minimum wavelength and the length of spiral needed to give the required resolution have to be determined. The major limitation to the number of spiral arms is the radial width of the spiral. The arms need to be well separated to avoid ghosting. For GIS a 10 arm spiral was chosen, with the outer 5 being used in the pattern (the wavelength of the inner arms being too short). With this and the maximum amplitude, the length of the spiral arc can be calculated, and scaled to match the length of the anode.

The minimum electrode wavelength should be no smaller than 8 times the pitch to avoid convolution leading to unacceptable radius reduction. For GIS, using the 10 arm spiral, the minimum wavelength (the 5th arm) comes out as 5 mm ($=13\times$pitch).

The MCP-anode gap and gap voltage also need to be determined to match the parameters. The gap was chosen to be 3 mm. The voltage was then selected empirically with the development detector as 350–500 V to give the smallest pulse height radius effect.

6.4. TESTING THE DETECTOR

Once the anode was designed and manufactured, it was tested and compared with the models used in the design. In §4.3. the non-uniformities arising from the MCP were discussed. The following sections give the results from pinhole and flat field experiments with the full detector, anode and flight electronics.

6.4.1. Anode stimming

To test out the design and manufacture of the anode, one was mounted on a travelling microscope, with the connections made to a set of preamplifiers underneath and thence to the analogue card via the analogue test box. A small probe connected to a pulse generator was lowered close to the anode so that there was capacitive coupling between the probe and the anode. The probe point was surrounded by a grounded collar, to prevent the area of the coupling from being unrealistically large. The pulses thus mimicked charge cloud events as detected by the charge amplifiers, the difference in response between this and a real charge pulse being due to a difference in pulse shape and the absence of partition noise. The probe could be moved evenly along the length of the anode or across it on the travelling microscope mechanism. The analogue test box

sent the anode signals from the analogue card to a PC where *ALLSINGN* was used to display the output.

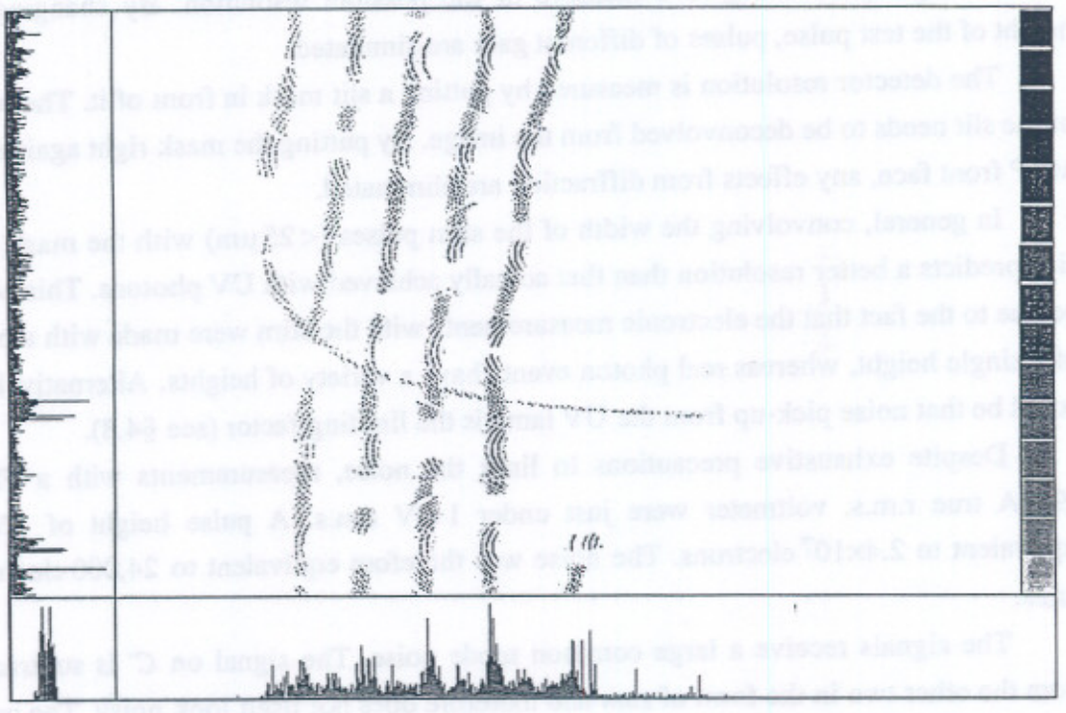

Figure 126. Spiral image obtained using stim probe, anode and travelling microscope.

Using the anode stim, it was possible to show that the front end electronics and the anode itself were working as expected. Near perfect spirals were obtained, showing that the design and laser-machining of the anode were accurate. Figure 126 shows one such plot. The stim shows up fixed patterning well because there are no charge cloud effects or PHD to mask it.

6.4.2. Resolution measurement

As described in §4.8. the resolution depends largely on the electronic noise level. It is difficult to simulate the flight grounding scheme in the laboratory, because nearly every piece of equipment is separately grounded to the mains supply. To overcome the large number of ground loops thus created, the chamber was chosen as the grounded star point. All pieces of electrical equipment were grounded to the chamber via thick screen cable and were isolated from mains earth by use of distribution boards and isolation blocks. There was still radiative noise from the UV lamp due to the magnetic field produced when the glow discharge is struck. Isolating the lamp did not stop this noise, which, on the oscilloscope, looked like a noisy pulse sitting on top of every real event. Screening the analogue card helped a little.

The contribution of the processing electronics to the resolution was measured by stimulating the anode directly using the stim pads and a pulse generator. The histograms of the images produced give a measure of the possible resolution. By changing the height of the test pulse, pulses of different gain are simulated.

The detector resolution is measured by putting a slit mask in front of it. The width of the slit needs to be deconvolved from the image. By putting the mask right against the MCP front face, any effects from diffraction are eliminated.

In general, convolving the width of the stim pulses (< 25 µm) with the mask hole size predicts a better resolution than that actually achieved with UV photons. This could be due to the fact that the electronic measurements with the stim were made with a pulse of a single height, whereas real photon events have a variety of heights. Alternatively, it could be that noise pick-up from the UV lamp is the limiting factor (see §4.8).

Despite exhaustive precautions to limit the noise, measurements with a Fluke 8920A true r.m.s. voltmeter were just under 1 mV r.m.s. A pulse height of 1 V is equivalent to 2.4×10^7 electrons. The noise was therefore equivalent to 24,000 electrons r.m.s.

The signals receive a large common mode noise. The signal on C' is subtracted from the other two in the form of *sum* and therefore does not itself look noisy. The noise appears as ballooning in the A' and B' region of the polar plot. The ballooning became more severe after the bias resistors between the electrodes were reduced to 100 kΩ (see §6.5.7.), although the noise increase was predicted to be negligible.

6.4.2.1. Modulation transfer function

A mask was made out of 30 µm thickness nickel shim material to clamp against the front face of the QM detector. The mask consisted of a series of square holes. One half of the mask has the holes in a square wave configuration for the measurement of the modulation transfer function (see Figure 127). Starting with a hole of sides 1 mm and a space of 1 mm (½ line-pair mm^{-1}), the hole and space size is decreased to 500 µm, then 200 µm, 100 µm, 50 µm, 40 µm and finally 25 µm. Each hole type occupies a 2 mm length of the mask. The contrast in the image produced is used as a measure of the resolution.

The contrast for each section of the MTF mask is found from:

$$C = \frac{I_{max} - I_{min}}{I_{max} + I_{min}} \qquad (109)$$

where I_{max} is the maximum intensity in the region, and I_{min} is the minimum.

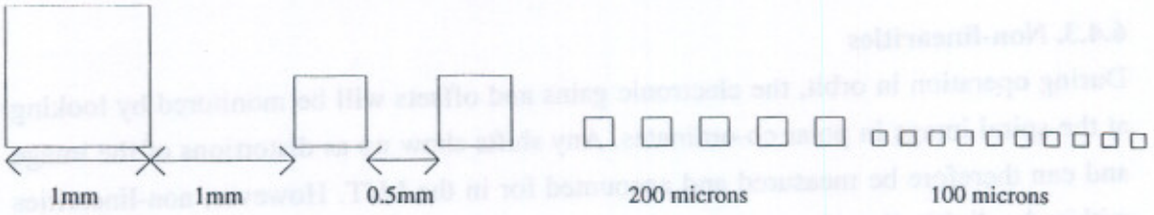

Figure 127. Part of Modulation Transfer Function mask.

To make the measurement, the QM detector was used with the filament as a source of electrons. A very low count rate was used ($100\,c\,s^{-1}$) to prevent any gain depression. Because most of the events fall in the large holes, an integration of 2×10^6 events was taken in order to obtain sufficient counts in the small holes. The high frequency noise, mostly due to fixed patterning, was removed using a fast Fourier transform routine. The smoothed image was then measured for maximum and minimum intensities. The graph in Figure 128 was obtained. The contrast is reduced to zero by 20 line pairs per mm. This therefore is the limit to the resolution, and corresponds to 50 μm, or 2 pixels.

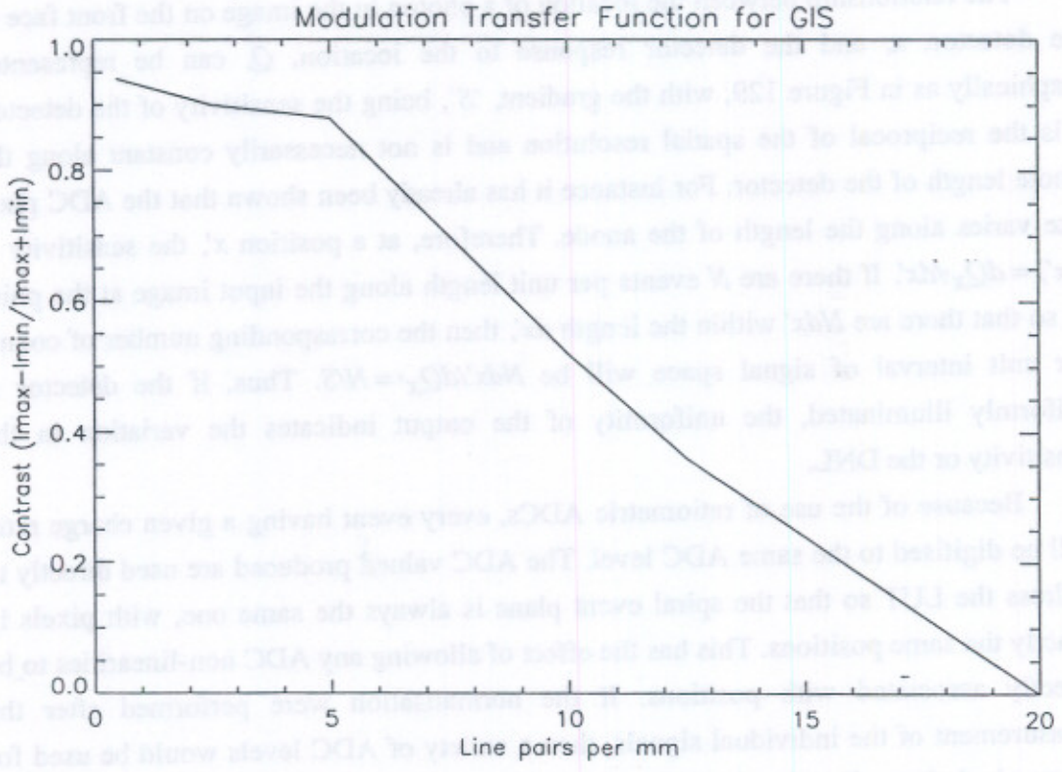

Figure 128. MTF for the QM detector with flight electronics.

6.4.3. Non-linearities

During operation in orbit, the electronic gains and offsets will be monitored by looking at the spiral image in polar co-ordinates. Any shifts show up as distortions of the image and can therefore be measured and accounted for in the LUT. However, non-linearities within the digitisation electronics or in the electronic gain of the amplification stage can lead to non-linearities in the output image.

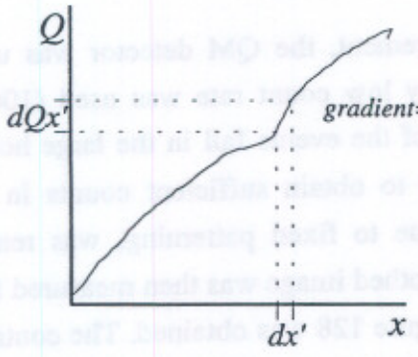

Figure 129. Detector response plotted against position.

The relationship between the location of a photon in the image on the front face of the detector, x, and the detector response to the location, Q, can be represented graphically as in Figure 129, with the gradient, 'S', being the sensitivity of the detector. S is the reciprocal of the spatial resolution and is not necessarily constant along the whole length of the detector. For instance it has already been shown that the ADC pixel size varies along the length of the anode. Therefore, at a position x', the sensitivity is $S(x') = dQ_{X'}/dx'$. If there are N events per unit length along the input image at the point x', so that there are Ndx' within the length dx', then the corresponding number of counts per unit interval of signal space will be $Ndx'/dQ_{x'} = N/S$. Thus, if the detector is uniformly illuminated, the uniformity of the output indicates the variation in the sensitivity or the DNL.

Because of the use of ratiometric ADCs, every event having a given charge ratio will be digitised to the same ADC level. The ADC valued produced are used directly to address the LUT so that the spiral event plane is always the same one, with pixels in exactly the same positions. This has the effect of allowing any ADC non-linearities to be directly associated with positions. If the normalisation were performed after the measurement of the individual signals, then a variety of ADC levels would be used for every pixel depending on the pulse height. In other words, a large number of spiral

planes would be used in the first instance, later reduced to one plane by normalisation. This would reduce the effect of any ADC non-linearity.

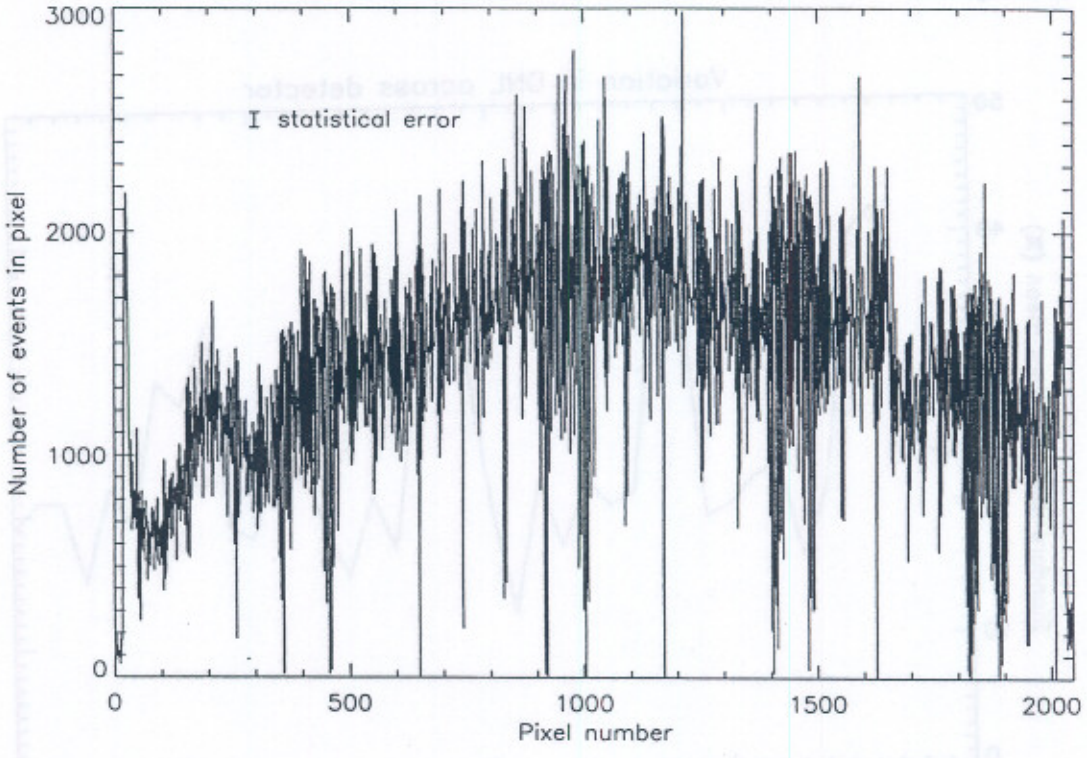

Figure 130. Flat field for differential non-linearity measurement taken with the QM detector with the mercury lamp illumination at a low count rate of 200 c s^{-1}.

Figure 130 shows a flat field taken for the purpose of measuring the DNL of the detector system with flight-style electronics. The setup was the same as that used for the lifetesting (§4.7.) with the QM detector. The Penray UV lamp was allowed to illuminate the whole detector front face at a low count rate, until 3 million events were collected. In order to measure the DNL, the mean counts per pixel and the standard deviation were calculated for each 50 pixel section. Dividing into sections minimised any contribution from the variation in the illumination level across the detector. The results are plotted in Figure 131.

The mean number of counts per pixel is 1455, for which Poisson statistics predict a random error of 2.6 %. The mean deviation is 27%, so the DNL contributes 26.8%. It can be seen that the linearity is limited by fixed patterning, which gives a non-linearity much higher than predicted by a purely random distribution. The error follows the phase

angles of the spiral arms, with four minima corresponding to the regions of maximum ballooning, as described in §6.4.2. At this phase angle the events cover many ADC digitisation elements. This confirms the fact that a wide spiral arm reduces fixed patterning.

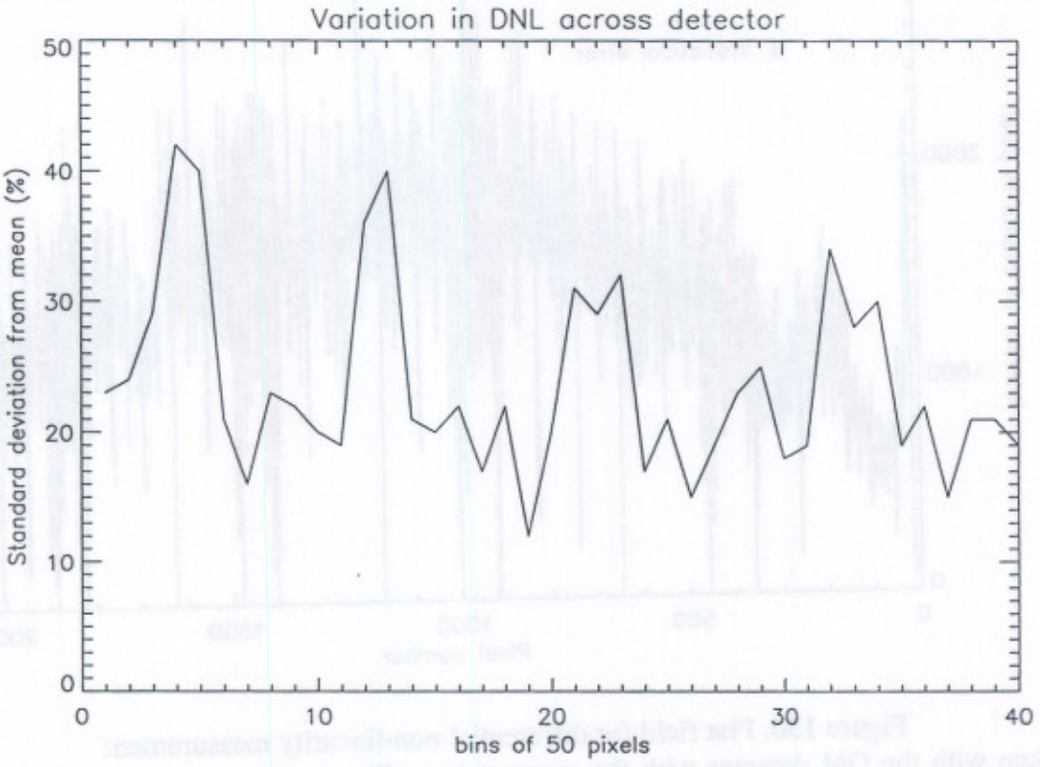

Figure 131. Standard deviation from the mean for the flat field illustrated in Figure 130, divided into 50 pixel sections. The mean deviation is 27±7% of 1455 c pixel^{-1}.

The mean deviation of 27% compares well with the values of 20–25% obtained from *GIS_SIM* for a variety of electronic noise levels. The shape of the flat field closely matches that of Figure 102.

Section §4.3.1.2. presented a similar measurement with the RM detector using 10-bit electronics and a beam of illumination scanning the front face. The measured DNL was 3.1%, which is considerably lower than in this case. Comparing the results illustrates the increase in DNL with the 8-bit fixed patterning.

To measure the integral non-linearity of the same detector, the calculated and measured positions of the centres of the holes in the MTF mask were compared. For the larger slits, the image was flat-topped and the centre position was calculated by

measuring the position of the edges of the image. For the narrower slits, the images were fitted with Gaussians and the centre found in that way.

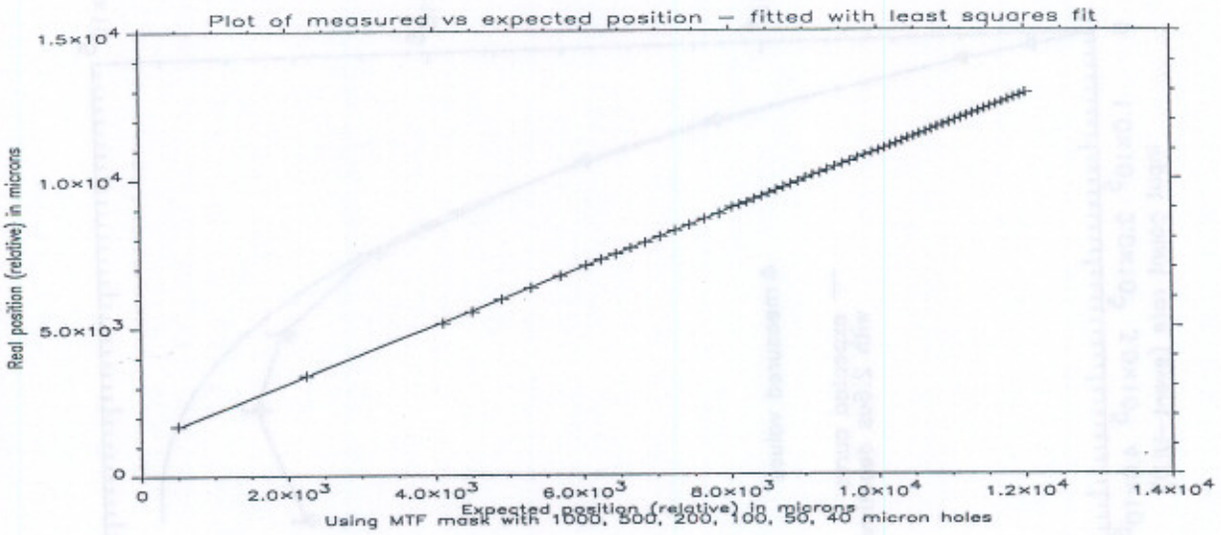

(a)

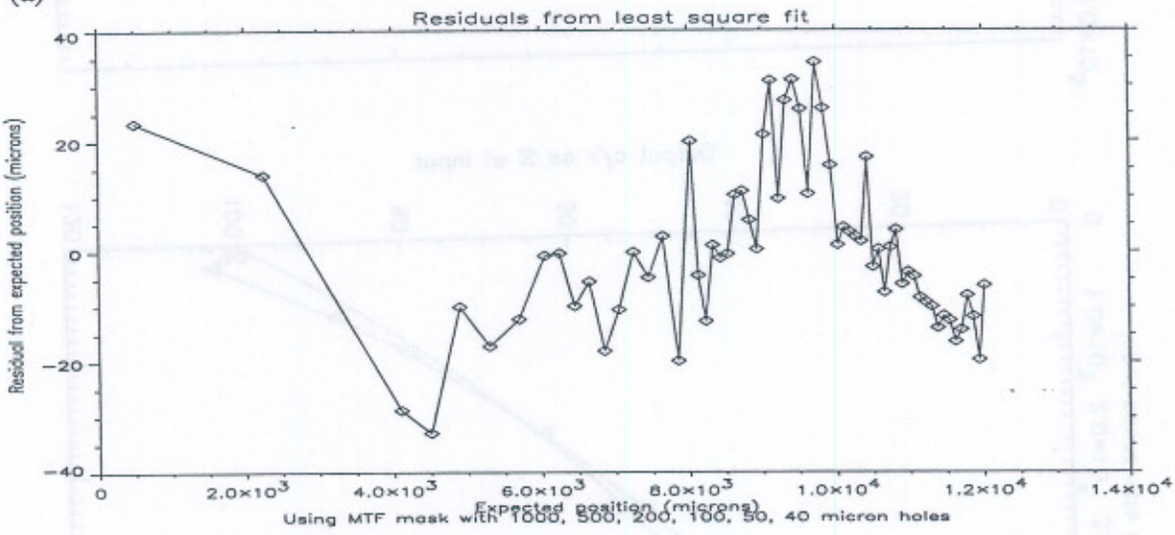

(b)

Figure 132. Integral non-linearity as measured using MTF mask.

Figure 132 (a) shows the measured positions plotted against calculated positions. A least squares fit line is plotted over the top. The scale is in microns. The origin for calculation and measurement was arbitrary, so the line does not go through (0,0). Figure 132 (b) shows the residuals of the measured position from the least squares fit line. It suggests that measuring the centre position of the larger images is not as accurate as measuring the smaller images using Gaussian fitting. If these larger holes are ignored,

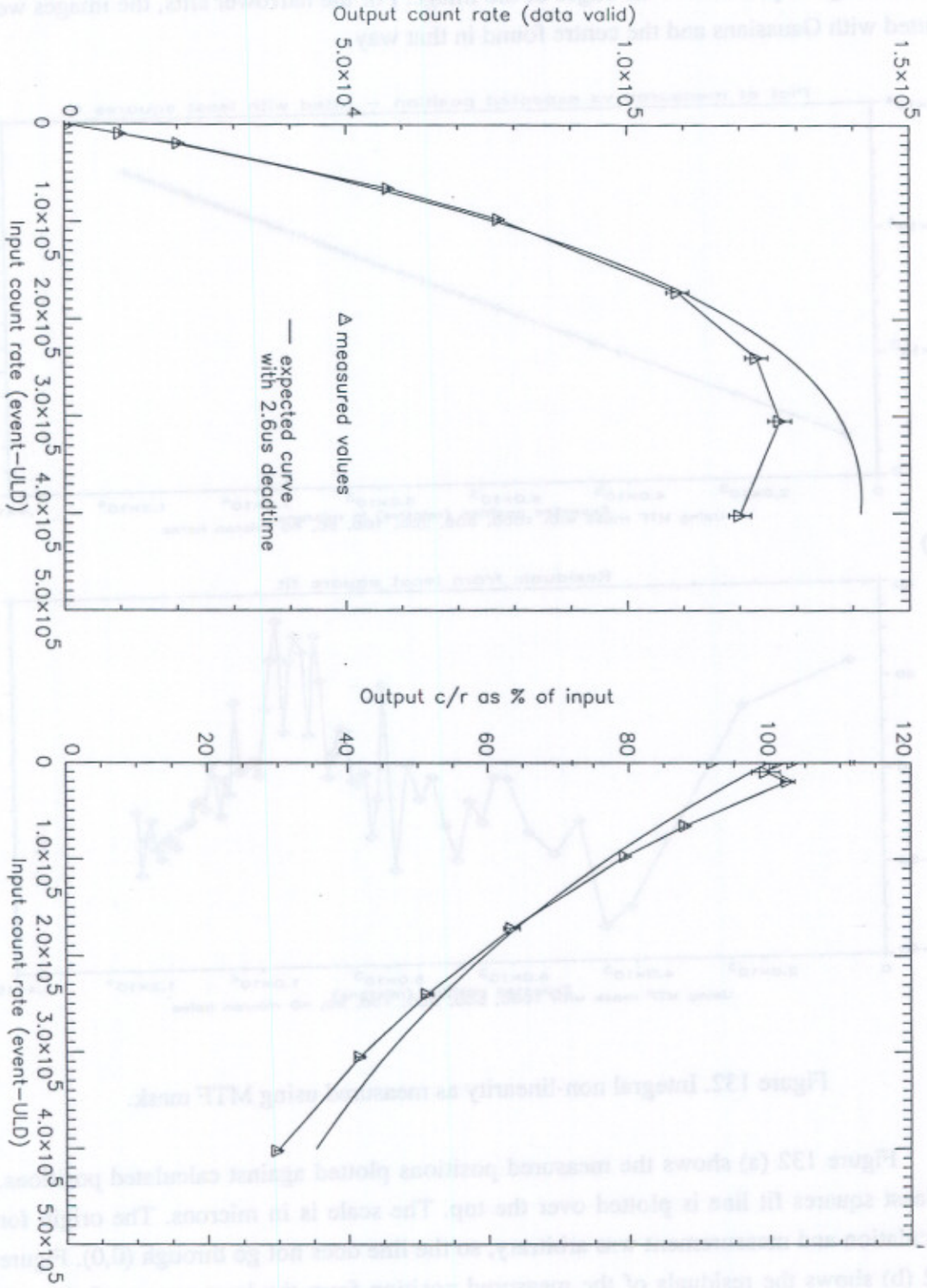

Figure 133. Plot of relationship between output and input count rates. The dead time used in the fit is 2.6 μs. The curve rolls over at higher count rates leading to a reduction in output count rate at very high input count rates.

then the maximum non-linearity is +34 µm to −19 µm or ±26.5 µm or ±1.06 pixels. The distortion parameter, as described in §4.3.2., for this data is 0.03%. This is within the requirement of 0.1% non-linearity and is similar to the values of ±19 µm predicted by the model (see §5.2.5). This level of non-linearity compares favourably with the measurements made with laboratory electronics and given in §4.3.2., where the poor performance of one channel produced a non-linearity of ±2 pixels with a distortion parameter of 0.08%. The prediction in §4.3.2. was that a distortion parameter of 0.025% should be obtained for ADCs meeting the INL requirement of 0.5 LSB.

6.4.4. Throughput

The maximum count rate for an individual detector is limited by the analogue dead time. An experiment was devised to measure this using the QM detector, analogue card, analogue test box and a count rate meter. The setup was the same as that used to measure the detector DNL, with the UV Penray lamp illuminating the whole front face of the detector.

The analogue test box has various test pins for the connection of oscilloscope probes to examine the 'event', 'data valid' and 'ULD' signals. The probes could be plugged into the count rate meter instead of an oscilloscope. The event signal is high whenever an event is large enough to reach the LLD or above, and is counted as the raw data count rate by the GIS processor. The data valid signal is only high if the pre- and post-event dead times are empty of other events, and if the event is not sufficiently large to reach the ULD. This becomes the processed event count rate. In normal operation, the data valid signal is not reset until the event is read by the processor (or the PC). It had to be adapted for this experiment to reset after every event.

A gain was chosen that gave very few ULD events. The input count rate was altered by opening and closing the diaphragm in front of the lamp. For every rate, both the event and data valid count rates were averaged over at least 20 readings. The difference between them is due to the analogue dead time and is plotted in Figure 133. The expected curve, with 2.6 µs dead time, is plotted on the graph for comparison. In fact, a 2.8 µs dead time curve fits better. The MCA was used to check the readings and was consistent up to about 1×10^4 c s^{-1}, at which rate the MCA dead time started to dominate.

Locking

During the all-up test, with all four detectors plugged into the GIS electronics box for the first time, there was blocking of data between the detectors. With the stims on, occasional data from only one detector was received in the science stream although the

count rate monitors on all four detectors looked normal. However, the data was always received correctly with only one detector enabled.

Two effects became apparent. First, the routing of the signal cables from the detectors was too close to one another in the vacuum chamber and the stim signals were synchronising with each other. This led to the second effect which was due to the detector selection, where the detectors are serviced on a first-come-first-served basis. The events from only one detector were being reliably received if the other detector signals were following close behind. The selection process rejects both events if they arrive too close together in time.

The problem was corrected by filtering the signal line on the detectors so that the stim oscillators did not lock together. However, the question arose as to how the count rates were correct while the events were not in fact being seen. This was understood by looking at the logical sequence in the GIS digital electronics (see Figure 134). When an event is detected on the analogue card, a raw event counter is incremented. A 'data valid' signal is sent from the relevant analogue card to the '1 of 4 select'. The data valid increments a processed event counter. A 'select data' signal is sent in reply to the detector sending a data valid signal, which then delivers the data to the FIFO. Meanwhile a 'not Acknowledge' signal is sent to the other three to prevent them from producing another event until the first one has been received at the FIFO. If another event is registered within 600 ns it is therefore ignored and the processed count is not incremented.

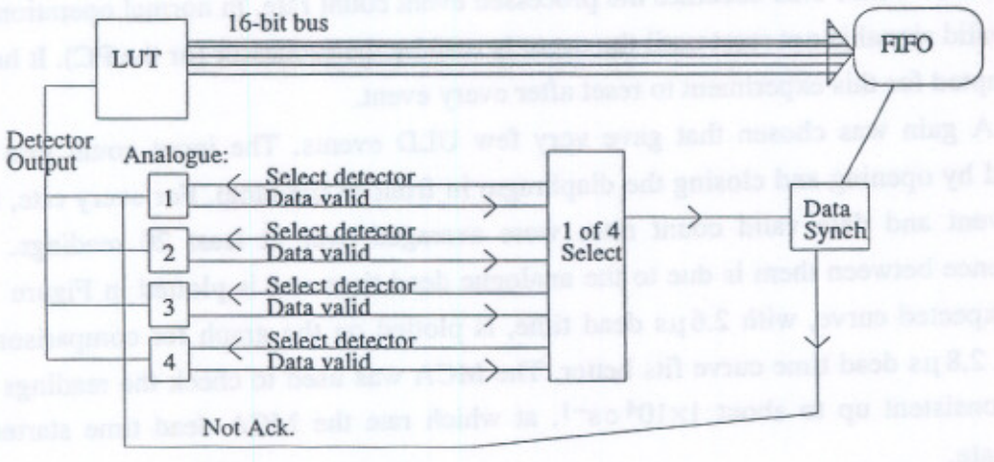

Figure 134. Simplified diagram of detector selection process.
The raw count is measured in the analogue card. The processed count is measured from the data valid signal.

The discrepancy arises because it takes some 200 ps to send and receive the 'not Acknowledge' signal. An event occurring within the 200 ps following a selected event will therefore produce a data valid signal and be counted as a processed event. The 'data synchronisation' will subsequently throw out both events as being too close together.

Thus, if two events are more than 600 ns apart, they will both be counted and processed correctly. Less than 600 ns apart, the second one should not be counted nor processed. Less than 200 ps apart, both events will be counted but neither processed. This explains the effect described above where all four detectors were apparently counting events correctly but nothing was being seen. The events were synchronised to within 200 ps of each other.

This was tested by setting up a pulse generator with a splitter and delay to control the time between two identical events.

If the detectors are not locking together and are all running at their maximum rate of 1×10^5 c s^{-1} with random data, where the mean time between events (t) is 2.5 µs, the probability of obtaining any events within $\tau = 200$ ps follows a Poisson probability distribution. It is one minus the probability of obtaining none:

$$P = 1 - \frac{\mu^x}{x!} e^{-\mu} = 0.008\% \qquad (110)$$

where µ is the mean number of events received within the time period (τ/t); and $x = 0$. In an integration of 12,500 events, one will be incorrectly processed, at 1×10^5 c s^{-1}.

6.5. POLAR IMAGE DISTORTIONS

Throughout the detector development, problems were encountered in obtaining a perfect spiral which would give the theoretical straight lines in polar co-ordinates.

6.5.1. Crossing arms

The very first 'spirals' obtained, using an anode and capacitive stim probe were very distorted, like pigs' tails. The arms even crossed one another. This was due to severe offsets in the ADCs and, in particular, the ADC which was measuring the *sum* signal. As the probe moved along the length of the anode, it did not maintain exactly the same distance from the surface. The centre of the spiral moved as the probe scanned across the surface.

The reason for this effect was the fact that the voltage of the stimulated signal altered with the change in distance. If the input pulse height was varied while keeping the probe in the same position, the signal on A/Σ went up from (hex) A0 to A4, and on B/Σ from 9E to A2. Using different parts of the summing ADC was giving different answers.

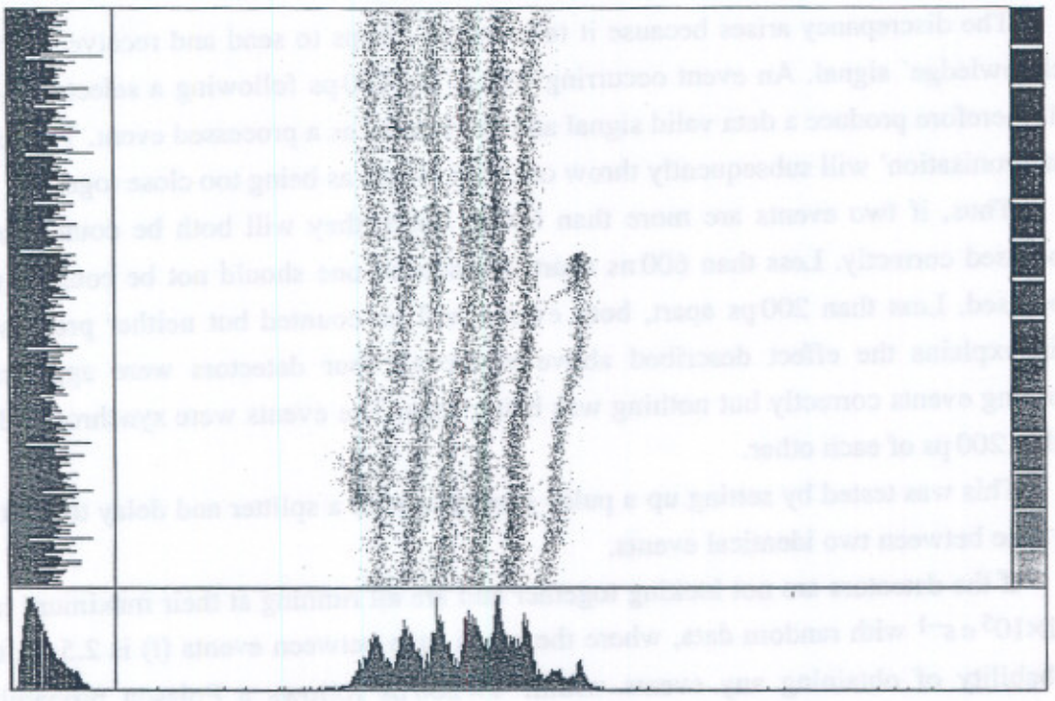

Figure 135. Early polar plot from development detector with laboratory electronics. It can be seen that there are no significant distortions in this output, but the arms are very close together.

6.5.2. Wiggles

Once the summing ADC offsets were removed, the polar plots obtained with the scanning probe were near perfect (see Figure 126). However, distortions still occurred in normal use of the detectors. The distortions took a variety of forms.

The development detector demonstrated straight lines in the polar plot. Figure 135 illustrates one of the early plots. Although the lines are easily resolvable and are straight, it was decided that for the flight design there should be fewer spiral arms, further apart, the more easily to accommodate any changes in radius. The distortions in the spirals obtained with the development model detector later, or with the optics model detector, are shown in Figure 136. These are 'negative wiggles' in that the radius is enlarged in the direction of the *A*, *B* and *C* minima.

The wiggles are positive with the flight-style detectors and electronics, *i.e.* with the FM, QM and EM detectors. The radius is enlarged in the direction of the *A*, *B* and *C* maxima. The wiggles are more pronounced in the outer arms. Figure 137 is an example of this type of distortion.

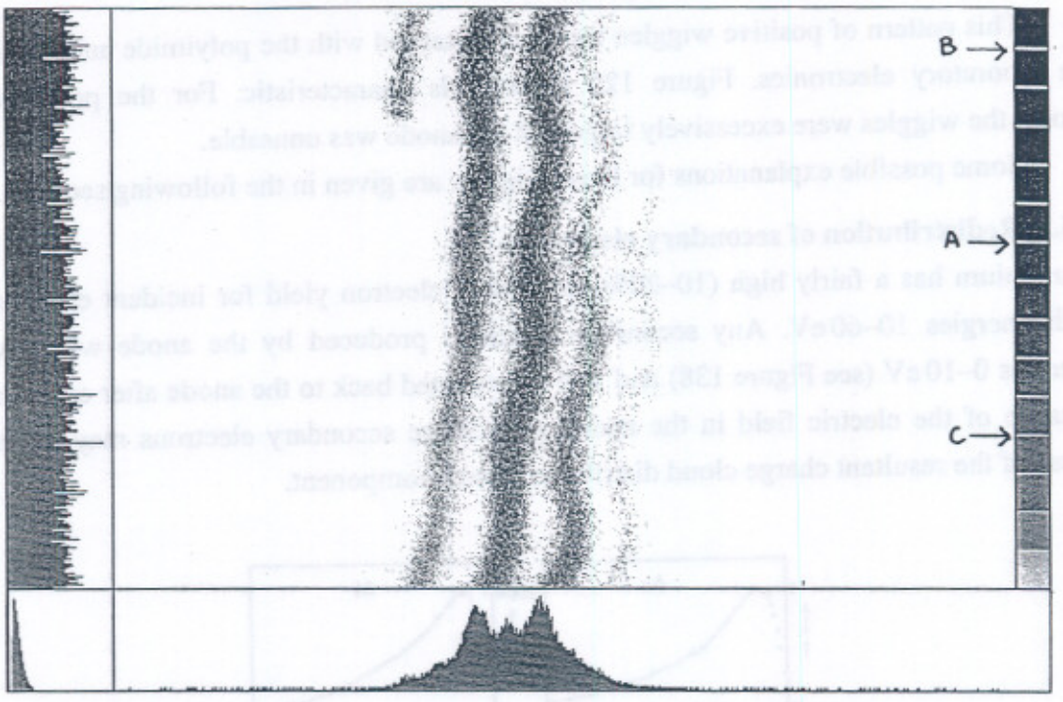

Figure 136. Output from development detector showing negative wiggle distortions. This spiral, as with Figure 135, was taken with laboratory electronics, but with different MCPs and anode design.

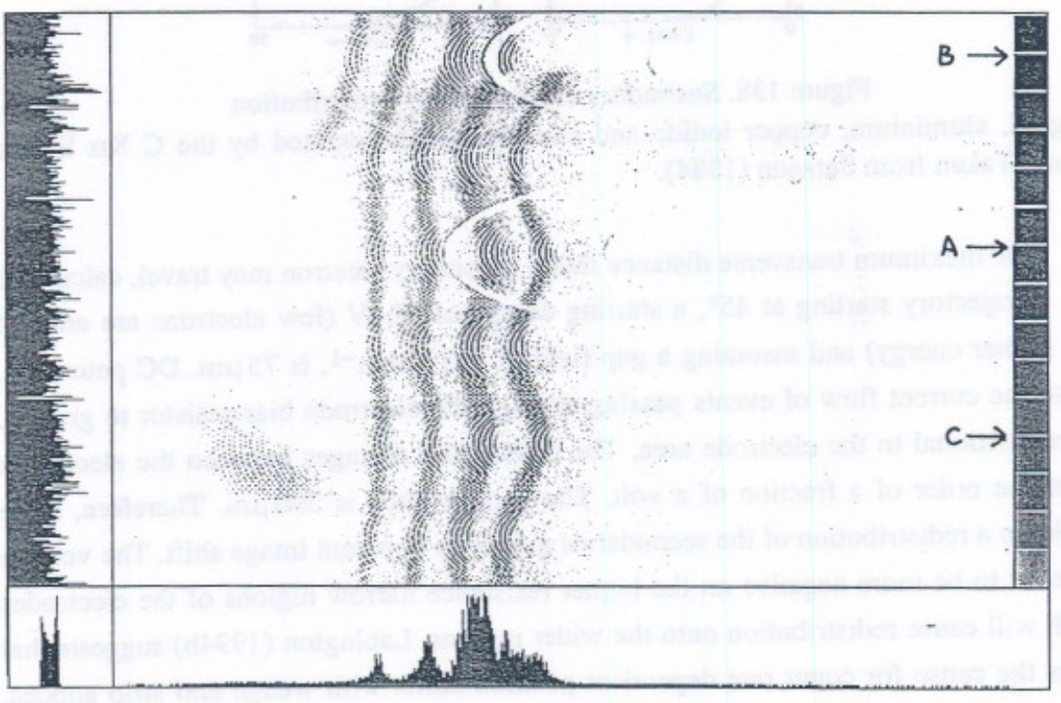

Figure 137. Polar plot obtained from flight detector showing positive wiggle distortion, increasing towards the outer arms.

This pattern of positive wiggles was also observed with the polyimide anode with the laboratory electronics. Figure 125 shows this characteristic. For the polyimide anode, the wiggles were excessively large and the anode was unusable.

Some possible explanations for these wiggles are given in the following sections.

6.5.3. Redistribution of secondary electrons

Aluminium has a fairly high (10–20%) secondary electron yield for incident electrons with energies 10–60 eV. Any secondary electrons produced by the anode will have energies 0–10 eV (see Figure 138) and will be attracted back to the anode after emission because of the electric field in the anode gap. These secondary electrons may be the cause of the resultant charge cloud distribution's soft component.

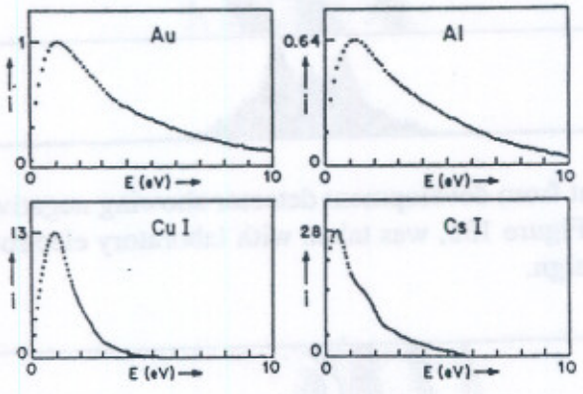

Figure 138. Secondary electron energy distribution for gold, aluminium, copper iodide and caesium iodide, excited by the C Kα line at 4.4 nm. Taken from Samson (1984).

The maximum transverse distance that a secondary electron may travel, calculated with a trajectory starting at 45°, a starting energy of 10 eV (few electrons are emitted with higher energy) and assuming a gap field of 133 V mm^{-1}, is 75 µm. DC potentials, due to the current flow of events passing through the electrode bias resistor to ground, are proportional to the electrode area. The differential voltages between the electrodes are of the order of a fraction of a volt. The pattern pitch is 390 µm. Therefore, there should be a redistribution of the secondaries giving an apparent image shift. The voltage will tend to be more negative on the higher resistance narrow regions of the electrodes which will cause redistribution onto the wider regions. Lapington (1994b) suggests that this is the cause for count rate dependent position shifts with wedge and strip anodes. This could also be an explanation for the positive wiggle distortions seen in Figure 137. The severe wiggles in Figure 125 can also be explained by this mechanism, if the

polyimide anode has different secondary electron properties and lower resistance than the equivalent quartz anode.

The spatial size of the charge cloud is related only to the gain, given constant anode-MCP gap conditions. The radius is therefore inversely proportional to the pulse height. However, with high count rate lines the radius can be reduced by more than would be expected simply by the effect of gain depression on the PHD. This result was seen in the RM detector where the pulse height could be tightly windowed but the spiral arm deformation still showed. This is believed to be due to the charging of the electrodes, thereby increasing the distance the secondary electrons move, causing a very large cloud spread.

Lapington (1994b) uses a grid between the anode and the MCP to suppress the secondary electron emission or confine its redistribution. This technique results in considerable improvements in linearity. Without this option on the GIS detectors, the large changes in radius cause ghosting. This was a considerable problem during calibration (see Chapter 8).

The nature of the secondary electron redistribution of the charge cloud could account for the fact noted by Siegmund *et al.* (1984), that distortions are reduced when the field strength decreases towards the anode.

It would be interesting to repeat the split strip experiment (§6.1.2.) with the suppressing grid to find out whether the wing component in the double exponential charge cloud model is indeed due to secondary electrons.

6.5.4. Dynamic crosstalk

Crosstalk does not produce distortions, but simply shrinks the spiral towards the origin. This can be shown by considering one point on the side of an electrode maximum, and another in a minimum direction (Figure 139).

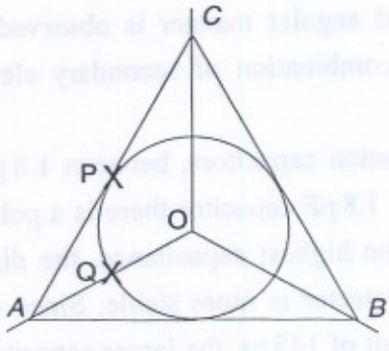

Figure 139. Two co-ordinates on the spiral plane at the same distance from the origin. The circle marks the limit of the possible spiral. P is at the minimum of *B*; Q is at the maximum of *A*.

The co-ordinates of point O are (0,0,0), point P ($^1/_2$,0,$^1/_2$) and Q ($^2/_3$,$^1/_6$,$^1/_6$). Crosstalk acts as a fraction δ being shared equally with the other two electrodes so that the signals become:

$$\begin{aligned} A &\equiv A - 2\delta A + \delta B + \delta C \\ B &\equiv B - 2\delta B + \delta A + \delta C \\ C &\equiv C - 2\delta C + \delta B + \delta A \end{aligned} \tag{111}$$

Inserting these into the co-ordinates P and Q, gives:

$$\begin{aligned} P &= \left(\tfrac{1}{2}(1-\delta), \delta, \tfrac{1}{2}(1-\delta)\right) \\ Q &= \left(\tfrac{2}{3}-\delta, \tfrac{1}{2}\left(\tfrac{1}{3}-\delta\right), \tfrac{1}{2}\left(\tfrac{1}{3}-\delta\right)\right) \end{aligned} \tag{112}$$

The components of the vectors A, B and C on the normalised spiral plane act at 60° from one another, so that the distance of P and Q from the origin can be found by vector addition. They both give the result $\frac{1}{2}(1-3\delta)$. They are both therefore moved inwards but by the same amount.

An explanation for the distortions in Figure 137, however, could lie in dynamic crosstalk between the preamplifiers. Unless the preamplifiers read the charge voltages at precisely the same time (unlikely if the voltages are of different sizes) they may give or take more or less charge as it is being measured. The support for this suggestion is the fact that the wiggles are reduced with increasing shaping time.

To distinguish between these causes, a pinhole image from the RM detector with laboratory electronics, may be examined, with each event associated with a pulse height. If the radius reduction is due to secondary electron convolution with the anode pattern, the pinhole image will be streaked radially on a spiral corrected for unmatched gains. If crosstalk is to blame, the pinholes will be streaked radially on the uncorrected spiral and will be distorted to a radial and angular error after correction. In fact, streaking of the pinhole in both a radial and angular manner is observed before and after correction, suggesting that there is a combination of secondary electron and dynamic crosstalk effects.

A variety of compensation capacitors, between 1.8 pF and 10 pF, was tried with the peak detectors. With the 1.8 pF capacitor there is a pole* at 8 ns, whereas with 10 pF the pole is at 47 ns. With the highest capacitance, the distortions were virtually non-existent, because the peak detector is more stable. Since 47 ns is still small compared with the shaping time constant of 145 ns, the larger capacitor should have little effect on the throughput.

* roll off of response curve where the reactance of the capacitor & resistor is the same. $\omega = \frac{1}{8ns}$

After adjusting the compensation capacitors to 10 pF for the QM detector, the polar plots gave almost perfect straight lines. This was therefore implemented on the flight boards.

6.5.5. Non-linearity of sum ADCs, peak detectors, preamplifiers

If there is an error in the *sum* multiplication factor (5/9) due to variation in the gain in the summing amplifier, a compensation can easily made in the decoding software or the LUT. This is the constant *zpln* described in §5.1.2.1. However, if the summing amplifier or ADC is non-linear the required *zpln* will vary with pulse height. This was observed in the pig tail spirals, where the centre of the spiral moved across the spiral plane as the voltage changed.

The two stim pads, built into the anode base plate, result in two event positions in the A/Σ, B/Σ plane. When the reference for the ADCs was fixed rather than normalising by using the *sum* signal, varying the magnitude of the stim pulses produced two straight lines which could be extrapolated to the origin (Figure 140). When the offsets had been calibrated out, the straightness of the lines reflected the linearity of the ADCs.

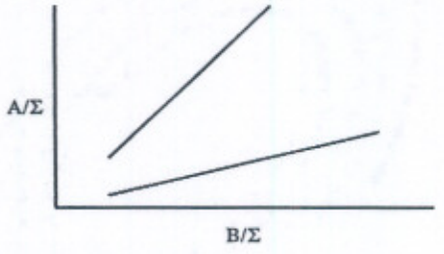

Figure 140. Stim signals with fixed reference to ADCs.

Drawing the spiral in ADC co-ordinates (*i.e.* plotting A' against B') shows up ADC non-linearities very clearly. There are distinctive gaps along the boundaries of the most significant nibbles, parallel with the two axes. This is due to the droop in the signal voltage during the peak and hold period, between setting the four most significant bits and the four least significant bits. It leads to a grid pattern in the normalised plot, with many events at the most significant nibble boundaries. A signal that starts at level A2(hex), will be digitised correctly to obtain the most significant A, but the signal leaks away before the 2 is measured and instead, a 0 may be measured, leading to a misplaced A0. The values 80, A0, C0 *etc.* are very frequent in the data (see Figure 141). The gaps are from the E's and F's of the LSBs. The same effect has been observed previously by *e.g.* Clampin *et al.* (1988), in the form of preferred binary codes. They assign the cause

to crosstalk and spurious noise pulses which are small and sampled by insufficient ADC codes. They also use a peak and hold circuit.

At first the ADCs were set up with only one sample per pulse. The data obtained with this setup showed a severe grid pattern. The manufacturers data sheet for the device was in error, implying that the ADCs needed only one stage, clocking the data to the ADC output on the next event. The data produced with the stims looked good, but this was due to the fact that the data was repetitive and therefore the second digitisation could be performed on the following sample pulse. In fact, two sample pulses were required. The timing between the triggering of the peak detectors and the two samples was crucial and required experimentation. The samples should be as far apart as possible without meeting the ends of the peak detection.

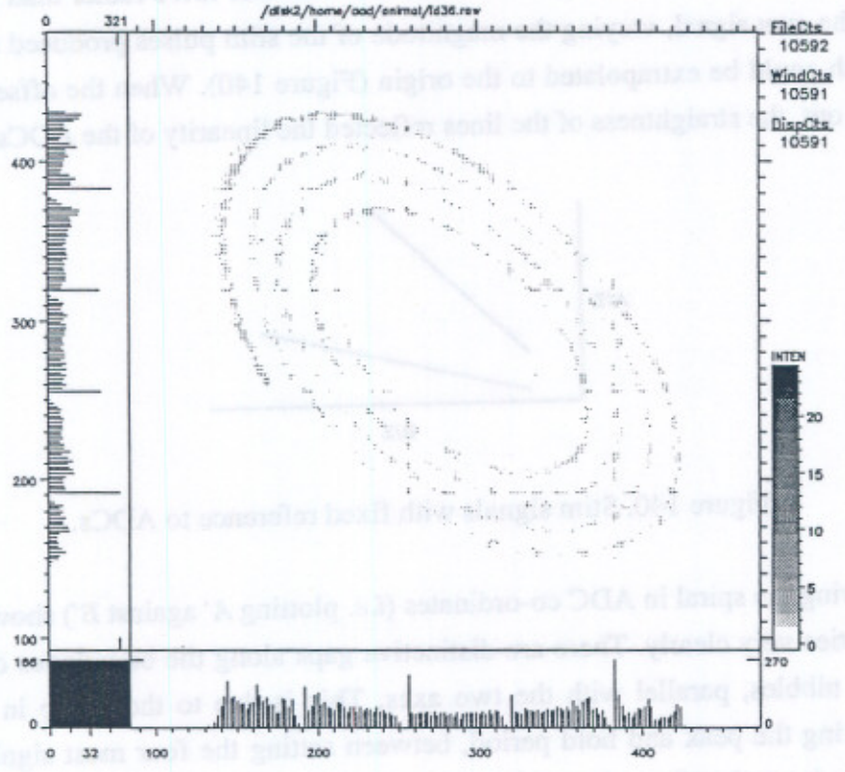

Figure 141. Incorrect digitisation giving an irregular grid picture taken with Isaiah at 3.6 kV, after the double sample was introduced but before the sample and hold times were adjusted. This plot is in ADC co-ordinates: B' plotted against A'.

A similar loss of least significant data is caused by the trigger amplifier firing from the negative side of an event. This was only seen when a pulse generator fed

square waves into the capacitive stim probe. Revising the grounding had an enormous benefit with respect to this problem.

6.5.6. Increase in radius with no MCP reservoir capacitors

If there is a breakdown at any point in the high voltage circuit, the high voltage reservoir capacitors (330 pF), connected between the MCPs and ground, discharge through the MCPs to the breakdown path. The capacitance of about 70 pF stored in each of the MCPs themselves was thought to be enough to supply charge for the events (~5 pF per event). The reservoir capacitors were therefore removed in the QM to reduce the risk of MCP damage in the case of breakdown, with an interesting result. The spiral picture grew in radius so that the outer arms passed the limit of the plane; the minimum electrode width appeared to be less than zero. It was necessary to reduce the *sum* multiplication factor from 9/5 to 3/2, to see the whole spiral again.

The reason for this effect is the capacitance between the back face of the bottom MCP and the anode. This capacitance is 42 pF, whereas the capacitance to ground is:

$$\left(3\times\frac{1}{70}\right)^{-1} = 23\,\text{pF} \tag{113}$$

with no reservoir capacitors. The ratio of capacitance between the MCPs and ground and the MCPs and anode is therefore large. A positive charge is left on the back face as the event strips the electrons from it. Because the impedance path to ground from the back face is increased, the time for the charge to be removed is increased. This charge spreads quickly over the conductive surface of the back face and induces a negative charge equally on all the electrodes of the anode. This looks like a reduction in signal on each of the electrodes. Signal A becomes $A-\delta$ *etc.*, and the *sum* signal becomes $\Sigma-3\delta$. This has the effect of enlarging the spiral and spreading out the arms.

One 330 pF capacitor was re-connected between the back face and ground to solve the problem.

6.5.7. Count rate dependent distortions

If the count rate was varied between 500 to 50,000 c s^{-1}, positive distortions like those in Figure 137 were seen to increase. This was due to the effect of 10 MΩ bias resistors between the anode electrodes. At a rate of 5×10^4 and a modal gain value of 4×10^7 this constitutes a current of 0.3 μA. At a position where one of the electrodes is at a maximum, it takes $0.3\times5/9 = 0.17$ μA, while $0.3\times2/9 = 0.07$ μA goes through each of the other two. The differential voltage could therefore be as much as a volt, between 1.7 V and 0.7 V. This would be enough to give a redistribution of the charge cloud or secondary electrons towards the electrode maxima, giving positive wiggles.

The remedy was to reduce the bias resistors, the disadvantage being an increase in noise. It was found that by reducing the bias resistors to 100 kΩ the noise increase was barely perceptible but the count rate distortions were much decreased.

CHAPTER 7.

FLIGHT DESIGN AND OPERATION

7.1. MODEL PHILOSOPHY

7.1.1. CDS

The CDS model programme was designed to separate the mechanical, electrical and optical aspects of the instrument. There are five CDS models: Structural Thermal Model (STM), Engineering Model (EM), Optics Model (OM), Flight Model (FM) and Flight Spare (FS). All except the OM were required to be delivered to ESA, although the EM was returned after delivery of the FM. Spares were produced at unit or subunit level *e.g.* spare electronic cards.

Breadboard models of all electrical subsystems (including detectors) were built to allow performance testing and optimisation before the EM build. The EM simulates the electrical properties of the instrument and is not structurally representative. The detectors, mechanisms, sun sensor and all associated electronics are built to be fully functioning. The EM is used on the EM spacecraft, for system level testing including EMC and thermal vacuum tests.

The STM is for structural testing. It simulates the mechanical and thermal properties of the instrument. All the subsystems are mass models with heaters to simulate power dissipation. The STM is used to qualify the structure in vibration testing and in thermal balance tests. It is also incorporated into the SM spacecraft.

The OM provides an accurate simulation of the optical properties of CDS. It incorporates detectors, gratings, slit and scan mirror mechanisms, as well as the prototype telescope. It is needed to test optical alignment, gratings *etc.* It was used in the first 'end to end' UV test and to simulate the calibration exercise.

The FM and FS are tested to flight acceptance levels. Alignment, UV testing and intensity calibration are carried out on the FM before delivery.

7.1.2. GIS detectors

GIS detectors were required for all CDS models except the STM: one detector for each of the EM and OM, four for the FM and two spares. An additional two detectors were

built: one as a QM to be used for integration and testing after delivery of the EM and OM; the other as the RM for use in detector physics experiments. Because there was no detector associated with the structural model, vibration and thermal testing were performed on the EM and QM. They were tested to qualification levels, which are higher than the acceptance levels for the FM, in order to verify the design. The OM was a fully functioning detector, but not built to flight standard and it had no flight-design electronics. The EM was built to flight standard but was delivered as an electrical model only, without functioning MCPs. The QM, FM and FS detectors were built to full flight specification. The RM incorporated a flight-style MCP stack and anode, but could be used with either flight-design or laboratory electronics.

7.1.3. Chronology

Table 15 is a brief summary of the work on the GIS detectors undertaken directly by the author, whilst collaborating with the other CDS team members in the development of the GIS electronics and software. From the table it can be seen that there were many simultaneous strands of work, so that development was scarcely complete before the flight detectors were built. It is also apparent that the flight detectors were built, tested and delivered within a few months, allowing insufficient time for a complete investigation.

At the beginning, the main need was to prove that the SPAN anode would meet the requirements. A development model detector was therefore built very simply, consisting of an MCP stack and anode mounted on a die cast box with connections to the vacuum flange. It has been described in §3.2.2. Some useful work on high voltage distribution, low noise electronics and some initial results on resolution and modulation were obtained with this detector, and have been presented in §4.8. and §6.1.4.

The first deliverable detector was the OM. It was to be used in the RAL instrument optics model, to test the optical alignment of the slits, grating, and detector on the RC. It was built to an early design and used laboratory electronics with three separate electronics channels. *ALLSINGN* was delivered with it and adapted to match the RAL 10-bit ADCs which differed from those at MSSL. The main problems with this detector were due to the attempt (eventually abandoned) to hold the anode at high voltage, as in the flight design. More work on clearances and insulation needed to be done before it was possible to operate successfully at HV. This was an on-going problem throughout the project, recurring even in the flight build stage. The OM, however, worked well throughout the optical calibration at RAL with the anode at ground potential and the MCPs at a high negative potential.

DATE:	1/11/88–11/4/90	11/4/90–22/3/91	22/3/91–22/10/91	22/10/91–6/5/92
SPAN:	Design and manufacture of first SPAN pattern. Measurement of anode resistances and capacitances. Capacitive stimming of anode.	Developing parameters. Reducing capacitance. Drawing at 45° to cope with backlash.	New designs. EM anode parameters decided. Alternative materials sought.	Connections to anode devised. *ALLSINGN* adapted for ratiometric ADCs. Effects of crosstalk and sum non-linearities examined. Hough routine worked on.
MODELLING:	Charge Cloud model written.	Started to create *GIS_SIM*.	Resolution with PHD and RMSIG. % loss with PHD. Linearity. Electronic noise. Comparison with dev. detector. Fixed patterning in flat fields.	90° anode compared with 120°. Noise effects on flat fields. PHD effects on flat fields. ADC offsets. Sum offsets. More on fixed patterning.
DM:	Built with first SPAN pattern and chevron MCPs. Resolution measurements made with pinhole mask. Capacitive stimming.	Measured modulation. Using triple thickness MCPs. Using z-stack MCPs. Tried using polycarbonate.	Scrubbing. Use of slit mask. Measuring noise, resolution, linearity, PHD. Varying anode gap voltage.	Polyimide coated, lased and stimmed. Built and run with polyimide anode. Abandoned HV anode. Ran polyimide anode at ground.
OM:				Created anode. Ran with lab electronics, with UV lamp. Problems with HV anode. Delivered to RAL (Feb. 92).
EM:			Created anode. Decided how to incorporate stims. First test of flight-style electronics with stim–small pig tail spiral and grid pattern.	Started building electronics. Built with new anode connections. Problems with: preamps ringing; breaking capacitors; ADC preferred codes. Made preamps more robust. Screen from optics bench. Calibrated preamps.
MISC.:			Set up new chamber, Rowland Circle and detector mounting. Set up MCP storage facility. Looked at brittle materials.	Commissioned UV source. Set up RC. Obtained MCA and PHD calibration scheme.

Table 15. Table of detector development chronology.
This is the work undertaken by the author to produce and characterise the detectors (continued overleaf).

DATE:	6/5/92–21/1/93	21/1/93–1/6/93
SPAN:	Added gain adjustment to *ALLSINGN*. Spectral lines. Spiral distortion investigations.	Radius pulse height relation examined. MCP stack capacitors effect on image. Calibration scheme suggestion. LUT and raw data handler.
MODELLING:	Added gap between electrodes.	Improved LUT generation. Worked on flat field, k and ϕ.
OM:	Made to work with RAL electronics.	Rebuilt with grounded anode. Used in Optical Cal. test at RAL.
EM:	Solved preferred codes problem with double sample. Replaced MCPs. Bias on Front face. Vibration test. Swapped plates back to integrate with GIS electronics. Anode stimming.	Instrument Thermal Vac. setup tested. Delivered.
QM:	Anode coated using RF, lased and built. Mounted onto RC with insulation and alignment studs. Ran with EM plates. UV spectral lines and Penning compared. Alignment studs. Integrated with GIS electronics. Worked on noise and resolution. HV return removed.	Vibration test. Instrument TV test. New MCPs. Breakdown and total rebuild. TV test at MSSL. Removed reservoir capacitors. Replaced one capacitor.
ISAIAH/JEREMIAH:		Work on anodes begun. Isaiah built, run, Kapton and Solithane added.
MISC.:		MCP scratching problem. Slit on RC calibrated. All MCP shims made. RM1 built.

Table 15 (cont.) of detector development chronology.

DATE:	1/6/93–28/9/93	29/9/93–6/4/94
SPAN:	Measured k, ϕ variation with gain on Jeremiah.	Gain correction factors in LUT. Raw data telemetry via either EGSE. More PHA bytes in raw data. Sorted out algorithm again. IDL raw data viewer. Raw data byte swap confusion. LUTs for FM stims. Ghosts.
MODELLING:	Transferred to Viglen PC. Started detector simulator with Chun.	Used for much of SPAN understanding.
ISAIAH/JEREMIAH:	Lased and baked Jeremiah. Rebuilt Isaiah with mended hardware. Measured stud alignment error, noise, gain etc. ALL-UP TEST	Test review. Changes in stims and filament images with temperature. Added filter to HV. Delivered to RAL (Oct 93). Removed HV screen. Integration at RAL. Filters on detectors to stop blocking. Delivered FM GIS box. (Mar 94) Calibration.
KINGS/LEVITICUS:	Baked, coated, built both. Kings breakdown problems. ALL-UP TEST	Test review. Added filter to HV. Found King's problem. Removed HV screen. Delivered to RAL (Nov 93). Integration at RAL. Filters added.
MALACHI/NEHEMIAH:		(Dec 93) Started making. Malachi wire bonds fell off. Rebuild. Count rate tests on Malachi. Used for electronics tests.
QM/RM 1 & 2:	RM1 abandoned.	Plan for RM2. Put QM at ZOD position. PHDs measured at ZOD position with QM. Set up RC again using SDDA to measure resolution. Since 6/4/94: Carry on characterising QM and RM in two vacuum chambers.

Table 15 (cont.) of detector development chronology.

Spectra were produced by *ALLSINGN* from the raw data collected. The spectral lines were in focus and their widths indicated that the detector was performing to a high resolution. This was very encouraging, although the effects of the flight electronics, 8-bit ADCs and the eventual grounding configuration were still unknown. It was noted in analysing the raw data that the best fit LUT had to be changed for each entrance slit and type of gas in the discharge lamp because of the changes in spectral line intensity and distribution. The real operating count rates were not appreciated at this point.

The EM detector was the next to be delivered to RAL. This had to be an electrical model only for ESA, but was used for early testing of the new flight design housing. It also permitted integration with the analogue EM electronics. This time the housing was adapted to take an anode without holes drilled in it and to have a wider aperture height. There was more space for HV protection. Improvements were included to make it easier to assemble the detector, and more attention was paid to the eventual alignment requirement with the RC. The build procedure was defined, and some specialist tools made. The EM was then delivered to ESA with contaminated MCPs as dummy plates for use as the electrical model.

The QM detector was, like the EM, representative of the flight detectors, for integrating the detector with GIS electronics and with the rest of the instrument. It was used in detector qualification vibration and thermal vacuum tests, and also to accompany the electronics and the whole CDS instrument in qualification tests. For the first time, the HV anode worked consistently, breaking down only once when a ground cable had been left off during a 'quick' test to check for breakdowns.

The four flight detectors (Isaiah, Jeremiah, Kings and Leviticus) were built using the experience gained on the previous models. There were a few obstacles to overcome with the electronics when having four detectors using a single processor.

Kings broke down in the first all-up test. The culprit was found to be a breakdown between the grounded stim pads and the HV anode through the gas trapped behind the anode in the base plate. The base plate was modified for Kings and for the two flight spares, which had not yet been built, in order to allow the air to escape more easily. Kings was completely re-furbished with new MCPs. Isaiah, Jeremiah and Leviticus were not modified because they had already been built and tested, without this problem being observed.

Apart from Kings, the flight detectors have worked consistently. They survived acceptance level vibration and thermal vacuum tests. In the instrument level thermal vacuum test, they were all used together at high voltage with the filaments as the source of stimulation. The first time they were used to view UV spectra together was in the

calibration test. There were initially problems with detectors tripping out, but the problem turned out to be that the HV units were ramping too fast and overshooting the current limits. This was overcome later by altering the GIS software to ramp the voltage slowly.

In the meantime, work started on another development detector, the RM, designed for further investigation of the anode and MCPs. In particular, the ultimate resolution obtainable and the quantum efficiency variation with incident angle were of interest. It was more representative of the flight detectors than the development model, with a flight-style anode and flight size MCPs. It could be fitted in the spectrometer, on the X-Y-rotary table, and operated with either flight-design or laboratory electronics, allowing work on PHD, gain depression *etc.*

Research on the development, QM and RM detectors is assumed to apply to the flight detectors, although the QM is the only one of these three which uses full flight-design electronics.

7.2. DESIGN

The choice of components and materials was controlled by the ESA Product Assurance requirements (ESA, 1995). Hazards, materials and components had to be documented. Procedures, inspections, trials and tests had to be recorded in documented histories for each subunit.

7.2.1. Mechanical design

The structure of CDS consists of two side frames machined from aluminium alloy plate connected together at discrete locations by bulkheads. Cross bracing between the bulkheads provides stiffness. An extremely stiff structure is needed to obtain the required minimum resonance frequency of 70 Hz. The telescope is attached to the front bulkhead via an invar ring. The scan mirror, gratings and detectors are all mounted on an optics bench, which is protected by removable covers to minimise contamination. The electronics boxes are mounted on a platform. The experiment power supply (EPS) and the CDHS are mounted remotely from CDS.

The telescope mirror surface roughness is less than 2 nm r.m.s. Aperture closure doors are provided to limit contamination of the optics during ground testing and launch. It may be necessary to close the doors to limit the solar flux under certain conditions or contamination during attitude manoeuvres. They can therefore be opened and closed on command in orbit.

7.2.2. Vibration

Every part of an instrument designed for space flight has to be built sufficiently robustly to withstand the launch conditions. To ensure this, the subsystems undergo a rigorous vibration test. Vibrations are performed in all three axes, in both sinusoidal and random modes. These were performed at MSSL for the individual detectors and electronics boxes. They were mounted on the vibrator using a special flange, protected by a downflow of clean air to maintain cleanliness.

Every part of the detector has to be considered and assessed for suitability for vibration. A variety of locking techniques is used for nuts and bolts. Kay lock nuts are deformed slightly so that they grip the bolt more tightly than a plain nut. Locking inserts, which are a coil of metal inserted into a tapped hole, hold screws in place. In the absence of these techniques, a nut or bolt head has to be locked using 24 hour Araldite. This is a low outgassing epoxy and therefore is suitable in small quantities. Even so its use has been avoided as far as possible on the actual detector head close to the MCPs and also on the sensitive optics bench, although it is used as a reinforcement to the spot-welding connecting the nickel MCP mid-contact shims to the Oxley feed through pins.

Twenty-four hour Araldite also locks some of the high voltage components onto the electronics cards. The cards, or regions of cards, without any HV components, are held steady and protected from any loose debris which might cause short circuits by a thin layer of solithane epoxy. Solithane is applied by painting or spraying after the circuits are fully built and tested. Disadvantages of this technique include the possibility of trapping air under the layer which could cause tracking when the instrument is evacuated. It is also very difficult to correct any problems with the board once it has been solithaned.

As for the MCPs, their mounting must not only be sufficiently delicate that no damage is caused to the brittle material, but strong enough to hold them sufficiently firmly to withstand launch. The MCP stack (Figure 20) is built up from a beryllium copper plate acting as the back MCP contact plate and defining the aperture with a chamfered edge. Polycarbonate spacers position the MCPs and a beryllium copper contact plate is placed onto the top MCP face and held in place by copper leaf spring clamps. The spring washer around the top edge of the MCPs holds the stack firmly in place, and also allows the load to be evenly distributed so that damage does not occur during launch. A certain amount of movement is allowed to reduce the impulse momentum on the MCPs. There is some flexibility in the spring clamp on the washer. The polycarbonate spacers, which themselves are elastic, do not fit too closely around the edges of the MCPs, so as to allow a little sideways displacement.

The same scheme is employed in mounting the anode. It is sunk into a polycarbonate base plate and is held in place by four spring clamps in the corners.

A wire is soldered to the beryllium copper bottom contact plate before baking. This wire is pushed through a tight hole in the anode base plate to get to the HV card behind. The hole must be tight to minimise the flow of air from the electronic boxes to the detector head during evacuation. All outgassing from electronics cards is extracted through the bottom box of the detectors, away from the optics bench.

The top contact is made via one of the four bolts on which the MCP stack is mounted. A lock nut makes a good contact between the bolt and the front face clamp bars and thence to the top of the MCP. The mid-MCP nickel shim contacts are made by spot-welding the shim tag to an Oxley pin which is mounted through the base plate, with wires soldered to the other side.

7.2.3. Mass

The detectors weigh 480 g each, which includes the HV distribution and preamplifier boxes and their contents. The dimensions are height: 150 mm, width: 70 mm and depth: 65 mm. The GIS processing box is 100×275×185 mm, and it weighs 3.01 kg.

7.2.4. Thermal environment

The instrument has to be able to maintain a stable temperature wherever it is located and pointing with respect to the sun and the Earth. Once SOHO is in its final orbit, there will only be long term seasonal changes in heating from the sun. The minimum will be 1353 $W\,m^{-2}$, and maximum 1447 $W\,m^{-2}$. A thermal balance is calculated to estimate the extremes which will be suffered by each part of the instrument in all possible states throughout its life. The spectrometer structure requires a nominal temperature of 20°C with a maximum rate of change of 1°C $hour^{-1}$. The primary and secondary telescope mirrors must be kept below 30°C.

CDS temperature is separately controlled, being conductively and radiatively de-coupled from the spacecraft. Multilayer insulation on all surfaces except the apertures and radiators will achieve the radiative de-coupling, whilst conductive de-coupling is maintained by insulated mountings. For cooling, the CCD in the NIS will be conductively coupled to a radiator to keep the CCD at –40°C. The electronics units on their own platform will radiate directly to space. Unwanted solar heat will be conductively coupled to a radiator.

For heating, 16 kapton thermofoil heaters are positioned within the instrument, with powers and locations calculated to maintain the required temperatures and temperature gradients (less than 2°C across the structure). These are thermostatically controlled by the electronics, according to associated temperature sensors, when the

instrument is powered up. For control of power consumption the heater circuit can be switched to a percentage of full duty cycle by command. When CDS is off the heating will be supplied to a lower thermal accuracy by the spacecraft via non-operational heaters. The CDHS and EPS, being separate from the spectrometer, will be thermally controlled by the spacecraft.

The detectors on the optics bench are expected to have a benign thermal range 10–30°C, but the CDHS and EPS are required to operate between −10°C and 40°C and to survive temperatures of between −15°C and +55°C.

7.2.5. Cleanliness and outgassing

Grazing incidence optics are particularly vulnerable to any surface contamination which may reduce the reflectivity.

The overall contamination limit is set to allow loss of throughput of less than 50% by the end of the instrument's life. About half of this is expected to occur in the ground phase and half in orbit. If each component (telescope surfaces, scan mirror, gratings and detectors) loses 10% efficiency over the lifetime, this will lead to a loss of 59% in all.

An upper limit of 100 nm of carbon contamination was set, allowing 20 nm pre-delivery, which is equivalent to 2 $\mu g\,cm^{-2}$. CDS is seven times more sensitive to Si than to C, but Si makes up only about a ninth of common contaminants.

To measure contamination, witness mirrors, witness plates and quartz crystal microbalances (QCM) have been used. The QCM can measure down to 0.01 $\mu g\,cm^{-2}$.

The inside of the optics bench box has to be maintained to high cleanliness standards. This is achieved by opening it only in an approved category clean room for the minimum time to carry out work. Only approved materials are allowed inside the optics bench. It is kept constantly purged with pure dry nitrogen to prevent entry of molecular contamination. All items have to be cleaned according to a documented cleaning schedule. There are four phases to the cleaning. First, removal of bulk debris and contamination by washing. Secondly, degreasing to remove oil and grease from workshop processes and handling. Thirdly, a surface clean in clean room conditions and finally a vacuum bake. For example, metal parts have to be washed in detergent solution and water, rinsed in de-mineralised water and dried. This is followed by an ultrasonic bath in Arklone P for 15 minutes. Acetone and IPA are used for a final grease removal. Lastly, the metal parts are baked in vacuum for at least 8 hours at 100°C. Gloves and tweezers are used for handling. All parts are kept in clean sealed containers, opened only in the clean room. The standard cleanliness procedures were adopted for all the detector parts, apart from the MCPs and anodes.

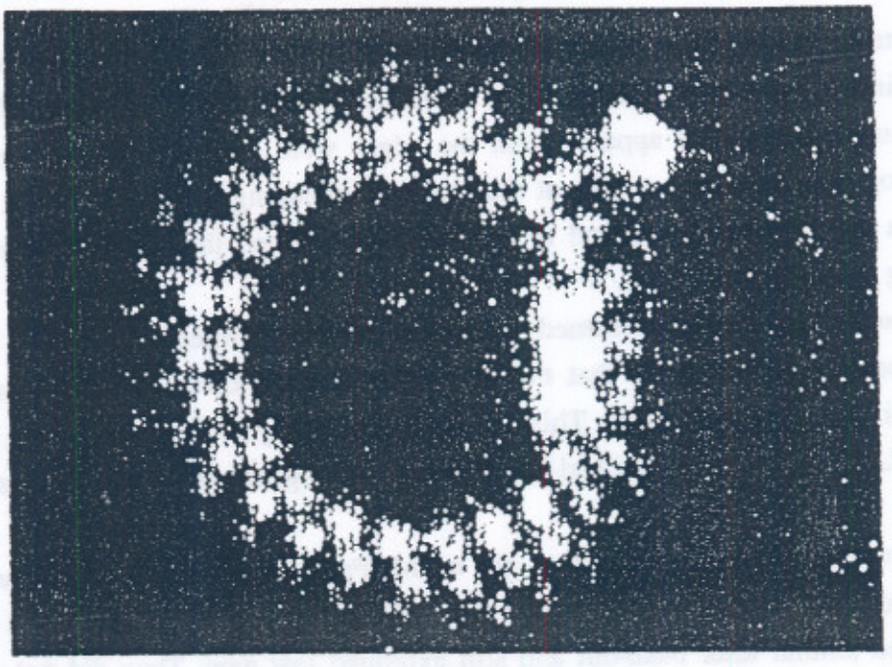

Figure 142. Spiral image obtained with contaminated MCPs at 5 kV. The detector was the EM. The MCPs were contaminated with Kapton in bake-out.

In §3.1.6. the need for cleanliness of the MCPs was explained. Particles remaining on the front face of the MCP will invariably give rise to hot spots when HV is applied. Contamination by substances such as oil or carbon was also mentioned as leading to a reduced gain. The substances may change the surface properties and conductivity of the MCP.

In building up the detector most of the solder joints are made in advance so that the solder flux can be removed before baking. The detector head is built up separately in a clean air flow bench and is wrapped securely while the last few solder connections between the head and the HV card are made, to prevent solder flux from contaminating it. This soldering is performed in the air flow bench and the joints cleaned with IPA.

An example of contamination was observed in the case of the MCPs in the EM detector. The MCPs were baked following the normal procedure described in Chapter 4, and built into the detector. On first switching on, it was observed that a small number of events appeared at 4.5 kV, but that all these events were at the ends of the detector. The PHD was exponential and did not saturate even when the voltage was pushed up to 5 kV. At 5 kV, the complete spiral was observed, but in a discontinuous form as in Figure 142.

Before baking the MCPs had been inspected and looked normal. After baking it was noticed that the MCP surfaces had become more greyish, and that the hexagonal

boule structure was visible to the naked eye. The edges of the MCPs, which had been supported in the grooves of the baking 'toast rack', were still the original black homogeneous surface. It is apparent that the edges were the only part of the MCP working properly and giving events at the expected operating voltage. The rest of the MCP had a severely depressed and non saturating gain, and the boule structure was contributing to the blobby image.

This set of MCPs was returned to Philips, who confirmed that it was indeed contaminated. Their belief was that the MCPs had been allowed up to atmospheric pressure while at high temperature. This was a real possibility as there had been a power cut at MSSL during the bake-out and there were no emergency protection valves fitted at that time.

On the strength of this, another set of MCPs was baked out to replace the contaminated ones. This time there were no power cuts. However, the second set of MCPs looked similar after bake-out and still exhibited low gain. They did not give a blobby spiral like the first set and were usable even though a higher voltage (4.5 kV) than planned had to be used.

Because of the poor performance of the second set, the bake-out chamber was examined very closely. The contamination was found to be due to some 'kapton' tape which had been used to hold thermocouples in place inside the chamber. This was supposed to be able to withstand the full 250°C but had become brittle and burnt. It turned out not to be the pure kapton tape, but a look-a-like which was not made of pure kapton.

Since that time, no tape has been used in the bake-out chamber! An emergency baffle valve has also been fitted in case of power failure.

The CDS doors will be kept closed on the telescope until about 50 days after launch to prevent contamination of the telescope and optics bench by the outgassing from CDS and other instruments. The instrument will be switched on after 10 days and should be outgassed through vents sufficiently to turn the detectors on after about 35 days. Quartz Crystal Monitors will measure any specific contamination inside the optics bench.

7.2.6. Electronic design

The GIS processor box contains five electronics cards as illustrated in Figure 143. Two cards each contain the analogue signal processing for two detectors. Another card contains the digital science data processing. Another holds the transputer processor. The fifth is a housekeeping card.

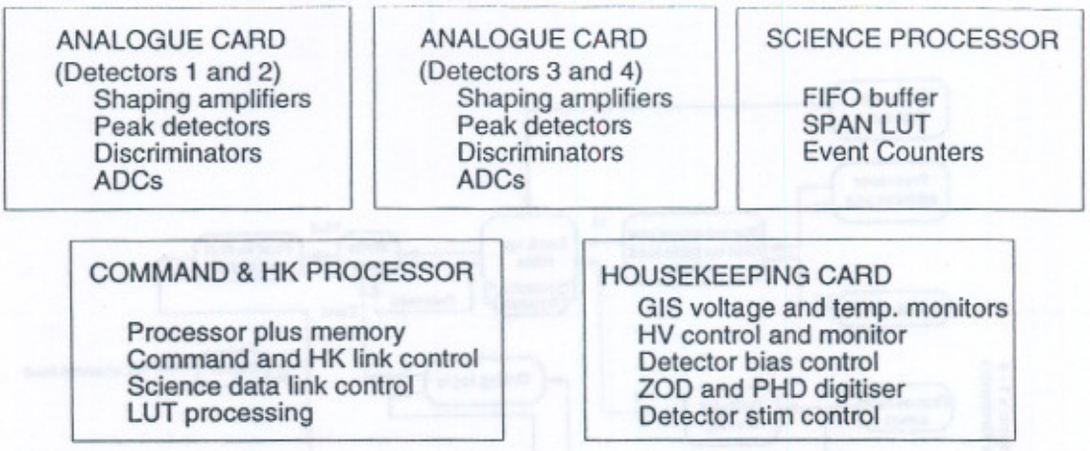

Figure 143. GIS electronics board allocations.

The two normalised anode signals *A* and *B* are passed from the analogue cards to the science processor. After the LUT, the 11-bit data from the four detectors is channelled one at a time into a common 1.25 MHz 13-bit serial stream to be passed to the CDHS. The science path uses non-programmable circuitry for maximum speed.

For commands to the detector system and status and health (housekeeping) monitoring, there is a bi-directional serial interface, 16-bits wide, which works at 62.5 kbits s^{-1}.

Figure 144 is a block diagram of the science processor circuit. An event coming from the detector is written into the FIFO in 600 ns. For a single detector this dead time appears in parallel with the 2.6 µs analogue dead time and thus has no effect. It does, however, limit the event to event resolution between detectors (see also §6.4.4).

The LUT is calculated by the on-board processor and stored in RAM. The 16-bit detector output plus 2-bits for detector identification is used as an address. The LUT output is 13-bits; 11-bits for the detector data (for the 2048 pixels), 2-bits for detector identification. A buffer stores up to 65,536 events at each pixel. Thus a 256k×16 bit RAM is used. The raw data is sent via the HK channel, because 16-bits are needed.

The command and housekeeping circuit is shown in Figure 145. An Inmos transputer T222 is used as a processor. The program code is held in EPROM. At power-up it is transferred to RAM where it is executed and patched if necessary. Code is written in Occam2 which allows parallel and sequential processes.

All commands are single 16-bit words. The most significant byte gives the actual command identification and the least significant byte is the parameter for that command, if there is one. A housekeeping table is updated every 2 seconds. It holds 105 parameters, which are a mixture of 1, 4, 8 and 16 bit values. A copy of the HK table is read out to the CDHS on demand.

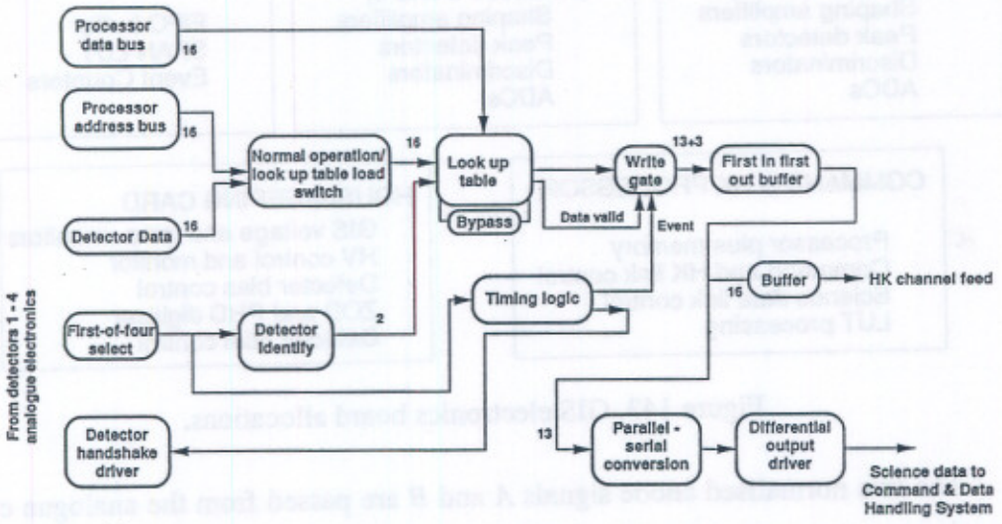

Figure 144. Block diagram of the science processing circuit from McCalden (1992).

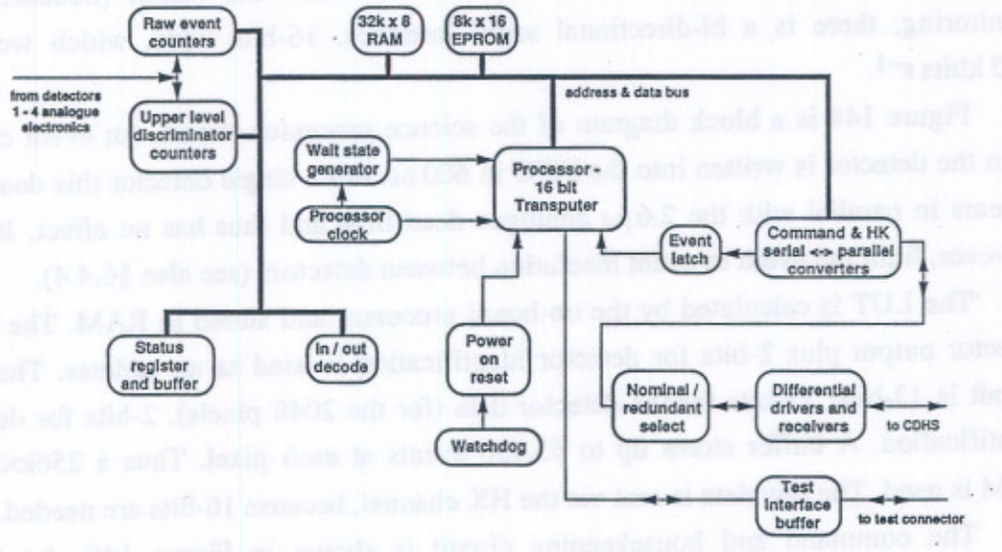

Figure 145. Block diagram of the command and housekeeping processor from McCalden (1992).

A watchdog timer is reset every 1.5 s by a processor instruction. If it does not receive this instruction, the watchdog will reboot the system. This allows controlled recovery in case of system faults.

There are 3 event counters per detector. Two 8-bit counters for the raw and processed events, and one 4-bit counter for the events above the ULD. A common latch

line is used to ensure that the count rates are sampled over identical periods. They are read every 2 ms and the values accumulated over 500 samples to give counts per second. This count per second value for raw and processed rates limits at 16-bits. The ULD does not limit but rolls over. It is very unlikely that the limits will be reached in normal use.

7.2.7. Power and HV supply

Power is supplied to SOHO by solar panels. The CDS power budget gives 56 W mean and 64 W maximum at 27.7 V. The power dissipation depends on the observation and the number of heaters being used. The CDHS and EPS consume about 9 W each. The power per detector including the MCPs and head electronics is 275 mW. The GIS processing box itself takes 5.51 W. The entire detector system, including the four detectors, HV units and processing, requires a total of 13 W from +5 V, ±12 V and +27 V power lines. A low current supply of a few mA is also available as a 'keep alive' line, to retain data in the LUT and processor RAM when the GIS is otherwise unpowered.

To minimise EMC susceptibility and generation, CDS internally regulated power is isolated from the spacecraft power bus. There is a single earth star point, at the chassis, for all regulated supplies, to avoid ground loops.

Without dedicated vacuums for the detectors, there was always a risk of high voltages being switched on during instrument testing, at atmospheric pressure. A number of safeguards and checks were written into the software to warn the operator about the possibility of hazards.

There are thus two modes of operation for the GIS HV supplies (one per detector). In 'enabled' mode, full HV is supplied with an absolute error of 5%, a rise time of 2.5 s and fall time of 10 s. The stability is to within 2% over 5,000 hours of operation. The 'disabled' mode, available for ground testing, gives an output of 3% of the commanded level. This allows the monitor and HV circuitry to be checked without endangering the detectors with high voltages. A remote disable plug is used for this purpose. The maximum output is 5.25 kV. There is a 390 kΩ current limiting resistor in series with the output. The HV return is biased to ±12 V by connection to the supply lines via series resistors, in order to bias the detector front faces. Both the HV and current are monitored directly. The rest of the detector system, from anode to output, could be tested at atmospheric pressure using the stims.

7.2.8. Radiation

It is estimated that the electronics, including detectors, will experience a total radiation dose of up to 20 krad inside their housings over a 6.5 year mission, with a large portion

being solar protons. There are two problems due to radiation: one is catastrophic failure and the other is single event upset.

To guard against catastrophic failure, the parts had to be carefully procured as 'rad-hard'. All components for general logic were specified as 40 krad tolerant. If 'rad-hard' components could not be purchased a batch had to be tested to prove their total dose tolerance and annealing properties. The Inmos parts were from a specially screened batch. FETs and MOS devices used in the charge amplifiers, discriminators and peak detectors were tested. The ADCs are MP7683 which maintained the specified performance after a total dose of 60 krad from a Cobalt-60 source followed by an annealing period of 60 days.

Single event upsets affect the processor and LUT RAM and general logic with bi-stable functions. For the processor RAM an IBM part was chosen with a well defined maximum total radiation dose of 1 Mrad and a single event upset rate of 1×10^{-9} errors per bit-day for standard Earth orbit. The EPROM and LUT RAM are rated at 20 krad total dose. Checksums are used to verify the integrity of the LUTs.

7.3. OPERATING THE GIS

7.3.1. Obtaining data

There are two means of receiving data from the GIS detectors. These are known as 'raw' and 'science' data. Figure 146 illustrates the procedure for setting up the GIS to give data.

The reasons for having the raw data mode are: (i) to allow the setting of the HV for each detector such that the PHD is inside the analogue signal window defined by the LLD and ULD; (ii) to allow an appropriate LUT to be written for that detector; (iii) to allow corrections to be made to the *science* data for any loss of intensity in a line through the use of a given LUT. The raw data can be tested with any LUT on the ground.

On receipt of a request for raw data, the GIS stops supplying full engineering data and fills packets with a mixture of raw and PHA data from the chosen detector. The 16-bit raw data packets are sent via the housekeeping stream from the GIS to the CDHS. The packets consist of the two 8-bit raw co-ordinates of events (A/Σ and B/Σ) as well as 8-bit PHA data. There are 88 PHA values to about 512 event raw data co-ordinates; the sampling times for the PHA values being evenly distributed throughout the time taken to fill the packet. A packet header with the detector number, front face bias, HV set and measured, MCP current, LLD setting, raw and ULD count rates is also included with the raw data.

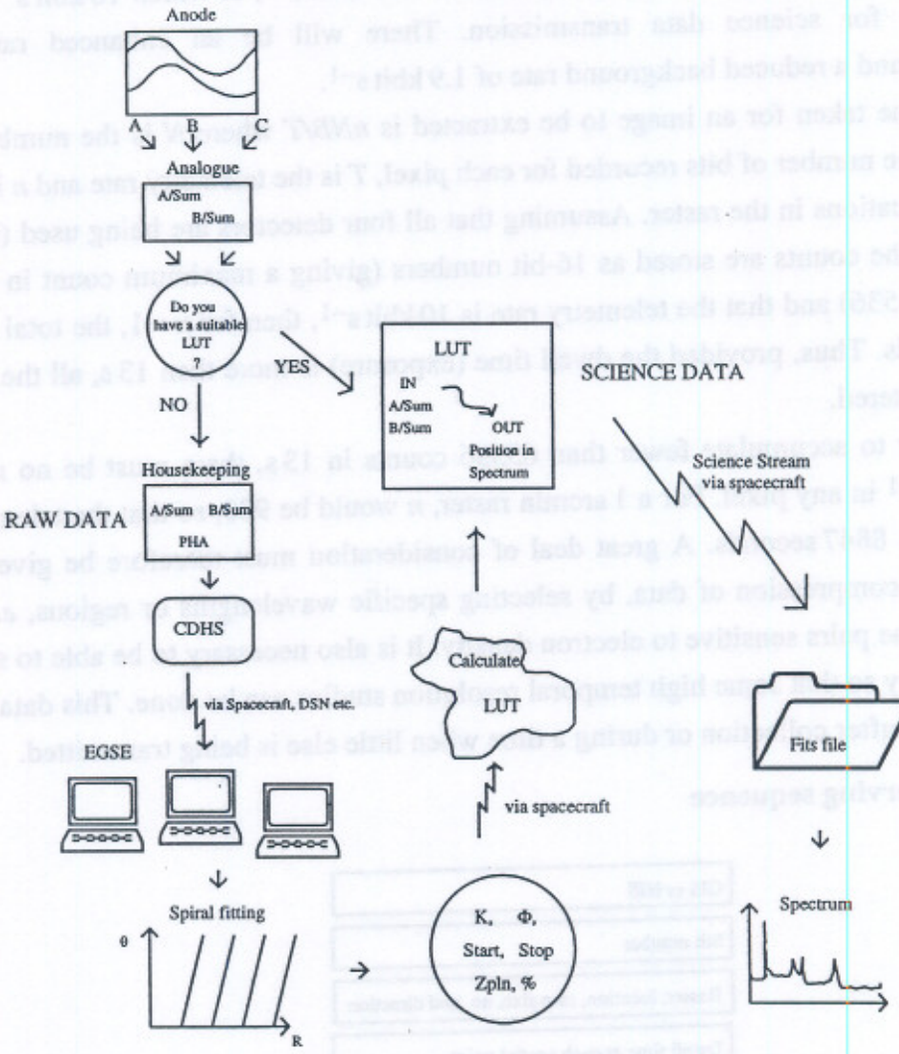

Figure 146. Flow diagram to illustrate how data is obtained from the detectors.

The CDHS recognises the raw data packets and sends them as special packets in the science stream. With one packet every two seconds, 1396 events per minute can be received. To obtain 10,000 events, therefore, takes about 7 minutes. A flat field of filament electron data is anticipated to take about 1 hour to collect.

In the science mode, the signals from the ADCs are put through a LUT on board. The purpose of this mode is to obtain large volumes of data from all four detectors, simultaneously and quickly. The data takes the form of a histogrammed spectrum, 4×2048 pixels long. Once on the ground, the spectra are put into FITS data files. A header with each file gives exposure time, slit and mirror positions *etc.*

There is a standard telemetry assignment of 11.3 kbit s^{-1}, of which 10 kbit s^{-1} will be available for science data transmission. There will be an enhanced rate of 22.6 kbit s^{-1} and a reduced background rate of 1.9 kbit s^{-1}.

The time taken for an image to be extracted is nNB/T where N is the number of pixels, B is the number of bits recorded for each pixel, T is the telemetry rate and n is the number of locations in the raster. Assuming that all four detectors are being used (8192 pixels), that the counts are stored as 16-bit numbers (giving a maximum count in each channel of 65536) and that the telemetry rate is 10 kbit s^{-1}, then for $n = 1$, the total time is 13.1 seconds. Thus, provided the dwell time (exposure) is more than 13 s, all the data can be telemetered.

In order to accumulate fewer than 65536 counts in 13 s, there must be no more than 5000 c s^{-1} in any pixel. For a 1 arcmin raster, n would be 900, so that the telemetry time becomes 8847 seconds. A great deal of consideration must therefore be given to selection and compression of data, by selecting specific wavelengths or regions, *e.g.* a selection of line pairs sensitive to electron density. It is also necessary to be able to store data in memory so that some high temporal resolution studies can be done. This data can be transmitted after collection or during a time when little else is being transmitted.

7.3.2. An observing sequence

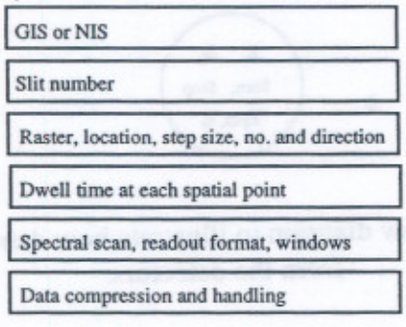

Figure 147. Block diagram of observing sequence parameters

To design an observing sequence, a number of choices has to be made, as summarised in Figure 147. A sequence consists of a set of instrument setup instructions, rasters and data handling activities. A raster is a specific succession of scan and slit movements and dwell times. The number of locations, the steps between each location for the slit and mirror, as well as the exposure time at each step, have to be selected. The shape of the raster pattern does not have to be rectangular and the centre of the raster may be offset from the centre of the CDS field. The same raster may be repeated any number of times. Data compression schemes and detector windows may be chosen. A description of a

sequence, which will be used extensively in the monitoring of calibration and for the design of other scientific studies, is given in Figure 148.

Spectral Atlas

Scientific Justification:

(i) To obtain a view of the whole wavelength range on quiet sun and active sun sites, at least once a month. (ii) To monitor the instrument spectral response against constant solar conditions.

Study Details:

Spectrometer:	Grazing Incidence
Slit:	2"×2"
Raster area:	30"×30"
Step (X,Y):	2", 2"
Raster locations:	15×15 = 225
Exposure time:	50 seconds
Duration of raster:	11293 sec (including overheads)
Number of rasters:	1
Total duration:	11293 sec
Line selection:	Full GIS output
Bins across line:	N/A
Telemetry/Compression:	26.2% 10 kbits/s. No compression.
Pointing:	To preplanned location.
Flags:	No flags used.
Solar feature tracking:	Not used in general. Sun will rotate 30" during raster.
Frequency:	Part of synoptic and monitoring programme to be performed at minimum once per month on both quiet and active sun.

Product:

Provides spectra for the four GIS wavelength bands for each of 225 locations of a raster covering an area of 30"×30" with 2"×2" resolution.

Joint Observations:

This study is complementary to SUMER POP number 05—the SUMER Solar Spectral Atlas.

Figure 148. The Spectral Atlas observing sequence from Harrison (RAL, private communication, 1995).

7.3.3. Inter-experiment flags

Inter-experiment flags will be used to transfer information from one scientific instrument on board SOHO to another to enable immediate action to be taken. The response can be within seconds—much faster than the time taken to downlink information, make a decision and uplink commands. This scheme will be used mainly for the purposes of pointing to interesting targets for studies of certain phenomena.

To meet the goals of SOHO it will be necessary to view highly transient events in the solar atmosphere. There are many likely targets and 5 instruments participating in the scheme. Thus the inter-experiment flag system is a complex arrangement of Master

and Receiver instruments, with multiple flags being appropriate for certain subsets of instruments. Some examples of flags relevant to CDS are for solar flares and microflares on a time scale of seconds; jets, turbulent events and bright points within a minute; eruptive prominences and coronal mass ejection within minutes; activated prominences and filaments over tens of minutes.

To avoid much complexity, only one inter-experiment flag type will be enabled at one time. The choice of the enabled flag, Master and Receivers will be decided in advance planning. The response of the Receivers will also be defined in advance. The contents of the flag will include the co-ordinates of the solar event and some identification data. The automatic identification of a solar event will be a significant rise or fall in brightness of a particular spectral line or a Doppler shift *etc.*

CDS therefore has to be able to generate and receive these flags as well as respond to them. In normal CDS operations no inter-experiment flags will be required.

CHAPTER 8.
PERFORMANCE—THE INSTRUMENT IN CALIBRATION

8.1. FLIGHT MODEL CALIBRATION

The instrument calibration tested the CDS instrument from end to end, as well as the instrument response to a known stimulus. Although much of the detail of the behaviour of the detectors had to be discovered by experimenting with them on their own, absolute intensity calibration was not performed with the GIS detectors separately.

Here I present my analysis of the detector performance from the flight calibration.

8.1.1. Requirements

The main goal of CDS is to measure accurate spectral line intensities, from which to deduce information about the solar atmospheres. A fine wavelength calibration is needed to measure flows and velocities from the spectral line shifts and broadenings.

8.1.1.1. Absolute and relative intensity calibration

A good absolute instrument sensitivity calibration versus wavelength is essential for establishing the absolute solar flux. It is required for much of the science, *e.g.* emission measure studies and abundances (see Chapter 1). An accurate calibration of the relative response to different spectral ranges is more important, but naturally follows from the absolute calibration. The accuracy to which the intensity calibration must be achieved depends on the accuracy to which the relevant atomic parameters are known. 20% is seen as the goal, while 50% is the lowest level worth attempting. Relative intensities need to be known to within 10%.

Variation in sensitivity from pixel to pixel affects the intensity calibration for absolute and relative measurements. The detectors have a small intrinsic variation but will vary more as time goes on because of LTGD.

8.1.1.2. Wavelength calibration

There is more emphasis on the measurement of intensities with CDS than on line shapes and shifts. For line identification as well as some flows analysis work, the wavelength calibration is required to 1 pixel for GIS.

8.1.1.3. Alignment

CDS needs to point to features with an accuracy of 10 arc seconds. Pointing must be stable to within the 2 arcseconds defined by the smallest field of view, for tens of minutes. CDS carries a sun sensor to monitor the pointing and to locate the solar disc. The ZOD, which is sensitive to visible and infrared light, will be used to check the alignment of the sun sensor with the optical axis.

8.1.1.4. Telescope PSF

The telescope calibration was performed separately at the Panter facility near Munich. A hollow cathode light source was placed behind a 5 µm pinhole, 125 m from the telescope. The image of the source at the telescope focus was detected using a two-dimensional intensified CCD detector which could be moved over the field of view. With a transputer driven centroiding algorithm, the detector was able to resolve down to the pore size of the MCP. The telescope PSF performance was within specification, with a FWHM spread of 1.2 and 1.7 arcsecs for the GIS aperture; and 1.2 and 1.5 arcsecs for the NIS aperture. The scatter from the PSF wings was also measured at 6.8 nm and found to fall from $10^{-4.3}$ at 20 arcsecs to $10^{-8.5}$ at 1000 arcsecs.

8.1.2. Apparatus

The CDS instrument was calibrated end to end at RAL with a pre-calibrated hollow cathode lamp as the ultraviolet source. Calibration took place in March 1994 and was a two-week 24 hour-a-day operation, to get enough data before delivering the instrument to Matra Marconi in Portsmouth, for integration with the rest of the payload.

At the EUV wavelengths viewed by CDS, no solid window materials exist, so the source must be inside the same vacuum chamber as the instrument, with an open optical path between the two. The only available continuum source in this wavelength range is a short-duration pulsed arc source which does indeed operate in vacuum. A line emission source was considered to be more suitable for CDS because it more nearly simulates the true solar spectrum. A hollow cathode lamp was selected which could be run at low pressure, minimising the gas bleeding into the instrument cavity. It was used as a radiometric transfer source standard (Danzmann *et al.*, 1988). The lamp was supplied by ETH in Zurich in collaboration with the PTB in Berlin.

The design of the lamp is similar to the one used in the MSSL UV facility, (see Figure 61): the latter, however, uses only a one-stage differential pumping system, which compares with the former use of a two-stage system, allowing higher pressures and hence a higher power. It emits intense unpolarized line radiation from a buffer gas (He, Ne, Ar or Kr) and the cathode material (Al). A current-stabilised power supply at

3 Amps, ~3 kV (10 times more than at MSSL) is used, with the voltage being adjusted by the gas pressure. The discharge burns reproducibly, with changes in spectral line emission of ≤5%, over more than 30 hours. After this period the anodes and glass spacers are cleaned with hydrochloric acid and the cathode inset is replaced. The emission values then remain steady for another 30 hours.

The radiances of the emitted spectral emission lines were pre-calibrated by radiant flux comparison with the Berlin electron storage ring BESSY, at the VUV-radiometric laboratory of PTB. The lamp was then transported to RAL and used for CDS. It was checked again at BESSY afterwards. Two rehearsals using the CDS optics model were performed, the second one including the OM detector. These trials served to test the calibration concept and also acted as an early proof of the suitability of the detector. An uncertainty in the source flux of the order of 6–8% was achieved for most lines.

Figures 149, 150 and 151 is a set of spectra from the detectors during FM calibration. They are all reversed so that increasing pixel number corresponds to increasing wavelength. Some lines on each detector are marked with their wavelengths in nanometres.

Twenty-one lines were identified in the hollow cathode spectra and calibrated against the storage ring. These were 3 neon lines on detector 1; 6 lines on detector 2 (1 helium and 5 neon); 4 neon lines on detector 3; and 4 lines on detector 4 (2 argon and 2 neon). A further 2 lines are produced on detector 1 from the aluminium cathode, with either neon or argon. The lines are listed in Table 16.

The beam fluxes are calibrated using the whole beam. Using the largest slit 6 (90"×240") ensures that the entire calibration beam is used. Those lines which are too close together to separate using this slit, were combined in the intensity measurements.

With slit 6, the total output from the GIS detectors, assuming they are 10% efficient and that all the flux falls on the detectors, would be 2.9×10^5 c s^{-1}. This is above the maximum that the GIS–CDHS link can handle if all the detectors are working at the same time. Detectors 3 and 4 individually also give count rates above the maximum (1.4×10^5 and 1.1×10^5 respectively). The lines 12, 17, 18, 23 and 24 were projected to give a count rate of more than 0.1 c s^{-1} $pore^{-1}$ with slits 6, 5 and 3, the highest being line 18. Table 17 shows how the slits are related in size and flux. The relative flux is measured by comparing the intensities on the NIS.

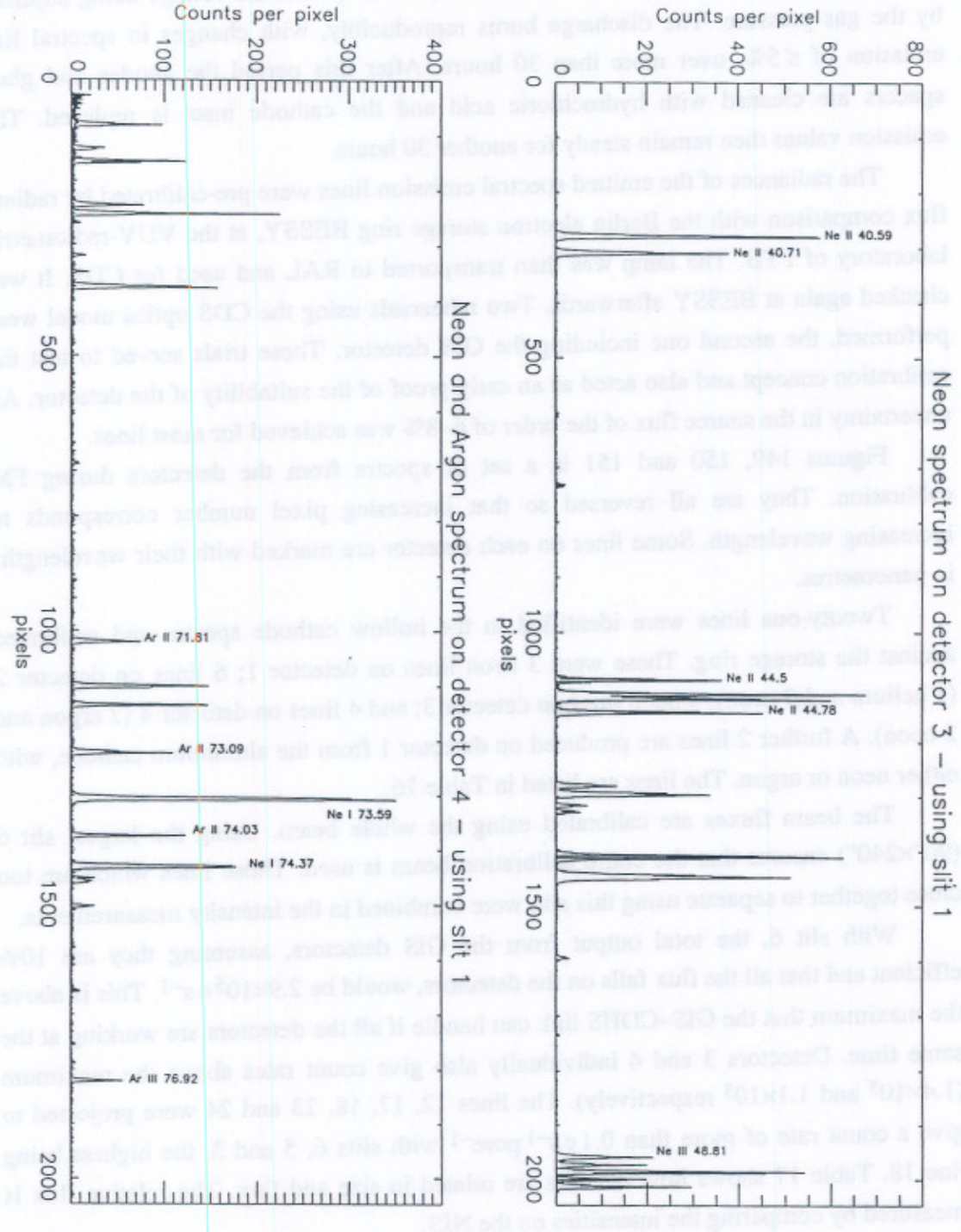

Figure 149. Examples of spectra obtained during calibration with slit 1.

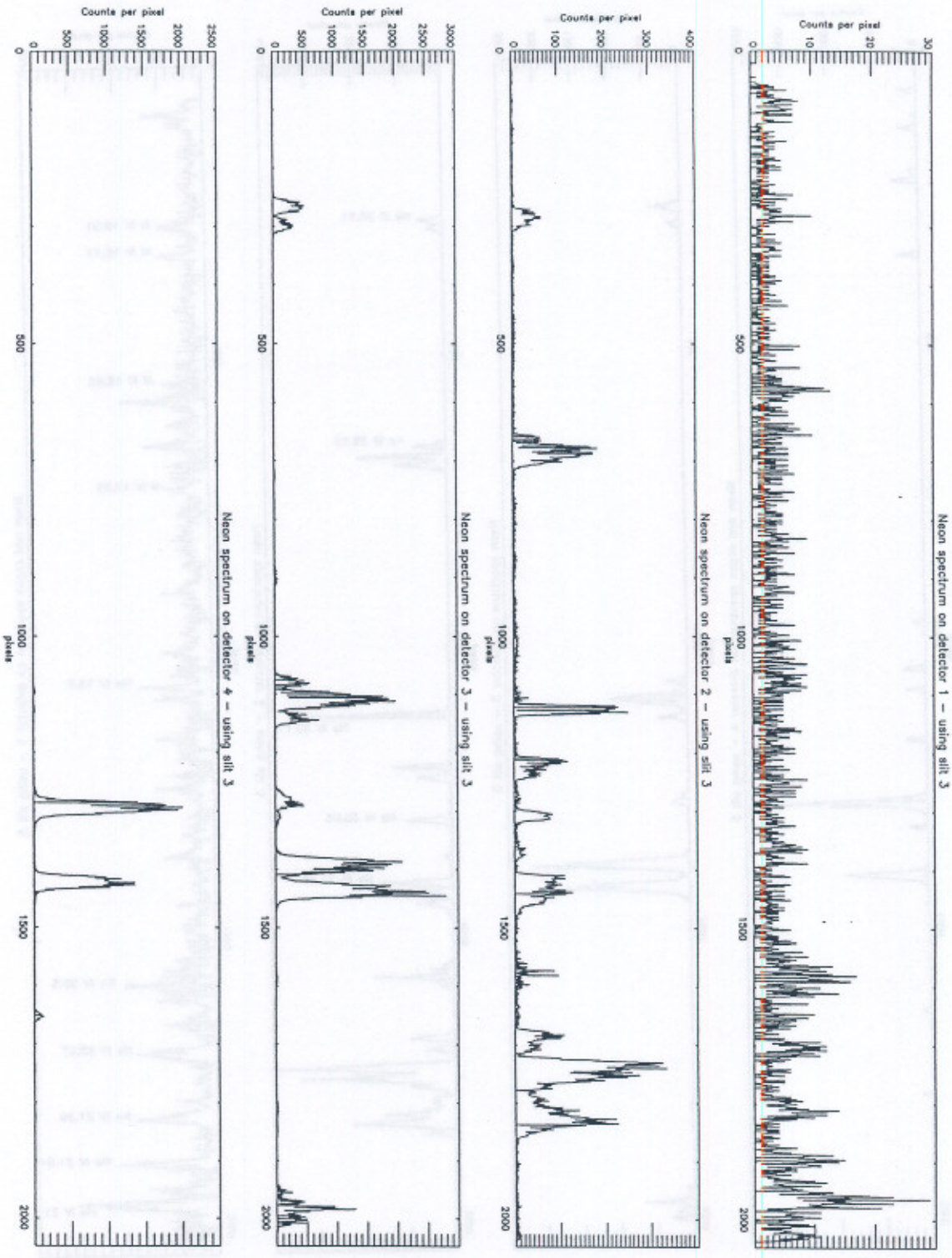

Figure 150. Examples of spectra obtained during calibration with slit 3.

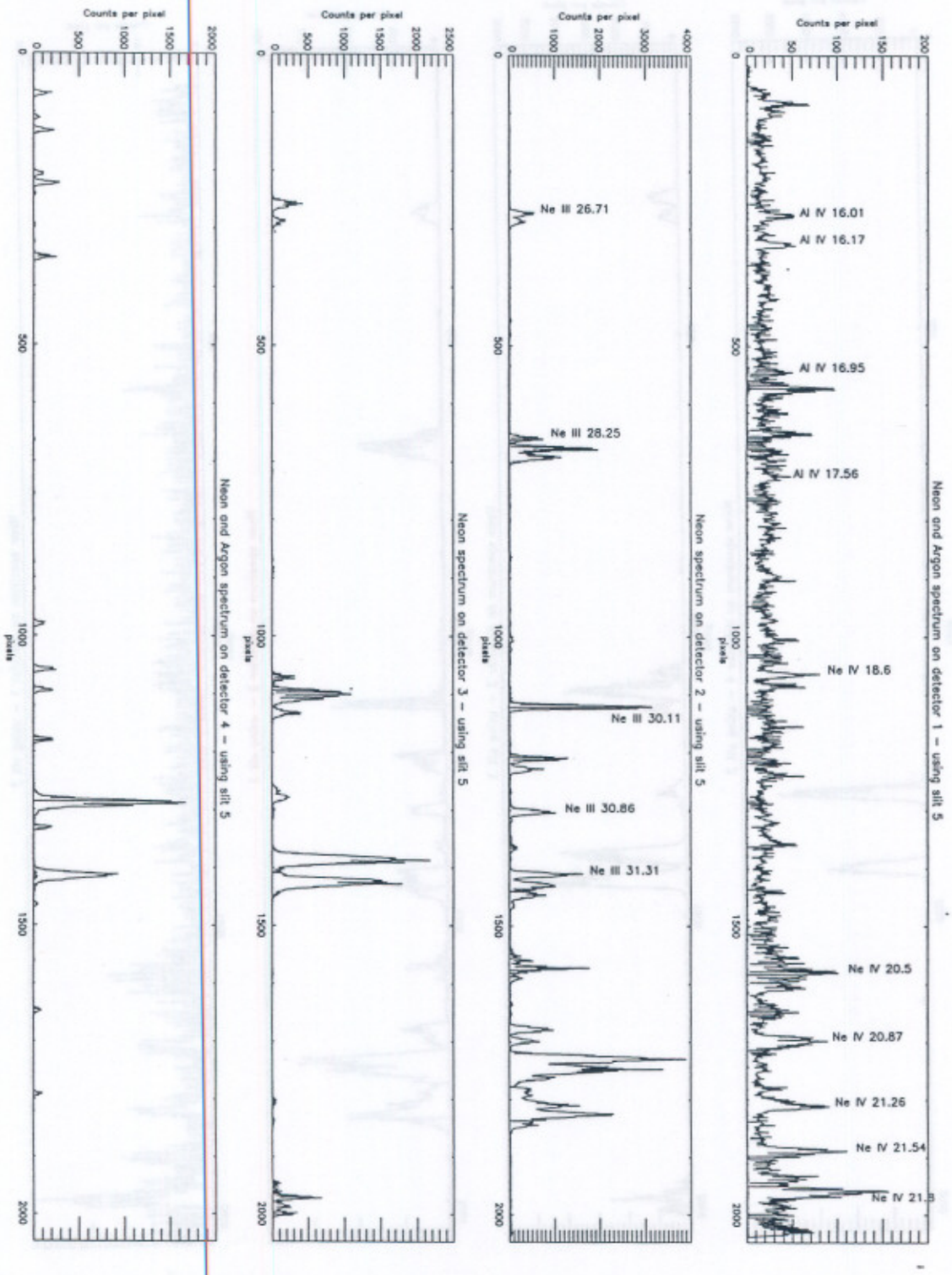

Figure 151. Examples of spectra obtained during calibration with slit 5.

Detector Number	Line number	Wavelength (nm)	Ion	Source beam intensity (photons s^{-1})	Photons at the detector[a] (photons s^{-1})
GIS 1	1	16.01/16.17	Al IV/Ne	5.35×10^{4}	321
GIS 1	2	16.95–17.56	Al III/Ne	1.17×10^{5}	702
GIS 1	3	16.01/16.17	Al IV/Ar	4.30×10^{4}	258
GIS 1	4	16.95–17.56	Al III/Ar	8.41×10^{4}	505
GIS 1	5	20.43–20.89	Ne IV	3.43×10^{5}	2058
GIS 1	6	21.26	Ne IV	1.21×10^{5}	726
GIS 1	7	21.54–21.88	Ne IV	4.81×10^{5}	2886
GIS 2	9	26.71–26.77	Ne III	9.83×10^{5}	5898
GIS 2	10	28.25–28.39	Ne III	2.58×10^{6}	1.5×10^{4}
GIS 2	11	30.11	Ne III	1.59×10^{6}	9540
GIS 2	12	30.38	He II	4.94×10^{7}	3.0×10^{5}
GIS 2	13	30.86	Ne III	6.06×10^{5}	3636
GIS 2 NIS 1	14	31.31–31.39	Ne III	1.97×10^{6}	1.2×10^{4}
NIS 1	15	37.93	Ne III	1.05×10^{7}	6.3×10^{4}
GIS 3	16	40.59/40.71	Ne II	1.96×10^{7}	1.2×10^{5}
GIS 3	17	44.50–44.78	Ne II	3.89×10^{7}	2.3×10^{5}
GIS 3	18	46.07–46.24	Ne II	1.57×10^{8}	9.4×10^{5}
GIS 3	19	48.81–49.11	Ne III	1.75×10^{7}	1.1×10^{5}
NIS 2	20	53.70	He I	7.08×10^{6}	8.5×10^{4}
NIS 2	21	58.43	He I	1.79×10^{8}	2.1×10^{6}
GIS 4	22	71.81–74.53	Ar II	2.53×10^{7}	1.5×10^{5}
GIS 4	23	73.59	Ne I	1.00×10^{8}	6.0×10^{5}
GIS 4	24	74.37	Ne I	5.88×10^{7}	3.5×10^{5}
GIS 4	25	76.92	Ar III	2.25×10^{6}	1.4×10^{4}

Table 16. Calibration line list.

[a] Expected rate, assuming a combined telescope, scan mirror and grating efficiency of 0.006

Although the GIS does not produce two-dimensional images, the grating does focus the spectrum as a series of images (one image for each spectral line) at the RC, with the width of the images dependent on the width of the slit. The number of pores illuminated is calculated assuming that each slit image is 16 mm high and the width is as measured in the calibration. This is therefore only an approximation because the images

are not all 16 mm high and the shape of the image is curved. The curvature is due to the loss of focus with distance from the plane of the grating and RC.

Slit Number	Size of slit in arcseconds	Size of slit in mm	Relative intensity of slit—measured on NIS	Number of pores illuminated by slit image
1	2×2	0.025×0.025	0.01	12300
2	4×4	0.050×0.050	0.05	16800
3	8×50.8	0.100×0.635	1	29500
4	2×240	0.025×3.0	0.31	12300
5	4×240	0.050×3.0	0.57	16800
6	90×240	1.125×3.0	10	185000

Table 17. Table of slits, sizes and pores.

8.1.3. Observations

The light from the lamp did not illuminate the whole aperture at once, but formed a pencil beam with a divergence of no more than 10". The instrument was on a motorised platform so that it could be moved relative to the beam in two orthogonal directions. This allowed the aperture to be scanned with the pencil beam so that the alignments could be checked and the response of a fully illuminated telescope reconstructed from the results. The aperture scans were performed with slit 6. Slit scans across the aperture were performed with all slits, using mostly 3-minute exposures at each position. Use of all the slits allowed any shifts in line position with movement of the source relative to the aperture to be measured.

In addition to the aperture, slit and mirror scans, intensity measurements were made by illuminating the instrument with the pencil beam near the centre of the aperture, with exposures of 30 minutes. All the slits were used. The intention was that slit 6 would provide definitive intensity measurements, while the other slits would give scaling factors to calculate the relative throughputs of the slits. Because of the very high count rates from slit 6 it was necessary to use the other slits for intensity measurements as well.

Lines from the hollow cathode lamp can be used for wavelength calibration, using the narrowest (2"×2") slit. The lines on the detectors are sufficiently well spread to obtain a good fit if the theoretical fit is known.

8.2. CALIBRATION CHALLENGES

8.2.1. Maintaining calibration until launch

One problem with the calibration of the CDS instrument is the long time between calibration and launch. Calibration took place in March 1994 and launch is predicted for November 1995. During storage, although the instrument is kept purged with dry nitrogen, there is a high likelihood that there will be significant drifts particularly in the gain of the MCPs.

In order to minimise drifts, a better method of storage would have been under vacuum. However, to have dedicated vacuum chambers would be impractical for this instrument configuration. Therefore, the detector responses will have to be re-calibrated after launch and compared with the pre-launch response.

8.2.2. Gain depression

Drifts in gain or a steady decline, as in LTGD, affects the maintenance of intensity calibration. Any change in the PHD relative to the acceptance window bounded by the discriminators will change the proportion of events imaged and thus change the apparent efficiency. In use, the gain therefore has to be continually monitored for changes.

CDGD and LTGD have the effect of reducing the gain at the position of individual lines producing a differential gain across the detector. The perceived intensities of all the lines on the detector are therefore not affected uniformly.

For uniform drifts or gain depression, the window or HV may be adjusted to keep the PHD in the same place relative to the window. For position dependent gain depression this is impossible for all lines at once. It is important to know which lines are being detected correctly.

With GIS the PHD is sampled randomly from the incoming events, according to the count rate. The pulse heights are not related to position, so that only the mean gain across the whole detector is known. Any small-scale changes due to high local count rates, giving CDGD or LTGD cannot be determined from the PHD, unless there are enough affected events to alter the mean PHD.

8.2.3. Puzzling PHD

At the start of the calibration some time was devoted to gathering raw data from the GIS detectors to set up the HVs and LUTs required. Very puzzling PHDs were produced from the raw data, as illustrated in Figure 152.

In many cases it was impossible to tell where the peak lay or indeed whether there was any peak at all. At low voltages the PHD was exponential. Higher, it became flat-

topped. Apparently the only peak was appearing above the ULD. The reasons for this did not become clear immediately.

There were four main reasons for the confusion. First, the discriminators (LLD and ULD) were not set at levels equivalent to the gains they were believed to be (see §4.4). The discriminators have since been changed to solve this problem.

Secondly, the counters wrapped round at 16-bits (65,000 c s^{-1}). This was not a problem with the smaller slits, but with slit 6 or using the filaments with +12 V bias on the front faces, the count rate could easily exceed 65,000 without it's being apparent. At such high count rates the PHD was depressed. The counters have been changed to limit at 65,000 c s^{-1}.

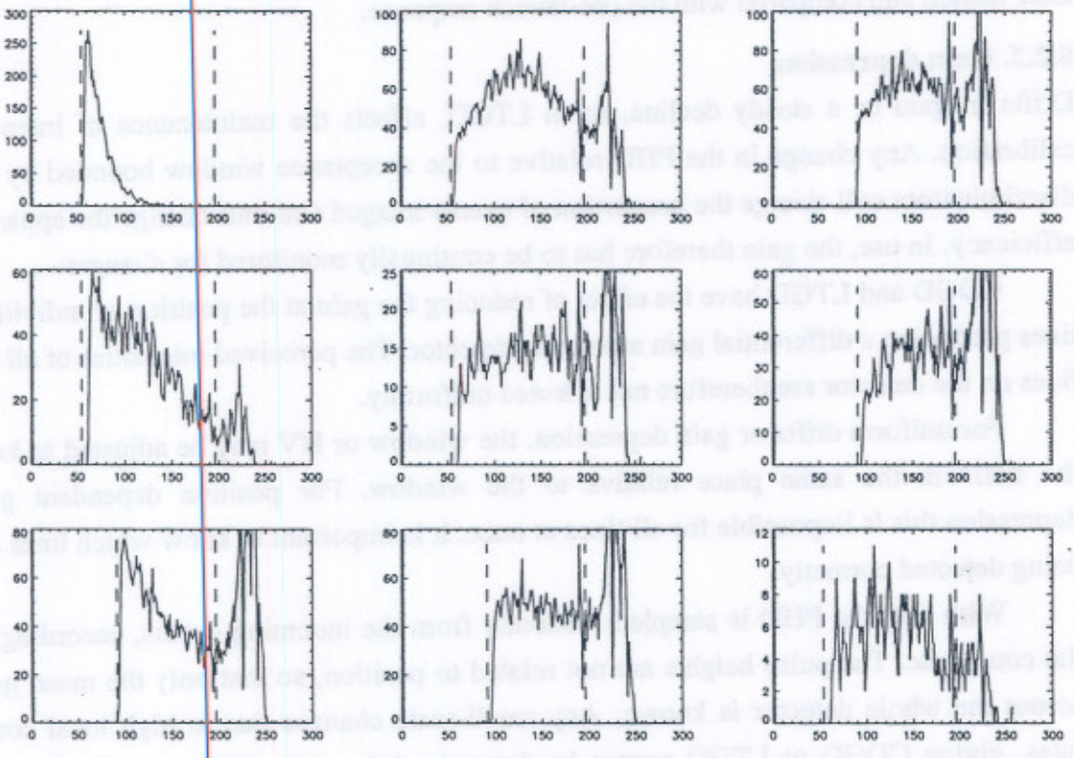

Figure 152. Examples of PHDs obtained during calibration.
The pulse height window is indicated by dashed lines in each case.

Thirdly, ion feedback was occurring because the pressure was not low enough. Although the gauges in the vacuum tank read less than 4×10^{-6} mbar, the pressure in the spectrometer must have been higher. The result was the appearance of a second peak near to or above the ULD. Instead of starting with an exponential at low voltages and gradually building up to a saturated peak with higher and higher voltage, the ion

feedback peak became dominant, distorting the PHD so that it was impossible to get the peak in the centre of the window. This ion feedback peak was not seen in the more recent spacecraft thermal vacuum test.

The fourth reason was CDGD. This was operating to broaden the peak by forcing many events towards the LLD. The gain was not equal across the plate.

Two distinct sets of intensity measurements were taken. For the first set of data (set A), the HVs were selected on the basis of a stable count rate within ±40 V of the selected HV value. The HVs were increased to compensate for high count rates with increasing slit size. For the second set of data (set B), the filaments were used to set up the HV at low count rates. However, the actual PHD generated by UV events turned out to have a lower gain, because of the change in front face bias altering the MCP voltage, often producing an exponential form at the chosen voltage. The chosen voltages were therefore increased slightly but there was not time to take sufficient raw data using the UV at these voltages to determine the correction factors for the LUT.

8.2.4. Choosing a look up table

An obstacle to repeatable intensity measurements is the existence of very bright lines leading to gain depression. The gain depression affects the count rate and also the position of the events in the spiral polar plot.

In order not to lose too many events, the LLD has to be set as low as possible, but then a large number of events with low pulse height may ghost onto the next spiral arm. Events falling between the arms and discarded to avoid ambiguity very often form a significant proportion of the line intensity.

For each slit there are different count rates. Changing the gas in the UV source gives lines in different positions. Changing detector voltages also alters the detected count rates and, because of gain depression, the positions of the lines in the spiral plot. These effects make it very difficult to find a set of LUT parameters which suits a variety of input spectra. Sometimes the gains and offsets have to be used creatively to allow the proper viewing of a line of particular interest.

For each detector, a set of LUT parameters and HVs were selected for a given slit and gas. For the set A intensity data, the HVs were reset for each slit to compensate for CDGD. Each detector had three different LUTs: one for slits 1, 2, another for slits 3, 4, 5 and another for slit 6. For the set B data, the HVs were kept constant, although the LUTs still had to be changed. The main purpose of this was to be able to produce the CDGD graphs using the increasing slit size to increase the incident count rate.

One thing that became abundantly clear in analysing the data after calibration, was the need to record exactly the conditions prevailing at the time of a particular observa-

tion: the HV, both set and measured; the LUT parameters; the LLD setting; count rates, raw and ULD. For the data analysis, the engineering telemetry had to be replayed to ascertain the relevant details, because the log book was not sufficient. The need for a variety of different HVs and LUTs made taking the data complex. There was a number of operator errors which could only be discovered by checking the telemetry afterwards. All these details are now included in the header of the FITS science data files.

8.2.5. Flat fielding

As mentioned in §8.1.1.1., in order to obtain accurate relative intensity measurements it is necessary to measure any pixel to pixel variations in sensitivity. The calibration scheme using a line source alone did not address this measurement.

Thermionic electron emission from the filament provides events across the whole detector surface but, with the +12 V front face bias the flux distribution is highly peaked, as the electrons from the filament are drawn straight towards the detectors. Because of the geometrical arrangement of the filaments relative to the detectors, the peak is towards one edge of the detectors. With the front faces biased to −12 V, the distribution is improved, although the intensity still varies by at least a factor of 2 (see Figure 154). The disadvantage with using −12 V is that the filaments have to be run at a much higher current (by about 20%), which will shorten their life time.

McComas and Bane (1982) observed that the distribution from such a filament at a number of radial positions in different directions varies by a factor of two or three. They also noticed that the non-uniformity changed with time and with slight variations in filament current. This could be caused by the effect on the local work function of crystal growth on the tungsten surface. They describe a way of obtaining a flat field from a filament. It involves mounting it inside a cylinder, with both filament and cylinder at ~−200 V, attracting the electrons out of the end of the cylinder with a flat plate at −190 V and then sideways through a mesh at ~−180 V, to a cylindrical grounded anode.

The pixel to pixel variations therefore were not measured on the instrument. The filaments were used only to monitor the change in sensitivity with time. From measurements in the laboratory the response across the detectors is smooth so that the intensities can be interpolated between the measured spectral lines.

8.3. RESULTS FROM CALIBRATION

The main results needed from the GIS calibration for the detectors were a wavelength calibration and the response to an input intensity relative to wavelength. Any measurement of the intensity has to be corrected for a number of instrumental

parameters: electronic dead times; losses from the LUT; ghosting; gain depression; detector dark count and scattered background. The error bars must also include uncertainty in the UV source output.

8.3.1. Long term gain depression

Periodically, throughout the calibration, base line count rate checks were made. These were records of raw, processed and ULD count rates using slit 6. Figure 153 shows the individual detector and total raw count rates recorded in the base line tests. Checks were made at all aperture positions. One check made at position G3,C5 followed immediately by one at G2,C5 allowed a correction factor to be determined for the change in position.

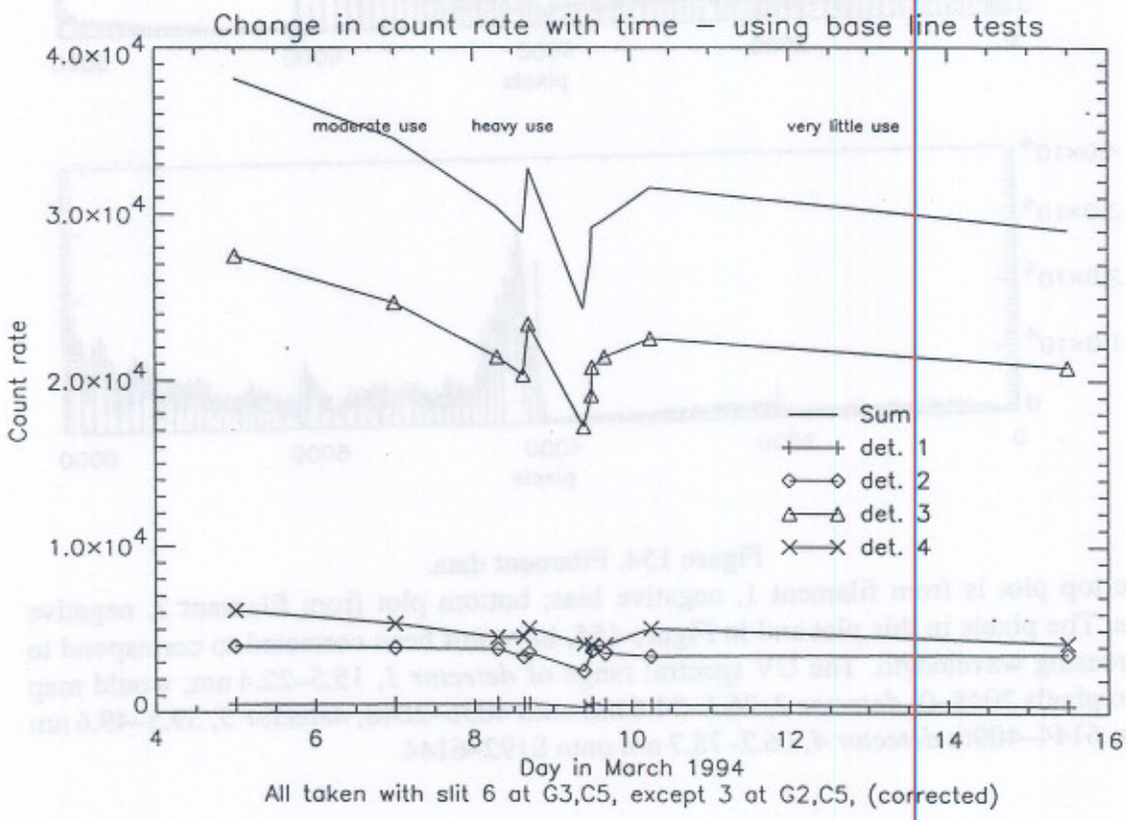

Figure 153. Decrease in count rate during the calibration period.
The total decreased to 76% of initial count rate by the end of the calibration.

It turned out to be too difficult to estimate the actual charge extracted during the calibration, but the amount of usage has been marked on the graph. There is some evidence of recovery during the latter half of the period when the GIS was not often in use.

It is evident that LTGD was taking place in detector 3 and 4, where the high count rate lines lay. They fell to 75% and 69%, respectively, of their initial count rate by the end of the calibration. Detectors 1 and 2 only fell to 89%. The fact that detectors 1 and 2

did reduce in count rate suggests that there is a slight overall decline in gain, possibly due to the gradual outgassing of the detectors, cleaning the plates and reducing ion feedback.

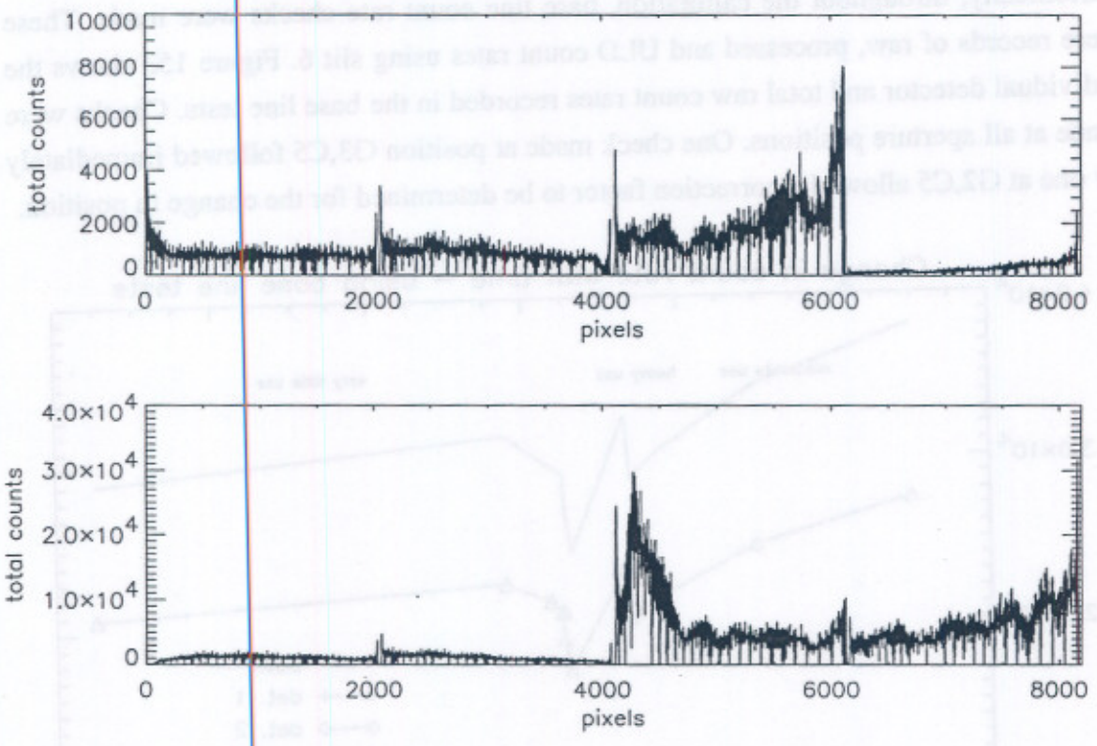

Figure 154. Filament data.

The top plot is from filament 1, negative bias; bottom plot from filament 2, negative bias. The pixels in this plot and in Figure 155, have **not** been corrected to correspond to increasing wavelength. The UV spectral range of *detector 1*, 15.5–22.4 nm, would map onto pixels 2048–0; *detector 2*, 26.1–34.6 nm onto 4096–2048; *detector 3*, 39.5–49.6 nm onto 6144–4096; *detector 4*, 66.2–78.7 nm onto 8192–6144.

8.3.1.1. Filament data

If the filament setting and detector settings are repeated identically after periods of use, changes in the detector performance can be monitored. This assumes the filament output does not change significantly.

Raw and science dumps of filament data (see Figure 154) were made near the beginning of the calibration period, on 5th March 1994, and near the end on 11th March. All the data was taken with the detector voltages set to the same value (3840 kV). The LUT was changed slightly between the two sets of data, but the effect was found to be insignificant when running the raw data through both LUTs.

The early observations with the same combination of filament and bias were summed together. All the data was smoothed with a simple boxcar average 2 pixels wide. This removed the zeros in the data to allow division. Any relative changes with time could be seen in the ratio of later data to equivalent early data (see Figure 155).

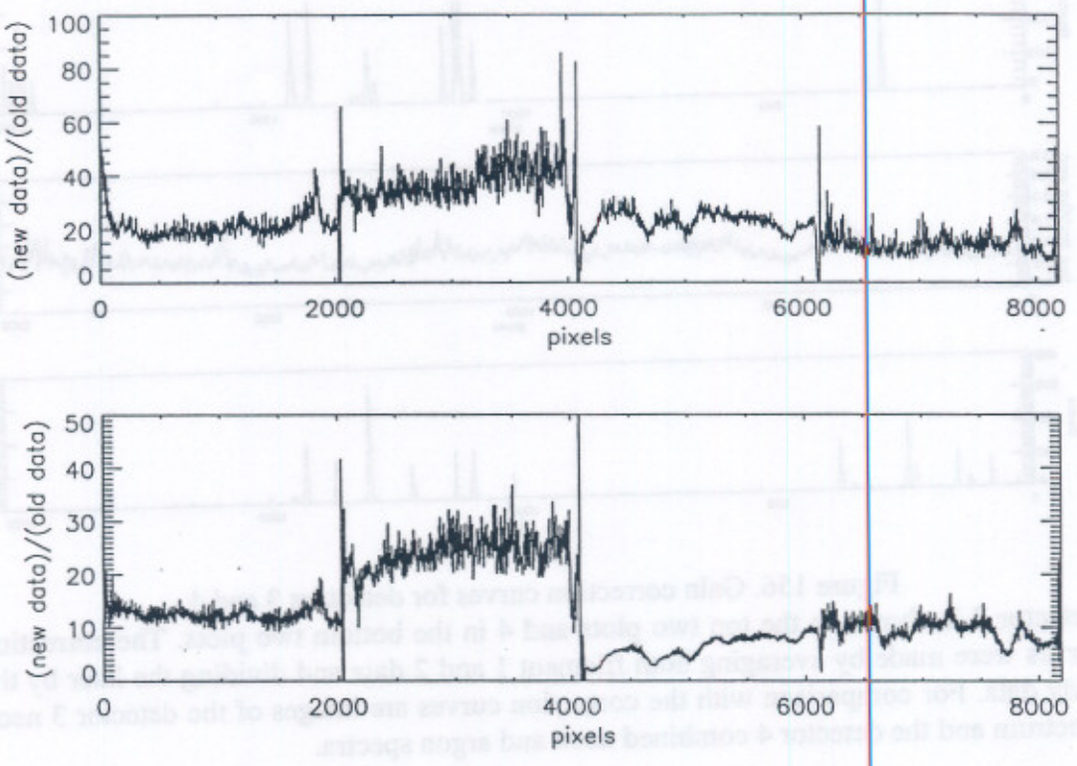

Figure 155. Plot of ratio of new data to old for filaments 1 (top) and 2 (bottom), using negative bias. Refer to caption to Figure 154 for explanation of pixel ranges.

Although the individual spectra for the two filaments were very different, the ratio plots were almost identical in shape. There were no significant features in the detector 1 and 2 data. An apparent increase in sensitivity at one end of detector 1 (Figure 155) was not consistent in all the data. Ratio plots of detectors 3 and 4 did have significant dips in them.

Superimposing neon spectra on top of the ratio plots (see Figure 156) showed that the dips in the detector 3 filament data were very closely aligned with the spectral line positions. For detector 3 the loss in count rate in those positions was clearly due to the LTGD from the intense lines 16, 17, 18 and 19. For detector 4 it was not so clear, but there were many more lines present.

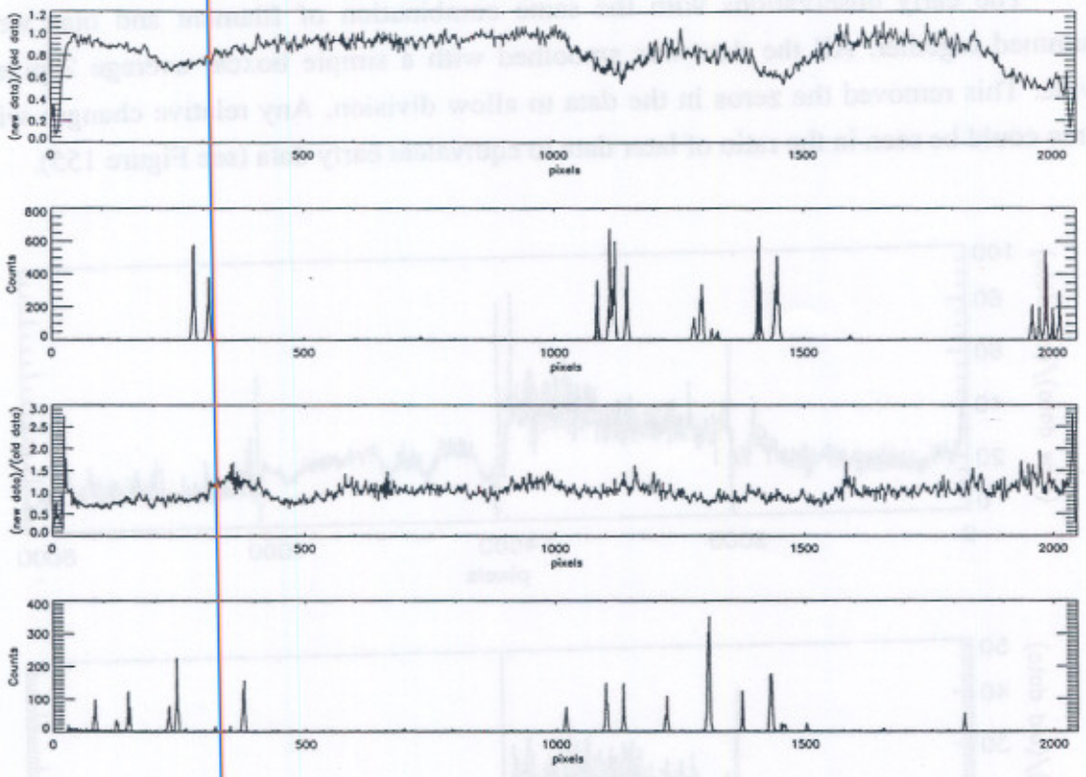

Figure 156. Gain correction curves for detectors 3 and 4.
Detector 3 is shown in the top two plots and 4 in the bottom two plots. The correction curves were made by averaging both filament 1 and 2 data and dividing the later by the early data. For comparison with the correction curves are images of the detector 3 neon spectrum and the detector 4 combined neon and argon spectra.

The plots from the two filaments were averaged together and the mean level set to unity. These plots were used as gain loss correction curves when analysing the later intensity data.

8.3.2. Wavelength calibration

The positions of the centres of many GIS lines were determined by Bromage of UCLAN and Kent of RAL, using both Gaussian fits and fits by eye. Figure 157 demonstrates the relationship between the spectral line wavelengths and the measured position in pixels. The lines are well spaced, allowing good fits to be done.

Although slit 1 gives the narrowest lines, because of the fixed patterning it was sometimes easier to fit to lines from the wider slits. Bromage found that the best wavelength fits were quadratic. There are three reasons for this: two associated with geometry and the third with the LUT. First, the detectors are flat whereas the spectral

axis is a curved Rowland circle, and the incident light is at a high grazing incidence angle. This leads to a quadratic displacement, of up to ±40 pixels.

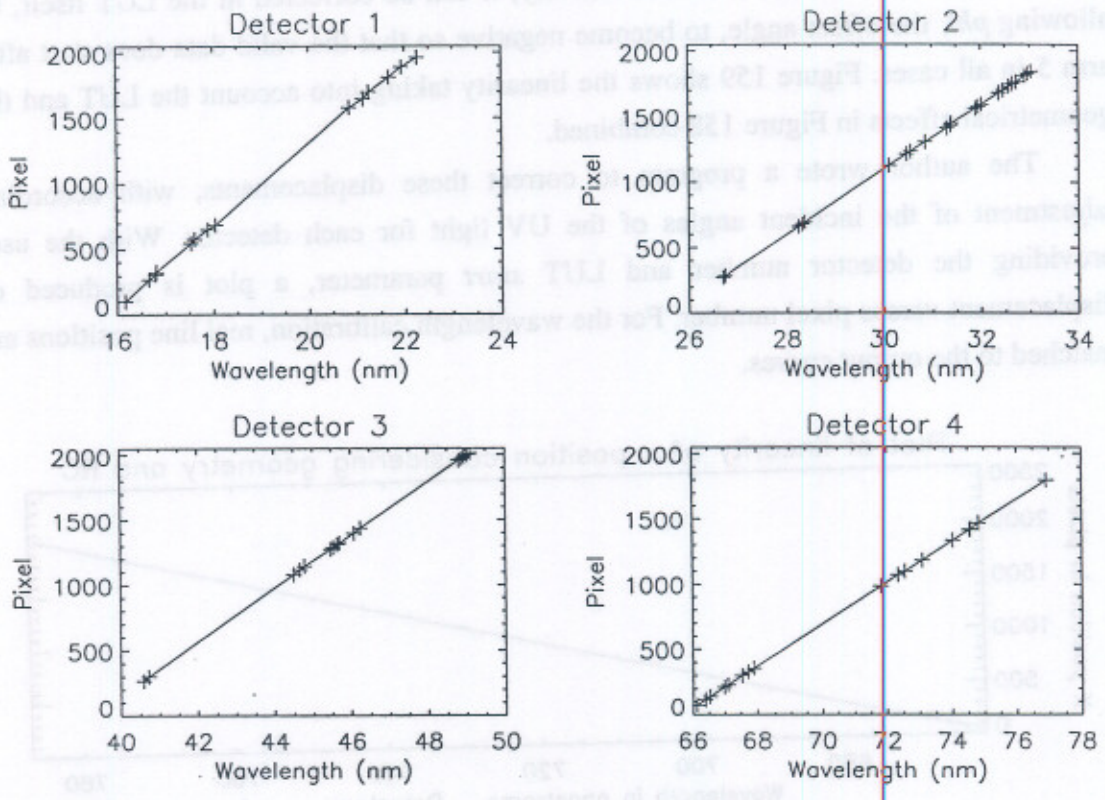

Figure 157. Spectral line position measurements.
The solid lines are not fits to the data, but just join up the points.

The second geometrical factor which has to be taken into account is the way in which the lines are mapped onto the RC. The arc length around the RC is not proportional to wavelength, but is proportional to the sine of the angle at which the light leaves the grating. This has the effect of partly compensating for the flatness of the detector, reducing the displacement from ±40 pixels to ±10 pixels. The mapping of the wavelength to pixels is demonstrated in Figure 158. The residuals are measured relative to a theoretical straight line crossing the RC at the same two points as the detector front face is actually designed to do.

The third reason, associated with the LUT, is that the convolution of the charge cloud with the anode leads to a reduction in spiral radius. Figure 123 shows how the shrinkage is not proportional to radius. When a spiral is fitted to the output, the result is a spiral with fewer arms than in the anode design. Because the position of a spectral line in this polar plane shifts only in radius and not in angle, the line may appear on arm 3

rather than arm 5. This results in another quadratic error in the wavelength calibration, but this time dependent on the amount of shrinkage. It can easily be calculated if the LUT parameter *start* is known. Alternatively, it can be corrected in the LUT itself, by allowing *phi,* the offset angle, to become negative so that the valid data does start after arm 5 in all cases. Figure 159 shows the linearity taking into account the LUT and the geometrical effects in Figure 158 combined.

The author wrote a program to correct these displacements, with according adjustment of the incident angles of the UV light for each detector. With the user providing the detector number and LUT *start* parameter, a plot is produced of displacement versus pixel number. For the wavelength calibration, real line positions are matched to the output curves.

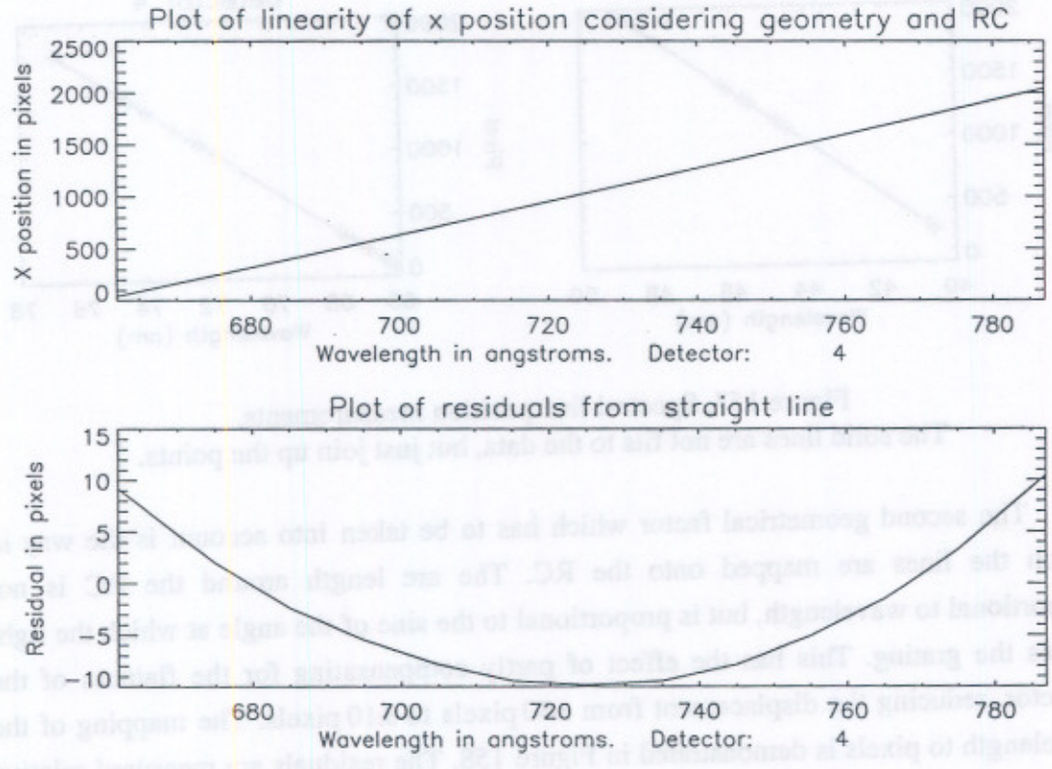

Figure 158. Non-linearity in wavelength calibration due to the geometry at detector 4 from the flatness of the detector on a curved RC, and the sine dependency of the spectral line positions.

Observations with different slits show a variation in the wavelength ranges of less than 0.1 nm between slits 1 and 5. However, the ranges were slightly different from expectation. This could be caused by small errors in the location of the detectors on the RC; along the RC radius; around the RC circumference or by rotation of the detectors

themselves so that they are not perfectly tangential to the RC. A rotation of the grating would also have an effect. As the ranges still cover the prime lines, the worst case would be if the whole offset in range was caused by movement of the detectors along the RC radius, because this would give the largest broadening of the lines.

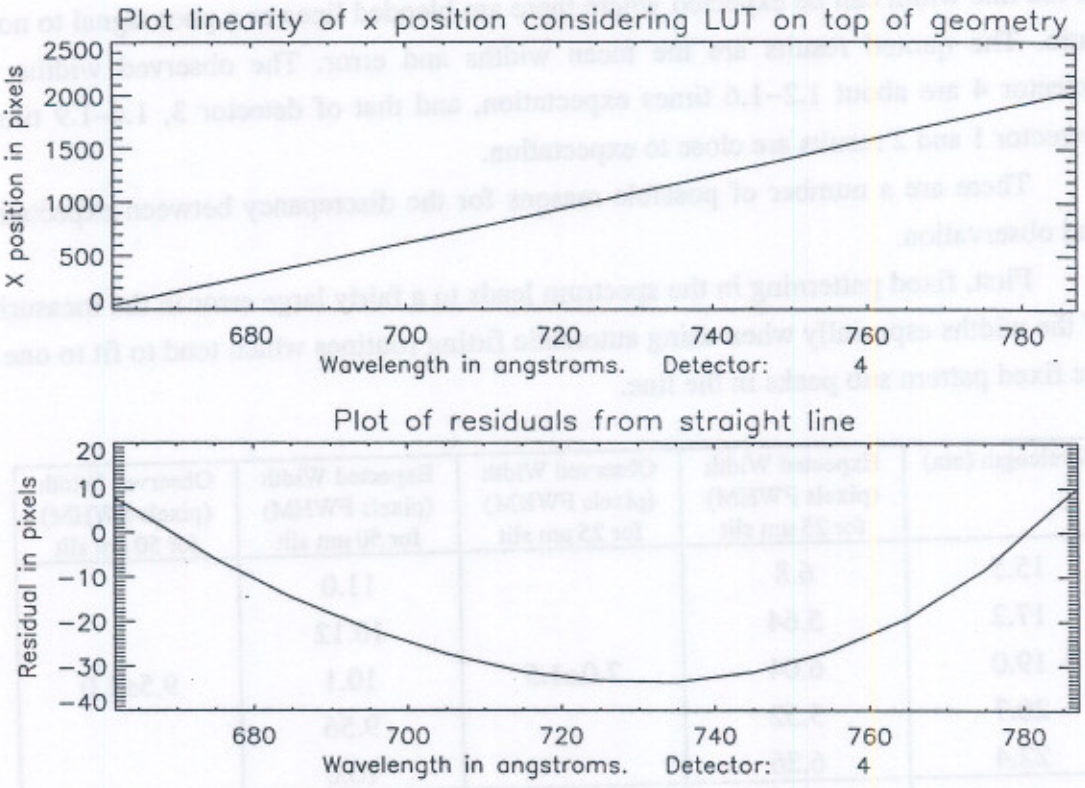

Figure 159. Non-linearity in wavelength calibration
after combining the effects of LUT, geometry and the RC line positions.

It was noticed that there were shifts in the line positions with changes in slit, mirror and aperture position. Scanning the full aperture gave shifts of 3–5 pixels, but because of the quadratic nature of the mapping, the size of the shift depends on the location of the line. This was also seen in the NIS. The shift implies a slight misalignment of the source and slits. The wavelength calibration has to depend on all these factors—slit number, slit and mirror position and the LUT *start* parameter, (Bromage, Breeveld and Kent, 1995). The shift in line position with the aperture scan implies a slight change in incident angle with the scan. If this is due to the response of the telescope, rather than the mounting of the source relative to the instrument, then illuminating the whole aperture will produce lines broadened by the number of pixels in the shift.

8.3.3. Line widths

The expected widths in terms of pixels for slits 1 and 2 are given in Table 18. The line widths were measured by Bromage using Gaussian fitting. Some lines were apparently narrowed by the fixed patterning, others were broadened. In some cases over estimation of the line width can be expected where there are blended lines or a poor signal to noise ratio. The quoted results are the mean widths and error. The observed widths for detector 4 are about 1.2–1.6 times expectation, and that of detector 3, 1.6–1.9 times. Detector 1 and 2 results are close to expectation.

There are a number of possible reasons for the discrepancy between expectation and observation.

First, fixed patterning in the spectrum leads to a fairly large error in the measuring of the widths especially when using automatic fitting routines which tend to fit to one of the fixed pattern sub peaks in the line.

Wavelength (nm)	Expected Width (pixels FWHM) for 25 μm slit	Observed Width (pixels FWHM) for 25 μm slit	Expected Width (pixels FWHM) for 50 μm slit	Observed Width (pixels FWHM) for 50 μm slit
15.5	6.8		11.0	
17.2	5.64		10.12	
19.0	6.04	7.0±1.5	10.1	9.5±1.0
20.7	5.52		9.56	
22.4	6.56		10.0	
26.1	4.75	5.5±1.0	9.5	9.5±1.0
34.6	4.05		8.1	
39.6	3.8	6.5±1.5	7.6	12.0±1.5
49.5	3.35		6.7	
66.2	3.6		5.8	
69.3	3.2		5.6	
72.4	3.2	5.8±1.0	5.5	6.5±1.0
75.5	3.1		5.4	
78.7	3.6		5.6	

Table 18. Comparing expected and observed line widths in terms of pixels. Ray tracing was performed for detectors 1 and 4, which represented the extremes, and the widths are taken from Table 8. The expected widths for detectors 2 and 3 are calculated from the projected slit widths for each end of the detectors. The observed numbers are the mean widths of all the lines on one detector in one exposure.

The largest expected broadening effect is the fact that only 3 mm of the grating was illuminated by the pencil beam. If a large part of the grating is illuminated, the resolving power of the grating is calculated using equation (114).

$$R \leq 2.3 \times \left[r^3 \lambda \frac{\cos\alpha \cos\theta}{\sin^2\alpha \cos\theta + \sin^2\theta \cos\alpha} \right]^{\frac{1}{4}} \times \left(\frac{n}{d} \right) \qquad (114)$$

where r ($=0.144$ m) is the radius of curvature of the grating, θ ($=84°$) is the angle of incidence onto the grating and α is the emergent angle. n ($=1$) is the order of the spectrum and d ($=1\times10^{-6}$ m) the pitch of the groove. At the two extremes of the wavelength range $\lambda = 15.5\times10^{-9}$ and 78.7×10^{-9} m, with $\alpha = 78.6°$ and $66.5°$. These give resolving powers of 3079–4882 respectively.

If only a small part of the grating is illuminated, the resolving power is calculated from

$$R \leq W\left(\frac{n}{d} \right) \qquad (115)$$

where W is the illuminated ruling width. Inserting 3 mm, gives a maximum resolving power of 3000. This is 1.6 times less than the best resolving power obtainable. The line widths on detector 4 might be expected to be broadened by this factor. This is indeed the additional factor measured on detector 4 in Table 18 using the 25 μm slit.

The expected widths calculated in Chapter 2 started with ray tracing which assumed parallel light from the sun. Any spread of angles in the beam from the calibration source would have to be added into the final value. The divergence of the beam is less than 10".

Another source of broadening is electronic noise in the detectors themselves. The size of this was estimated from the output produced by the two stims for each detector. Although these do not include any noise produced by the HV power supplies, they do include all other sources of front end noise. The image of the stims, taken as raw data, was fitted to a LUT covering the normal number of spiral arms. The stims appear in the image as two distinct and narrow peaks. Each of the stims for detectors 1, 2 and 3 occupied no more than one pixel. For detector 4 the stims spread to two pixels. The narrowness of the stim images suggests that electronic noise is not the limiting factor in the real line widths.

The deviations from the expected wavelength ranges mentioned in §8.3.2. could also imply a broadening of the line widths by the detector being displaced radially from the RC. Knowing the calculated wavelength range and the measured wavelength range,

the error in beam angle from the grating could be calculated ($d\alpha$) and hence an offset in radius (dR) for each end of each detector.

$$\sin(\alpha+d\alpha)=\sin(84.75^{\circ})-\frac{\lambda'}{1\times10^{-6}} \tag{116}$$

$$dR=\frac{\ell d\alpha}{\left(180^{\circ}-(\alpha+d\alpha)\right)} \tag{117}$$

where α is the incident angle on the detector, ℓ is the cord length between the grating and detector, 1×10^{-6} m is the grating ruling, 84.75° is the incident angle on the grating. The broadening due to the dR displacement can be calculated from:

$$W=2dR\left(\tan(\theta+\varphi)-\tan\theta\right) \quad \text{where} \quad \varphi=\tan^{-1}\left(\frac{25\cos\theta}{\ell}\right) \tag{118}$$

This width W has to be combined quadratically with the projected slit width as calculated in Table 8. This value dR includes the 200 µm displacement from the RC which is due to the detector crossing the RC at two places. An upper limit to the line width calculated by this method is given in Table 19.

Wavelength (nm)	dR (µm)	Width (pixels)	Wavelength (nm)	dR (µm)	Width (pixels)
15.5	374	17.2	39.6	185	7.5
22.4	240	10.9	49.5	272	7.2
26.1	387	12.3	66.2	464	7.2
34.6	613	13.5	78.6	125	5.1

Table 19. Table showing widths of lines broadened by displacement from RC for slit 2. (Column 1 contains the detector 1 and 2 values; column 2, detectors 3 and 4.) The values dR need to have 200 µm subtracted from them to find the error in positioning of the detectors.

In Figure 160 the observed widths, expected widths given in Table 18 and broadened widths due to the displacement given in Table 19 are plotted for detectors 1 and 4. The figure shows that the measured line widths for both detectors are within expectation if the additional sources of broadening are taken into account. Detector 2 also shows measured widths within those of Table 19. Detector 3 has poor widths despite apparently being well placed in terms of wavelength range. This is partly due to

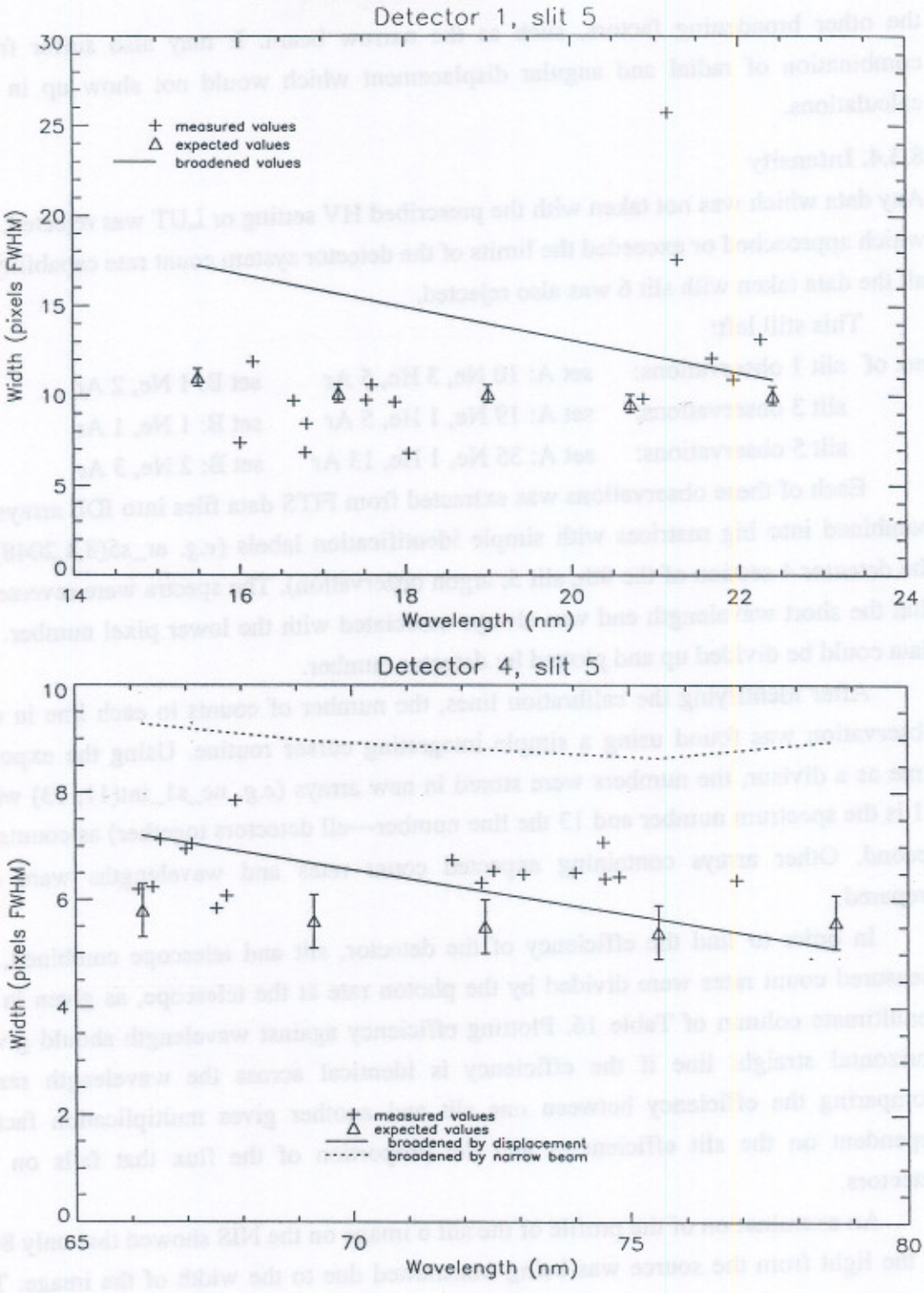

Figure 160. Comparing expected and measured line widths. The expected widths are those given in Table 18 for slit 2, assuming the detectors are perfectly positioned relative to the RC. The broadened values are calculated from the maximum displacement of the detectors from the RC. For detector 4 the broadening due to the narrow source beam is also marked.

the other broadening factors, such as the narrow beam. It may also suffer from a combination of radial and angular displacement which would not show up in these calculations.

8.3.4. Intensity

Any data which was not taken with the prescribed HV setting or LUT was rejected. Data which approached or exceeded the limits of the detector system count rate capability, *i.e.* all the data taken with slit 6 was also rejected.

This still left:

no. of	slit 1 observations:	set A: 10 Ne, 3 He, 5 Ar	set B: 1 Ne, 2 Ar
	slit 3 observations:	set A: 19 Ne, 1 He, 5 Ar	set B: 1 Ne, 1 Ar
	slit 5 observations:	set A: 35 Ne, 1 He, 13 Ar	set B: 2 Ne, 3 Ar

Each of these observations was extracted from FITS data files into IDL arrays and combined into big matrices with simple identification labels (*e.g.* ar_s5(8,4,2048) for the detector 4 section of the 8th, slit 5, argon observation). The spectra were reversed so that the short wavelength end was always associated with the lower pixel number. The data could be divided up and plotted by detector number.

After identifying the calibration lines, the number of counts in each line in each observation was found using a simple integrating cursor routine. Using the exposure time as a divisor, the numbers were stored in new arrays (*e.g.* ne_s1_int(11, 13) where 11 is the spectrum number and 13 the line number—all detectors together) as counts per second. Other arrays containing expected count rates and wavelengths were also prepared.

In order to find the efficiency of the detector, slit and telescope combined, the measured count rates were divided by the photon rate at the telescope, as given in the penultimate column of Table 16. Plotting efficiency against wavelength should give a horizontal straight line if the efficiency is identical across the wavelength range. Comparing the efficiency between one slit and another gives multiplication factors dependent on the slit efficiencies and the proportion of the flux that falls on the detectors.

An examination of the profile of the slit 6 image on the NIS showed that only 80% of the light from the source was being transmitted due to the width of the image. The photon rates at the detectors were therefore 0.8 times that expected from Table 16.

A number of other corrections had to be done to the measurements before the true efficiencies could be found. These are listed below. Apart from the electronic dead times, all the rest of the corrections need to be applied on a line by line basis.

8.3.4.1. Correction for electronic dead times

In §2.3.4. an analysis of the analogue dead time was described. It is necessary to apply that correction for dead time to the intensity measurements. The relationship between input and output count rates was plotted in Figure 133.

In fact, the count rate is limited ultimately by the rate at which information can be sent to the CDHS from the GIS box (see §2.3.4). The events from the four detectors are combined into one stream on a first come first served basis, with a detector to detector dead time of 600 ns. This method of choosing the events culminates in a global dead time but, as with the analogue dead time, does not affect the distribution of events.

To correct for the electronics dead times, the count rate for a particular detector and the total for all the detectors together allowed two dead time factors to be calculated. These factors were multiplied into all the line intensities for that spectrum, although in most cases the correction factor was tiny compared with the error. In the set B data in particular, the PHD was peaking below the LLD, or was exponential in shape. The detected count rates were therefore lower than expected.

8.3.4.2. Correction for LTGD

Between 5th and 11th March 1994 there was a decline in efficiency in the detectors as measured by the filament data in §8.3.1. For intensity measurements taken towards the end of this period, the differential gains would affect the flatness of the efficiency curve. For detectors 3 and 4, gain correction curves as in Figure 156, were divided into the data before the counts in each line were measured. Low gain areas have their count rates enhanced by this method.

The purpose of this correction was partly to correct the efficiency measurement, but it was also an attempt to obtain a flat response to check the consistency of the measurement with different wavelengths and lines of different count rates. The detectors will probably recover gain during the wait until launch, in which case the corrected efficiency will be more appropriate than the post-LTGD efficiency.

One problem is that the intensity data was taken at various times during the period, so that there will have been varying degrees of LTGD for each data set. The correction turned out to be of limited usefulness in obtaining a flat response. The count rate effects, UV source and telescope efficiency dominated the measurement.

8.3.4.3. Background subtraction

The detector dark count is less than $2\,c\,s^{-1}$ per detector. Background due to scattered light from the telescope, however, did need to be subtracted for detector 1.

The method for subtracting the background was to select a region containing no lines on either side of the line of interest. The mean count rate per pixel was found for these regions, and the number was subtracted from each of the pixels in the line of interest. This allowed for variation in the background intensity across the detector. The rates in the regions containing no lines were of the order of $0.015\,c\,s^{-1}\,pixel^{-1}$ for neon with slits 3 or 5, which is high compared with the intensities of the lines being measured, the weakest being about $0.05\,c\,s^{-1}\,pixel^{-1}$ with slit 5. This gives a large error (~30%) to the measurements on detector 1.

8.3.4.4. LUT corrections

With the parameter *percent* in the LUT set to anything less than 100%, events are rejected between the spiral arms. This is useful for reducing ambiguities and ghosting, but inevitably leads to an apparent loss of intensity. Using *VRAWNALL* and raw data, correction factors can be obtained for this loss. The method is to select the part of the arm containing the spectral line using *start* and *stop*. The number of events found within 100%, and also within *percent%* can then be measured. The ratio gives the correction factor. These correction factors are very dependent on the shape and fit of the data. It is for this reason that the reference raw file and knowledge of LUT *etc.* are so important.

ARM_LINE is useful to work out the position in terms of pixels of a line given in terms of spiral arms. *VRAWNALL* and *ARM_LINE* can also be used to assess the likelihood of ghosting.

Ghosts were corrected by adding the intensity in a ghost line to the intensity in the real line. Furthermore, it was necessary to measure correction factors for the ghosts in respect of data lost between the arms.

For most science observations, there were raw files which had been obtained for all four detectors, at the same voltages and with the same slit, gas *etc.* as the science observation. For every line, or group of lines, used in the intensity calibration, an appropriate correction factor was obtained by using the associated raw file with *VRAWNALL* and the LUT parameters. For some data, especially in set B, there was no raw file taken at the same voltage. In these cases the nearest voltage raw file was used.

The count rate measurements were multiplied by the correction factors to remove the effects of the LUT.

8.3.4.5. Correction for CDGD

Gain depression reduces the intensity as events move below the LLD. Above a certain input count rate the output count rate response curve becomes double valued, leading to confusion.

In order to obtain a CDGD curve, it would be ideal to view a line of known intensity and then to increase the intensity and measure the change in response. In the calibration, the intensity of the lamp was fixed, but there was a number of ways of approximating to this measurement.

The CDGD curve depends on the HV and also on the slit number which dictates the number of pores illuminated by the line image as well as the brightness. If a bright line is not too severely depressed, it may be restored by increasing the voltage to move the PHD back into the energy window. But lower intensity lines will be lost at the higher voltage due to the pulse heights being over the ULD. Figure 161 illustrates the expected form of the curves (see also the measured curves in Chapter 4). The linear part lies on the same straight line regardless of the HV setting. Therefore the choice of HV only affects the start and end points of the linear régime.

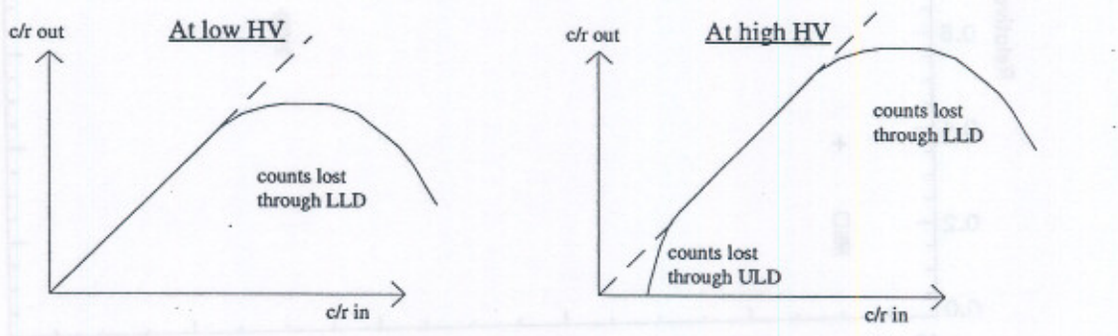

Figure 161. Expected form of CDGD curves.
Note that the linear parts of the curves lie on the same straight line (showed with a dashed line).

If a detector has lines with a variety of intensities falling on it, assuming that the response is equal across the detector, a plot of measured count rate versus intensity produces a curve. Unfortunately, not all detectors had a wide range of intensities—detectors 1 and 2 had mostly low count rates and detectors 3 and 4 high count rates. Note that lines grouped together for purposes of flux measurement (§8.1.2.) could not be used for CDGD.

However, it turned out that there was a large variation in measured intensity as the slit was scanned across the aperture (see Figure 162). This was first noticed when the spectra from all the FITS data files were plotted out as thumbnail plots. Comparing the spectra it could be seen that the ratios of intensities varied greatly. For example, the ratio of the intensities of the two bright neon lines on detector 3 swapped over as the slit was moved from above to below the centre of the aperture. Measuring the total count rate and plotting against position, it was clear that towards the edges of the aperture and at

certain aperture heights the intensity was weaker. This was due in part to structure in the source which meant that the small slits were not illuminated by the same part of the source in all positions. The plan to use slit 6 only for intensity measurements would have avoided this problem by using the whole beam.

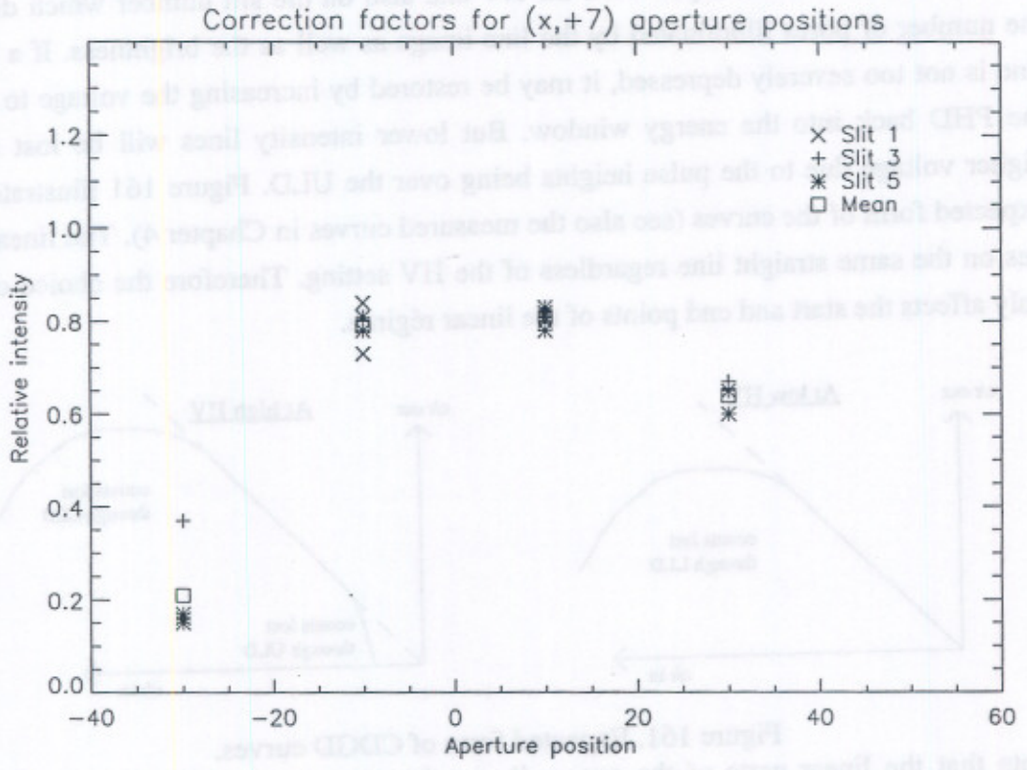

Figure 162. Variation in intensity across the aperture.
This plot was taken from observations at the same position in the y direction, using detector 2.

The variation in intensity with position was very useful in providing additional points to CDGD curve. It was necessary to find an independent means of calculating the input count rate at the various positions. This could be done by using the aperture scan measurements which used all detectors and slit 6. This did not take into account any effects due to source structure, but only due to the beam being lost from the edge of the aperture, which is of limited use for a smaller slit measurement. The factors were therefore found by using the total count rate on detector 2 at each position. This detector was the best one to use because it had a low scattered light background and low spectral line count rates. It turned out to provide reproducible results of relative intensities using slits 1, 3 and 5. The data in Figure 162 was from this detector and the mean values were used to correct the data from all the detectors.

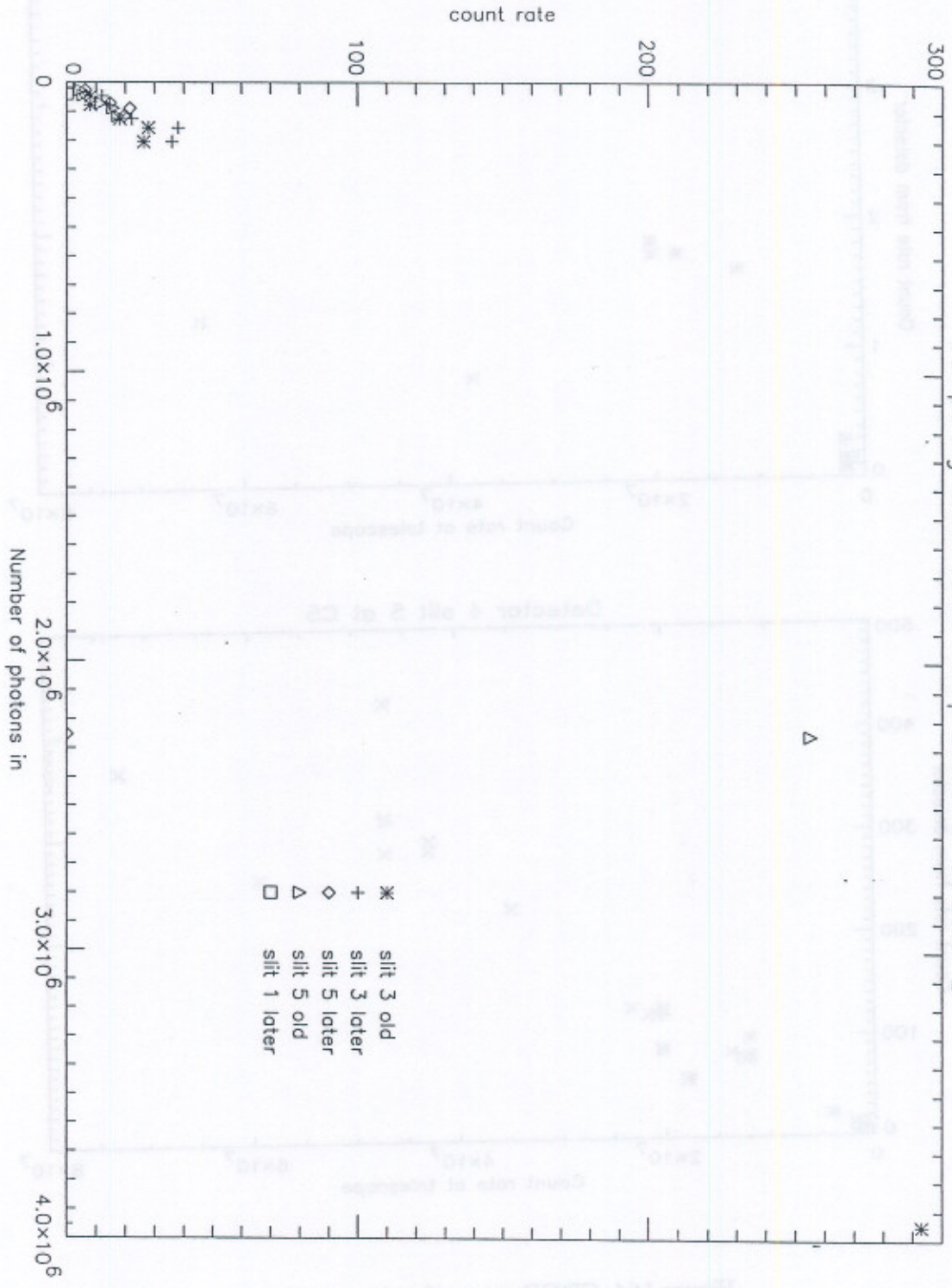

Figure 163. CDGD curve for detector 2.
This plot uses the number of photons detected per unit area to combine data from different slits.

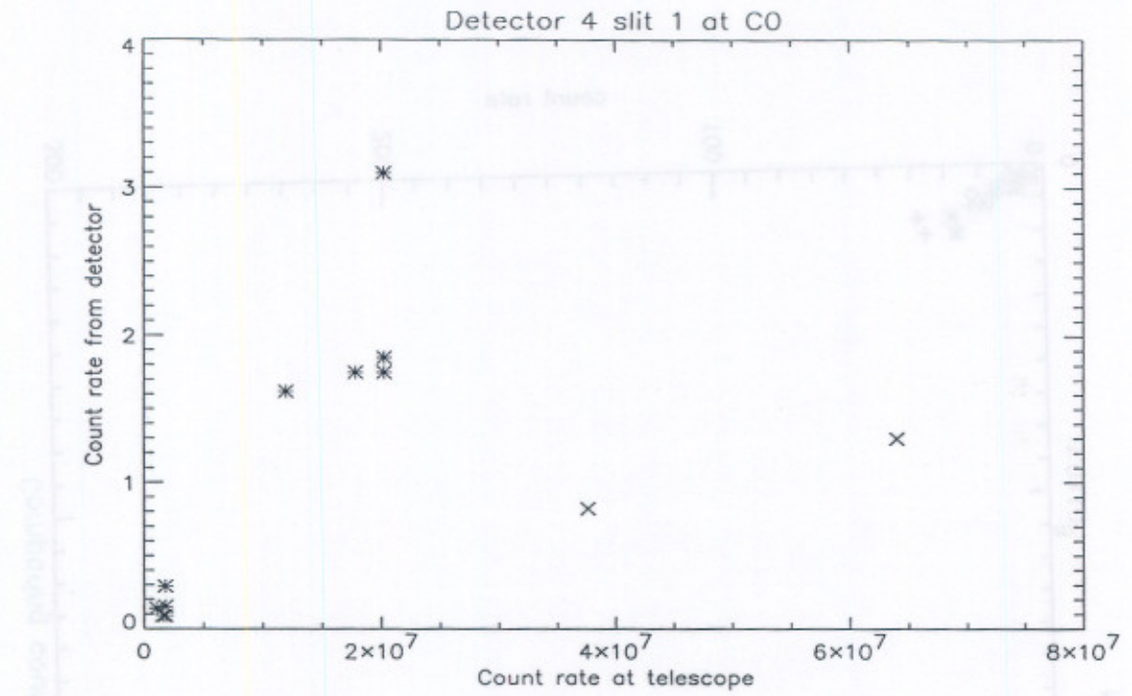

(a)

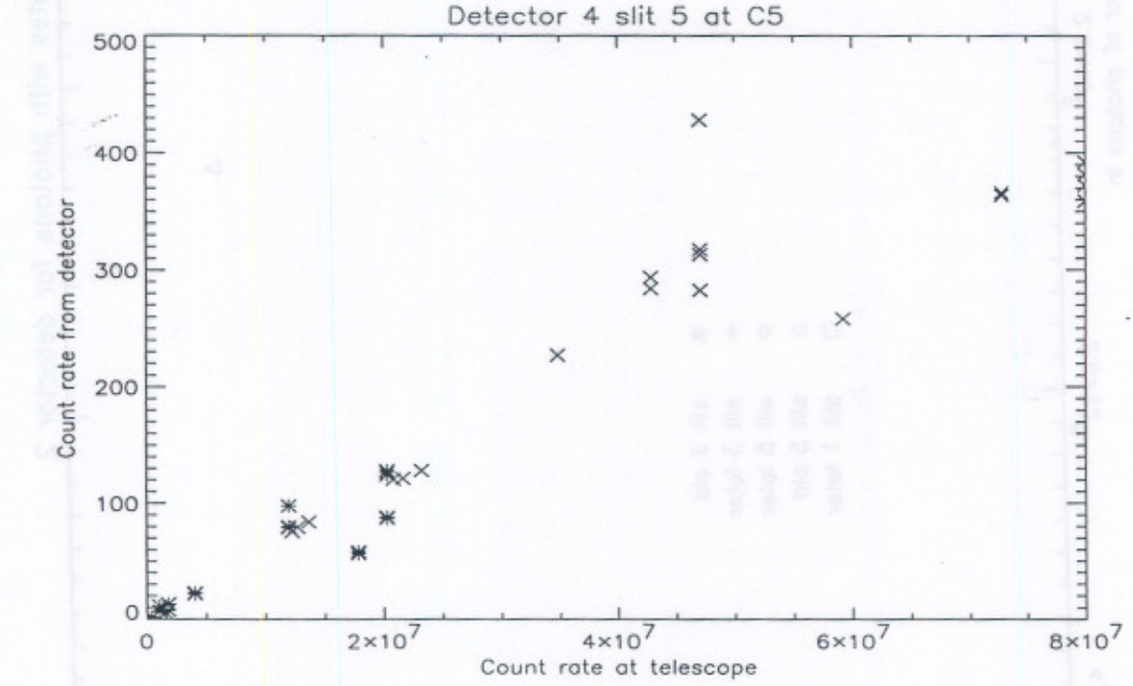

(b)

Figure 164. CDGD curves for detector 4.
*: neon lines, ×: argon lines. (a) is taken with slit 1 at a voltage of 3.84 kV. (b) is taken with slit 5 at 3.94 kV. Linearity is maintained to ~3 c s^{-1} for slit 1, and 300 c s^{-1} for slit 5, which illuminates ~100 times as many pores.

In using this data for the CDGD curve it is essential that the same voltage was used for all the measurements per detector. For some of the observations, *e.g.* detector 1, and for the set B data, the same voltage was used for measurements with all the slits. This provided another means of varying the input intensity. The wider slits give higher count rates, but also illuminate more pores. This had to be taken into account if the measurements from different slits were going to be put onto the same curve (see Figure 163 and 164).

For some detectors the curves could be produced at more than one voltage. The input count rate at which the CDGD curves loose linearity (maximum linear count rate) can be plotted against voltage. Figure 165 is a plot of maximum linear count rate per pore versus voltage, made using the CDGD curves from all the detectors.

8.3.4.6. Measured sensitivity

Once all the corrections had been applied, plots of efficiency versus wavelength were produced. For the central aperture data first selected, the curves were not smoothly varying. Detector 2 was the only one which seemed to follow a consistent trend. Detectors 3 and 4 were highly variable. Detector 1 data gave the largest errors in measuring the counts per line both because of the background and low count rates, but also because the extent of the lines is not well defined. Detectors 3 and 4 were dominated by gain depression.

After analysing the data from all the aperture positions, it became clear that the data was extremely reproducible with respect to position. At a given aperture position the curves were identical if repeated at different times over the calibration period. The smoothest varying curves for detectors 3 and 4 were those obtained at the edges of the aperture where the count rates were at a minimum.

This extreme aperture data was therefore selected for the intensity calibration, using the factors described above from detector 2 to calculate the actual incident flux at those positions. Figure 166 is a plot of the instrument efficiency versus wavelength obtained for slits 1, 3 and 5. The plot includes set A and B data, neon and argon lines wherever possible.

A number of factors was considered in the assessment of the errors in the efficiency plots:

$$\frac{\Delta\varepsilon}{\varepsilon}=\sqrt{\left(\frac{\Delta flux}{flux}\right)^2+\left(\frac{\Delta corr.\,factors}{corr.\,factors}\right)^2+\left(\frac{\Delta intensity}{intensity}\right)^2+\left(\frac{\sqrt{N}}{N}\right)^2} \qquad (119)$$

where ε is the efficiency, *flux* refers to the source flux, including any error in the correction factor due to aperture position, *corr. factors* are the LUT correction factors,

and *intensity* is the measurement of the number of counts in a spectral line, *N* being the number of counts.

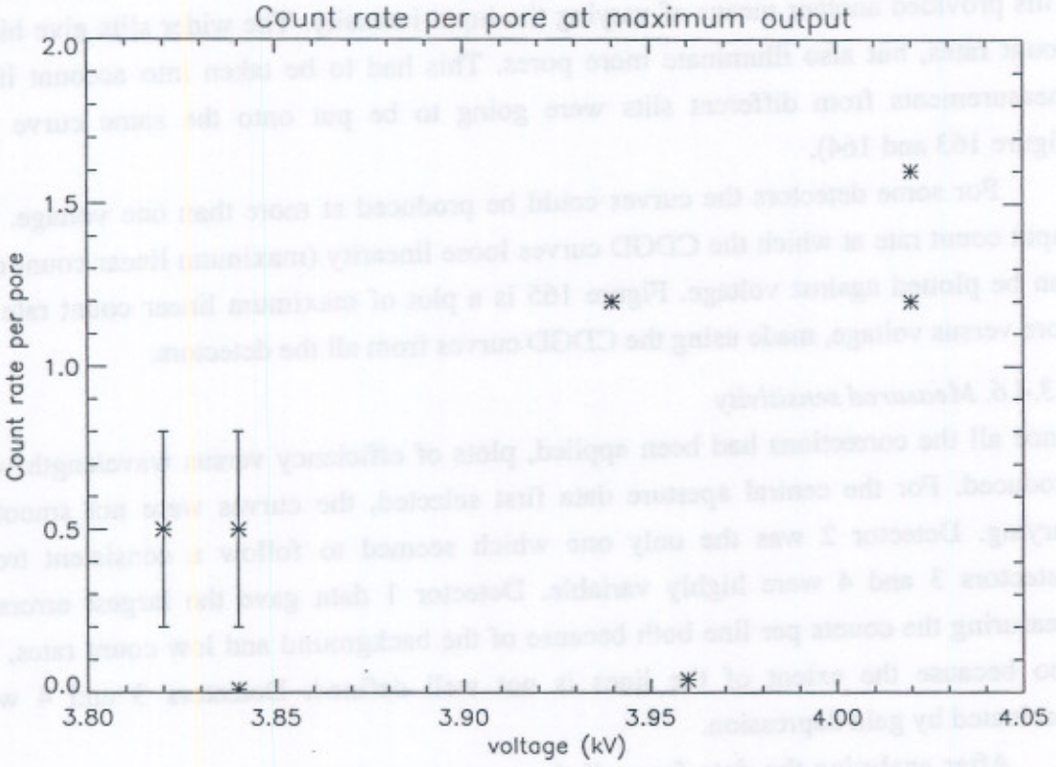

Figure 165. Maximum linear input count rates vs. voltage.
The large error bars on some of the points are due to the lack of data at the turn over point.

Three or four measurements of the intensities of the lines in the FITS files were made, and an error calculated. Ten percent error on the LUT correction factors was added—estimated by comparing the difference in correction factors for more than one raw file with the same LUT. A Poisson statistical error dependent on the number of counts in the line was also added in. These errors affect the relative response of different lines. Finally, a 12% error in the absolute UV source flux was added to all lines equally. The variation in flux from one measurement to the next should be less than 5%, except just before lamp refurbishment when the flux was less trustworthy. Additional error due to the polarisation of the lamp was believed to be negligible.

The *intensity* and Poisson factors depend on the line and background. For an average line, the error on ε was of the order of 60%.

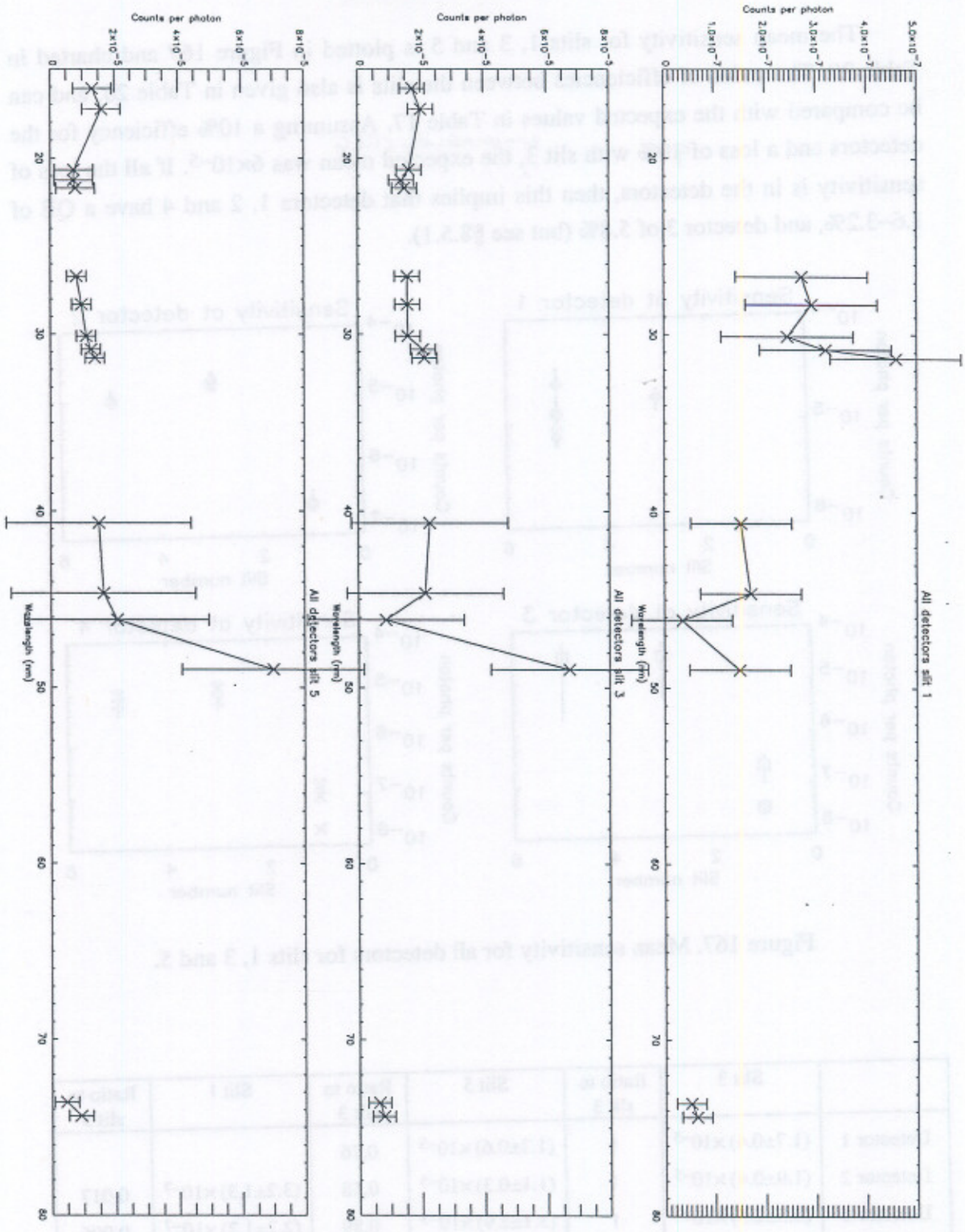

Figure 166. Sensitivity plot for slits 1, 3 and 5.

The mean sensitivity for slits 1, 3 and 5 is plotted in Figure 167 and charted in Table 20. The ratios of efficiencies between the slits is also given in Table 20, and can be compared with the expected values in Table 17. Assuming a 10% efficiency for the detectors and a loss of 10% with slit 3, the expected mean was 6×10^{-5}. If all the loss of sensitivity is in the detectors, then this implies that detectors 1, 2 and 4 have a QE of 1.6–3.2%, and detector 3 of 5.8% (but see §8.5.1).

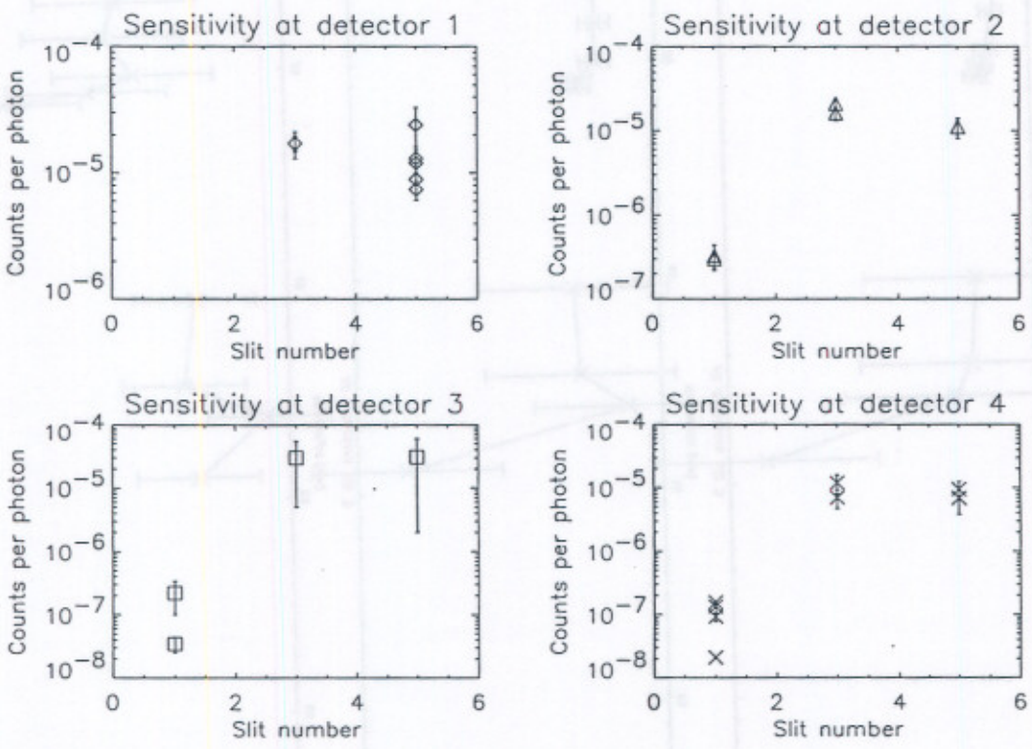

Figure 167. Mean sensitivity for all detectors for slits 1, 3 and 5.

	Slit 3	Ratio to slit 3	Slit 5	Ratio to slit 3	Slit 1	Ratio to slit 3
Detector 1	$(1.7\pm0.4)\times10^{-5}$	1	$(1.3\pm0.6)\times10^{-5}$	0.76		
Detector 2	$(1.9\pm0.4)\times10^{-5}$	1	$(1.1\pm0.3)\times10^{-5}$	0.58	$(3.2\pm1.3)\times10^{-7}$	0.017
Detector 3	$(3.5\pm2.5)\times10^{-5}$	1	$(3.1\pm2.9)\times10^{-5}$	0.89	$(2.2\pm1.2)\times10^{-7}$	0.006
Detector 4	$(9.5\pm3.6)\times10^{-6}$	1	$(7.7\pm3.8)\times10^{-6}$	0.81	$(1.3\pm0.3)\times10^{-7}$	0.013

Table 20. Mean sensitivities.

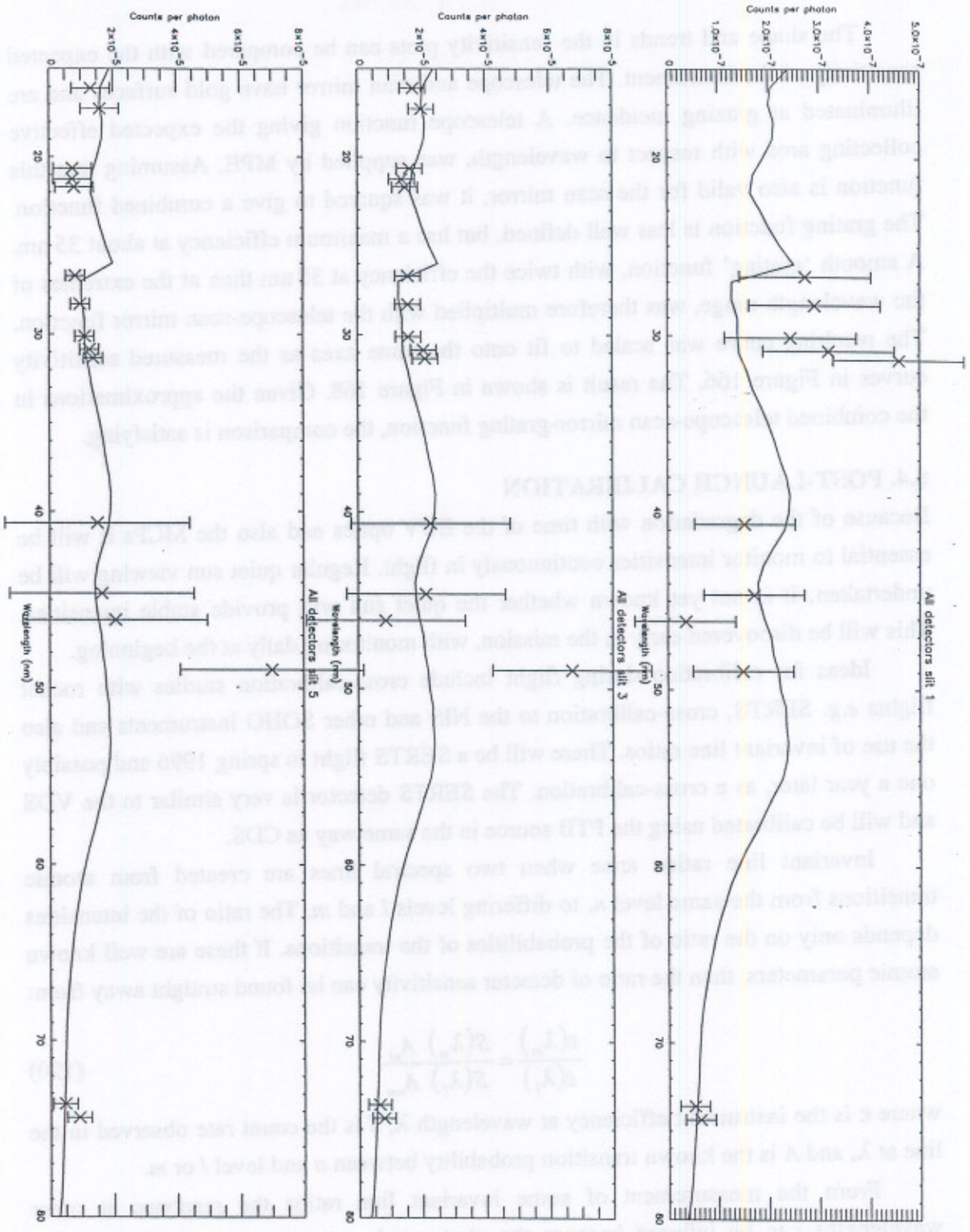

Figure 168. Shape of expected telescope-scan mirror-grating function compared with the measured sensitivity.

The shape and trends in the sensitivity plots can be compared with the expected sensitivity of the instrument. The telescope and scan mirror have gold surfaces and are illuminated at grazing incidence. A telescope function giving the expected effective collecting area with respect to wavelength, was supplied by MPE. Assuming that this function is also valid for the scan mirror, it was squared to give a combined function. The grating function is less well defined, but has a maximum efficiency at about 35 nm. A smooth 'grating' function, with twice the efficiency at 35 nm than at the extremes of the wavelength range, was therefore multiplied with the telescope-scan mirror function. The resulting curve was scaled to fit onto the same axes as the measured sensitivity curves in Figure 166. The result is shown in Figure 168. Given the approximations in the combined telescope-scan mirror-grating function, the comparison is satisfying.

8.4. POST-LAUNCH CALIBRATION

Because of the degradation with time of the EUV optics and also the MCPs it will be essential to monitor intensities continuously in flight. Regular quiet sun viewing will be undertaken. It is not yet known whether the quiet sun will provide stable intensities. This will be discovered early in the mission, with monitoring daily at the beginning.

Ideas for calibration during flight include cross-calibration studies with rocket flights *e.g.* SERTS, cross-calibration to the NIS and other SOHO instruments and also the use of invariant line ratios. There will be a SERTS flight in spring 1996 and possibly one a year later, as a cross-calibration. The SERTS detector is very similar to the VDS and will be calibrated using the PTB source in the same way as CDS.

Invariant line ratios arise when two spectral lines are created from atomic transitions from the same level n, to differing levels l and m. The ratio of the intensities depends only on the ratio of the probabilities of the transitions. If these are well known atomic parameters, then the ratio of detector sensitivity can be found straight away from:

$$\frac{\varepsilon(\lambda_m)}{\varepsilon(\lambda_l)} = \frac{S(\lambda_m)}{S(\lambda_l)} \frac{A_{nl}}{A_{nm}} \tag{120}$$

where ε is the instrument efficiency at wavelength λ, S is the count rate observed in the line at λ, and A is the known transition probability between n and level l or m.

From the measurement of some invariant line ratios the response at other wavelengths can be inferred because the photometric response across CDS, at least initially, is not a steep function of λ.

The GIS and NIS can be cross-calibrated within the wavelength ranges listed in Table 21. Some overlap with the wavelength range of the SUMER instrument on board SOHO allows cross-calibration between 51.7 and 78.6 nm. A stable UV (17.0–70.0 nm)

full-sun monitor is included on SOHO. This device should allow monitoring of absolute sensitivity changes in time.

31.0–34.6 nm	NIS 1st order	GIS 1st order
31.0–38.0 nm	NIS 1st order	GIS 2nd order
52.2–63.3 nm	NIS 1st order	GIS 2nd order
66.2–76.0 nm	NIS 2nd order	GIS 1st order

Table 21. GIS and NIS cross-calibration ranges.

Wavelength calibration can be repeated in flight, but then it will be necessary to remove any velocity shifts. There are a few 'cool' chromospheric lines within the CDS wavelength ranges. SUMER has particular need for accurate wavelength calibration because the main purpose is to look at flows and velocities. Cross-calibration of wavelengths will therefore be useful.

The telescope PSF may also be tested in flight, using stars passing within 1° of the sun as point sources. Stars further away than this would require the whole of SOHO to repoint to view them.

8.4.1. Monitoring long term gain depression

There are two problems here. One is the global decay of gain across the whole detector—caused by outgassing, plate ageing, filament usage *etc.* The other is differential decay caused by the fact that the spectrum is always illuminating the same parts of the detector. Both will affect the long term maintenance of the intensity calibration.

Any regions suffering from differential decay will appear as a region of lower count rate. The filament electrons illuminate the whole detector surface. The problem with using filaments to monitor global decay is the output will not stay constant with time, but it should be possible to use them for differential decay. Ideally the filament and HV should be set up to give the same count rate in non-bright-line regions at all times. Then, dividing the later spectrum by the earlier will give unity in non-bright-line regions, and less where there has been loss of sensitivity.

A second method of detecting the loss of sensitivity in particular lines is to follow a sequence to observe the quiet sun, using first the smallest slit (2×2") to define the locations of the line centres, *i.e.* the sites of most likely depletion, then to open up to the widest slit (8×50"). The centre of the wider slit image should show any depletion.

The global decay may be monitored by using repeated quiet sun measurements, background count rates or continuum. If quiet regions of the sun are considered to be stable, then any decrease in intensity can be monitored with regular viewing of quiet sun regions. There are already observations designed to do this on a regular basis.

8.5. LATEST DEVELOPMENTS

8.5.1. Sensitivity

The sensitivity measurements presented in §8.3.4.6. must now be considered as a lower limit, for four reasons. First, the calculations above assumed that 20% of the source light would be eliminated by the CDS apertures. Analysis of the aperture scans (Bromage, 1995) show that, in fact, 26% was lost. Thus all the measurements should be increased by 8%.

Secondly, the fine structure in the source meant that the illumination level was not as high as intended for most observations, particularly with the smaller slits. Even at the zero aperture position used for the intensity corrections the smaller slits were not necessarily well aligned with the source. Comparing the peak value in aperture scans at different aperture heights suggests that the results from many of the intensity observations used for the GIS should be multiplied by a factor of 2.4 (Bromage, 1995).

Thirdly, the HVs could have been set higher for the bright lines to compensate for CDGD. The HVs were selected using the raw and processed count rates rather than the count rates in individual lines, which would have involved data analysis of the raw files at a number of voltages.

Finally, since the calibration exercise, the levels of the lower and upper discriminators have been altered to give a pulse height window approximately 20% wider.

The true efficiency is, therefore, more than twice as high as the measurements presented here, giving detector efficiencies of greater than 3.2–6.4% for detectors 1, 2 and 4; 11.6% for detector 3. These efficiencies exceed the prediction presented in Chapter 3 of 2–5%.

8.5.2. Fringing

During a simple functional test of the instrument on board the spacecraft, it was observed on one occasion that for a few seconds, each single line image from a stim appeared to be split up into about 8 lines. An example is given in Figure 169. Checking through previous data revealed the same effect occurring a number of times, though never previously noticed, at a frequency of anything between a few minutes and hours,

lasting for just a few seconds. The events which should have appeared in the stim lines were being displaced into the fringes.

After investigation, the fault was traced to the FIFO on the processor 1 card within the GIS electronics box. It consists of a pair of 512×9 bit, GEC-Plessey type MA7001, connected in parallel between the detector LUTs and the science serial output shift register (see §7.2.6). Their purpose is to provide a de-randomizing buffer between the random events from all four detectors and the interface to the CDHS. They are also used to buffer raw data.

The 13-bit detector data (11 bit pixels plus the detector identity) is split between the two parallel FIFOs as the 8 LSBs in one FIFO and the 3 MSBs plus detector identity in the other. Under certain rare conditions the two FIFOs become desynchronised so that the 8 LSBs from one event get assigned to the wrong event. If each detector image is divided into 8 segments, the 3 MSBs plus identity bits uniquely describe a segment of one particular detector. Thus, the events from one stim get distributed into eight lines within the segment, each fringe line corresponding to a set of LSBs from a different stim.

In bench tests with the two FS detectors, *DET_SIM* and the Pseudo-random detector simulator (see §2.4.2.), the effect could be readily reproduced provided the total combined count rate exceeded the maximum rate for the interface to the CDHS, $8.9\times10^4\,c\,s^{-1}$. At this rate, the FIFO is full most of the time. The total count rate from all eight detector stims is just above this rate. The frequency of fringing decreases rapidly as the science count rate is reduced. Note that the science data rate is lower than the sum of the individual detector processed count rates because of pile up rejection between the detectors and events being rejected by the LUT.

Between spurious events, the system functions correctly and recovers completely after a few seconds, or when the count rate is reduced below the maximum. Testing at a count rate of $10{,}000\,c\,s^{-1}$ over an 18 hour period showed an average of 1 displaced event per 10^4. A count rate of $440\,c\,s^{-1}$, over a 36 hour period, gave approximately 1 displaced event in 10^6.

The cause of fringing is associated with a 10 μs FIFO read enable pulse, which creates another undesirable effect in the form of a 10 μs dead time. This is not an extending dead time and can be calculated theoretically for the combined detector count rates.

In addition, if the input rate exceeds the 8.9×10^4, a dramatic fall in the total count rate to 50% is observed, because the entire contents of the full FIFO are alternately lost, as the full and empty FIFO flags become indeterminate. Thus, count rates out of the

FIFO above 5×10^4 become ambiguous, although in principle, some of this ambiguity could be resolved by use of the raw count rates.

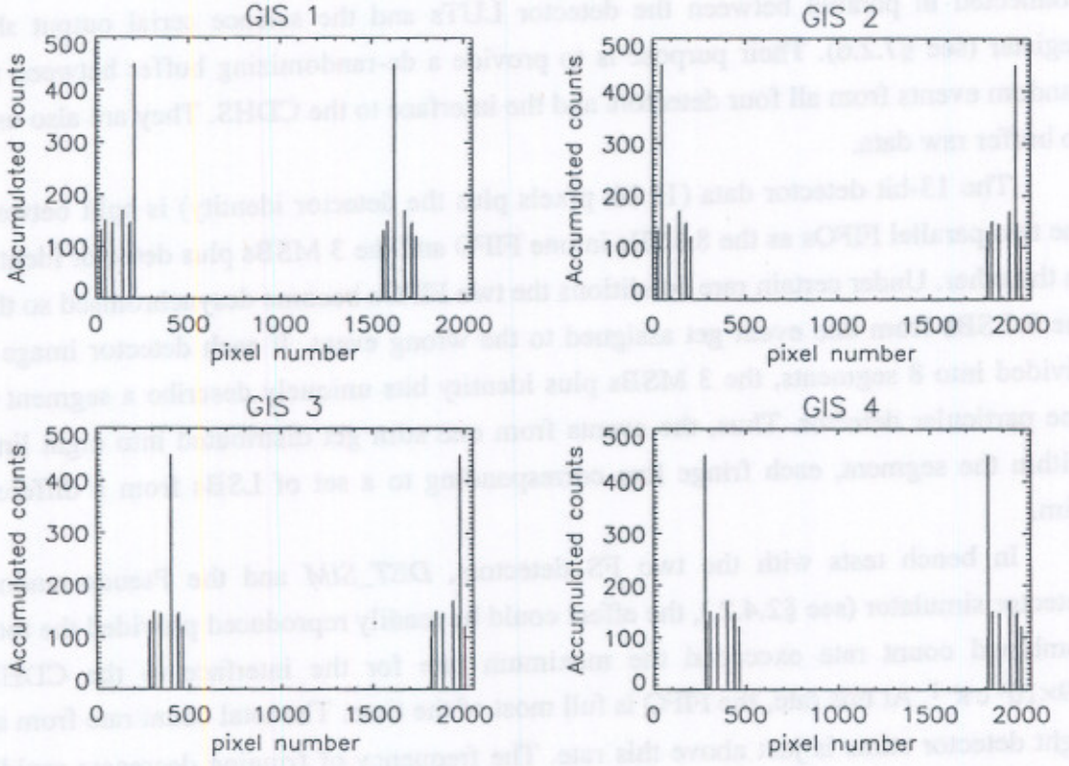

Figure 169. Fringing of the stim images on the flight detectors.

Although a modification was designed and tested to cure the problem, it was decided that no change should be made for the following reasons. First, the risks involved with making a design modification late in a flight programme are relatively high. Secondly, the predicted count rates for normal operation of the GIS are below 4000 c s^{-1}. Therefore, the data loss and corruption will be at a very low level. The largest GIS slit (3) may still be used if the total count rate is kept below 5×10^4. The predicted rate for quiet solar conditions are less than this figure. In the extreme, the He 30.4 nm line, which will provide about 90% of the counts, could be blocked out in the LUT. A standard correction can be applied for the 10 μs dead time.

8.6. CONCLUSIONS

This thesis has described the development of GIS detectors, concentrating on two novel aspects: use of MCPs to detect UV light at high (>67°) angles of incidence, and the theory and implementation of the SPAN anode for photon arrival-position encoding.

I first explored the requirements for the detectors by looking at the solar science expected using GIS. Besides the practical considerations of the detector design and building for space flight, I described experiments from which I chose to use a *z*-stack of MCPs with two interplate conductive shims, giving a gain of 4×10^7, with a PHD of 100% FWHM. In a series of experiments designed to characterise the detector with laboratory electronics, the background event rate was measured as less than $0.16\,c\,s^{-1}\,cm^{-2}$; well below the requirement of $1\,c\,s^{-1}\,cm^{-2}$. The response was found to be uniform to within a range of 17% across the surface, and non-linearities were measured: DNL 3.1% r.m.s. and INL 0.08%. An experiment examining the effect of high angles of incidence on the MCP showed that while there is a fall in efficiency at high angles, there is no hard cut-off in response, the reduction following a $\cot(\theta)$ curve, as predicted by theory.

With a description of the detailed design and manufacture of the FM detector anode, I gave results from tests on the full flight system, including electronics. The resolution was shown to be better than 50 μm FWHM; the INL is 0.03%; and the detectors can give a maximum throughput of $1.3\times10^5\,c\,s^{-1}$, consistent with a 28 μs dead time. However, the DNL was shown to be 27% because of the high level of fixed patterning. Computer model predictions compared well with experimental results.

I included analysis of data taken during the instrument flight calibration, which reveals that the detector sensitivity is better than 3–6% for detectors 1, 2 and 4; 12% for detector 3. There is apparently considerable variation in sensitivity along the wavelength range, but most of this can be attributed to the response of the telescope and diffraction grating. The very high count rates from the calibration line source meant that the results are associated with high CDGD. Other results from the flight calibration are the wavelength ranges and line widths, which are broader than predicted. The detector resolution, however, contributes very little to the observed line widths (minimum measured 145 μm FWHM).

The requirements have thus been met, but there are limitations which will affect the scientific usefulness in both key aspects of the detector: MCPs and SPAN.

A detailed study of the response of the MCPs to high count rates showed that the output count rate becomes non-linear for a spectral line input count rate greater than about $2000\,c\,s^{-1}$ (CDGD). This is a problem for GIS if any of the larger slits (3–6) are used. LTGD was also assessed by use of two lifetests; one using a spectral-line-sized slit

and the other a flat field. The results suggest that, although the HV will have to be raised from time to time to preserve the gain, it will not have reached the 5 kV limit after the nominal two years. However, as the positions of the spectral lines on the detectors do not change, the detectors will suffer from different LTGD in different regions. It can be compensated for with increasing HV, but is complicated by the variety of line strengths on each detector, and by the fact that the pulse height information is divorced from the positional information. Thus careful trend analysis and monitoring will be needed to prevent the detector calibration quickly becoming obsolete in flight. A discussion in Chapter 3 shows that scrubbing the detectors would not have helped.

The main problem with the SPAN anode is that of fixed patterning. This has the effect of displacing events by one or two pixels, distorting line shapes and reducing the useful resolution. Ghosting and data loss are likely because of polar image distortions: radius pulse height dependence, count rate dependent distortions, secondary electron emission and ballooning due to electronic noise. All of these effects make the fitting of LUTs very difficult. The successful operation of SPAN for GIS was compromised by an attempt to reach a very high throughput, which neither matched the real expectation of solar output, nor the MCPs.

Looking to the future, for certain low count rate applications, *e.g.* photon counting astronomy, SPAN could be satisfactory. However, alternatives may now be preferred, making use of new developments. The Vernier anode, briefly mentioned in the thesis, removes the problem of radius pulse height dependence and gives less fixed patterning by a special method of combining the output from the ADCs. Alternatively, if low power, fast ADCs of higher digitisation and good linearity are now available, a Wedge and Wedge anode may still be best choice. Further research into alternatives to MCPs would also be welcome. In particular, it is expected that CCDs will contribute the majority of the future detector applications for space flight.

In conclusion, the quality of observations for any experiment is ultimately limited by systematic errors. In the complex detector systems employed in modern research it is vital to limit these errors by a very full and detailed knowledge of the system performance over the full range of potential operating parameters. From the computer models and experimental data presented in this thesis, it has been shown that there are errors associated with the SPAN anode due to the interaction of the charge clouds with the anode and also with the ADC digitisation. MCP limitations have also been explored. The sources of these errors have been analysed and the results from the models shown to be consistent with experiment. In general, the errors are such that with careful choice of operating parameters, detector and anode dimensions, the errors can be minimised.

APPENDIX A.

SPIRAL ARC LENGTH

$$d\ell = \sqrt{dr^2 + rd\theta^2}$$

From spiral equation $r = k\theta$, so $dr = kd\theta$

$$\therefore \quad d\ell = \sqrt{k^2 d\theta^2 + k^2\theta^2 d\theta^2} = k\left(1+\theta^2\right)^{\frac{1}{2}} d\theta$$

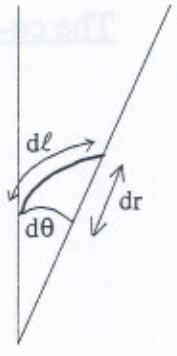

$\therefore$ length of arc from $\theta = 0$ to α:

$$\ell = k\int_0^{\alpha}\left(1+\theta^2\right)^{\frac{1}{2}} d\theta$$

Let $\theta = \sinh x$, so that $d\theta = \cosh x.dx$

$$\therefore \quad \ell = k\int_0^{X} \cosh^2 x.dx, \text{ where } X = \sinh^{-1}\alpha \text{ or } \alpha = \sinh X$$

$$\cosh x = \tfrac{1}{2}\left(e^x + e^{-x}\right), \text{ so } \cosh^2 x = \tfrac{1}{4}\left(e^{2x} + e^{-2x} + 2\right)$$

$$\therefore \quad \ell = \tfrac{k}{4}\int_0^{X}\left[e^{2x} + e^{-2x} + 2\right]dx = \tfrac{k}{4}\left[\tfrac{1}{2}e^{2x} - \tfrac{1}{2}e^{-2x} - 2x\right]_0^X = \tfrac{k}{4}\left[\tfrac{1}{2}e^{2X} - \tfrac{1}{2}e^{-2X} - 2X\right]$$

$$= \tfrac{k}{4}\left[\sinh 2X - 2X\right] = \tfrac{k}{2}\left[\sinh X \cosh X - X\right] \qquad (121)$$

Using $\cosh^2 X = 1 + \sinh^2 X = 1 + \alpha^2$

$$\cosh X = \tfrac{1}{2}\left(e^X + e^{-X}\right) = \sqrt{1+\alpha^2} \qquad (122)$$

$$\sinh X = \tfrac{1}{2}\left(e^X - e^{-X}\right) = \alpha \qquad (123)$$

Adding equations (122) and (123):

$$e^X = \alpha + \sqrt{1+\alpha^2} \quad \therefore \quad X = \ln\left(1 + \sqrt{1+\alpha^2}\right)$$

Inserting into equation (121), with equation (122) and (123), the length of the spiral arc from 0 to α is:

$$\ell = \tfrac{k}{2}\left[\alpha\sqrt{1+\alpha^2} - \ln\left(\alpha + \sqrt{1+\alpha^2}\right)\right]$$

APPENDIX B.

CO-ORDINATE TRANSFORM

The co-ordinate transform from 3d to 2d using dot product method

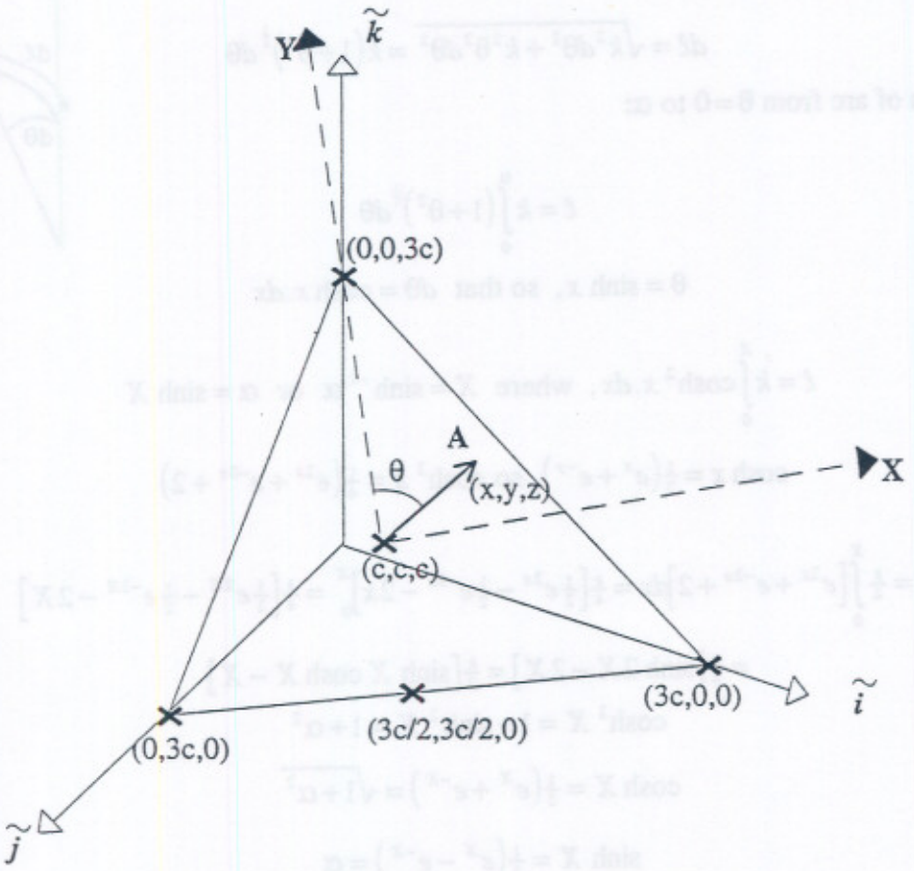

Projection of A onto Y axis:

$$A_y = |A|\cos\theta$$

Projection of A onto X axis:

$$A_x = |A|\cos(90^\circ - \theta)$$

Dot Product:

$$\vec{A}.\vec{Y} = |A||Y|\cos\theta \quad \therefore \quad A_y = \frac{\vec{A}.\vec{Y}}{|Y|}$$

Similarly:

$$A_x = \frac{\vec{A}.\vec{X}}{|X|}$$

$$\vec{Y} = -c\tilde{i} - c\tilde{j} + 2c\tilde{k} \quad \text{and} \quad |Y| = \sqrt{c^2 + c^2 + 4c^2} = \sqrt{6}.c$$

$$\vec{X} = \left(3c - \frac{3c}{2}\right)\tilde{i} + \left(0 - \frac{3c}{2}\right)\tilde{j} = \frac{3c}{2}\tilde{i} - \frac{3c}{2}\tilde{j} \quad \text{and} \quad |X| = \sqrt{\frac{9c^2}{4} + \frac{9c^2}{4}} = \frac{3c}{\sqrt{2}}$$

$$\vec{A} = x\tilde{i} + y\tilde{j} + z\tilde{k}$$

$$\therefore \quad A_y = \frac{-xc\tilde{i} - yc\tilde{j} + 2cz\tilde{k}}{c\sqrt{6}} = \frac{-x\tilde{i} - y\tilde{j} + 2z\tilde{k}}{\sqrt{6}} \quad \text{and}$$

$$A_x = \frac{\frac{3c}{2}x\tilde{i} - \frac{3c}{2}y\tilde{j}}{\frac{3c}{\sqrt{2}}} = \frac{x\tilde{i} - y\tilde{j}}{\sqrt{2}}$$

These last two equations are the ones used to transform from three signals to the two dimensional spiral plane. If x and z are swapped then the spiral will be reflected and rotate in the opposite direction.

REFERENCES

Adams J. and Manley B.W., "Mechanism of Channel electron multiplication", IEEE Trans. Nucl. Sci., p.86, June (1966), ... *105*

Adams J. and Manley B.W., "The Channel Electron Multiplier", Electronic Engineering, p.180 March (1965), ... *88*

Allington-Smith J.R. and Schwarz H.E., "Imaging Photon Detectors for Optical Astronomy", Q. Jl R. Astr. Soc. 25 p.267–289 (1984), ... *48*

Allinson N.M., "Solid-state imaging arrays for X-ray detectors", Nucl. Instrum. Meth. 201, p.53 (1982), ... *47*

Allison J., Barlow R.J., Canas R., Duerdoth I.P., Loebinger F.K., Macbeth A.A., Murphy P.G. and Stephens K., "Diamond shaped cathode pads for the longitudinal co-ordinate from a drift chamber", Nucl. Instrum. Meth. A236 p.284–288 (1985), ... *46*

Amnicoli, MSc Thesis M.I.T., (1985), ... *145*

Anacker D.C. and Erskine J.L., "Analysis of microchannel plate response in relation to pulsed laser time-of-flight photoemission spectroscopy", Rev. Sci. Instrum. 62(5), p.1246–55, (1991), ... *149*

Audier M., Delmotte J.C. and Boutot J.P., "Multiplicateur a galette de microcanaux–amélioration des performances de gain et de dynamique de détection", Revue de Physique Appliquée Vol.13, p.188-194, (1978), ... *104*

Barstow M.A., Fraser G.W., Milward S.R., "Imaging Microchannel Plate Detectors for XUV Sky Survey experiments", Proc. SPIE 597, p.352 (1985), ... *100*

Barstow M.A., Lees J.A. and Fraser G.W., "Observation of microchannel plate multifibre structure in soft X-ray images", Nucl. Instrum. Meth. A286, p.350–354, (1990), ... *137*

Becker T.H., Gross E.E., Trammell R.C., "Characteristics of high-rate energy spectroscopy systems with time-invariant filters", IEEE Trans. Nucl. Sci. NS-28, p.1 (1981), ... *81*

Bowyer S., Kimble R., Paresce F., Lampton M. and Penegor G., "Continuous-readout extreme-ultraviolet airglow spectrometer", Applied Optics Vol.20, no.3, p.477, (1981), ... *127*

Breeveld A.A. and Thomas P.D., "The Grazing Incidence Detectors for the SOHO Coronal Diagnostic Spectrometer,", Proc. ESA Symp. on Photon Detectors for Space Instrumentation, SP-356, p.237-241, (1992), ... *49*

Breeveld A.A., "Detector Characterisation Plan", MSSL, 1992, ... *87*

Breeveld A.A., Edgar M.L., Lapington J.S. and Smith Alan, "The effects of charge cloud size and digitisation on the SPAN anode", Proc. SPIE, Vol.1743, p.315, (1992), ... *231*

Breeveld A.A., Edgar M.L., Smith A., Lapington J.S. and Thomas P.D., "A SPAN MCP detector for the SOHO Coronal Diagnostic Spectrometer", Rev. Sci. Instrum. 63(1), Jan. (1992), ... *35*

Broadfoot A.L. and Sandel B.R., "Self-scanned anode array with a microchannel plate electron multiplier; the SSANACON", Applied Optics Vol.16 no.6 p.1533 June (1977), ... *38*

Bromage B., Breeveld A.A. and Kent B., "Report of the CDS Calibration of March 1994", In preparation, (1995), ... *315*

Browning R., Lidiard K.A., "CDS Optics Definition Document", SC-CDS-RAL-DS-89-0004, Feb. (1991), ... *63*

CDS Response to ESA/NASA announcement of opportunity, EID Part B, July (1987), ... *59*

Ceckowski D.H., Eberhardt E. and Carney E., "Proximity focused microchannel plate photomultiplier tubes", IEEE Trans. Nucl. Sci. NS-28 no.1, p.677 Feb. (1981), *.39*

Chappell J.H. and Murray S.S., "Position Modelling for the AXAF High Resolution Camera (HRC)", Proc. SPIE Vol.1159, p.460, (1989), ... *40*

Chauvet G., Brenac A. and Baptist R., "Simple electronic device for position-sensitive detectors in VUV spectrometry", Rev. Sci. Instrum. 58(2), Feb. (1987), ... *43*

Cho D.J. and Morris G.M., "Local dead-time effects in microchannel-plate imaging detectors", Proc. SPIE Vol.976, August (1988), ... *142*

Clampin M. and Edwin R.P., "Large format imaging photon detector for astronomical spectroscopy", Rev. Sci. Instrum. 58(2), p.167 Feb. (1987), ... *44*

Clampin M. and Paresce F., "Photon-counting imaging with a GaAs photocathode; evaluation of the Red-RANICON for astronomical imaging", Astron. Astrophys. 225 p.578–584 (1989a), ... *44*

Clampin M. and Paresce F., "Spatial resolution characteristics of a GaAs-photocathode RANICON", Rev. Sci. Instrum. 60(6), p.1092 June (1989b), ... *44*

Clampin M., Crocker J, Paresce F., and Rafal M., "Optical RANICON detectors for photon counting imaging I", Rev. Sci. Instrum. 59(8), p.1269–1285, (1988), ... *44*

Cotton D.M., Chakrabarti S. and Siegmund O.H.W., "Calibration of the Berkeley EUV Airglow Rocket Spectrometer", Proc. SPIE Vol.1159 p.404, (1989), ... *38*

Courtney S.H. and Wilson W.L., "Multichannel time-correlated single photon counting; Spectroscopy and time-gated imaging using a resistive anode photomultiplier tube", Rev. Sci. Instrum. 62(9), Sept. (1991), ... *43*

Culhane J.L., "Position Sensitive Detectors in X-ray Astronomy", Proc. 2nd Position Sensitive Detectors Conference, London, 1990, Nucl. Instrum. Meth. A310, p.1 (1991), ... *36*

Danzmann K., Günther M., Fischer J., Kock M. and Kühne M., "High current hollow cathode as a radiometric transfer standard source for the extreme vacuum ultraviolet", Applied Optics Vol.27, no.23, p.4947, Dec. (1988), ... *298*

Dunkelman L, Fowler W.B. and Hennes J., "Spectrally Selective Photodetectors for the Middle and Vacuum Ultraviolet", Applied Optics Vol.1, No.6, p.695, Nov. (1962), ... *134*

Durrant C.J., "The Atmosphere of the Sun", Adam Hilger IOP Publishing Ltd. ISBN 0-85274-375-0 (1988), ... *26*

Eberhardt E.H., "An Operational Model for Microchannel Plate Devices", IEEE Trans Nucl. Sci. NS-28, no. 1, Feb. (1981), ... *106*

Eberhardt E.H., "Gain model for microchannel plates", Applied Optics Vol.18, No 9, p.1418, May (1979), ... *106*

Edgar M.L., "A High Performance, Microchannel Plate Based, Photon Counting Detector For Space Use", PhD Thesis, University of London, (1993), ... *205*

Edgar M.L., Kessel R., Lapington J.S., Walton D.M., "The spatial charge distribution of Microchannel Plates," Rev. Sci. Instrum. Vol.60, p.3673 (1989), ... *72*

Edgar M.L., Lapington J.S. and Smith A., "The Spatial Extent of Gain Depression for MCP Based Photon Detectors", SRI 91, Rev. Sci. Instrum. 63, p.816, (1992a), *147*

Eng W. and Landecker P.B., "Properties of the channel electron multiplier arrays (CEMs) for the solex solar X-ray spectrometer/spectroheliograph", Nucl. Instrum. Meth. 190, p149, (1981), ... *136*

ESA SOHO CDS Experiment Interface Document Part B. Updated (1995), ... *283*

Evans D.S., "Low Energy Charged-Particle Detection Using the Continuous-Channel Electron Multiplier", Rev. Sci. Instrum. Vol.36 No.3 March (1965), ... *99*

Firmani C., Ruiz E., Carlson C.W., Lampton M. and Paresce F., "High-resolution imaging with a two-dimensional resistive anode photon detector", Rev. Sci. Instrum. 53(5) May (1982), ... *44*

Floryan R.F. and Johnson C.B., "Resistive-anode position-sensing photomultiplier tube operational modelling", Proc. SPIE Vol.1072 Image Intensification (1989), ...*104*

Fraser G.W. and Mathieson E., "Signal Location by Uniform Resistive Anodes", Nucl. Instrum. Meth. 179, p.591–604, (1981), ...*44*

Fraser G.W. and Pearson J.F., "The direct detection of thermal neutrons by imaging microchannel-plate detectors", Nucl. Instrum. Meth. A293 p.569–574 (1990), .*102*

Fraser G.W., "Imaging Detectors for FUV and EUV wavelengths", Adv. Space Res. 11, p.155–166 (1991), ...*98*

Fraser G.W., "Microchannel Plate Detectors for Space Astronomy", Proc. ESA Symp. on Photon Detectors for Space Instrumentation, SP-356, p.97, (1992), ...*149*

Fraser G.W., "The Electron Detection Efficiency of MCPs", Nucl. Instrum. Meth. 206, p.445–449, (1983), ...*101*

Fraser G.W., "The operation of open-window microchannel plate (MCP) detectors"; Report for RAL, contract SC/26/9/90, Nov. (1990), ...*150*

Fraser G.W., "The soft X-ray quantum efficiency of microchannel plates", Nucl. Instrum. Meth. 195, p.523-538, (1982), ...*132*

Fraser G.W., "X-ray Detectors in Astronomy", Cambridge Astrophysics Series, Cambridge University Press, ISBN 0 521 32663 X (1989), ...*36*

Fraser G.W., Barstow M.A. and Pearson J.F., "Imaging Microchannel Plate Detectors for X-ray and XUV Astronomy", Nucl. Instrum. Meth. A273, p.667–672, (1988a), ...*186*

Fraser G.W., Barstow M.A., Pearson J.F., Whiteley M.J. and Lewis M. "The Soft X-ray detection efficiency of coated microchannel plates", Nucl. Instrum. Meth. 224, p.272–286 (1984), ...*132*

Fraser G.W., Barstow M.A., Whiteley M.J. and Wells A. "Enhanced soft X-ray detection efficiencies for imaging microchannel plate detectors", Nature, letters, Vol.300, p.509, (1982), ...*134*

Fraser G.W., Pain M.T., Lees J.E., "Microchannel plate operation at high count rates—further studies", Nucl. Instrum. Meth. A327, p.328, (1993), ...*145*

Fraser G.W., Pain M.T., Lees J.E., Pearson J.F., "The Operation of Microchannel Plates at high count rates", Nucl. Instrum. Meth. A306, p.247–260, (1991), ...*142*

Fraser G.W., Pearson J.F. and Lees J.E., "Dark noise in microchannel plate X-ray detectors", Nucl. Instrum. Meth. A254, p.447–462, (1986), ...*100*

Fraser G.W., Pearson J.F. and Lees J.E., "Evaluation of long life (L2) Microchannel plates for X-ray photon counting", IEEE Trans. Nucl. Sci. NS-35 no.1 Feb. (1988b), ...*98*

Fraser G.W., Pearson J.F., Smith G.C., Lewis M. and Barstow M.A., "The gain characteristics of microchannel plates for X-ray photon counting", IEEE Trans. Nucl. Sci. NS-30, no. 1, p.455, Feb.(1983a), ... *104*

Gabriel A.H. and Mason H.E., "Solar Physics", Applied Atomic Collision Physics Vol.1 (1982), ... *23*

Gatti E., Oba K. and Rehak P., "Study of the Electric Field Inside Microchannel Plate Multipliers", IEEE Trans. Nucl. Sci. NS-30, no.1, Feb. (1983), ... *105*

Gerdes J.W., "The design, development, testing, fabrication, calibration and integration of a High Resolution Imager (HRI) for the Roentgen Satellite (ROSAT)", Progress report, Smithsonian Astrophysical Obs., Cambridge, MA. (1985), ... *38*

Giudicotti L., Bassan M., Pasqualotto R. and Sardella A., "Simple analytical model of gain saturation in microchannel plate devices", Rev. Sci. Instrum. 65(1), p.247 Jan. (1994), ... *108*

Guest A.J., "A computer model of channel multiplier plate performance", Acta Electronica Vol.14 no.1 p.79–97 (1971a), ... *93*

Guest A.J., "Channel multiplier plates for image intensification", UDC 621.383.81, Mullard Ltd., (1971b), ... *91*

Guest A.J., "The Modulation Transfer Function of a Channel Plate in an Image Tube", P.R.L. Annual Review, p.15, (1978), ... *233*

Hailey C.J., Lupton J.H., Siegmund O.H.W., Stewart R.E. and Ziock K.P., "An X-ray image intensifier system for precision wavelength dispersive X-ray spectroscopy", Rev. Sci. Instrum. 61(8), Aug. (1990), ... *38*

Harrison R.A. and Fludra A., "The Coronal Diagnostic Spectrometer for the Solar Heliospheric Observatory", Scientific Report Version 6, SC-CDS-RAL-SN-95-0001, (1995), ... *34*

Harrison R.A. and Kent B.J., "CDS Telescope", RAL Memo 18th Jan. (1994), ... *35*

Harrison R.A. and Sawyer E., "SOHO—The Scientific Payload", SC-CDS-RAL S/93/386 (1993), ... *59*

Harrison R.A., "Scientific Demands on Optical Specifications", SC-CDS-RAL-SN-91-0003 (Feb. 1991), ... *63*

Harrison R.A., (The Blue Book), "The Coronal Diagnostic Spectrometer for SOHO", Scientific Report Version 5, SC-CDS-RAL-SN-93-0007 (1993), ... *60*

Henkel P., Roy R. and Wiza J., "High Gain Microchannel Plates", IEEE Trans. Nucl. Sci. NS-25, no.1 Feb. (1978), ... *96*

Henry J.P., Kellogg E.M., Briel U.G., Murray S.S., Van Speybroeck L.P. and Bjorkholm P.J., "High Resolution Imaging X-ray Detector for Astronomical Measurements", Proc. SPIE Vol.106, p.196–205, (1977), ... *38*

Hier R.G., Beaver E.A., Zheng W., Schmidt G.W. and McIlwain C.E., "CCD-Digicon detector system performance parameters", Proc. SPIE Vol.1072 Image Intensification p.81 (1989), ... *48*

Holland, Steckelmacher and Yarwood, "Vacuum Manual", Published by E. & F. N. Spon, London, (1974), ... *154*

Johnson C.B., "Status of high-speed optical detector technologies at ITT/EOPD", Proc. SPIE Vol.1072 (1989), ... *39*

Jorden P.R., "CCDs for the 1990s", Proc. SPIE Instrumentation in Astronomy VII, (1990), ... *48*

Kersten H (editor), de Bruijn D., van Deenen P., Dijkkamp D., Holsboer H., van Oven C., "Microchannel Plate Report", Fom-Instituut voor atoom-en molecuulfysica, Kruislaan 407—1098 SJ Amsterdam-Watergraafsmeer, FOM no. 54.246a, Amolf no. 89/82 (1982), ... *94*

Knibbeler C.L.C.M., Hellings G.J.A., Maaskamp H.J., Ottevanger H. and Brongersma H.H., "Novel two-dimensional position-sensitive detection system", Rev. Sci. Instrum. 58(1) p.125 Jan. (1987), ... *46*

Koshida N. and Hosobuchi M., "Energy distribution of output electrons from a microchannel plate", Rev. Sci. Instrum. 56(7), July (1985), ... *231*

Koshida N. and Yoshida S., "Energy distribution of output electrons from a single channel electron multiplier", Rev. Sci. Instrum. 50(2), Feb.(1979), ... *231*

Koshida N., "Effects of electrode structure on output electron energy distribution of microchannel plates", Rev. Sci. Instrum. 57(31), March (1986), ... *231*

Koshida N., Kunii M. and Yoshida S., "Narrow energy distribution of output electrons from modified single channel electron multiplier", Rev. Sci. Instrum. 51(3), p.365, (1980), ... *231*

Koshida N., Midorikawa M. and Kiuchi Y., "Output Energy Distribution of a Microchannel Plate", Advances in Electronics and Electron Physics Vol.648, p.337, (1985), ... *232*

Kowalski M.P., Fritz G.G., Cruddace R.G., Unzicker A.E. and Swanson N., "Quantum efficiency of cesium iodide photocathodes at soft X-ray and extreme ultraviolet wavelengths", Applied Optics Vol.25, No.14, p.2440-2446, (1986), ... *127*

Lampton M. and Malina R.F., "Quadrant anode image sensor", Rev. Sci. Instrum. 47 no.11 p.1360 Nov. (1976), ... *42*

Lampton M. and Paresce F., "The Ranicon; A resistive anode image converter", Rev. Sci. Instrum. Vol.45, no.9 Sept. (1974), ... *44*

Lampton M., Siegmund O. an Raffanti R., "Delay line anodes for microchannel-plate spectrometers", Rev. Sci. Instrum. 58(12) p.2298 Dec. (1987), ... *43*

Lapington J.S. and Edgar M.L., "The Size and Spatial Distribution of Microchannel Plate Output Electron Clouds", Proc. SPIE Vol.1159, p.565, (1989), ... *237*

Lapington J.S. and Schwarz H.E., "The Design and Manufacture of Wedge and Strip Anodes", IEEE Trans. Nucl. Sci. NS-33, No. 1 Feb. (1986), ... *46*

Lapington J.S., "A Photon Counting Image Tube for Space- and Ground-based Applications", Proc. SPIE, Vol.2198 part 2, p.851, Hawaii, March (1994a), ... *234*

Lapington J.S., "Investigation of Image Non-linearities in a Photon Counting Image Tube", Proc. SPIE Vol.2209, p.549, 'Space Optics 1994 – Earth Observations and Astronomy', Garmisch-Partenkirchen, (1994b), ... *270*

Lapington J.S., Breeveld A.A., Edgar M.L. and Smith A., "Performance characteristics of SPAN position readout systems", Proc. SPIE 1743, p.303-314 (1992), ... *61*

Lapington J.S., Breeveld A.A., Edgar M.L. and Trow M.W., "A novel imaging readout with improved speed and resolution", Nucl. Instrum. Meth. A 310, p.299, (1991), ... *196*

Lapington J.S., Breeveld A.A., Edgar M.L., Tandy J.A., Trow M.W., "SPAN—A Novel High Speed High Resolution Position Readout", Proc. SPIE. Vol.1344, p.324 (1990), ... *52*

Lapington J.S., Breeveld A.A., Edgar M.L., Trow M.W., "A novel imaging readout with improved speed and resolution", Nucl. Instrum. Meth. A 310, p.299 (1991), ... *52*

Lapington J.S., Kessel R. and Walton D.M., "Spatial resolution limitations of microchannel plate/conductive charge division readout devices", Nucl. Instrum. Meth. A273, p.663–666, (1988), ... *234*

Laprade B.N. and Reinhart S.T., "Recent advances in small pore microchannel plate technology", Proc. SPIE 1072, p.119–129, (1989), ... *90*

Leonov N.B., Tyutikov A.M. and Shishatskii N.A., "Characteristics of pulse-operated microchannel plates", Instruments and Experimental Techniques Vol.23, p.200–203, (1980), ... *107*

Leskovar B., "Microchannel plates", Physics Today, p.42–49, Nov. (1977), ... *88*

Lewis R.A., Fore N.S., Helsby W., Hall C., Jones A., Parker B., Sumner I, Worgan J.S. and Budtz-Jorgensen C., "High Counting Rate Gaseous X-ray Detectors for Synchrotron Radiation Applications", Rev. Sci. Instrum. Vol.63, no.1, p.642 (1992), ... *42*

Lidiard K.A., "CDS Spectrometer Optics Review", SC-CDS-RAL-RV-91-0002 July (1991a), ... *59*

Lidiard K.A., "Effects of radius of curvature error for manufactured GI grating, and analysis of sensitivity to positional errors", SC-CDS-RAL-TN-91-0053, Feb. (1991b), ... *69*

Loty C., "Saturation effects in channel electron multipliers", Acta Electronica Vol.14, no.1, p.107–119, (1971), 107

Malina R.F. and Coburn K.R., "Comparative lifetesting results for Microchannel plates in windowless EUV photon detectors", IEEE Trans. Nucl. Sci. NS-31, No.1, Feb. (1984), ... *102*

Marsden R.G., "Ulysses Explores the South Pole of the Sun", ESA Bulletin No.82 May (1995), ... *25*

Martin C. and Bowyer S., "Quantum efficiency of opaque CsI photocathodes with channel electron multiplier arrays in the extreme and far ultraviolet", Applied Optics Vol.21, No.23, p.4206, (1982), ... *127*

Martin C., Jelinsky P., Lampton M., Malina R.F. and Anger H.O., "Wedge-and-Strip anodes for centroid-finding position-sensitive photon and particle detectors", Rev. Sci. Instrum. 52(7), p.1067 July (1981), ... *46*

Mason I.M., Branduardi-Raymont G., Culhane J.L., Corbet R.D.H., Ives J.C. and Sanford P.W., "The EXOSAT imaging X-ray detectors", IEEE Trans. Nucl. Sci. NS-31, p.795–800 (1984), ... *38*

Mathieson E., Smith G.C. and Gilvin P.J., "The graded-density Cathode", Nucl. Instrum. Meth. 174 p.221–225 (1980), ... *42*

Matsuura S., Umebayashi S., Okuyama C and Oba K., "Current status of the micro channel plate", IEEE Trans. Nucl. Sci., NS-31, No.1, p.399–403, (1984), ... *98*

McCalden A.J., "Data Processing System For Flight Spectrometer", Proc. ESA Symp. on Photon Detectors for Space Instrumentation, SP-356, p.349-352, (1992), ... *290*

McClintock W.E., Barth C.A., Steele R.E., Lawrence G.M. and Timothy J.G., "Rocket-borne instrument with a high-resolution microchannel plate detector for planetary UV spectroscopy", Applied Optics 21, no.17, p.3071, (1982), ... *40*

McComas D. and Bane S.J., "Radially uniform electron source", Rev. Sci. Instrum. 53(9), p.1490, Sept.(1982), ... *308*

McComas D.J., Baldonado J.R., Bame S.J. and Barraclough B.L., "Channel electron multiplier compatibility with Viton and Apiezon-L vacuum grease", Rev. Sci. Instrum. 58(12), p.2331, Dec. (1987), ... *153*

Mullard Ltd, "Microchannel Plates", Technical Information no.31, TP1561, (1976), .. *89*

Natallo Garcia R., "Investigations of Pore Paralysis in Microchannel plates", MSc Thesis, University College London, (1990), ... *142*

Negus C.R., "Grazing-Incidence Mirror System for Use with a Grating Spectrometer in the Extreme Ultraviolet", Applied Optics Vol.13, no.5, p.1216 May (1974), ... *32*

Oba Koichiro, "Microchannel Plate Photodetectors Characteristics and Applications", Hamamatsu TV Co. Ltd., Application res-0792-01 (1976), ... *102*

Papaliolios C., Nisenson P. and Ebstein S., "Speckle imaging with the PAPA detector", Applied Optics Vol.24 no.2 p.287 Jan. (1985), ... *41*

Parkes W., Gott R. and Pounds K.A., "Soft X-ray Studies of Channel Multipliers and Multiplier Arrays", IEEE Trans. Nucl. Sci. NS-17, p.360, (1970), ... *163*

Patchett B.E., "XUV Observations of the inner corona–the coronal diagnostic spectrometer on SOHO", Adv. Space Res. Vol.11, No.1, p.(1)369–(1)375, (1991), ... *29*

Patchett B.E., Harrison R.A., Sawyer E.C., "The Coronal Diagnostic Spectrometer–A solar EUV experiment for the SOHO mission", Journal of The British Interplanetary Society, Vol.43, p.181-184, (1990), ... *27*

Patchett B.E., Norman K., Gabriel A.H. and Culhane J.L., "The Coronal Helium Abundance Experiment on Spacelab 2", Space Science Reviews Vol.29, p.431 (1981), ... *37*

Patchett B.E., Harrison R.A., Sawyer E.C., Aschenbach, Culhane, Doschek, Gabriel, Huber, Jordan, Kjeldseth-Moe, Mason, McWhirter, Parkinson, Poland, Priest, Schmitt, Thomas, Timothy, Tondello, Trumper, "CDS–The Coronal Diagnostic Spectrometer", ESA SP-1104, p.39, (1989), ... *28*

Peacock A., Andresen R.D., Manzo G, Taylor B.G., Villa G, Re S., Ives J.C. and Kellock S., "The Gas Scintillation Proportional Counter on EXOSAT", Space Science Reviews 30, p.525–534, (1981), ... *37*

Pearson J.F., Fraser G.W., Whiteley M.J., "Variation of Microchannel Plate Resistance with temperature and applied voltage", Nucl. Instrum. Meth. A258, p.270 (1987), ... *97*

Pearson J.F., Lees J.E. and Fraser G.W., "Operating Characteristics of Sandwich Microchannel Plates", IEEE Trans. Nucl. Sci. NS-35 p.520 (1988), ... *97*

Phillips A., "Solar A BCS digitisation Errors", MSSL (1992), ... *225*

Phillips K.J.H., "Guide to the Sun", Cambridge University Press, ISBN 0 521 39483 (1992), ... *27*

Rasmussen A. and Martin C., "Development and testing of a prototype mosaic wedge and strip anode detector", Proc. SPIE Vol.1159, p.538 (1989), ... *80*

Read P.D., van Breda I.G., Norton T.J., "Performance of a 40 mm unfilmed microchannel plate intensifier", Proc. SPIE Vol.1235 p.305 (1990), ... *39*

Richter L.J. and Ho W., "Position-sensitive detector performance and relevance to time-resolved electron energy loss spectroscopy", Rev. Sci. Instrum. 57(8), August (1986), ... *101*

Sams B.J., "The effect of microchannel plate gain depression on PAPA photon counting cameras", Rev. Sci. Instrum. 62(3), March (1991), ... *41*

Samson James A.R., "Photocathodes; their efficiency and stability", Nucl. Instrum. Meth. 222, p.215–220, (1984), ... *134*

Schecker J.A., Schauer M.M., Holzscheiter K. and Holzscheiter M.H., "The performance of MCP at cryogenic temperatures and in high mag. fields, and the detection efficiency for low energy positive hydrogen ions", Nucl. Instrum. Meth. A320 p.556–561 (1992), ... *141*

Schmidt K.C. and Hendee C.F., "Continuous channel electron multiplier operated in the pulse saturated mode", IEEE Trans. Nucl. Sci., p. 100, June (1966), ... *56*

Seah M.P. and Smith G.C., "Energy and spatial dependence of the electron detection efficiencies of single channel electron multipliers used in electron spectroscopy", Rev. Sci. Instrum. 62(1) Jan. (1991), ... *37*

Sharma A. and Walker J.G., "Effect of local dead time in imaging detectors", Quantum Opt. 1 p.11–16 (1989), ... *141*

Siegmund O. H. W., Vallerga J. and Wargelin B., "Background Events in Microchannel Plates", IEEE Trans. Nucl. Sci. Vol.35, no.1, Feb. (1988), ... *98*

Siegmund O.H.W., Clother S., Thornton J., Lemen J., Harper R., Mason I.M. and Culhane J.L., "Application of the wedge and strip anode to position sensing with microchannel plates and proportional counters", IEEE Trans. Nucl. Sci. NS-30, p.503–507, (1983), ... *188*

Siegmund O.H.W., Coburn K. and Malina R.F., "Investigation of Large Format Microchannel Plate Z Configurations", IEEE Trans. Nucl. Sci. NS-32 (1985), ... *104*

Siegmund O.H.W., Everman E., Vallerga J.V. and Lampton M., "Extreme Ultraviolet Quantum Efficiency of Opaque Alkali Halide Photocathodes on Microchannel Plates", Proc. SPIE Vol.868, p.18, (1987b), ... *135*

Siegmund O.H.W., Lampton M., Bixler J., Bowyer S. and Malina R.F., "Operational Characteristics of Wedge and Strip Image Readout Systems", IEEE Trans. Nucl. Sci. Vol.33, No.1, p.724, Feb. (1986), ... *144*